GEM TN-92-131

Responses to the December 1991 PAC Report

Barry Barish
California Institute of Technology

July 8, 1992

Abstract:

This document contains GEM responses to the comments and questions in the December 1991 PAC Report. It is written in question/answer format to directly respond.

RESPONSE TO DECEMBER 1991 PAC REPORT

1. Copy of PAC Report dated December 15 - 17, 1991

2. Responses to PAC Report in Question/Answer Format

A. 3.2 Physics

B. 3.3.1 Magnet — pages 1 - 8

C. 3.3.2 Calorimetry
Question 1 — pages 1 - 13
Question 2 — pages 1 - 11
Question 3 — pages 1 - 6
Question 4 — pages 1 - 4
Question 5 — pages 1 - 12
Question 6 — pages 1 - 2

D. 3.3.3 Muon System — pages 1 - 24

E. 3.3.4 Tracking
Questions 1 - 6 — pages 1 - 7

F. 3.3.5 DAQ & Trigger — pages 1 - 4

Report of the
Superconducting Super Collider Program Advisory Committee

December 15-17, 1991

SSC Laboratory, Dallas Texas

1. Introduction

The Program Advisory Committee met from December 15 to 17 at the SSC Laboratory in Dallas. A copy of the agenda is attached. The Committee heard reports on the progress of the project and on the experimental program, including the decision to locate the major detectors on the east side of the ring.

Director Roy Schwitters also reviewed the Laboratory policy for the funding of the major detectors. SSCL policy is to allocate $550M for two large detectors from project funds. The remainder of the needed funds will have to come from other sources, foreign and domestic. The total cost of each major detector should not exceed approximately $500M. At this time, the Laboratory did not seek additional advice from the PAC on this policy.

The PAC heard a progress report from George Trilling, spokesman for the Solenoidal Detector Collaboration (SDC), and presentations of the Gammas, Electrons, and Muons (GEM) collaboration's Letter of Intent (LoI) from GEM co-spokesmen Barry Barish and William Willis. The PAC then met separately with the spokesmen of both collaborations and some of their colleagues to discuss various issues related to their presentations. The Committee's conclusions and recommendations are given below.

2. SDC

Trilling reported on the technical progress and the schedule for the preparation of a Technical Design Report (TDR). He also discussed the evolution of the collaboration, the status of the choices of subsystem technologies, R&D plans for FY 1992, the latest cost estimates, and possible sources of funds.

Overall, the SDC is making good progress. The group has selected scintillating tile with wavelength-shifting fiber readout as the technology for the barrel calorimeter. In addition, they have settled on iron as the choice of

absorber, allowing the flux return for the magnet to be integrated into the calorimeter. The thickness of the calorimeter has been increased to 10 absorption lengths (from the 9 presented at the October review) and the segmentation of the hadron calorimeter has been coarsened from 0.05 x 0.05 to 0.1 x 0.1, although the collaboration plans to preserve the ability to recover the finer granularity in the future.

In the central tracker, the total area of silicon microstrip detectors has been reduced substantially. In addition, the hybrid scintillating-fiber/straw-tube outer tracker option has been abandoned. The all-straw-tube option, with the number of superlayers reduced to four, has been selected for inclusion in the TDR. In February, the group will decide whether or not to continue with the all-scintillating-fiber system as an option for the outer tracking system as well, and will finally select a design for the muon chambers.

The collaboration has proposed a budget request for R&D/engineering in FY 1992 at a funding level of $19.9M. The PAC is impressed by the high quality of R&D carried out to date by SDC. In addition, the overall scope of the R&D plan and the funding request seem appropriate for this stage of a project of this magnitude. We feel that the SDC request should be supported by the SSCL.

Our overall impression is that the group is handling the process of making difficult choices in an effective way. However, the Committee is concerned about insufficient SDC top management integrated into the SSC Laboratory. A project of this scale needs full time on-site leadership and management in order to ramp up smoothly to a full scale construction project. It is imperative that this problem be solved within the next few months.

The collaboration asserts that it cannot descope the detector further without substantially degrading the physics performance of the detector. The evidence made available to us so far is insufficient to substantiate this claim. The size of this project demands that the essential design parameters be justified in terms of the physics performance. We expect that such documentation will be included in the TDR.

The Committee is still concerned about the gap between the apparently available funds and the projected costs. It reiterates that the TDR must include a credible funding plan for the experiment.

3. GEM

3.1 General

The PAC was impressed with the progress made by the GEM collaboration in the relatively short time since its inception. The collaboration has put together an effective interim structure and is working toward an organization capable of constructing a major SSC detector. They have made considerable progress in defining the design and making the necessary technological choices.

The collaboration has also been successful in adding substantial new strength. The collaboration should be encouraged in its effort to increase its strength further and to enlist additional non-U.S. participants with major responsibilities in the project.

As is noted below, the PAC has several concerns and questions with respect to the GEM design and technology that were not answered in the LoI. Nevertheless the PAC recommends that the GEM collaboration be supported to proceed towards the development of a Technical Design Report (TDR).

The PAC requests that a review of GEM progress be made at the July 1992 PAC meeting. This timing seems appropriate as it allows time for the collaboration to carry out significant new work. It will follow the GEM cost review planned for the spring of 1992. The PAC requests a written report prepared by the collaboration for the July review. The report should include responses to the specific issues that are raised in the sections below.

While the submission of a TDR in the fall of 1992 would be desirable from the point of view of schedules and of balanced progress for the two detectors, the PAC is concerned that sufficient time be available to refine and optimize the design, to build a team capable of carrying out a project of this scale and complexity, and to make the TDR a document of the quality and completeness necessary for a decision to proceed on a major SSC detector. The date for submission of the TDR and the decision to proceed with initial procurement steps for the magnet would be subject to the outcome of the July review.

3.2 Physics

We have considered the physics capabilities of the GEM experiment assuming the detector parameters as presented in the LoI. In general, it appears that if the performance of the detector can really be established as claimed, then the physics reach of the experiment will be adequate to the tasks.

In comparison with SDC, the GEM detector has emphasized photons, leptons and robustness at high luminosities. Excellent photon resolution is important for the Higgs search at low masses and can also be an advantage for the discovery of new physics. For example, GEM, with either a BaF_2 calorimeter or a liquid argon option operating with a resolution at least as good as $7\%/\sqrt{E}$ combined with a constant term of about 0.5 %, should be significantly better than SDC for observing a low mass Higgs in the $\gamma\gamma$ mode. It would be interesting to repeat some of the studies of the calorimeter performance with somewhat more conservative assumptions about the resolution ($10\%/\sqrt{E}$ for liquid argon and 1-2% for the constant term for either the liquid argon or crystal option).

The GEM LoI also emphasizes the importance of electrons and muons both with respect to precision energy measurement and with respect to running at high luminosity. In the Committee's view, further study of the calorimeter thickness and more realistic simulations are necessary to demonstrate that GEM's muon measurement goals can be met. The GEM muon measurement system has the potential to be more robust at high luminosity than that of SDC, which relies on its inner tracker. It also must be demonstrated that it is possible to trigger on muons at high luminosity, especially in the forward direction where the bending is significantly reduced. Excellent muon identification in the vicinity of jets is a potential advantage for heavy flavor tagging. However, the present LoI does not make a strong case as to how this information can be used.

The ability of the GEM detector to identify electrons at high luminosity is much less clear. The inner tracking is potentially more difficult for GEM than for SDC, since the track measurements must be performed at smaller radii. While the occupancy of the silicon detector for GEM is sufficiently small at 10^{34}, pattern recognition has not been demonstrated and it has not been shown how long the silicon will survive.

In general, we were positively impressed by the study done by the GEM collaboration of the physics problems proposed by the Committee, although we feel that further study and deeper analysis of several issues are vital. We now briefly comment on some of the important physics problems studied in the LoI.

(a) Intermediate Mass Higgs: $H \rightarrow \gamma\gamma$

One of the strengths of the detector is its excellent photon detection and mass resolution. Thus, the performance of the detector in the search for the Higgs

in the $\gamma\gamma$ mode is considered in some detail in the LoI. Its conclusion is that the Higgs can be observed even at a mass as low as 80 GeV. However, the final result on signal over background depends crucially on the resolution of the calorimeter. While the result is best for a BaF_2 calorimeter, the liquid argon option also leads to good results with an assumed $7\%/\sqrt{E}$ resolution.

Also, the analysis should be implemented in several ways. For example, the background from mis-identified electrons was not considered, even though it could be significant. In general, a more realistic simulation of the detector should be pursued. Another important omission is the study of the associated production channels, W + H and $t\,\bar{t}\,H$, which lead to a small number of events relatively free of background. The study of these channels in the GEM detector will also be important for a direct comparison with SDC. In fact, SDC can only detect a low mass Higgs through the associated production channels and it would be important for the GEM collaboration to demonstrate its capabilities in these modes. Finally, we comment that the performance of the detector for $\gamma\gamma$ detection at high luminosities has not been studied. It could be particularly important for the relatively rare associated production events.

(b) Intermediate Mass Higgs: $H \rightarrow Z\,Z^* \rightarrow$ 4 leptons

The assumed characteristics of the calorimeter lead to good evidence for the signal in this channel, with especially remarkable resolution in the 4-electron channel. However, also in this case, it would be interesting to see the corresponding results with a $10\%/\sqrt{E}$ resolution for the liquid argon calorimeter. We also point out that, in general, the overall efficiency for electron identification in the end-cap region has not been demonstrated.

(c) Heavy Higgs

The mass region between 0.2 and 0.6 TeV is the ideal interval for observing the Higgs in the $H \rightarrow ZZ \rightarrow$ 4-lepton mode. As the mass increases beyond 0.8 TeV, the signal detection becomes more and more difficult. The performances of the GEM and SDC detectors turn out to be quite comparable in this region, except that for high Higgs masses, GEM could have some advantage due to its robustness at high luminosity. In this connection, we note that the ability to detect electrons at high luminosities has not been studied in the LoI.

(d) Other

The PAC was generally satisfied with the GEM detector capabilities to answer the other physics questions posed. However, there are many remaining questions and concerns. Heavy quark decays may be observable and useful in the study of various high mass events, but no convincing case was made for GEM's special abilities to use leptons for heavy flavor tagging. Also, the case presented for the observation of a 300 GeV gluino was not completely convincing and needs further study.

3.3 Subsystems

3.3.1 Magnet

The PAC notes that SSCL has tentatively accepted the unshielded single coil for GEM. However, we are still concerned about the effects of the external field. We reiterate that the consequences of the stray field to SSCL, e.g., increased cost of machine and detector components that must tolerate the stray field, should be further examined before final approval. The forward field shaping scheme should be specified promptly to permit optimization of the detector subsystems.

The absence of bypasses for the machine and garage positions in the interaction areas means that GEM's (and SDC's) installation and commissioning are likely to be completely interlocked with commissioning of the machine, which gives strong constraints on the commissioning schedule for SSC and the experiments. Since the magnet appears to be a critical path item for the GEM detector, it is important to carry out the magnet engineering R&D without delay, and the PAC endorses the collaboration's request for these funds.

Permission to make commitments in the procurement process should not be given before a performance and cost optimization for the muon measurement has been performed and the major detector subsystems have been sufficiently specified. We would anticipate that these steps can be made by the time of the July meeting.

3.3.2 Calorimetry

The GEM collaboration has two options for their calorimetry, one based on liquid argon/krypton, and the other based on BaF_2 (electromagnetic) and on lead/scintillating fiber (hadronic). The PAC considers both options potentially viable. It is, however, concerned about the problems of radiation damage and the lack of longitudinal segmentation of the BaF_2 calorimeter, as

well as the potential inhomogeneity of response and the difficulty of longitudinal segmentation in the lead/scintillating fiber calorimeter. Also, the effect on the constant term of the hadronic energy resolution, when employing very different compositions for the electromagnetic and hadronic parts, needs to be quantified.

Furthermore, the PAC recognizes that in the accordion design of the liquid argon/krypton calorimeter, a $7\%/\sqrt{E}$ performance has not yet been demonstrated (even for a moderate size prototype) and that a substantial engineering R&D effort will be needed.

The PAC endorses the collaboration's plan to make a choice between the proposed options. Such a decision will help the collaboration to allocate its efforts and resources effectively toward a balanced support of all subdetector systems.

The PAC is concerned that there be sufficient absorptive power of the calorimetric sections for hadrons, so as not to impair the triggering capabilities of the GEM detector for muons.

Also, the PAC notes that the capability of the forward calorimeter to help determine missing transverse energy has not yet been demonstrated.

3.3.3 Muon System

High-quality measurement of muons is stated as a major goal of the GEM experiment (as a benchmark, the proponents specify $\Delta P_t/P_t \equiv 5\%$ at 500 GeV/c.) The system proposed to do this employs three distinct technologies for technical reasons. Drift tubes (either pressurized or limited streamer) with ~100 micron position resolution are used for momentum measurement in the barrel region. Cathode strip chambers are proposed for the end-cap region, where higher particle fluxes must be handled. The group has chosen resistive plate counters in the barrel region to trigger on muons and to provide sufficient time resolution to identify the muon's bunch crossing.

These technologies seem appropriate, but each constitutes a major detector subsystem requiring its own R&D and design team. The PAC feels that a larger effort will be needed to evaluate prototypes and to establish a complete design in time for submission of the TDR.

While the system specifications are proceeding well, the following issues should be addressed by the proponents to demonstrate that the performance goals of the muon system can actually be accomplished.

1. Since the rapidity region covered by the resistive plate counters for triggering is quite narrow, $0 < \eta < 1.32$, the proposed trigger based on pad chambers will need to be demonstrated.

2. The collaboration has not yet demonstrated that resistive plate counters and limited streamer tubes are suitable choices for muon detection.

3. The thickness of the calorimeters must be sufficient so that the triggering effectiveness will not be compromised by hadron punch-through and thus the system will remain robust at high rates.

4. There are three levels of alignment: wires, chambers, and chamber packages in the global frame. Each presents its own challenge and will require considerable engineering and significant interaction among the physicists and engineering groups.

The goals of the FY 1992 R&D effort for the muon system are appropriate, as is the funding request. The choice of drift-tube technology (pressurized versus streamer tubes) should be made as quickly as possible. The Committee fully supports the "Texas Test Rig" plan for conducting cosmic ray tests of these technologies in a standard way at the SSCL.

3.3.4 Tracking

The GEM group has defined the performance goals for the central tracking system:

(a) identification of the primary interaction vertex;

(b) separation of electrons and photons;

(c) isolation of electron, muon, gamma from conversions and Dalitz pairs;

(d) momentum measurement to enhance electron-hadron separation and reduce hadron backgrounds to muons; and

(e) determination of the sign of the electron up to a few hundred GeV/c.

While the Committee considers the stated goals desirable, it is not convinced that the proposed system is optimized and that all these goals are achievable,

in particular in the forward direction. Specifically, we have the following concerns:

1. The projected momentum resolution demands very good intrinsic resolution in the silicon and the interpolating pad chambers (IPCs), and places challenging demands on the alignment and stability of the complete system.

2. The total amount of material in the silicon layers and the IPCs (including support frames, electronics, cooling systems and cables) is very substantial and will generate substantial background. It needs to be kept as small as practical to avoid major difficulties, especially in the forward direction. The choice of single-sided silicon detectors doubles the amount of silicon. It is not clear that this choice would substantially increase the radiation hardness.

3. In the forward direction, the placement of a large number of detectors at a radial distance of 10 cm represents a serious risk to their operation. Furthermore, it is not proven that the proposed performance goals can be achieved in this region.

4. The proposed R&D program focuses on the IPCs, their read-out electronics and chamber prototyping, and a demonstration of a position resolution of 1% of the strip width, as well as mechanical engineering of a light weight support structure of high precision and rigidity. This effort should be fully supported. Due to the similarity of the designs, the silicon detector R&D should be closely coordinated with the parallel effort by the SDC collaboration on mechanics and read-out electronics.

5. Detailed Monte Carlo studies to evaluate the pattern recognition problems in the central and forward tracker, taking into account realistic background effects as well as integration and dead times, have not yet been presented.

6. The tracking group is at present seriously understaffed.

3.3.5 DAQ and Trigger

The data acquisition and trigger systems appear to be following a "conventional" approach utilizing a three level trigger with synchronous delay before level 1, followed by asynchronous buffering before level 2. While the preliminary design and strategy is well thought out, the amount of work remaining for a TDR is prodigious. A detailed schedule including

functional specification, design and review, prototype development and system testing, and production plans should be developed and compared with projected physicist and engineering manpower. The cost estimates appear low, and the review process ought to include comparison with SDC estimates. The R&D effort should be fully supported.

3.3.6 Management and Cost

The collaboration is vigorously narrowing the choices for the detector subsystems, but at the time of submission of the LoI (November 30, 1991) the detector had not been specified in detail. The collaboration has chosen not to give a detailed estimate of the detector costs. The collaboration aims at a target figure of $500M for the total detector cost.

At the time of the PAC meeting, the collaboration provided the report GEM-IN-91-2, "Summary of the GEM Cost Estimate Status," in which the cost estimating plan and the current status of the subsystem cost estimates are presented. We understand that the collaboration is preparing for a detailed laboratory cost review in March/April 1992.

No plan has been presented on how the necessary funds could be raised in the United States and abroad.

The management structure of the collaboration is evolving. The responsibilities are being shared by several persons and coordinating bodies. The collaboration must strive to broaden the participation in the coordinating bodies. We note with approval that the collaboration plans to review the management structure and the redistribution of responsibilities at the time of the TDR. This review will be particularly appropriate in light of the then undoubtedly enlarged collaboration.

The collaboration already has a significant representation from the SSC Laboratory, and several senior members of GEM have taken up residence at SSCL to provide project management.

3.2 Physics

CHAPTER 3 PROGRESS REPORT ON GEM PHYSICS SIMULATIONS

3.1 Introduction and Overview

The purpose of this chapter is three-fold:

- To report on the progress and status of the GEM physics simulations program since the beginning of 1992.
- To respond to the PAC's concerns regarding simulation of physics processes in the GEM Letter of Intent.
- To catalog the physics simulations to be carried out for the GEM Technical Design Report.

The GEM Physics Group has simulated a large number physics processes and their backgrounds to provide a broad and incisive test of the detector's capabilities. Given our ignorance of the details of the mechanism of electroweak symmetry breaking, not to mention other new physics that may be lurking in the TeV energy region, it is clear that such a list of processes cannot be unique. For this report, we have chosen to emphasize those physics processes considered in the GEM Letter of Intent (LoI) [1], especially those that the PAC expressed concern about in its report on the LoI [2]. For the Technical Design Report (TDR), we shall in addition examine several new processes whose simulation increases our understanding of GEM's capabilities.

Detailed detector simulations for a long list of physics processes are impossible at this stage. Indeed, the detector design now changes significantly on a time scale much shorter than the one required to carry out such simulations. Consequently, we have constructed a parameterized model of the detector in our physics studies. This parameterization is based on GEANT simulations [3] of the major subsystems as described in the GEM Baseline document [4]. Trigger-related issues are also included in this computer model of GEM. The first GEM baseline (Baseline I) was issued on April 23. Preparations for the parameterized Baseline I simulation, known as FAST1, were completed in June. The FAST1 model of GEM is described in section 3.2. When Baseline II is issued, an updated, FAST2, parameterization will be developed and put into use as rapidly as possible.

FAST1 simulations of physics processes of concern to the PAC have been carried out. Most were completed in June; other studies are still underway. The topics receiving particular attention include the search for the intermediate mass Higgs boson in its photon and electron decays, tagging heavy top quarks via inclusive muons, processes involving lepton identification and measurement at $\mathcal{L} = 10^{34}\,\mathrm{cm}^{-2}\,\mathrm{s}^{-1}$, missing-$E_T$ physics signals and backgrounds, and jet energy measurement at high-p_T. These are discussed in section 3.3.

We will also note there which PAC concerns are still under investigation. Finally, section 3.4 outlines the processes we plan to study for the TDR by the FAST parameterization model of GEM.

3.2 The FAST1 Model of the GEM Detector

While complete GEANT simulations are important for determining detector parameters, they are far too slow to analyse the large samples of events needed to study signatures and backgrounds, at least at this stage in the evolution of GEM. A much faster simulation, known as FAST1, has therefore been created to simulate the gross features of the GEM Baseline 1 detector and to study its physics performance. It is adequately fast, about 3 sec/event on an HP 9000/720, and most of the physics studies reported here are based on it. A major exception is the analysis of $H^0 \rightarrow \gamma\gamma$ which has been done with an independent, more detailed electromagnetic calorimeter simulation.

3.2.1 Overall Framework

While the individual detector system parameterizations can be used independently, FAST1 also provides an overall framework for event simulation which calls a physics event generator, simulates the the response of each subsystem to each particle, and stores the results in a data structure for further analysis.

At present events can be generated with ISAJET [4], PYTHIA and JETSET [5], or a single particle generator. A uniform interface has been written for the different generators. Events can be read from files in various formats. In all cases, the event information is stored in the STDHEP format [6], and the STDHEP codes are used for particle types. This allows the same analysis to be used for different generators and should make it simple to incorporate additonal generators as needed.

The response to each generated particle is then simulated. The overall geometry is approximated as a series of nested cylinders, one each for the central tracker, electromagnetic calorimeter, hadron calorimeter, and muon system, as shown in Fig. 3.2-1. Particles are transported through each of these cylinders in a uniform magnetic field. Particles such as K_S and Λ can also be decayed in flight. Beyond this simple transport, the interaction of a particle with the detector is described using parameterizations of resolutions and acceptances based on full GEANT simulations of the actual baseline detectors. For example, an electron would be tracked along a helix through the tracker; it would then deposit its energy in calorimeter cells using the parameterized energy resolution and shower shape. The parameterizations for each detector subsystem are described in more detail below.

So far pileup has been included only as equivalent noise in the calorimeter and as an overall inefficiency in the central tracker.

The output of FAST1 is stored in two common blocks. One contains the energies in each tower of the electromagnetic and hadronic calorimeters. The other contains lists of all the measured momenta of particles in the central tracker and in the muon system above a specified minimum p_T. Various utility routines such as a simple jet-finding algorithm are also provided.

3.2.2 Central Tracker Parameterization

The central tracker is perhaps the most difficult system to parameterize, since its performance depends so much on occupancy. Nevertheless, the occupancy is quite low in the GEM Baseline 1 design, so a parameterization should be sufficient to describe the most important aspects. The FAST1 parameterization includes:

(1) Resolution on momentum, both with and without a vertex constraint, including the expected chamber resolution, bending in the magnetic field, and the effect of multiple scattering;

(2) Resolutions on the impact parameter and the z position of the vertex, based on Gaussian parameterizations of full GEANT simulations of the Baseline 1 design;

(3) Photon conversions and resolution effects from the tracker material as a function of η and ϕ, again based on a full GEANT simulation of the tracker.

As an example the resolution as a function of η for various values of p_T is shown in Fig. 3.2-2.

The major limitations of the existing FAST1 simulation of the central tracker are that it treats a single particle at a time, so that inefficiencies correlated with the whole event are not properly reproduced, and that inefficiency or additional occupancy from backsplash from the calorimeter is not included. Work on these topics is continuing.

3.2.3 Liquid Argon Calorimeter Parameterization

The FAST1 parameterization of the Baseline 1 liquid argon central calorimeter incorporates approximate parameterizations of the energy and position resolution, transverse and longitudinal shower shapes, and pileup and electronic noise.

The calorimeter is taken to be uniformly segmented in η and ϕ, with $\Delta\eta = \Delta\phi = 0.032$ for the electromagnetic (EC) part and $\Delta\eta = \Delta\phi = 0.08$ for the hadronic (HC) part. This is not exactly correct but is adequate for the central region. Five EC cells are matched to two HC ones. The energy resolution is taken to be of the form

$$\frac{\Delta E}{E} = \sqrt{\frac{a^2}{E} + b^2}\,.$$

For electromagnetic particles a varies with η from 0.07 to 0.08 depending on the angle of incidence on the accordion structure, and $b = 0.005$. For hadronic particles $a = 0.6$

and $b = 0.05$. Jet resolutions are obtained by summing over the individual particles. The calorimeter resolutions for single electrons and pions are shown in Fig. 3.2-3 and Fig. 3.2-4.

The energy of both electromagnetic and hadronic particles is shared between the EC and HC sections of the calorimeter, although the subdivisions of each are not taken into account. The sharing is based on the Bock parameterization [7]:

$$\frac{1}{E}\frac{dE}{dx} = \frac{w}{X_0}\frac{b^a}{\Gamma(a)}s^a e^{-bs} + \frac{(1-w)}{\Lambda}\frac{d^c}{\Gamma(c)}t^c e^{-dt}$$

where X_0 and Λ are the radiation and interaction lengths of the material, $s = x/X_0$, $t = x/\Lambda$, and a, b, c, d, and w are linear functions of $\log E$. The interaction point is picked according to an exponential distribution, and the above formula is integrated to determine the sharing. Energy is also shared transversely using a parameterization as a sum of exponentials fit to the full GEANT simulation. No fluctuations in shower shape other than the shower starting point are taken into account, so the fluctuations are underestimated.

The position resolution for an EC shower is assumed to be $4.4\,\mathrm{mm}/\sqrt{E}$, based on the full GEANT simulation. The angular resolution has not been simulated, but $100\,\mathrm{mrad}/\sqrt{E}$ is a reasonable estimate.

Finally, thermal noise and pileup are taken into account, treating the latter as an additional noise term [8]. The distributions are taken to be Gaussians with the following mean values:

EC:	thermal	$E = 35\,\mathrm{MeV/cell}$
	pileup	$E_T = 35\,\mathrm{MeV/cell}$
HC:	thermal	$E = 250\,\mathrm{MeV/cell}$
	pileup	$E_T = 200\,\mathrm{MeV/cell}$

(summed over the longitudinal sections of each part.) Note that thermal noise gives a constant E per cell, whereas pileup gives a constant E_T.

3.2.4 BaF_2/Scintillator Parameterization

The BaF_2 calorimeter parameterization in FAST1 is based on a detailed GEANT simulation of its performance. The segmentation is $\Delta\eta = \Delta\phi = 0.04$ in the EC calorimeter and twice that in the HC calorimeter. The energy resolution is

$$\frac{\Delta E}{E} = \sqrt{\frac{a^2}{E} + b^2}\,.$$

with $a = 0.02$, $b = 0.005$. Transverse and longitudinal shower sharing is handled using a Bock-type parameterization with parameters fit to the GEANT results. The thermal and pileup noise are smaller than for liquid argon and so have been neglected.

The hadronic calorimeter simulation uses the same code as the liquid argon simulation with appropriate changes in the parameters.

Most of the physics processes discussed below have been studied using the liquid argon parameterization. Those for which the stochastic term, a, is important – specifically intermediate-mass Higgs boson process – have been studied with the LAr and BaF_2 and with a wider range of resolutions, as requested by the PAC [2].

3.2.5 Forward Calorimeter Parameterization

The principle goal of the forward calorimeter is to measure $\not{E}_T$, so only the p_T resolution has been parameterized. The p_T resolution is determined mainly by the limited angular resolution caused by transverse shower spreading. To determine this resolution, full GEANT 3.14 showers using the standard cuts were generated for single charged pions with $p = 10$, 200, 500, and 2000 GeV distributed randomly over the $3 < \eta < 7$. Each section of the calorimeter was described as a single block of homogeneous material filled with a GEANT mixture of tungsten alloy and liquid argon. The deposited energy was then binned into cells, taking into account the slightly nonprojective geometry of the baseline design, hadronic smearing, e/h suppression, and electronic noise. This energy deposition was then used to calculate the observed $p_{T,\mathrm{in}}$ and $p_{T,\mathrm{out}}$ in and out of the plane of the primary particle. The resolution for $p_{T,\mathrm{in}}$ is shown in Fig. 3.2-5.

Based on the limited available statistics, a few hundred events per point, the resolution appears to be Gaussian. Therefore, particles in the forward calorimeter were smeared with a Gaussian whose width is determined by interpolation from the calculated points in p_T and η. This has been used only to calculate $\not{E}_T$. Understanding the reconstruction of jets in the forward calorimeter would require a more detailed parameterization of the shower spreading, which is not yet available.

3.2.6 Calorimeter Trigger Parameterization

Calorimeter triggers dominate the trigger rate and so have received the most attention. The FAST1 simulation calculates a number of trigger "primitives" from which it can be determined if the Level 1 or Level 2 trigger is satisfied. The electromagnetic cells are combined in 5×5 trigger towers, matched to 2×2 hadronic trigger towers. These trigger towers are also combined 3×3 groups to give 'jet' trigger towers. For these towers, the number of electromagnetic towers above several thresholds, the number of these satisfying an isolation cut, the number of 'jet' towers above threshold, and the number of EC cells above thresholds subject to a hadronic energy test are all calculated and compared with specified thresholds.

An example of such a trigger is the number of EC towers above a threshold of $E_T = 8$, 16, 50, and 80 GeV subject to the requirements that the hadronic energy $E_{T,\mathrm{had}} < 0.1 * E_T$ and that the E_T in the eight neighboring EC towers is less than 7.5 GeV. This is the basic trigger for photons and for isolated electrons.

Little work has yet been done on the Level 3 trigger, which presumably uses a less sophisticated version of the final analysis cuts.

3.2.7 Muon System and Trigger Parameterization

The muon resolution was calculated using a GEANT simulation taking into account the detailed Baseline 1 magnetic field, the geometry and expected resolution of the chambers, and multiple scattering in these chambers. No central tracker information was used. This resolution was then parameterized as a function of p_T and η. In FAST1 the resolution is simulated as a Gaussian in $1/p$ with this width, which is shown in Fig. 3.2-6.

Energy loss in the calorimeter was calculated using GEANT with a GEANT mixture of lead and liquid argon including both dE/dx and hard bremsstrahlung. The energy loss distribution was parameterized as a function of p_T and η, and this is used in FAST1 to generate both the muon's energy deposition in the calorimeter and its energy entering the muon system.

The muon acceptance and trigger efficiency was calculated based on a detailed GEANT simulation and parameterized. The simulation took into account the cracks in ϕ and η in the Baseline 1 design, radiation from the muon producing extra hits in the chambers, and the probability that a muon would bend enough to satisfy the trigger criteria for a given threshold. The probability of reconstructing the muon track was also taken into account based on a preliminary reconstruction algorithm.

Finally, distributions of the number and momenta of tracks and their distances and angles from the primary muon were generated using GEANT. These were parameterized and can be used to estimate the efficiency for reconstructing both isolated muons and muons in hadronic jets.

3.2.8 Future Developments

The fast parameterization has achieved the goal of allowing for the accumulation of high statistics in a short period of time. However, improvements are needed, especially for studies for the Technical Design Report. The FAST1 simulation will also evolve as the detector evolves. As experimental data and a full overall GEANT simulation become available, the parameterizations will be based on more detailed knowledge. Specific features that should be added are noted:

(1) Central Tracker: Simulation of track reconstruction efficiency, effects of high luminosity, efficiency of finding the correct vertex and probability of of finding a track stub are among features that are needed.

(2) Calorimeter: Integration of the central region endcap with the forward calorimeter is needed to better study $\not{E}_T$ questions. There are two possible "seamless approaches": (1) treating the whole calorimeter as a tabulated response function, as is done now for the forward calorimeter, or (2) treating it with cells and jet finding, but with the $\eta = 3$ transition and the $\eta = 5.5$ edge region given special smearing functions. Each of two approaches has its uses in different contexts. Transverse fluctuations should be added in a way that is separate from position resolution.

Figures and Figure Captions for Section 3.2

Fig. 3.2-1 Overall FAST1 geometry, showing the nested cylinders used for tracking.

Fig. 3.2-2 FAST1 central tracker resolution versus η (averaged over ϕ) for various p_T.

Fig. 3.2-3 FAST1 electromagnetic calorimeter resolution versus η (averaged over ϕ) for various p_T.

Fig. 3.2-4 FAST1 hadron calorimeter resolution versus η averaged over ϕ for various p_T.

Fig. 3.2-5 Single pion resolution for various p and η as calculated from GEANT for the GEM baseline forward calorimeter.

Fig. 3.2-6 FAST1 muon resolution versus η (averaged over ϕ) for various p_T.

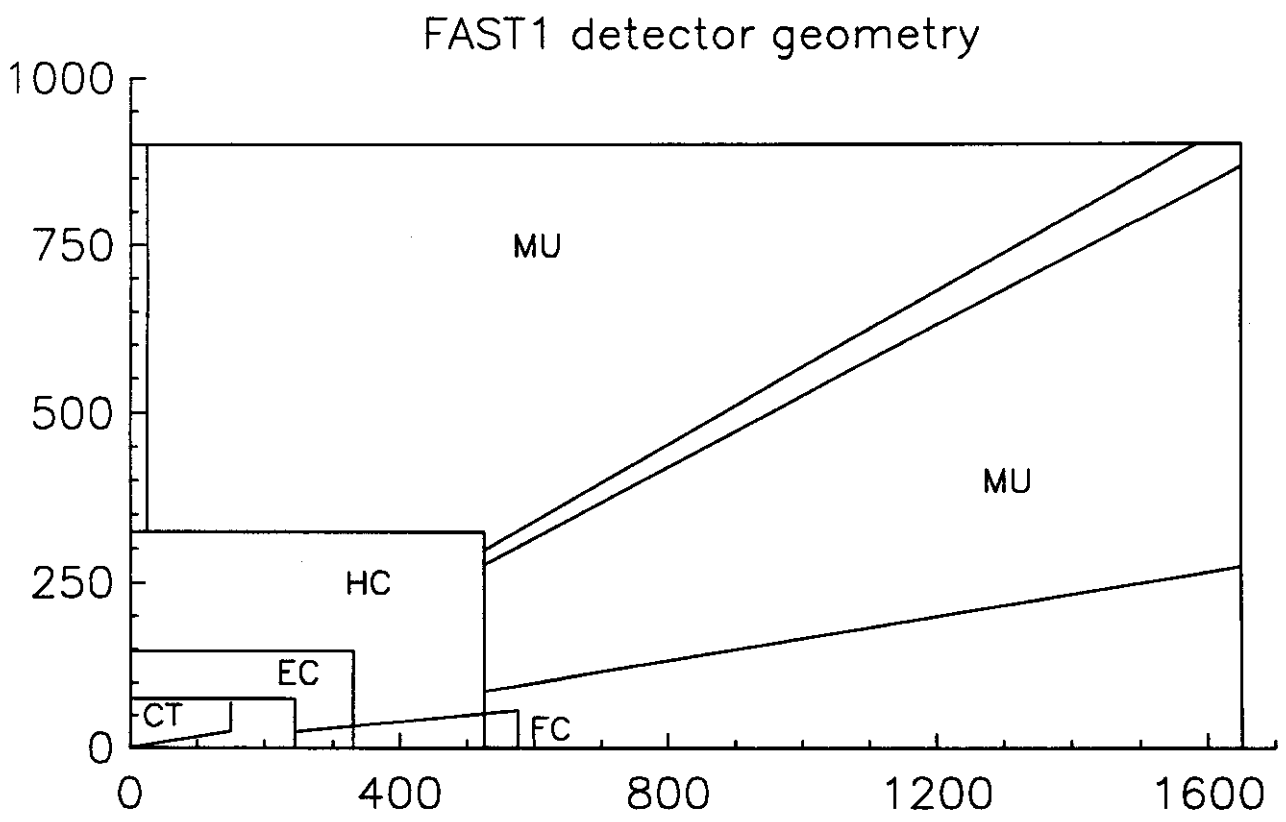
FAST1 detector geometry
1000
750
500
250
0
0
400
800
1200
1600
MU
MU
HC
EC
CT
FC

FIG. 3.2-1

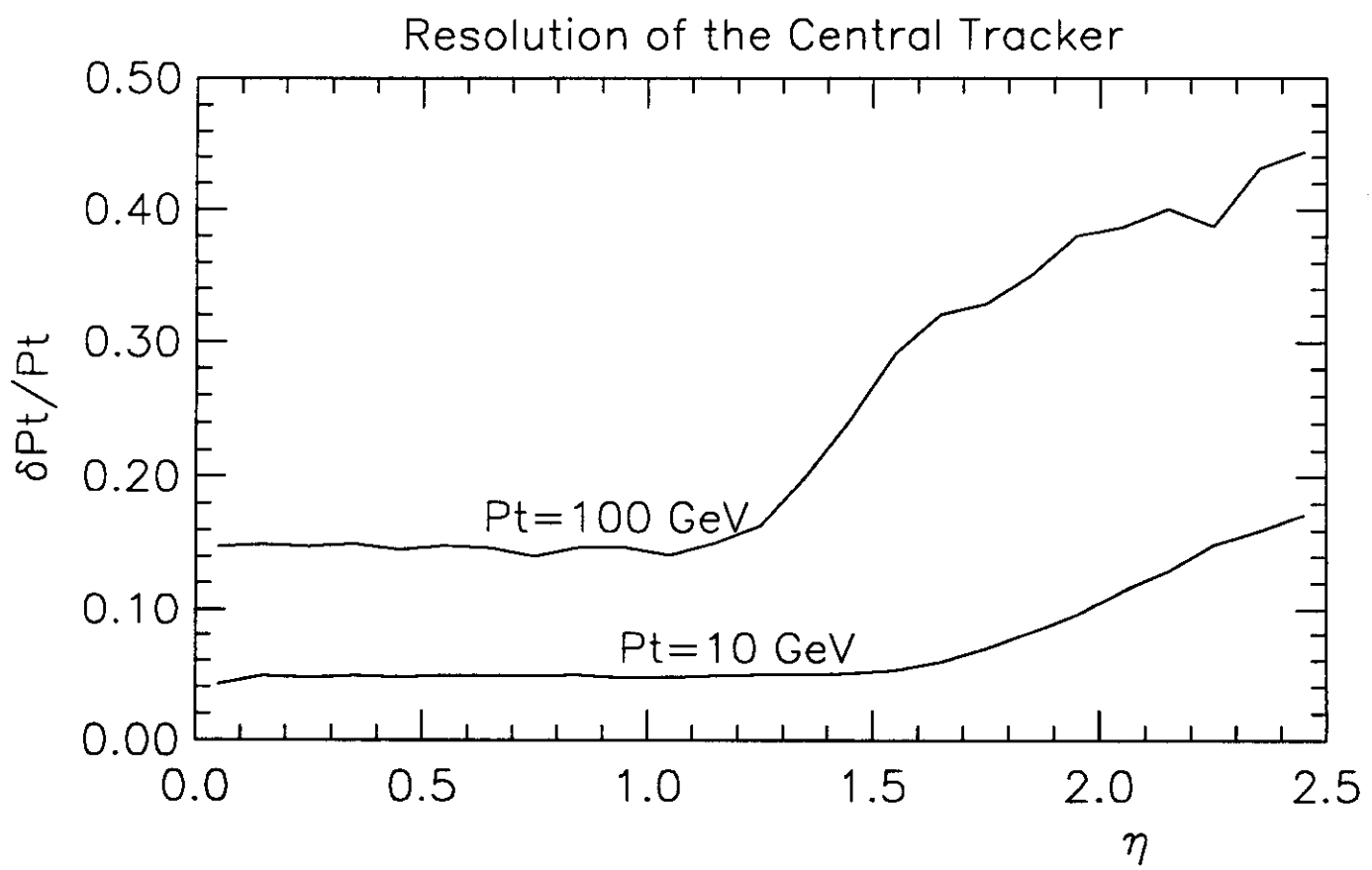
Resolution of the Central Tracker
0.50
0.40
0.30
0.20
0.10
0.00
δPt/Pt
Pt=100 GeV
Pt=10 GeV
0.0
0.5
1.0
1.5
2.0
2.5
η

FIG. 3.2-2

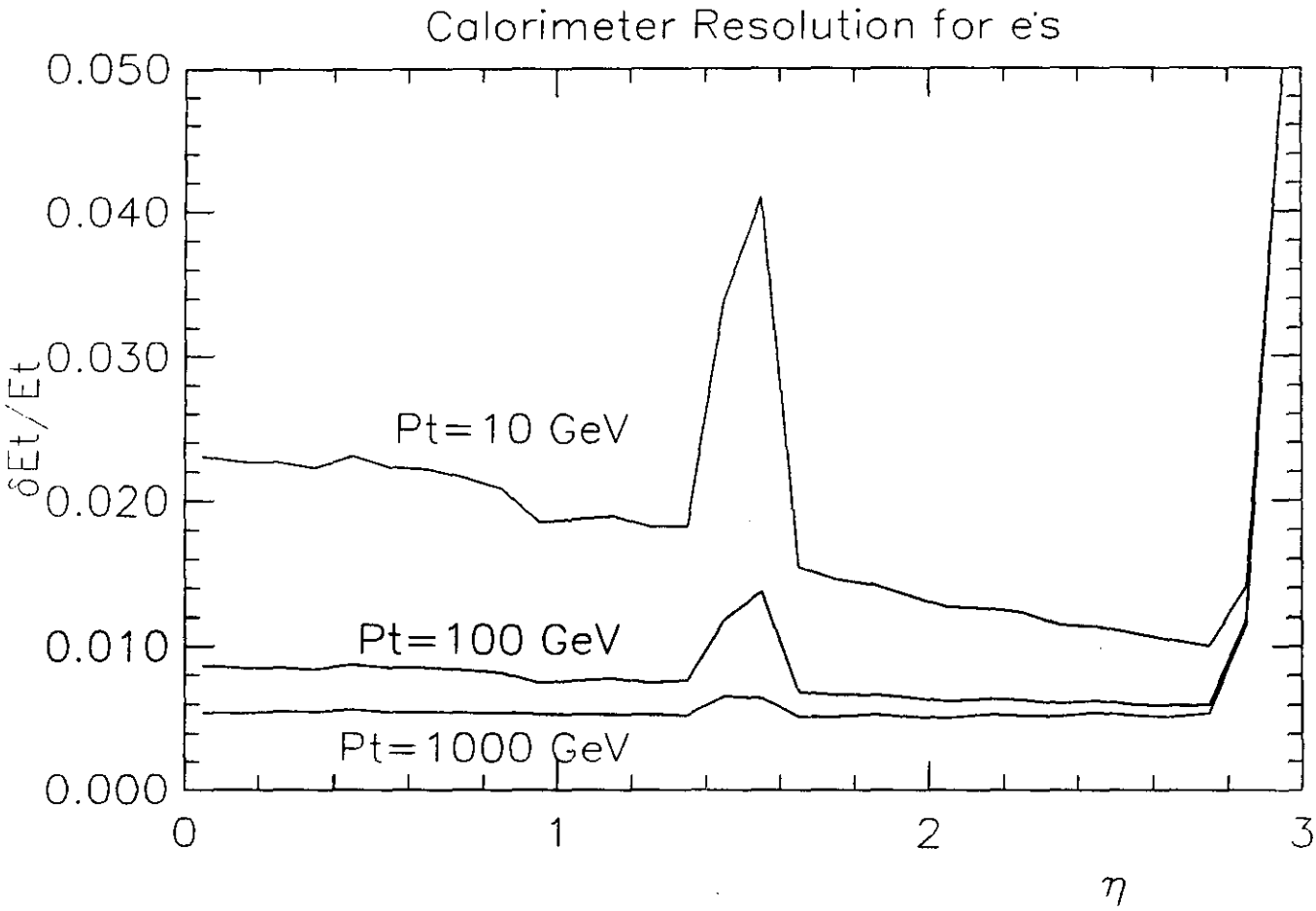
Calorimeter Resolution for e's
0.050
0.040
0.030
0.020
0.010
0.000
δEt/Et
Pt=10 GeV
Pt=100 GeV
Pt=1000 GeV
0
1
2
3
η

FIG. 3.2-3

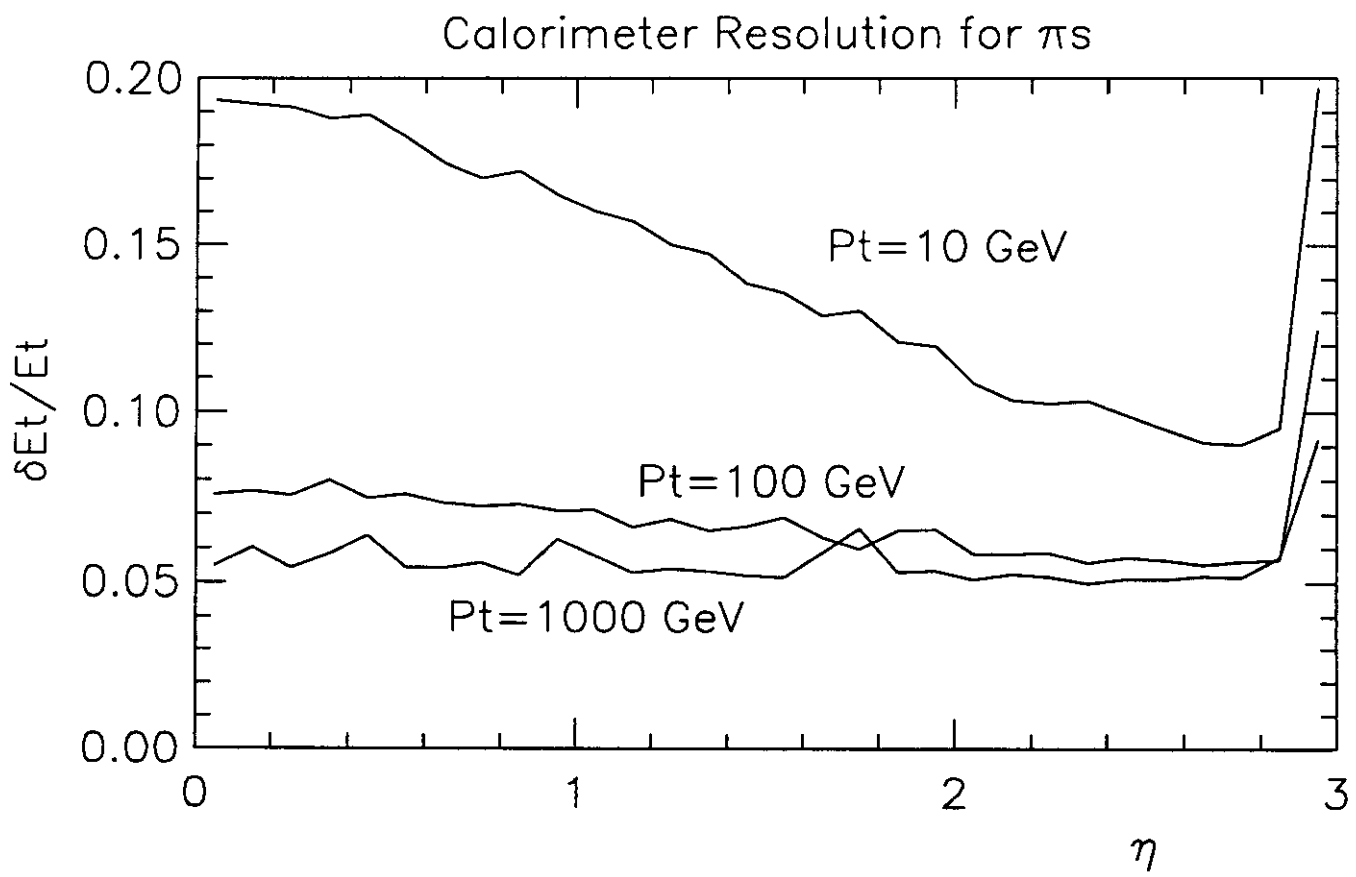
Calorimeter Resolution for πs
0.20
0.15
0.10
0.05
0.00
δEt/Et
Pt=10 GeV
Pt=100 GeV
Pt=1000 GeV
0
1
2
3
η

FIG. 3.2-4

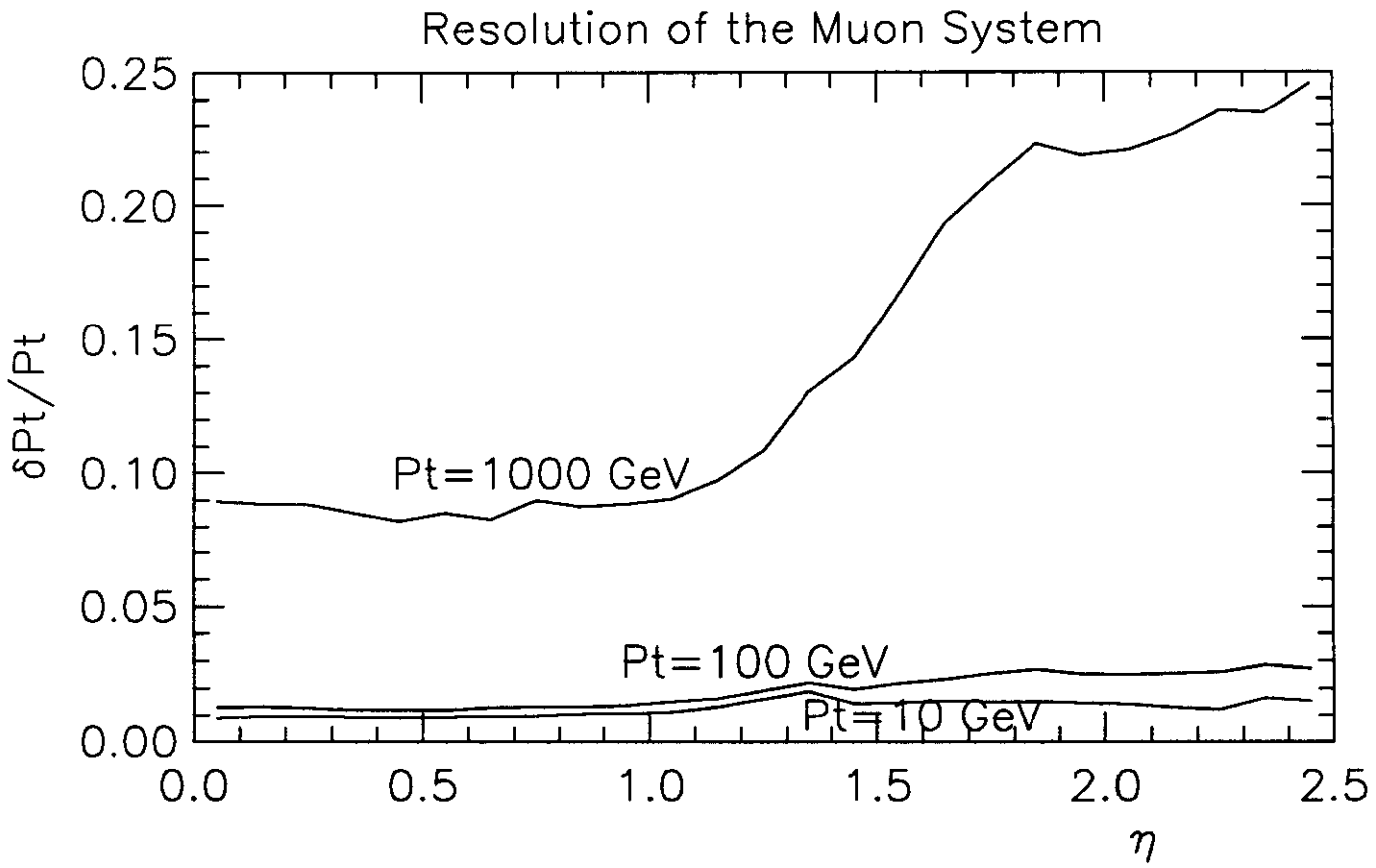
Resolution of the Muon System
0.25
0.20
0.15
0.10
0.05
0.00
δPt/Pt
Pt=1000 GeV
Pt=100 GeV
Pt=10 GeV
0.0
0.5
1.0
1.5
2.0
2.5
η

FIG. 3.2-6

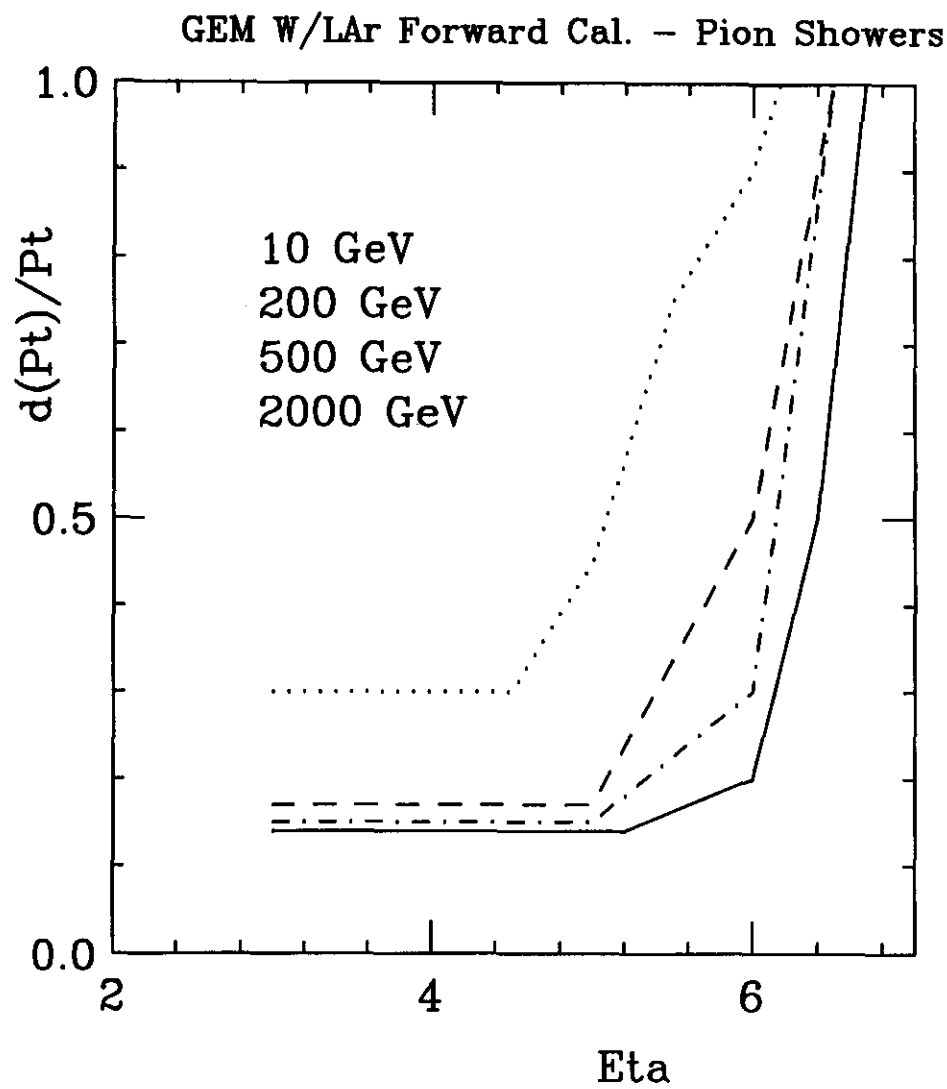
GEM W/LAr Forward Cal. - Pion Showers
1.0
0.5
0.0
d(Pt)/Pt
10 GeV
200 GeV
500 GeV
2000 GeV
2
4
6
Eta

FIG 3.2-5

3.3 FAST1 Studies of Selected Physics Processes

The GEM Letter of Intent was submitted in November 1991 [1]. The LoI was reviewed by the SSC Program Advisory Committee, which issued its report in January 1992 [2]. In its report, the PAC expressed concern about several aspects of the physics simulations carried out for the GEM LoI and suggested that broadened and/or sharpened studies be performed. We have addressed the PAC's concerns with studies in the following areas:

1. Intermediate mass Higgs boson physics in γ and e final states:
   $H^0 \to \gamma\gamma$ ($M_H \cong 80 - 150\,\mathrm{GeV}$).
   $t\bar{t}/W^{\pm} + H^0 \to \ell\gamma\gamma + X$ ($M_H \cong 80 - 150\,\mathrm{GeV}$).
   $H^0 \to ZZ^* \to e^+e^-e^+e^-$ ($M_H \cong 140 - 180\,\mathrm{GeV}$).

2. Heavy flavor tagging with inclusive muons:
   Discovery and mass measurement for a heavy top quark ($t \to W^+b$ with $m_t = 200 - 300\,\mathrm{GeV}$) in $t\bar{t}$ processes with two isolated leptons and one inclusive muon.

3. Lepton identification and measurement at $\mathcal{L} = 10^{34}\,\mathrm{cm}^{-2}\,\mathrm{s}^{-1}$:
   $H^0 \to Z^0Z^0 \to e^+e^-\mu^+\mu^-$ ($M_H = 800\,\mathrm{GeV}$).
   Signal and backgrounds for a 4 TeV $Z'^0 \to e^+e^-$.
   Signal and backgrounds for quark – lepton substructure at the scale $\Lambda = 25\,\mathrm{TeV}$ in the Drell-Yan process $\bar{q}q \to \mu^+\mu^-$

4. Missing-E_T physics:
   The $\not{E}_T$ signal and backgrounds for pair-production of a 300 GeV gluino.
   The likesign-dilepton signal and backgrounds for pair-production of a 300 GeV gluino.
   $H^0 \to Z^0Z^0 \to \ell^+\ell^-\nu\bar{\nu}$ ($M_H = 800\,\mathrm{GeV}$).

5. Jet energy measurement and the calorimetric e/h response:
   Signal and detector-induced backgrounds in a search for quark substructure in high-p_T jet production.

In all these studies, except the one for the heavy top quark, a mass $m_t = 140\,\mathrm{GeV}$ was used.

3.3.1 Intermediate Mass Higgs Boson Physics in γ and e Final States [9]

<u>$H^0 \to \gamma\gamma$ ($M_H \cong 80 - 150\,\mathrm{GeV}$)</u>

The PAC expressed concern over several aspects of the simulation of the signal and backgrounds for $H^0 \to \gamma\gamma$:

1. The degree of realism of the detector simulation.
2. The assumed resolution of the BaF_2 and LAr electromagnetic calorimeter (EC) options.
3. The backgrounds from misidentified electrons.
4. Performance of the detector for $\gamma\gamma$ detection at high luminosities (by which we presume the PAC meant $\mathcal{L} \gtrsim 10^{34}\,\mathrm{cm}^{-2}\,\mathrm{s}^{-1}$).

All of these issues have been reconsidered in detail and are discussed in Ref. [9], which is attached as an appendix to this report. Here we summarize the principal results of this study.

Realism of the Detector Simulation

The study of the search for the intermediate mass Higgs in γ and e final states is based on full GEANT simulations of both the BaF_2 and LAr (and LKr) accordion options for the electromagnetic calorimeter (EC). These simulations were carried out to determine a parameterized energy resolution for each option (see references 4 and 5 in Ref. [9]). They included the effects of electrical noise, photoelectron statistics, geometry – including shower leakage and dead material, physics noise – including shower fluctuations and uniformity of cell response, and intercalibration error. For the electromagnetic energies of interest here, the resolution of the EC may be parameterized by

$$\frac{\Delta E}{E} = \frac{a}{\sqrt{E}} \oplus b\,,$$

with $a = 2.0$, $b = 0.5$ for BaF_2 and $a = 7.5\,(5.5)$, $b = 0.5$ for the LAr (LKr) accordion. Effects of departures from these baseline resolutions on the discovery potential for the intermediate mass Higgs boson are discussed below.

The acceptance of both EC options for photons and electrons was studied for all the intermediate mass Higgs processes considered here, taking into account dead material and regions where the resolution is poor. Both options for the EC extend to $|\eta| = 3$, but only the region with tracking coverage, $|\eta| < 2.5$, is considered active. In addition, these options are dead in the regions

$$|\eta| = 0 - 0.0125\,,\ 1.348 - 1.388 \qquad (BaF_2)\,;$$
$$|\eta| = 1.22 - 1.39 \qquad (\mathrm{LAr})\,.$$

To allow for leakage into these inactive regions, a pessimistic assumption is to extend the boundaries of these ranges by $\Delta\eta = 0.04$, approximately one cell width (except for the $|\eta| = 1.39$ transition in LAr). The geometric acceptance (A_G) for both optimistic

and pessimistic assumptions was studied for all H^0 processes using the event selections employed for each search mode. In all cases, the geometric acceptance was found to be well-approximated by

$$A_G = \left(\frac{5 - \Delta\eta_{\rm dead}}{5}\right)^{n_{\gamma/e}},$$

where $n_{\gamma/e}$ is the number of photons and electrons to be detected.

Precise determination of the photon (or electron) direction is also important for background suppression. The design shower position resolution at the front face of the EC is $\delta x = \delta y = 1\,\mathrm{mm}$. The design resolution on the vertex position as determined by the central tracker (CT) is $\delta z = 1\,\mathrm{mm}$. The effects of departures from these design resolutions was studied and is discussed in [9].

Finally, the effects of thermal and pileup noise in the two calorimeter options were studied and taken into account in selecting the isolation cone sizes and E_T cuts for the $H^0 \to \gamma\gamma$ and other processes. Again, see Ref. [9].

Effects of Electromagnetic Calorimeter Resolution

The $H^0 \to \gamma\gamma$ signal and background events were generated using PYTHIA 5.6 and JETSET 7.3 [5]. The signal cross section rises from 124 fb at $M_H = 80\,\mathrm{GeV}$ to 211 fb at 120 GeV and then falls to 53 fb at 160 GeV. A recent calculation of QCD radiative corrections to the $gg \to H^0$ process shows that these rates should be increased by a factor of 1.5 [10]. Because the radiative corrections have not yet been computed for $gg \to \gamma\gamma$, we do not include this factor here.

The irreducible $\gamma\gamma$ background is 276 pb for $\hat{p}_T^\gamma > 20\,\mathrm{GeV}$ and $75\,\mathrm{GeV} < M_{\gamma\gamma} < 165\,\mathrm{GeV}$. The event selections on the signal and irreducible background are the same as in the LoI, namely: $|\eta_\gamma| < 2.5$; $E_T^\gamma > 20$ GeV; $|\cos\theta_\gamma^*| < 0.9$; and $|\eta_{\gamma\gamma}| < 3.0$. This retains approximately 50% of the signal while reducing the $\gamma\gamma$ background to 42 pb.

Even if all other backgrounds are under control, two-photon production swamps the signal unless the EC has sufficiently good resolution. For the large numbers of events accumulated in one SSCY, the significance S of the signal is given by

$$S = \frac{N_S}{\sqrt{N_B}} = \frac{A_S \cdot A_R \cdot 0.68\,\sigma(H^0 \to \gamma\gamma) \cdot \int \mathcal{L}\,dt}{\sqrt{A_B \cdot A_R \cdot 2\sigma_{M_{\gamma\gamma}} R_B \cdot \int \mathcal{L}\,dt}} \propto \sqrt{\frac{A_R \cdot \int \mathcal{L}\,dt}{\sigma_{M_{\gamma\gamma}}}}.$$

Here, A_S and A_B are the absolute acceptance of signal and background. The relative acceptance A_R is the product of the geometric acceptance A_G, discussed above, and the $\gamma\gamma$ identification efficiency. When such effciencies are needed for numerical purposes, they

shall be assumed to be 90% for each photon and electron. The background rate at the Higgs mass is R_B. Finally, the $M_{\gamma\gamma}$ resolution, $\sigma_{M_{\gamma\gamma}}$, is given by

$$\frac{\sigma_{M_{\gamma\gamma}}}{M_{\gamma\gamma}} = \frac{1}{2}\sqrt{\left(\frac{\Delta E_1}{E_1}\right)^2 + \left(\frac{\Delta E_2}{E_2}\right)^2 + \left(\cot\frac{\theta}{2}\Delta\theta\right)^2},$$

where $E_{1,2}$ are the energies of the two photons and θ is the angle between them.

The expression for S emphasizes that a larger geometric acceptance and smaller mass resolution are equivalent to a shorter discovery time. The average of optimistic and pessimistic geometric acceptances is $A_G = 0.90$ for BaF_2 and 0.85 for LAr. Then, a reasonably conservative estimate of A_R for the $\gamma\gamma$ processes is $0.81 A_G$.

The mass resolution was studied by varying the stochastic and constant terms in the EC resolution, a and b, over the ranges

$$2.0\% \leq a \leq 15\%$$
$$0.5\% \leq b \leq 2.0\%.$$

The shower position and vertex z resolutions were held fixed at 1 mm for this study. Then, to a good approximation, the contribution of the angular error to $\sigma_{M_{\gamma\gamma}}$ is negligible and it was found that

$$\frac{\sigma_{M_{\gamma\gamma}}(M_H)}{M_H} \cong \frac{1}{\sqrt{2}}\left(\frac{\Delta E}{E}\right)_{M_H/2} \cong \sqrt{\frac{2a^2/M_H + b^2}{2}}.$$

The time factors for discovery of $H^0 \to \gamma\gamma$, relative to the BaF_2 baseline design goal of $a = 2$ and $b = 0.5$, are listed in Table 3.3-1 as a function of a and b. Note that these time factors do not include the acceptances A_G and $A_{S,B}$.

Table 3.3-1: Time Factor in discovering a $H^0 \to \gamma\gamma$ as function of a and b.

a	2.0	3.0	5.5	7.5	10	15
			$M_H = 80$ GeV			
$b = 0.5$	**1.0**	1.1	1.5	1.9	2.4	3.4
$b = .75$	1.4	1.5	1.7	2.1	2.6	3.6
$b = 1.0$	1.8	1.8	2.1	2.4	2.8	3.8
$b = 1.5$	2.6	2.6	2.8	3.1	3.4	4.2
$b = 2.0$	3.4	3.5	3.6	3.8	4.1	4.8
			$M_H = 150$ GeV			
$b = 0.5$	**1.0**	1.1	1.3	1.6	2.0	2.8
$b = .75$	1.4	1.5	1.7	1.9	2.3	3.0
$b = 1.0$	1.8	1.9	2.0	2.2	2.5	3.2
$b = 1.5$	2.6	2.7	2.8	3.0	3.2	3.7
$b = 2.0$	3.6	3.6	3.7	3.8	4.0	4.4

The effects of varying the resolution on the shower position and the vertex z-coordinate were also studied and are tabulated in [9]. For the shower position ($\delta x = \delta y$), the time factor for the BaF_2 baseline resolution rises from 1.0 for $\delta x \leq 1.5\,\mathrm{mm}$ to 1.2 for $\delta x = 5\,\mathrm{mm}$. For the LAR baseline resolution, the time factor rises from 1.9 for $\delta x \leq 1.5\,\mathrm{mm}$ to 2.0 for $\delta x = 5\,\mathrm{mm}$. Increasing δz from 1 mm to 10 mm (50 mm) increases the discovery time by a factor of 1.5 (5.4) for the BaF_2 resolution. The relative time factor for LAr increases from 1.9 to 2.2 (5.6) for $\delta z = 10$ mm (50 mm). All these time factors refer to the case $M_H = 80\,\mathrm{GeV}$, but their dependence on M_H is weak.

At $\mathcal{L} = 10^{33}\,\mathrm{cm}^{-2}\,\mathrm{s}^{-1}$, the event vertex is reliably selected on the basis of multiplicity. There are only 1.6 minimum bias events per beam crossing. Then, Monte Carlo studies using PYTHIA and ISAJET minimum bias events show that the high-multiplicity vertex is the correct one 85% – 95% of the time [9]. It is expected that assigning tracks to vertices and selecting the high-multiplicity vertex will be straightforward at 10^{33}; a study of this is underway for the GEM tracker.

Backgrounds, including Misidentified Electrons

Given energy and position resolutions sufficient to see a Higgs signal above the $\gamma\gamma$ background in 1–3 SSCY, the most serious remaining background is the QCD γ + jet and 2-jet background in which jets fake photons. These backgrounds were discussed at length in the GEM LoI [1] and again in [9]. They were reduced first by isolation cuts. To simulate these cuts, dijet and γ-jet events were generated, and the EM energy and a GEANT-determined part of the hadronic energy were deposited in the EM calorimeter cells with parameterized shower spreading. A photon candidate with transverse energy E_T^{photon} was found by summing a 3×3 cluster of EC cells surrounding the one hit by the photon. No charged particles, which were tracked through the 8 kG magnetic field, were allowed to hit the cluster. The photon candidate was rejected if it did not pass the calorimetric isolation cut

$$\sum_R E_T - E_T^{\mathrm{photon}} \leq E_T^{\mathrm{cut}} + 0.1\, E_T^{\mathrm{photon}} \ ,$$

where the sum is over the E_T of the cells in a cone of size $R = \sqrt{(\Delta\eta)^2 + (\Delta\phi)^2}$ about the photon cell. The probability $R(\gamma/\mathrm{jet})$ that a jet mimics an isolated single photon must be no more than a few 10^{-4}. Based on the expected thermal and pileup noise of the two calorimeter options, the following isolation parameters were chosen:

$$\begin{array}{lll} R = 0.75 & E_T^{\mathrm{cut}} = 5\,\mathrm{GeV} & (BaF_2) \\ R = 0.60 & E_T^{\mathrm{cut}} = 10\,\mathrm{GeV} & (\mathrm{LAr}) \ . \end{array}$$

After isolation cuts, the QCD background is expected to have the same shape as the $\gamma\gamma$ spectrum. This makes it easy to estimate the effect of these backgrounds on the signal significance. In the case of BaF_2, the QCD backgrounds may be reduced to the level of $\gamma\gamma$ by isolation cuts and a shower shape analysis. In the case of LAr, a preradiator may be needed to reduce the QCD backgrounds to this level. The reason for this is that thermal and pileup noise levels in LAr do not permit as tight an isolation cut as may be implemented for BaF_2. Alternatively, isolation cuts using two concentric cones may be more effective in reducing the QCD background for the LAr calorimeter. The effect of a preradiator on the EC resolution has not been studied yet, but it is not expected to be very significant for either EC option.

Isolated electrons can fake photons if they are not identified by the CT. We denote by $R(\gamma/e)$ the probabilty of such a fake. It is also possible that a jet can fake an isolated electron with probability R(e/jet). Hence, a jet fakes an isolated photon with total probability $R(\gamma/\text{jet}) + R(\gamma/e)R(e/\text{jet})$.

The largest source of isolated e^+e^- production is ordinary Drell-Yan production, with the bulk of it coming near $M_{e^+e^-} = M_Z$. After $\gamma\gamma$ event selections, the e^+e^- cross section at the Z^0 peak is 160 pb/GeV, 250 times larger than the $\gamma\gamma$ rate there. The two rates are comparable above $M_{e^+e^-} = 120\,\text{GeV}$. Thus, if the GEM CT can provide a rejection factor of $R(\gamma/e) < 3\%$ over the rapidity range $|\eta| < 2.5$ at $\mathcal{L} = 10^{33}\,\text{cm}^{-2}\,\text{s}^{-1}$, the Drell-Yan background will be eliminated. The second largest isolated e^+e^- background comes from $t\bar{t}$ production. This source is as large as the Drell-Yan background for $M_{e^+e^-} > 110\,\text{GeV}$. Thus, a 3% rejection of electrons renders this background source negligible as well.

A real calculation of the $Z \to e^+e^-$ veto inefficiency requires a hit level Monte Carlo for the tracker, which does not yet exist. Since it is not necessary to reconstruct the electron track, only to veto it, a simple estimate shows that it is easy to obtain $R(\gamma/e) < 3\%$. The tracker has 12 planes of silicon and 8 planes of IPCs. It is sufficient to require hits in 5 of the first 8 planes of the silicon. The inefficiency per hit is estimated to be less than 3%, so the probability that an electron will fail to give 5 hits is approximately $\frac{8!}{5!3!}(.03)^3(.97)^5 = 1.3 \times 10^{-3} \ll 3\%$. The occupancy of the silicon is everywhere less than 0.22%. If a road 1 mm or 20 strips wide is used, the occupancy on this road is less than 4% per plane. Even if the occupancy were completely correlated between planes, which is extremely conservative, the loss of signal events would be small.

The probability $R(e/\text{jet})$ was studied for QCD dijets and $\gamma+$ jet events by using isolation cuts similar to those for selecting isolated photon candidates plus the requirement that a charged track hit the center EC cell. Most of the isolated electron candidates consist of energetic photons overlapping a low-momentum charged track. A relatively loose $E - p$

matching criterion (such as $p_{\rm track}/E_{\rm cal} < 0.5$) may be used to cut away these events. For an isolation cone radius of 0.6, the fake $\gamma - e$ rate was reduced to 2.8 pb, while the fake e^+e^- rate was .01 pb. With a 3% misidentification of photons as electrons, these constitute negligible backgrounds to $H^0 \to \gamma\gamma$.

Table 3.3-2 lists the total background cross sections, integrated over $75\,\mathrm{GeV} < M_{\gamma\gamma} < 165\,\mathrm{GeV}$, at each stage of the cuts in the BaF_2 and LAr-accordion options. The background scaling factor, BF, is the total background rate divided by the irreducible $\gamma\gamma$ rate. Assuming that the shape of $\gamma\gamma$ invariant mass spectra from all background sources is the same, the total background spectrum may be obtained by scaling the irreducible $\gamma\gamma$ background by BF.

Table 3.3-2: Total $H^0 \to \gamma\gamma$ background cross-sections (pb) after cuts.

	BaF_2 System					LAr System				
Process	$\gamma\gamma$	γ-jet	2jets	Total	BF	$\gamma\gamma$	γ-jet	2jets	Total	BF
Isol.	31	33	46	110	3.5	34	90	220	344	11
S.S.	31	21	20	72	2.3	34	50	120	204	6.6
P.R.	31	17	13	61	2.0	34	24	20	78	2.5
Irr.	31	14	7.3	52	1.7	34	14	10	58	1.9

Figure 3.3-1 shows the spectra of Higgs signals For $M_H = 80$, 100, 120, 140 and 160 GeV superimposed on the total background after shower shape analysis (a) and preradiator rejection (c) for the BaF_2 calorimeter. The corresponding background subtracted spectra are shown in Fig. 3.3-1 (b) and (d). The significances of these signals in one SSCY are 3.0, 5.7, 9.2, 10 and 3.9 after the shower shape analysis and 3.3, 6.1, 9.9, 11 and 4.9 after the preradiator rejection. The corresponding plots for for the LAr calorimeter are shown in Fig. 3.3-2.. The significances of the Higgs signals in one SSCY are 1.3, 2.8, 4.7, 5.1 and 2.0 after shower shape analysis, and 2.3, 4.4, 7.6, 8.2 and 3.3 after preradiator rejection. These significances do not include the geometric and other acceptances and the γ-detection efficiencies. Nor do they include the potential factor of 1.5 enhancement of signal over background [10].

Performance at Ultrahigh Luminosity

Finally, there is the question of searching for $H^0 \to \gamma\gamma$ at ultrahigh luminosity, $10^{34}\,\mathrm{cm}^{-2}\,\mathrm{s}^{-1}$. At nominal SSC energy and luminosity, there are several hundred signal events – after cuts and background subtractions – for any Higgs mass in the range $80\,\mathrm{GeV} \lesssim M_H \lesssim 150\,\mathrm{GeV}$. Assuming that our resolution goals are met, ultrahigh luminosity is neither needed nor likely to be desirable for this search. Many tools of the

search are much more difficult to use at this luminosity, including background rejection via isolation cuts, vertex finding for photon momentum pointing, rejection of misidentified electrons, and so on. In general, we believe that ultrahigh luminosity is most readily used and best reserved for very high mass scale physics whose signals are isolated energetic ($\gtrsim 1\,\mathrm{TeV}$) photons, electrons and muons. We shall discuss this view in more detail in section 3.3.3.

$\underline{H^0 + t\bar{t}/W \to \gamma\gamma\ell + X\ (M_H \cong 80 - 150\,\mathrm{GeV})}$

Associated production of H^0 with $t\bar{t}$ or $W^\pm$ and the decay of this system to $\gamma\gamma$ plus an isolated $\ell^\pm$ is an attractive search mode for the intermediate mass Higgs because the true and fake $\gamma\gamma$ backgrounds discussed above are eliminated by the isolated-lepton tag [11]. On the other hand, the signal cross section at the SSC (dominated by $t\bar{t}H^0$) is only a few fb, and the backgrounds are still formidible and not yet entirely under computational control. Here we summarize a study of detection of the $\gamma\gamma\ell^\pm$ signal for the baseline BaF_2 and LAr resolutions, as well as the case $\Delta E/E = 15\%/\sqrt{E} \oplus 1\%$, at $\mathcal{L} = 10^{33}\,\mathrm{cm}^{-2}\,\mathrm{s}^{-1}$. The issues involved in detecting this signal at $\mathcal{L} = 10^{34}\,\mathrm{cm}^{-2}\,\mathrm{s}^{-1}$ have not been studied yet.

The main backgrounds are $t\bar{t}\gamma\gamma$ ($\sigma = 80\,\mathrm{fb}$), $b\bar{b}\gamma\gamma$ (2 pb), $W^\pm\gamma\gamma$ (23 fb), and ordinary $t\bar{t}$ production (16 nb). The hard scattering processes for the first three backgrounds were generated using PAPAGENO [12] while initial and final state radiation, hadronization and decays were treated by PYTHIA 5.6.

The $t\bar{t}$ process is nettlesome because it is not rendered negligible by the cuts to select isolated photons. Events with a tagged isolated lepton have four quark jets. Our studies show that the rejection factors achieved by a photon isolation cut with, e.g., $E_T^{\mathrm{cut}} = 5\,\mathrm{GeV}$ and $R = 0.6$ are about 3×10^{-4} for gluon jets, but only 1.3×10^{-3} for quark jets. This leads to a $t\bar{t} \to \gamma\gamma\ell^\pm + X$ rate with $75\,\mathrm{GeV} < M_{\gamma\gamma} < 165\,\mathrm{GeV}$ of 30 fb, about 15–25 times the signal. An important additional factor of 3 rejection can be achieved by requiring that the p_T of the di-photon system be greater than 40 GeV. The other cuts on the data are:

- $|\eta_\ell| < 2.5$, $p_T^\ell > 20\,\mathrm{GeV}$, and isolation cone radius $R = 0.3$;
- $|\eta_\gamma| < 2.5$, $p_T^\gamma > 20\,\mathrm{GeV}$, and isolation cone radius $R = 0.3, 0.45, 0.6$;
- Isolation cut: $\sum_R E_T - E_T^{\mathrm{photon}} \leq E_T^{\mathrm{cut}} + 0.1\,E_T^{\mathrm{photon}}$;
- Shower shape analysis.

The signal and background events accumulated in one SSCY after these cuts are displayed in Fig 3.3-3 for the BaF_2 and LAr baseline resolutions as well as for $\Delta E/E = 15\%/\sqrt{E}\oplus 1\%$. The Higgs mass values considered are $M_H = 80, 100, 120, 140$ and 160 GeV. The largest background is still the fake $\gamma\gamma$ events from $t\bar{t}$ production. Figure 3.3-4 shows

the results of three SSCY worth of data. The relative acceptances of 62% and 56% for BaF_2 and LAr are not included in these figures. It is clear that precision electromagnetic energy resolution is also important for discovering the intermediate mass Higgs boson in the associated production channels in a reasonable period of time.

Since the number of associated production events are so low, some care must be taken in determining the significance of the signals. The analysis of the significance is discussed in Ref. [9]. The results are displayed as a function of standard SSCY in Fig. 3.3-5.

$\underline{H^0 \to ZZ^* \to e^+e^-e^+e^- \ (M_H \cong 140 - 180\,\mathrm{GeV})}$

The PAC expressed concern about two aspects of the search for $H^0 \to ZZ^* \to e^+e^-e^+e^-$. The first was the effect of degraded EC resolution on the signal and discovery time. This effect is summarized in Table 3.3-3 below. For more details, see Ref. [9]. The PAC's second concern was that the LoI did not demonstrate electron identification in the end-caps. As of this writing, this question is still being investigated; it will be reported upon on in the TDR.

Table 3.3-3 shows the effect of varying the EC resolution on the discovery time factors, relative to the BaF_2 baseline design resolution, $a = 2.0$, $b = 0.5$.

Table 3.3-3: Time factor in discovering $H^0 \to ZZ^* \to e^+e^-e^+e^-$ as function of a and b.

a	2.0	3.0	5.5	7.5	10	15
			$M_H = 140\,\mathrm{GeV}$			
$b = 0.5$	**1.0**	1.1	1.6	2.0	2.5	3.7
$b = 1.0$	1.8	1.9	2.1	2.5	3.0	4.0
$b = 1.5$	2.6	2.7	2.9	3.1	3.5	4.3
$b = 2.0$	3.4	3.5	3.7	3.9	4.4	5.0
			$M_H = 170\,\mathrm{GeV}$			
$b = 0.5$	**1.0**	1.0	1.2	1.6	2.0	3.0
$b = 1.0$	1.5	1.6	1.8	2.0	2.3	3.2
$b = 1.5$	2.1	2.2	2.3	2.6	2.7	3.3
$b = 2.0$	2.7	2.8	3.0	3.1	3.4	4.1

3.3.2 Heavy Flavor Tagging with Inclusive Muons [13]

In this section we discuss GEM's ability to identify heavy top quarks ($m_t \simeq 250\,\mathrm{GeV}$) via isolated leptons and inclusive b-decay muons. The top-quark mass may be determined from several different distributions, depending on the t-decay mode. The two most accurate determinations of m_t come from measurements of:

1) The invariant mass, $M_{\ell\mu}$, of an isolated lepton and an inclusive muon arising from the semileptonic decay chain $t \to W^+ b$; $W^+ \to \ell^+ \nu_\ell$ and $b \to c\mu^- \overline{\nu}_\mu$.
2) The invariant mass, M_{jjj}, of the three jets arising from nonleptonic top-decay $t \to W^+ b \to 3$ jets.

In this report, we discuss a precision measurement of m_t via the $M_{\ell\mu}$-distribution. The issues of jet-energy measurement involved in the M_{jjj} measurement and of non-standard top-quark decays will be discussed in the TDR.

ISAJET was used to generate 50K $t\bar{t}$ events for each of the three masses $m_t = 200$, 250, 300 GeV. The t-quarks were required to have $50\,\text{GeV} < p_T < 1000\,\text{GeV}$. The $W^\pm$ were required to decay to $\ell^\pm \nu_\ell$ ($\ell = e,\ \mu$). The b from t-decay was forced to decay to $c\mu^- \overline{\nu}_\mu$, while the $\overline{b}$ from $\overline{t}$ was allowed to decay into all possible channels. The signal events are those with one isolated electron, one isolated muon and one non-isolated muon. The isolated leptons were required to have opposite charges. Choosing isolated leptons of different flavors eliminates backgrounds involving $Z^0 \to \ell^+\ell^-$. The signal cross sections (assuming $B(W \to \ell\nu) = B(b \to \mu^- + X) = 1/9$) for the three top-masses were found to be 10.1 pb, 4.12 pb and 1.93 pb, respectively.

The selection criteria on the leptons were taken to be:

Isolated $e^\pm$: $\sum_{R=0.2} E_T > 20\,\text{GeV}$, $\sum_{R=0.3} E_T - \sum_{R=0.2} E_T^{\text{EM}} < 5\,\text{GeV}$.

Isolated $\mu^\pm$: $p_T > 20\,\text{GeV}$, $\sum_{R=0.2} E_T - \sum_{R=0.1} E_T < 5\,\text{GeV}$.

Inclusive $\mu^\pm$: $p_T > 5\,\text{GeV}$, $\sum_{R=0.2} E_T - \sum_{R=0.1} E_T > 5\,\text{GeV}$.

Here, E_T is the transverse energy in a cell of the combined calorimeter and E_T^{EC} is the transverse energy in EC cell. These selections were chosen to optimize the separation between isolated leptons from W-decay and non-isolated leptons from b-decay. The acceptances of these cuts were found to be 0.089 for $m_t = 200\,\text{GeV}$, 0.116 for 250 GeV, and 0.145 for 300 GeV. Thus, before taking into account lepton identification efficiencies, the number of signal events in one SSCY are 1.81×10^4 ($m_t = 200\,\text{GeV}$) 9730 (250 GeV), and 5865 (300 GeV).

The identification and measurement of inclusive muons from b-decay have been studied using a hit-level Monte Carlo. The details are in Chapter 2.3 of this report. Effects of muon interactions in the calorimeter and punchtrough from the c-jet and other interactions were included. Two potential problems for muon pattern recognition were considered. The first was the probability that the hit in a cell through which the muon passes is in fact caused by another charged particle. For inclusive muons resulting from the decay of a 250 GeV top quark with $p_T \lesssim 500\,\text{GeV}$, it was found that there are less than or equal to

three such "shared cells" (out of 20) 90% of the time. The second problem considered was the number of neighboring cells along the muon's trajectory in which there was a hit. For the same muon sample, there are ≤ 3 neighboring hits 90% of the time. These non-overlap frequencies are independent of m_t over its plausible range of values. Thus, a conservative estimate the efficiency of tagging the b-quark by an inclusive muon is 80%. The efficiency for identifying the isolated muon should be close to 100%. The efficiency for identifying the isolated electron is expected to be at least 80%.

The backgrounds from $W^{\pm}Z^0$, $Z^0 b\bar{b}$ and $W^{\pm}b\bar{b}$ production were studied. After the selections above, these processes were found to contaminate the signals by at most a few per cent.

The $M_{e\mu}$, $M_{\mu\mu}$ and $M_{\ell\mu} = M_{e\mu} + M_{\mu\mu}$ distributions are shown in Fig. 3.3-6 (a,b,c) for m_t = 200, 250, and 300 GeV. These plots do not include the lepton identification efficiencies. The average value of the $M_{\ell\mu}$ distributions are 47 GeV, 58 GeV and 66 GeV, respectively. The cases of m_t = 230 and 270 GeV have also been simulated, though with only 10K events generated. The mean value of $M_{\ell\mu}$ is plotted against m_t in Fig. 3.3-7. A statistical error of 1.3 GeV on the mass of a 250 GeV top quark is expected after one SSCY. The systematic error is under study and it is expected to be larger.

3.3.3 Lepton Identification and Measurement at $\mathcal{L} = 10^{34}\,\mathrm{cm}^{-2}\,\mathrm{s}^{-1}$

The PAC expressed concern about GEM's capabilities for lepton detection at ultrahigh luminosity and the extent to which they were demonstrated in the LoI. Such detector-specific issues as calorimeter thickness and punchthrough, muon triggering (especially in the forward direction), and tracking capabilities surviving at $10^{34}\,\mathrm{cm}^{-2}\,\mathrm{s}^{-1}$ are addressed in the appropriate subsystem chapters of this report. Here we use the FAST1 model to investigate in greater depth several processes that were highlighted in the LoI as opportunities for ultrahigh luminosity experimentation. Before presenting our results, however, we want to spell out what we believe ultrahigh luminosity at the SSC is to be used for.

At $\mathcal{L} = 10^{34}\,\mathrm{cm}^{-2}\,\mathrm{s}^{-1}$ there are, on average, 16 events per beam crossing and $O(1000)$ charged particle tracks in the central rapidity range, $|\eta| < 2.5$. While these particle densities do not represent insuperable challenges to experimentation, they do make detection of many low-energy signals much more problematic. We have already noted this in one example, $H^0 \to \gamma\gamma$. There, given sufficient resolution of the electromagnetic calorimeter, the whole game is isolation and shower shape cuts to remove background, plus identification of the event vertex to define the photon momenta. Both are much more difficult at $\mathcal{L} = 10^{34}$ than at 10^{33}. Fortunately, the SSC design energy is high enough to permit experiments at 10^{33} to reach this and most other examples of TeV-region physics.

In our view, then, one should resort to ultrahigh luminosity mainly to access high-mass physics with small cross sections and simple signals. In practice, at the SSC this usually means isolated-lepton signals with $\sigma \cdot B \sim 1 - 10\,\text{fb}$. Fortunately, much new high-scale physics that might be expected to be within reach of the SSC involves isolated-lepton signals. These phenomena are related to the origin and breakdown of electroweak symmetry and quark-lepton flavor symmetry and/or to extensions the standard electroweak gauge group. Examples include very heavy Higgs bosons and technihadrons decaying to weak gauge bosons, quark-lepton substructure, and new extra-heavy gauge bosons.

The processes considered here for ultrahigh luminosity studies were discussed in varying degrees of detail in the LoI. They are: (1) the search for an 800 GeV H^0 decaying to $e^+e^-\mu^+\mu^-$; (2) precision measurements of the width of a 4 TeV Z'^0 decaying to e^+e^-; (3) detailed study, via the Drell-Yan process $\bar{q}q \to \mu^+\mu^-$, of the contact interaction induced by quark-lepton substructure at the scale $\Lambda = 25\,\text{TeV}$. The reports on these topics are somewhat preliminary because event selection cuts have not been fully optimized. Nevertheless, we are reasonably confident that the results described here will be essentially unaltered by more detailed scrutiny.

$H^0 \to Z^0 Z^0 \to e^+e^-\mu^+\mu^-$ ($M_H = 800\,\text{GeV}$) at $\mathcal{L} = 10^{34}\,\text{cm}^{-2}\,\text{s}^{-1}$ [14]

There are strong theoretical reasons to believe that, if $M_H \gtrsim 650\,\text{GeV}$, the standard model breaks down in the sense that new, unspecified degrees of freedom are needed to describe the physics of electroweak symmetry breaking [15]. Nevertheless, detailed studies of techniques designed to discover a very heavy Higgs boson in a variety of "standard" decay modes are useful because they test a detector's capabilities to observe these modes above known backgrounds, regardless of the source of the signal. The search for an 800 GeV Higgs boson decaying into $e^+e^-\mu^+\mu^-$ is studied here. The signal is very clean, but the rate is very small, 30 events per year at standard luminosity before event selection and background rejection. Thus, we consider a search for this mode in one year at $\mathcal{L} = 10^{34}\,\text{cm}^{-2}\,\text{s}^{-1}$.

PYTHIA 5.5 was used to generate 10K signal events – far higher statistics than can ever be obtained. The production cross section, including branching ratios, of 2.6 fb yields 260 events per SSCD (one SSCD corresponds to $\int \mathcal{L}\,dt = 10^{41}\,\text{cm}^{-2}$). The irreducible $Z^0Z^0 \to e^+e^-\mu^+\mu^-$ background rate is 45.9 fb for $M_{ZZ} > 300\,\text{GeV}$. The most important reducible physics background is due to $t\bar{t}$ production. The $t\bar{t}$ cross section is 9.2 nb for $M_{t\bar{t}} > 200\,\text{GeV}$ and $p_T(t,\bar{t}) > 20\,\text{GeV}$. Recall that the factor of 1.5 enhancement of $gg \to H^0$ may mean that the signal-to-background ratio is as much as 50% higher than considered here [10]. It is expected that muon backgrounds from punchthrough and pion decays in flight can be reduced by momentum matching between the CT and muon system,

but this study has not yet been carried out using FAST1.

Events were selected with two electron and two muon candidates in the rapidity range $|\eta| < 2.5$; 76% of the signal events satisfy this fiducial cut; 65% of the signal events had two muons accepted by FAST1. Further event selections to reduce the Z^0Z^0 and $t\bar{t}$ backgrounds and the data flow for the signal are summarized as follows:

1. The isolation energy for the muon is

$$E_T^{\rm cut}(\mu) = \sum_R E_T - 0.3 p_T(\mu) .$$

   Here, E_T is the transverse energy deposited in the cells of the combined calorimeter and the sum is over an $\eta - \phi$ cone of radius $R = 0.3$. The cut was chosen to be $E_T^{\rm cut}(\mu) < 0$, and this accepted 63% of the signal events.
2. Electron and muon candidates were required to have $E_T > 20\,\mathrm{GeV}$; 60% of the signal passed this cut.
3. The isolation energy for electron candidates is

$$E_T^{\rm cut}(e) = \sum_{R_2} E_T - 1.1 \sum_{R_1} E_T^{EC} .$$

   In this study, cone radii $R_1 = 0.1$ and $R_2 = 0.3$ were used. The cut was chosen to be $E_T^{\rm cut}(e) < 0$, and 53% of the signal was passed.
4. The energy ratio for electron candidates is defined to be

$$\rho_{\rm EM} = \frac{\sum_{R_1} E_T^{EC}}{\sum_{R_2} E_T} .$$

   The cut was taken to be $\rho_{\rm EM} > 0.9$, passing 50% of the signal.
5. The number $n_{\rm ch}$ of charged particles, including the candidate lepton, with $p_T > 5\,\mathrm{GeV}$ in a surrounding cone of radius $R_{\rm ch} = 0.15$ was studied. Only events with $n_{\rm ch} = 1$ were accepted; this kept 48% of the signal.
6. The dilepton invariant mass, $M_{\ell^+\ell^-}$ was required to satisfy $|M_{\ell^+\ell^-} - M_Z| < 10\,\mathrm{GeV}$. This cut passed only 39% of the signal. Such a large signal reduction is somewhat surprising and the reason for it is still under study.

These cuts reduced the $t\bar{t}$ background, including punchthrough to the muon system from this source, to below the level of the irreducible background. The signal and irreducible background at this level are shown in Fig. 3.3-8. There are 103 signal events over a background of 62 in the mass range $600\,\mathrm{GeV} < M(e^+e^-\mu^+\mu^-) < 1100\,\mathrm{GeV}$. Finally, a

cut on the transverse momentum of the Z^0 bosons, $p_T(Z^0) > 150\,\mathrm{GeV}$, was made. This cut retained 37% of the signal, amounting to 96 signal events over a background of 41 from the $Z^0 Z^0$ background (see Fig. 3.3-9).

$\underline{Z'^0 \to e^+e^- \ (M_{Z'} = 4\,\mathrm{TeV})\ [16]}$

In principle, GEM's electromagnetic calorimetry makes possible a very precise measurement of the width and, modulo energy-scale uncertainties, the mass of a very heavy Z'^0 boson by studying its e^+e^- decay mode. In extended gauge models of the electroweak interactions, where the couplings are $O(e)$, one typically has $\Gamma_{Z'} \simeq 1 - 5\%\, M_{Z'}$. For $M_{Z'} \gtrsim 1\,\mathrm{TeV}$, the electron energy $E_e \gtrsim 500\,\mathrm{GeV}$ and only the 0.5% constant term in the EC resolution matters for the width and mass measurements. Naively, then, one would expect $\delta M_{Z'} \cong (0.5\%/\sqrt{2}) M_{Z'}$, smaller than $\sigma_{Z'} = \Gamma_{Z'}/2.35$.

For a multi-TeV Z'^0, with production cross section of several fb, it is clearly desirable to run at $10^{34}\,\mathrm{cm}^{-2}\,\mathrm{s}^{-1}$ in order to collect in a reasonable time the $O(1000)$ $Z'^0 \to e^+e^-$ events needed for a precision measurement of $\Gamma_{Z'}$. At ultrahigh luminosity and energy, several new issues must be faced:

1.) Mass resolution depends also on electron momentum pointing, which must be achieved either by the CT or by longitudinal segmentation in the EC.
2.) Pileup at $10^{34}\,\mathrm{cm}^{-2}\,\mathrm{s}^{-1}$ may degrade the EC resolution.
3.) The initial-state radiation accompanying high-mass Z'^0 production may degrade EC resolution. Here again, CT operation at $10^{34}\,\mathrm{cm}^{-2}\,\mathrm{s}^{-1}$ is important.
4.) Energy leakage from the EC into the HC is not completely negligible for multi-TeV electrons.

Our goal is that GEM should be able to distinguish two different Z'^0 models by using the e^+e^- mode to measure $\Gamma_{Z'}$. The two models studied here with FAST1 are those discussed in the LoI.

1. The LR model, in which $SU(2)_L \otimes SU(2)_R \otimes U(1)$ breaks down to $SU(2)_L \otimes U(1)$. The $SU(2)_R$ coupling was taken to be the same as the $SU(2)_L$ one. We call the extra Z-boson of this model Z_1.
2. A model in which the grand-unification group $SO(10)$ breaks down to $SU(5) \otimes U(1)$, then to $SU(2)_L \otimes U(1)$. Such a model may have an extra $Z'^0 \equiv Z_2$ well below the unification scale.

The left-and right-handed couplings to quarks and leptons in the two models are given

by [17]

$$g_{u\,L} = \beta/2\,, \quad g_{u\,R} = (\beta+\gamma)/2\,;$$
$$g_{d\,L} = \beta/2\,, \quad g_{d\,R} = (\beta-\gamma)/2\,;$$
$$g_{\nu\,L} = -3\beta/2\,, \quad g_{\nu\,R} = -(3\beta-\gamma)/2\,;$$
$$g_{\ell\,L} = -3\beta/2\,, \quad g_{\ell\,R} = -(3\beta+\gamma)/2\,.$$

The parameters are

$$\beta = 0.1043\,, \quad \gamma = -0.7545 \qquad \text{(Model 1)}$$
$$\beta = 0.1958\,, \quad \gamma = -0.3916 \qquad \text{(Model 2)}\,.$$

In calculating the Z'^0 decay widths, it is assumed that there are three generations of quarks and leptons and that right-handed neutrinos exist and are much lighter than $M_{Z'}$. The widths are given by

$$\Gamma(Z'^0 \to f_i\overline{f}_i) = \frac{2\alpha M_{Z'} C_i}{3\sin^2 2\theta_W}\left(g_{i\,L}^2 + g_{i\,R}^2\right)\,,$$

where $C_i = 3$ for quarks and 1 for leptons.

PYTHIA 5.5 was used to generate 1000 events of $Z'^0 \to e^+e^-$ for each the two models with $M_{Z'} = 4\,\text{TeV}$. The production cross sections were 7.2 fb for the Z_1 (LR) model and 5.6 fb for the Z_2 ($SO(10)$) model. The PYTHIA-generated widths were found to be:

$$\Gamma(Z_1) = 121.2\,\text{GeV}\,, \qquad \Gamma(Z_2) = 78.3\,\text{GeV}\,.$$

The $M_{e^+e^-}$ distributions for a perfect, full-acceptance detector are shown in Fig. 3.3-10(a,b) for the two Z'^0 models. The acceptance for electrons with $|\eta_e| < 2.5$ and $p_T > 500\,\text{GeV}$ was found to be 92%.

The principal physics background to $Z'^0 \to e^+e^-$ arises from QCD jet production, with the high-energy jets faking isolated electrons. The event rate is 250 pb for dijets with $3\,\text{TeV} < M_{\text{jj}} < 5\,\text{TeV}$, $|\eta| < 2.5$ and $p_T > 500\,\text{GeV}$. Thus, a rejection factor of less than 225 per jet is needed to remove the jet background completely from this mass region. This factor may be achieved using energy-ratio and isolation cuts.

The first rejection of the jet background comes from a cut on the energy ratio $\rho_{\text{EM}} = \sum_{R_{\text{EC}}} E_T^{ec} / \sum_{R_{\text{CA}}} E_T$. This ratio was studied for $R_{\text{EC}} \simeq 0.05$ (a 3×3 cluster of EC cells) and various R_{CA}. For signal events, it was found that ρ_{EM} is roughly independent of R_{CA} for $0.075 \leq R_{\text{CA}} \leq 0.225$. A cut at $\rho_{\text{EM}} = 0.8$ was made; this gives a QCD-jet rejection factor of 45.

Two features of $\rho_{\rm EM}$ are worth noting here. (1) The $\rho_{\rm EM}$-peak is slightly below one due to energy leakage from the EC into the HC. This leakage is typically 2–3% for $E_e \simeq 2\,\mathrm{TeV}$. Thus, even though this energy is relatively poorly measured in the HC, it does not degrade the overall resolution significantly. (2) There is a long, low tail below $\rho_{\rm EM} \simeq 0.8$ due to energy deposited in the HC by initial state radiation and pileup. These effects, which can degrade the mass resolution, are discussed below.

The isolation cut on the QCD-jet background is made using the variable

$$E_T^{\rm cut} = \sum_{R_2} E_T - 1.02 \sum_{R_1} E_T \,.$$

This is the transverse energy deposited in an annulus of the calorimeter of inner radius R_1 and outer radius R_2. The subtraction of an extra 2% of the energy in the small cone is intended to put a strict cut on pileup and other sources of degradation for the electron energy. Balancing the need to cut away jets while retaining electrons, the cone radii $R_1 = 0.075$, $R_2 = 0.225$ and $E_T^{\rm cut} = 20\,\mathrm{GeV}$ were chosen for the isolation cut. This gave a jet rejection factor of 2.8 while eliminating 20% of the $Z'^0 \to e^+e^-$ events.

These two cuts give an overall rejection of 1.6×10^4 on QCD jets. The rejection factor for $t\bar{t}$ jets is about 80, but these constitute only 0.1% of the QCD jets. Thus, these cuts completely remove the QCD-jet background in the resonance region. Approximately 20% of the $Z'^0 \to e^+e^-$ events are lost by these cuts. The choice of cut parameters is still being studied to optimize signal retention and background rejection.

Finally, it is necessary to consider the complications due to initial state radiation and pileup, both of which send particles in the direction of the electrons. Indeed, the initial-radiation jet tends to be correlated with one of the electrons because of the directional correlations between the radiation and the colliding quark and between the quark and the outgoing $e^\pm$. These effects can degrade the Z'^0 mass measurement both by depositing additional energy in the calorimeter and by making more difficult the determination of the electron direction by the tracker.

Information from the CT pad chambers was used to match the calorimeter shower position with the electron track. In this analysis, only those events were accepted which had exactly one hit in each of three pads close to the shower position. In this case a track position accuracy of a few 100 microns can be obtained, even at ultrahigh luminosity. The track-shower matching resolution of 1 mm in the (r, ϕ)-plane is dominated by the measurement of the electron shower position. The 3 mm resolution in the (r, z)-plane is dominated by vertex resolution. After the isolated track was matched with the shower, it was required to have $p_T > 50\,\mathrm{GeV}$. Approximately 12% of the $Z'^0 \to e^+e^-$ events were lost by these requirements.

Figure 3.3-11 shows the final $M_{e^+e^-}$ distributions expected in one SSCD for the two models. The acceptance of the $Z'^0 \to e^+e^-$ events at $\mathcal{L} = 10^{34}\,\mathrm{cm}^{-2}\,\mathrm{s}^{-1}$ is 61%. The measured widths for are

$$\Gamma_{\mathrm{meas}}(Z_1) = 125.9\,\mathrm{GeV}\,, \qquad \Gamma_{\mathrm{meas}}(Z_2) = 83.3\,\mathrm{GeV}\,.$$

The accuracy of the $\Gamma_{Z'}$ measurement in one SSCD is 5.4%. Thus, these measured widths are consistent with the true widths of 121.2 GeV and 78.3 GeV and clearly separate the two models. By way of comparison, the overall acceptance is 73% at $\mathcal{L} = 10^{33}\,\mathrm{cm}^{-2}\,\mathrm{s}^{-1}$ and the error on the width measurement in one standard SSCY is 14%.

Quark – Lepton Substructure via $\bar{q}q \to \mu^+\mu^-$ [18]

If quarks and leptons are composite entities with structure at the scale Λ, the most visible manifestation of this at subprocess energies $\sqrt{\hat{s}} \ll \Lambda^2$ is the presence of four-fermion contact interactions, $\mathcal{L}_\Lambda$, involving the composite quarks and leptons [19]. These interactions induce deviations of order $\pi\hat{s}/\Lambda^4$ from standard model predictions of dijet and dilepton production cross sections, leading to significant excesses at these "low" $\hat{s}$. It is known from experiments at e^+e^- and hadron colliders that $\Lambda \gtrsim 1-2\,\mathrm{TeV}$. Thus, $\mathcal{L}_\Lambda$ must be $SU(3)\otimes SU(2)\otimes U(1)$ invariant and the composite quark and lepton fields appearing in it are electroweak, not mass, eigenstates. It is technically natural to assume that all fermions are composite at the scale Λ and that $\mathcal{L}_\Lambda$ is at least symmetric under interchanges of the three generations of quarks and leptons. Then the Drell-Yan processes $pp \to \ell^+\ell^-$ have equal rates for electrons and muons (up to detector-related effects, of course). Modifications to $pp \to \mu^+\mu^-$ only are considered here. The few physics backgrounds to this process are easy to simulate and to eliminate.

The modifications to dimuon production can be observed in two ways: There will be an excess of events at high $M_{\mu^+\mu^-} = \sqrt{\hat{s}}$ [20] and there will be a deviation in the angular distribution of the outgoing μ^- relative to the incoming quark [21]. In [20] it was shown that a "perfect" SSC detector could, in one SSCY, detect a significant factor-of-two excess in the dimuon rate for a generic contact interaction with $\Lambda < 20 - 25\,\mathrm{TeV}$. In [21] it was determined that a perfect SSC detector could, in one SSCY, distinguish different chiral structures for the contact interaction for $\Lambda \lesssim 15\,\mathrm{TeV}$. Here we demonstrate GEM's potential for isolated muon processes at $10^{34}\,\mathrm{cm}^{-2}\,\mathrm{s}^{-1}$ by a one-SSCD study of two different chiral forms for the contact interaction arising from substructure at $\Lambda = 25\,\mathrm{TeV}$. The goal is to distinguish these two models by their muon angular distribution. Both models considered here received preliminary treatment in the GEM LoI [1].

In the first model considered, left-handed quarks and leptons are composite and the contact interaction is the product of two weak-isoscalar currents (the "ISO" model):

$$\mathcal{L}_{\rm ISO} = -\frac{4\pi}{\Lambda^2}\,\overline{Q}_{La}\gamma^\mu Q_{La}\,\overline{L}_{Lb}\gamma_\mu L_{Lb}\ ,$$

where $Q_{La} = (u_a, d_a)_L$ and $L_{La} = (\nu_a, \ell_a)_L$ are left-handed quark and lepton fields and $a, b = 1, 2, 3$ label generations. This interaction, together with the standard Drell-Yan processes, produces the subprocess cross section

$$\frac{d\hat{\sigma}(q_i\overline{q}_i \to \ell^-\ell^+)}{d(\cos\theta)} = \frac{\pi\alpha^2}{24\hat{s}}\,\left[A_i(\hat{s})\,(1+\cos\theta)^2 + B_i(\hat{s})\,(1-\cos\theta)^2\right]\ ,$$

where

$$\begin{aligned} A_i(\hat{s}) =& \left[\frac{\hat{s}}{\alpha\Lambda^2} + Q_i + \frac{4}{\sin^2 2\theta_W}\,(T_{3i} - Q_i\sin^2\theta_W)\,\left(\tfrac{1}{2} - \sin^2\theta_W\right)\left(\frac{\hat{s}}{\hat{s}-M_Z^2}\right)\right]^2 \\ &+ \left[Q_i + Q_i\tan^2\theta_W\left(\frac{\hat{s}}{\hat{s}-M_Z^2}\right)\right]^2; \end{aligned}$$

$$\begin{aligned} B_i(\hat{s}) =& \left[Q_i - \frac{1}{\cos^2\theta_W}\,(T_{3i} - Q_i\sin^2\theta_W)\left(\frac{\hat{s}}{\hat{s}-M_Z^2}\right)\right]^2 \\ &+ \left[Q_i - \frac{1}{\cos^2\theta_W}Q_i\,\left(\tfrac{1}{2} - \sin^2\theta_W\right)\left(\frac{\hat{s}}{\hat{s}-M_Z^2}\right)\right]^2. \end{aligned}$$

Here, $\sin^2\theta_W = 0.23$, $(T_{3i}, Q_i) = (\frac{1}{2}, \frac{2}{3})$ for $q_i = u_i$ and $(-\frac{1}{2}, -\frac{1}{3})$ for $q_i = d_i$, and it is assumed that $\hat{s} - M_Z^2 \gg M_Z\Gamma_Z$. The angle θ is between the direction of the incoming quark and the outgoing ℓ^- in the subprocess center-of-mass (cm) frame. At large $\hat{s}$, the angular distribution of ℓ^- relative to q_i is approximately $(1+\cos\theta)^2$.

The second case studied involves a helicity nonconserving contact interaction (the "HNC" model) given by

$$\mathcal{L}_{\rm HNC} = \frac{4\pi}{\Lambda^2}\,\epsilon_{ij}\overline{Q}_{Lia}u_{Ra}\,\overline{L}_{Ljb}\ell_{Rb} + \text{hermitian conjugate}\ ,$$

where $i, j = 1, 2$ label indices in an electroweak doublet and $\epsilon_{12} = -\epsilon_{21} = 1$. This interaction is theoretically unlikely because it is not invariant under separate transformations on left- and right-handed fields with the same the color and electric charge. It is studied here because it generates an angular distribution that becomes isotropic at large $\hat{s}$:

$$\frac{d\hat{\sigma}(u_i\overline{u}_i \to \ell^-\ell^+)}{d(\cos\theta)} = \frac{\pi\alpha^2}{24\hat{s}}\,\left[A_u(\hat{s})(1+\cos\theta)^2 + B_u(\hat{s})(1-\cos\theta)^2\right] + \frac{\pi\hat{s}}{12\Lambda^4}\ ,$$

where $A_u(\hat{s}) = \lim_{\Lambda\to\infty} A_{i=u}(\hat{s})$ and $B_u(\hat{s})$ were given above for the ISO model.

It is clear from the cross sections above that powerful information on the chiral structure of the contact interaction can be obtained by measuring the muon's angular distribution in the subprocess cm frame. For this measurement, one must determine the muons' charges, the incoming quark's direction and the subprocess frame itself. The criterion that the muon charges are known is conservatively taken to be $\Delta p_T/p_T < 40\%$ for *both* muons. The muon rapidities, $\eta_{\mu^\pm}$, are used to determine the μ^- angular distribution, as described next.

First, define the "boost rapidity", $\eta_B = \frac{1}{2}(\eta_{\mu^-} + \eta_{\mu^+})$. For events with $M_{\mu^+\mu^-} > 2\,\text{TeV}$, assume that the quark direction is determined by the sign of η_B. Next, define the angle θ^* by

$$\cos\theta^* = \text{sgn}(\eta_B)\,\tanh\left(\frac{\eta_{\mu^-} - \eta_{\mu^+}}{2}\right).$$

If one may ignore the transverse motion imparted to the subprocess frame by initial state radiation and if the quark is harder than the antiquark, it follows that $\eta_B = \pm\frac{1}{2}\ln(x_q/x_{\bar{q}})$ and $\cos\theta^* = \cos\theta$. Here, x_q is the fraction of its parent proton's momentum carried by the quark and the sign depends on whether the quark is moving to right(+) or the left(−).

To address the question of initial state radiation, the true, unsmeared transverse momentum distribution $|\vec{p}_{T_1} + \vec{p}_{T_2}|$ for the two highest-p_T muons was studied for the ISO model with $\Lambda = 25\,\text{TeV}$. Events were generated with (unsmeared) $M_{\mu^+\mu^-} > 2\,\text{TeV}$ and $p_T^\mu > 160\,\text{GeV}$ and were then required to have at least two muons with $|\eta| < 2.5$ accepted by the FAST1 MU simulation. About 55% of the events have $|\vec{p}_{T_1} + \vec{p}_{T_2}| < 100\,\text{GeV}$ and 70% have $|\vec{p}_{T_1} + \vec{p}_{T_2}| < 200\,\text{GeV}$. These proportions are unchanged by the event selections made to enhance the substructure signal. Thus, the effect of initial radiation on the motion of the subprocess cm frame can be neglected for $M_{\mu^+\mu^-} > 2\,\text{TeV}$.

A parton model study of the probability that the quark is harder than the antiquark was carried out using the EHLQ Set 1 distribution functions [20]. To the extent that initial state radiation can be ignored, this is also the probability that $\cos\theta^* = \cos\theta$. For $M_{\mu^+\mu^-} > 2\,\text{TeV}$, it was found that $x_q > x_{\bar{q}}$ at least 75% of the time. So long as the experiment can collect enough events with well-measured muons, this is quite adequate to distinguish the angular distributions of the ISO and HNC models.

PYTHIA 5.5 was used to generate 1500 events each for the standard Drell-Yan and substructure models with $\Lambda = 25\,\text{TeV}$ [22]. These events had true $M_{\mu^+\mu^-} > 2\,\text{TeV}$ and $p_T^\mu > 160\,\text{GeV}$, the minimum p_T for a muon at $|\eta| = 2.5$. Pileup noise in the calorimeter corresponding to $10^{34}\,\text{cm}^{-2}\,\text{s}^{-1}$ was included in FAST1. The cross section for these processes were found to be $\sigma_{\text{DY}} = 3.38\,\text{fb}$, $\sigma_{\text{ISO}} = 11.0\,\text{fb}$ and $\sigma_{\text{HNC}} = 8.90\,\text{fb}$.

Signal events were processed through FAST1 and the two highest-p_T muons in each event with $|\eta| < 2.5$ were selected. A cut of $p_T > 20\,\mathrm{GeV}$ was imposed to eliminate events in which the second highest-p_T particle in the muon system was a muon from π/K decay. No other constraints (such as charge identification) were imposed. The numbers of events produced per SSCD that remain at this stage are 230 (DY), 765 (ISO) and 630 (HNC), corresponding to acceptances of 70%. Of these events, at least 95% had identified opposite sign dimuons ($\Delta p_T/p_T < 40\%$).

Non-physics backgrounds to the dimuon signal include π and K decays in flight and other sources of punchthrough. As noted, FAST1 allows for π/K decays in flight, but only at $\mathcal{L} = 10^{33}\,\mathrm{cm}^{-2}\,\mathrm{s}^{-1}$. Nevertheless, they are not a serious background to multi-TeV muon detection. Punchthrough rates are discussed in Chapter 2.3 of this report. Most serious for the measurement of multi-TeV muons are the showers produced by muon energy loss near the back of the calorimeter. The identification and measurement of muons with $1\,\mathrm{TeV} < p_T 3\,\mathrm{TeV}$ was studied with a hit-level Monte Carlo for $\mathcal{L} = 10^{33}\,\mathrm{cm}^{-2}\,\mathrm{s}^{-1}$. This study is identical to the one carried out for inclusive muons from b-quarks originating from t-decay (section 3.3.2 above) and the results are the same: The probability that a muon shares three or fewer cells with another track is 90%, as is the probability that there are hits in three or fewer neighboring cells along the muon's trajectory. This result is not expected to change significantly at ultrahigh luminosity. Thus, a conservative estimate for the dimuon measurement efficiency is 80%. This efficiency was not included in the final event rates quoted below.

Physics backgrounds to the Drell-Yan process come from $t\bar{t}$ production, $b(\bar{b}) + g \to t(\bar{t}) + W$, and W^+W^- production. For $t\bar{t}$, tW and WW invariant masses greater than 2.5 TeV and $p_T(t, W) > 125\,\mathrm{GeV}$, the total cross sections are $\sigma(t\bar{t}) = 9.36\,\mathrm{pb}$, $\sigma(t/\bar{t}+W) \simeq 0.13\,\mathrm{pb}$, and $\sigma(W^+W^-) \simeq 0.03\,\mathrm{pb}$ [23]. Only the $t\bar{t}$ background is of any importance.

PYTHIA 5.5 was used to generate 400K $t\bar{t} \to \mu^+\mu^- + X$ events with $M_{t\bar{t}} > 2.5\,\mathrm{TeV}$, $p_T(t) > 125\,\mathrm{GeV}$, $M_{\mu^+\mu^-} > 2\,\mathrm{TeV}$, and $|\eta_\mu| < 2.5$. For a total $t\bar{t}$ cross section of 9.36 pb, W-boson decays will produce 11.6K dimuons in one SSCD. Of these, only 62 events were found with $M_{\mu^+\mu^-} > 2\,\mathrm{TeV}$ and $|\eta_\mu| < 2.5$. The angular distribution of these muons is sharply peaked at $\cos\theta^* = 1$, reflecting the fact that the high-energy muons follow the parent t-quarks which themselves have an angular distribution sharply peaked in the beam direction. These events are completely removed by the isolation cut on the muons

$$\sum_{R=0.5} E_T - E_T^\mu \leq 25\,\mathrm{GeV} + 0.02\,E_T^\mu\,.$$

Four $t\bar{t} \to \mu^+\mu^-$ events with $M_{\mu^+\mu^-} > 2\,\mathrm{TeV}$ were found to pass this cut. Only one event of this sample has $M_{\mu^+\mu^-} > 2.5\,\mathrm{TeV}$.

Figure 3.3-12 shows the standard and modified dimuon mass distributions for isolated, identified $\mu^+\mu^-$ with $M_{\mu^+\mu^-} > 2.5\,\text{TeV}$. The numbers of events for each model are 92 (DY), 440 (ISO) and 390 (HNC), corresponding to only 27% of the original DY sample, but 70% of the ISO and HNC samples. The $\cos\theta^*$ distributions comparing DY with ISO and with HNC are shown in Figs. 3.3-13(a) and 3.3-13(b). The high-energy expectations of a $(1+\cos\theta^*)^2$ distribution for the ISO model and a flat distribution for the HNC model are evident in these figures. Departures from the pure forms are due almost entirely to the 25% misidentification of the quark direction and the uderlying Drell-Yan background. The forward-backward asymmetry for DY and the two substructure models are

$$A_{FB}(\text{DY}) = 0.268 \pm 0.101$$
$$A_{FB}(\text{ISO}) = 0.316 \pm 0.045$$
$$A_{FB}(\text{HNC}) = 0.131 \pm 0.050\,.$$

Clearly, the two substructure models are separated from the standard model and from each other. Preliminary studies indicate that $\Lambda \simeq 40 - 50\,\text{TeV}$ can be reached in one SSCD. Such scales generate a 50% excess (5σ statistical) over the Drell-Yan expectation.

3.3.4 Missing Energy Signals

For a variety of possible SSC physics signatures it is important to measure the missing transverse energy $\not{E}_T$ in the range $\not{E}_T \gtrsim 100\,\text{GeV}$. The forward calorimeter is crucial for this, since without it the $\not{E}_T$ cross section would be dominated by missing jets.

The calorimeter parts of the FAST1 simulation were used for this analysis. For the forward calorimeter, FAST1 calculates a smeared transverse momentum for each particle based on a parameterization of results from a full GEANT simulation. For the central calorimeter it includes the energy resolution, the average transverse shower shape, energy sharing between the electromagnetic and hadronic sections, and electronic noise, and pileup treated as an additional noise term. The transverse spreading could cause energy to leak beyond the edge of the calorimeter at $\eta = 3$. This has not yet been included in FAST1, but an earlier GEANT simulation showed that this leakage is well enough measured by the forward calorimeter that it does not significantly degrade the $\not{E}_T$ resolution. [24] Therefore, leakage beyond $\eta = 3$ was added to the last bin of the calorimeter and assumed to be correctly measured with the usual energy resolution.

Search for a 300 GeV Gluino Using Jets and $\not{E}_T$

For the gluino analysis the minimal supersymmetric extension of the standard model (MSSM) was assumed with two Higgs doublets and superpartners of all the standard

particles, including four neutralinos $\widetilde{\chi}_i^0$ and two charginos $\widetilde{\chi}_i^\pm$. [20] If the gluino is lighter than the squarks, then it will decay into $q\bar{q}\widetilde{\chi}_i^0$ or $q\bar{q}'\widetilde{\chi}_i^\pm$; the $\widetilde{\chi}$'s will in turn decay via a cascade until the lightest supersymmetric particle $\widetilde{\chi}_1^0$ is reached. This is stable and escapes from the detector, giving a $\not{E}_T$ signature. Other signals such as like-sign dileptons are also possible.

As in the GEM LOI analysis, all of the decay modes were calculated assuming a gluino mass $M_{\widetilde{g}} = 300\,\mathrm{GeV}$, a supersymmetric Higgs mass $\mu = -300\,\mathrm{GeV}$, and a ratio of vacuum expectation values $\tan\beta = v_2/v_1 = 2.0$. The squark masses were taken to be 600 GeV. Gluino pair production and decay were simulated using ISAJET 6.43. Since the gluinos will typically be produced with $p_T \sim M_{\widetilde{g}}$, one expects a signal with multiple jets plus large $\not{E}_T$. The dominant physics background for this signal comes from missing neutrinos from heavy quarks. It was shown in the LOI that the other physics backgrounds, e.g., $Z \to \nu\bar{\nu}$ at high p_T, are negligible in this mass range, although they do contribute for higher gluino masses. In addition there are detector-induced backgrounds from mismeasured jets.

ISAJET 6.43 was used to generate 10K gluino signal events, including all the decays of the MSSM, and 1.8M QCD jet events distributed in ten bins covering $50 < p_T < 1600\,\mathrm{GeV}$. Other than the minimum p_T of the hard scattering, no preselection of the events to contain real missing energy was made. This is necessary to obtain the correct cross section for mismeasured jets. All events were run through the FAST1 simulation, $\not{E}_T$ was calculated as described above, and jets were found using a fixed-cone algorithm with $R = 0.7$.

In the inclusive $\not{E}_T$ cross section the background is large compared to the signal. To reduce the background, at least four jets with $p_T > 75\,\mathrm{GeV}$ were required in the central calorimeter. Jets in the forward calorimeter are not used, so its ability to recognize them is not an issue. In addition the sphericity in the transverse plane S_T was calculated from the central calorimeter cells with $E_T^{\mathrm{cell}} > 0.5\,\mathrm{GeV}$, and a cut $S_T > 0.2$ was made. After these cuts the signal to background ratio S/B is about 2 for $\not{E}_T \sim 250\,\mathrm{GeV}$.

Semileptonic decays of gluinos would of course be important to study; for example, isolated like-sign dileptons $\ell^\pm\ell^\pm$ provide a signal for the Majorana nature of the gluino. However, making a lepton veto further improves the S/B for the $\not{E}_T$ distribution. Events were vetoed if they contained a muon or an isolated electron with $p_T > 20\,\mathrm{GeV}$ and $\eta < 2.5$. Isolated electrons were defined by requiring that the total energy in the electromagnetic and hadronic calorimeter in a cone $R = 0.1$ match the momentum, $|E/p - 1| < 0.1$. This effectively combines a HC/EC cut and an EC/p cut. It is intended to select those electrons which could plausible be identified, mainly those from direct t decay. The efficiency of the lepton identification has not been simulated in detail in this study, but it cannot be very crucial, since even if it were perfect there still would be remaining background from τX

decays of b's and t's. The signal and background remaining after these cuts are shown in Fig. 3.3-14(a). The ratio $(S+B)/B$ is shown in Fig. 3.3.-14(b) and reaches about 5 for the GEM baseline calorimeter.

Fig. 3.3.-14(b) also shows the $(S+B)/B$ ratio obtained using the same cuts but calculating $\not{E}_T$ from the the missing ν and $\tilde{\chi}_1^0$ momenta. While the GEM calorimeter increases the background at low $\not{E}_T$, it provides reasonable agreement with the perfect detector result in the region for which the ratio is large.

The statistical significance of the signal is not an issue. The t, W and Z backgrounds can be checked using isolated lepton samples; the b and c backgrounds can be checked using muons in jets. The $\not{E}_T$ resolution of the detector can be checked using inclusive data on QCD jets and $\gamma+$jets events. Given all these constraints, the background should be reliably known, so observation of a $\not{E}_T$ cross section 5 times that expected from the standard model should be very convincing.

Search for a 300 GeV Gluino Using Jets and $\ell^\pm\ell^\pm$

In addition to the $\not{E}_T$ signature described above, there are many other signatures for supersymmetry. In particular, since the gluino is a self-conjugate Majorana fermion, gluino pairs can give isolated $\ell^\pm\ell^\pm$ pairs. Observing these likesign pairs is essential for understanding the nature of any $\not{E}_T$ signal [26]. The dominant standard model background is expected to be from $t\bar{t}$ events in which either a $\overset{(-)}{b} \to \ell X$ lepton appears isolated or an isolated lepton sign is wrongly determined. Since the cross section for a 300 GeV gluino is large, one can rely just on $\mu^\pm\mu^\pm$ events, for which the signs are well determined in GEM. Nevertheless it seems useful to see whether $e^\pm e^\pm$ can also be observed in GEM.

ISAJET 6.43 was used to generate 10K events each of the $\tilde{g}\tilde{g}$ signal and $t\bar{t}$ background using the same minimal supersymmetric model parameters as in the previous section. The gluino pairs were forced to decay into $\tilde{W}^-\tilde{W}^-X$ and thence into e^-e^-X. The $t\bar{t}$ pairs were forced to decay by $t \to b$, $b \to e^-X$, and $\bar{t} \to e^-X$. The additional background from $t\bar{t}$ events in which the lepton sign was wrongly deterimined was found to be small, since the electrons from the gluinos typically have $p_T \lesssim 200\,\mathrm{GeV}$ whereas the tracker provides good sign selection up to $p_T \approx 400\,\mathrm{GeV}$.

The events were then simulated using FAST1. Pileup and noise at $\mathcal{L} = 10^{33}\,\mathrm{cm}^{-2}\mathrm{sec}^{-1}$ were included using the calorimeter simulation CALOED. Jets were found using CJETS with $R = 0.7$, and at least four jets with $p_T > 40\,\mathrm{GeV}$ in the central calorimeter ($\eta < 3$) were required. Electrons were called isolated if after detector simulation they had an additional hadronic energy $E_{\mathrm{had}} < 5\,\mathrm{GeV}$ in a cone $R = 0.3$, and at least two isolated electrons with $p_T > 10\,\mathrm{GeV}$ and $\eta < 2.5$ were also required. Since this cut was made on

total rather than transverse energy, it is quite severe in the forward direction. Isolated electrons were assumed to be identified with perfect efficiency; this is believed to be a reasonable approximation and in any case should affect signal and background equally. Such electrons were removed from the jets found by CJETS by vetoing any jet with $R < 0.5$ from an electron. No cut was made on $\not{E}_T$.

After these cuts, 2212/10000 like-sign pairs from the gluino events and 61/10000 like-sign pairs from the $t\bar{t}$ events survived. When the production cross sections and branching ratios are taken into account and different charges are summed, this corresponds to 6.6×10^4 signal events and 2.1×10^4 $t\bar{t}$ background events accepted per year, giving $S/B = 3.1$ after only minimal optimization of the cuts. Work to refine the cuts is continuing, but it is already clear that GEM can observe a 300 GeV gluino in the $e^{\pm}e^{\pm}$ channel.

<u>Search for $H \to ZZ \to \ell^+\ell^-\nu\bar{\nu}$</u>

For a standard model Higgs with $M_H \gtrsim 600$ GeV the rate for $H \to \ell^+\ell^-\ell^+\ell^-$ becomes small, and other modes need to be considered. The mode $H \to \ell^+\ell^-\nu\bar{\nu}$ has six times the branching ratio. The most serious background to detection of this mode is from the QCD production of Z^0 + jets, and discrimination is based on the $\not{E}_T$ of the event. This makes the measurement very sensitive to the calorimeter coverage at high eta. ISAJET 6.46 was used to generate 10000 Higgs events with $M_H = 800$ GeV and 50000 Z^0 + jets events in five p_T ranges covering $50 < p_{T,Z} < 1600$ GeV.

The signal and background events were first analyzed for perfect detector coverage up to $\eta = 5.5$. In this analysis, neutrinos were excluded, and muons were considered to deposit 3 GeV equivalent in the calorimeter. The events were also analysed using the GEM FAST1 simulation routines. Specifically, for this study FCSMEAR was used to give the response in the forward calorimeter, and MUFAST was used to give the muon detector response. The forward calorimeter studied here was the tungsten and liquid argon option of the current GEM baseline detector. The full machinery of the central and endcap parameterization, CALO, was not needed because this measurement is insensitive to central calorimeter segmentation, but the CALO energy response functions were used for $\eta < 3.0$. In the current study, only the mode $Z^0 \to e^+e^-$ was analyzed.

The analysis began by reconstructing the Z^0 and making a loose requirement that the mass be within 20 GeV of M_Z. The reconstructed Z^0's were required to have a $p_T >$ 350 GeV and be centrally produced with $\eta < 1.5$. In Higgs events, then, this sample has a large $\not{E}_T$, whereas Z^0 + jets events exhibit jet activity on the side opposite the Z^0. The separation is not perfect because the Higgs events have spectator jets which balance the Higgs p_T, and because in Z^0+jets events the jets occasionally fluctuate to produce high-p_T neutrinos.

To characterize the jet activity, the scalar p_T of all particles in the semi-cylinder opposite the Z^0 is summed. Using this broad angular range allows for the p_T of the Higgs, which is typically of order 100 GeV. This summed scaler p_T is shown for a perfect detector in Fig. 3.3.-15. The signal events lie at low p_T and are uncontaminated by background up to 360 GeV. There are 38 events for one SSC year at $\mathcal{L} = 10^{33}\,\mathrm{cm}^{-2}\mathrm{sec}^{-1}$ up to this cut. The same sample of events is shown after processing with the GEM FAST1 simulation in Fig. 3.3.-16. The more realistic coverage at high eta has degraded the measurement at low p_T, but it is possible to apply a cut at 120 GeV and have an uncontaminated sample of 22 signal events in one SSC year.

Future work in this area includes study of the liquid-scintillator forward calorimeter option, further optimization of the liquid argon design, study of the $Z^0 \to \mu^+\mu^-$ modes, and finally, using the full GEM GEANT detector simulation to incorporate effects such as p_T crossover in the $\eta \approx 3$ transition region. Backgrounds due to $gg \to ZZ$ and $q\bar{q} \to ZZ$ will also be considered. The emphasis of the current study was to determine the effect of the p_T response of the GEM baseline design on detection of a massive Higgs in this mode. The baseline design seems adequate to detect the signal with an acceptable tightening of the cuts compared to an idealized detector.

3.3.5 Jet Energy Measurement and the Calorimetric e/h Response

Although detectors have grown more sophisticated, the signal for compositeness has remained the same: a surplus of hard scattering events with large p_T. The model for the four-quark contact interaction used here is essentially the one discussed in Ref. [20], except that all quarks are considered to be composite and, as in our discussion of quark-lepton substructure signals, the interaction is flavor-conserving. The energy scale at which the quarks start to behave as composite particles is characterized by the variable Λ where $\Lambda =$ infinity corresponds to no substructure. PYTHIA 5.5 was used to generate the jet events for QCD and the quark substructure signal [22]. Similar models, with $\Lambda < 950$ GeV have been eliminated by CDF [27].

It was decided to see how large a value of Λ could be ruled out by taking a year's worth of data at a luminosity of 10^{33}. The methodology is outlined below.

- Establish trigger requirements
- Set jet clustering algorithm
- Identify and eliminate backgrounds
- Collect inclusive jet E_t spectrum in high p_T (signal region). Save jet for every event so that various systematic errors can be addressed.

- Compare spectrum with results using various compositeness scales.

Trigger requirements

Jet physics dominates the high p_T cross section. For a $\sum p_T$ requirement of 1600 GeV, $|\eta_{jet}| < 3.0$, the total cross section is 1.2E-6 mb. Running at 10^{33} gives a trigger rate of 1.2/s, a reasonable rate which would need no prescaling. Naturally the events in this study must be generated with a higher p_T cut, since the the 30 million expected in an SSC year cannot be simulated in a reasonable amount of time. Roughly speaking, this corresponds to generating events only in the signal region. In the real experiment, the lower part of the spectrum would be used to normalize out uncertainties in the luminosity, which would probably be of order 10%.

Event selection and jet clustering

We define inclusive jet production as the process $pp \rightarrow$ JET + X, with $|\eta| < 3.0$, the nominal coverage of the GEM calorimeter. While it is true that most of the composite signal is at central η, the extremely high jet p_T cut, 2.5 TeV, keeps the jets far from the beam pipe. The jet clustering is done with a fixed cone algorithm, where all cells within an $\eta - \phi$ radius of .7 from the jet center are included.

Detector energy scale and resolution

For any reasonable detector, energy resolution is not a terribly important issue in a compositeness search. Its main effect is to change very slightly the shape of the jet p_T curve. The more important issue is the jet energy scale, which, for the GEM calorimeter, is, quite simply, unknown. In particular, one needs to know how non-linear the response might be from 100 GeV up to 5 TeV. High p_T jets whose p_Ts drift upward can easily fake a compositeness signal.

The non-linear response of calorimeters to jets can be understood in terms of a simple model. Suppose that a calorimeter is divided into an electromagnetic and a hadronic section and that the relative response of each to electromagnetic (π^0s and ηs) and hadronic (mainly charged pions) is given by e/h_{em} and e/h_{ha}. Typical values of e/h range from from 1 (a so-called compensating calorimeter) to 2 (in the case of barium fluoride) or more. The electromagnetic calorimeter is calibrated with electrons and the hadronic calorimeter with charged pions which are mimimum-ionizing in the electromagnetic calorimeter. " Jet calibrations" can be made by having a proton slam into a steel bar and looking at the calorimeter's response to the multi-particle event.

Suppose that the electromagnetic calorimeter is made of barium fluoride ($e/h = 2$), and the hadronic calorimeter is a matrix of copper and scintillating fiber ($e/h = 1$). For low

energy jets, much of that energy is left in the electromagnetic calorimeter. The response of the electromagnetic calorimeter will be low. If the electromagnetic calorimeter is required get a hadron's electromagnetic energy right, and since $e/h_{em} = 2$ the hadronic part of that hadron's shower will be underweighted. As the jet and average particle energy increase, two effects must be considered. The first is that the average fraction of π^0s in a charged pion shower increases. For charged pions which shower in the electromagnetic calorimeter, this means that the response becomes enhanced and more nearly reflects the true charged pion energy. The increase in average particle energy also means that the charged pion showers reach further into the hadronic calorimeter, which has the same effect. Of course, the detector can be calibrated at any available energy, but at energies far from its calibration point the response of the calorimeter will be inaccurate.

However, Wigmans and Paar have shown, that in the case of a detector with a non-compensating electromagnetic section and compensating hadronic section, it is possible to construct a simple algorithm with which to correct jet energies [28]. See Figure 3.3-17. The y axis is the energy left by a jet in the electromagnetic calorimeter, and the x-axis, the total energy in both electromagnetic and hadronic sections. In both calorimeters, the energy response is normalized, arbitrarily, to the hadronic component of the hadronic shower. Within a few percent, the coordinates for jets of a given energy lie tightly clustered about the line connecting the points $(E_{jet}, 0)$, where all the energy is left in the compensating hadronic calorimeter and $(2{*}E_{jet}, 2{*}E_{jet})$ where the jet fluctuates into all π^0s and its energy is left in the non-compensating barium fluoride detector. Spread along the line is caused by fluctuations in the jet's multiplicity, fluctuations in the jet's π^0 fraction and fluctuations in shower development. Changing the fragmentation function moves the cluster of points along the line. One line is associated with each true jet energy, which can be obtained, again to a few percent, by extrapolating back along a line of slope e/h_{em}. Thus, knowing the relative amount of energy left in the electromagnetic and hadronic sections, one can make a good guess as to the true jet energy. Moreover, muliparticle events created in test beams can be used to calibrate these sets of lines, despite the fact that such events do not have the same fragmentation properties as true jets, because at a given energy, the real and phony jets will lie along one and the same line. This feature is particularly important in the event that a test beam of several TeV is available at the SSC. In that case, the few percent non-linearities mentioned above can be calibrated out.

If the hadronic section of the calorimeter is also noncompensating, the responses to jets of a given energy are again tightly correlated, but no longer lie along a straight line. Moreover, the extrapolation of this curve toward the horizontal axis, which corresponds to a change in fragmentation function, depends on the details of that fragmentation function.

Multiparticle events therefore cannot be used to simulate jets.

However, a non-compensating calorimeter cannot be dismissed out of hand. It has been stated that compensation is unnecessary on the grounds that current uncertainties in the structure functions produce larger uncertainties in the inclusive jet p_T spectrum than the distortions produced by a non-compensating calorimeter. It has also been suggested that like CDF, the GEM collaboration can create its own jet energy correction scheme, perhaps even with the help of the SDC tracker.

There are two objections to the first argument. One is that our knowledge of the structure functions is likely to improve in the next 10 years, particularly as results come in from HERA. The second is that the distortions of the jet p_T distribution produced by a non-compensating calorimeter depend on the chosen fragmentation function, which as we've noted, is completely unknown for jets at SSC energies. It could be better or worse.

The objections to the second argument are simple practical ones. Does GEM wish to invest an enormous amount of manpower in creating a jet energy correction function, as CDF did? That correction function was several years in the making and while fairly well-tested, has not received the critical attention it might have had CDF seen evidence of a compositeness signal.

Eliminating backgrounds

It may seem strange to talk about backgrounds to a QCD process, but since a compositeness signal may consist of a relative handful of events, the high p_T part of the spectrum must be clean. The main background is cosmic ray bremsstrahlung, which can be removed by eliminating events with a lot of out-of-time energy, showers with unusual energy deposition, and, in general, events with large missing p_T.

Jet energy correction

A full experimental analysis would include the development of a jet energy correction function and an unsmearing procedure for the the inclusive p_T spectrum. The jet correction function would include underlying event, energy-out- of-the-clustering-cone and detector noise corrections. While these corrections are reasonably well-understood, they are not very important for high p_T jets. The most important issue is the uncertainty in the GEM jet energy scale, of which very little is known and since the FAST1 simulation does not include separate responses to the electromagnetic and hadronic parts of hadron showers, using it to create such a correction function would not be realistic. The jet p_T spectra were not corrected. Instead, the raw p_T spectra, made by running events (with and without compositeness) through our detector simulation were compared. The effect an incorrect energy scale was assessed by its effect on these same raw spectra.

Generating the data

In the real experiment, there would be several $\sum p_T$ triggers, all but the highest of which would be prescaled. Presumably the region covered by the prescaled triggers would be used for normalization, while that covered by the highest would be the (possible) signal region. Our run size was set so that we could generate all the events in 1 day - about 20,000. This is roughly 1/500th of the high p_T events one would collect in an SSC year. Our $\sum p_T$ threshold (4.8 TeV) was therefore set such that the corresponding cross-section was 1/500th of that at the SSC. Compositeness signals were sought in the jet p_T spectrum above 2.5 TeV.

Analysis

The analysis of the data is very simple. The principal task is to calculate a χ^2 based on the statistical error, that is, to estimate how likely are the various finite Λ spectra, given the expected infinite-Λ spectrum which is measured. For large bin contents (about 30) the statistical error is adequately given by the familiar Gaussian form but for a few thinly populated bins, Poisson errors are required. To assess the effect of systematic energy measurement, the finite-Λ data were rescaled, rebinned and re-examined.

Results

Events were run at various compositeness scales: 22.5, 25.0, 27.5 and 30.0 TeV as well as infinity, i.e. no compositeness. Figure 3.3-18 shows the total cross section for jets above 2.4 TeV computed using the EHLQ set I (1986 revised) structure functions. Above 22.5 GeV the variation in total cross section is much smaller than the anticipated uncertainty in luminosity. Also plotted are the Λ = infinity total cross sections for the Duke-Owens I and Morfin-Tung I structure functions. The long extrapolation in q^2 results in large uncertainties.

Figure 3.3-19 shows the inclusive p_T distribution for jets made by simply clustering the final-state particles produced by PYTHIA. Neutrinos are ignored. The upper, dashed curve is Λ = 22.5 TeV, the middle, dotted curve is Λ = 27.5 TeV and the bottom, solid curve is Λ = infinity. If we ignore structure function uncertainties, it is clear that barring severe detector effects, a compositeness signal with scale Λ = 22.5 TeV should be quite obvious. A comparison of each compositeness curve with the no-compostiteness curve, using the χ^2 described above is shown in Table 3.3-4. With the usual criterion that a theory is only rejected if the χ^2 is 3 or 4 σ out on the tail, Λ = 22.5 TeV appears easy to eliminate. Elininating Λ = 25 TeV in one SSCY is borderline, while 27.5 TeV and 30 TeV appear out of reach.

Λ (TeV)	χ^2
22.5	207
25	104
27.5	44
30	53

χ^2 for p_T distributions with various Λs. PYTHIA particle clustering only. 25 degrees of freedom.

Detector effects

The FAST1 program was used to simulate the calorimeters. FAST1 employs the Bock parameterization to describe the longitudinal development of showers and spreads the energy transversely with two Gaussians: a narrow one for electromagnetic energy and a wider one for hadronic energy. The size of energy fluctuations is determined by particle type: the response to electrons and photons varies as the electromagnetic resolution and the response to hadrons varies as the hadronic resolution, whether the hadronic shower begins in the hadronic calorimeter or not. The detectors are almost featureless apart from a small section of degraded resolution in the liquid argon electromagnetic section. Detector non-linearities are not modeled.

The p_T spectra for PYTHIA particle clustering and two detector resolutions, 50% and 75% over the square root of the energy are compared in Fig. 3.3-20. Since there is very little difference between the liquid argon and scintillating fiber calorimeters as modeled in FAST1, only the liquid argon option was studied. As the only difference between the two is a little energy smearing and the loss of the odd muon in the latter two cases, it is not surprising that they're all quite similar. The corresponding χ^2 for detector clustering (50% smearing) and various compositeness scales are listed in Table 3.3-5. Energy smearing by itself will not fake a compositeness signal.

Λ (TeV)	χ^2
22.5	218
25	118
27.5	48
30	53

χ^2 for p_T distributions with various Λs, simulated jets in the GEM calorimeter

Non-linearities are a different matter. If we take the no-compositeness spectrum and boost all the jet energies by 10% we have a curve that looks like that for $\Lambda = 25$ TeV; see Fig. 3.3-21. As mentioned above, such distortions could result if our detectors are only calibrated at low energy or, in the case of a totally non-compensating calorimeter, the

fragmentation function at high jet p_T is very different from that expected.

Structure Functions

As mentioned above, we ran with two sets of structure functions which gave very different results for the high p_T cross section. In Fig. 3.3-22 we plot the relative jet p_T distribution for the EHLQ set I and Duke-Owens structure functions. The increase in cross section is comparable to that produced by a compositeness scale of $\Lambda = 15$ TeV.

Conclusion

The reach of the GEM calorimeter in searching for compositeness signals has been investigated with the help of the FAST1 detector simulation. If structure function uncertainties are small at the SSC, then a compositeness scale of 22.5 TeV should be quite obvious. The search for compositeness is essentially a counting experiment and, if CDF experience can be used as a guide, any compositeness limit will be set principally on the basis of statistics, as statistical errors should dominate over systematic errors at high p_T. FAST1 provides no insight as to whether or not this will be the case but simple arguments demonstrate how dangerous a misestimated jet energy scale can be. A compensating calorimeter may not be absolutely required for the measurement but would make it considerably easier and, in the event of a signal, would make the result far more credible.

Figures and Figure Captions for Section 3.3

Fig. 3.3-1 $H^0 \to \gamma\gamma$ signals for M_H =80, 100, 120, 140 and 160 GeV, superimposed on all backgrounds, for the BaF_2 calorimeter: (a) after shower shape analysis and (c) after preradiator rejection. Corresponding background-subtracted spectra are shown in (b) and (d). Data are for one SSCY.

Fig. 3.3-2 Same as Fig. 3.3-1 for the LAr-accordion calorimeter.

Fig. 3.3-3 $t\bar{t}/W + H^0 \to \ell^{\pm}\gamma\gamma + X$ signals for M_H = 80, 100, 120, 140 and 160 GeV, superimposed on all backgrounds. Data are for one SSCY and the indicated EC resolutions.

Fig. 3.3-4 $t\bar{t}/W + H^0 \to \ell^{\pm}\gamma\gamma + X$ signals for M_H = 80, 100, 120, 140 and 160 GeV, superimposed on all backgrounds. Data are for three SSCY and the indicated EC resolutions.

Fig. 3.3-5 Significance of the $t\bar{t}/W + H^0 \to \ell^{\pm}\gamma\gamma + X$ signals for M_H = 80, 100, 120, 140 and 160 GeV, as function of EC resolution and data-taking time.

Fig. 3.3-6 Isolated lepton plus inclusive muon invariant mass distributions for m_t = 200 GeV (solid), 250 GeV (dotted) and 300 GeV (dashed). (a) $M_{e\mu}$ distribution; (b) $M_{\mu\mu}$ distribution; (c) $M_{\ell\mu} = M_{e\mu} + M_{\mu\mu}$ distribution. Data are for one SSCY.

Fig. 3.3-7 The mean value of $M_{\ell\mu}$ plotted against m_t. Error bars represent Monte Carlo statistical errors.

Fig. 3.3-8 Signal and irreducible Z^0Z^0 background rates for an 800 GeV $H^0 \to Z^0Z^0 \to e^+e^-\mu^+\mu^-$ after all cuts *except* $p_T(Z^0) > 150\,\text{GeV}$. Data are for one SSCD.

Fig. 3.3-9 Same as Fig. 3.3-8, after the $p_T(Z^0) > 150\,\text{GeV}$ cut.

Fig. 3.3-10 $M_{e^+e^-}$ distributions for two Z'^0 models in a perfect detector;(a) the LR model; (b) the $SO(10)$ model. Distributions are based on 1000 generated events.

Fig. 3.3-11 $M_{e^+e^-}$ distributions for two Z'^0 models after background rejection and resolution smearing: (a) the LR model; (b) the $SO(10)$ model. The numbers of events correspond to one SSCD.

Fig. 3.3-12 Dimuon mass distributions after event selections for the ISO model (upper solid), HNC model (dashed) and standard Drell-Yan (lower solid). Λ = 25 TeV. Data are for one SSCD.

Fig. 3.3-13 $\cos\theta^*$ distributions for dimuon production in (a) the ISO model and (b) the HNC model. The dashed histograms are the underlying contribution from standard Drell-Yan dimuon production. $\Lambda = 25\,\text{TeV}$. Data are for one

SSCD.

Fig. 3.3-14 (a) Gluino signal and QCD background versus $\not{E}_T$ after the jet and sphericity cuts and the lepton veto described in the text. (b) Solid: Ratio of $(S+B)/B$ from (a). Dotted: Same ratio using $\not{E}_T$ calculated from the ν and $\tilde{\chi}_1^0$ momenta.

Fig. 3.3-15 E_T opposite $Z \to e^+e^-$ after cuts for 800 GeV Higgs and Z^0 + jets background with a perfect calorimeter covering $\eta < 5.5$.

Fig. 3.3-16 Same as Fig. 3.3-15 for the GEM baseline calorimeter.

Fig. 3.3-17 Electromagnetic calorimeter energy versus total energy for 100 GeV jets.

Fig. 3.3-18 Total cross section for high p_T jets versus Λ.

Fig. 3.3-19 p_T distribution for jets. PYTHIA particle clustering. The curves shown are from the top, Λ =22.5 TeV, 25 TeV and infinity.

Fig. 3.3-20 A comparison of PYTHIA (solid) and GEM detector (dotted) jet p_T spectra.

Fig. 3.3-21 Overlays of $\Lambda = 22.5$ (left) and $\Lambda = 25$ (right).

Fig. 3.3-22 Jet p_T distributions for the EHLQ set I (lower) and Duke-Owens Set I (upper) structure functions.

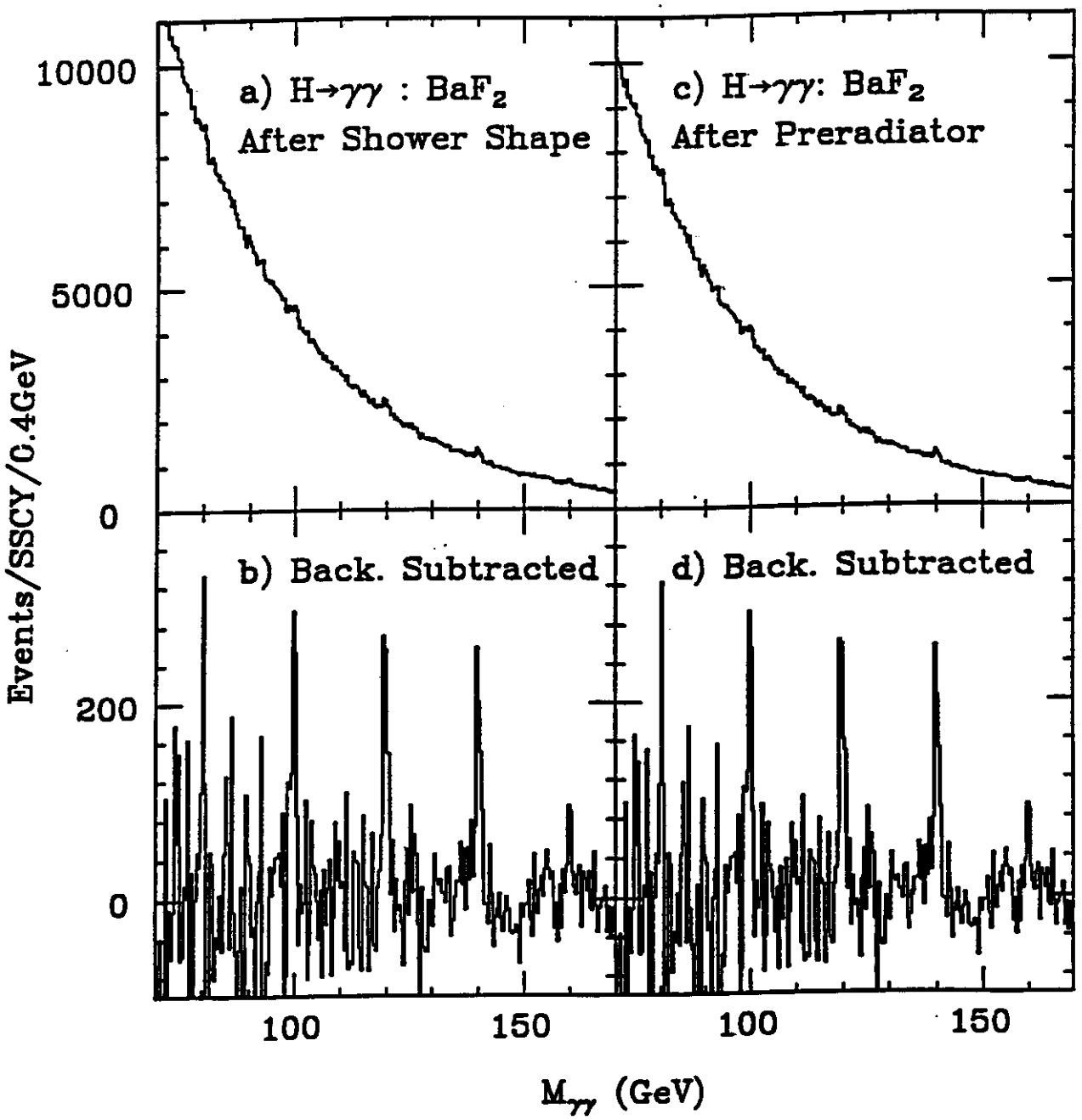
a) H→γγ : BaF2
After Shower Shape
c) H→γγ: BaF2
After Preradiator
b) Back. Subtracted
d) Back. Subtracted
10000
5000
0
200
0
100
150
100
150
Events/SSCY/0.4GeV
Mγγ (GeV)

FIG. 3.3-1

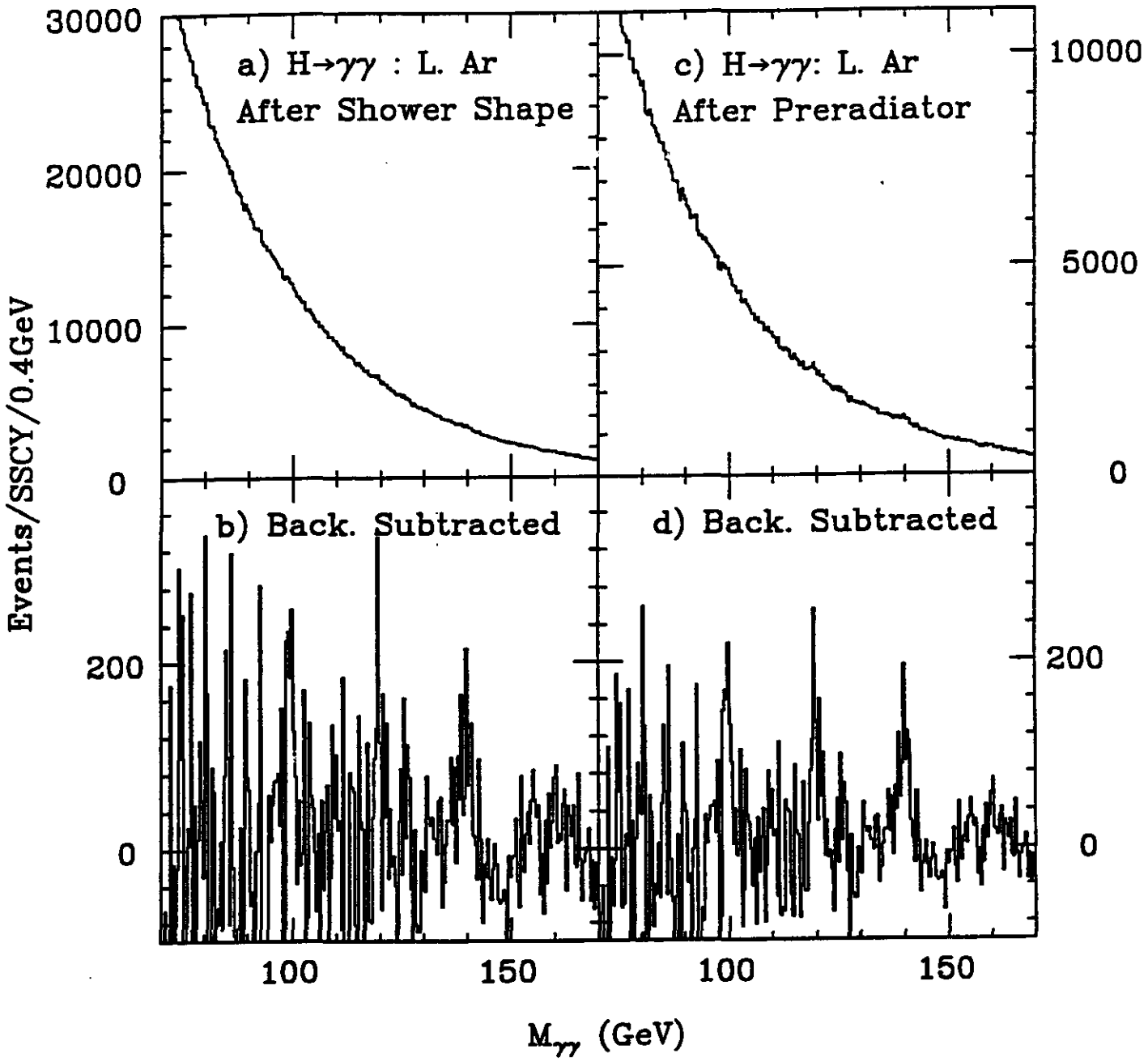
a) H→γγ : L. Ar
After Shower Shape
c) H→γγ: L. Ar
After Preradiator
b) Back. Subtracted
d) Back. Subtracted
30000
20000
10000
0
10000
5000
0
200
0
200
0
100
150
100
150
Events/SSCY/0.4GeV
$M_{\gamma\gamma}$ (GeV)

FIG. 3.3-2

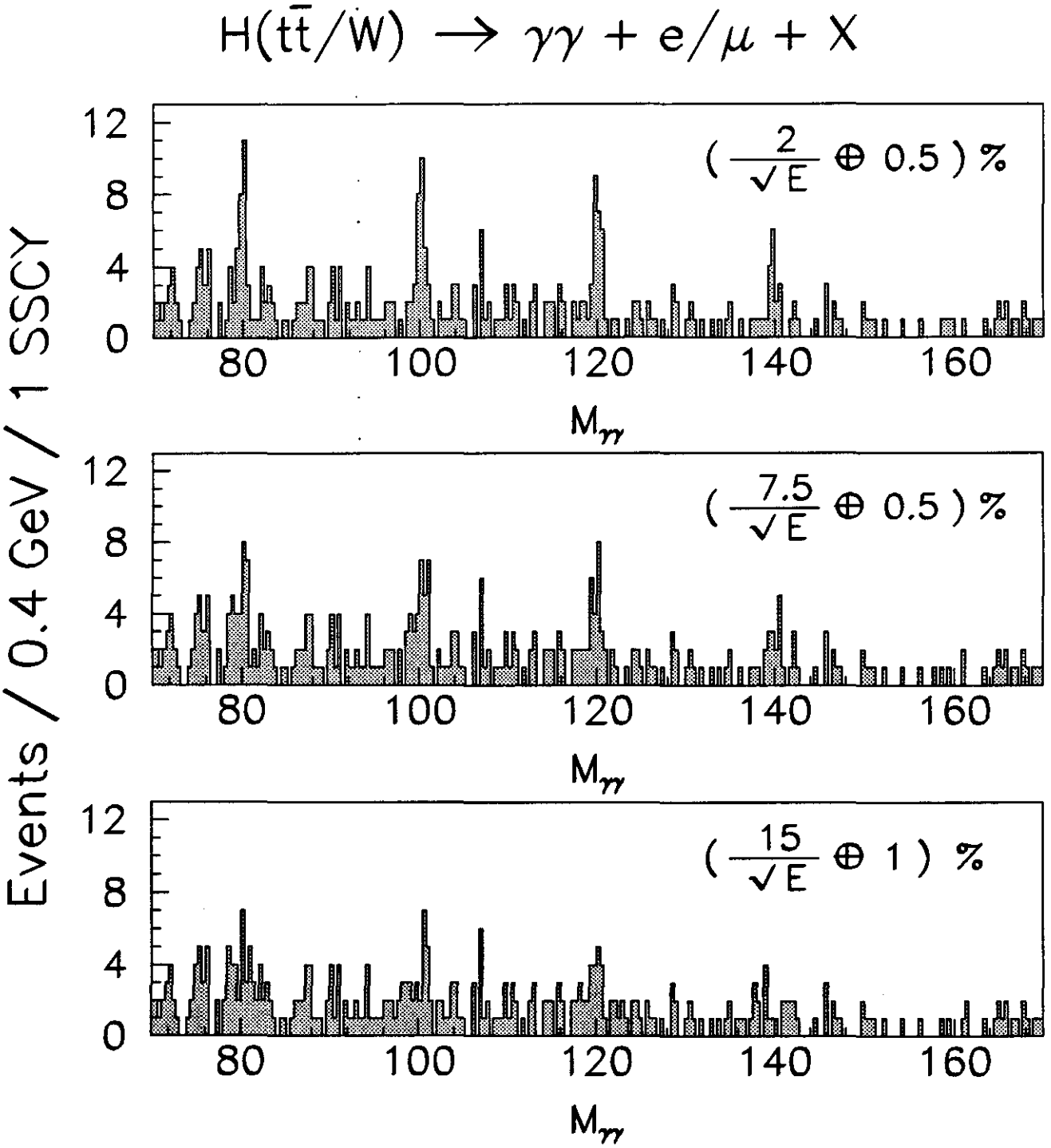
H(tt̄/W) → γγ + e/μ + X
Events / 0.4 GeV / 1 SSCY
(2/√E ⊕ 0.5) %
(7.5/√E ⊕ 0.5) %
(15/√E ⊕ 1) %
M_γγ
0
4
8
12
80
100
120
140
160

FIG. 3.3-3

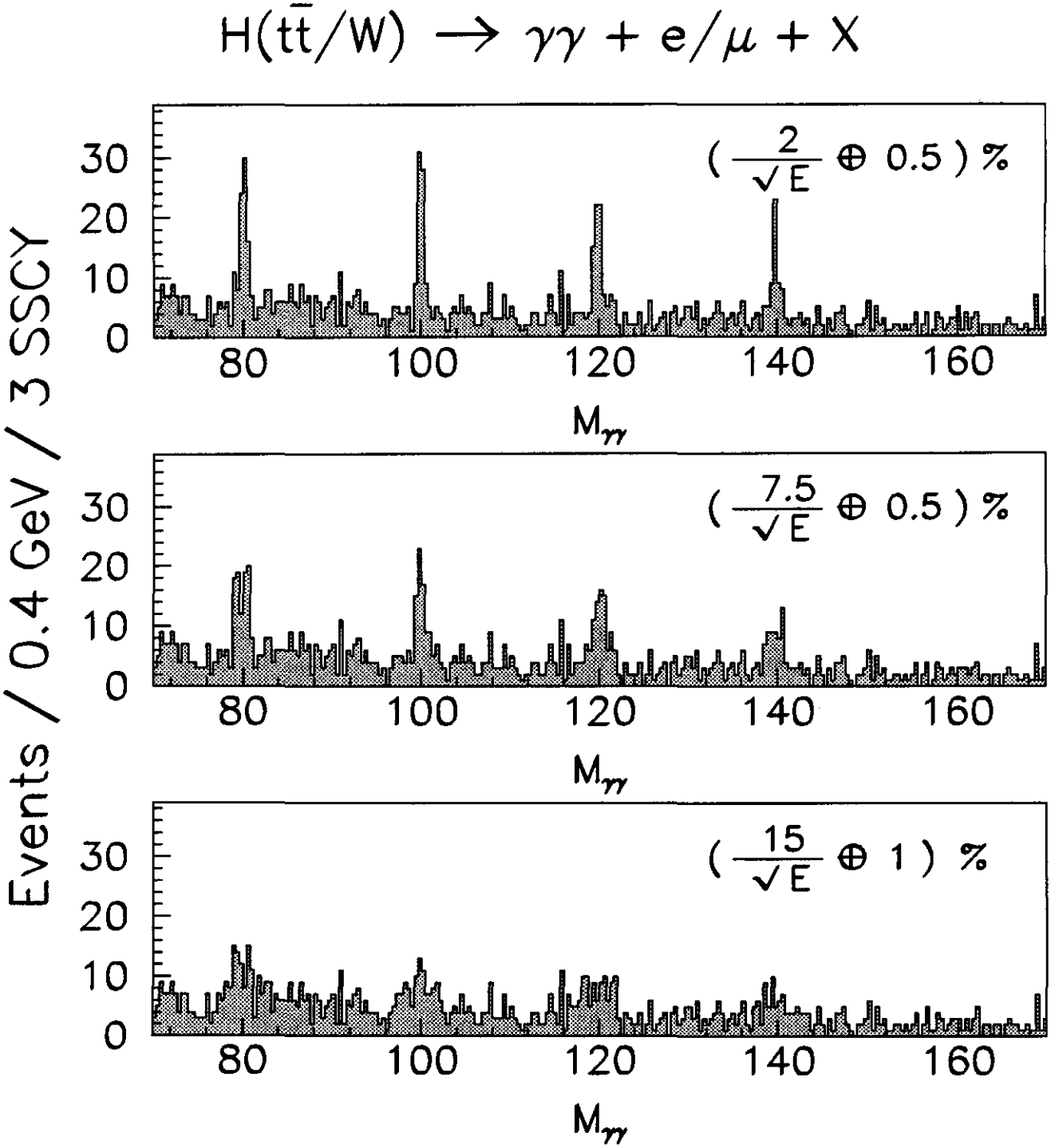
H(tt̄/W) → γγ + e/μ + X
Events / 0.4 GeV / 3 SSCY
(2/√E ⊕ 0.5) %
(7.5/√E ⊕ 0.5) %
(15/√E ⊕ 1) %
M_γγ
0
10
20
30
80
100
120
140
160

FIG. 3.3-4

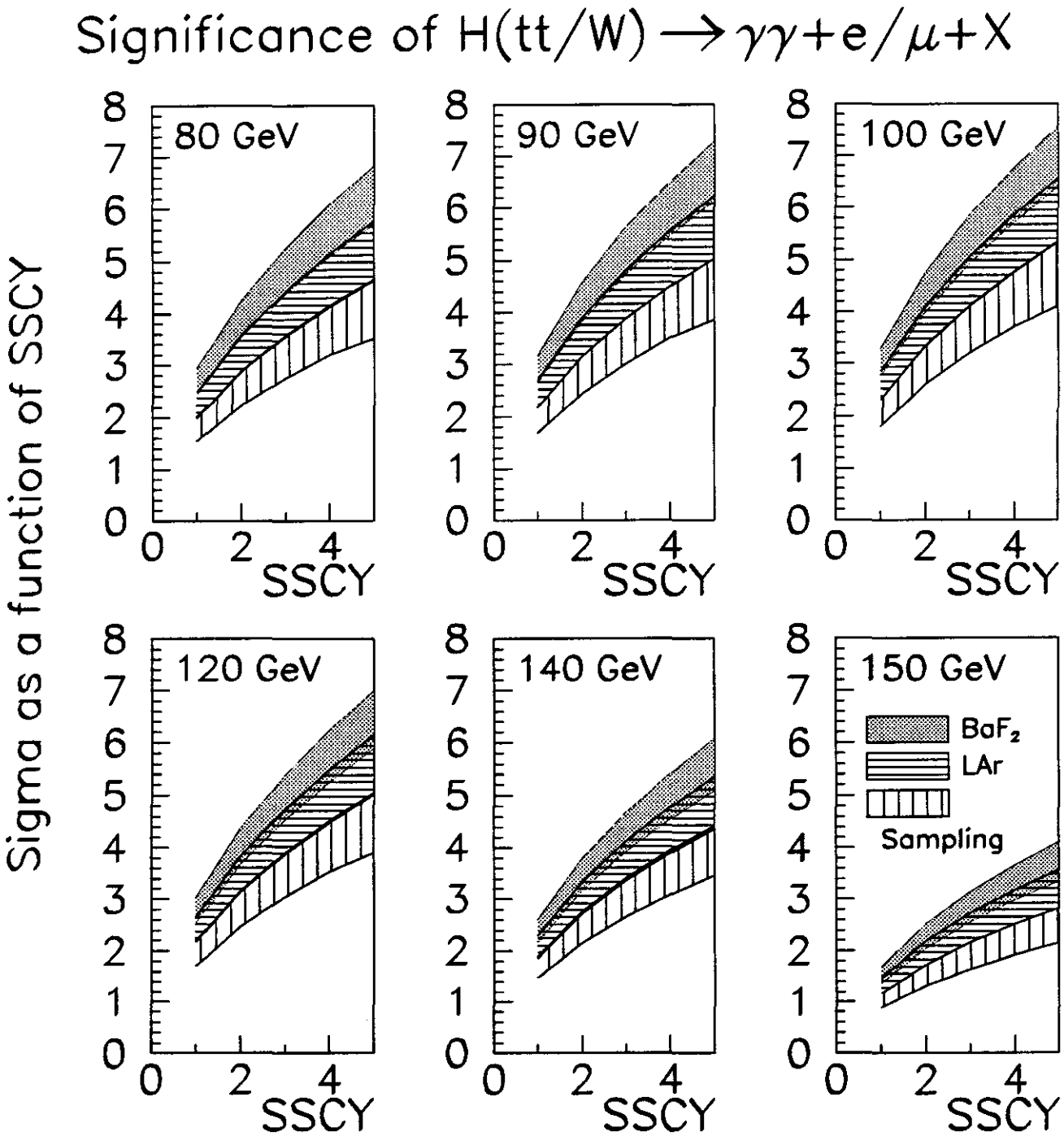
Significance of H(tt/W) → γγ+e/μ+X
Sigma as a function of SSCY
80 GeV
90 GeV
100 GeV
120 GeV
140 GeV
150 GeV
BaF₂
LAr
Sampling
SSCY

FIG. 3.3-5

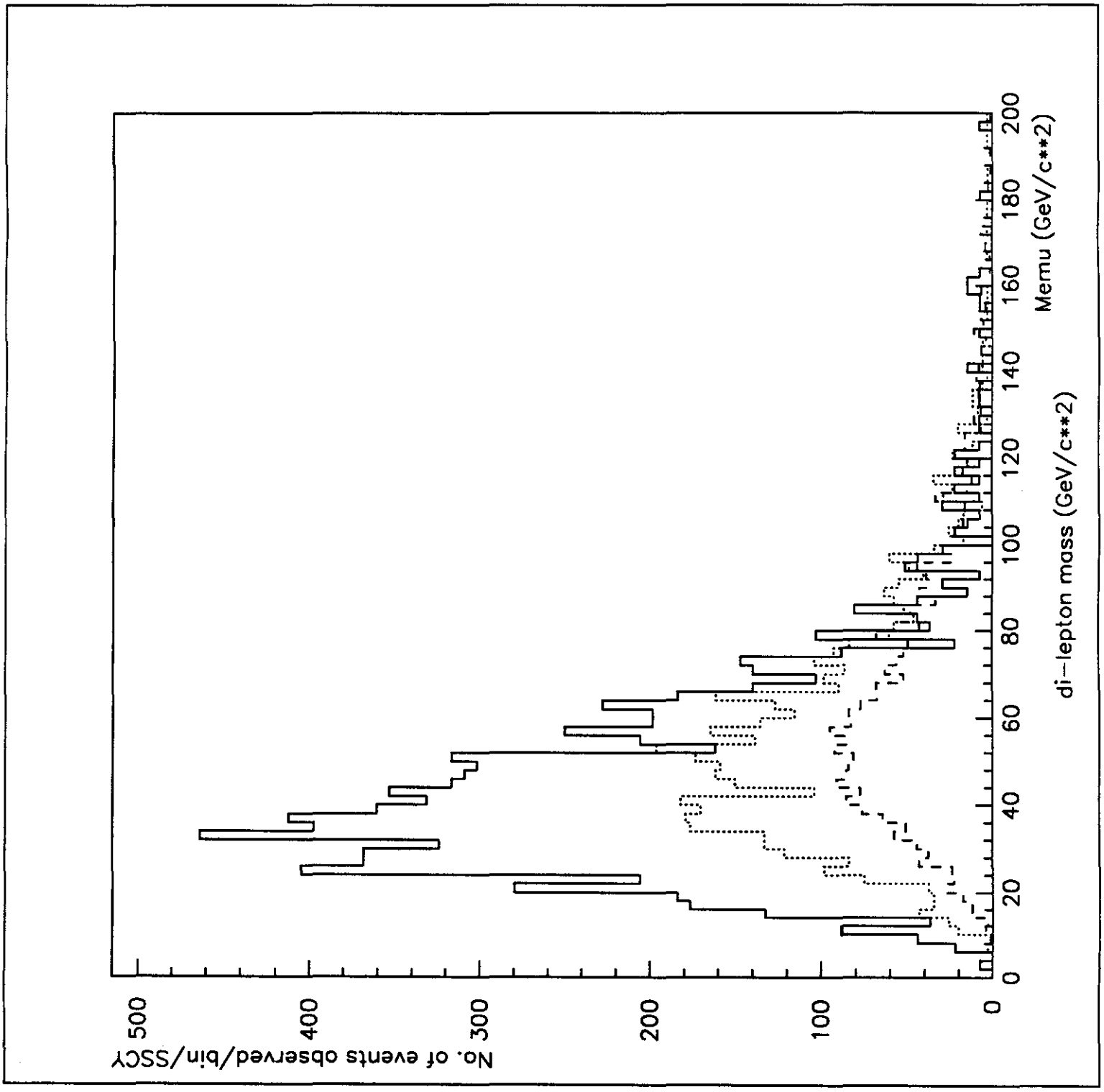
No. of events observed/bin/SSCY
500
400
300
200
100
0
0
20
40
60
80
100
120
140
160
180
200
di-lepton mass (GeV/c**2)
Memu (GeV/c**2)

FIG. 3.3-6(a)

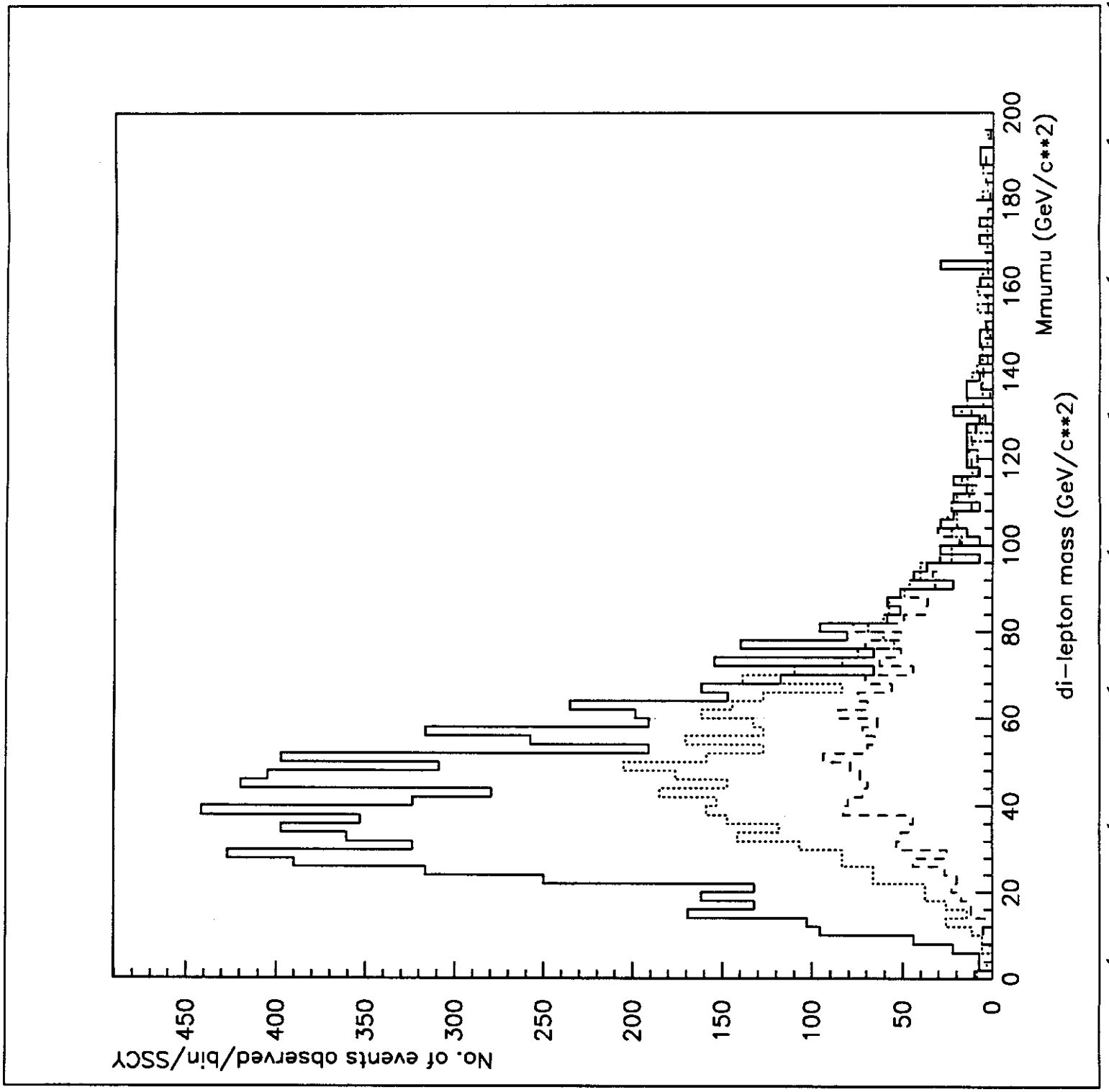
No. of events observed/bin/SSCY
450
400
350
300
250
200
150
100
50
0
0
20
40
60
80
100
120
140
160
180
200
di-lepton mass (GeV/c**2)
Mmumu (GeV/c**2)

FIG. 3.3-6(b)

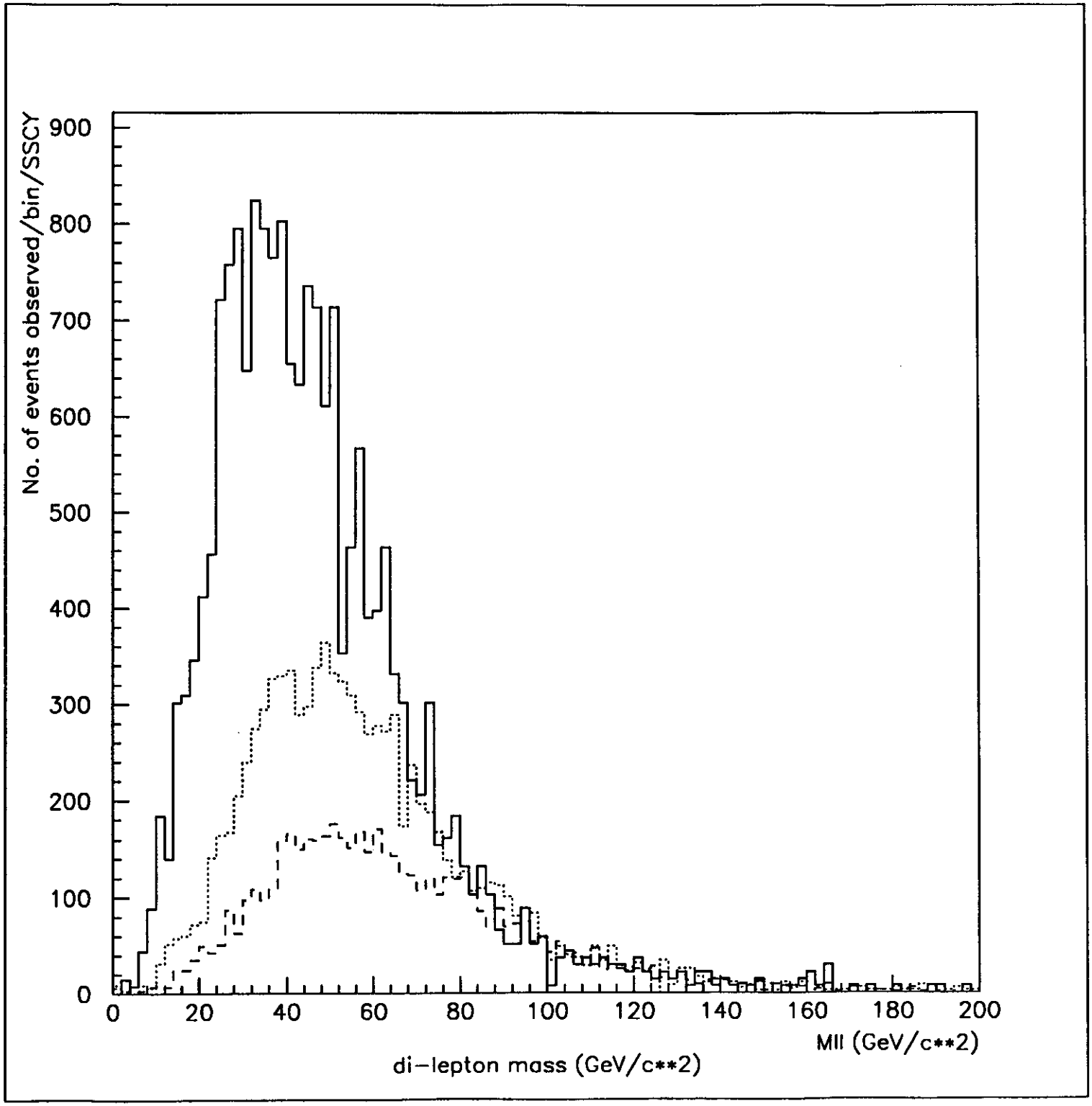
No. of events observed/bin/SSCY
900
800
700
600
500
400
300
200
100
0
0
20
40
60
80
100
120
140
160
180
200
MII (GeV/c**2)
di-lepton mass (GeV/c**2)

FIG. 3.3-6(c)

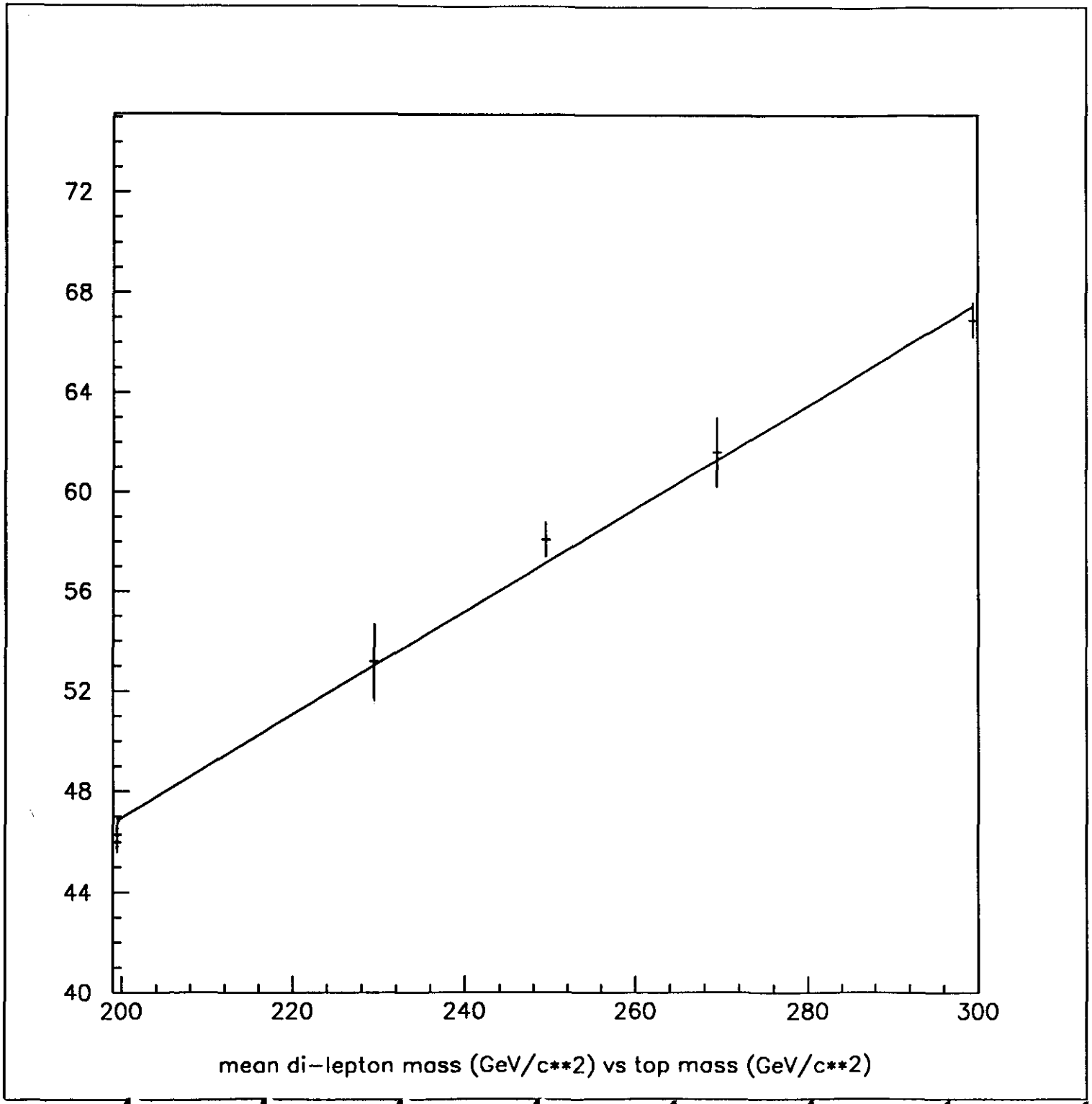
72
68
64
60
56
52
48
44
40
200
220
240
260
280
300
mean di-lepton mass (GeV/c**2) vs top mass (GeV/c**2)

FIG. 3.3-7

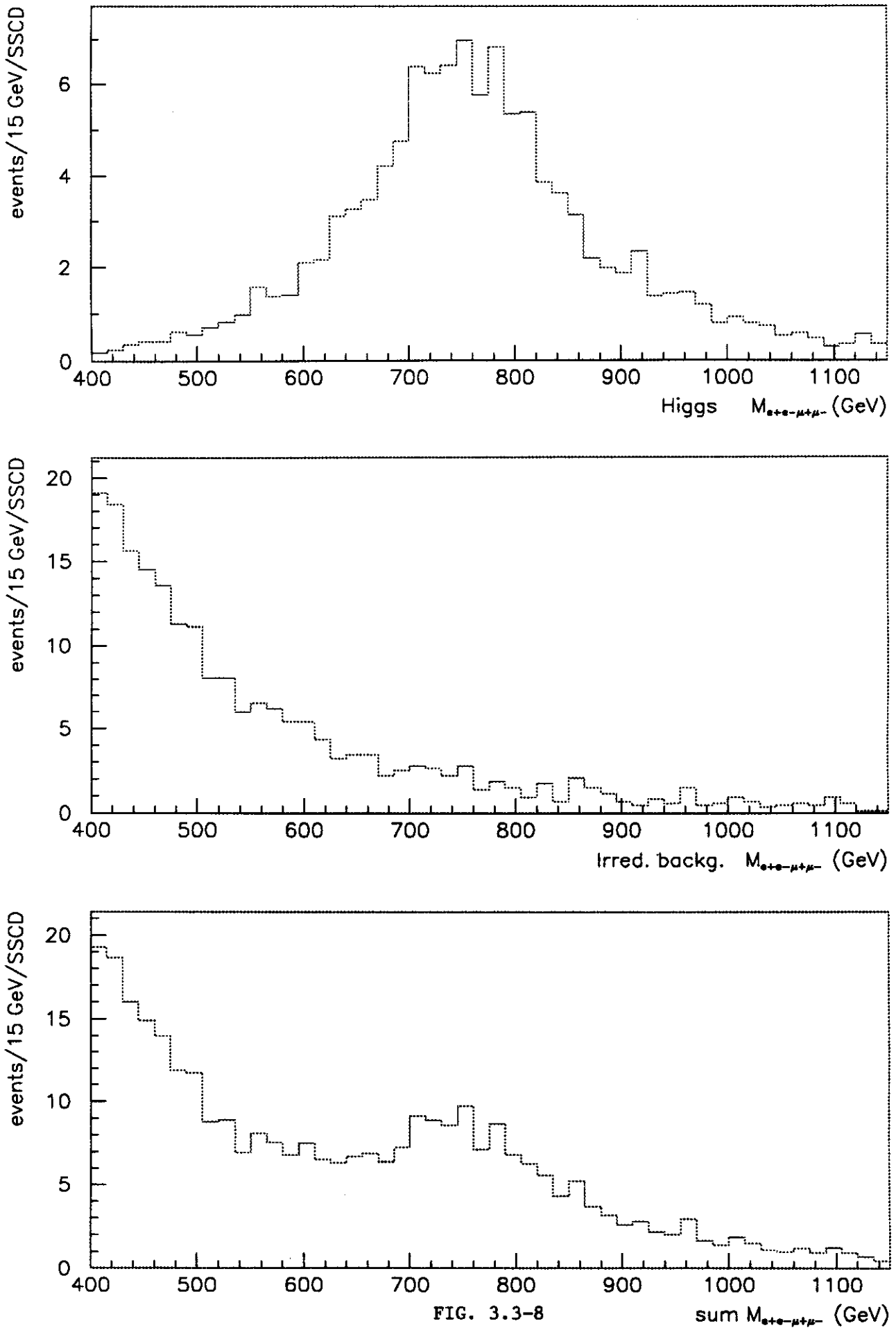
events/15 GeV/SSCD
0
2
4
6
400
500
600
700
800
900
1000
1100
Higgs $M_{e^+e^-\mu^+\mu^-}$ (GeV)
events/15 GeV/SSCD
0
5
10
15
20
400
500
600
700
800
900
1000
1100
Irred. backg. $M_{e^+e^-\mu^+\mu^-}$ (GeV)
events/15 GeV/SSCD
0
5
10
15
20
400
500
600
700
800
900
1000
1100
sum $M_{e^+e^-\mu^+\mu^-}$ (GeV)

FIG. 3.3-8

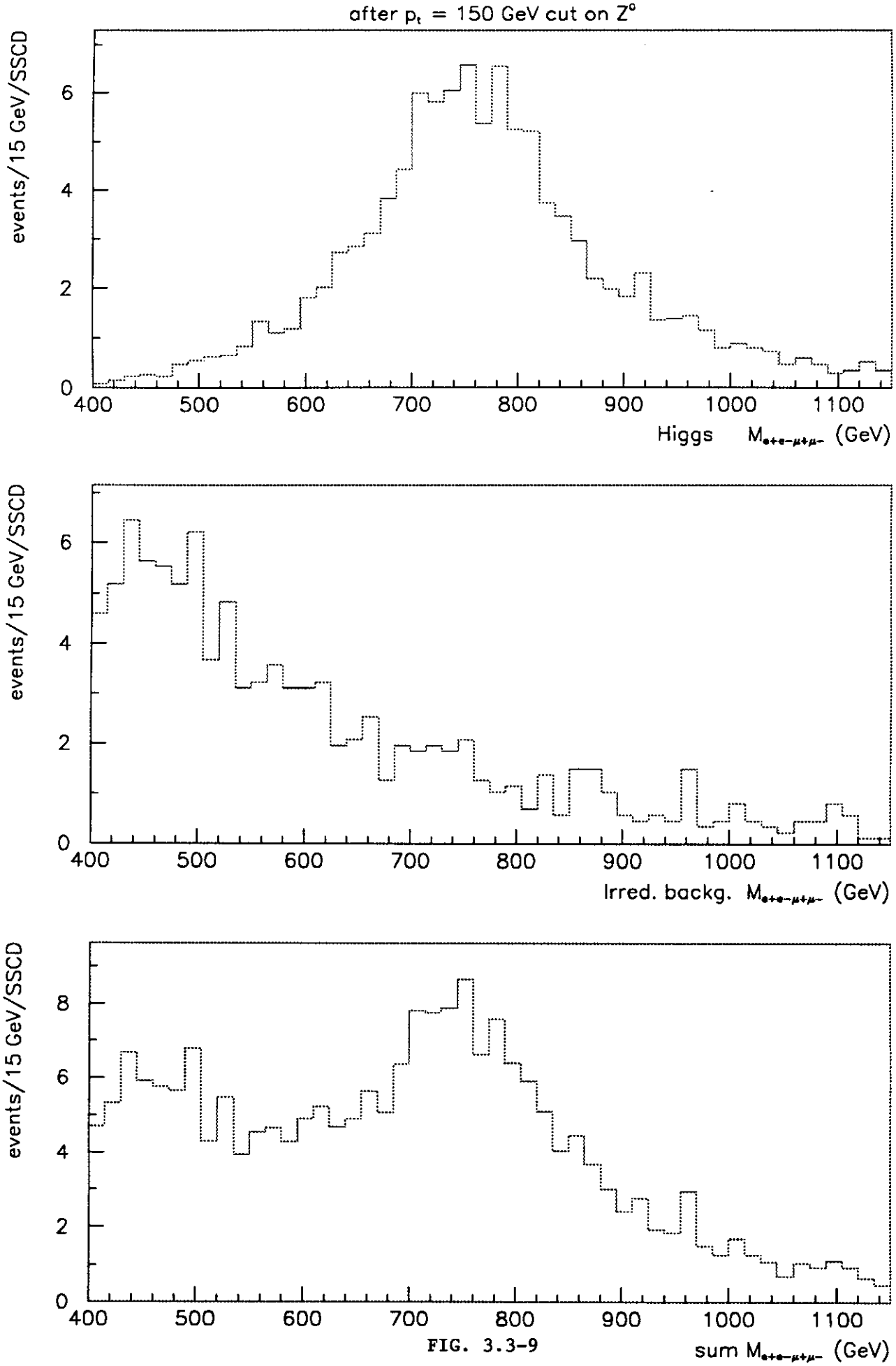
after p_t = 150 GeV cut on Z^0
events/15 GeV/SSCD
Higgs $M_{e+e-\mu+\mu-}$ (GeV)
events/15 GeV/SSCD
Irred. backg. $M_{e+e-\mu+\mu-}$ (GeV)
events/15 GeV/SSCD
sum $M_{e+e-\mu+\mu-}$ (GeV)

FIG. 3.3-9

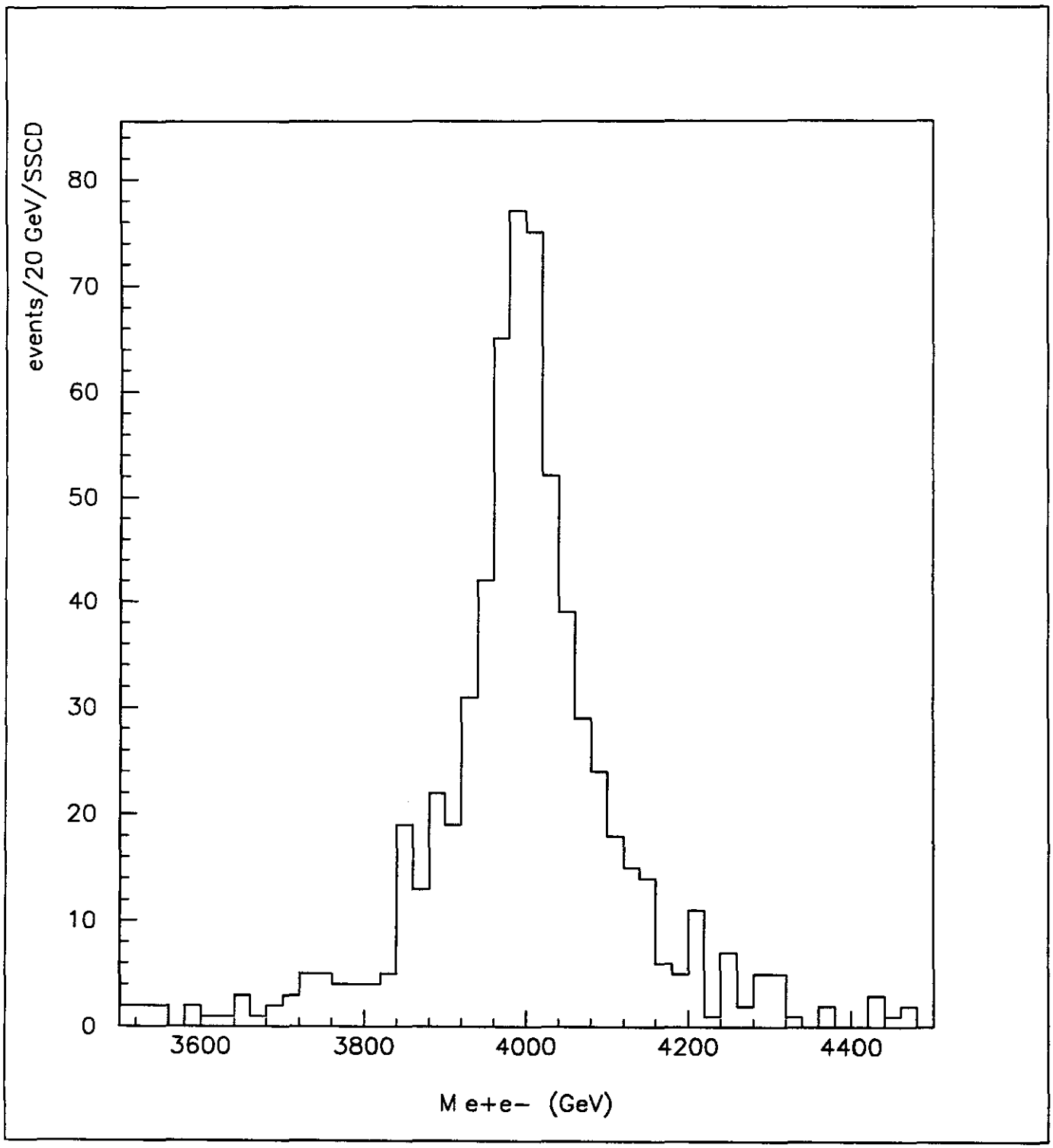
events/20 GeV/SSCD
80
70
60
50
40
30
20
10
0
3600
3800
4000
4200
4400
M e+e- (GeV)

FIG 3.3-10(a)

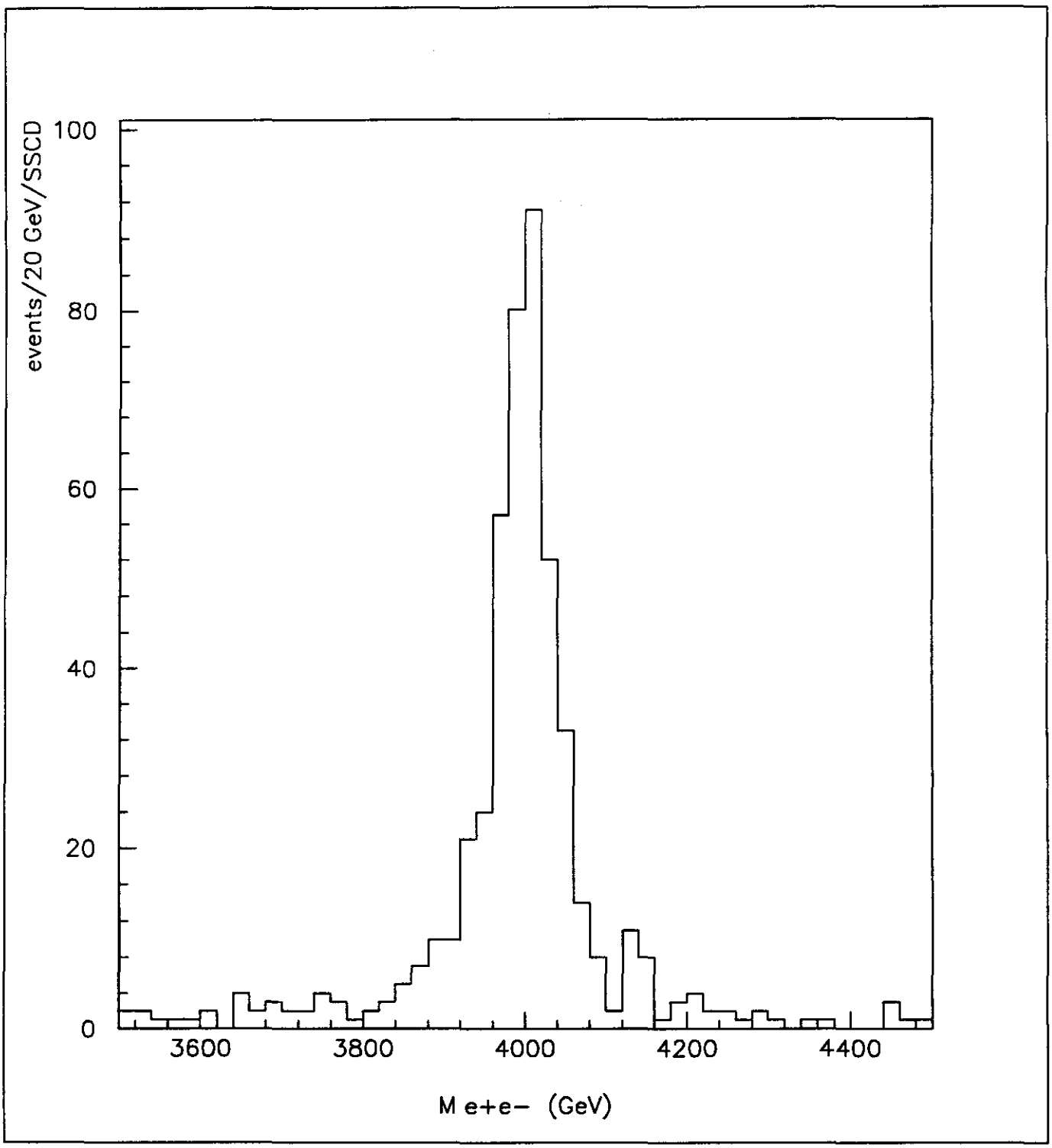
events/20 GeV/SSCD
100
80
60
40
20
0
3600
3800
4000
4200
4400
M e+e− (GeV)

FIG 3.3-10(b)

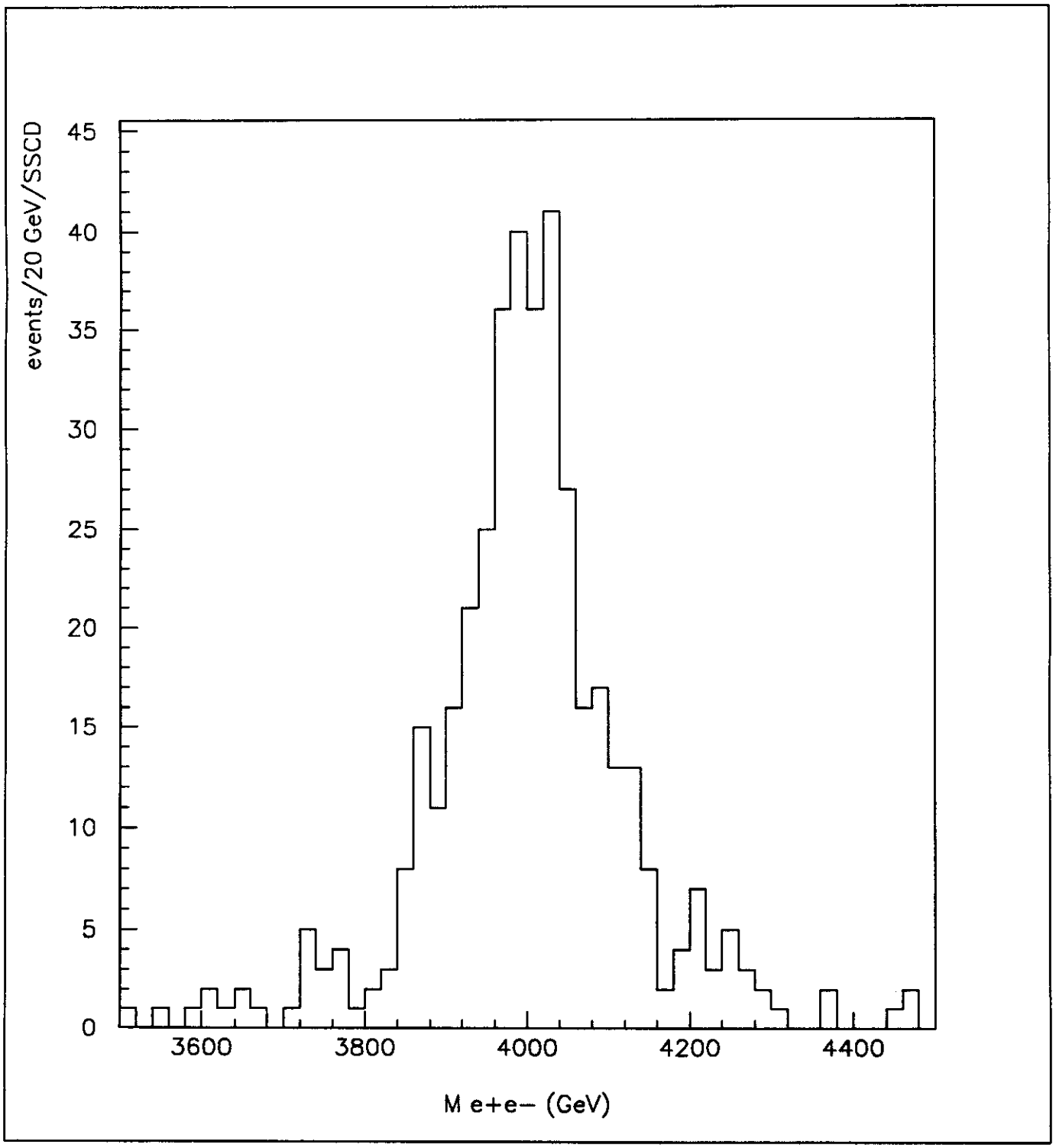
events/20 GeV/SSCD
45
40
35
30
25
20
15
10
5
0
3600
3800
4000
4200
4400
M e+e− (GeV)

FIG. 3.3-11(a)

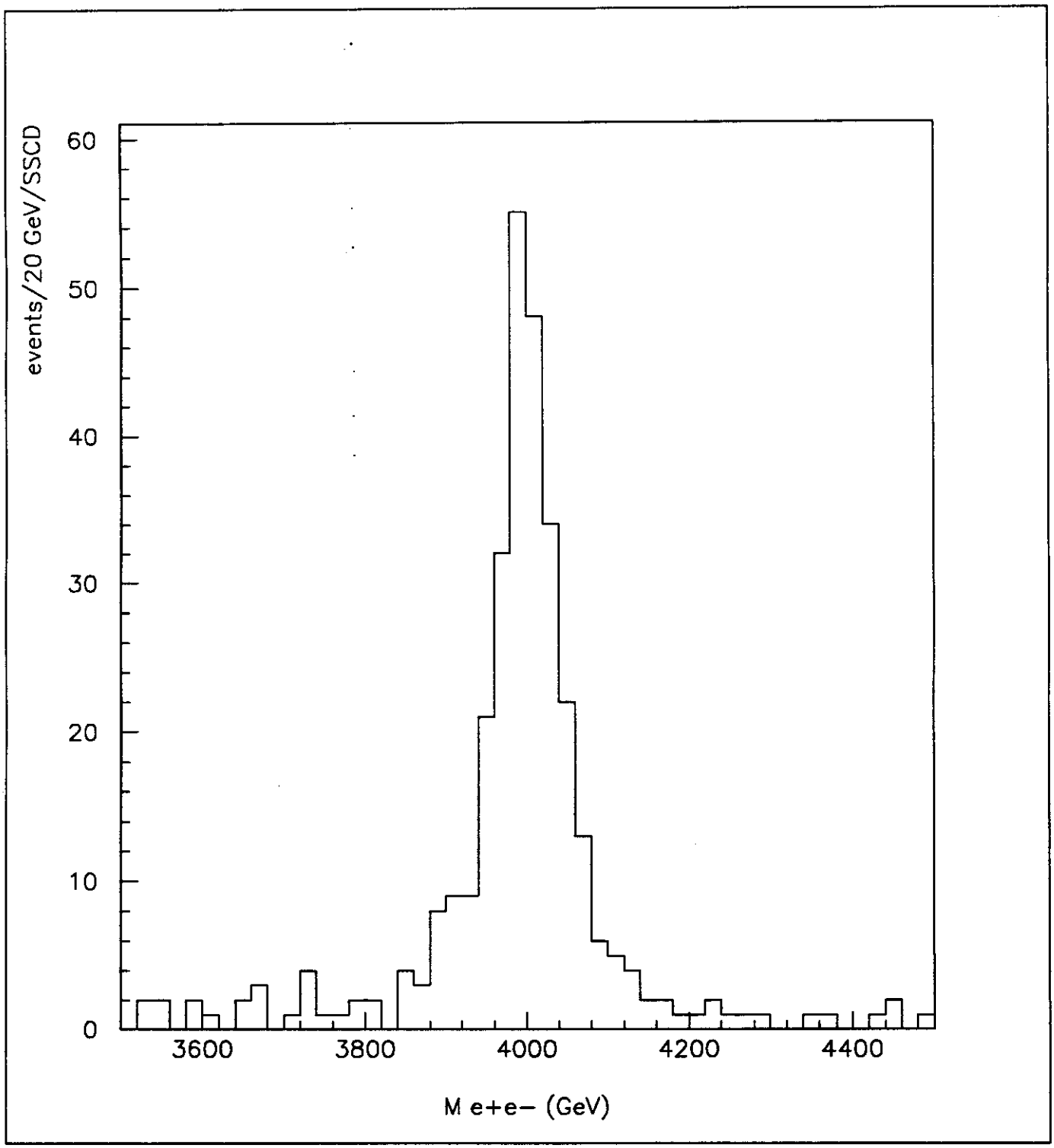
events/20 GeV/SSCD
60
50
40
30
20
10
0
3600
3800
4000
4200
4400
M e+e− (GeV)

FIG. 3.3-11(b)

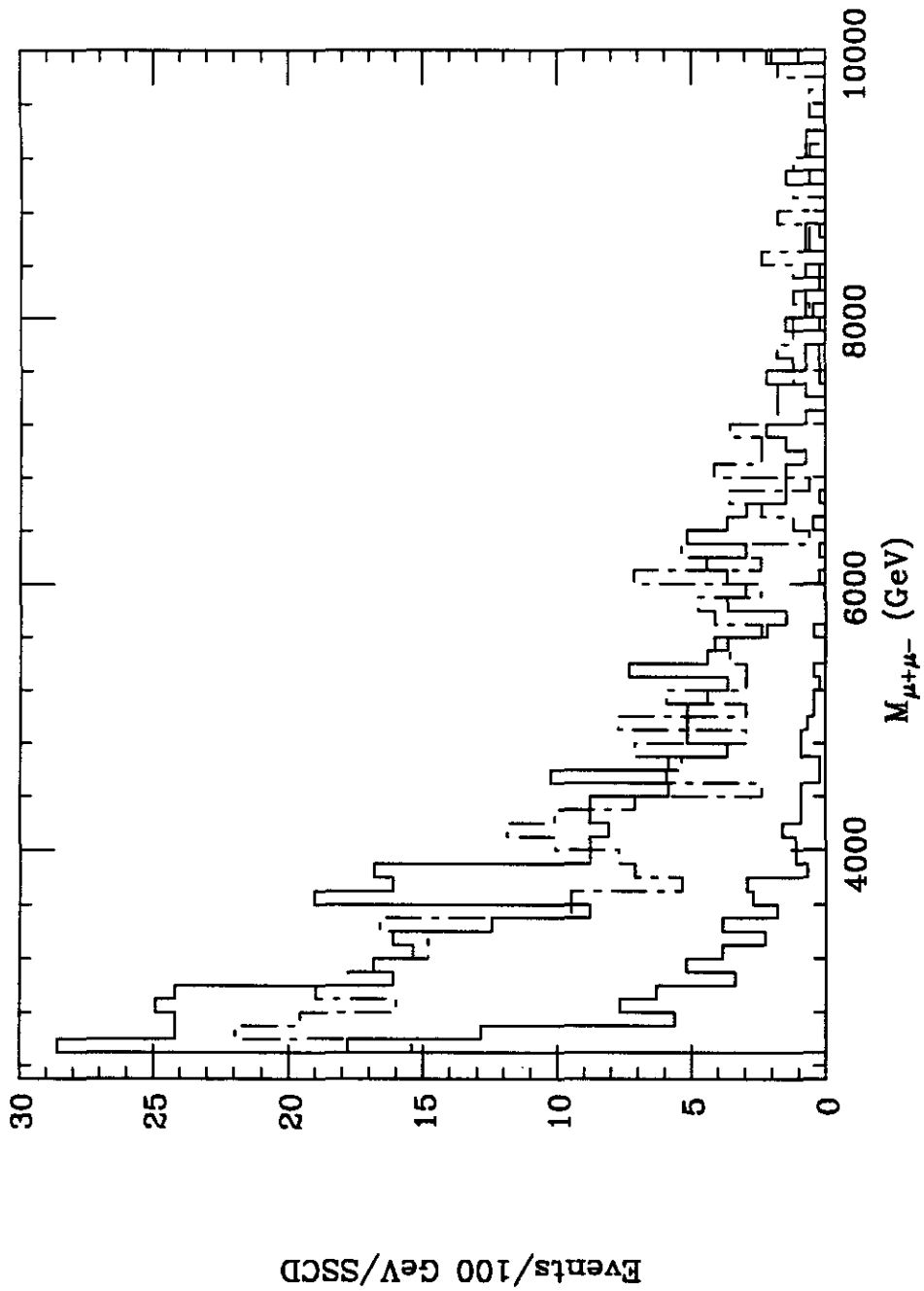
30
25
20
15
10
5
0
4000
6000
8000
10000
$M_{\mu^+\mu^-}$ (GeV)
Events/100 GeV/SSCD

FIG. 3.3-12

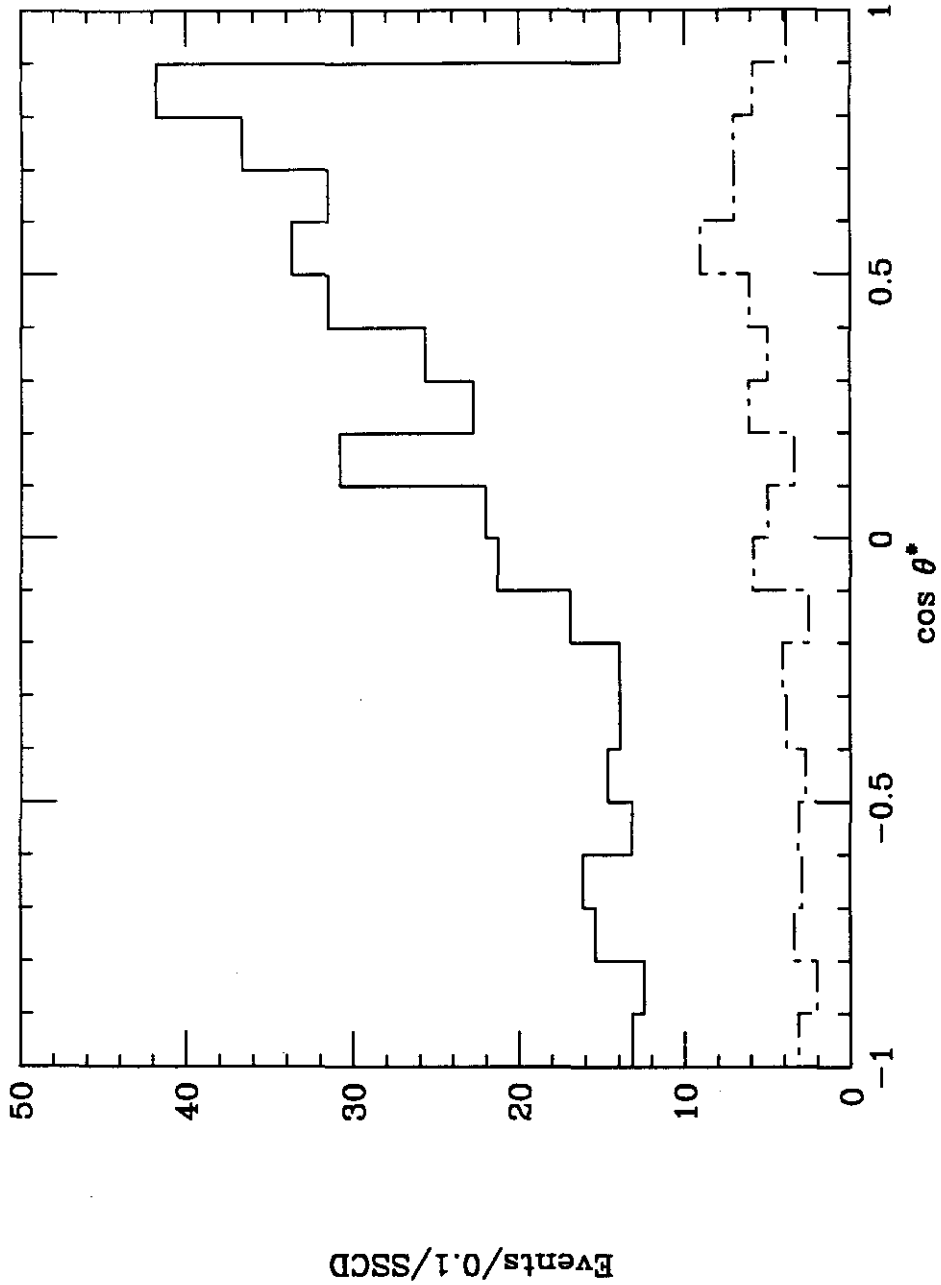

FIG. 3.3-13(a)

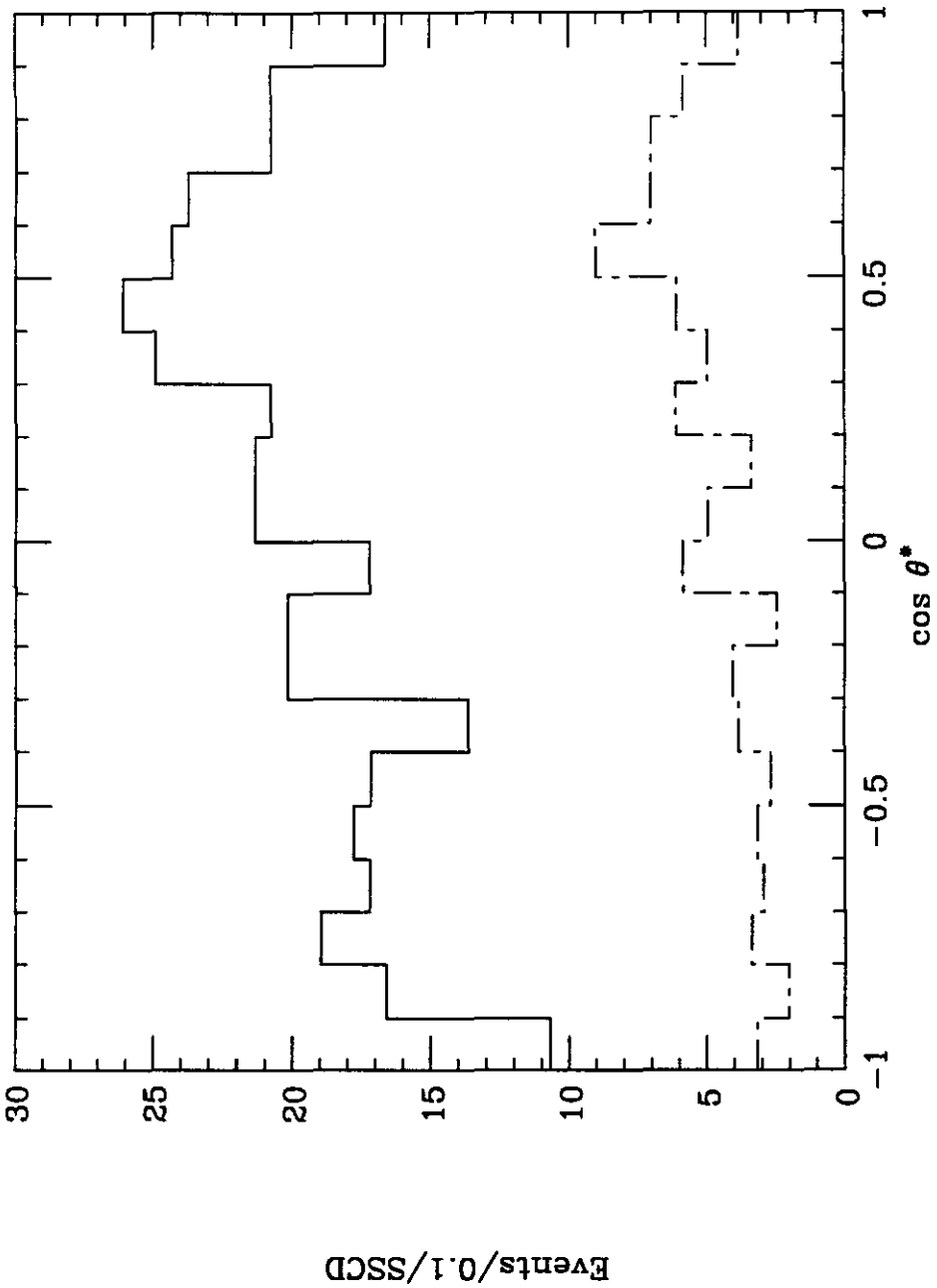

FIG. 3-13(b)

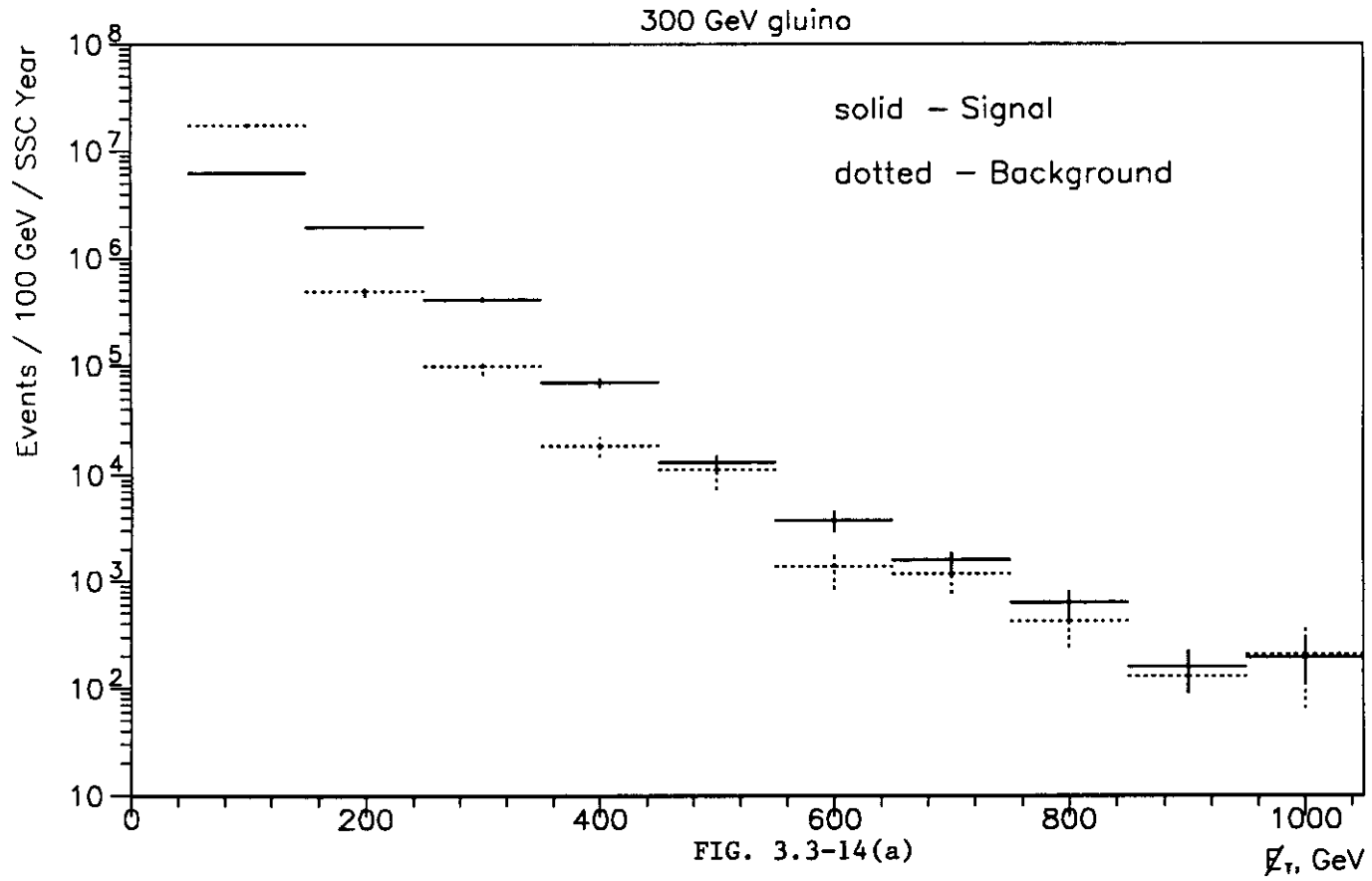

FIG. 3.3-14(a)

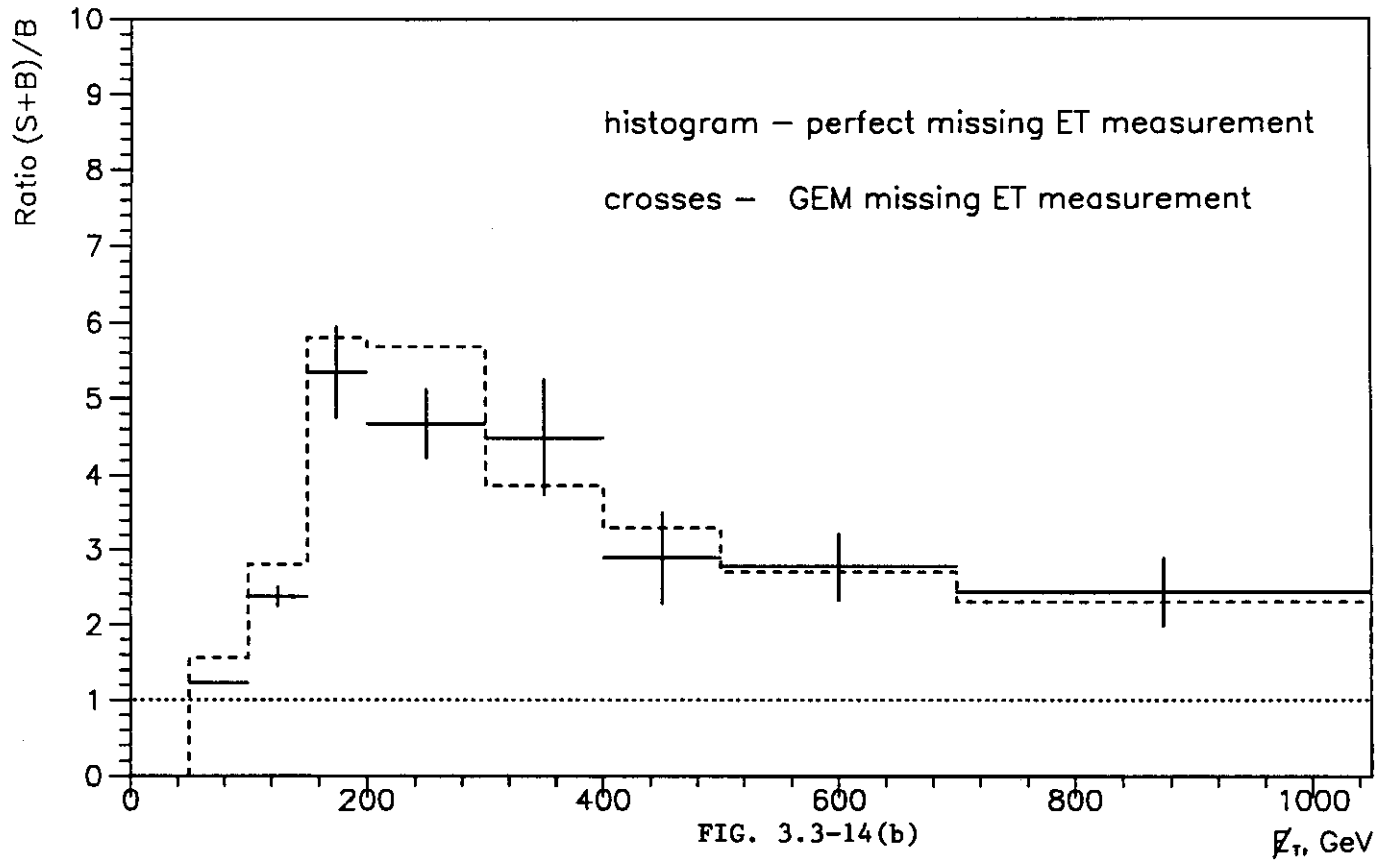

FIG. 3.3-14(b)

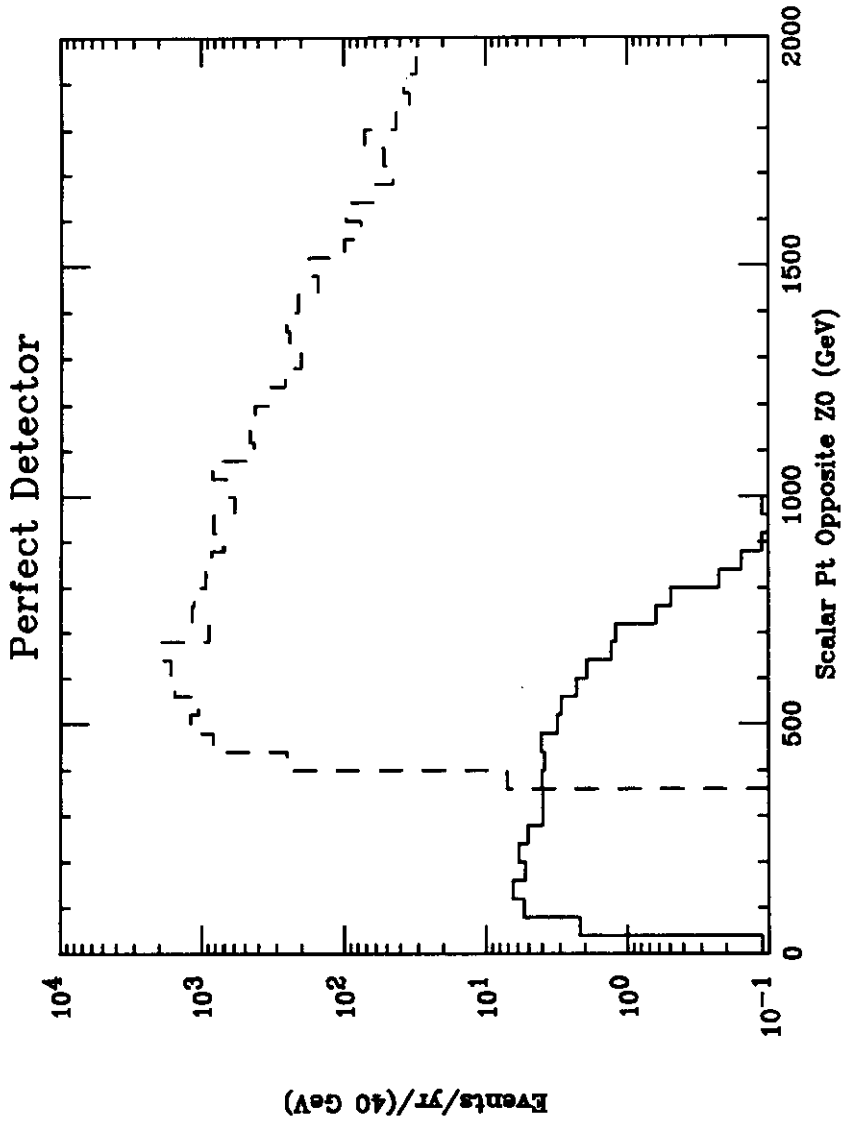
Perfect Detector
Events/yr/(40 GeV)
10^4
10^3
10^2
10^1
10^0
10^{-1}
0
500
1000
1500
2000
Scalar Pt Opposite Z0 (GeV)

FIG. 3.3-15

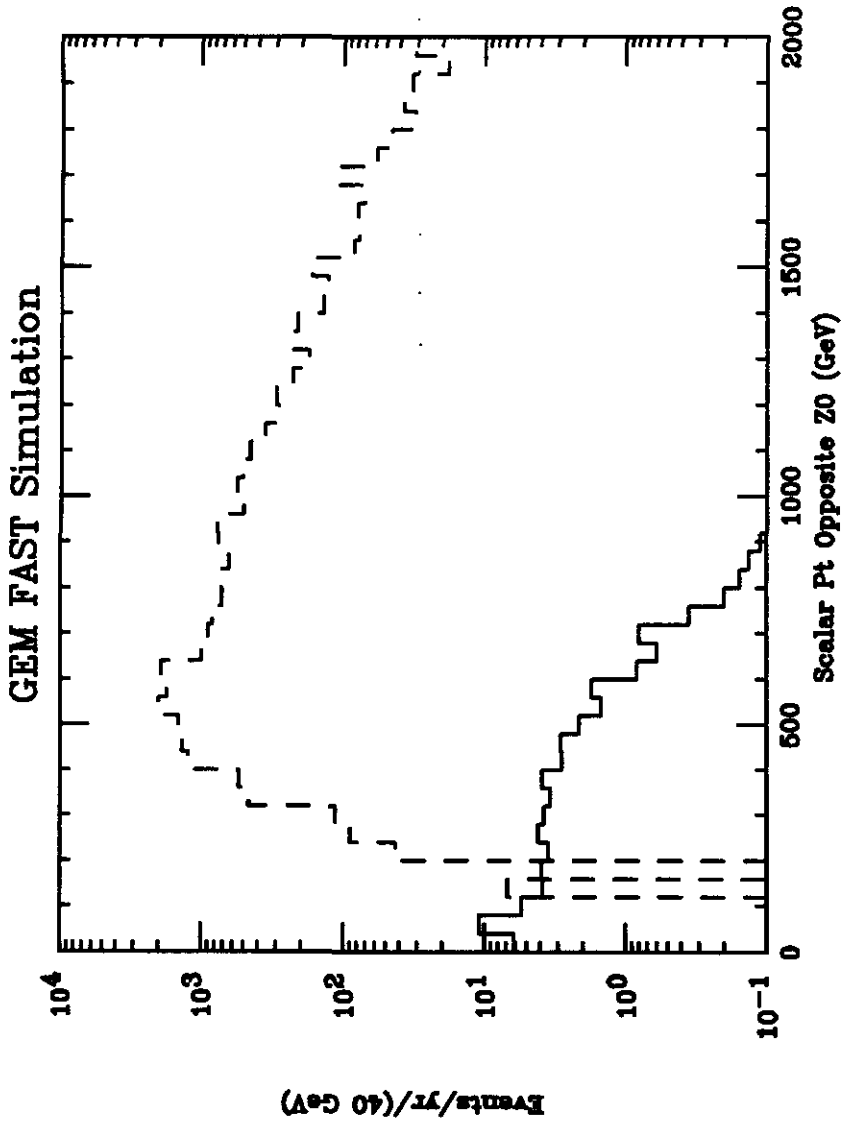
GEM FAST Simulation
Events/yr/(40 GeV)
10^4
10^3
10^2
10^1
10^0
10^{-1}
0
500
1000
1500
2000
Scalar Pt Opposite Z0 (GeV)

FIG. 3.3-16

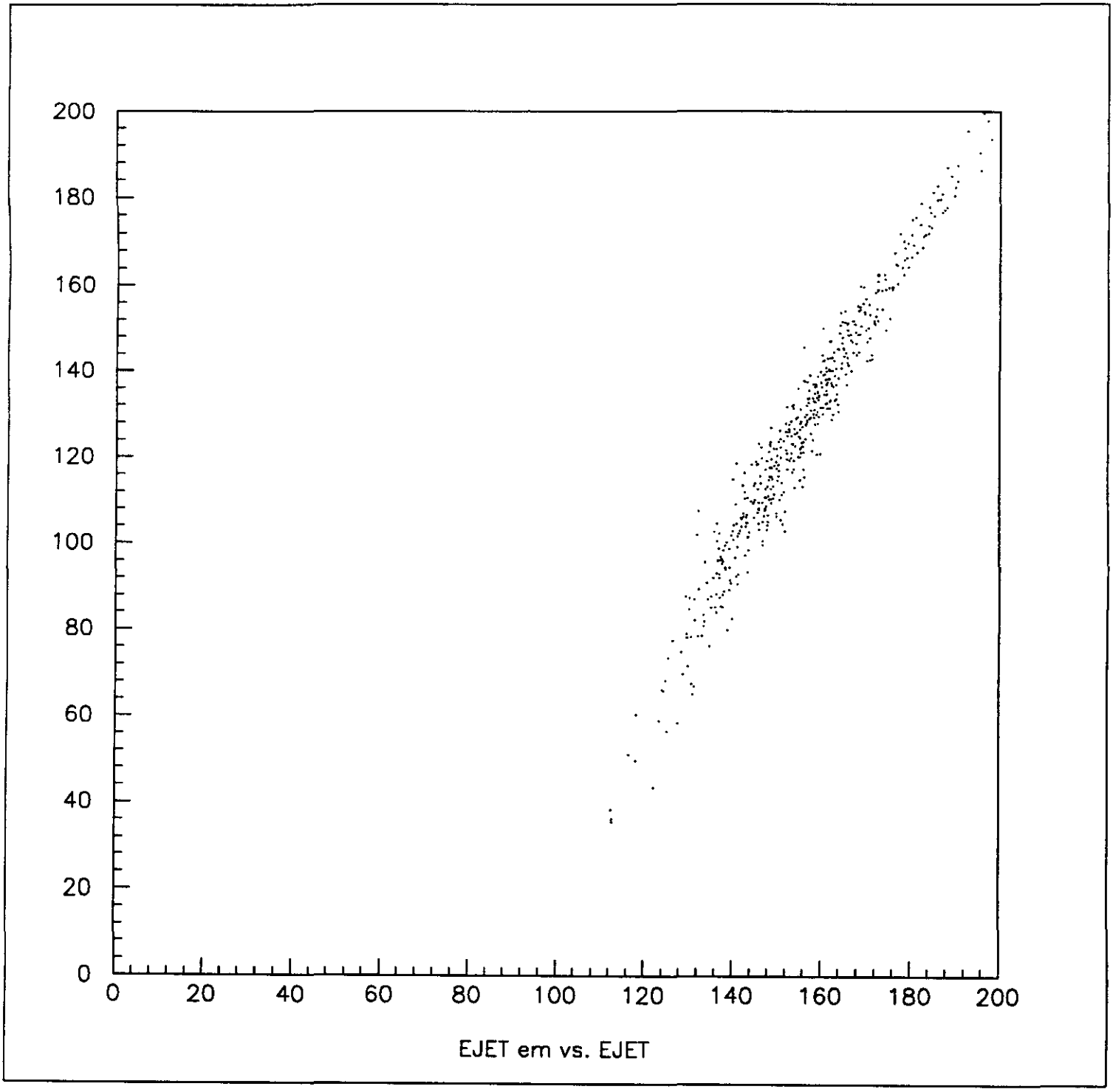
200
180
160
140
120
100
80
60
40
20
0
0
20
40
60
80
100
120
140
160
180
200
EJET em vs. EJET

FIG. 3.3-17

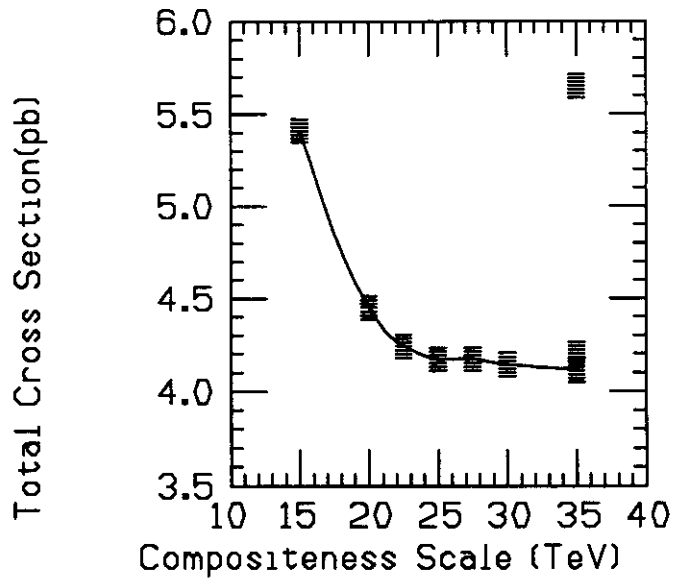
6.0
5.5
5.0
4.5
4.0
3.5
10 15 20 25 30 35 40
Compositeness Scale (TeV)
Total Cross Section(pb)

FIG. 3.3-18

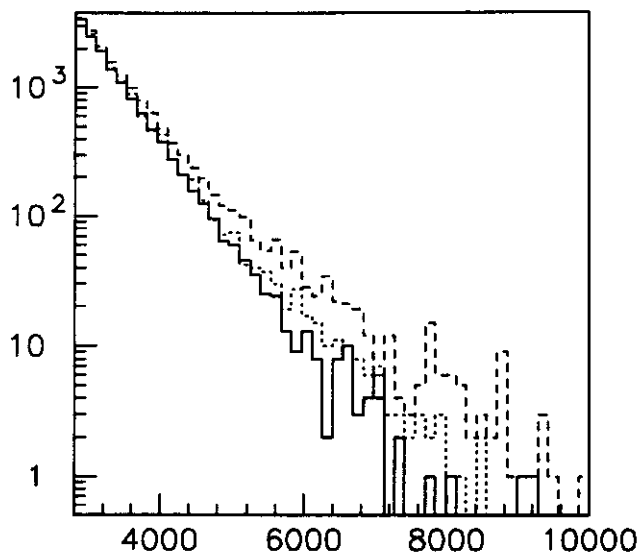

Inclusive Jet Pt Distribution

FIG. 3.3-19

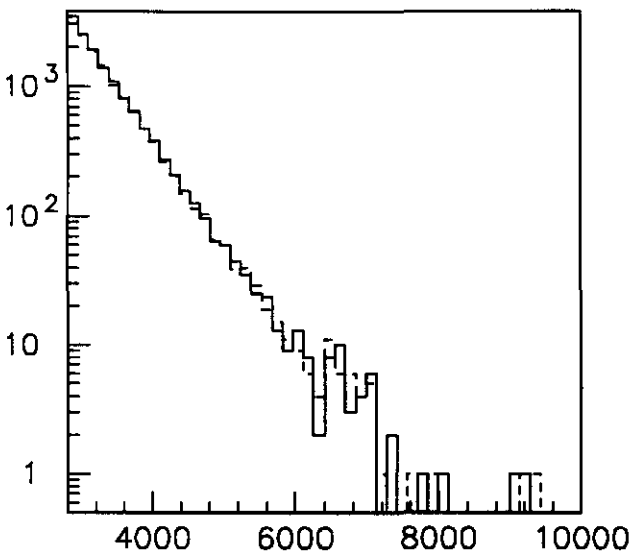

Pythia and Detector Jets

FIG. 3.3-20

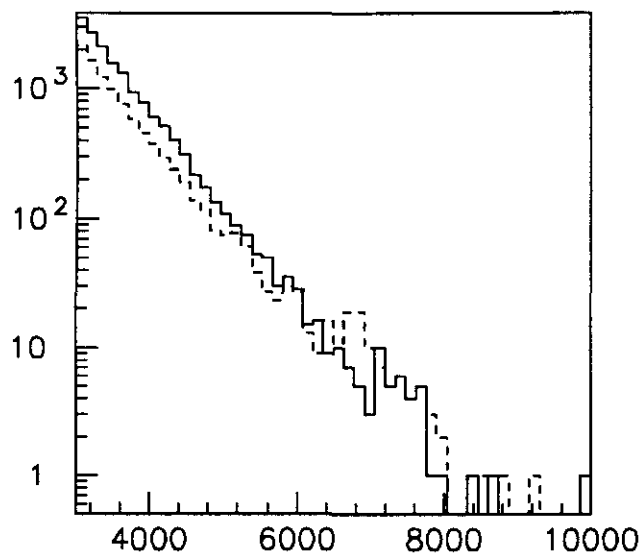

The effect of non−linearity

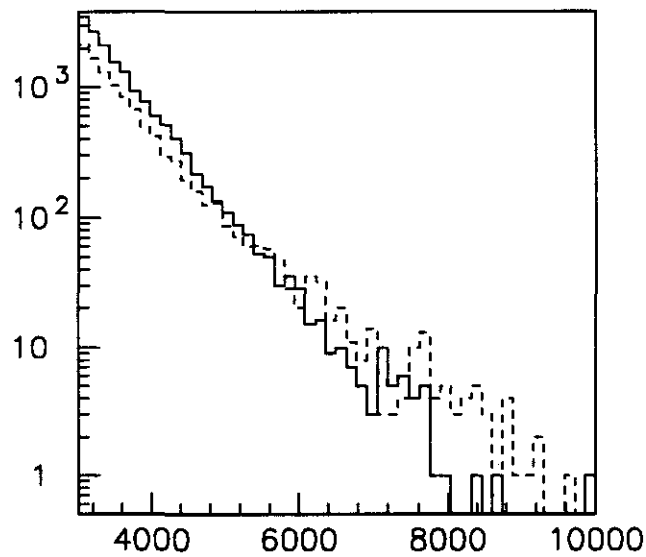

The effect of non−linearity

FIG. 3.3-21

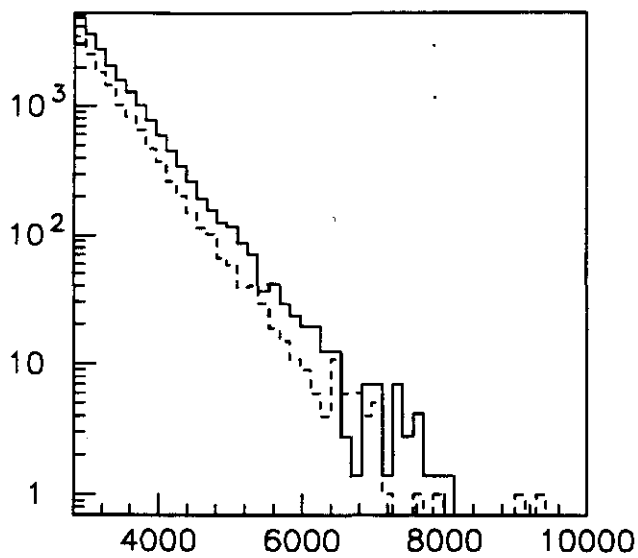

Two different structure Functions

FIG. 3.3-22

3.4 FAST Physics Simulations for the Technical Design Report

The principal design goals of the GEM detector remain precise measurements of electromagnetic energy and muon momenta with systems robust enough to operate well above the nominal SSC design luminosity. Hadronic energy will be well-measured over the central region, $|\eta| \lesssim 3.0$. Central tracking coverage to $|\eta| = 2.5$ will be an important adjunct to the calorimeter, helping to realize its potential for electromagnetic energy measurement over the entire range of energies, from 25 GeV to several TeV, and up to ultrahigh luminosity. Forward calorimeter coverage to $|\eta| \simeq 5.5$ will determine $\not{E}_T > 100\,\mathrm{GeV}$ with adequate accuracy.

In preparation for the Technical Design Report, technology choices for the GEM calorimeter, muon, and tracking systems will be made by September. With the major elements of the GEM design essentially frozen until the TDR, a FAST parameterization of this "final" version will be executed. The GEM Physics Group then will study an extensive set of processes chosen both for their usefulness in testing the broadest possible range of GEM capabilities and for their physics interest. This effort has two goals: (1) To provide feedback on detector performance to the designers in a timely enough fashion to influence the design and enhance the physics performance of the detector. (2) To provide as accurate as possible a picture of the expected performance capabilities of all of GEM's major subsystems. The processes we plan to study are listed below. Many of them are familiar from recent submissions (including this report) by GEM and other collaborations. Other processes have not received detailed scrutiny before and will require encoding in the event generators.

3.4.1 Standard Model Higgs Physics

1. $H^0 \to \gamma\gamma$ ($M_H \cong 80 - 150\,\mathrm{GeV}$)
2. $t\bar{t} + H^0 \to \ell\gamma\gamma + X$ ($M_H \cong 80 - 150\,\mathrm{GeV}$).
3. $H^0 \to Z^0 Z^0 \to \ell^+\ell^-\ell^+\ell^-$ for $\ell = e, \mu$ ($M_H \cong 140 - 800\,\mathrm{GeV}$).
4. $H^0 \to Z^0 Z^0 \to \ell^+\ell^-$ jet jet ($M_H \simeq 800\,\mathrm{GeV}$).
5. $H^0 \to Z^0 Z^0 \to \ell^+\ell^-\nu\bar{\nu}$ ($M_H \simeq 800\,\mathrm{GeV}$).

3.4.2 Heavy Flavor Physics

1. $t\bar{t}$ production for $m_t \simeq 250\,\mathrm{GeV}$ in standard ($t \to W^+ b$) and non-standard ($t \to H^+ b$) decay modes and mass measurement via the $M_{\ell\mu}$ and multijet distributions.

2. Leptoquark pair-production $gg, \overline{q}q \to \pi_{\overline{L}Q}\pi_{\overline{Q}L}$, with decays to heavy flavors such as $\pi_{\overline{L}Q} \to \tau^+ b$ and $\mu^+ b$.
3. Single technieta production, $gg \to \eta_T \to t\overline{t}$.
4. Color-octet technihadron production, $gg, \overline{q}q \to \rho_T^8 \to \pi_{\overline{Q}Q}\pi_{\overline{Q}Q}$ with technipion decays to heavy quark pairs, e.g., $\pi_{\overline{Q}Q} \to b\overline{b}, t\overline{b}, t\overline{t}$.

3.4.3 Jet Physics

1. Quark substructure in high-p_T and invariant mass jet production (deviation from QCD cross sections at $p_T \gtrsim 4\,\text{TeV}$).
2. Color-octet technirho or axigluon resonances in dijet production, $gg, \overline{q}q \to \rho_T^8 \to$ jet jet.
3. Color-octet technihadron production, $gg, \overline{q}q \to \rho_T^8 \to \pi_{\overline{Q}Q}\pi_{\overline{Q}Q}$ with technipion decays to light quark pairs.
4. $\widetilde{g}\widetilde{g}$ detection via a complicated multijet signature.

3.4.4 Physics at Ultrahigh Luminosity

1. Signal and backgrounds for quark – lepton substructure at the scales $\Lambda \gtrsim 25\,\text{TeV}$ in the Drell-Yan process $\overline{q}q \to \mu^+\mu^-$.
2. Signal and backgrounds for quark – lepton substructure at the scales $\Lambda \gtrsim 25\,\text{TeV}$ in the Drell-Yan process $\overline{q}q' \to \mu^\pm\nu$. Chiral structure of the contact interaction will be probed via the η_μ distribution.
3. Signal and backgrounds for $Z'^0 \to \ell^+\ell^-$, with $\ell^\pm = e^\pm, \mu^\pm$. Precision measurements of the mass and width (via e^+e^-) and asymmetries (via $\mu^+\mu^-$); determination of the reach in $M_{Z'}$.
4. Signal and backgrounds for $W'^\pm \to \ell^\pm\nu_\ell$. Precision measurements of the mass, width and asymmetry; determination of the reach in $M_{W'}$.
5. Signal and backgrounds for color-singlet $\rho_T^\pm \to Z^0W^\pm \to \ell^+\ell^-\ell^\pm + \not{E}_T$ and $\ell^+\ell^-$ jet jet.

3.4.5 Other Topics

1. Neutral and charged Higgs-like color-singlet scalars (H'^0) and ($H^\pm$) found in extensions of the standard model, supersymmetry and technicolor.

(a) $H'^0 = h^0, \pi_T^0 \to \gamma\gamma$ ($M_{H'^0} < 2M_W$).

(b) $t \to H^+b$, for $m_t > M_{H^+}$, with $H^+ \to c\overline{s}$ and $\tau^+\nu_\tau$.

(c) Electroweak pair-production of H^+H^-, with $H^+ \to t\overline{b}$ ($M_{H^+} > m_t$).

2. $H^0 \to \ell^+\ell^-\tau^+\tau^-$ at $M_H \simeq 800\,\mathrm{GeV}$.

3. Alternatives to $H^0 \to \gamma\gamma$ will be studied for the intermediate mass Higgs and similar particles (h^0 and π_T^0). Some possibilities are $gg \to H^0 \to \tau^+\tau^-$ and $t\bar{t} \to t\bar{t}H^0$ with $H^0 \to \tau^+\tau^-$ and/or $b\bar{b}$.

4. For either technical or financial reasons, certain subsystems or parts of subsystems may have to be staged. We need to determine alternative search modes and evaluate the backgrounds for new physics processes whose discovery is threatened by staging.

References

1. *GEM Letter of Intent*, The GEM Collaboration (November 30, 1991).
2. Report of the Superconducting Super Collider Program Advisory Committee, December 15 – 17, 1991, SSC Laboratory, dallas, TX.
3. GEANT reference.
4. GEM Baseline I, GEM-TN-76 (April 23, 1992).
5. F. E. Paige and S.D. Protopopescu, BNL-38774 (1986).
5. *A Manual to the Lund Monte Carlo for Hadronic Processes*, H. -U. Bengtsson and T. Sjostrand; *The Lund Monte Carlo for Jet Fragmentation and e+e- Physics*, T. Sjostrand.
6. Lynn Garren, FNAL report PM0050 (1991).
7. R.K. Bock, et al. NIM **186**, 533 (1981).
8. Cleland reference.
9. R. -Y. Zhu and H. Yamamoto, *Intermediate Mass Higgs Searches with the GEM Detector*, GEM-TN-92-126 (1992).
10. A. Djouadi, M. Spira and P. M. Zerwas, Phys. Lett. **B264**, 440 (1991).
11. W. J. Marciano and F. E. Paige, BNL Preprint, **BNL-45805**; J. F. Gunion, et al., SDC report, **SDC-91-00057**; R. Kleiss et al., Phys. Lett. **B253**, 269 (1991); Z. Kunszt, et al. Phys. Lett. **B271**, 247 (1991).
12. I. Hinchliffe, *A Monte Carlo Parton Generator*, unpublished.
13. This analysis was performed by C. Yanagisawa.
14. This analysis was performed by J. Antos.
15. See, e.g., R. S. Chivukula, in Proceedings of the GEM Meeting, Tucson, AZ (March 1992).
16. This analysis was done by A. Sumarokov.
17. The expressions for the couplings and their values that appear below correct transcription errors made in the LoI.
18. This analysis was done by M. Golden, K. Lane and E. Simmons.
19. E. J. Eichten, K. D. Lane and M. E. Peskin, Phys. Rev. Lett. **50**, 811 (1983).
20. E. Eichten, I. Hinchliffe, K. Lane and C. Quigg, Rev. Mod. Phys. **56**, 579 (1984).
21. R. S. Chivukula and L. Randall, Phys. Lett. **202B**, 429 (1988).
22. We are greatly indebted to T. Sjostrand for embedding the quark and lepton compositeness routines in PYTHIA and for continued help on the event simulations.
23. The $t\bar{t}$ cross section was determined by generating 400K PYTHIA 5.5 events; other cross sections come from parton-level calculations.

24. G. E. Forden, AZPH-EX-91-31, Aug 1991.
25. H. E. Haber and G. L. Kane, Phys. Rept. **117**, 75 (1985).
26. H. Baer, et al., Phys. Rev. **D45**, 142 (1992).
27 F. Abe et al., The CDF Collaboration, "Inclusive Jet Cross section in $\overline{p}p$ Collisions at $\sqrt{s}$ =1.8 TeV", Phys. Rev. Lett. **68**, 1104 (1992); Fermilab-PUB-91/231-E.
28 H. Paar and R. Wigmans, "Jet-Energy Measurements with a Noncompensating Calorimeter System", GEM Technical Note, March, 1992.

GEM TN-92-126

Intermediate Mass Higgs Searches with GEM Detector

$$H \rightarrow \gamma\gamma$$
$$H(t\bar{t}/W) \rightarrow (\mu/e)\gamma\gamma X$$
$$H \rightarrow e^+e^-e^+e^-$$

Ren-yuan Zhu and Hiro Yamamoto

Lauritsen Laboratory
California Institute of Technology
Pasadena, CA 91125

July 7, 1992

Part of GEM Physics Report to PAC

Abstract

This report summarizes a study on signal and background for intermediate mass Higgs searches at SSC by using precision electromagnetic calorimeters proposed by GEM collaboration. Searches by using $H \rightarrow \gamma\gamma$, including lepton associate production channel $H(t\bar{t}/W) \rightarrow (\mu/e)\gamma\gamma X$, and $H \rightarrow e^+e^-e^+e^-$ are discussed. Various physics as well as detector design issues were investigated. The backgrounds from real photons and electrons and misidentified photons and electrons originated from jets are elaborated.

1 Introduction

As a precision lepton photon detector, the discovery potential of the GEM (Gamma-Electron-Muon) detector is shown in its ability of detecting Higgs particles in intermediate mass range between 80 and 180 GeV through its $\gamma\gamma$ and 4ℓ (ZZ^*) modes [1], where ℓ refers to electron or muon (e/μ). While the 4ℓ decay mode will allow GEM to detect a Higgs with a mass heavier than 140 GeV, the $\gamma\gamma$ decay mode will cover a gap between the upper limit for Higgs detection at LEP Phase II (80 GeV) [2] and 140 GeV.

$H\rightarrow \gamma\gamma$ detection places stringent requirements to the overall detector design, especially to the design of the electromagnetic calorimeter (EMC). Because of the small production cross-section (60 to 200 fb) and the narrow decay width (5 to 10 MeV) of the Higgs boson in this mass range, and because of the huge irreducible direct $\gamma\gamma$ background (276 pb) and the QCD jet background, precision EMC's, capable of measuring $\gamma\gamma$ invariant mass to a high precision, are pursued by GEM. Two subsystems were proposed: a barium fluoride (BaF_2) crystal calorimeter and a liquid argon (LAr) accordion calorimeter with liquid krypton (LKr) option.

The main course of this note reports a study on signal and background of Higgs searches by using $H\rightarrow \gamma\gamma$ channel. Large fraction of this work, including Higgs searches by using lepton associate production channel $Ht\bar{t} \rightarrow \ell\gamma\gamma$, was carried out by one of the authors for GEM LoI study, and has been reported in a GEM note [3]. The analysis, since then, has been supplemented by additional studies to address a broader range of physics issues in $H\rightarrow \gamma\gamma$ searches. To be complete, Higgs searches by using $H\rightarrow e^+e^-e^+e^-$ channel are also discussed.

The background from real photons and electrons, as well as misidentified photons and electrons from jets are investigated. For jet background rejection, the consequence of thermal as well as pileup noise in an isolation cone is discussed.

The Monte Carlo program used in this study is PYTHIA 5.6 [4], and the top quark mass is assumed to be 140 GeV. An SSC year (SSCY) is defined as 10^{40} cm^{-2} integrated luminosity.

2 γ/e Response of GEM EM Calorimeters

The responses of GEM detector to isolated photons or electrons were simulated according to parametrized energy, position and vertex z resolutions. The parametrization was obtained by using rigorous GEANT simulations for each proposed subsystems [5,6]. Key parameters of detector performance were varied to investigate their influences to the physics performance.

In this section we discuss the parametrization of energy resolution and detector coverage. A global parametrization of GEM detector response used in event acceptance and jet background study is also described in this section. The detailed procedure of GEANT simulation and justification of all parameters used in analysis can be obtained in corresponding GEM notes: reference [5] for BaF_2 simulation and reference [6] for LAr simulation. In a short summary, the parametrization of detector performance is as follows:

- **Energy Resolution:**
  - $(2.0/\sqrt{E} \oplus 0.5)\%$ for homogeneous BaF_2 calorimeter; and
  - $(7.5/\sqrt{E} \oplus 0.5)\%$ for LAr accordion and $(5.5/\sqrt{E} \oplus 0.5)\%$ for LKr accordion.
- **Position Resolution:** $\delta x = \delta y = 1$ mm at front surface of EMC are used for both calorimeters;
- **Vertex z Resolution:** $\delta z = 1$ mm are used for both calorimeters. Photon momentum vector is assumed to be reconstructed by using its impact point at the front surface of the EMC and the primary event vertex, which is determined by using central tracker at standard SSC luminosity $\mathcal{L} = 10^{33}$ cm^{-1} s^{-1} (see section 3.6 for the details).

2.1 Parametrization of γ/e Energy Resolution

The energy resolution of an electromagnetic calorimeter can be parametrized as:

$$(\frac{\Delta E}{E})^2 = (\frac{a_0}{E})^2 + (\frac{a_1}{\sqrt{E}})^2 + b^2 \qquad (1)$$

where

- $\mathbf{a_0}$ is the contribution from electrical noise, summed over detector readout channels within a few Moliere radii around the center of the lateral shower distribution;
- $\mathbf{a_1}$ is the contribution from the photoelectron statistics;
- the systematic term **b** has three contributions:

$$\mathbf{b^2 = b_n{}^2 + b_G{}^2 + b_C{}^2} \tag{2}$$

  - $\mathbf{b_G}$ represents the geometry effect, including shower leakage at the front, side and back of the detector and inactive material between cells;
  - $\mathbf{b_n}$ represents physics noise, including fluctuations and uniformity of response from active media etc.;
  - $\mathbf{b_C}$ represents intercalibration error.

At low energy, the dominant contribution to the energy resolution is the noise term ($\mathbf{a_0}$), which decreases quickly with increasing energy. The sampling term ($\mathbf{a_1}$) dominates in the range of medium to high energies until a high energy limit is reached, where the systematic term (**b**) dominant. While term $\mathbf{a_0}$, and term $\mathbf{a_1}$ for a total absorption calorimeter, can be calculated analytically, terms $\mathbf{b_G}$, $\mathbf{b_n}$, and term $\mathbf{a_1}$ for a sampling calorimeter, must be studied with realistic GEANT simulations. If systematic effects from $\mathbf{b_n}$ and $\mathbf{b_C}$ are under control, a GEANT simulation on energy deposition in active media may provide the best resolution an EMC can achieve.

In this report, for simplicity, we parametrize the energy resolution of an EMC as a function of parameters **a** and **b**:

$$\frac{\Delta E}{E} = (\frac{\mathbf{a}}{\sqrt{\mathbf{E}}} \oplus \mathbf{b})\% \tag{3}$$

where $\oplus$ denotes an addition in quadrature.

2.1.1 BaF_2 Simulation

A detailed GEANT simulation was carried out to estimate the effect of shower leakage and non-active material for the BaF_2 design [5]. The BaF_2 matrix used in this simulation, which consists of 121 (11 × 11) BaF_2 crystals with the proposed size: 3 × 3 cm^2 at the front, 5 × 5 cm^2 at the back and 50 cm long. Effects included in the simulation are:

- 250 μm carbon fiber wall between crystals;

- shower leakage because of summing a limited number (3×3 or 5×5) of crystals; and
- 0.30 radiation lengths of aluminum, representing the beam pipe, tracker, and carbon fiber mechanical support, at the front of the BaF_2 array.

Particles were shoot uniformly at the front surface of the center crystals of the array. The energies deposited in each crystal, in the carbon fiber walls between crystals, in the aluminum and leaking out sideways were recorded. The result of this simulation for electrons with different energies (5, 10, 20, 50, 100, 200 and 500 GeV), in terms of σ of the peak, full width at half maximum (FWHM) divided by 2.35, is listed in Table 1.

Table 1: Energy Resolution (%) of BaF_2 Calorimeter

E (GeV)	5	10	20	50	100	200	500
Electrical Noise	0.4	0.2	0.1	0.04	0.02	0.01	0.004
Photoelectrons	0.2	0.14	0.1	0.063	0.045	0.03	0.02
GEANT (b_G)	0.60	0.43	0.32	0.30	0.30	0.30	0.36
Intercalibration (b_C)	0.40	0.40	0.40	0.40	0.40	0.40	0.40
Total	0.85	0.63	0.53	0.51	0.50	0.50	0.54

Table 1 summarizes the BaF_2 resolution, including the contributions from electrical noise, photoelectron statistics, intrinsic resolution from GEANT simulation and the intercalibration. Based upon the discussion in reference [5], a precision of intercalibration of 0.4% is assumed. Note, in this table the light response uniformity (b_n) was assumed to be under control. The real effect of light response uniformity is discussed in details in reference [5]. The result of the energy resolution is shown in Fig. 1b. It can be parametrized as $2\%/\sqrt{E} \oplus 0.5\%$, which is also shown in Fig. 1b as a solid line.

As a comparison, Fig. 1a shows the energy resolution measured with 4000 BGO crystals (half barrel) in a CERN test beam [7]. In the energy range beyond 20 GeV, the dominant contribution to the energy resolution is the systematic intercalibration uncertainties. The resolution of the L3 BGO calorimeter may also be parametrized as $2\%/\sqrt{E} \oplus 0.5\%$, shown as a solid line in Fig. 1a.

2.1.2 LAr Simulation

As detailed in reference [6], an accordion geometry was used in GEANT simulation to evaluate the intrinsic resolution of LAr calorimeter. The result shows that at 90° incident the energy resolution of LAr accordion calorimeter with 1 mm Pb plate can be parametrized as $\mathbf{a} = 7$ in Equation 3.

A study on incident angle dependence shows that the energy resolution of LAr calorimeter is about the same at $|\eta| = 1$ but rises to $\mathbf{a} = 8.5$ at $|\eta| = 1.3$ for a constant plate thickness. However, we plan to change the thickness of the absorber plate at a convenient angle to keep the resolution at $|\eta| = 1.3$ to be about the same value as at $\eta = 0$.

Taking into account of various systematics in Equation 1, we thus use $\mathbf{a} = 7.5$ and $\mathbf{b} = 0.5$ for LAr energy resolution parametrization. This resolution can be further improved by replacing liquid argon with liquid krypton. In this case, the GEANT study shows that $\mathbf{a} = 5.5$ and $\mathbf{b} = 0.5$ are the design goal.

2.2 γ/e Acceptance

The detailed design of GEM calorimeters is evolving in time. A realistic estimation of γ/e acceptance may only be provided after the completion of detailed design of the calorimeter. Here we discuss general principle of our treatment of acceptance problem. Both geometry acceptance and e/γ identification efficiency are discussed in this section.

Although both calorimeter options are designed to cover up to $|\eta| < 3.0$, the effective geometry acceptance is $|\eta| < 2.5$ because of the rapidity coverage of GEM central tracker. In both BaF_2 and LAr calorimeters, there are dead spaces and regions where the energy resolution is extremely bad. In the following rapidity regions, the energy resolution is expected to be very bad, or EM energy may not be measured at all:

- BaF_2 $\quad |\eta| = 0 - 0.0125$ and $|\eta| = 1.348 - 1.388$;
- LAr $\quad |\eta| = 1.22 - 1.39$.

When an electron or γ hits the calorimeter close to these dead regions, some of the showers leak into the dead region, and large corrections might be necessary. The exact effect on energy resolution in these region can only be investigated by using detailed

GEANT simulation. A most pessimistic estimation of this effect, however, may be obtained by excluding the boundary and its vicinity of $\Delta\eta = \pm\ 0.04$ if the boundary has dead material in its neighbour. We thus have the following dead regions:

- BaF_2 $\quad |\eta| = 0 - 0.0525$ and $|\eta| = 1.308 - 1.428$;
- LAr $\quad |\eta| = 1.18 - 1.39$.

The effect of these dead regions was studied to investigate the overall physics acceptance for $H \to \gamma\gamma$, $Ht\bar{t} \to \gamma\gamma\ell$ and $H \to e^+e^-e^+e^-$. Assuming the muon acceptance is 90%, Table 2 shows the result of geometry acceptance (GA) by using our standard event selection cuts, described in this report, for these physics processes. For each calorimeter option both optimistic (O) and pessimistic (P) dead region assumptions were investigated, and the event is accepted if none of the γ/e hits the dead region.

Table 2: Geometry Acceptance (GA) of GEM EM Calorimeters

Process	BaF_2 (O)	BaF_2 (P)	LAr (O)	LAr (P)	Abs. Efficiency
$H \to \gamma\gamma$	0.95	0.86	0.87	0.83	0.49
$Ht\bar{t} \to \gamma\gamma\mu X$	0.86	0.77	0.77	0.74	0.16
$Ht\bar{t} \to \gamma\gamma eX$	0.93	0.81	0.79	0.74	0.16
$H \to ZZ^* \to 4e$	0.91	0.75	0.73	0.67	0.45
$H \to ZZ \to 4e$	0.90	0.74	0.74	0.68	0.50

The geometry acceptance listed in Table 2 does not depend on the Higgs mass, and is entirely determined by the number of electrons or gammas being detected. The last column of Table 2 is the average absolute event selection efficiency, assuming no dead region in $|\eta| < 2.5$. This efficiency, however, is Higgs mass dependent. The numbers given here are for a quick reference purpose.

It is clear from above table, that the effect on acceptance caused by dead region in calorimeter can be understood as

$$\left(\frac{5. - \Delta\eta(dead)}{5.}\right)^{\#\ e's\ and\ \gamma's\ to\ detect} \tag{4}$$

The average geometry acceptance of most optimistic and pessimistic cases is listed in Table 3. Assuming 90% identification efficiency for each μ, e and γ, Table 3 also

lists the final relative acceptance (RA) for each physics process. Since this relative acceptance is applied to both signal and background, its real consequence in discovery potential is a loss of significance of $\sqrt{RA}$ (see Equation 5 for the details), or an increase of discovery time of 1/RA.

Table 3: Average GA and Final Relative Acceptance (RA)

	Average GA		RA	
Process	BaF_2	LAr	BaF_2	LAr
$H \rightarrow \gamma\gamma$	0.90	0.85	0.73	0.69
$Ht\bar{t} \rightarrow \gamma\gamma\mu X$	0.82	0.76	0.60	0.55
$Ht\bar{t} \rightarrow \gamma\gamma eX$	0.87	0.77	0.63	0.56
$H \rightarrow ZZ^* \rightarrow 4e$	0.83	0.70	0.54	0.46
$H \rightarrow ZZ \rightarrow 4e$	0.82	0.71	0.54	0.47

To facilitate comparison, this relative acceptance has not been applied to the tables and figures in this report. Its consequence on signal significance, however, is discussed for each physics process.

2.3 Parametrized Response of Calorimeters

For event acceptance and jet background rejection calculation, a parametrized response of ideal calorimeter systems was used. The ideal calorimeters were defined in $|\eta| < 2.5$, and were segmented to $\Delta\eta \times \Delta\phi = 0.04 \times 0.04$ in both EMC and hadron calorimeter (HCAL) sections. No longitudinal segmentation in EMC or HCAL was assumed.

The longitudinal energy division between EMC and HCAL was assigned based upon a GEANT study for BaF_2 calorimeter [8]. γ's or electrons have 100% of their energies deposited in EMC. All muons are minimum ionizing, i.e. deposit minimum ionizing energy (MIE) in EMC. For charged hadrons, if its energy is less than 2 MIE then all its energy were deposited in EMC, otherwise it has 25% probability of depositing MIE in EMC, and 75% probability of depositing a fraction of its energy in EMC with the rest in HCAL. This fraction was determined according to a uniform distribution between MIE and about 80% of the energy of the hadron.

The energies deposited in EMC and HCAL were further divided to 50 pieces and

deposited to cells according to lateral shower profile. This process provides a first order approximation of lateral energy distribution in EMC/HCAL cells.

A reconstruction procedure was developed to identify isolated electrons or photons. The program looks cells with the highest energy comparing with its eight neighbours first, and sum the energy of 3×3 cells to define the energy of the isolated EM cluster. The program further requires no or one charged track hits the center cell to distinguish photon and electron. An isolation cut was used to reject QCD background, as described in Section 4.1.

This program is used in calculations of event acceptance and jet background rejection. It was also used in a trigger rate study [8] for physics processes discussed in this report.

3 Signal and Irreducible Background

3.1 Signal Cross Section

Figure 2 shows the production cross-sections of standard model Higgs in three interesting decay modes: (a) $\gamma\gamma$, (b) $(t\bar{t}/W)H \rightarrow \gamma\gamma\ell X$, and (c) $ZZ^*/ZZ \rightarrow e^+e^-e^+e^-$, before event selection cuts. These cross sections were calculated by using PYTHIA 5.6 program.

For the Higgs mass range between 80 to 150 GeV, the $\gamma\gamma$ decay mode provides 1200 to 2100 events per SSC year, while $t\bar{t}H \rightarrow \gamma\gamma\ell X$ together with $WH \rightarrow \gamma\gamma\ell X$ provide 70 to 240 events without lepton tagging, or 20 to 70 events with electron or muon tagging. The 4 electron decay channel ($ZZ^* \rightarrow e^+e^-e^+e^-$) provides 20 to 80 events per SSC year. Combining electron and muon, 80 to 320 would be produced before cuts. Table 4 lists production cross-section and number of events accepted after passing event selection cuts described in this report. Note, the event numbers listed in this table are for a perfect calorimeter, covering $|\eta| < 2.5$. The acceptance loss discussed in section 2.2 is not included in the table.

Taking into account a recent calculation of high order QCD corrections to the Higgs production [9], the production cross sections of $H \rightarrow ZZ^* \rightarrow e^+e^-e^+e^-$ and $H \rightarrow \gamma\gamma$ should be increased by a K factor of around 1.5 for Higgs mass below $t\bar{t}$ threshold. However, since we do not have a consistent picture of high order QCD corrections to the background processes, we choose not to change the signal cross section in this report. The consequence of this increase of signal cross section to the significance of the physics signal will be discussed individually for each relevant physics process.

3.2 Irreducible $\gamma\gamma$ Background

The main background in $H \rightarrow \gamma\gamma$ searches is direct photon production [10]. The cross-section of this background was calculated to be 276 pb for $\hat{p}_T > 20$ GeV:

- $q\bar{q} \rightarrow \gamma\gamma$: 78 pb; and
- $gg \rightarrow \gamma\gamma$ via a box diagram: 198 pb.

The event topology of $H \rightarrow \gamma\gamma$ and this background are similar. This so-called *"irreducible background"* therefore has to be reduced by event selection cuts. Figure 3

Table 4: Production Cross-Section and Events/SSCY

M_H(GeV)	$\sigma_{H(\gamma\gamma)}(fb)$	$N_{\gamma\gamma}$	$\sigma_{LH(\gamma\gamma)}$ (fb)	$N_{l\gamma\gamma}$	$\sigma_{H(4e)}(fb)$	N_{4e}
80	124	510	8.4	18		
90	144	610	8.0	20		
100	169	730	7.8	21		
120	211	990	6.9	18		
140	180	880	4.2	14	6.5	27
150	128	630	2.6	8	7.9	39
160	52.6	270	0.87	3	3.7	16
170					2.3	14

shows the distributions of photon rapidity (η_γ), photon transverse energy (E_T^γ), rapidity of the 2 photon system ($\eta_{\gamma\gamma}$) and $\cos\theta^*$, where θ^* is the polar angle of photons in the $\gamma\gamma$ rest frame, for H$\rightarrow \gamma\gamma$, $q\bar{q} \rightarrow \gamma\gamma$ and $gg \rightarrow \gamma\gamma$.

Event selection cuts used to reduce this background are:

- $|\eta_\gamma| < 2.5$;
- $E_T > 20$ GeV;
- $|cos\theta_\gamma^*| < 0.9 \Rightarrow$ reduce $gg \rightarrow \gamma\gamma$;
- $|\eta_{\gamma\gamma}| < 3 \Rightarrow$ reduce $qq \rightarrow \gamma\gamma$.

After event selection cuts, the cross-section of irreducible background is reduced to 42 pb for $M_{\gamma\gamma} > 75$ GeV, while the acceptance of H$\rightarrow \gamma\gamma$ events is about 50%.

3.3 Significance of Higgs Peaks

Because of large numbers of irreducible background events, the significance (S) of Higgs peaks can be calculated by dividing the number of signal events counted within a mass interval of $M_H \pm \sigma_{M_{\gamma\gamma}}$ by the square root of the corresponding background events in

the same mass interval, where $\sigma_{M_{\gamma\gamma}}$ is the $\gamma\gamma$ invariant mass resolution. We thus have

$$S = \frac{N_S}{\sqrt{N_B}} = \frac{\int \mathcal{L}dt\ A_S\ RA\ 0.683\sigma_{H\to\gamma\gamma}}{\sqrt{\int \mathcal{L}dt\ A_B\ RA\ 2\sigma_{M_{\gamma\gamma}}\ R_B}} \propto \sqrt{\frac{RA\int \mathcal{L}dt}{\sigma_{M_{\gamma\gamma}}}} \tag{5}$$

where A_S and A_B are the absolute acceptance of signal and background respectively, RA is the relative acceptance discussed in section 2.2, and R_B is the background rate at Higgs mass. It is clear from Equation 5 that a better mass resolution or a large relative acceptance is equivalent to a shorter discovery time.

3.3.1 $\gamma\gamma$ Mass Resolution

Analytically, the mass resolution reconstructed by using two photon energy vectors can be expressed as:

$$\frac{\sigma_{M_{\gamma\gamma}}}{M_{\gamma\gamma}} = \frac{1}{2}\sqrt{(\frac{\Delta E_1}{E_1})^2 + (\frac{\Delta E_2}{E_2})^2 + (\cot\frac{\theta}{2}\Delta\theta)^2} \tag{6}$$

where E_1 and E_2 are energies of two photons and θ is the opening angle between them.

In this analysis, mass resolution was calculated by using Higgs events passing event selection cuts. Events were generated by using PYTHIA 5.6 program. The primary event vertex position and photon impact point at front surface of the EMC were used to reconstruct the photon momentum vectors, taking into account the effects of energy resolution assumed, 1 mm position resolution at the front surface of EMC and 1 mm vertex z resolution. It was assumed that the primary event vertex can be determined by using central tracker at standard SSC luminosity 10^{33} cm^{-2} s^{-1} (see section 3.6 for the details).

3.3.2 Significance

Figure 4 shows $\gamma\gamma$ invariant mass spectra collected in one SSCY with Higgs signals (80, 100, 120, 140 and 160 GeV) superimposed over the irreducible background for three energy resolutions: $(2/\sqrt{E} \oplus 0.5)\%$ (BaF_2), $(7.5/\sqrt{E} \oplus 0.5)\%$ (LAr) and $(15/\sqrt{E} \oplus 1)\%$ (Sampling). Corresponding background subtracted spectra are shown in Figure 5.

Table 5 summarizes production cross-section and number of signal events (N_S) in $M_H \pm \sigma_{M_{\gamma\gamma}}$ for different Higgs masses. Also listed in Table 5 are mass resolutions ($\sigma_{M_{\gamma\gamma}}$) and significances (S) for three nominal energy resolutions.

Table 5: Significance of H$\rightarrow \gamma\gamma$ Searches in one SSCY

$\Delta E/E$ (%)			$2/\sqrt{E} \oplus 0.5$		$7.5/\sqrt{E} \oplus 0.5$		$15/\sqrt{E} \oplus 1.0$	
M_H (GeV)	$\sigma_{\gamma\gamma}$ (fb)	N_S	$\sigma_{M_{\gamma\gamma}}$ (GeV)	S	$\sigma_{M_{\gamma\gamma}}$ (GeV)	S	$\sigma_{M_{\gamma\gamma}}$ (GeV)	S
80	124	360	0.34	4.6	0.66	3.2	1.3	2.3
90	144	430	0.37	6.1	0.70	4.5	1.4	3.2
100	169	510	0.40	8.6	0.73	6.3	1.45	4.5
120	211	690	0.45	14	0.77	11	1.5	7.7
140	180	620	0.53	16	0.89	12	1.7	8.9
150	128	450	0.58	13	0.95	10	1.9	7.3
160	52.6	190	0.65	5.9	1.1	4.7	2.0	3.4

Figure 6 shows the significance of Higgs search as a function of SSCY for Higgs masses of 80, 90, 100, 120, 140, 150 and 160 GeV. In this figure the significance is plotted as a band for each energy resolution. While the up bound corresponds to the background of irreducible $\gamma\gamma$ background only, the low bond corresponds to a total irreducible QCD background as discussed in Section 4.2.

Note, the event numbers, listed in this table and in Figure 4 and 5, are for a perfect EMC without including the acceptance loss discussed in section 2.2. Taking into account the relative acceptance listed in Table 3, the numbers of both signal and background events should be reduced to 73% and 69% respectively for BaF_2 calorimeter and LAr calorimeters. The corresponding significance should be reduced to 85% and 83% respectively.

On the other hand, taking into account high order QCD corrections to the Higgs production [9], i.e. the K factor of 1.5, the corresponding numbers of signal events and the significance should both be increased by a factor of 1.5. Note, the dominant irreducible background of gg$\rightarrow \gamma\gamma$ is an $O(\alpha_s^2)$ process.

Table 5 shows clearly the importance of excellent energy resolution in pursuing this physics. In summary, there is a factor of $\sqrt{1.8}$ difference in significances of H$\rightarrow \gamma\gamma$ detection, or a factor of 1.8 difference in time needed to achieve certain significance, between two neighboring energy resolutions in above table.

According to Equation 5, an easy way to evaluate detector performance in terms of physics discovery potential is to look its $\gamma\gamma$ mass resolution. In the rest of this section, we discuss the consequences of deviations from the designed resolutions.

3.4 Effect of Energy Resolution

To study systematically the effect of energy resolution, we parametrize the energy resolution of an EMC as a function of parameters **a** and **b**, as defined in Equations 3. The result of this analysis, listed in Table 6, shows the ratio of H$\rightarrow \gamma\gamma$ peak width as a function of energy resolution (**a** and **b**), normalized to the case of **a** = 2 and **b** = 0.5, for Higgs mass of 80 GeV and 150 GeV. Because of the high statistics of the background, this ratio corresponds to the time factor needed to discover a narrow $\gamma\gamma$ resonance, as indicated in Equation 5.

Table 6: Ratio of H$\rightarrow \gamma\gamma$ Peak Width as Function of **a** and **b**.

a	2.0	3.0	5.5	7.5	10	15
M_H = 80 GeV						
b=0.5	**1.0**	1.1	1.5	1.9	2.4	3.4
b=.75	1.4	1.5	1.7	2.1	2.6	3.6
b=1.0	1.8	1.8	2.1	2.4	2.8	3.8
b=1.5	2.6	2.6	2.8	3.1	3.4	4.2
b=2.0	3.4	3.5	3.6	3.8	4.1	4.8
M_H = 150 GeV						
b=0.5	**1.0**	1.1	1.3	1.6	2.0	2.8
b=.75	1.4	1.5	1.7	1.9	2.3	3.0
b=1.0	1.8	1.9	2.0	2.2	2.5	3.2
b=1.5	2.6	2.7	2.8	3.0	3.2	3.7
b=2.0	3.6	3.6	3.7	3.8	4.0	4.4

3.5 Effect of Position Resolution

It is also interesting to see the effect of shower position resolution. Table 7 shows the ratio of H$\rightarrow \gamma\gamma$ peak width as a function of the shower position resolution (δx) and energy resolution (a and b), for Higgs mass of 80 GeV. The numbers in the table are normalized to the case of a = 2, b = 0.5 and $\delta x = \delta y = 1$ mm. It is clear that the shower position resolution of an order of few mm will not compromise the discovery potential of a precision EM calorimeter.

Table 7: Ratio of H$\rightarrow \gamma\gamma$ Peak Width as Function of δx, a and b.

δx (mm)		0.5	1.0	1.5	2.0	2.5	3.0
a=2	b=0.5	0.97	1.0	1.0	1.1	1.1	1.2
a=5.5	b=0.5	1.5	1.5	1.5	1.6	1.6	1.6
a=7.5	b=0.5	1.9	1.9	1.9	1.9	2.0	2.0
a=15	b=3.7	3.8	3.8	3.8	3.8	3.8	3.8

3.6 Effect of Vertex z Resolution

As discussed above, a precise event vertex z position determination is very important for the discovery of Higgs in its $\gamma\gamma$ decay mode. The GEM central tracking system is designed to locate the event vertex with an accuracy of 1 mm in the z direction. However, with the standard luminosity of $\mathcal{L} = 10^{33}$ cm^{-2} s^{-1} and a bunch crossing frequency of 62.5 MHz, there are 1.6 minimum bias events (MBE) per bunch crossing, and the correct primary Higgs event vertex should be selected to achieve good mass resolution.

The selection of primary Higgs vertex with overlapping MBE's was studied by one of authors [11]. The algorithm follows an early study by L* [12], i.e. using the charged particle multiplicity coming out of each vertex in the event. The Monte Carlo programs used in simulation are PYTHIA 5.6 for Higgs signal and ISAJET 6.4.6 for the MBE's.

The vertex selection is done in two steps. In the first selection, all those vertices with good vertex position measurements are selected as the candidates. This cut is fairly arbitrary so long as the vertex location is well measured; and the loss of the

Higgs signal is small. In this study it was required that a vertex should have at least 12 charged tracks with $p_t \geq 200$ MeV in $|\eta| \leq 2.5$. This selection keeps more than 98% of the Higgs signal, and the average number of MBE's is 1.43 per bunch crossing after this cut.

In the second selection, the vertex with the largest charged multiplicity is selected as the primary Higgs vertex. The cut used in selecting charged tracks is $p_t \geq 1$ GeV in $|\eta| \leq 2.5$. The study also shows that the result of the second selection is not sensitive to the cuts used in the first selection.

By using above two cuts, the probability of selecting the correct primary Higgs vertex is around 96%, which is not sensitive to the Higgs mass between 80 to 160 GeV. This probability is also not sensitive to the track reconstruction efficiency, provided that it is better than 80%.

Note, the production of MBE's has theoretical uncertainty. In this simulation ISAJET was used, since its phenomenological parametrization for the MBE's agrees well with the available hadron collider data. However, it is not sure that the center of mass energy dependence is correctly implemented in ISAJET. To evaluate the model ambiguity, MBE's were also generated by using PYTHIA program. The probability of selecting correct primary Higgs vertex is found to be around 85%, which is independent of Higgs mass between 80 to 160 GeV.

Figure 7 shows a distribution of charge multiplicity of Higgs events after $p_T > 1$ GeV and $|\eta| < 2.5$ cuts. Also shown in the figure are corresponding distributions of MBE's generated with PYTHIA and ISAJET programs.

Taking into account theoretical uncertainties, we conclude that the correct primary Higgs vertex can be determined with a better than 90% confidence. This indicates

Table 8: Ratio of H$\rightarrow \gamma\gamma$ Peak Width as Function of δz, a and b

δz (mm)		1.0	2.0	3.0	5.0	10.	50.
a=2	b=0.5	1.0	1.0	1.1	1.1	1.5	5.4
a=5.5	b=0.5	1.5	1.5	1.6	1.6	1.9	5.5
a=7.5	b=0.5	1.9	1.9	1.9	2.0	2.2	5.6
a=15	b=1.0	3.8	3.8	3.8	3.8	3.9	6.5

that 90% of the Higgs event will have a vertex z position resolution of 1 mm, while the other 10% of Higgs events will have vertex z resolution of 5 cm.

To be complete, Table 8 shows the ratio of H$\rightarrow \gamma\gamma$ peak width as function of the vertex z coordinate resolution (δz), energy resolution (**a** and **b**), assuming shower position resolution $\delta x = 1$ mm, for Higgs mass of 80 GeV. The numbers in this table are normalized to the case of $\mathbf{a} = 2$ and $\mathbf{b} = 0.5$. It is clear one must determine vertex z to a level of better than 5 mm so that the discovery potential of a high energy resolution EM Calorimeter is not compromised.

4 Isolated Photon Background from QCD Jets

If there were no other background, the analysis for H$\rightarrow \gamma\gamma$ searches would have been finished in section 3. However, there are copious π^0's, and thus photons, produced in QCD jets. There are two major background from QCD jets: γ-jet and 2 jets final states. The production cross-section of γ-jet is 237 nb for $\hat{p}_T > 20$ GeV, including the following processes:

- qg$\rightarrow \gamma$q: 226 nb; and
- qq$\rightarrow \gamma$g: 11 nb.

The production cross section of QCD 2jets is 2 mb for $\hat{p}_T > 20$ GeV, including the following final states:

- gg: 1.54 mb;
- gq: 0.44 mb; and
- qq: 0.043 mb.

A narrow neutral jet consisting of multiple photons would fake an isolated photon. Single photons may also be produced in parton shower through bremsstrahlung process. To identify real photon and to reject QCD jet background, isolation cuts, shower shape analysis and preradiator may be used. The huge cross-section of these background processes make an accurate GEANT simulation not feasible in near future with foreseen computer power. Thus, a GEANT based parametrization, as described in Section 2.3, was used to obtain a realistic estimation of the background cross-section.

It is interesting to note that at "parton" level[1] distributions of the invariant mass of $\gamma\gamma$, γ-jet and 2jets are similar at high mass end, as shown in Figure 8. After implementing the isolation cut described below, the energy vector of a fake isolated photon, in general, follows that of its parent parton. It is thus reasonable to assume that the $\gamma\gamma$ spectra from all three background processes have similar shape. Therefore, we need only to calculate γ/jet rejection ratio for a given rejection cut, and to deduce contribution cross-section from corresponding background process.

We further use relevant integrated cross-section, e.g. in a mass range between 75 and 165 GeV, to calculate total background cross-sections, and find significances for a

[1] We denote photon as one of the partons together with quarks and gluons.

given Higgs signal by scaling. Note, the shower shape and preradiator cuts described in this section do not change cross-sections of the Higgs signal and the irreducible $\gamma\gamma$ background very much, since the efficiency for single isolated photon passing these cuts are required to be larger than 95%.

4.1 Isolation Cut

The isolation cut uses the following procedure:

- Generate γ-jet or 2jets, use only jets within detector acceptance and with $E_T >$ 20 GeV. Deposit energies of complete events in calorimeter cells, as described in Section 2.3. Mark cells which were hit by charged track in 8 kG field.
- Search through all cells to identify those cells hit by photons only, find E_T^{cell}.
- Charge Veto:

  Search through neighboring 8 cells, if any cell is hit by a charged track or its E_T^{cell} is larger than that of the central cell $\Rightarrow$ **Reject**;
- Define the sum of E_T^{cell}'s of these 9 cells ($\sum_{9cells} E_T^{cell}$) as the E_T^{photon};
- Isolation Veto:

  if the sum of the transverse energies in a cone of radius R ($R = \sqrt{\Delta\eta^2 + \Delta\phi^2}$), excluding the E_T^{photon}, is larger than 10% of the E_T^{photon} plus an isolation energy cut (E_T^{cut}):

$$\sum_{r<R} E_T - E_T^{photon} > (E_T^{cut} + 0.1 E_T^{photon}) \Rightarrow \textbf{Reject}. \tag{7}$$

Table 9 shows the result of R(γ/jet), defined as a probability of a jet passing above cuts and thus faking an isolated photon, as function of the size of isolation cone (R) and the E_T^{cut}, for two QCD processes.

It is interesting to note that the R(γ/jet) from γ-jet background is different comparing R(γ/jet) from 2jets background. This can be explained by different jet composition of these two processes. Since QCD 2jets have 12% quark jets and 88% gluon jets, while γ-jet have 95% quark jets and 5% gluon jets, we deduce that the isolation rejection ratio is about 10^{-3} for the quark jet and 2×10^{-4} for the gluon jet

Table 9: R(γ/jet) (10^{-4})

Process	2jets			γ-jet		
E_T^{cut}	R=0.45	R=0.60	R=0.75	R=0.45	R=0.60	R=0.75
5 GeV	5.3	4.1	3.1	16	13	9.6
10 GeV	8.8	6.8	6.2	30	26	22
15 GeV	13	10	8.6	40	34	32
20 GeV	16	14	13	54	47	43

when the tightest isolation cut is used, i.e. 5 GeV E_T^{cut} in a 0.75 cone. We further attribute this factor of 5 difference in isolation rejection to:

- gluon jet is more broader than the quark jet in fragmentation; and
- gluon jet has lower probability of producing a hard photon through bremsstrahlung.

4.2 Further Rejection of Isolated Photon Candidate

The isolation cut alone can not reduce the QCD jets background to below irreducible $\gamma\gamma$ background level. Looking at the isolated photon candidate (IPC) in details, however, one finds that many IPC's consist of more than one photons, and thus can be rejected by using shower shape analysis or preradiator. Figure 9 shows distributions of number of photons in isolated photon candidates after an isolation cut of R = 0.75 and E_T^{cut} = 10 GeV for 100k events each of a) γ-jet and b) 2jets events.

A calculation was carried out to select IPC's passing a rough isolation cut: R = 0.45 and E_T^{cut} = 20 GeV. Events samples with one IPC from 2jets process and two IPC's from γ-jet process were recorded in data files on physics detector simulation facility (PDSF) disk at SSCL for further analysis.

To identify how close the IPC's are to a real photon, an energy weighted mean opening angle, $\bar{\theta}$, is calculated for each IPC:

$$\bar{\theta} = \frac{\sum_i E_i \theta_i}{\sum_i E_i} \tag{8}$$

where

$$\cos\theta_i = \frac{\vec{E}_i \cdot \vec{n}}{E_i}, \quad \vec{n} = \frac{\sum_i \vec{E}_i}{|\sum_i \vec{E}_i|}, \tag{9}$$

and $\vec{E}_i$ is the energy vector of the ith photon in the isolated photon candidate.

Table 10: QCD "$\gamma\gamma$" Background Cross-Sections (pb) between 75 and 165 GeV

After Isolation						
Process	2jets			γ-jet		
E_T^{cut}	R=0.45	R=0.60	R=0.75	R=0.45	R=0.60	R=0.75
5 GeV	140	81	46	55	45	33
10 GeV	370	220	180	100	90	76
15 GeV	780	510	360	140	120	110
20 GeV	1200	940	800	190	160	150
After Shower Shape Analysis						
Process	2jets			γ-jet		
E_T^{cut}	R=0.45	R=0.60	R=0.75	R=0.45	R=0.60	R=0.75
5 GeV	73	34	20	31	26	21
10 GeV	160	120	89	54	50	42
15 GeV	250	210	140	68	59	57
20 GeV	310	260	230	83	73	66
After Preradiator						
Process	2jets			γ-jet		
E_T^{cut}	R=0.45	R=0.60	R=0.75	R=0.45	R=0.60	R=0.75
5 GeV	20	16	13	19	17	17
10 GeV	25	20	13	24	24	19
15 GeV	34	29	20	24	24	24
20 GeV	34	34	29	26	26	26
Irreducible QCD Jet Background						
Process	2jets			γ-jet		
E_T^{cut}	R=0.45	R=0.60	R=0.75	R=0.45	R=0.60	R=0.75
5 GeV	10	10	7.3	17	14	14
10 GeV	13	10	7.3	19	14	14
15 GeV	16	16	13	21	17	17
20 GeV	16	16	16	21	19	17

Figure 10 shows $\bar{\theta}$ distributions of isolated photon candidates after an isolation cut of R = 0.75 and E_T^{cut} = 10 GeV obtained from 100k events each of a) γ-jet and b) 2jets events. It is clear that those IPC's with a large $\bar{\theta}$ may be rejected by using shower shape analysis.

A detailed GEANT study by one of the authors shows that in average, IPC's with $\bar{\theta} > 5$ mrad may be rejected by using a shower shape cut [14]. This analysis is based upon a fit on lateral shower profile in BaF_2 to an oval Gaussian distribution, and reject those IPC's with large minor. The simulation includes a rotation of all particles in IPC's, making $\vec{n}$ aiming at random at the full area of the central crystal. The vertex z position, where IPC's originated from, were smeared by 5 cm as a Gaussian. All particles in IPC's were shoot to an array consisting of 11 $\times$ 11 BaF_2 crystals. A full GEANT simulation was carried out to deposit energies in BaF_2 crystals. An effective cut on minor of fitted oval, keeping more than 90% of real photons, was found to be consistent to $\bar{\theta} > 5$ mrad. Although the calculation was done for BaF_2 simulation, the same strategy can also be used for any fine segmented EMC, such as LAr accordion calorimeter.

Assuming that IPC's with $\bar{\theta} > 1$ mrad would be rejected by a preradiator, we can also estimate the corresponding background cross-sections after a preradiator cut. Several preradiator designs were proposed for GEM. See [14] for the details of a preradiator design for BaF_2.

As seen from Figure 9, there are single photons in IPC's which are originated from QED process in parton shower. These single photons would provide an irreducible QCD jet background for $H \rightarrow \gamma\gamma$.

Table 10 summaries the result of the QCD background cross-sections as a function of the size of the isolation cone (R) and the E_T^{cut}. The cross-sections are calculated in a $\gamma\gamma$ mass range between 75 and 165 GeV.

5 Misidentified Electron Background

In the last two sections we discussed backgrounds of real photon and fake isolated photons from QCD jets. Because of limited efficiency of central tracker, however, in a real detector an electron may also fake a photon if there is no charged track stub found at the front of the EM shower. A jet may fake an isolated electron and may further be recognised as an isolated photon.

Taking into account the misidentified electrons, the background against H$\rightarrow \gamma\gamma$ thus may be summarized as a sum of the following misidentification related contributions:

$$\begin{aligned}\sigma_{\text{"}\gamma\gamma\text{"}} &= \sigma_{ee}\, R^2(\gamma/e) + \sigma_{\gamma-jet}\, [R(\gamma/jet) + R(e/jet)R(\gamma/e)] + \\ &\quad \sigma_{2jets}\, [R(\gamma/jet) + R(e/jet)R(\gamma/e)]^2 \end{aligned} \tag{10}$$

where the first term is from a pair of isolated e^+e^-, such as Drell-Yan, the second term is from γ-jet final state, and the third term is from 2jets final state. R(e/jet) and R(γ/jet) are the probability of a jet faking an isolated electron and photon respectively, and R(γ/e) is the probability of misidentification of an isolated electron as an isolated photon.

5.1 Background from Isolated Electrons

The largest isolated e^+e^- background is Drell-Yan e^+e^- production, which has a production cross section of 2 nb. The event topology of Drell-Yan e^+e^- pair is very similar to H$\rightarrow \gamma\gamma$. If the overall detector design has no ability to distinguish γ versus electron, this background would seriously compromise H$\rightarrow \gamma\gamma$ measurement.

Figure 11 shows the invariant mass distribution of Drell-Yan e^+e^- after event selection cuts (dashed line). 41% of Drell-Yan e^+e^- events were accepted by the event selection cuts. The e^+e^- mass has a peak at Z^0 mass with a cross section of around 160 pb/GeV. As a comparison, the irreducible $\gamma\gamma$ background is also plotted in the figure as a solid line. The $\gamma\gamma$ cross section at Z^0 mass is about 650 fb/GeV.

At the Z^0 peak, the Drell-Yan cross section is about 250 times larger than the irreducible $\gamma\gamma$ background. They are at the same level at the off resonance tail when $M_{e^+e^-}$ is larger than 120 GeV. A detector, which has an R(γ/e) of less than 3%, would provide a 10^{-3} reduction to the Drell-Yan background. The Drell-Yan e^+e^- background after this reduction is also plotted in Figure 11 as a dotted histogram. It is clear that

such an ability would not compromise the H$\rightarrow \gamma\gamma$ physics.

Note, a conventional tracker with small radius, such as L3 Time Expansion Chamber (TEC) at the front of BGO crystal calorimeter, may provide 2×10^{-4} rejection for $\gamma\gamma$ to Bhabha, which corresponds to 1.4% single track misidentification [13]. It is expected that GEM central tracker will provide an R(γ/e) of better than 1% [15]. The Drell-Yan e^+e^- background thus is not a problem for H$\rightarrow \gamma\gamma$ detection.

The second largest isolated e^+e^- background is the e^+e^- pair production in the $t\bar{t}$ production. The electron pair in the $t\bar{t}$ is of the same size as the Drell-Yan background when M(e^+e^-) is larger than 110 GeV. A 1% rejection is more than enough to reduce it to a negligible level.

5.2 Jet Faking an Electrons

The probability of a QCD jet faking an isolated electron, R(e/jet), was studied by using the isolation strategy described in section 4.1 with an additional requirement of a charged track hitting the center cell.

Most of the isolated electron candidates (IEC) passing isolation cuts have a topology of overlapping energetic γ's with a low momentum charged track. To reduce these candidates, a very rough E-p matching is used:

$$|E_{Cal} - p_{track}| < 5\sqrt{\sigma_{Cal}^2 + \sigma_{track}^2} \tag{11}$$

where

$$\frac{\sigma_{Cal}}{E} = (\frac{10}{\sqrt{E}} \oplus 2)\%, \; and \; \frac{\sigma_{track}}{p^2} = 0.25\% \tag{12}$$

These energy resolution and momentum resolution are very conservative. A more conservative cut

$$\frac{p_{track}}{E_{Cal}} \leq 0.5 \tag{13}$$

works equally well.

All the candidates which pass these two cuts contain real electrons accompanying no γ or a few low momentum γ's. The total electron candidate which passes these cuts were 6 among 300k 2jets events, and 2 among 300k γ-jet events. In these samples, all IEC's are from heavy quark decays (c, b and t), and when tighter cuts are applied, only decays from b and t quarks remained.

Table 11 lists the result of the calculation by using E_T^{cut} = 5 GeV and three cone size R = 0.3, 0.45 and 0.6. 300k events each for 2jets and γ-jet final states were generated in this calculation. Also shown in the table is R(e/jet) after E-p matching and final cross sections of "γ-e" and "e-e" configurations.

Table 11: R(e/jet) and Fake Electron Related Background Cross Section

	2jets			γ-jet		
R	0.30	0.45	0.60	0.30	0.45	0.60
R(e/jet) by isolation (10^{-5})	21	12	8.1	22	12	9.8
R(e/jet) by E-p match (10^{-5})	5.6	4.0	3.0	3.7	3.7	3.7
R(γ/jet) by isolation (10^{-4})	7.4	5.3	4.1	21	16	13
$\sigma_{"\gamma-e"}$ (pb) $M_{"\gamma-e"} \geq 75$ GeV	22	11	6.4	1.3	1.3	1.3
$\sigma_{"e-e"}$ (pb) $M_{"e-e"} \geq 75$ GeV	0.8	0.4	0.2			

The probability of a jet faking an isolated electron, R(e/jet), can be compared to the probability of a jet faking an isolated photon, R(γ/jet) as listed in Table 9. It is interesting to note that

- contrary to the case of faking a photon, both gluon jet and quark jet have a similar probability of faking an isolated electron; and
- R(e/jet) is more than 10 times smaller than R(γ/jet).

The consequence of fake isolated electrons to H$\rightarrow \gamma\gamma$ detection can be observed from the last two lines of Table 11, where background cross sections of "γ-e" and "e-e" are listed. These cross sections are negligible, compared to the irreducible $\gamma\gamma$ background cross section of 43 pb for $M_{\gamma\gamma} > 75$ GeV, taking into account the R(γ/e) of a few %.

6 H$\rightarrow \gamma\gamma$ for two GEM Calorimeter Systems

In Section 4.2, we calculated the "$\gamma\gamma$" background cross sections from QCD jets after various rejection cuts for the case of a jet faking an photon. In Section 5 we discussed the "$\gamma\gamma$" background cross sections from Drell-Yan and QCD jets for the case of a jet faking an electron and/or an electron faking a photon. In this section, we will discuss the consequence of the detector noise and the final significance of Higgs peaks over the sum of all backgrounds.

6.1 Thermal and Pileup Noise

It is clear that a tighter isolation cut (large isolation cone and lower threshold) would provide more effective rejection. However, if R is too large or the threshold is too low, the signal acceptance would degrade. The values applicable in analysis depends on detector performance, especially the sum of thermal and pileup noise in a large cone.

Two calorimeter systems were proposed by GEM [16].

- One is a BaF_2 crystal EMC followed by a scintillation calorimeter HCAL. While the segmentation of BaF_2 is 0.04×0.04, the segmentation is 0.08×0.08 for SHCAL. Since both BaF_2 and SHCAL have low thermal noise (3 MeV/channel), the dominant contribution to the noise in a large area is the pileup noise.
- The other is a liquid argon accordion EMC followed by a LAr HCAL which is designed to have:
  - thermal and pileup noise of 20 and 32 MeV respectively for each 0.032×0.032 channel in EMC; and
  - thermal and pileup noise of 130 and 118 MeV respectively for each 0.08×0.08 channel in HCAL.

Note, the design of LAr system was optimised so that the thermal and pileup noise contributions are roughly equal in a trigger tower [18].

These thermal and pileup noise defined in GEM baseline document [16] can be used to scale the corresponding noise in a large cone according to the following rule:

- pileup noise is proportional to $\sqrt{t_{integration}}$, where $t_{integration}$ is the integration time

of the detector, which is 16, 32, 40 and 100 ns respectively for BaF_2, SHCAL, LAr accordion and LAr HCAL [16];

- pileup noise is proportional to $\text{Area}^{0.6}$, taking into account jet correlation;
- thermal noise is proportional to $\text{Area}^{0.5}$, assuming no jet correlation.

Table 12 lists the result of this calculation, where σ_t and σ_p are the thermal and pileup noise respectively, and σ_{EMC}, σ_{HC} and σ_{TOT} are the sum of noise in EMC, HCAL and EMC + HCAL, respectively.

Table 12: Thermal and Pileup Noise (GeV) of Two GEM Calorimeter Systems

	BaF_2				LAr Accordion			
	0.04^2	R=0.45	R=0.60	R=0.75	0.032^2	R=0.45	R=0.60	R=0.75
σ_t	0.003	0.12	0.16	0.20	0.020	0.50	0.66	0.83
σ_p	0.026	0.95	1.3	1.8	0.032	1.5	2.1	2.8
σ_{EMC}	0.026	0.96	1.3	1.8	0.038	1.6	2.2	2.9
	SHCAL				LAr HCAL			
	0.08^2	R=0.45	R=0.60	R=0.75	0.08^2	R=0.45	R=0.60	R=0.75
σ_t	0.003	0.03	0.04	0.05	0.13	1.3	1.7	2.2
σ_p	0.068	1.1	1.5	2.0	0.12	1.9	2.7	3.5
σ_{HC}	0.068	1.1	1.5	2.0	0.18	2.3	3.2	4.1
σ_{TOT}	N/A	1.5	2.0	2.7	N/A	2.8	3.9	5.0

6.2 Isolation Threshold in Isolation Cone

Requesting 95% of signal acceptance, we choose a threshold E_T^{cut} of $1.65\sigma_{noise}$, which corresponding to 4.5 GeV in a 0.75 cone for BaF_2 or 4.6 GeV in a 0.6 cone for LAr. We thus use R = 0.75 and E_T^{cut} = 5 GeV for BaF_2 case and R = 0.45 E_T^{cut} = 5 GeV for LAr.

Note, the study carried out in this report is a straightforward one. One may try more sophisticated isolation algorithms, e.g. using central tracker or part of calorime-

ter etc., to relax the requirements to the calorimeter noise. We discuss briefly two algorithms of this sort which use full calorimeter information.

An algorithm summing only cells in isolation cone with energy deposition larger than 3σ of noise was tested by author. Although less sensitive to the noise, this technique was found to provide a similar result to what presented in this report with some improvement. It is understood that when raising the energy threshold in each cell, the sensitivity to the associate jet energies in the isolation cone is also degraded. Another algorithm proposed by H. Ma [17] sums transverse energies in two cones with different size, both centered at IPC, and uses different E_T^{cut} threshold in these two cones. The result of this algorithm also improves rejection efficiency.

Because of the uncertainty in estimating the thermal and pileup noise, in this analysis we choose a conservative threshold. By using the data in Table 10, Table 13 lists the total background cross-sections from $\gamma\gamma$, γ-jet and 2jets processes for the cases of after isolation cut (isol.), shower shape analysis (S.S.) and preradiator rejection (P.R.). The irreducible QCD $\gamma - \gamma$ background cross-section (Irr.), which corresponds to real isolated photon pairs from each process, is also calculated. Table 13 also lists sums of $\gamma\gamma$ background from these three processes. Finally, the background scaling factor (B.F.), which is the total background cross-section normalized to the irreducible $\gamma\gamma$ background of 31 pb, is listed for each selection cut.

Table 13: Total Background Cross-Section (pb) for H$\rightarrow \gamma\gamma$ Searches

	BaF_2 System					LAr System				
Process	$\gamma\gamma$	γ-jet	2jets	Total	B.F.	$\gamma\gamma$	γ-jet	2jets	Total	B.F.
Isol.	31	33	46	110	3.5	31	55	140	226	7.3
S.S.	31	21	20	72	2.3	31	31	73	135	4.4
P.R.	31	17	13	61	2.0	31	19	20	70	2.3
Irr.	31	14	7.3	52	1.7	31	17	10	58	1.9

6.3 Siginicance of H$\rightarrow \gamma\gamma$ Searches

Assuming that the shape of $\gamma\gamma$ invariant mass spectra from all background sources is the same, total background spectrum may be obtained by scaling the irreducible $\gamma\gamma$

background with a factor of B.F. Figure 12 shows two spectra: Higgs signals of 80, 100, 120, 140 and 160 GeV superimposed on total background after shower shape analysis and corresponding background subtracted spectrum. Figure 13 and 14 show similar spectra after shower shape analysis and preradiator rejection for LAr calorimeter.

Table 14: Significance of H$\rightarrow \gamma\gamma$ Searches in one SSCY

M_H (GeV)	BaF_2 System			LAr System		
	S.S.	P.R.	Irr.	S.S.	P.R.	Irr.
80	3.0	3.3	3.5	1.5	2.1	2.3
90	4.0	4.3	4.7	2.1	3.0	3.3
100	5.7	6.1	6.6	3.0	4.2	4.6
120	9.2	9.9	11	5.2	7.3	8.0
140	11	11	12	5.7	7.9	8.7
150	8.6	9.2	10	4.8	6.6	7.3
160	3.9	4.2	4.5	2.2	3.1	3.4

Table 14 lists the significance of H$\rightarrow \gamma\gamma$ searches for these two calorimeter systems after these jet rejection cuts for Higgs mass of 80, 90, 100, 120, 140, 150 and 160 GeV. Note, the event numbers shown in Figures 12, 13 and 14 are for a perfect EMC without including the acceptance loss discussed in section 2.2. Taking into account the relative acceptance listed in Table 3, the numbers of both signal and background events should be reduced to 73% and 69% respectively for BaF_2 calorimeter and LAr calorimeters. The corresponding significance in Table 14 should be reduced to 85% and 83% respectively.

On the other hand, taking into account high order QCD corrections to the Higgs production [9], i.e. the K factor of 1.5, the corresponding numbers of signal events and significance should both be increased by a factor of 1.5. This is reasonable, since the dominant irreducible background of gg$\rightarrow \gamma\gamma$ is an $O(\alpha_s^2)$ process. This increase of of a factor of 1.5 in signal events may cancel the B.F. listed in Table 13 for BaF_2 after shower shape analysis or for LAr after preradiator rection, according to Equation 5. The up bound of the significance shown in Figure 6 thus can also be taken as the significance of H$\rightarrow \gamma\gamma$ searches for BaF_2 without preradiator and for LAr with preradiator.

7 $H(t\bar{t}/W) \rightarrow \gamma\gamma\ell X$ Searches

Both $Ht\bar{t} \rightarrow \gamma\gamma\ell X$ and $HW \rightarrow \gamma\gamma\ell X$ are complementary channels which can be used to cover the Higgs mass range below 140 GeV [19]. As shown in Figure 2, the signal cross-section of sum of these two channels is in an order of few fb. However, with a lepton (ℓ) tagging the irreducible background for $H \rightarrow \gamma\gamma$ can be eliminated. The $\gamma\gamma$ invariant mass spectrum of these two processes thus has much less background.

In this section we discuss searches for intermediate mass Higgs boson by using these two channels. Since we are looking for $\gamma\gamma$ invariant mass to locate Higgs signal, most elaboration on effect of detector resolutions to the Higgs peak width discussed in section 3 is also applicable to this search. The main differences are:

- with an associate charged lepton in final state and the fine resolution of its impact parameter, the Higgs vertex determination would be more accurate;
- the statistics of both signal and background is low, so that the effect of high resolution is not directly correlated to the discovery time, as shown in Equation 5. The consequence of $\gamma\gamma$ mass resolution to the significance will be discussed in section 7.2.

7.1 Signal and Background

The main backgrounds against $H(t\bar{t}/W) \rightarrow \gamma\gamma\ell X$ searches are:

- $t\bar{t}\gamma\gamma$: 80 fb for $\hat{p}_t^{\gamma} \geq 20$ GeV, and $|\hat{\eta}^{\gamma}| \leq 3$;
- $b\bar{b}\gamma\gamma$: 2 pb for $\hat{p}_t^{\gamma} \geq 20$ GeV, $|\hat{\eta}^{\gamma}| \leq 3$ and $M_{b\bar{b}\gamma\gamma} \geq 70$ GeV;
- $W\gamma\gamma \rightarrow \ell\gamma\gamma$: 23 fb for $\hat{p}_t^{\gamma,\ell} \geq 20$ GeV, $|\hat{\eta}^{\gamma,\ell}| \leq 3$, $R^{\ell,\gamma} \geq 0.3$, $R^{\gamma,\gamma} \geq 0.3$ and 60 GeV $\leq M_{\gamma\gamma} \leq 180$ GeV, where R is the distance in $\eta - \phi$ space as defined in Section 4.1.
- $t\bar{t}$: 16 nb.
- $q\bar{q}/gg \rightarrow Z\gamma \rightarrow \ell^+\ell^-\gamma$: 14.4 pb for $\hat{p}_t^{\gamma,Z} \geq 10$ GeV.

  This process becomes the background either by the QED radiation from one of the leptons ($Z\gamma \rightarrow \ell^+\ell^-\gamma\gamma$) or by the misidentification of one of the electrons as gamma ($Z\gamma \rightarrow e^{\text{“}}\gamma^{\text{”}}\gamma$).

The process gg$\rightarrow$ Zγ was not available in PYTHIA, and it was accounted for by increasing the background from $q\bar{q} \rightarrow Z\gamma$ by 20% [20].

- $q\overline{q'} \rightarrow W\gamma \rightarrow \ell^{\pm}\gamma\gamma$[2]: 54 pb for $\hat{p}_t^{\gamma,Z} \geq 10$ GeV.

  This process becomes the background by the QED radiation from the lepton ($W\gamma \rightarrow \ell\gamma\gamma$).

A combination of Monte Carlo programs is used to simulate the first three backgrounds. The hard scattering processes are generated by using PAPAGENO 3.6 [21]. To apply the isolation cut in the particle level and to properly simulate transverse motion, the initial and final state parton radiation, hadronization and decays are generated by using PYTHIA 5.6 [4],

The $t\bar{t}$ background was generated with PYTHIA 5.5 program with QED radiation option turned on. The study was done with 2.6M events. It is interesting to note that the isolation cut alone can not reduce $t\bar{t}$ background to a negligible level. With a lepton tagging, the $t\bar{t}$ final state has 4 quark jets. According to Table 9, an effective isolation cut can achieve 1.4×10^{-3} rejection for $E_T^{cut} = 5$ GeV and R = 0.6. Together with a combinatory factor of 6, the isolation would provide a rejection of 10^{-5}, which leads to a background cross-section of $t\bar{t} \rightarrow \ell X$ of 90 fb, or 20 to 100 times higher than the $Ht\bar{t} \rightarrow \gamma\gamma\ell X$ signal.

Since the $\gamma\gamma$ invariant mass distribution obtained from IPC's from $t\bar{t}$ process was spread out, a cut on interesting mass interval between 75 and 165 GeV would reduce the background by a factor of less than 2. It was also found that the two photon system from signal has a large p_T than that from background. A cut on joint p_T of $\gamma\gamma$ system in an order of 40 GeV would effectively reduce background by another factor of 3.

It should be pointed out that calculating background from the $t\bar{t}$ with QED radiation turned on in PYTHIA might cause double counting to $t\bar{t}\gamma\gamma$ process. A detailed check, however, found most isolated photon candidates from $t\bar{t}$ sample are isolated π^0s. The double counting is therefore negligible.

All final state QED radiation was simulated by PYTHIA with QED radiation turned on. After isolation and joint p_T cuts, there is no effective cut to reduce this background. The isolation cut reduced background events with small $M_{\ell\gamma}$. After isolation cut, the $M_{\ell\gamma}$ distribution for 80 GeV Higgs is similar to that of QED background.

[2]This background is different from $W\gamma\gamma$ listed above where both γ's are radiated from quark lines. In this process one γ is from the quark line, but the other is from a lepton.

We therefore decided do not use $M_{\ell\gamma}$ cut. For higher mass Higgs, the distributions are narrow, but the $M_{\ell\gamma}$ cut does not improve the significance.

For electron faking photon, an $R(\gamma/e)$ of 3% was used. Although the GEM design value of $R(\gamma/e)$ is 1% [15], a conservative value is assumed here. It is also interesting to note that while a larger cone helps in rejecting jet background, the best cone size for lepton isolation is 0.3, which helps to maintain high signal acceptance.

The following cuts are therefore used in our $H(t\bar{t}/W) \rightarrow \gamma\gamma\ell X$ searches:

- $|\eta_\ell| < 2.5$, $P_T^\ell > 20$ GeV, R = 0.3;
- $|\eta_\gamma| < 2.5$, $P_T^\gamma > 20$ GeV, R = 0.3, 0.45 or 0.6;
- isolation cut $\Rightarrow$ reject $t\bar{t}$:

$$\sum_{r<R} E_T - E_T^{photon} < 5GeV + 0.1E_T^{photon}$$

- p_T of di-photon $> p_T^{cut} \Rightarrow$ reject $t\bar{t}$;
- Shower Shape Analysis: $\bar{\theta} < 5$ mrad, as discussed in section 4.

Table 15 lists signal and background events, calculated in a range of 75 GeV $\leq M_{\gamma\gamma} \leq$ 165 GeV, after these cuts. As a comarison, the signal and background events without using joint p_T cut are also listed. The $b\bar{b}\gamma\gamma$ background is rejected by the isolation cut to a negligible level. It is clear from this table, that the largest background is the fake $\gamma-\gamma$ pairs from $t\bar{t}$ production and the QED radiation $Z\gamma \rightarrow \ell^+\ell^-\gamma\gamma$, and p_T^{cut} applied to joint momentum of $\gamma-\gamma$ pair is an effective cut to reduce these background.

Figure 15 shows $\gamma\gamma$ invariant mass spectra collected in one SSCY with Higgs signals of 80, 100, 120, 140 and 160 GeV superimposed over a sum of all backgrounds for three energy resolutions: $(2/\sqrt{E} \oplus 0.5)\%$, $(7/\sqrt{E} \oplus 0.5)\%$ and $(15/\sqrt{E} \oplus 1)\%$. The cuts used are R = 0.45, $p_T^{cut} = 40$ GeV and $\bar{\theta} < 5$ mrad.

Note, the event numbers shown in Table 15 and Figure 15 are for a perfect EMC without including the acceptance loss discussed in section 2.2. Taking into account of the relative acceptance listed in Table 3, the numbers of both signal and background events should be reduced to 62% and 56% respectively for BaF_2 calorimeter and LAr calorimeters.

Table 15: Numbers of Signal and Background Events in One SSCY for $H(t\bar{t}/W) \rightarrow \ell\gamma\gamma X$ Searches

	No p_t^{cut}			p_t^{cut} = 40 GeV		
R	0.30	0.45	0.60	0.30	0.45	0.60
Higgs (80 GeV)	28	23	18	21	18	14
Higgs (90 GeV)	30	25	20	24	20	17
Higgs (100 GeV)	30	25	21	25	21	17
Higgs (120 GeV)	24	20	16	22	18	15
Higgs (140 GeV)	17	15	13	15	14	11
Higgs (150 GeV)	10	8	7	9	8	6.5
Higgs (160 GeV)	4	3.4	2.7	3.6	3	2.5
$t\bar{t}\gamma\gamma$	58	48	34	52	44	32
$W\gamma\gamma$	26	25	25	15	15	15
$t\bar{t}$	308	246	185	123	61	61
$Z\gamma \rightarrow e^{\text{“}}\gamma^{\text{”}}\gamma$	53	51	47	34	32	30
$Z\gamma \rightarrow \ell^+\ell^-\gamma\gamma$	206	177	151	122	96	79
$W\gamma \rightarrow \ell\gamma\gamma$	135	108	76	54	43	43

7.2 Significance

Since the statistics of both signal and background is low, Equation 5 can not be used to estimate the significance. We thus estimate the significance by using a convolution of two Poisson probability distributions.

We assume a signal peak with defined width is observed over some background. The expected number of signal events in mass interval of $M_H \pm \sigma_{\gamma\gamma}$ is N_s, and the corresponding number of background events is N_B. The probability of observing certain number of events (n) follows a Poisson statistics:

$$P_n(\lambda) = \frac{\lambda^n e^{-\lambda}}{n!} \tag{14}$$

where λ is the expected value, i.e. N_S for the signal and N_B for the background.

If one observe n events, the probability of these events caused by background

fluctuation is:

$$\sum_{m=n}^{\infty} P_m(N_B) \tag{15}$$

Taking into account the fluctuation of observed events, which has an expectation value of $N_B + N_S$, the final probability of observing a signal which is caused by background fluctuation is:

$$Prob = \sum_{n=0}^{\infty}[P_n(N_B + N_S) \times \sum_{m=n}^{\infty} P_m(N_B)] \tag{16}$$

It is also interesting to note, that when N_B and N_S are large Equation 16 can be used to deduce Equation 5 used in estimating significance of $H \rightarrow \gamma\gamma$ searches. The deduction is shown below. If the expected number is large, the Poisson distribution becomes a Gaussian distribution, and Equation 16 can be written as

$$\begin{aligned} Prob &= \sum_{n=0}^{\infty}[P_n(N_S + N_B) \times \sum_{m=n}^{\infty} P_m(N_B)] \\ &\approx \frac{1}{2\pi\sqrt{N_B(N_S+N_B)}} \int_0^{\infty} dx \int_x^{\infty} dy\ e^{-\frac{(x-N_S-N_B)^2}{2(N_S+N_B)}}\ e^{-\frac{(y-N_B)^2}{2N_B}} \\ &\approx \frac{1}{\sqrt{2\pi}} \int_{\frac{N_S}{\sqrt{N_B}}}^{\infty} dy\ e^{-\frac{y^2}{2}} \end{aligned} \tag{17}$$

The last term in Equation 17 is the exact probability used in defining $N_s/\sqrt{N_b}$ as the significance in terms of standard deviation (σ) for a Gaussian distribution. For example Prob = 0.0027 is mapped to 3σ, and 0.000057 is 5σ etc.

Table 16 lists significance calculated according to Equation 16 for $H(t\bar{t}/W) \rightarrow \gamma\gamma\ell X$ searches with three energy resolutions in one SSCY. Because of the uncertainty in background estimation for such small number of background events, we also calculate the significance by assuming the background events is twice as much. In this table, the two numbers in the significance column correspond to the expected and double of the expected number of backgrounds events.

Figure 16 shows the significance of this search as a function of SSCY calculated for three energy resolutions and 6 different Higgs masses. The up bound of the band corresponds to the calculated background, while the low bound of the band corresponds to the background scaled up by a factor of two. It is clear that high resolution also corresponds to a short discovery time.

Table 16: Signicance of H($t\bar{t}$/W)$\rightarrow \ell\gamma\gamma$X Search in one SSCY

ΔE/E (%)			$2/\sqrt{E} \oplus 0.5$		$7.5/\sqrt{E} \oplus 0.5$		$15/\sqrt{E} \oplus 1.0$	
M_H (GeV)	$\sigma_{\ell\gamma\gamma}$ (fb)	N_S	$\sigma_{M_{\gamma\gamma}}$ (GeV)	S	$\sigma_{M_{\gamma\gamma}}$ (GeV)	S	$\sigma_{M_{\gamma\gamma}}$ (GeV)	S
80	8.4	12	0.34	2.9/2.5	0.66	2.5/2.0	1.3	2.0/1.5
90	8.0	14	0.37	3.2/2.7	0.70	2.7/2.2	1.4	2.2/1.7
100	7.8	14	0.40	3.3/2.8	0.73	2.8/2.3	1.45	2.3/1.8
120	6.9	13	0.45	3.0/2.5	0.77	2.7/2.2	1.5	2.2/1.7
140	4.2	9	0.53	2.6/2.2	0.89	2.3/1.9	1.7	1.9/1.5
150	2.6	5.4	0.58	1.7/1.4	0.95	1.5/1.2	1.9	1.2/0.9

Note, the significance shown in Table 16 and Figure 16 are for a perfect EMC without including the acceptance loss discussed in section 2.2. Taking into account of the relative acceptance listed in Table 3, the numbers of the significance should be reduced.

8 $H \to ZZ^* \to e^+e^-e^+e^-$ Searches

As shown in Table 4 and Figure 2, for Higgs mass above 130 GeV considerable Higgs would decay to 4 electrons through ZZ/ZZ^* decay, where Z^* denotes a virtual Z. The signal in this search has a distinguished feature of four isolated electrons, and has a cross section of a few fb.

Our study shows that that requiring four isolated leptons would reduce all QCD jet background to a negligible level, except for the $t\bar{t}$ production process. In addition to $t\bar{t}$ background, there are irreducible ZZ^* background and $Zq\bar{q}$ (q is a heavy quark b or t) backgrounds. Both may provide four isolated electrons. The cross section of these backgrounds are:

- $q\bar{q}/gg \to ZZ^* \to e^+e^-e^+e^-$: 9.9 fb for $M_{Z^*} \geq 10$ GeV, 120 GeV $\leq M_{ZZ^*} \leq 190$ GeV;
- $Zt\bar{t} \to e^+e^-t\bar{t}$: 460 fb;
- $Zb\bar{b} \to e^+e^-b\bar{b}$: 105 pb for $M_{Zb\bar{b}} \geq 130$ GeV;
- $t\bar{t}$: 16 nb.

The cross section of $gg \to ZZ^*$ has not been calculated. The contribution of this process is estimated by using the calculated ratios of $\sigma(gg \to ZZ)/\sigma(q\bar{q} \to ZZ) = 60$ - 70% and $\sigma(gg \to Z\gamma)/\sigma(q\bar{q} \to Z\gamma) = 15$ - 30% [20]. Based on these calculations, the cross section of $q\bar{q} \to ZZ^*$ is multiplied by 1.65 to account for the contribution of $gg \to ZZ^*$ process.

The following cuts were used to reduce these backgrounds:

- $|\eta_e| < 2.5$;
- Use four electrons with largest E_T;
- Second largest $E_{T_e} \geq 10$ GeV;
- All electrons with $E_{T_e} \geq 5$ GeV;
- isolation cut $\Rightarrow$ reduce decay from Heavy Quarks:

$$\sum_{r<0.3} E_T - E_T^{(e)} < 5\text{GeV} + 0.1E_T^{(e)}$$

- 10 GeV $\leq M_{ee}^{(l)} \leq$ 96 GeV and 60 GeV $\leq M_{ee}^{(h)} \leq$ 96 GeV $\Rightarrow$ suppress continuum background, where $M_{ee}^{(l)}$ and $M_{ee}^{(h)}$ are low and high invariant masses of two e^+e^- pairs.

The mass cut on $M_{ee}^{(h)}$ is much lower than the intrinsic width of Z, because the Bright-Wigner tail is power-like damping and the tail toward the lower mass side is enhanced by the increase of the available kinematical phase space [22]. According to PYTHIA, if one require only 86 GeV to 96 GeV for $M_{ee}^{(h)}$, the efficiency decreases by around 20%.

Table 17: Number of Events in one SSCY for $H \rightarrow ZZ/ZZ^* \rightarrow e^+e^-e^+e^-$ Searches

	Cross section	Event Number
Higgs (140 GeV)	6.5 fb	27
Higgs (150 GeV)	7.9 fb	39
Higgs (160 GeV)	3.7 fb	16
Higgs (170 GeV)	2.3 fb	14
$Zb\bar{b}$	105 pb	22
$Zt\bar{t}$	456 fb	4
ZZ^*	6.0 fb	14
$t\bar{t}$	16 nb	6

Table 17 shows cross section and event number after event selection cuts, obtained in one SSCY for both Higgs signal and various backgrounds. The number of background events are in the mass range between 130 and 180 GeV. Figure 17 shows $e^+e^-e^+e^-$ invariant mass spectra collected in one SSCY for Higgs signals of 140, 150, 160 and 170 GeV superimposed over a sum of all backgrounds for three energy resolutions: $(2/\sqrt{E} \oplus 0.5)\%$, $(7/\sqrt{E} \oplus 0.5)\%$ and $(15/\sqrt{E} \oplus 1)\%$.

The Higgs mass resolution and significance of the signals calculated by using Equation 16 is listed in Table 18. The two numbers in the significance column correspond to the expected and double amount of the expected number of background events. Figure 18 shows the significance of this search as a function of SSCY calculated for three energy resolutions and 4 different Higgs masses. The up and low bounds of the band correspond to the exact background calculated and the double amount of the background.

Table 18: Significance of $H \to ZZ/ZZ^* \to e^+e^-e^+e^-$ Searches in one SSCY

$\Delta E/E$ (%)			$2/\sqrt{E} \oplus 0.5$		$7.5/\sqrt{E} \oplus 0.5$		$15/\sqrt{E} \oplus 1.0$	
M_H (GeV)	σ_{4e} (fb)	N_S	$\sigma_{M_{4e}}$ (GeV)	S	$\sigma_{M_{4e}}$ (GeV)	S	$\sigma_{M_{4e}}$ (GeV)	S
140	6.5	18	0.43	4.3/4.0	0.86	4.0/3.7	1.72	3.7/3.4
150	7.9	23	0.48	5.2/4.9	0.89	4.9/4.6	1.89	4.6/4.1
160	3.7	11	0.54	3.4/3.4	1.06	3.2/2.8	2.04	2.9/2.5
170	2.3	7.1	0.72	2.6/2.3	1.15	2.4/2.1	3.01	2.0/1.6

Note, the event number and significance shown in Table 17 and 18 and Figure 17 and 18 are for a perfect EMC without including the acceptance loss discussed in section 2.2. Taking into account of the relative acceptance listed in Table 3, the numbers of both signal and background events should be reduced to 54% and 46% respectively for BaF_2 calorimeter and LAr calorimeters. Corresponding significance should also be reduced. However, the K factor of 1.5 would be enough to compensate the loss of acceptance and significance. The significance number in Table 18 and Figure 18 thus

Table 19: Ratio of $H \to e^+e^-e^+e^-$ Peak Width as Function of a and b

a	2.0	3.0	5.5	7.5	10	15
M_H = 140 GeV						
b=0.5	1.0	1.1	1.6	2.0	2.5	3.7
b=1.0	1.8	1.9	2.1	2.5	3.0	4.0
b=1.5	2.6	2.7	2.9	3.1	3.5	4.3
b=2.0	3.4	3.5	3.7	3.9	4.4	5.0
M_H = 170 GeV						
b=0.5	1.0	1.0	1.2	1.6	2.0	3.0
b=1.0	1.5	1.6	1.8	2.0	2.3	3.2
b=1.5	2.1	2.2	2.3	2.6	2.7	3.3
b=2.0	2.7	2.8	3.0	3.1	3.4	4.1

can be treated as the exact.

Similar to Table 6, Table 19 shows the ratio of of $H \rightarrow e^+e^-e^+e^-$ peak width as function of **a** and **b**, normalized to the BaF_2 crystal calorimeter resolution: $2\%/\sqrt{E} \oplus 0.5\%$, for Higgs mass of 140 and 170 GeV.

References

[1] GEM Collaboration, Letter of Intent to the SSCL, November 30, 1991.

[2] CERN Green Book, *"ECFA Workshop on LEP 200"*, Aachen, September, 1986.

[3] R.Y. Zhu, GEM Internal note **GEM TN-91-32**, November 30, 1991.

[4] H-U. Bengtsson and T. Sjostrand, *"A Manual to the Lund Monte Carlo for Hadronic Processes"*, PYTHIA version 5.6, September, 1991.

[5] R.Y. Zhu, GEM Internal note **GEM TN-92-48 Rev A.**, January 18, 1992.

[6] M. Seman, Talk given in GEM Council Meeting, June 4, 1992.

[7] L3 Collaboration, *Nucl. Instr. and Meth.* **A289** (1990) 35.

[8] R.Y. Zhu, Proceedings of ECFA LHC Workshop, Aachen, October 1990, Volume III p. 411.

[9] A. Djouadi, M. Spira and P. M. Zerwas, Phys. Lett. **B264** (1991) 440.

[10] D. Dicus and S. Willenbrock, Phys. Rev. **D37** (1988) 1801.

[11] H. Yamamoto, GEM Internal note **GEM-TN-92-127**.

[12] L* Collaboration, Report to the PAC, July 7, 1990.

[13] Y. Karyotakis *et al.*, Final State Photons, L3 Internal Note, February 1992.

[14] H. Yamamoto, GEM Internal note **GEM-TN-91-33**.

[15] GEM Central Tracker Physics Performance Specifications, July 1992.

[16] GEM Baseline 1, GEM Internal note **GEM-TN-92-76 Rev B**.

[17] H. Ma, GEM Internal note.

[18] BNL Report, **BNL 52244**, Ed. B.Yu and V. Radeka.

[19] W.J. Marciano and F. Paige, BNL Preprint, **BNL-45805**
J.F. Gunion *et al.*, SDC report, **SDC-91-00057**
R. Kleiss *et al.*, Phys. Let. **B253** (1991) 269;
Z. Kunszt *et al.*, Phys. Let. **B271** (1991) 247.

[20] J.J. van der Bij and E.W.N. Glover, Phys. Lett. **B206** (1988) 701;
E.W.N. Glover and J.J. van der Bij, Nucl. Phys. **B321** (1989) 561.

[21] I. Hinchliffe, A Monte Carlo Parton Generator, unpublished.

[22] T. Sjostrand, private communication.

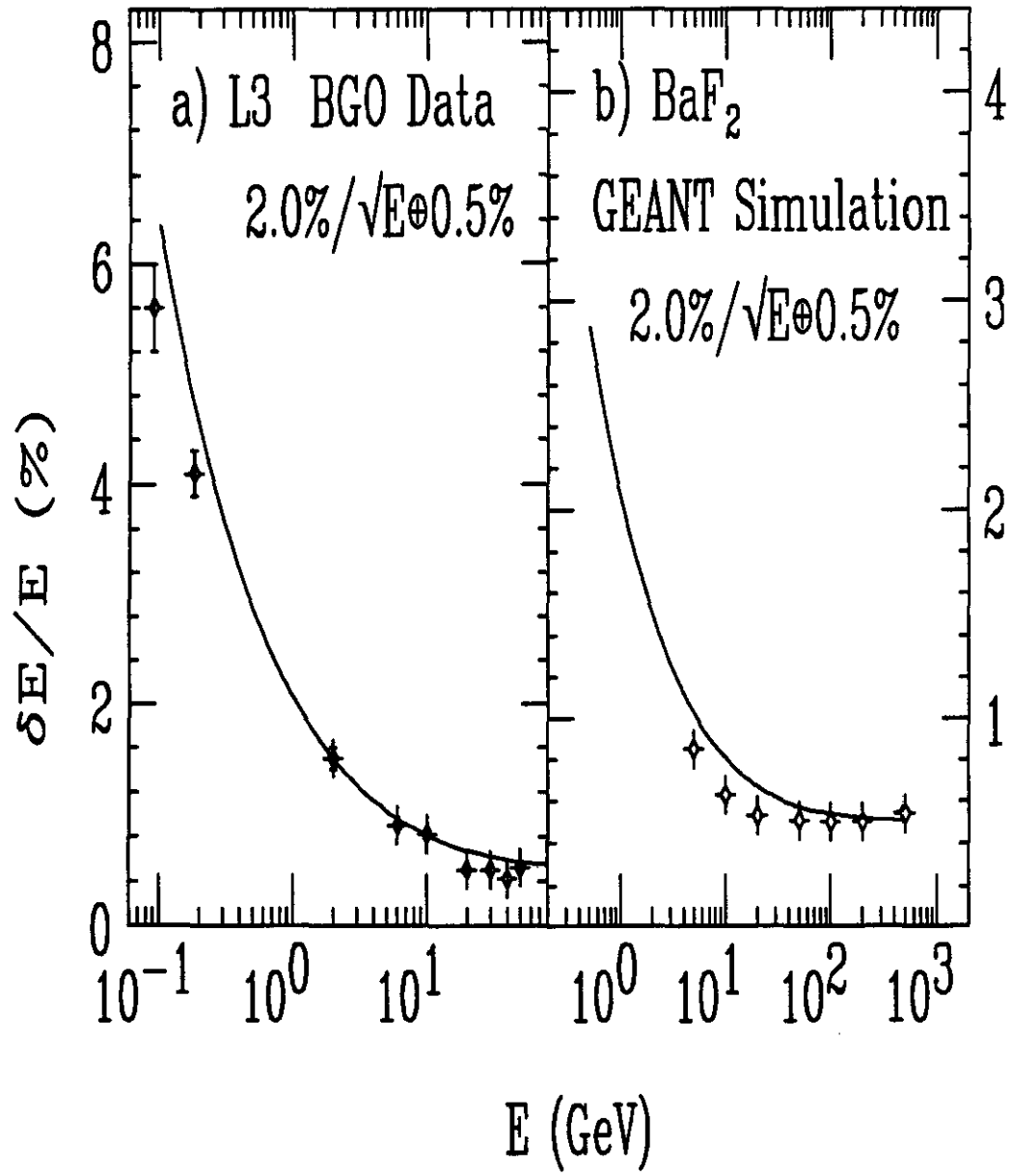

Figure 1: Energy Resolutions of (a) L3 BGO calorimeter, measured at CERN test beams with 4000 crystals, and (b) BaF_2 calorimeter, calculated with GEANT simulation. The solid curves represent a simple parametrization of $2\%/\sqrt{E} \oplus 0.5\%$.

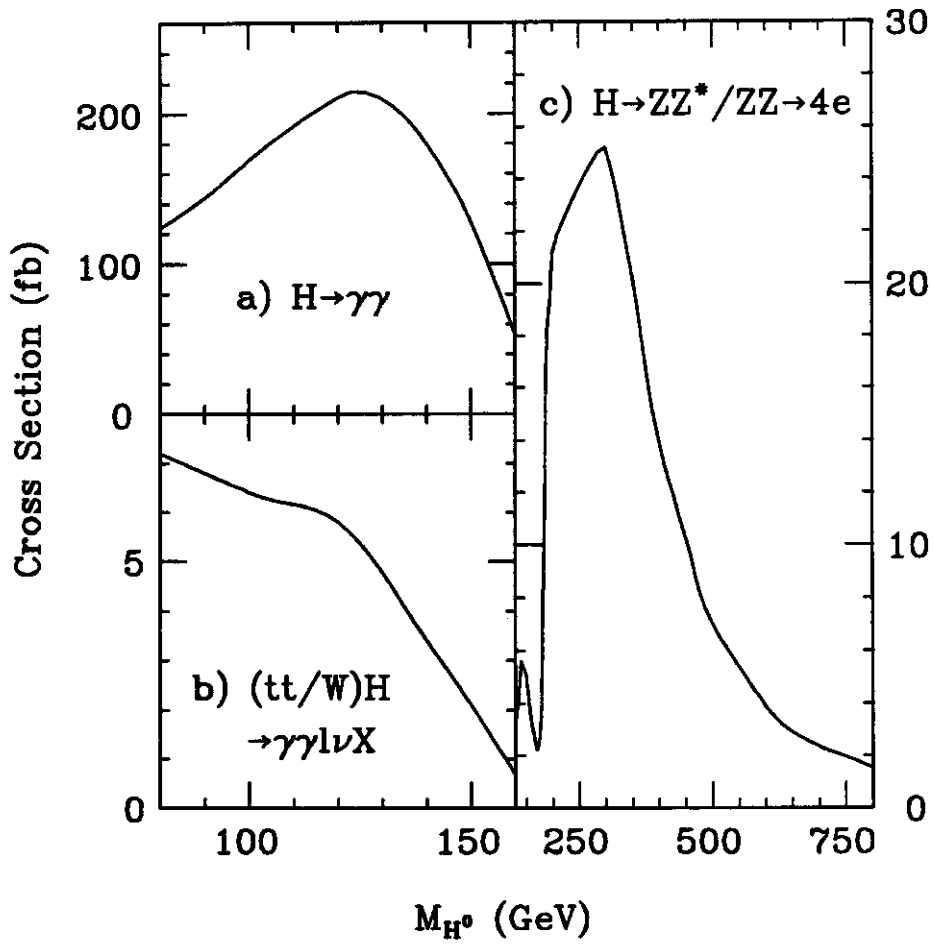

Figure 2: Cross sections of (a) $H \to \gamma\gamma$, (b) $H(t\bar{t}/W) \to \gamma\gamma\ell X$ and (c) $H \to ZZ^*/ZZ \to e^+e^-e^+e^-$ at the SSC are shown as functions of Higgs mass.

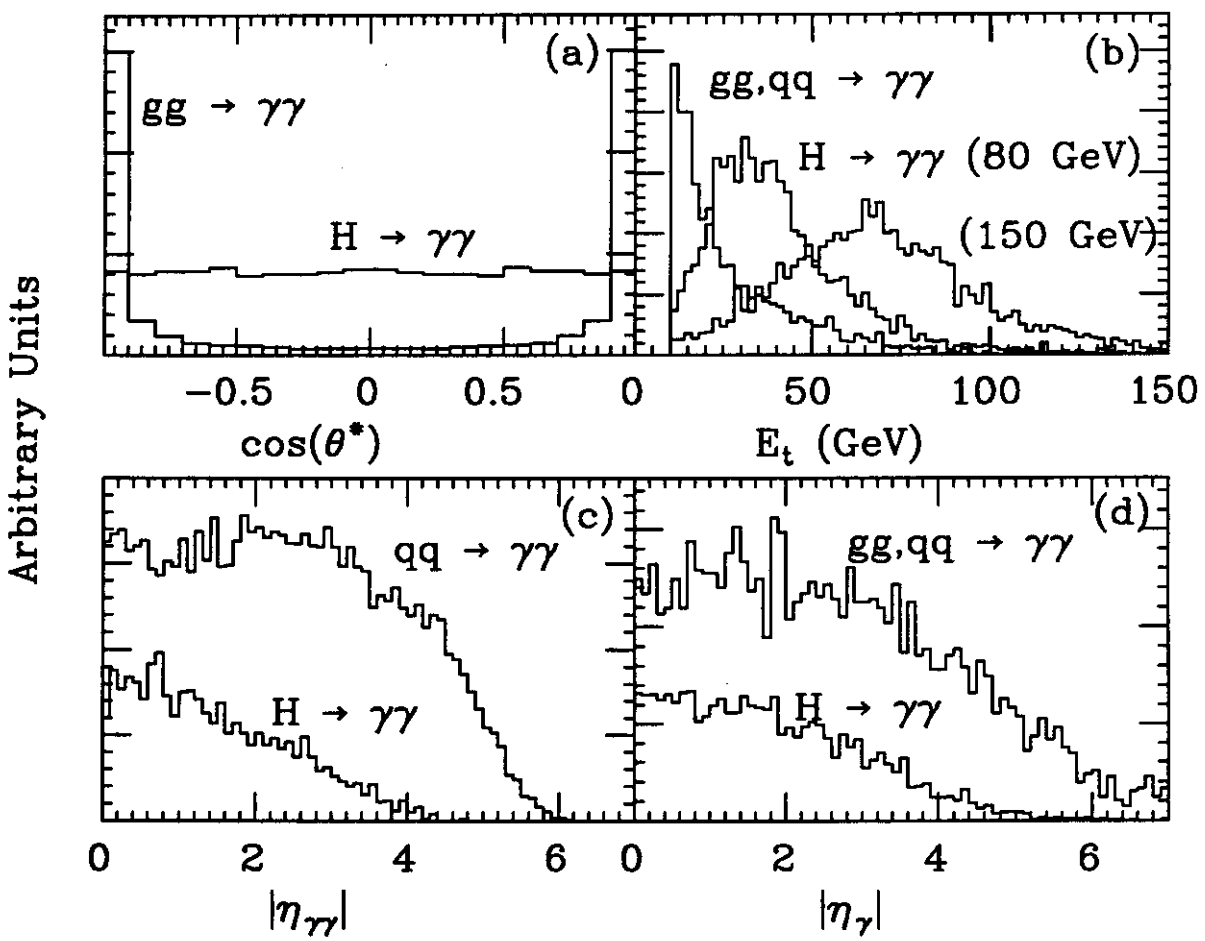

Figure 3: Compariosn of distributions between H→ $\gamma\gamma$ and irreducible background: (a) $\cos\theta^*_\gamma$, (b) E^γ_T, (c) $|\eta_{\gamma\gamma}|$; and (d) $|\eta_\gamma|$.

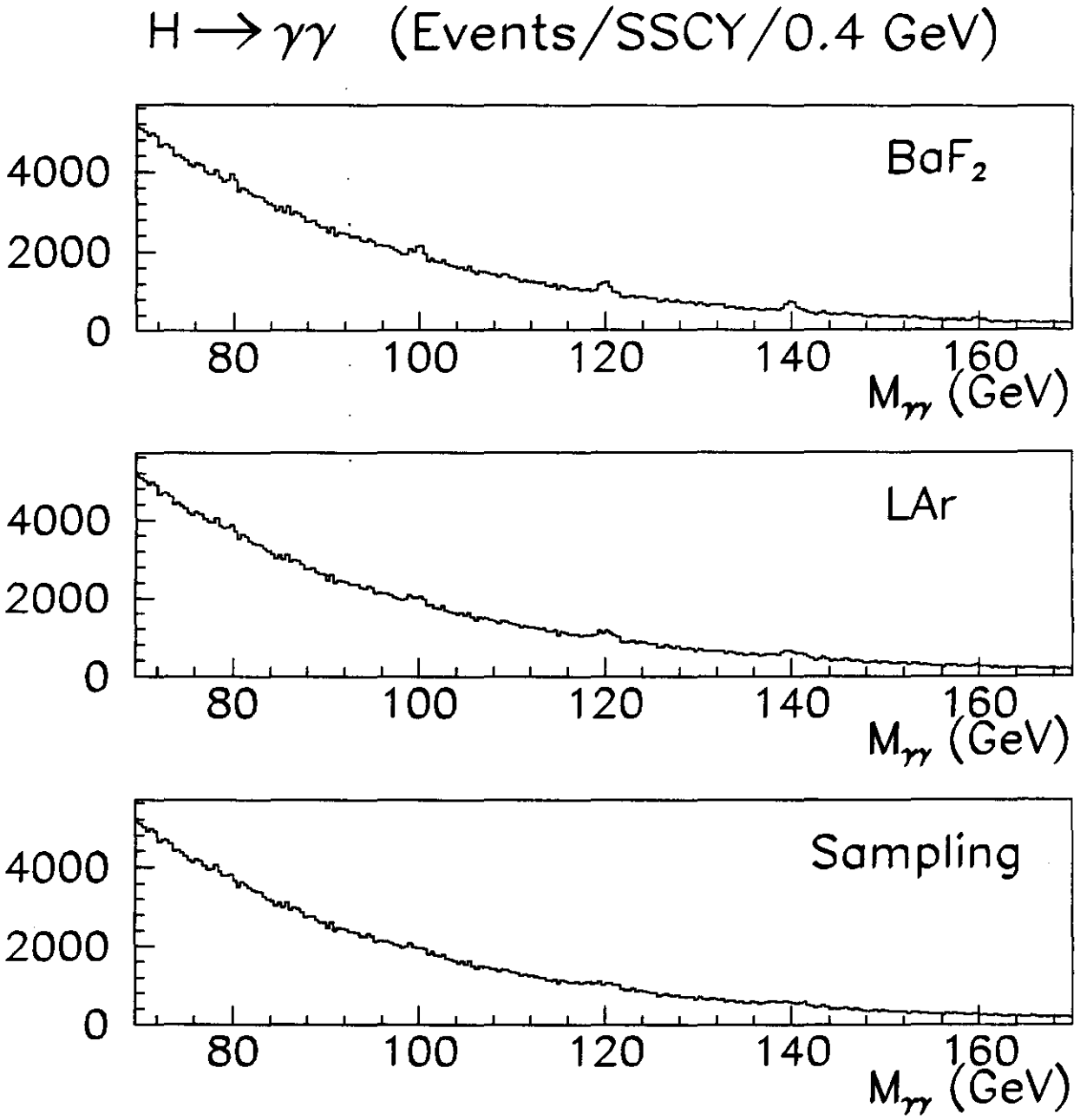

Figure 4: $\gamma\gamma$ **invariant mass spectra obtained within 1 SSCY for Higgs signals of 80, 100, 120, 140 and 160 GeV superimposed on irreducible background are shown for three energy resolutions:** $(2/\sqrt{E} \oplus 0.5)\%$ **(BaF$_2$),** $(7.5/\sqrt{E} \oplus 0.5)\%$ **(LAr) and** $(15/\sqrt{E} \oplus 1.0)\%$ **(Sampling).**

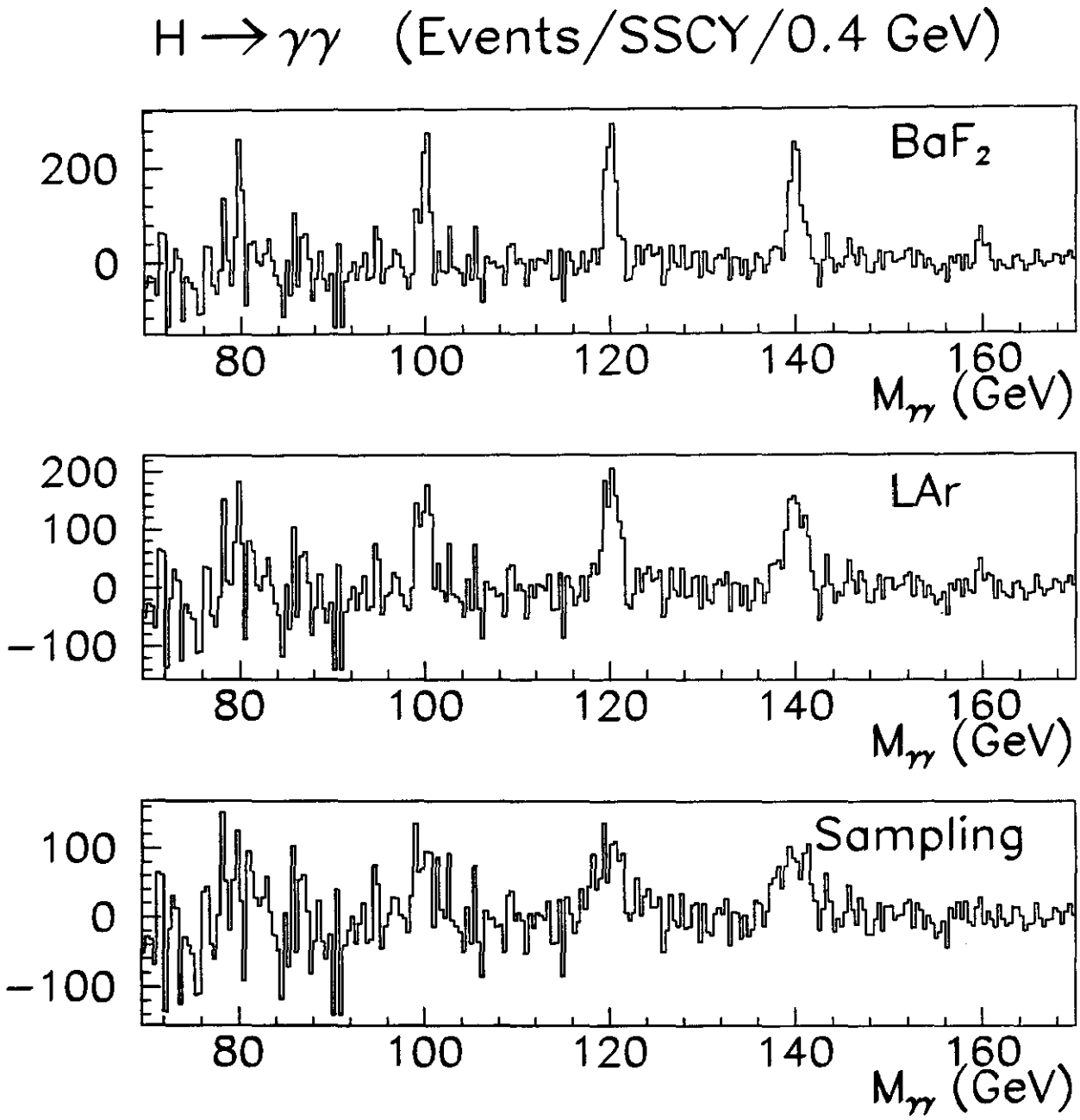

Figure 5: Background subtracted $\gamma\gamma$ invariant mass spectra obtained within 1 SSCY for Higgs signals of 80, 100, 120, 140 and 160 GeV are shown for three energy resolutions: $(2/\sqrt{E} \oplus 0.5)\%$ (BaF_2), $(7.5/\sqrt{E} \oplus 0.5)\%$ (LAr) and $(15/\sqrt{E} \oplus 1.0)\%$ (Sampling).

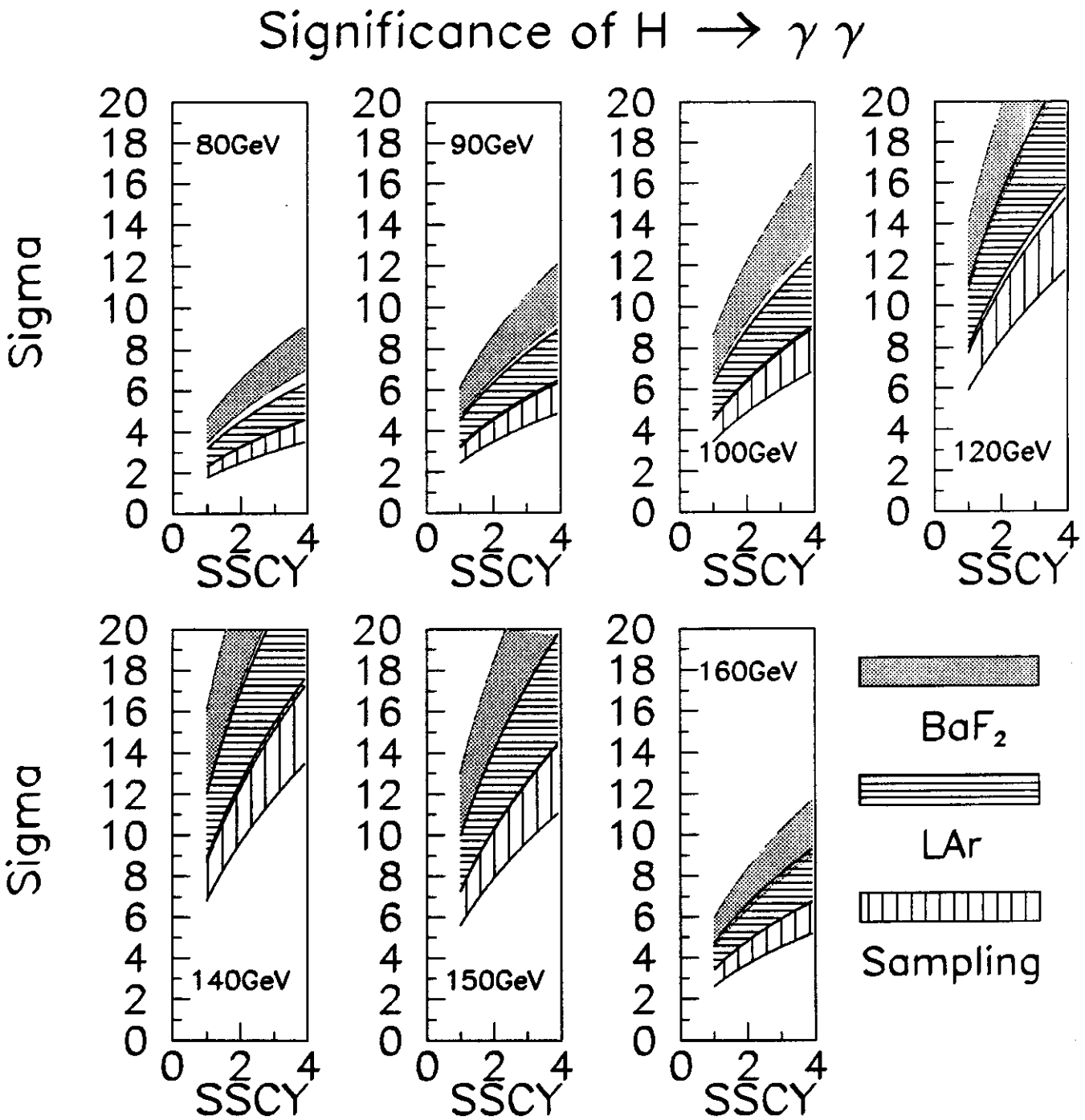

Figure 6: The significance obtainable in H→ $\gamma\gamma$ search is shown as a function of SSCY for Higgs masses of 80, 90, 100, 120, 140, 150 and 160 GeV for three energy resolutions: $(2/\sqrt{E} \oplus 0.5)\%$ (BaF_2), $(7.5/\sqrt{E} \oplus 0.5)\%$ (LAr) and $(15/\sqrt{E} \oplus 1.0)\%$ (Sampling).

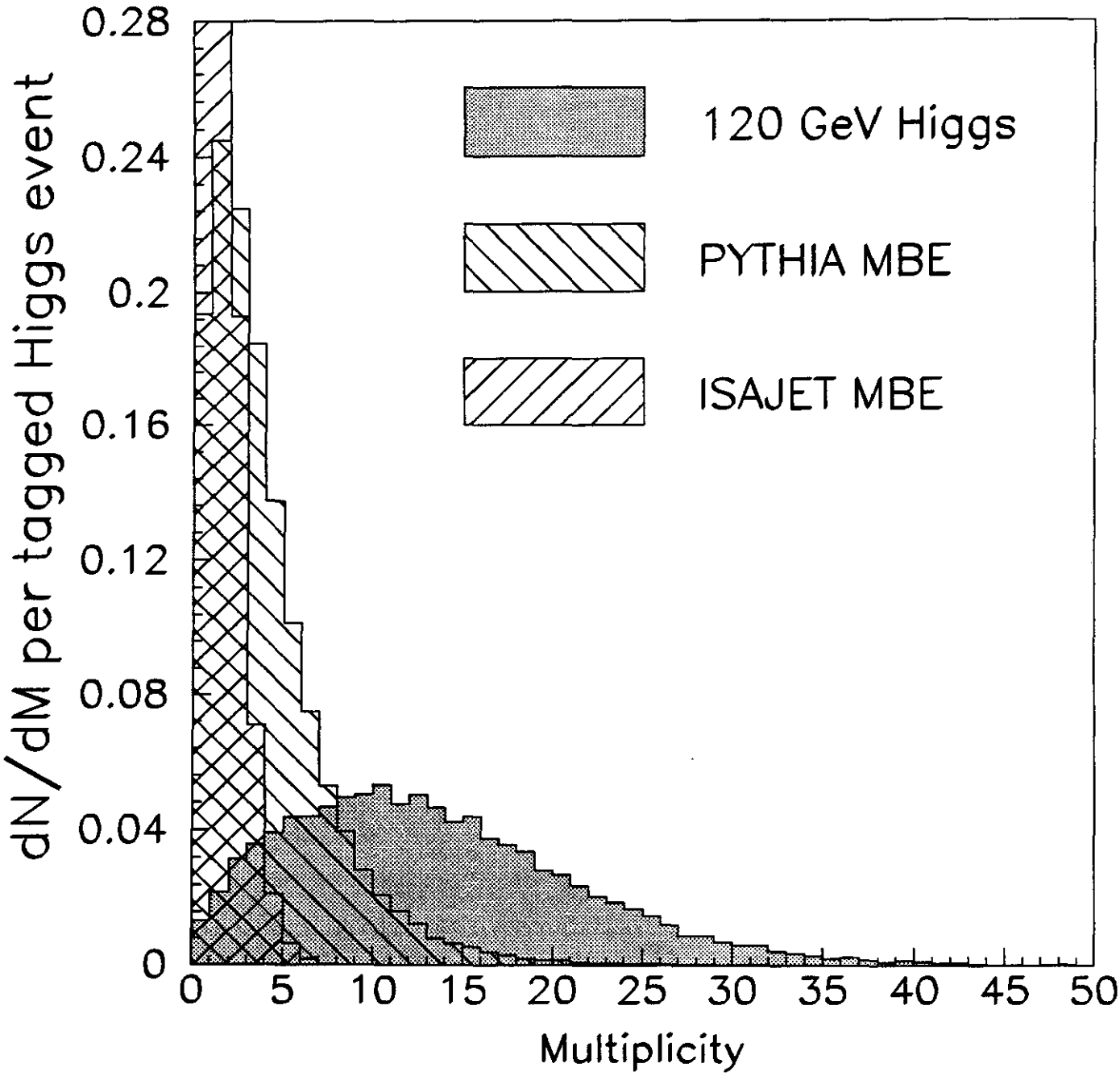

Figure 7: Charge multiplicity distributions after $p_T > 1$ GeV and $|\eta| < 2.5$ cuts for a 120 GeV Higgs signal and minimum bias events backgrounds generated by using PYTHIA and ISAJET programs.

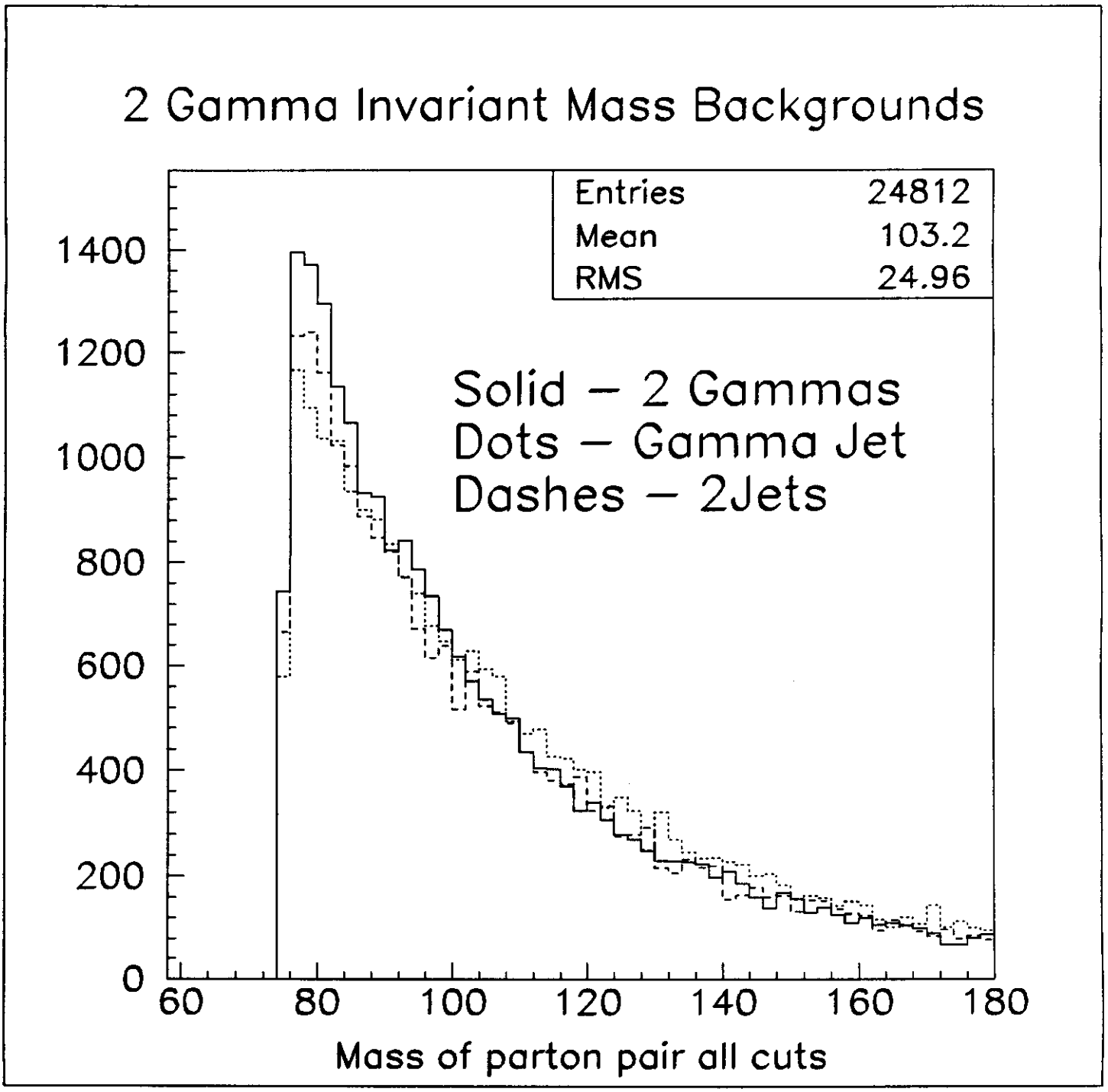

Figure 8: Comparison of parton invariant mass spectra from three QCD processes: $\gamma\gamma$, γ-jet and 2jets.

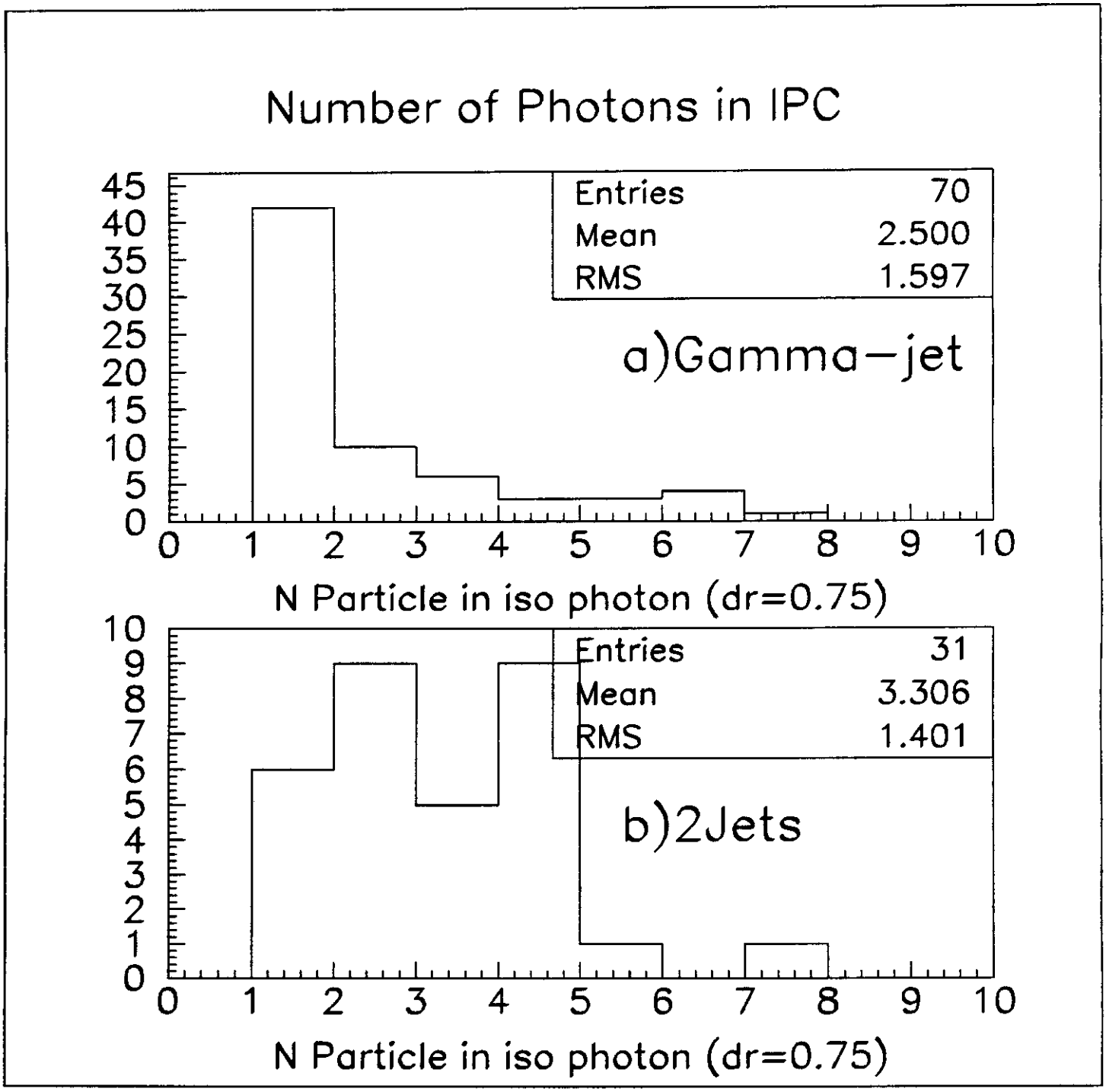

Figure 9: Distributions of photon numbers in isolated photon candidates, passing an isolation cut of R = 0.75 and E_T^{cut} = 10 GeV from 100k events each of (a) γ-jet and (b) 2jets.

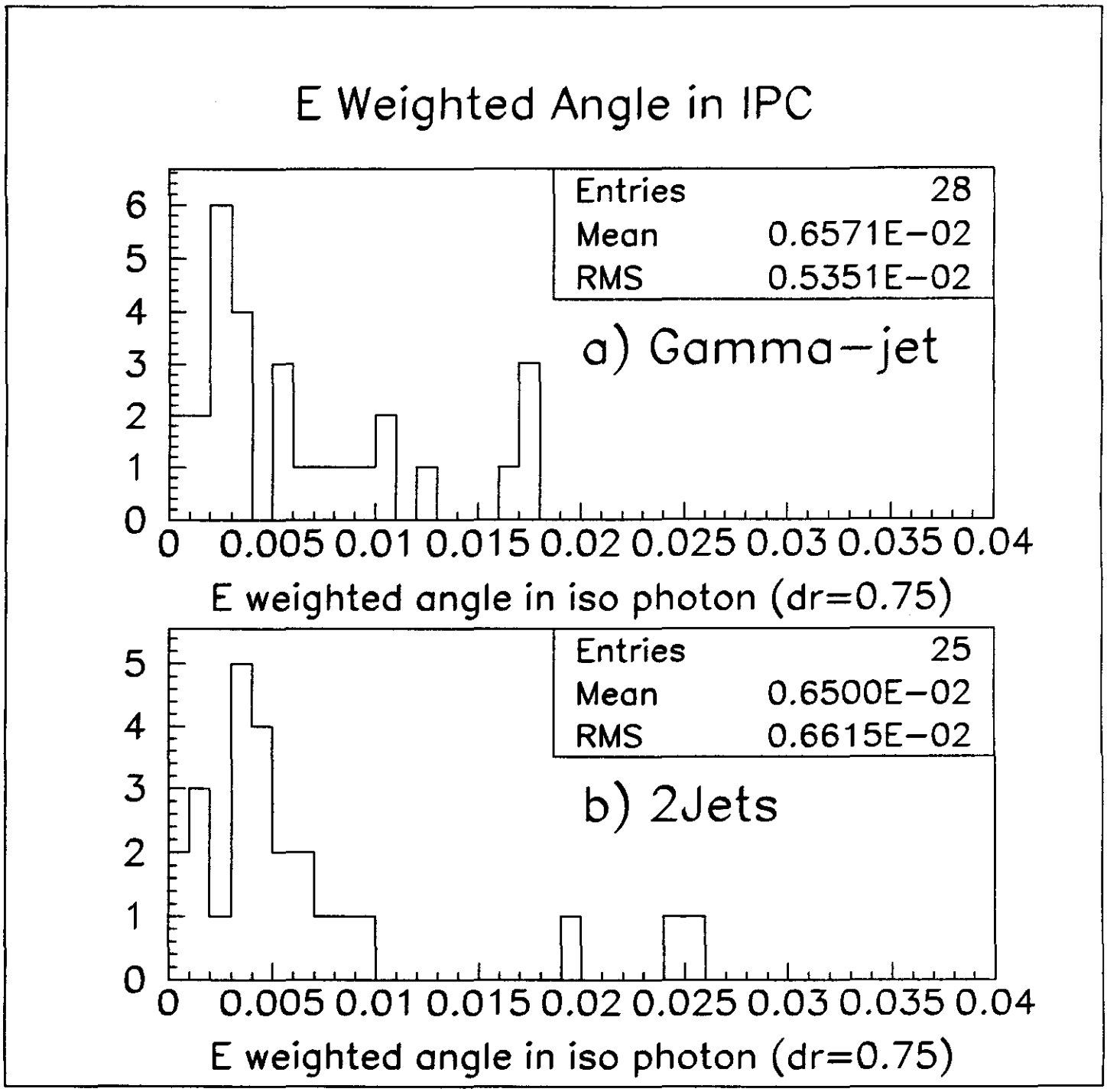

Figure 10: Distributions of $\tilde{\theta}$ of isolated photon candidates, passing an isolation cut of R = 0.75 and E_T^{cut} = 10 GeV from 100k events each of (a) γ-jet and (b) 2jets.

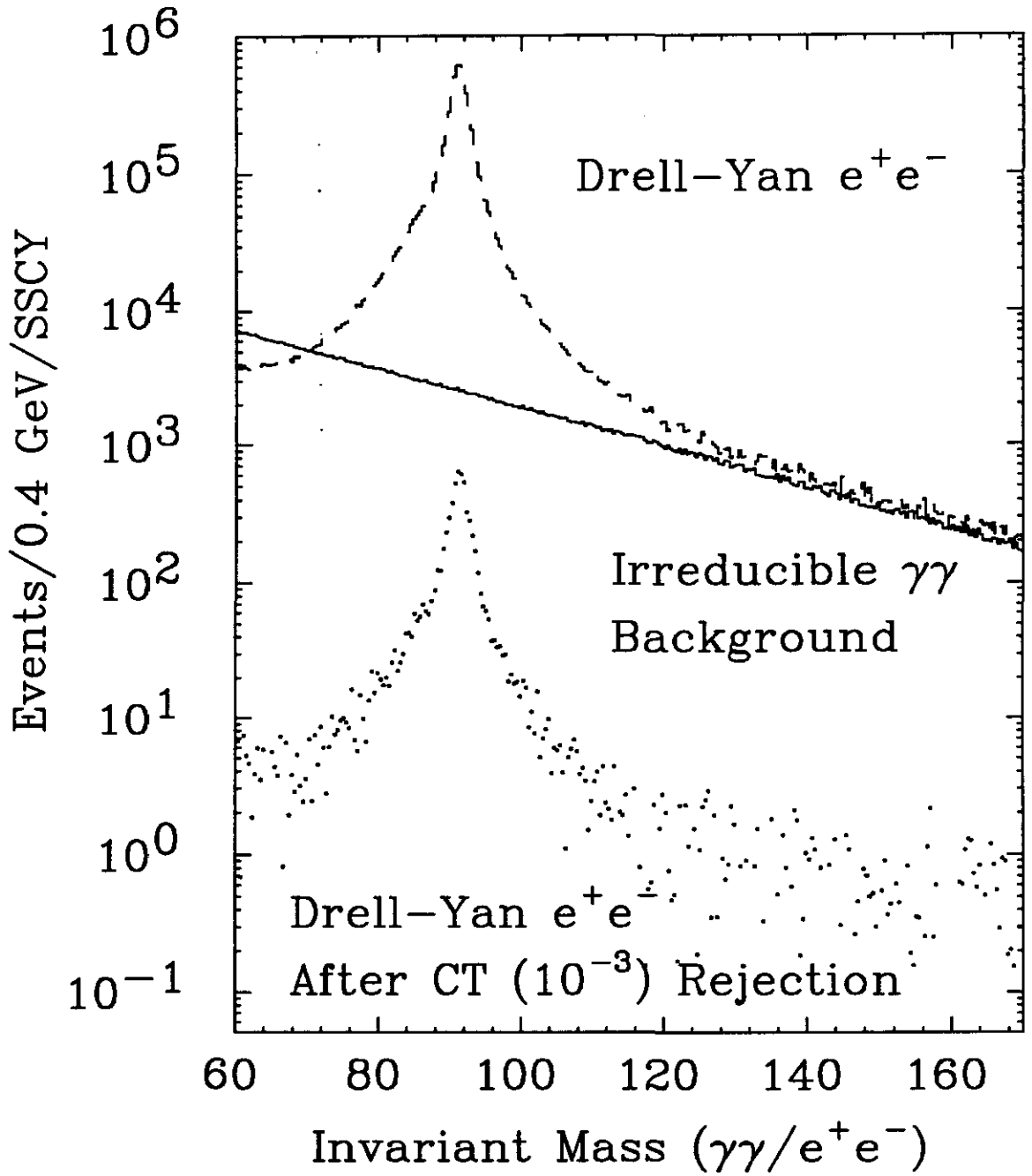

Figure 11: $\gamma\gamma$ and e^+e^- invariant mass distribution of Drell-Yan e^+e^- after event selection cut with no γ/e separation (dashed) is compared with irreducible $\gamma\gamma$ distributions (solid). Also shown in the figure is the Drell-Yan distribution, if 3% of electrons would misidentified as a photon.

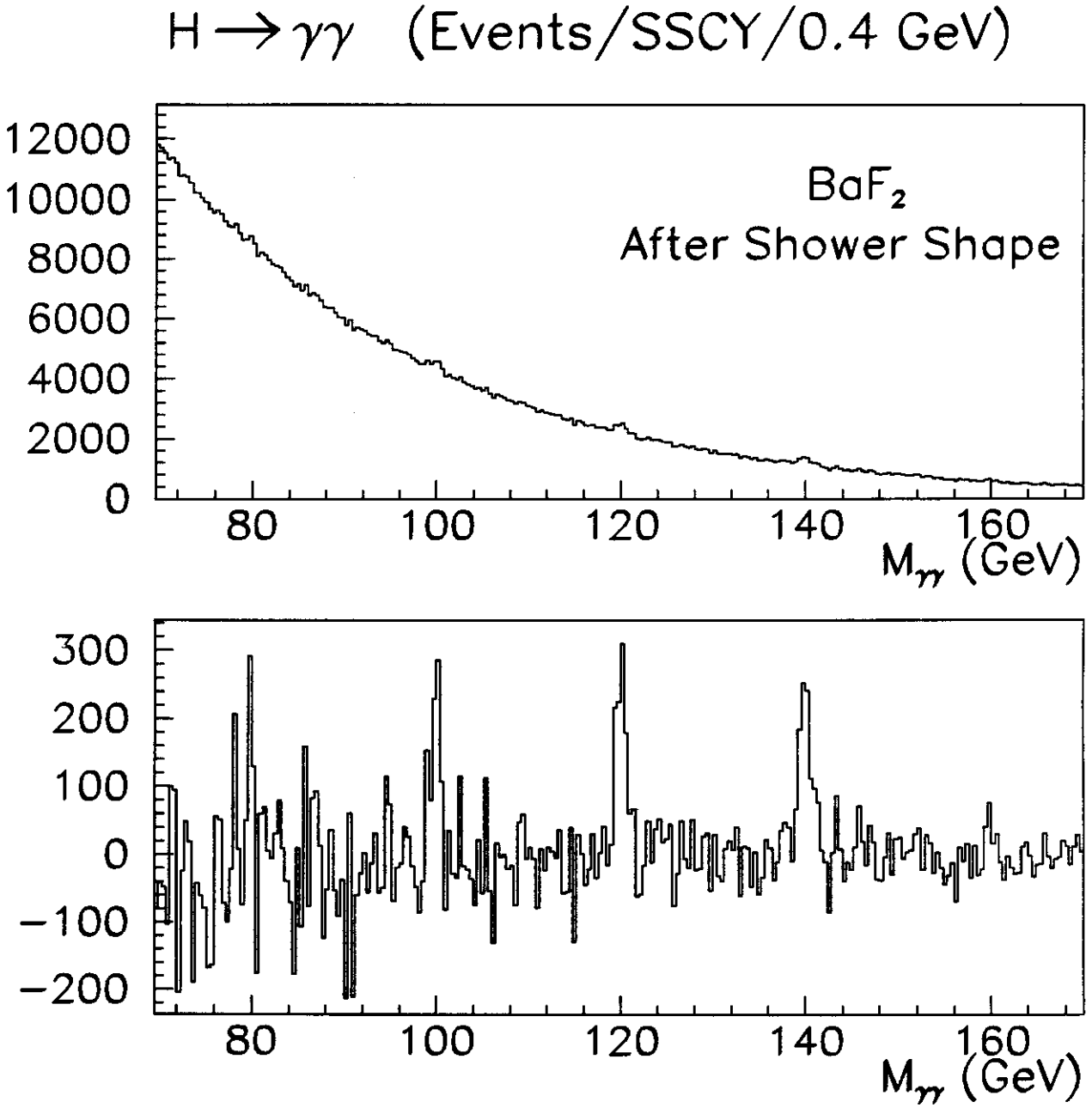

Figure 12: H→ $\gamma\gamma$ signals of 80, 100, 120, 140 and 160 GeV superimposed on all backgrounds and corresponding background subtracted spectra are shown for BaF_2 calorimeter after shower shape analysis.

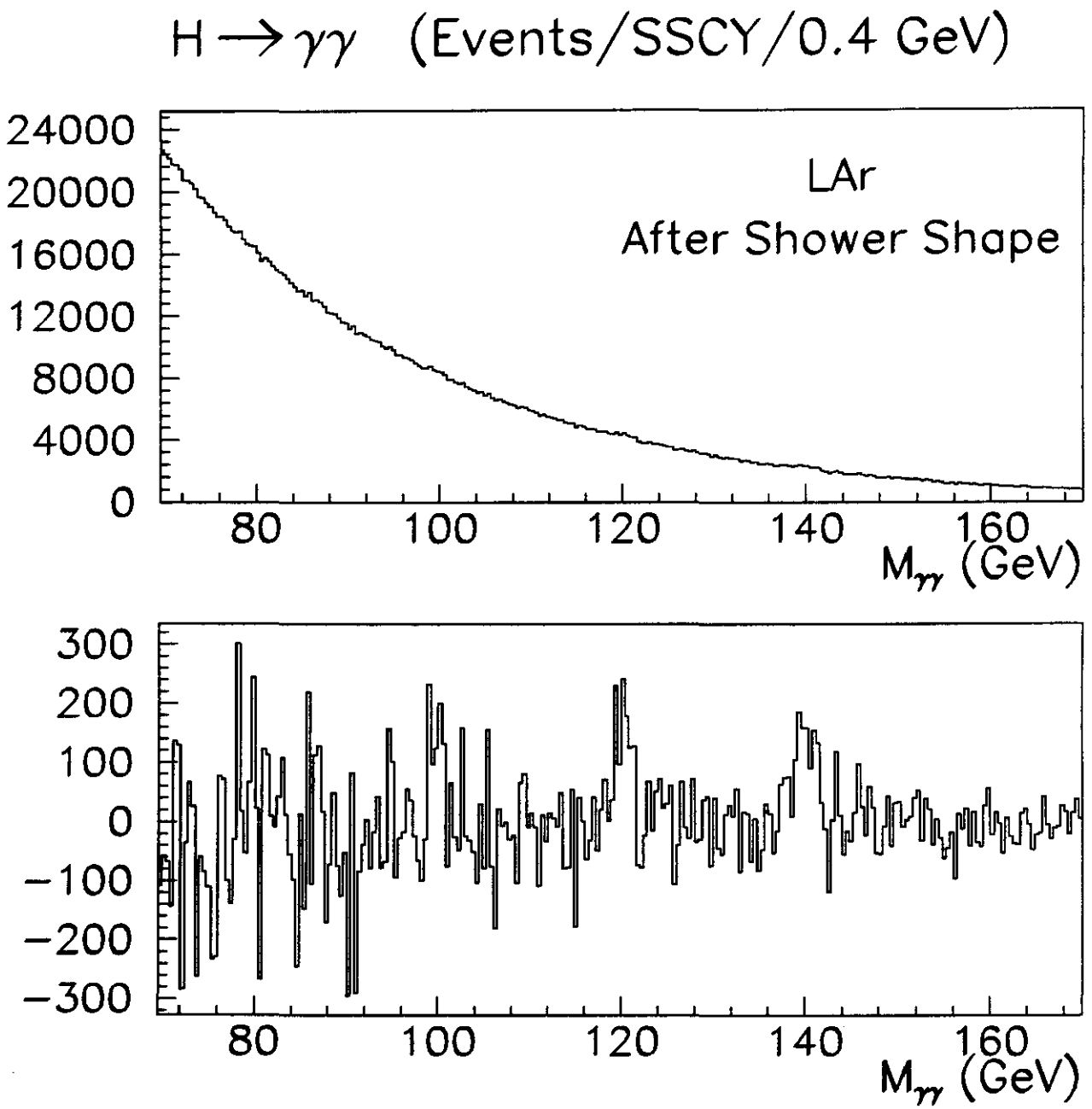

Figure 13: H→ $\gamma\gamma$ signals of 80, 100, 120, 140 and 160 GeV superimposed on all backgrounds and corresponding background subtracted spectra are shown for LAr calorimeter after shower shape analysis.

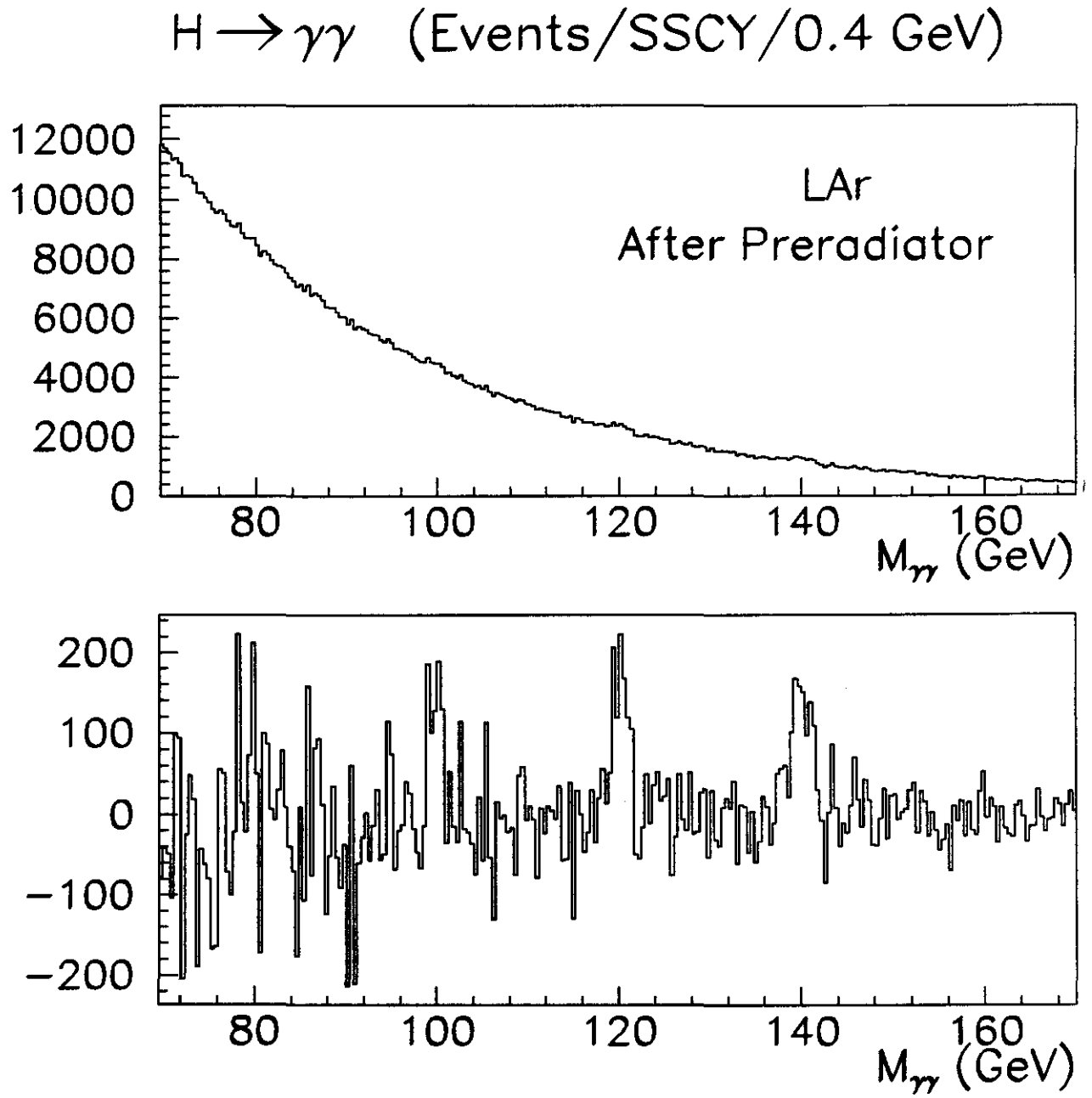

Figure 14: H→ $\gamma\gamma$ signals of 80, 100, 120, 140 and 160 GeV superimposed on all backgrounds and corresponding background subtracted spectra are shown for LAr calorimeter after preradiator rejection.

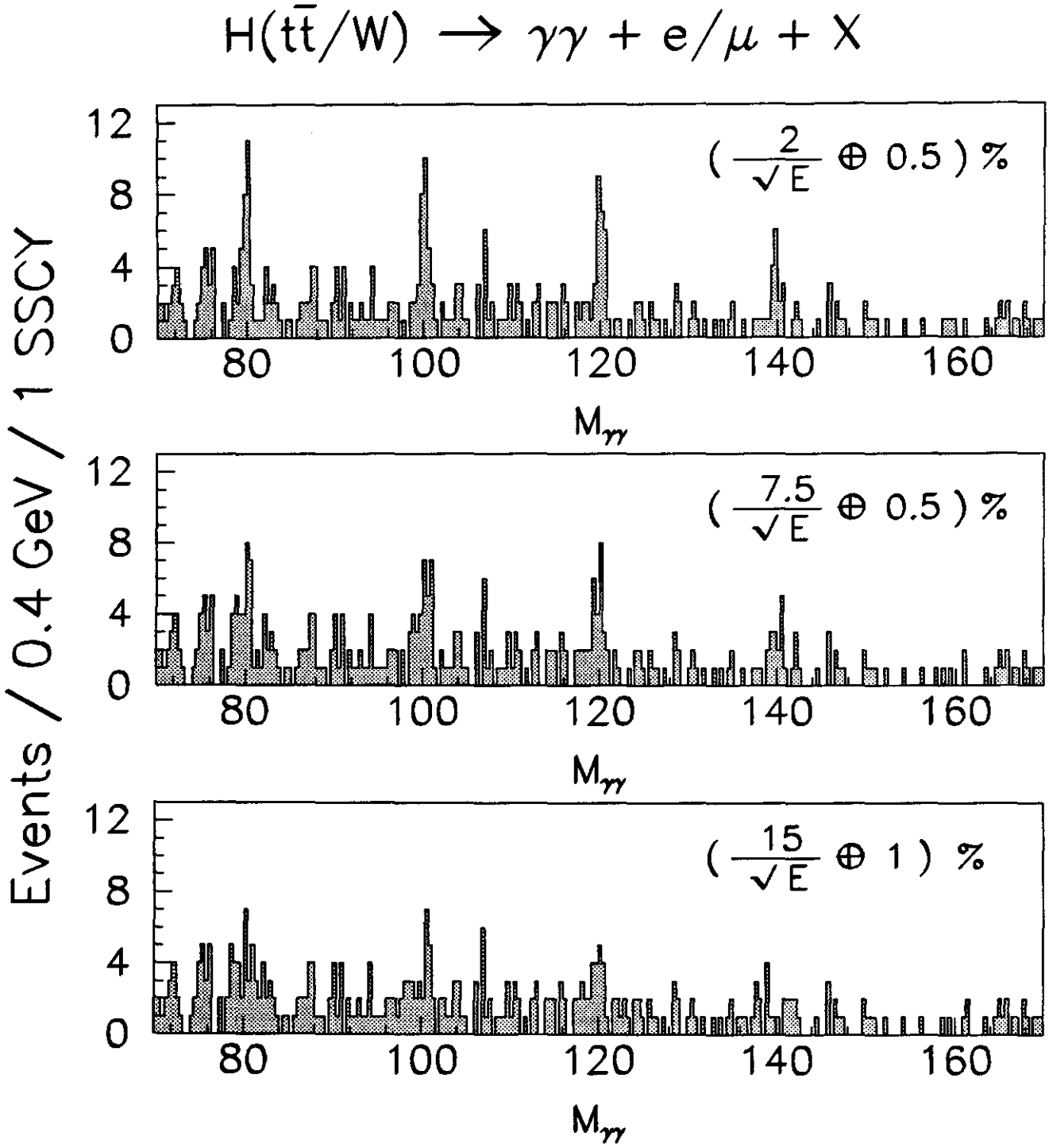

Figure 15: H($t\bar{t}$/W)→ $\ell\gamma\gamma$X signals of 80, 100, 120, 140 and 160 GeV, superimposed on all backgrounds are shown for three different energy resolutions: $(2/\sqrt{E} \oplus 0.5)\%$, $(7.5/\sqrt{E} \oplus 0.5)\%$ and $(15/\sqrt{E} \oplus 1.0)\%$.

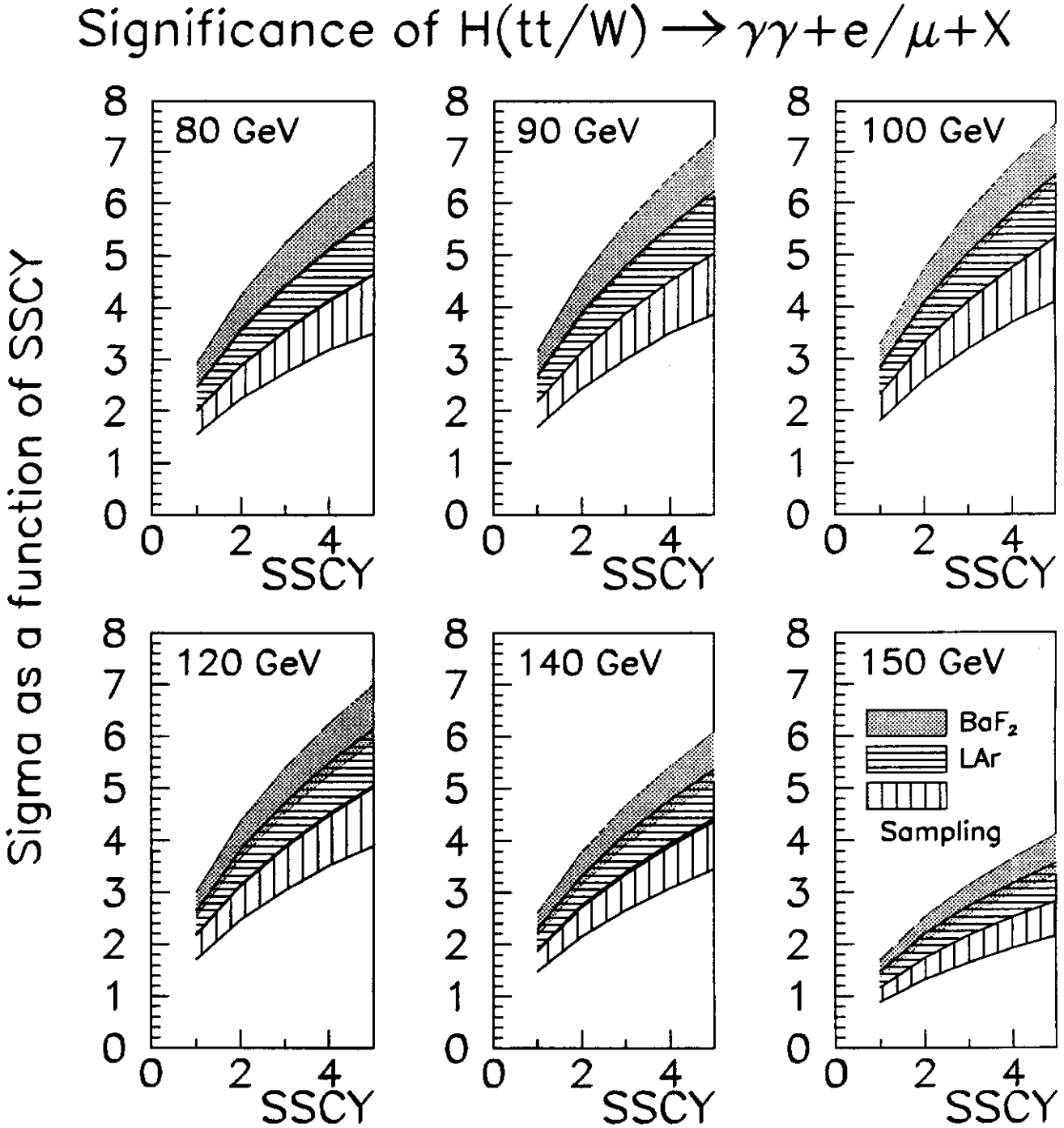

Figure 16: Significance of $H(t\bar{t}/W) \rightarrow \ell\gamma\gamma X$ searches as function of SSCY for Higgs mass of 80, 90, 100, 120, 140 and 150 GeV, shown for three different energy resolutions: $(2/\sqrt{E} \oplus 0.5)\%$, $(7.5/\sqrt{E} \oplus 0.5)\%$ and $(15/\sqrt{E} \oplus 1.0)\%$.

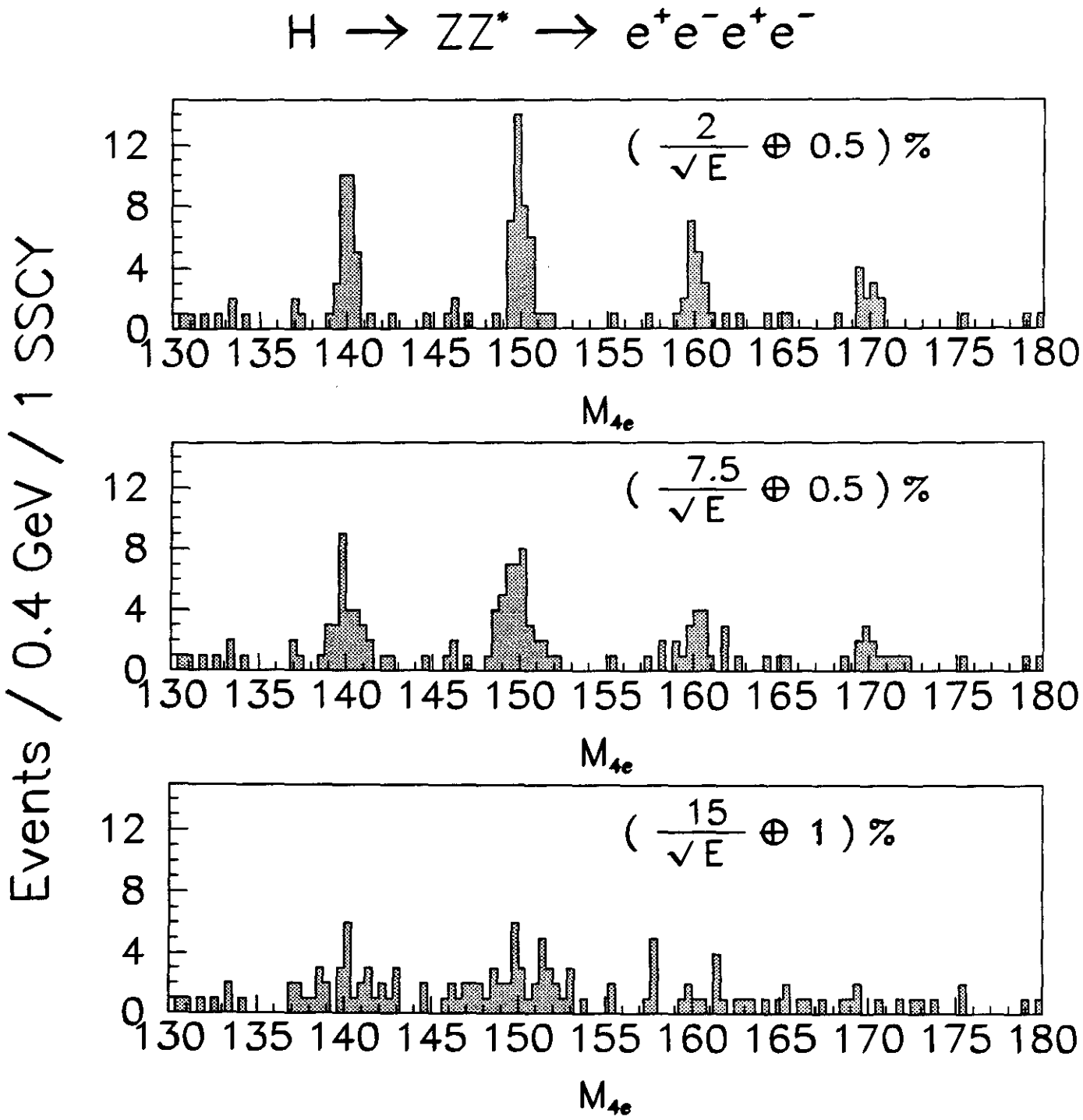

Figure 17: H→ZZ/ZZ* →$e^+e^-e^+e^-$ signals of 140, 150, 160 and 170 GeV, superimposed on all backgrounds are shown for three different energy resolutions: $(2/\sqrt{E} \oplus 0.5)\%$, $(7.5/\sqrt{E} \oplus 0.5)\%$ and $(15/\sqrt{E} \oplus 1.0)\%$.

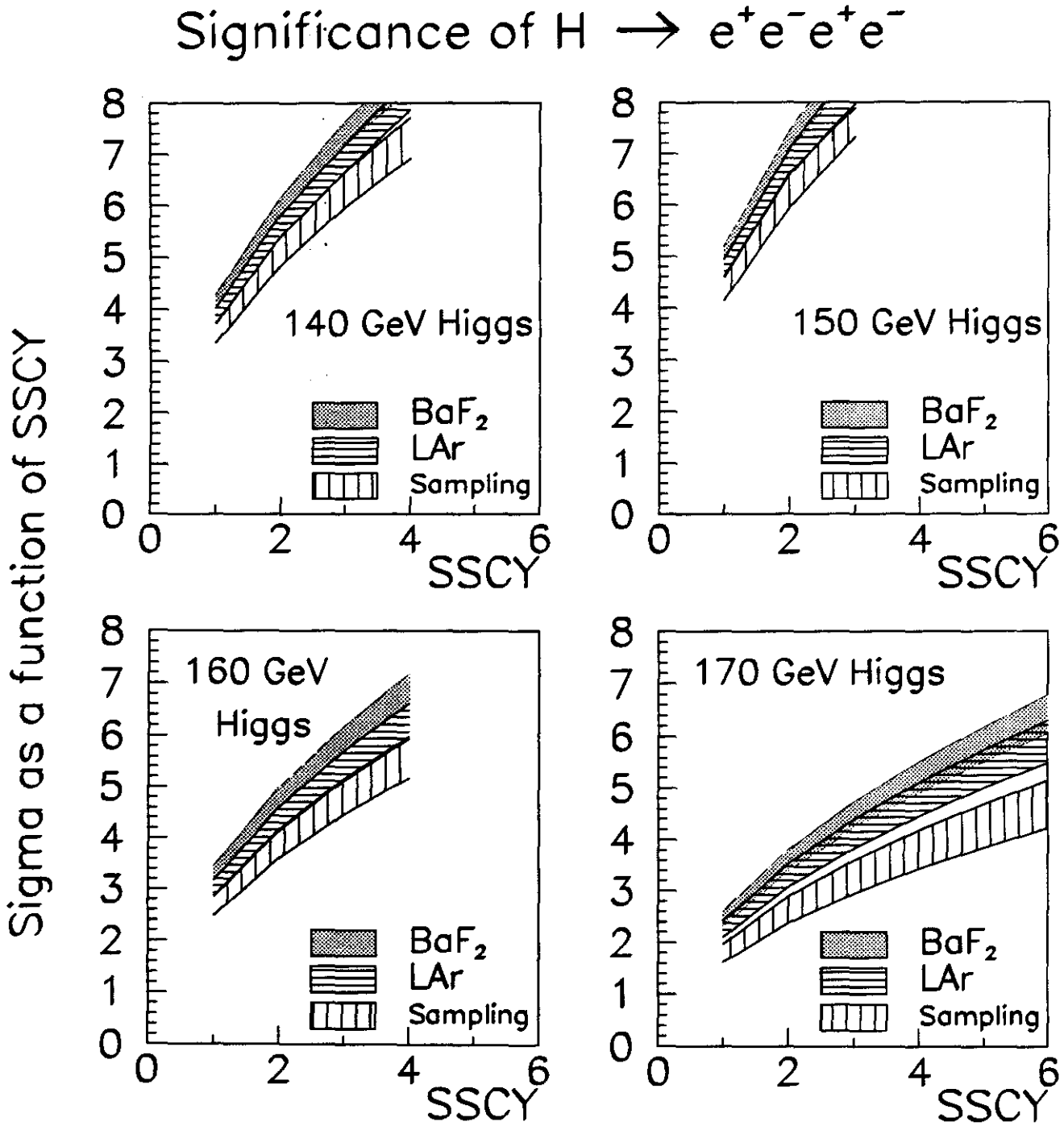

Figure 18: Significance of H→ZZ/ZZ* →$e^+e^-e^+e^-$ searches as function of SSCY for Higgs mass of 140, 150, 160 and 170 GeV, shown for three different energy resolutions: $(2/\sqrt{E} \oplus 0.5)\%$, $(7.5/\sqrt{E} \oplus 0.5)\%$ and $(15/\sqrt{E} \oplus 1.0)\%$.

3.3.1 Magnet

3.3.1 Magnet

Question 1: We are still concerned about the effects of the external field. We reiterate that the consequences of the stray field to SSCL/e.g. increased cost of machine and detector components that must tolerate the stray field, should be further examined before final approval.

The GEM magnet does not have a return yoke. As a result fringe magnetic field will be present in the experimental hall and on the surface during magnet operation. The surface level fringe field is small. It peaks at 44 gauss above the center of the detector hall and decreases to normal earth magnetic field level at the fenced boundary of IR5. Posting of the 10 gauss perimeter is planned.

The fringe field in the experimental hall and access shafts varies rapidly from about 0.2 T near the Forward Field Shapers to about 50 gauss in the access shafts and near the ends of the IR hall. Adequate experience from national laboratories and many MRI hospital facilities exists of shielding electrical (switches, lights, power supplies etc.) and cryogenics equipment (pumps, valves, etc.) from such field. An estimate of the incremental cost of shielding has been added to the magnet WBS cost estimate. It also includes a cost of shielding of the 20x20x4m counting room with a 338t iron plates.

We have also investigated an effect of the fringe field on the accelerator components. The main concern is the size and corrections for the radial field component at the final focus quadrupoles. The radial field of the GEM magnet was found to be rather small. For the magnet centered on the beam line the radial field component will be less then 50 gauss at 20 m from the interactional point and less then 2 gauss at 35 m. The integral of the radial field component along the beam envelope is also very small. A proposal to change the optics of the final focus so that ends of the quadrupoles start at 35 m is being studied by the accelerator group. In either position however, the shielding of the quadrupoles from the radial field component is quite simple.

Question 2: The forward field shaper scheme should be specified promptly to permit optimization of the detector subsystems.

The design of the GEM magnet presented in the LOI was of an open field solenoid only. In that design, the muon momentum resolution in the forward direction, 1.5<eta<2.5 was unacceptably poor. Our studies indicated that the resolution in this rapidity region was relatively insensitive to the radius and length of the solenoid. A number of local field shaping options was considered (see Table 1) and a simple, passive iron field shaper was chosen for the GEM baseline.

Table 1 Forward field Design Options Considered

Options	Design Objective	Performance	Disadvantage
longer superconducting solenoid	improved forward performance, lower cost, improved access	poor	
superconducting solenoid with end compensation	improved field uniformity	poor	high technical risk
forward pinch coils	improved forward performance	moderate-good	costly, complex
forward oppos. field coil	improved forward performance	moderate-good	costly, complex
flat steel poles with coil windings	improved forward performance	moderate	costly, complex
conical steel field shaper	improved forward performance	good	costly, complex
conical steel field shaper with coil windings	improved forward performance	good	costly, complex
conical steel field shaper	improved forward performance	good	

The iron forms a truncated cone around the beam axis in the region of 10 to 18 meters from the interaction point. It introduces flux concentration and a large field gradient in the region of forward muon chambers allowing for the 13% momentum resolution at eta=2.5 for a muon emitted with 500 GeV/c transverse momentum. The momentum resolution at different values of transverse momentum is shown in Figure 1.

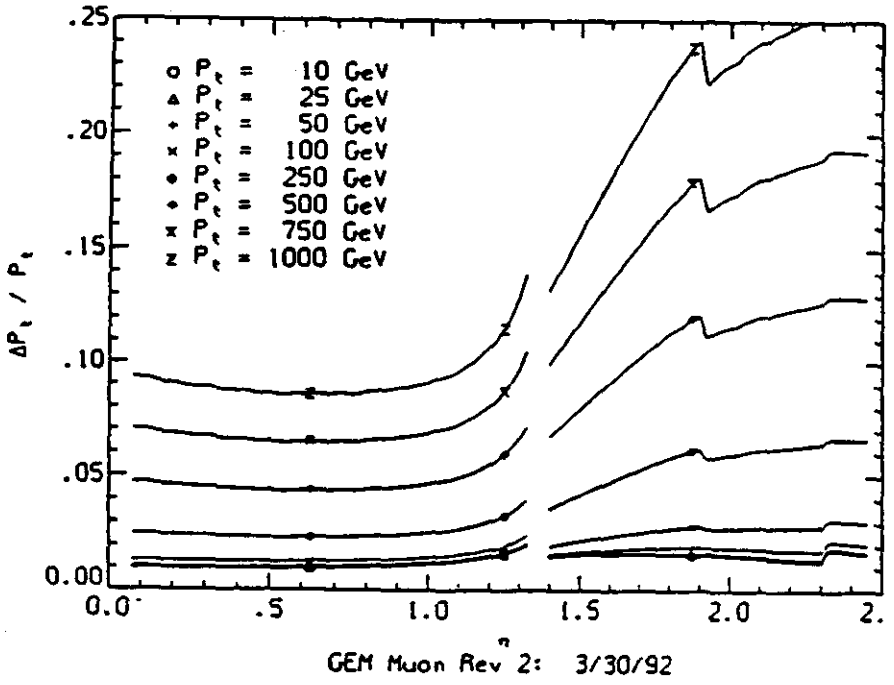

Figure Momentum resolution versus pseudorapidity at constant p_t. These curves correspond to the mean position of the endcap muon chambers. The gap at η 1.35 corresponds to the transition between the barrel and endcap chambers.

The field shaper represents a simple, but massive structure weighing approximately 1000 tons. It will have a support structure, independent of that of the magnet which will also allow for an independent movement and alignment of the iron. The back of the cone will be notched to provide space for beam line vacuum pipes. Detailed design of the forward field shaper and its support structure as well as the structural analysis of gravitational and magnetic loads can be found in Magnet Technical Design Report.

Question 3: Since the magnet appears to be a critical path item for the GEM detector, it is important to carry out the magnet engineering R&D without delay.

Gem has given high priority to the design of the magnet and related R&D. This has absorbed a large fraction of the GEM budget. Most of the effort has gone into the design of the magnet, resulting in a technical design report. conductor R&D has now begun at MIT. Our FY92 funding is detailed below, accompanied by Table 1, which shows the budget by design institution, and Table 2, which lays out the conductor development plan for MIT (this plan extends into FY93). Finally, we include our plans for FY93, along with Table 3, which contains a list of activities and costs.

FY92 Funding

The original FY92 budget for Magnet Design and R&D was $5M. As of June 30, a total of $4.5M of that has been allocated to LLL, MIT< RAL and SSC, plus consultants, who have assisted us in the preparation of the draft RFP. These funds have been used to accomplish the following:

A. A conceptual design of sufficient breadth for a reasonably realistic cost estimated to be made. The magnet technical design report is the principal deliverable for the activity.

B. Develop a cost estimate for the GEM magnet and to defend it to the internal review committee and to the DoE. That work is now complete and was reviewed last week.

C. Initiate a comprehensive R&D program to verify the conductor design, to demonstrate that the "CIC" conductor can be made in sufficient lengths for subsequent experiments on conductor bending, winding, current carrying capability, etc.; to demonstrate satisfactory performance of the joints that must be made between coil segments of the solenoid and to initiate design approaches to the winding of coils. This work is just getting under way.

D. Prepare an RFP for industry to bid on as the prime contractor for magnet final design, fabrication, assembly and test. The draft RFP is completed and being reviewed by industry.

E. Prepare an RFP for the GEM magnet conductor. That work has already been started. The draft Statement of Work has been prepared.

Of the total allocation of $4.5M, design and associated activities account for $3.750M; ($2.1M at LLL, $1.25M at MIT and $0.4M for SSC). Funding for the R&D program has just been allocated to MIT at a level of $0.76M for this year. The expenditures to date on the budget of $4.5M is about $2M. The earlier ramp up at MIT and LLL had been accomplished and we believe most of the remaining funds will be costed or accrued by the end of FY92.

FY92 Funding

Because of the tremendous size of the GEM magnet and the associated field fabrication, assembly and installation issues, we believe it is critical to the overall design effort that the prime contractor come on board as soon as possible so that the people who do the final design are also the ones who built it. Form the GEM magnet point of view, we assume that we do have the frozen design and can proceed to build it according to the base line specifications in order to meet the overall GEM schedule. We intend to bring the contractor on board in FY93 with a Phase I award of about $5M for engineering effort and $2M for long lead procurement of coil winding tooling.

Table 1

FY92 BUDGET

LLNL - 2.1M$	Design of Vacuum Vessel and Cold Mass Support, Development of Assembly and Installation Approaches
MIT - 1.240M$	Design of Cold Mass
MIT - 0.760M$	R&D on Conductor, Joint Design, Coil Winding Approaches with Industry
SSC - 0.400M$	Design and Mangement Staff, Consultants, RAL, Small Contracts

TOTAL = 4.5M$

table C

GEM DETECTOR DEVELOPMENT PLAN for MIT

MAGNET DESIGN (Procurement/Fabrication) (MIT Cold Mass Engineering - FY 1992)	
Description	**M&S/Labor Dollars**
TDR Approval	
S.C. Wire	
Early SC strand production/hand cabling	6K
R&D strand production (315,000)	162K
Strand verification	8K
Total S.C. Wire:	**176K**
Cabling	
Manufacture Cu Cable (cabling trials, tube *mill practice-development winding)*	11K
Development Winding (400m)	43K
Cable 100m + 600m SC strand	9K
Total Cabling:	**63K**
Conduit	
Manufacture Strainless Strip (reestablish *tube mill operation)*	106K
Development Winding conduit (conduit ver.)	60K
Total Conduit:	**166K**
Al Sheath	
Sheath material evaluation	25K
Manufacture 100m Al sheath	11K
Total Al Sheath:	**36K**
Joints	
Cu joints (Fab. first sample joint Cu)	17K
Fab. early SC joint & test	18K
Cryostat, leads, mods	36K
Data acquisition, etc.	36K
Helium	27K
Evalutate alternative joints	18K
Total Joints:	**152K**
Winding and Tooling	
Conductor bending experiments	80K
Tooling design	69K
Total Winding and Tooling:	**149K**
Additional Miscellaneous	18K
FY92 Cold Mass Engineering @ MIT	240K
Previously Approved Dollars	1000K
PAGE TOTAL:	**2000K**

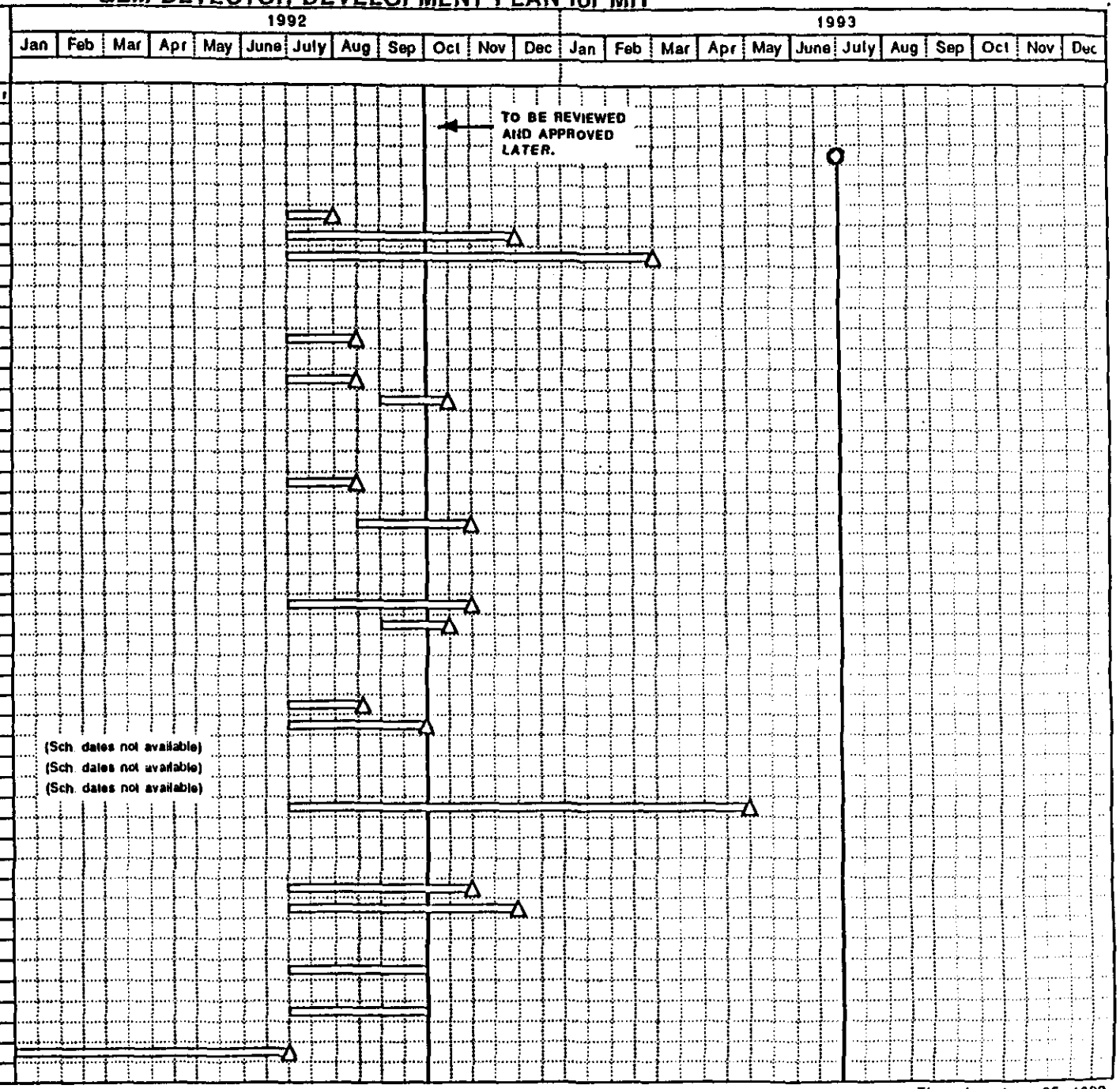

Thursday, June 25, 1992

Table 3

GEM MAGNET FY 93 PLAN

MAGNET DESIGN
R&D Procurement/Fabrication
(FY93 Program - SSC, MIT, LLL)

Description	M&S/Labor Dollars
Collaboration Design Effort	3000K
Prime Contractor Engineering	3000K
S.C. Wire (FY92 Program Cont.)	
Strand verification	10K
Cabling (FY92 Program Cont.)	
Cable 100m + 600m SC strand	54K
Conduit (FY92 Program Cont.)	
Encapsulate 100m + 600m SC cable (Encap. 600m)	140K
Al Sheath (FY92 Program Cont.)	
Fabricate 1150m Al Sheath	149K
Joints (FY92 Program Cont.)	
Fabricate SC joints	54K
Helium	41K
Evaluate alternative joints	10K
TOTAL JOINTS	105K
Winding & Tooling (FY92 Prog. Con	
Conductor Assy./Spooling	67K
Tooling Design	46K
TOTAL WINDING & TOOLING	113K
Winding and Tooling	
Devel winding tool design/tooling setup site	46K
Fab. development winding tooling	500K
Assemble cu cable in sheath	67K
Fabricate joint components	44K
Wind first development winding	320K
Make joint/issue winding & joint fab. specs.	73K
TOTAL WINDING AND TOOLING	1050K
Bobbin	
Spec. develop winding coil bobbin	17K
Place order for develop wind coil bobbin	119K
Fabricate first bobbin	364K
TOTAL BOBBIN	500K
Conductor Procurement by SSCL (partial)	500K
Additional Engineering (SSC, MIT, LLL and Prime Contractor)	2000K
Simulated Service Coil	
Model Coil Tooling Design/spec for Model Coil	36K
Fab Modify/Assy Model Coil Conduct/Cryostat	15K
Fabricate Model Coil Tooling	71K
Wind Model coil	40K
Model Coil tests (includes Helium)	50K
Make model coil joints and test	20K
Assemble model coil into cryostat	50K
Miscellaneous Funds	18K
TOTAL SIMULATED SERVICE COIL	300K
Procure Four more Coil Conductor Segments	2000K
Long Lead Procure by Prime (Winding Tool)	2200K
Set-up and Wind Second Development Coil	500K
GRAND TOTAL	15,621K

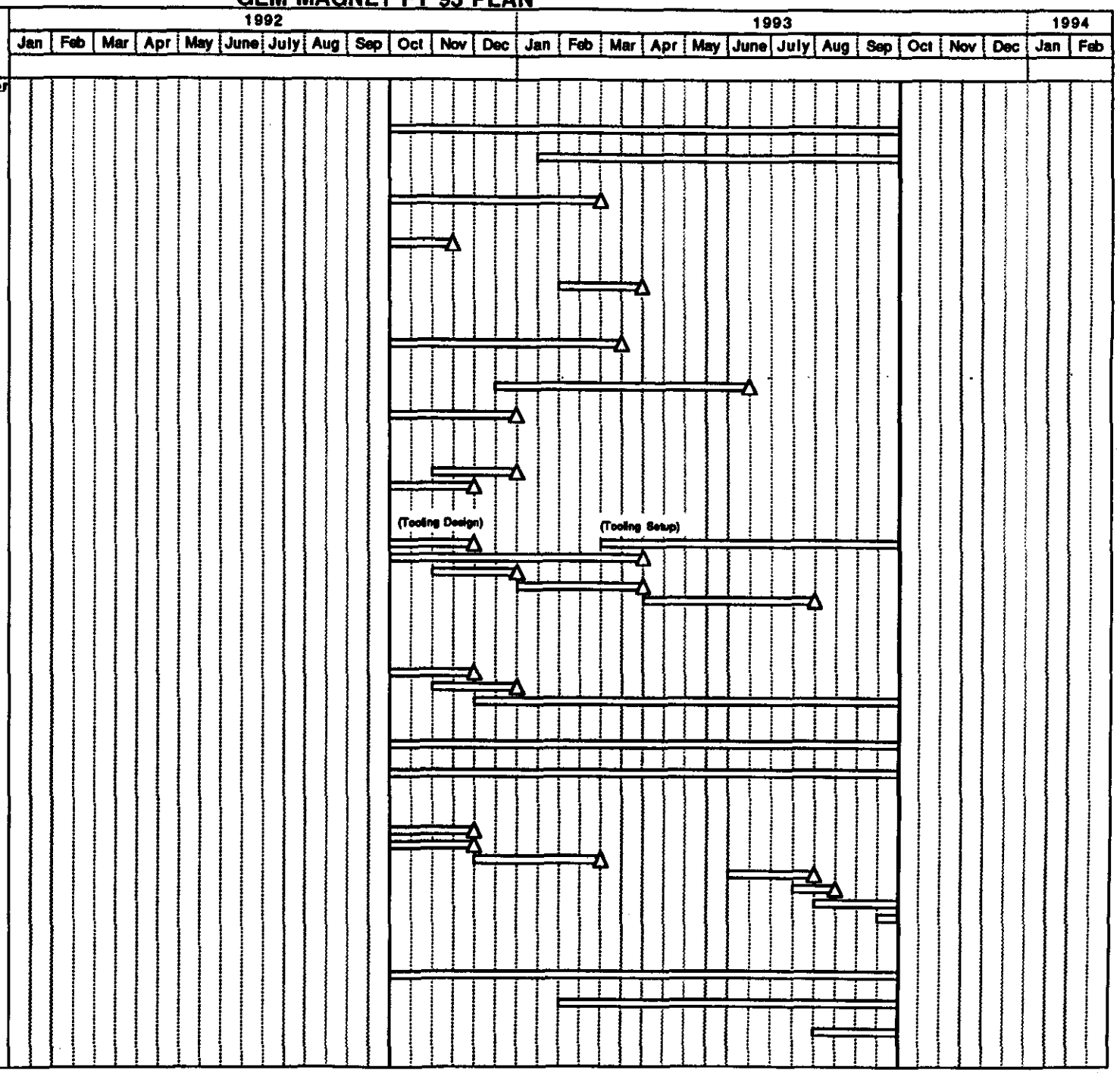

FY93 funding & out year funding will be reviewed/approved later.

Thursday, July 2, 1992

Fallback Plan

GEM MAGNET FY 93 PLAN

MAGNET DESIGN
R&D Procurement/Fabrication
(FY93 Program - SSC, MIT, LLL)

Description	M&S/Labor Dollars
- BASE PROGRAM -	
(Results in one year schedule slippage)	
Collaboration Design Effort	3000K
Prime Contractor Engineering	3000K
S.C. Wire (FY92 Program Cont.)	
Strand verification	10K
Cabling (FY92 Program Cont.)	
Cable 100m + 600m SC strand	54K
Conduit (FY92 Program Cont.)	
Encapsulate 100m + 600m SC cable (Encap. 600m)	140K
Al Sheath (FY92 Program Cont.)	
Fabricate 1150m Al Sheath	149K
Joints (FY92 Program Cont.)	
Fabricate SC joints	54K
Helium	41K
Evaluate alternative joints	10K
TOTAL JOINTS	105K
Winding & Tooling (FY92 Prog. Cont	
Conductor Assy/Spooling	67K
Tooling Design	46K
TOTAL WINDING & TOOLING	113K
MISCELLANEOUS FUNDS	20K
SUBTOTAL FY92 PROGRAM CONT.	600K
Winding and Tooling	
Devel winding tooling design/tooling setup site	46K
Fab development winding tooling	500K
Assemble cu cable in sheath	67K
Fabricate joint components	44K
Wind first development winding	320K
Make joint/issue winding & joint fab. specs.	73K
TOTAL WINDING AND TOOLING	1050K
Bobbin	
Spec develop winding coil bobbin	17K
Place order for develop wind coil bobbin	119K
Fabricate first bobbin	364K
TOTAL BOBBIN	500K
Conductor Procurement by SSCL (partial)	500K
PROGRAM	8650K

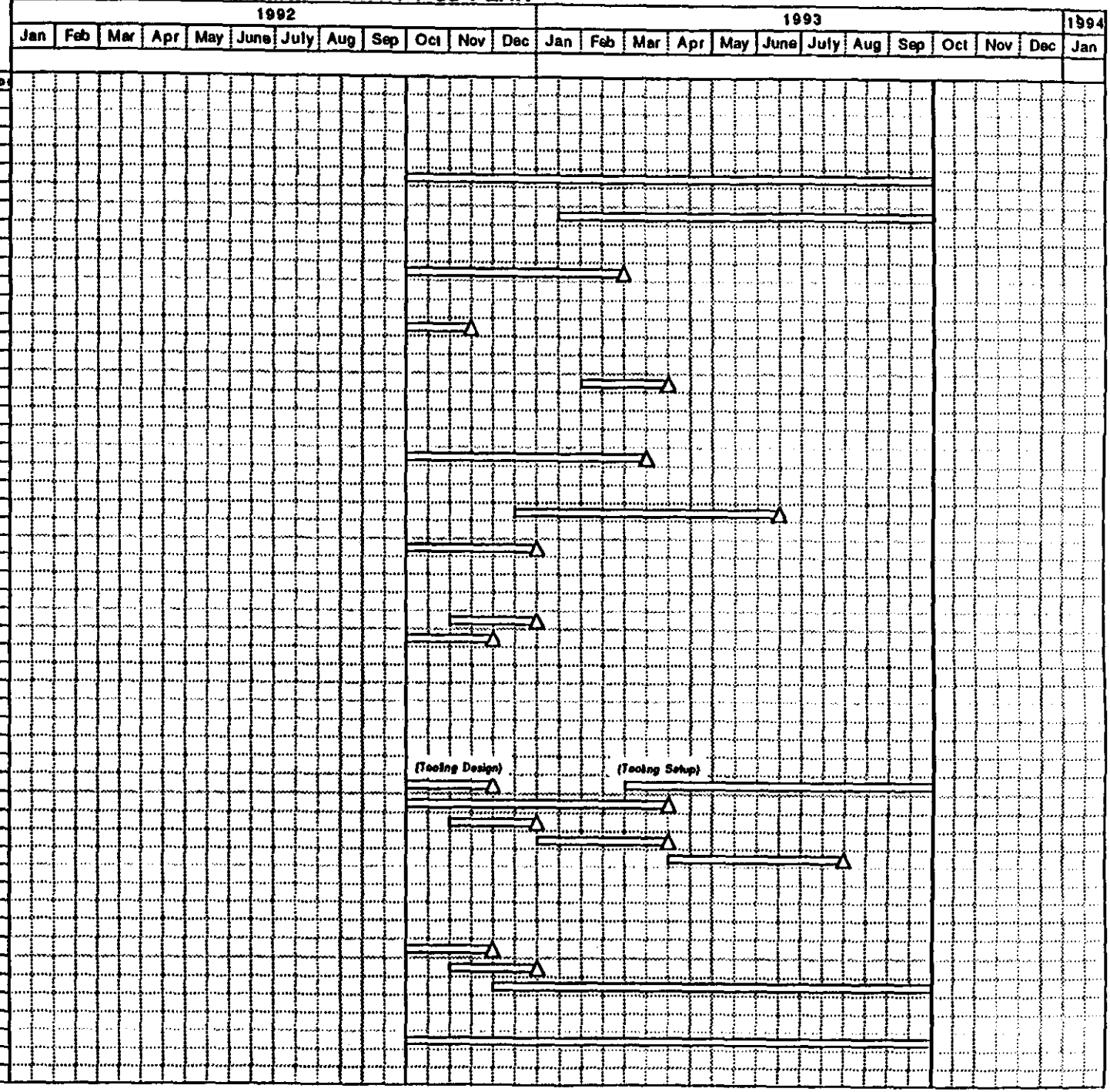

FY93 funding & out year funding will be reviewed/approved later.

Friday, June 26, 1992

3.3.2 Calorimetry

1 Q: The PAC ... is concerned about the problems of radiation damage and the lack of longitudinal segmentation of the BaF_2 calorimeter.

1.1 R&D Program To Produce Radiation Hard BaF_2 Crystals

An extensive R&D program to produce radiation hard Barium Fluoride crystals for GEM is underway. Substantial progress on the production of large crystals with improved radiation hardness, and on the determination of the key factors and the basic mechanism responsible for the radiation damage has been made since the last PAC Meeting. Large crystals approaching the GEM specifications, and small demonstration crystals meeting the specified rad hardness, are expected within the next two months, in time for the GEM choice of calorimeter technologies.

The R&D program on radiation damage is being carried out by the GEM Collaboration (Caltech, BNL and LLNL in the U.S.; SIC, BGRI and Tongji University in China), in coordination with expert research teams in the fields of materials characterization (Charles Evans & Associates and the Naval Research Lab: trace element and microstructural defect analysis), pure crystal growth and manufacture (Optovac and the LLNL group of Kway *et al.*), and the identification of the specific "color centers" responsible for the damage using paramagnetic and low temperature absorption spectroscopy (Univ. of West Virginia Optoelectronics Group).

The radiation damage research effort includes some key members of the BaF_2 Expert Panel, which was formed by the SSCL to review the radiation damage problem in BaF_2, and to assist with the design and execution of a further R&D program if the prospect of solving the problem was sufficiently promising. The Panel met in December, 1991 and again in January 1992 following a site visit to the Shanghai Institute of Ceramics (SIC) and Beijing Glass Research Institute (BGRI) by selected Panel members and the GEM Spokesmen. A summary of the Panel's conclusions and the R&D progress over the last six months is presented below.

1.1.1 Conclusion of BaF_2 Expert Panel

The principal conclusion of the Panel's February 1992 report is "there is no apparent fundamental reason why BaF_2 can not be made radiation hard" [1]. The Panel stated:

- While it is not possible at this time to guarantee that crystals of sufficient radiation hardness to meet the GEM specifications can be produced within the time frame allowed, the recent progress looks very promising.
- A coordinated, comprehensive plan of research should be (drawn up) to efficiently use all the talent that is available for solving the radiation damage problem... The Panel strongly encourages R&D work to develop the necessary technology to reach this goal.

The conclusion from BaF_2 panel is based upon existing data obtained by that time. Some highlights are summarized below:

- The BaF_2 radiation damage caused by photons shows clear saturation. Both transmittance and light output measured after irradiation do not degrade further after initial dosage of a few tens kRad to 100 kRad, depending on the quality of the BaF_2 crystals; (Figures 12 and 14 of [2])
- There is no permanent damage caused by either photons or neutrons. All damage recovers in full after an annealing at 500°C for three hours; (Figures 12 and 17 of [2])
- There is no spontaneous annealing of the radiation damage of BaF_2 under room temperature measured up to 68 days after irradiation; (Figures 15 and 16 of [2])
- The radiation damage of BaF_2 has no dose rate dependence; (Figure 17 of [2])
- There is evidence that the damage of BaF_2 is caused by formation of color centers, which cause self-absorption of the scintillation light as it is transmitted through the crystal. There is no apparent damage to the scintillation mechanism itself, so that the intrinsic scintillation light yield by the crystal is unaffected (Section 5.4 of [2]).

- Large size (20-25 cm long) BaF_2 crystals produced by SIC in December 1991 have considerably better radiation resistance than the crystals from previous batches. The transmittance of two 20 cm long crystals is ~50% at 220 nm after 1 MRad irradiation which corresponds to a light attenuation length of 35—40 cm. (Figures 18 and 19 of [2])

In addition to work already proceeding in the U.S. and China to test the radiation damage properties, and to produce improved crystals, the Panel recommended an additional program of R&D. Highlights include:

- Impurity and Defect Analysis:
  Correlate radiation effects with measurable impurities and/or microstructural properties of crystals.
- Surface Preparation:
  Develop and verify a preparation process that results in a polished surface free of impurities and subsurface imperfections that are associated with increased radiation damage.
- Radiation Damage Measurements:
  - Correlate the surface quality (mechanical damage, degradation due to water) with radiation-induced effects.
  - Measure the relative radiation-induced effects due to photons, neutrons, and charged hadrons.
  - More extensive simulations and lab tests to study the effects of changes in the uniformity of response over time, and its effects on the resolution. Determination of the requirements for uniformity to be maintained over time.

Based on systematic studies of the energy resolution of a precision EMC, specifications have been set for the dimensional tolerances, and for the UV transmittance before and after irradiation of a 50 cm long crystal pair. The radiation resistance requirement is that the attenuation length for the fast component (at 220 nm) must be ~100 cm, after the crystal has been irradiated to saturation. (See Section 7 of [2] for details.)

The Expert Panel will meet again in August, to assess the status and progress of the BaF_2 radiation damage study, shortly before the GEM calorimetry decision.

1.1.2 Progress in 1992

The 1992 BaF_2 R&D program program closely follows the guidelines set by the BaF_2 Expert Panel, and is focused on meeting the requirements set by the GEM Executive Committee in February 1992 following its review of the BaF_2 Expert Panel Report [3]. The requirements, aimed at demonstrating the BaF_2 calorimeter's ability to maintain its stability and thus its high resolution *in situ*, are:

- Demonstration of substantial improvement in 20—25 cm long BaF_2 crystals, with an light attenuation length $\lambda > 60$ cm after 1 MRad;
- Production of small rad-hard crystals with $\lambda > 95$ cm after 1 MRad, meeting the GEM final specifications.

Since January 1992 a great deal has been learned about BaF_2 radiation damage properties, the underlying mechanism leading to light absorption in the UV, and the influence of impurities and microstructural defects on the radiation damage. Some of the main results are summarized below.

- Trace element and microstructural analysis at Charles Evans and Associates shows clearly the difference between crystals produced in December 1991 and that from previous batches [4]. It was discovered that
  - new crystals have Sr and rare earth concentrations which are much lower, by one to two orders of magnitude;
  - impurities are concentrated in microscopic inclusions; and
  - new crystals show different properties:
    - large regions with no inclusions;
    - fewer total inclusions;
    - inclusions are clustered together, and lie along crystal planes
- Oxygen, fast cooling and their correlation with damage at SIC and BGRI:

- Crystals produced under poor vacuum have poor radiation resistance [5];
- Improper annealing (fast cool down) leads to decreased radiation hardness [6];
- Crystals with more O_2 show larger structural changes under the microscopy [6].

- Studies of the radiation damage mechanism, especially the key roles of O and H, have been carried out by Tongji University in China and the West Va. University in US:
  - OH^- doped crystals, produced by annealing the crystal in humid air at high temperature, show absorption bands both in the UV and in the infrared, at wavelengths which precisely match those computed for interstitial H and substitutional O^- [7];
  - electron paramagnetic resonance (EPR) spectra obtained with OH^- doped crystals show clearly identified O^- and Hydrogen atom signals, which are correlated with the UV absorption bands. The same paramagnetic signals seen in small OH^- doped samples are seen in larger undoped crystal samples [8]. These measurements establish the key role of oxygen and hydrogen, in combination with preexisting color centers due to other trace impurities (such as rare earths) in the crystals. They also confirm that much of the production mechanism for the UV-absorbing color centers is now understood.

- There is no spontaneous annealing of the BaF_2 radiation damage at room temperature measured up to 210 days after irradiation. (See Figure 1)

- A 25 cm long BaF_2 crystals produced by SIC shows that the light output is reduced to around 40% (due to self-absorption of the scintillation light) after Co^{60} doses up to 1 MRad. The crystal was produced recently at SIC with improved processing techniques, aimed at reduction of oxygen and water. Saturation of the radiation is observed at a dose of around 20—50 kRad. (See Figure 2)

- A small BaF_2 crystal (1" diameter $\times$ 1" long) from SIC was irradiatied by neutrons obtained by proton-induced stripping from a Be target at the University of Lowell Van de Graaff facility. The fluence at typical points in the crystal varied from 5 to 8 $\times 10^{13}$ n/cm^2. The neutron energy spectrum was roughly flat from 0 to 2.2 MeV, with little background of thermal neutrons (0.1% of the flux) and

a low associated dose of photons (estimated between 1 and 2 kRad). The absorbence of this crystal as a function of wavelength was measured at BNL by Woody *et al.*. The result, shown in Figure 3, indicates that the high fluence of MeV neutrons had little effect. Curves 1 and 2 of Fig. 3 show the results before and after the neutron irradiation. In order to separate out the effects of the associated photon dose, the crystal was annealed at 500°C after neutron dase, and was then reirradiated with 1 kRad of Co^{60} γ's (curves 3 an 4). As seen in the figure, the absorbence from the run at the Van de Graaff can be explained (within dosimetry errors) by the photon dose alone. It is also noteworthy that the radiation damage is fully annealable.

- A study of the effects of irradiations by hadrons was started at BNL during the last half of June. Large crystals from Optovac (25 cm), an older 25 cm crystal from SIC (Part of the 1991 Fermilab test matrix) and a 20 cm SIC crystal produced at the end of 1991 are being irradiated by placing the crystals near one of the primary production targets at the AGS. The crystals have so far received a dose of only a few tens of kRad, as measured by TLD's placed inside the target cave along with the crystals. Preliminary results from transmission scans taken at a few intermediate doses indicate that the radiation - induced effects for hadrons may be substantially less than for photons in BaF_2. We emphasize these results are at present preliminary, and not yet fully understood. However, we note that similar effects have been observed in BGO and GSO(Ce) by by Kobayashi *et al.*. Further measurements at higher doses, to be followed by annealing, and then further irradiation with photons, are now being carried out at BNL.

  Another important result of this measurement is that the activation of BaF_2 by hadron irradiation is low. Following the irradiation dose of 13.4 kRads, the induced radioactivity was measured to be 0.8 milliRem/hr on contact.

All these results will be systematically presented to the BaF_2 Expert Panel at the SSCL in the next panel meeting. A new batch of large BaF_2 crystals is currently being prepared in China. Based on the knowledge accumulated, these new crystals may demonstrate considerable progress, as compared with crystals produced in December 1991.

Following the BaF_2 panel's suggestions, small size crystals are being produced at LLNL by a group with extensive experience in the production of pure fluoride crystals

[10]. These crystals are supposed to be as pure as possible, using pure raw materials and technological refinements which inlude: pretreatments with reactive gas, the use of crucibles made by non-reactive "noble" metals instead of carbon, and zone refining to increase the crystals' purity. Tests of these small crystals as well as of new radiation hard crystals from China are scheduled in July and August, directly following the production, and the refined cutting and polishing procedures developed at LLNL.

1.2 Longitudinal Segmentation

The longitudinal segmentation of a precision EMC is useful, provided the segmentation does not cause degradation of energy resolution of the calorimeter. The potential improvements in detector performance are as follows:

- measurement of the photon direction without using the information from the central tracker;
- improve π/e rejection by providing longitudinal information on the shower development; and
- improve the energy resolution, especially at high energies when rear shower leakage is an issue.

The GEM BaF_2 total absorption crystal calorimeter design has no longitudinal segmentation. This is a compromise made in detector design between performance and cost. Should sufficient financial resources become available for additional photodevices and preamplifiers, the crystal-pair can be read out at both the front end and the rear end. This scheme would provide longitudinal segmentation without degrading the energy resolution.

Simulation studies also show that a thin position detector installed at a depth of $5X_0$, and containing up to 0.1 radiation length of inactive material, would not degrade the energy resolution of BaF_2 [11]. This configuration would provide a photon direction measurement with a precision of 7 mrad and an additional ability to veto high momentum π_0's from jets. This would indeed be a proper design in an LHC-like environment.

At luminosities of $\mathcal{L} = 10^{33}$ cm^{-2} s^{-1}, however, there are alternative methods which can do as well or even better without longitudinal segmentation. As a matter

of fact, all GEM physics simulations for the LoI, and the recent physics report to the PAC, do not use longitudinal segmentation. Here, we briefly discuss the three issues related to longitudinal segmentation.

- Photon direction:

  For H$\rightarrow \gamma\gamma$ physics, a precision measurement of the photon vectors is crucial. This can be achieved with a longitudinally segmented EMC, having a typical 6—10 mrad resolution. An alternative is to determine the the primary Higgs vertex by using the difference in event topology between high p_T Higgs event and low p_T minimum bias events. GEM's specification of vertex z resolution is about 1 mm which is much better than is needed to maintain the high energy resolutions proposed by GEM. The probability of finding a correct primary Higgs vertex with overlapping minimum bias events was calculated to be 95% and 85% respectively for minimum bias events generated by using ISAJET or PYTHIA. This probability also is not sensitive to the track reconstruction efficiency, provided it is better than 80%. (See section 3.6 of [9].) This alternative, however, does not work at the LHC.

- π/e rejection:

  Although the longitudinal information can help improve the π/e separation, an alternative is to use lateral shower information. For a precision EMC with fine granularity, the lateral shower shape is a powerful tool which can be used in electron identification. Study shows that π/e rejection at the level of 10^{-4} can be achieved by using only lateral shower development and a matching hadron calorimeter veto [12].

- Shower leakage:

  A detailed GEANT simulation was carried out to estimate the effect of shower leakage and non-active material for the BaF_2 design [2]. The result of the simulation is shown in Table 1.

  It is clear that up to 500 GeV there is no significant leakage would degrade the energy resolution, and thus the H$\rightarrow \gamma\gamma$ physics is not compromised. At higher energies, energy leaked into hadron calorimeter may be measured, to improve the overall resolution.

Table 1: Energy Resolution (%) of BaF_2 Calorimeter

E (GeV)	5	10	20	50	100	200	500
Electrical Noise	0.4	0.2	0.1	0.04	0.02	0.01	0.004
Photoelectrons	0.2	0.14	0.1	0.063	0.045	0.03	0.02
GEANT	0.60	0.43	0.32	0.30	0.30	0.30	0.36
Intercalibration	0.40	0.40	0.40	0.40	0.40	0.40	0.40
Total	0.85	0.63	0.53	0.51	0.50	0.50	0.54

References

[1] S. Majewski, BaF_2 Expert Panel Report, Febryary 1992.

[2] R.Y. Zhu, GEM Internal note **GEM TN-92-48 Rev A.**, January 1992.

[3] Y. Kamyshkov, GEM Internal note **GEM TN-92-85**, March 1992.

[4] M. Struthman, Report on material characterization of BaF_2 samples, June 1992.

[5] G. Chen *et al.*, GEM Internal note **GEM TN-92-78**, March 1992.

[6] P.J. Li *et al.*, GEM Internal note **GEM TN-92-77**, March 1992;
Z.W. Yin, Talk given in First East Asia/Pacific – US Symposium on SSC, May 1992.

[7] L.M. Wang *et al.*, *The Optical and Radiation Damage Properties of Barium Fluoride Crystals*, talk presented in Shanghai BaF_2 Workshop, Shanghai, May 1991.
L.Y. Chen *et al.*, *The Radiation Damage of BaF_2 Crystals*, talk prepared for GEM BaF_2 Panel meeting, Shanghai, December 1991.

[8] L. Halliburtoon *et al.*, Identification and Chracterization of Radiation-Induced Point Defects in BaF_2, University of West Virginia Optoelectronics Group Technical Reports, April - June 1992.

[9] R.Y. Zhu and H. Yamamoto, GEM Internal note **GEM TN-92-126**, July 1992.

[10] C. Wuest, GEM Internal note **GEM TN-92-94**, May 1992.

[11] R.Y. Zhu, *Physics Requirements to the Precision of Electromagnetic Calorimeter at SSC*, GEM TN-91-06, August 1991.

[12] R.Y. Zhu, Proceedings of ECFA LHC Workshop, Aachen, October 1990, Volume III p. 411.

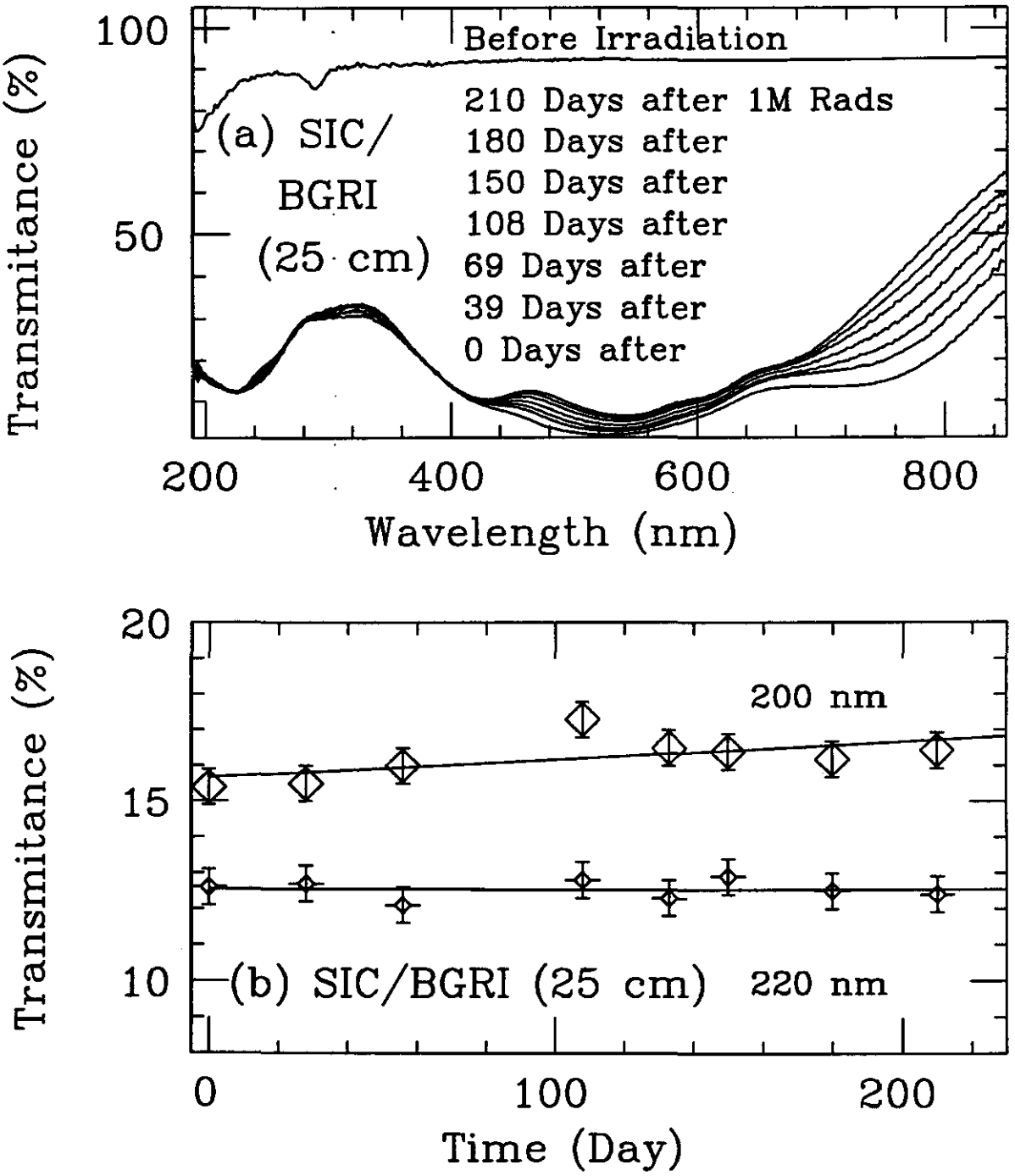

Figure 1: Transmittance recovery of radiation damage measured under room temperature for a 25 cm long BaF_2 crystal produced at SIC in early 1991.

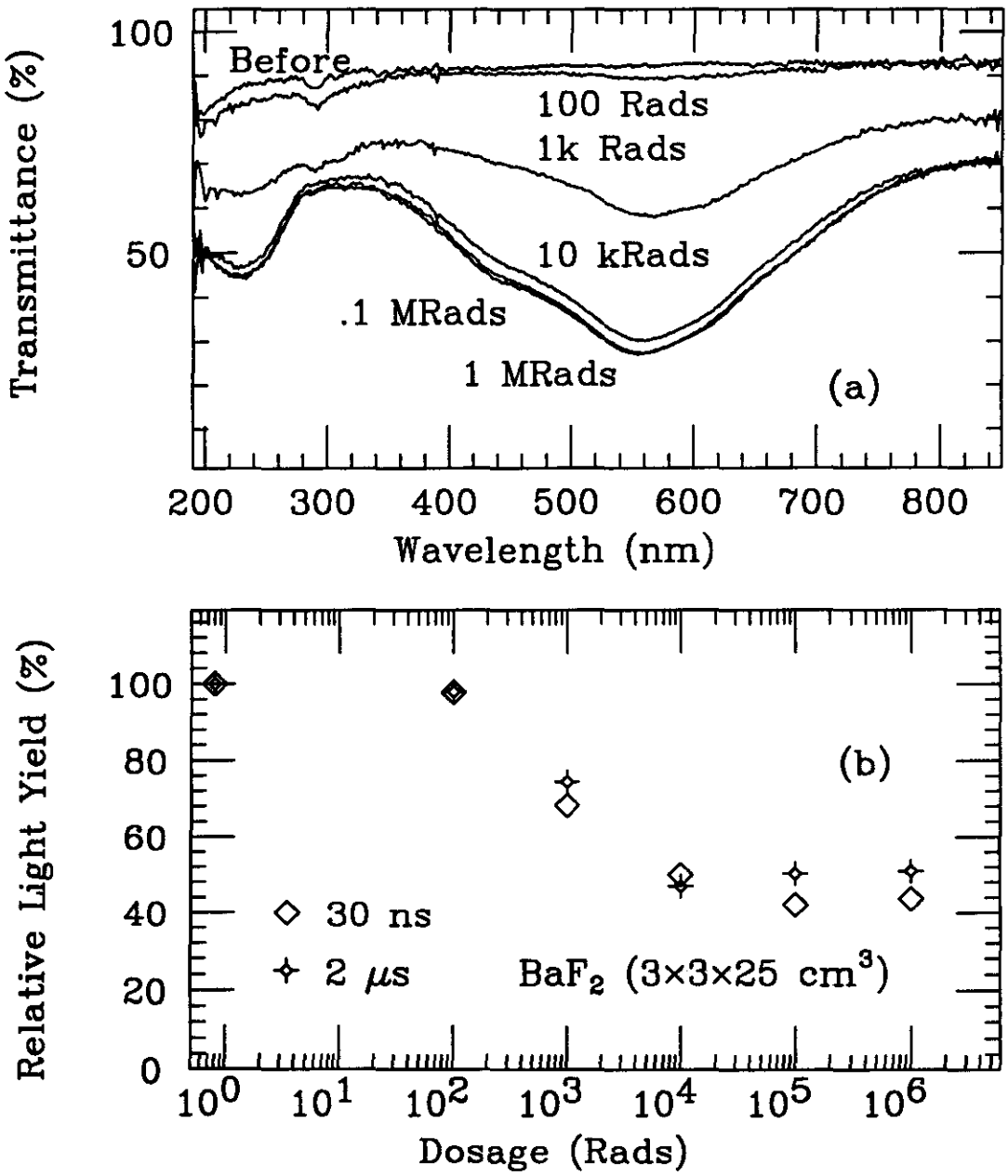

Figure 2: (a) Transmittance and (b) light output measured for a 25 cm long BaF_2 crystal produced recently at SIC.

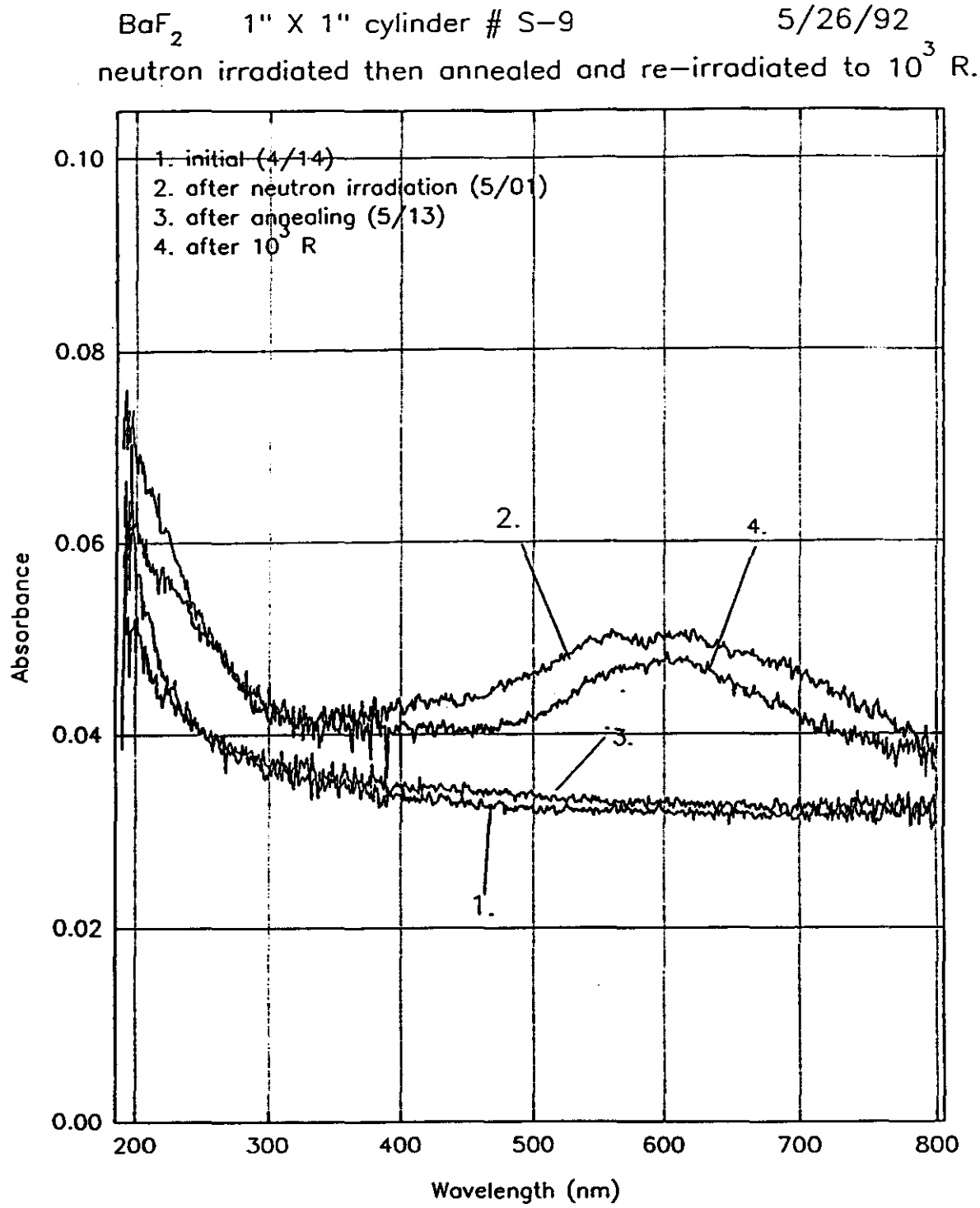

Figure 3: Absorbence of a 1"×1" SIC crystal: (1) before neutron irradiation; (2) after neutron irradiation; (3) after subsequent high temperature annealing; and (4) after re-irradiation with 1 kRad of $Co^{60}\gamma$'s.

3.3.2 Calorimetry

Question #2 : The PAC is concerned ... about the potential inhomogeneity and the difficulty of longitudinal segmentation in the lead/scintillating fiber calorimeter. Also, the effect on the constant term of the hadronic energy resolution, when employing very different compositions for the electromagnetic and hadronic parts, needs to be quantified.

Answer #2a : (Inhomogeneity) Talking about signal non-uniformity (inhomogeneities), one should distinguish between two types: a) Geometrical effects, e.g. the position dependence of the light collection efficiency in BGO or BaF2 crystals. b) Random effects.

In a fiber calorimeter, the latter may occur when a certain batch of fibers has optical characteristics significantly different from the rest. These effects are the most worrysome. Edge effects are repetitive and can usually be easily corrected for, random effects tend to go unnoticed.

The SPACAL Collaboration at CERN has spent a lot of effort in trying to understand and eliminate signal nonuniformities in fiber calorimeters. Most of the studies were done with electrons, whose signals are much more sensitive to inhomogeneities than for pions. It was demonstrated experimentally that, in a detector with cylindrical geometry, edge effects could be completely eliminated by properly mixing the light from the fibers from one cell. The shape and the dimensions of the light guide are of crucial importance for this purpose (Figure 2a-1 from NIM A294 (1990) 193). Tests of the big SPACAL detector with high-energy electron beams showed excellent signal uniformity in the boundary regions between cells. On the other hand, the same tests showed a random effect due to a bad fiber batch, which lowered the electron response locally by about 8% (Fig. 2a-2 from NIM A308 (1991) 481). The effect of this local nonuniformity on the signals from 80 GeV pions was found to be about 3%.

For the production of GEM fiber calorimeter modules we plan to employ the automatized quality acceptance procedure for every fiber to avoid random effects.

The RD1 Collaboration has constructed up to now two hadronic prototype detectors, both projective and modular. The first detector, which was tested last year, showed rather large edge effects. Electrons detected in the boundary regions between modules gave signals up to 20% smaller than electrons hitting the center of a module. Similar effects were observed for pions, albeit that the amplitude of the dip was clearly smaller than for electrons. The effect was also dependent on the pion energy, it was more pronounced at higher energies, where a larger fraction of the shower energy goes into the narrow e.m. core. At 80 GeV, it was about 12%, at 20 GeV 8%. However, these edge effects were very repetitive and could be easily corrected for. A grid scan with 80 GeV electrons covering a large area of the detector's front face gave a distribution of the mean values of the signals with a sigma(RMS) of 2.9%. By applying a simple algorithm accounting for the edge effects, this width was reduced to 0.8%.

At least part of the edge effects observed by RD1 was due to the construction of the modules. Since the fibers that start at a certain depth inside the calorimeter have to be cut perpendicular to their axis and cannot stick out of the module, a local depletion of sensitive material occurs in the boundary region, which causes a local decrease in the shower sampling fraction. In the new detector recently built by RD1 this problem has been eliminated by means of a "staircase" structure. This detector was tested for the first time only a few days ago. It is still too early to quote results, which require a careful offline analysis to be meaningful. When one takes the on-line data at face value, there is no sign of any edge effects. However, it should be realized that the particles are hitting the detector at a small angle with respect to the fiber axis. Therefore, the longitudinal fluctuations in the starting point of the pion showers translate into a lateral smearing on a scale of a few centimeters, which completely washes out any edge effects. This smearing has to be unfolded off-line.

Answer #2b : (Lack of longitudinal segmentation)

Longitudinal segmentation should be important to tag the late developing

hadronic showers and radiatively showering muons which bring debris into muon system. In GEM baseline design of Cu-scintillating fiber hadron calorimeter we have the last two lambda of scint. fiber modules equipped with additional separate fiber readout (with sampling fraction 0.3 - 0.5%).

The longitudinal segmentation of the hadron calorimeter might appear to be useful also for the detection of e-m showers, pion/e rejection, corrections for muon radiative losses and corrections for radiation damage. These issues are considered below.

a) Detection of e-m showers : For high energy electrons, for example from heavy Z' decaying into e+e-, significant fraction (up to few percent) of e-m energy can escape from the back of e-m calorimeter which is 25 X0 deep and result in the loss of the precision of the Z' mass reconstruction (for some fraction of events). Figure 2b-1 shows 1 TeV isolated electron energy deposit in 24.5 X0 e-m calorimeter and energy distribution corrected for leakages measured in scintillating fiber hadron calorimeter without longitudinal segmentation as simulated in GEANT 3.15 code. E-m energy resolution in the hadronic section is assumed to be 40%/sqrt(E). Thickness of dead material between e-m and hadronic section of 2.82 X0 simulates either the cryostat walls of the LKr e-m calorimeter or readout system of BaF2 crystal calorimeter together with structural materials of scint. fiber calorimeter support.

b) Pion/e rejection. Pion/e rejection at 100 GeV for 25 X0 e-m calorimeter followed by hadronic scintillating fiber calorimeter having no longitudinal segmentation is shown in Figure 2b-2 as simulated in GEANT code. Pion rejection up to factor 1000 can be reached for 96% of electron efficiency. This pion suppression can be used in the trigger for isolated electrons.

c) Muon radiative energy losses in hadron calorimeter. Radiative energy losses of muons are originated uniformly along the muon path in the hadron calorimeter. The finite light absorbtion length in the fibers (typically 3-5 m) can contribute into accuracy of muon radiative energy losses measurements in the hadron calorimeter. Results of GEANT simulation of the 500 GeV muons passing through scint. fiber

hadron calorimeter are shown in Figure 2b-3. Error to the overall muon momentum measurement due to correction for radiative losses measured in scint. fiber hadron calorimeter is 0.5%.

d) Radiation damage Since the radiation dose in the hadron calorimeter has strong radial dependance, longitudinal nonuniformity produced by accumulated dose will be integrated into scintillating fiber calorimeter responce. Relative calculated response of fibers vs calorimeter depth is shown in Figure 2b-4 for undamage fibers and for fibers accumulated the dose equivalent to 2 and 5 years of SSC operation at luminosity 10**34. [Fiber radiation damage effects vs dose are parametrized according to data from measurements of A.Maio et al, CERN 90-10, ECFA 90-133 vol 3, Dec 3, 1990]. In these simulations 25 X0 BaF2 e-m calorimeter was assumed in front of scintillating fiber calorimeter at eta=3. Jet resolution for undamaged and damaged calorimeter at eta=3 is shown in Figure 2b-5. After two years of SSC operation at luminosity 10**34 the jet resolution will not deteriorate significantly. We plan to exchange fibers in GEM hadron calorimeter for eta region between 2.5-3.0 after integrated luminosity of 2x10**41.

Answer #2c : (Constant term in energy resolution)

For the combined calorimeter system where e-m calorimeter is non-compensating material with e/h in the range 1.4-1.7 the resolution of jet energy reconstraction might expected to be affected. We have addressed this question in GEM LoI where it was shown by MC simulations that for given e/h in the e-m section the best hadronic jet resolution can be obtained with compensated hadronic section. GEM baseline Cu - scintillating fiber hadron calorimeter with 3% fiber volume fraction is expected to be compensated, so that the overall jet resolution of 50%/sqrt(E) + 2% can be achieved.

In GEM note GEM TN-92-67 the combined calorimeter system consisting of BaF2 e-m section (where e/h=2.0 was assumed) followed by scintillating fiber section with e/h=1 was studied. The weighting algorithm was developed which takes account of the event-to-event fluctuations in the energy deposits in the two

calorimeter sections. If the hadronic calorimeter is compensating, all input data required for the method can be measured in beamtests of prototype calorimeter modules, using single electron and pion beam, and multiparticle beam (obtained from a target in a single pion beam). If the hadron calorimeter is noncompensating, additional knowledge is required regarding the jet fragmentation function and the electromagnetic energy fraction in hadronic shower development at SSC energies.

In figure 2c-1 the single pion and jet resolution vs energy are shown. Uncorrected jet resolution corresponding to non-compensated calorimeter is shown to be above 10% in the whole energy range. Using weighting correction procedure jet resolution improves down to the constant term of below 2%.

RESULTS OF PROTOTYPE STUDIES FOR A SPAGHETTI CALORIMETER

D. ACOSTA [1], S. BUONTEMPO [2], L. CALÔBA [3], M. CARIA [4], R. DESALVO [5], A. EREDITATO [2], R. FERRARI [6], M. FRATERNALI [7], G. FUMAGALLI [6], O. GILDEMEISTER [5], F.G. HARTJES [8], TH.H. HENKES [9], A. HENRIQUES [5,10], L. LINSSEN [5], M. LIVAN [4], A. MAIO [10], L. MAPELLI [5], K.H. MEIER [5], B. ONG [1], H.P. PAAR [1], F. PASTORE [6], M. PEREIRA [10], L. POGGIOLI [11], C.V. SCHEEL [5,8], J.M. SEIXAS [3], A. SIMON [12], M. SIVERTZ [1], P. SONDEREGGER [5], M.N. SOUZA [3], Z.D. THOMÉ [3], V. VERCESI [5] and R. WIGMANS [5,8]

[1] *University of California, San Diego, USA*
[2] *Università di Napoli and INFN Sezione di Napoli, Italy*
[3] *COPPE/EE/UFRJ, Rio de Janeiro, Brazil*
[4] *Università di Cagliari and INFN Sezione di Cagliari, Italy*
[5] *CERN, Geneva, Switzerland*
[6] *Università di Pavia and INFN Sezione di Pavia, Italy*
[7] *Università di Palermo and INFN Sezione di Pavia, Italy*
[8] *NIKHEF-H, Amsterdam, The Netherlands*
[9] *Max Planck Institut, Heidelberg, FRG*
[10] *LIP, Lisbon, Portugal*
[11] *LPNHE, Université Paris VI, Paris, France*
[12] *Universität Heidelberg, Heidelberg, FRG*

Received 12 February 1990

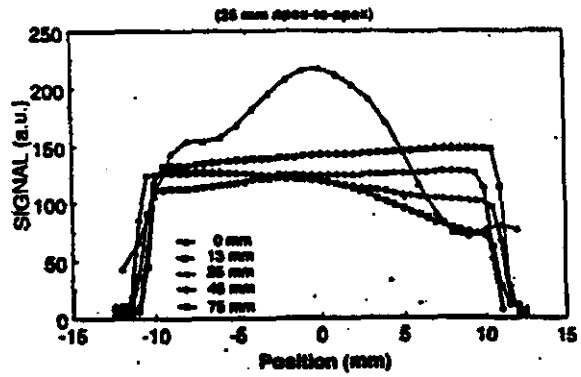

Fig. 7. Response to a fibre scanning the surface of a hexagonal light guide/PM combination, for various lengths of the light guide.

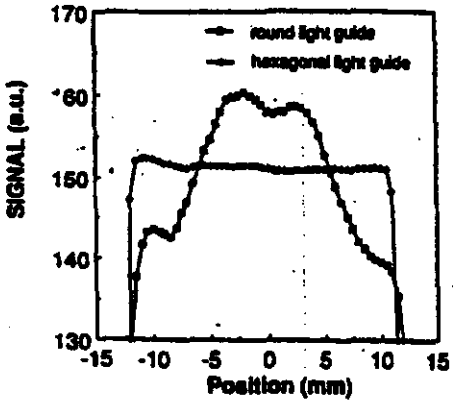

Fig. 6. Response to a fibre scanning the surface of a light guide/PM combination. Results for circular and hexagonal cylindrical light guides with the same length, using the same PM. Note the blown-up vertical scale.

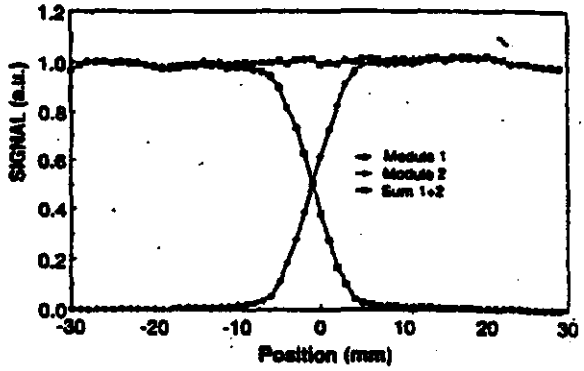

Fig. 8. Calorimeter response to a collimated β-source scanning the boundary between two SPACAL modules.

Fig 2a-1

Electron, pion and multiparticle detection with a lead/scintillating-fiber calorimeter

D. Acosta [a], S. Buontempo [b], L. Calôba [c], M. Caria [d], R. DeSalvo [f], A. Ereditato [b], R. Ferrari [h], G. Fumagalli [h], G. Goggi [e,h], W. Hao [g,l], F.G. Hartjes [i], A. Henriques [e,j], P. Jenni [e], L. Linssen [f], M. Livan [d], A. Maio [j], L. Mapelli [e], M.R. Mondardini [k], B. Ong [a], H.P. Paar [a], F. Pastore [h], L. Poggioli [l], G. Polesello [e,h], F. Riccardi [b], A. Rimoldi [h], C.V. Scheel [f,l], J. Schmitz [i], J.M. Seixas [c,e], A. Simon [m], M. Sivertz [a], P. Sonderegger [e], M.N. Souza [c], Z.D. Thomé [c], V. Vercesi [h], Y. Wang [g,l], R. Wigmans [e,j], C. Xu [g,l] and K. You [g,l]

[a] *University of California, San Diego, USA*
[b] *Università di Napoli and INFN Sez. Napoli, Italy*
[c] *COPPE/EE/UFRJ, Rio de Janeiro, Brazil*
[d] *Università di Cagliari and INFN Sez. Cagliari, Italy*
[e] *CERN, Geneva, Switzerland*
[f] *CERN/LAA project, Geneva, Switzerland*
[g] *CERN (Worldlab fellow), Geneva, Switzerland*
[h] *Università di Pavia and INFN Sez. Pavia, Italy*
[i] *NIKHEF-H, Amsterdam, The Netherlands*
[j] *LIP, Lisbon, Portugal*
[k] *Cornell University, Ithaca, USA*
[l] *LPNHE, Université Paris VI & VII, Paris, France*
[m] *Universität Heidelberg, Heidelberg, Germany*

Received 22 May 1991

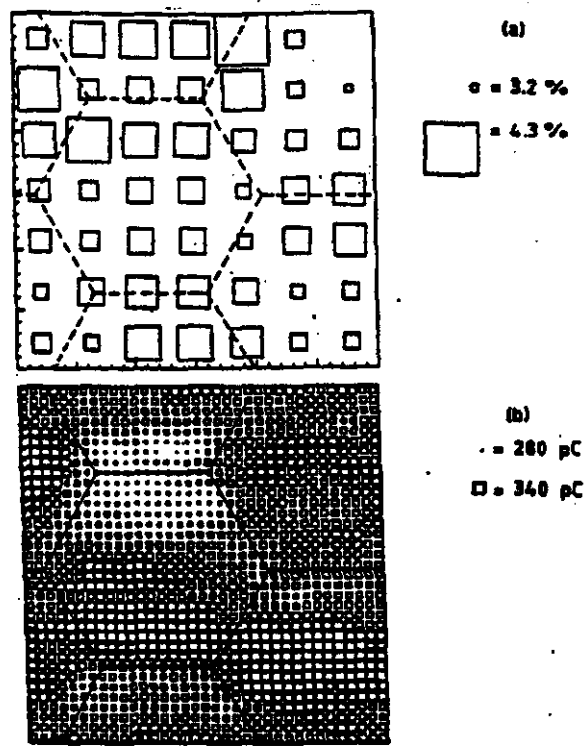

Fig. 8. The energy resolution (a) and the average signal (b) for 80 GeV electrons entering the central region of the calorimeter at a large number of impact points. The size of the squares indicates the numerical value (not proportional!).

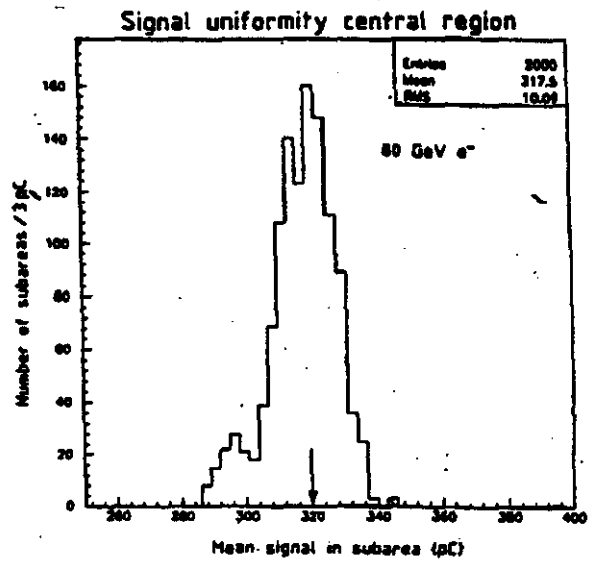

Fig. 10. Distribution of the calorimeter response to 40 GeV electrons measured over an area of 144 cm^2 in the form of a grid scan. Each entry in the histogram corresponds to the average response in a subarea of $\sim 3\times3$ mm^2. The electron response measured in the center of the calorimeter is indicated by an arrow.

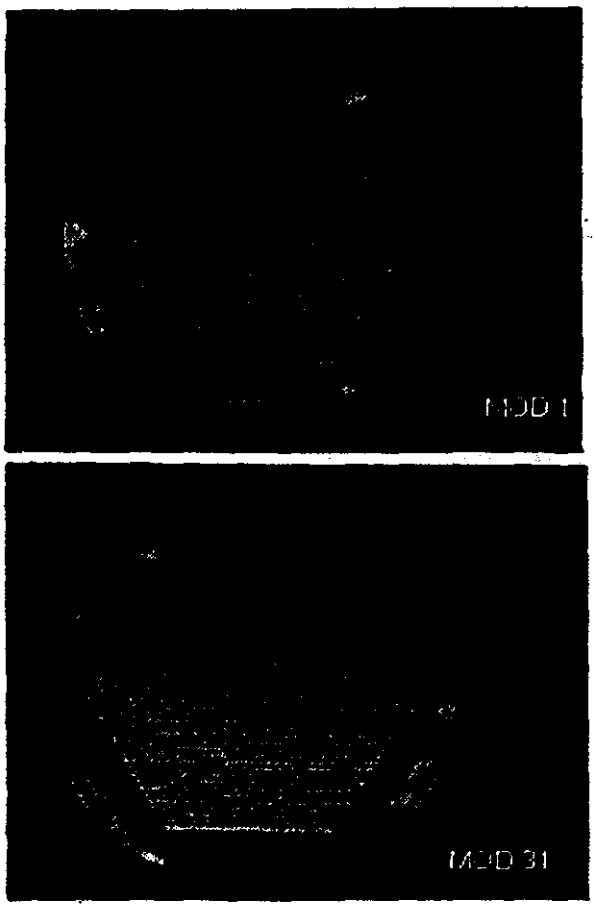

Fig. 9. Results of light transmission measurements with a CCD camera. Shown are the bunches of fibers from 4 individual towers. There are 1141 fibers in each bunch. The upper left picture shows the central tower of the detector, the others were chosen at random.

Fig 2a-2

24.5 X0 E−M calorimeter

2.8 X0 dead material between E−M and Hadronic section

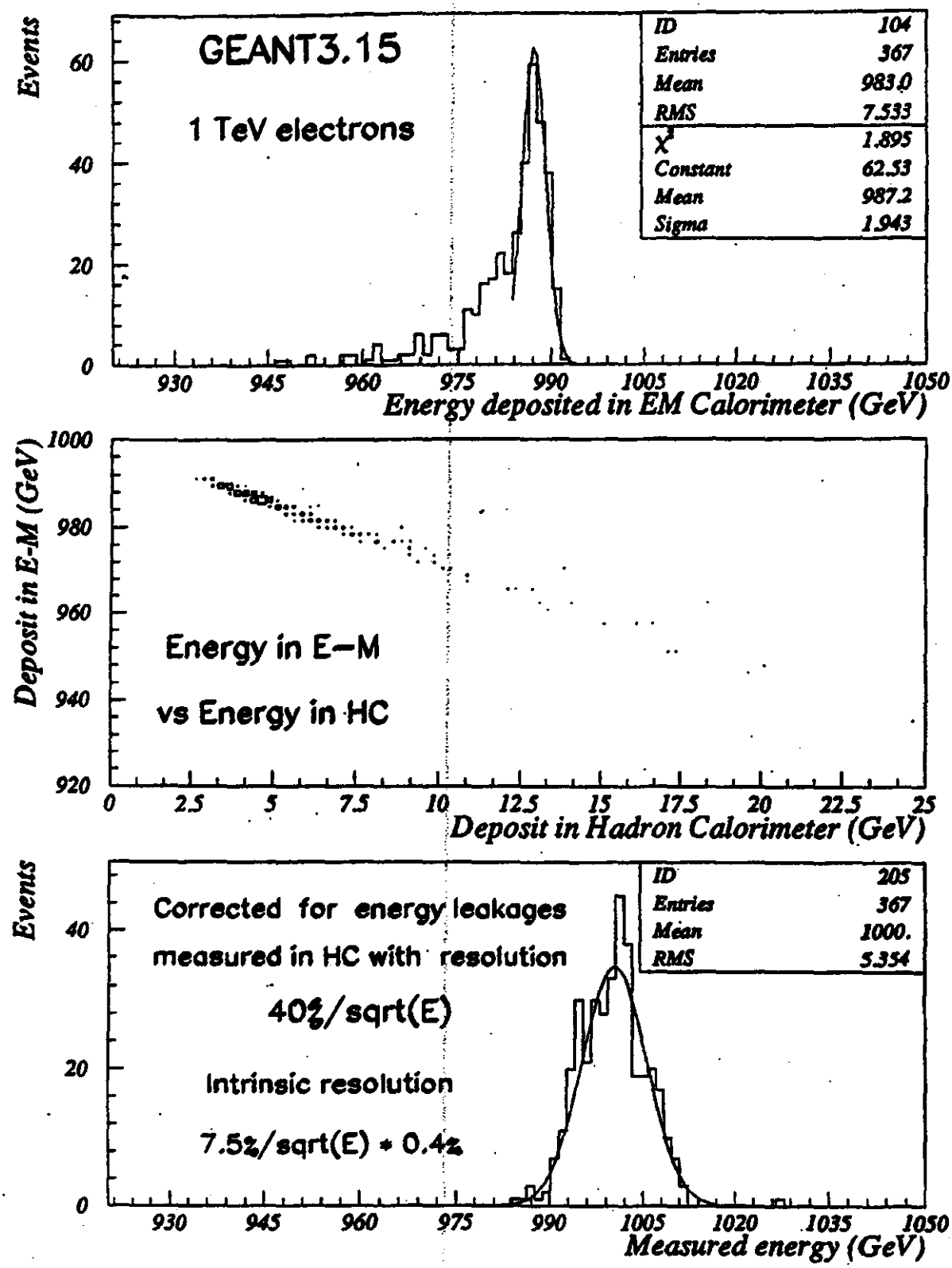

Fig 2b-1

Pion rejection factor

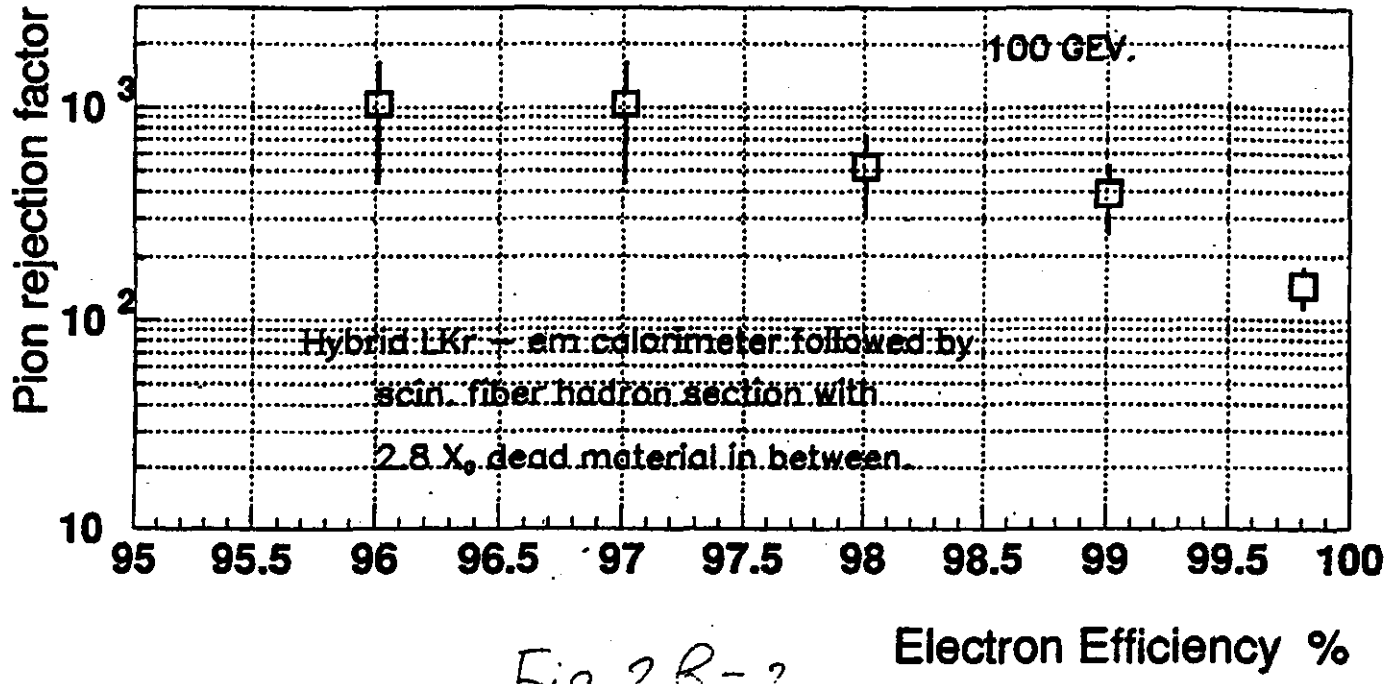

Fig 2B-2

500 GEV μ

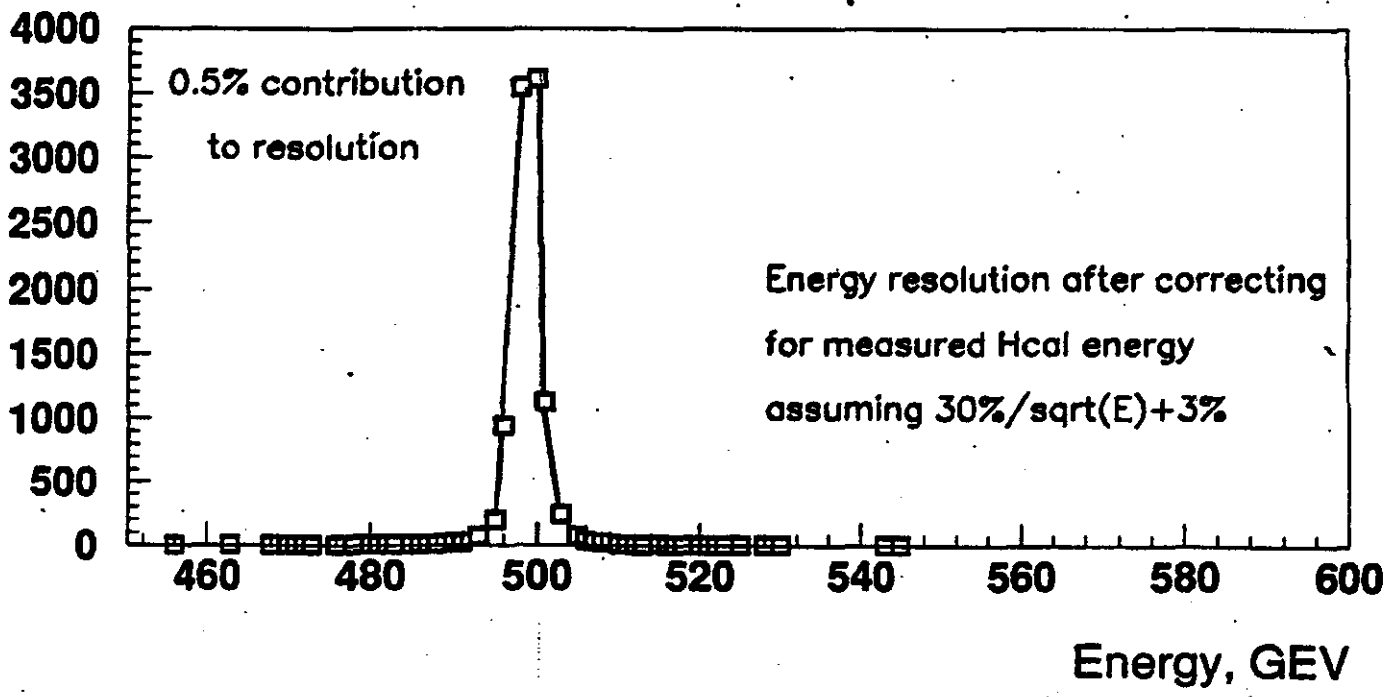

Fig 2b-3

Spagetti calorimeter

Nonuniformity of response

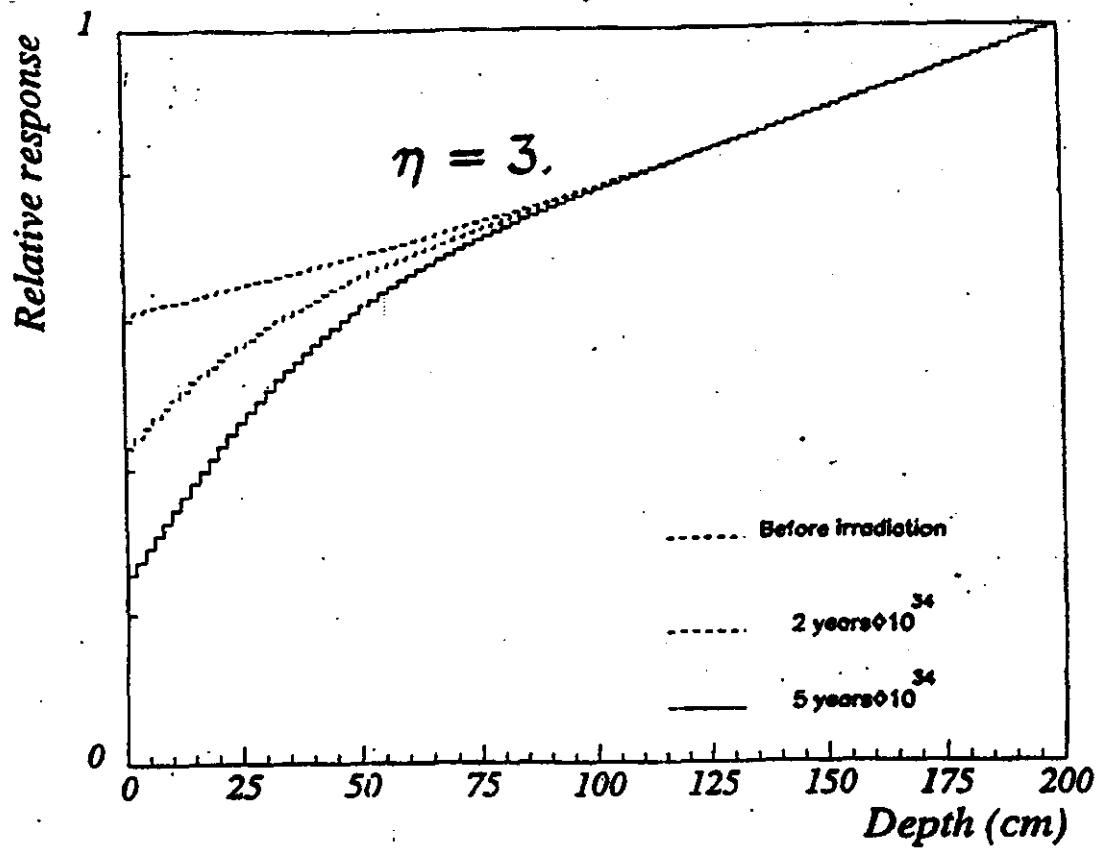

Fig 2b-4

JET RESOLUTION - GEANT3

BaF_2 + Spagetti HC

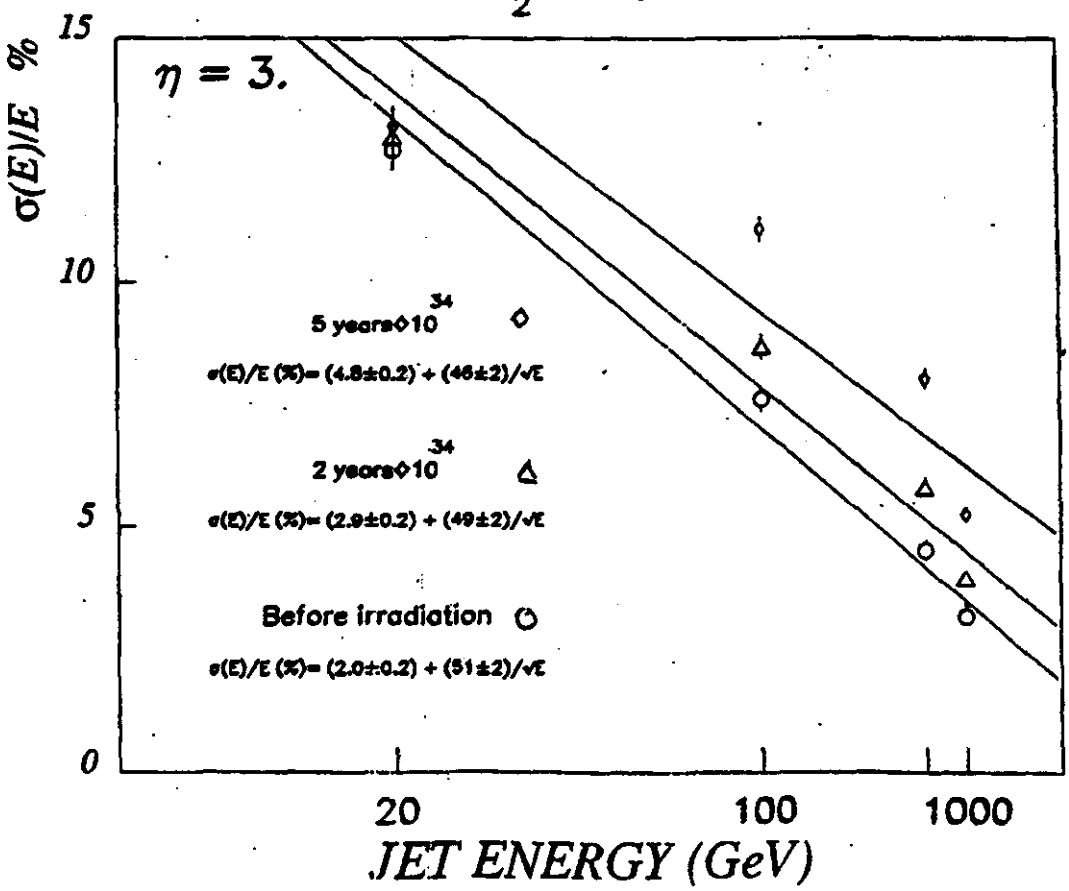

Fig 2b-5

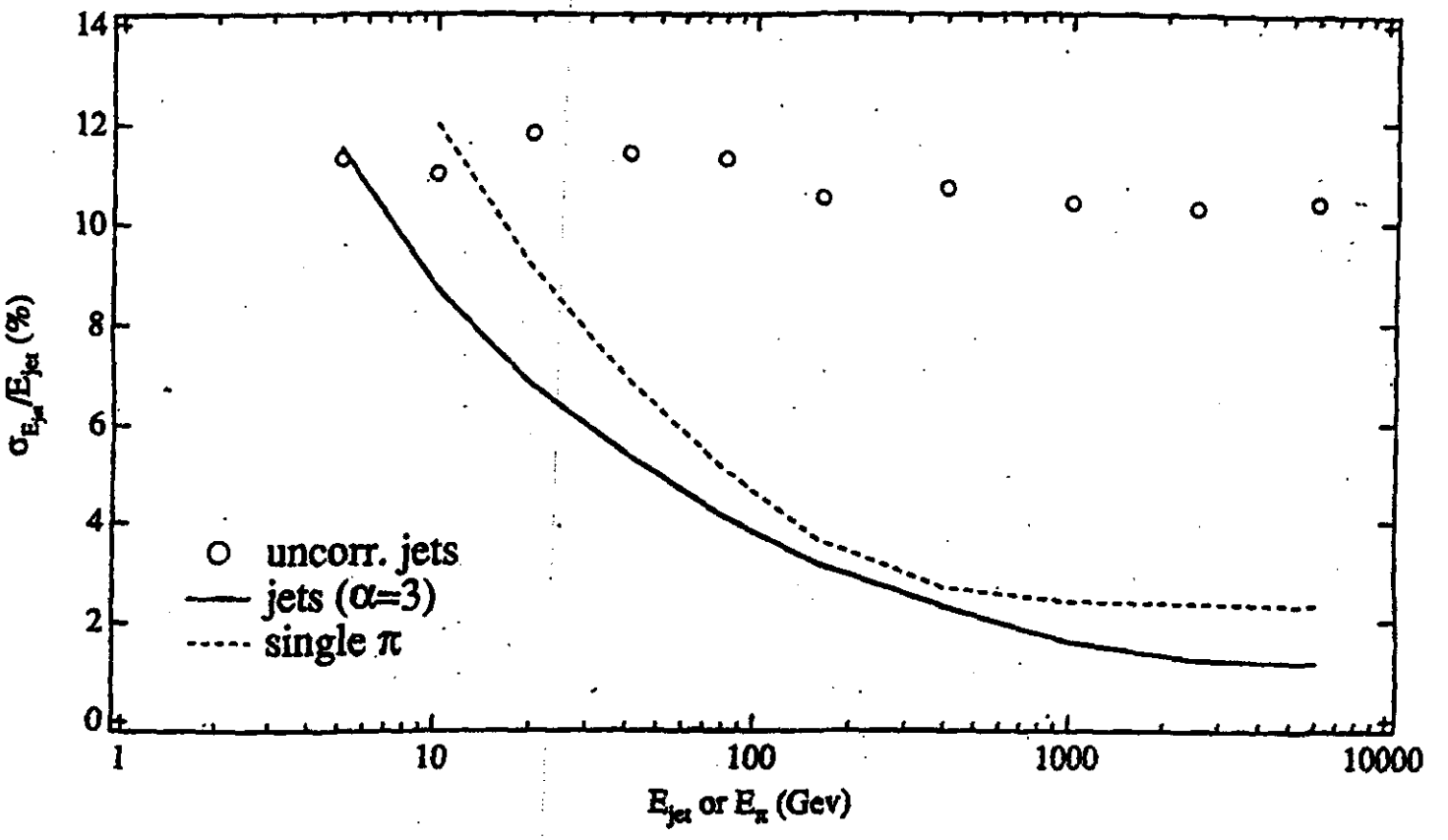
14
12
10
8
6
4
2
0
1
10
100
1000
10000
$\sigma_{E_{jet}}/E_{jet}$ (%)
E_{jet} or E_π (Gev)
uncorr. jets
jets (α=3)
single π

Fig 2C-1

3.3.2 Calorimetry

3.3.2 Calorimetry

Question #3: Accordion design argon/krypton, a 7%/sqrt(E) performance has not yet been demonstrated ...

At this writing (June 28), there are three new accordion stacks in liquid argon in the A3 beam at BNL awaiting the beam. We expect to start taking beam in the next few days. The three stacks include both options mentioned in the GEM LoI: the "2 mm" option and the "1 mm" option, see Figures 1 and 2. The third stack also uses "2 mm" absorber plates but the electrodes, instead of being rectangular, are in the shape of chevrons to optimize the position resolution in the η direction. We have borrowed 250 liters of liquid krypton from our GEM collaborators from the Budker Institute of Nuclear Physics in Novosibirsk, Russia. The krypton arrived in April.

We will be studying the energy and position resolution of these accordion stacks with electrons from 0.5 to 20 GeV. The chevron stack has been designed to simulate the accordion near η=1 and so we will also be studying the change in the energy resolution in this η range. We expect the energy resolution of the 2 mm stack with krypton to be about the same as the 1 mm stack with argon and both in the neighborhood of 7.5%/sqrt(E). We are also testing a new calibration system based on switching a DC current. In bench tests, this system has shown the ability to calibrate the electronics chain to a precision of 0.1% over the full dynamic range for the SSC: 100 MeV to several TeV.

A fourth stack based on parallel plates has also been fabricated and is at BNL awaiting the final electronics installation. It will be tested in a separate dewar with the same electronics chain and readout as the accordions. Expected resolution with Kr filling is about 5%/sqrt(E) (stochastic term) with small constant term (to be studied by MC simulations and beam tests at much higher energy).

While the above accordion tests are all in the non-projective geometry, there has been substantial progress on projective geometry. Our colleagues in the RD3

collaboration at CERN have been successful in producing 2 m long projective EM accordion absorber plates with a new "crocodile" machine. A stack using these plates will be beam tested in the Fall in CERN.

Michael Seman and Misha Leltchouk of Nevis have obtained significant results in simulating a projective structure for both the barrel and endcap GEM EM calorimeters. For the barrel, the optimum resolution was obtained using lead plates of 0.96 mm with 2x1.9 mm krypton gap. In this case the energy resolution is 5.4%/sqrt(E) at 90 degrees (Fig. 3) and 5.8%/sqrt(E) at 30 degree (between 57 and 30 degree absorber in the barrel has 0.44 mm lead cladded with thicker SS plates such that the total thickness of absorber plates remain constant).

We have also adopted a novel geometry for the endcap (Fig. 4) which is a cylinder with a vertical axis (similar to the barrel geometry with horizontal axis) however, with the folds starting and ending in the appropriate place to allow a planar monolith. This endcap structure is truly projective and has no cracks.

1992 GEM Test Beam Cryostat at AGS

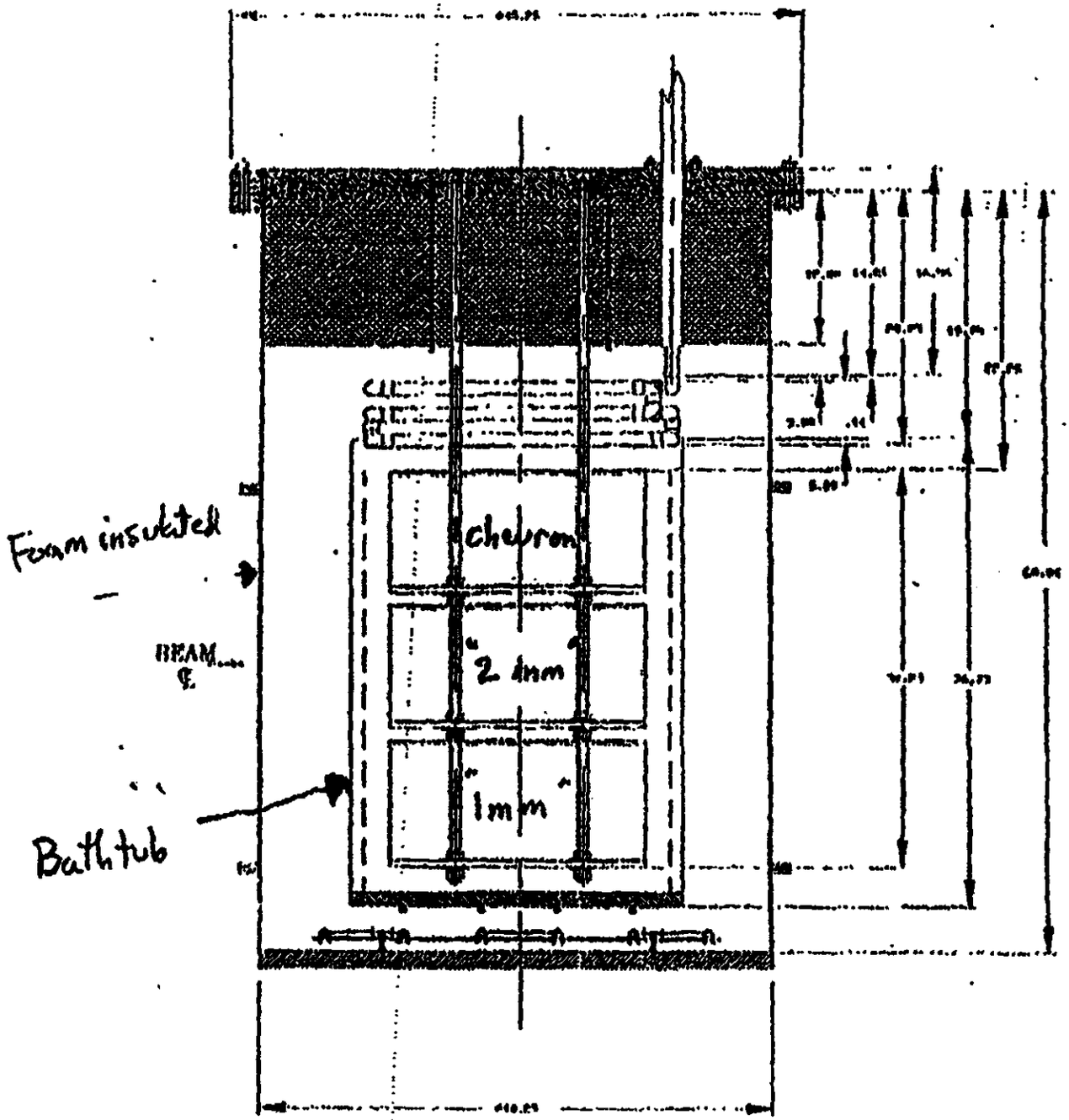

Figure 1. 1992 GEM Test Beam Cryostat at the AGS

3/26/92

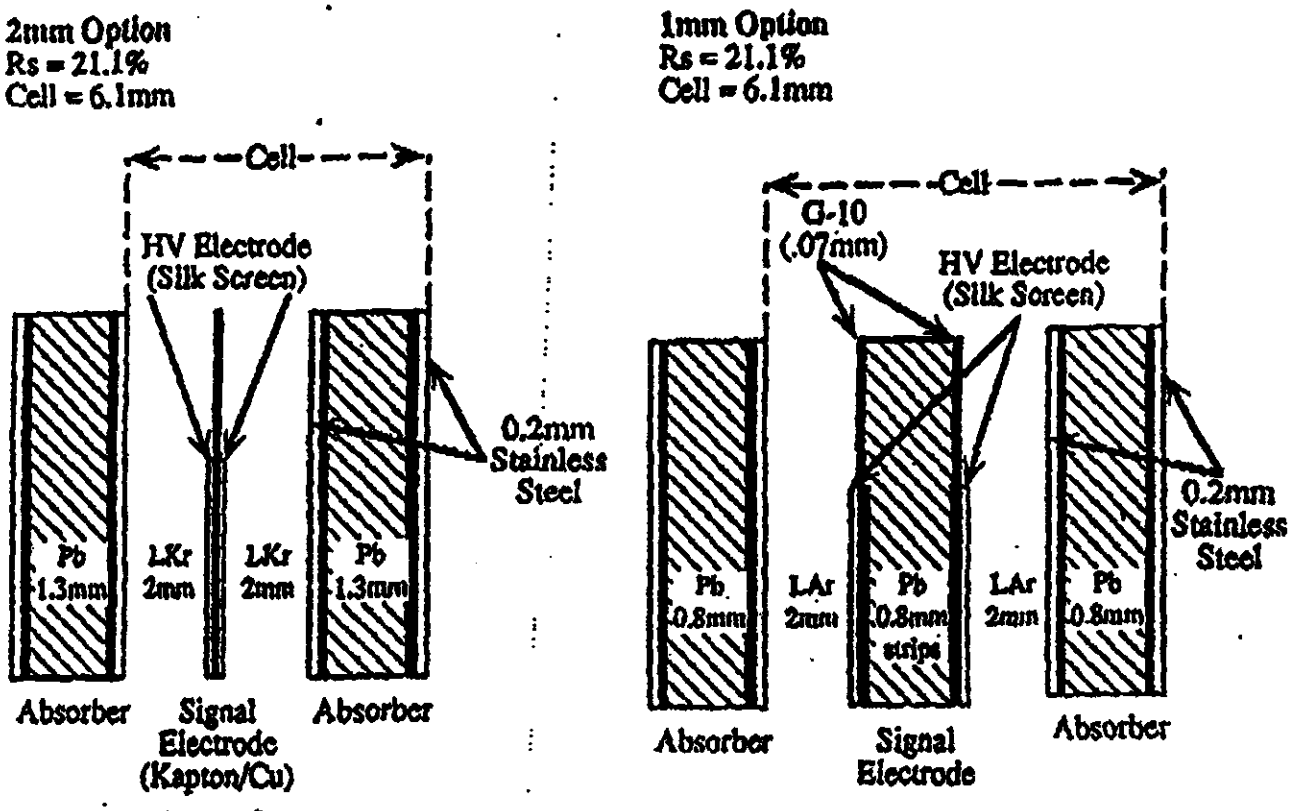

Figure 2

Electrode Structure for 1mm and 2mm Option

Figure 3

RESOLUTION AT ENERGIES ≥ 120 GeV ..
IS CORRECTED FOR LEAKAGE. ! ?

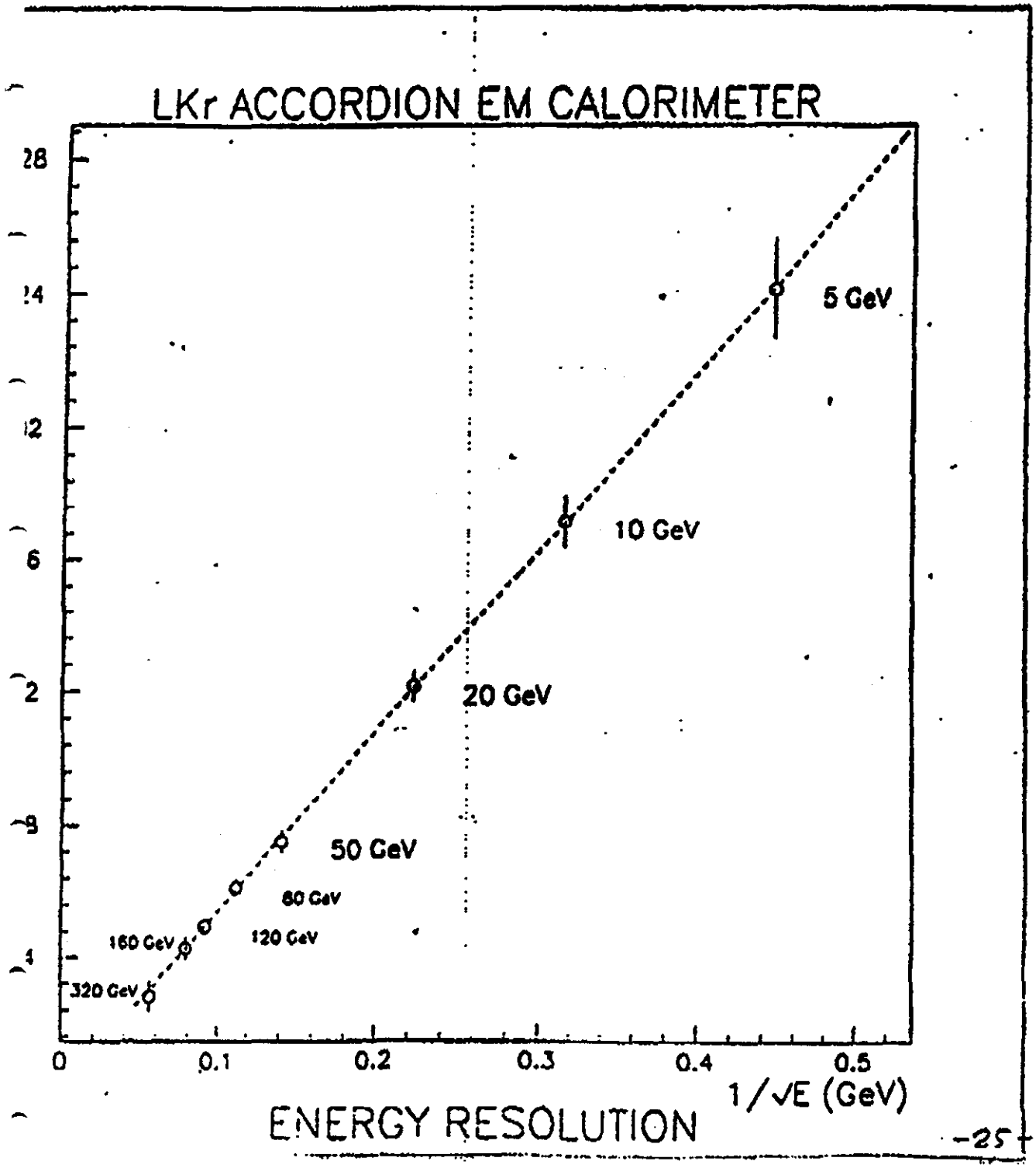

Figure 4

Endcap Accordion EM

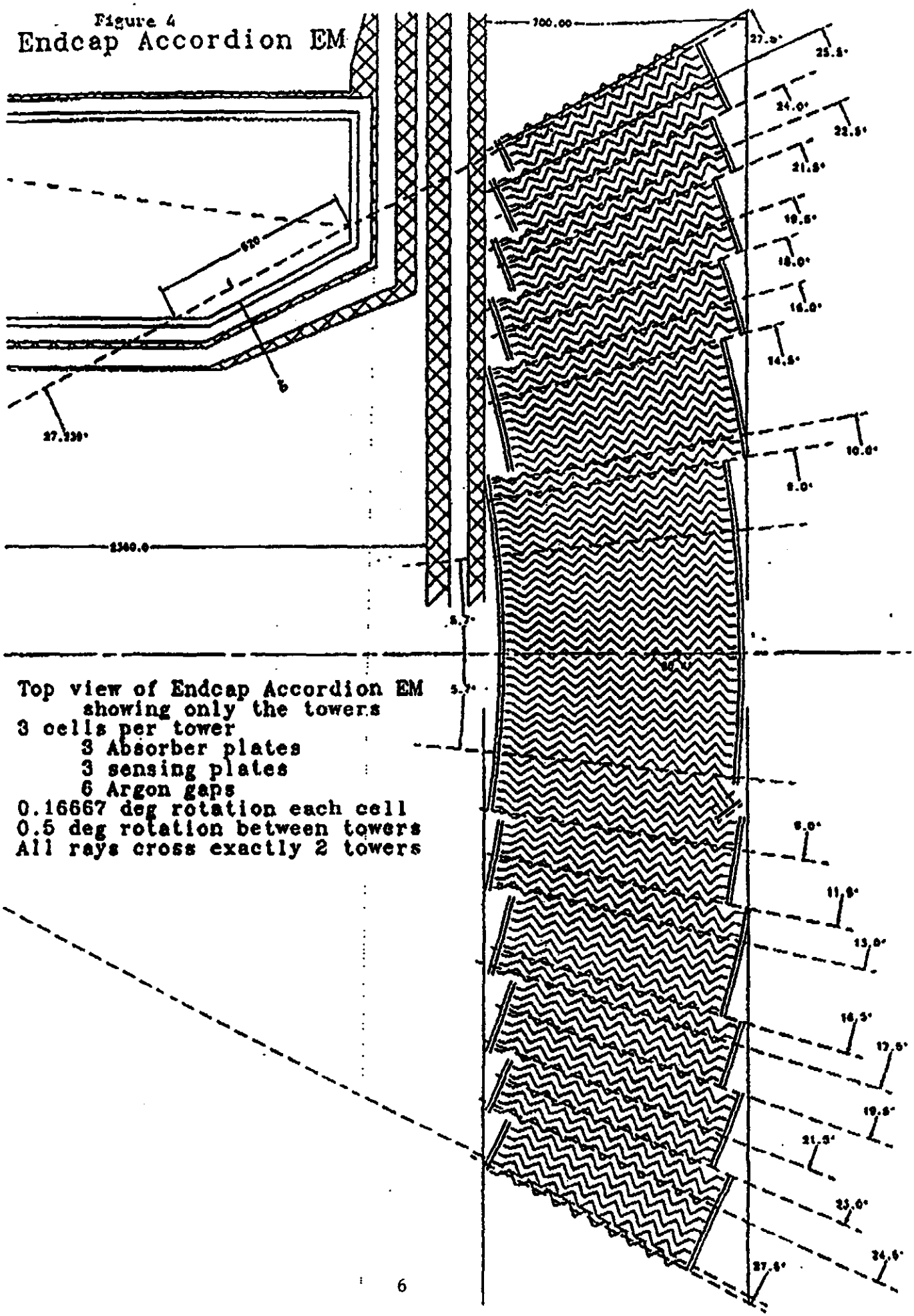

Top view of Endcap Accordion EM
showing only the towers
3 cells per tower
3 Absorber plates
3 sensing plates
6 Argon gaps
0.16667 deg rotation each cell
0.5 deg rotation between towers
All rays cross exactly 2 towers

3.3.2 Calorimetry

Question #4: PAC endorses collaborations plan to make choice between the proposed options.

Collaboration decided to proceed with two major R&D for e-m option till August 92, when the decision for choice of e-m calorimeter option for TDR will be made. Depending on the status of open questions at the time of making the decision, a strategy will be developed for continuing the development of the second technology at a considerably lower level, while these outstanding issue are resolved for the primary option and to allow the proponents to smothly finish their R&D program.

The R&D plans for both e-m technologies has been carefully discussed at the GEM Executive Committee meeting in February 92 and a list of requirements that each technology has to meet by the August decision time have been prepared. (This documment is supplied in an Addendum 1). Since GEM LoI considerable progress has been made by both BaF2 and LAr techniques (This progress is reproduced in a number of GEM technical reports and meeting procedings).

BaF2 Expert panel has been created by SSC in the fall 91 to review the status of the radiation damage of BaF2 crystals. The recomendations of the panel, due begining of August, will be regarded by the Collaboration as an important constaraint for the decision.

GEM internal Engineering panel has been created to evaluate the status and viability of the mechanical design of the LKr/Ar e-m and hadronic calorimeter - the major R&D issue for this technology. The recomendations of this panel are due beginning of August.

The series of meeting is planned by Collaboration in August - begining of September to discuss various aspects of both e-m techniques (incuding physics performance, calibration, design, cost, international participation, and other aspects). A final decision will be made after the final discussions at the Collaboration Council Meeting of September 3.

3.3.2 Calorimetry

Addendum 1 for question #4

GEM Executive Committee requirements to BaF2 and LAr-Kr technologies

The Executive Committee at the meeting Feb. 20th has reviewed the status of e-m calorimetry R&D Programs and has formulated the list of requirements for each technology which should be met before the management of the Collaboration will proceed with the choice of one of the options. Our plan is to make the choice before the end of August 92, and preferably earlier. Response to the requirements must be reported to Collaboration management by the specified date or earlier, in order to allow proper consideration. It was noted by the Executive Committee that the BaF2 technology has a lower probability of success in its R&D Program, because of possible radiation damage and other effects which can destroy the small constant term in energy resolution.

A. Requirements for BaF2 technology

1. Demonstrate substantial improvement in radiation resistance of large BaF2 crystals (20-25 cm long) towards the GEM specifications - reach absorbtion length of at least > 60 cm at 220 nm after 1MRad irradiation with photons, and if possible high energy hadrons. Present a detailed plan to obtain final GEM quality crystals, along with evidence of manufacturability and cost, including work required to prepare crystals after delivery.

   by August 1, 1992

2. As proposed by the expert panel, produce small radiation-hard crystals to demonstrate there are no fundamental limitations in making rad hard BaF2 crystals. (eg. absorbtion length >= 95 cm at 220 nm after 1 MRad)

   by August 1, 1992

3. Address in detail questions of preradiation, wrapping, residual non-uniformity, etc. in crystals we can practicably expect to manufacture. Cosmic ray transverse measurements in produced crystals could provide useful

data. Provide detailed practical plan for calibration of BaF2 system in-situ :describe calibration strategy, RFQ layout, required calibration time for each proposed technique to achieve necessary accuracy.

by July 1, 1992

4. Show by MC and by lab tests that the following effects do not destroy the resolution of the BaF2 system (maximum tolerable constant term is 0.6%):

   - residual non-uniformity (as installed);
   - non-uniformity developed by possible further radiation damage of "saturated" crystals and/or by possible annealing; (note - the expert panel and executive committee are not convinced of the proposal to preradiate the crystals);
   - accuracy of intercalibration (see point 3);
   - short term instabilities of readout system;
   - linearity, linearity calibration and dynamic range of readout system.

by July 1, 1992

B. Requirements for LAr-Kr technology

1. Demonstrate by beam tests stochastic term in resolution for non-projective geometry <= 7%/sqrt(E). Determine angular dependence of this resolution.

by August 1,1992

2. Produce detailed mechanical design/analysis of e-m barrel and end caps with optimization of gap between barrel and end cap, wall thicknesses, etc.

by July 1,1992

3. Demonstrate by MC simulations for realistic projective geometry and full angular range (between 90 and 5.7 degrees) the resolution $<= 7\%/sqrt(E) +$ 0.4% and physics consequences of the gap between barrel and end cap, wall thicknesses, etc.

by July 1, 1992

DECISION

In August, a decision will be made between the two technologies based on our best judgement of the expected performance of each technology, balanced against the cost and risk involved in each. A primary choice will be made for our e-m calorimeter for the TDR. Depending on the status of open questions at the time of making the decision, a strategy will be developed for continuing the development of the second technology at a considerably lower level, while these outstanding issues are resolved for the primary option and to allow the proponents to smoothly finish their R&D program.

The final decision will be made by the spokesmen, after considering the evidence presented for each technology and receiving the advice of the Executive Committee.

Additional requirements for LAr-Kr technology

(proposed by individual members of exec. committee and members of calorimeter group)

by the time of e-m decision

1. Show Higgs $\rightarrow > 2\gamma$ spectra (mass range 80-150 GeV) for realistic e-m LAr-Kr detector and background simulations..
2. Provide detailed practical plan for calibration of LAr-Kr detector in situ. Provide an evidence that electronic calibration is equivalent to the detector calibration with the required accuracy.
3. Provide experimental proof of radiation stability of LAr-Kr e-m system (for actually used materials).
4. Provide the results of the benchmark tests of LAr-Kr electronics which demonstarate required linearity, dynamic range, white and coherent noise in the real accordion system, cross talks and means of linearity calibration.

3.3.2 Calorimetry

Question 5: The PAC is concerned that there be sufficient absorptive power of the calorimetric sections for hadrons, so as not to impair the triggering capabilities of the GEM detector for muons.

1. Introduction

A very important consideration in the design optimization of the muon spectrometer is the level of backgrounds from hadron punchthrough and decay. These backgrounds not only affect the ability to observe signals from rare processes at the SSC, but also the ability to form a low-rate muon trigger. An outstanding issue which must be understood before embarking on the construction of the muon spectrometer is the minimum hadron absorber thickness demanded by SSC physics needs. This is particularly important in the GEM detector where all the absorbing material lies inside of the muon system as expensive calorimetry. The thickness of hadron absorber therefore sets the scale in size and cost for both the muon spectrometer and the calorimeter if more depth is required for punchthrough suppression than is required for good hadron energy resolution (9-10 λ [1]). In this era of "design to cost" it is therefore very important to study and determine the calorimeter thickness necessary to effectively trigger, identify, and measure muons of physics interest while not overwhelming the GEM detector budget. The current design requirements for calorimeter thickness in the GEM Baseline 1 [2] are 12 λ in the barrel region ($\eta < 1.3$) and 14 λ in the endcap region ($2.5 > \eta > 1.3$).

The depth of calorimetry before the muon system was an issue raised by the PAC in its report on the GEM LOI and has been the focus of considerable simulation effort over the past months. Simulation studies of particle rates in the muon spectrometer as a function of calorimeter thickness were performed for both the barrel (section 2.1) and endcap regions (section 2.2). For the study, TWOJET events were generated via ISAJET and particle rates outside the calorimeter were determined including prompt muons from quark leptonic decays, muons π/K decays occurring in the inner tracking region, and hadron induced charged particles

exiting the calorimeter (punchthrough). Neutrons and associated gammas are not considered in the studies. Additional thickness of calorimeter for neutron suppression is not cost effective. Other means to suppress the neutron rate exist; for example, addition of layers of polyethylene doped with Boron. Design requirements for the suppression of the neutron background are currently being studied.

To estimate the punchthrough rate, the PCHTHR code [3] was utilized. The PCHTHR code produces 4-vectors for the punchthrough particles and was derived from GEANT simulation of single pions of various momenta incident on iron absorber of various thickness. The resultant punchthrough showers were recorded and probability tables prepared for the punchthrough probability, shower multiplicity, individual particle type, momentum, spatial position, and exiting angle relative to the incident track. The probability tables are incorporated into a single subroutine which is called for stable hadrons particles. incident on the calorimeter. The PCHTHR code, while superior to simple parameterizations, assumes that a λ of Fe is equivalent to a lambda of any material. It has been found from GEANT simulation that Pb has slightly more absorptive power per λ than solid Fe. The PCHTHR code also assumes no magnetic field in the calorimeter material. The addition of a non zero magnetic field in the calorimeter should serve to suppress the punchthrough. The PCHTHR code can thus be considered a conservative estimate of the punchthrough background.

2.1 Barrel Region [4]

For the muon system, the limiting factor will be the rate of particles in the first muon detector layers after the calorimeter. This rate should be sufficiently low that a level 1 muon trigger can be formed which is efficient for muons of interest, namely muons from Ws and Zs (about 10–20GeV/c in transverse momentum). In considering criteria for evaluating the calorimeter depth, it is useful to consider the source of the particles exiting the calorimeter. Charged particles entering the barrel muon system will be mainly of three sources: 1) Prompt muons from quark decays, 2) the muons from π/K decays in the inner tracking volume before the calorime-

ter, and 3) the hadron-induced particles leaking out the back of the calorimeter (hadron punchthrough). The rate of prompt muons is irreducible. Muons from π/K decays are suppressed in GEM by the very compact tracking region (less than half the size of SDC's). The first two sources produced muons before entering the calorimeter and so the calorimeter material serves merely to range out these muons. Therefore the reason for calorimeter depth beyond that needed for good hadron energy resolution is to reduce the rate of hadron punchthrough. Assuming therefore that the calorimeter is not already so thick that it serves only to range muons, then the following two criteria can be defined by which we can gauge the benefits of additional calorimeter thickness:

Criteria 1: The overall particle rate exiting the calorimeter from hadron punchthrough should be much less than the sum of the rates from prompt muons and muons from π/K decays.

Criteria 2: The rate of particles with transverse momentum above a trigger threshold from hadron punchthrough should be much less than that from prompt muons and muons from π/K decays.

For the determination of particle rates after the calorimeter, TWOJET events have been generated using the ISAJET generator in the JET P_T range 4 $GeV/c < P_T < 5000$ GeV/c and top quark mass $M_t = 140$ GeV/c^2. The event sample was compiled in various P_T subintervals in order to have increased statistics at high P_T while generating the entire SSC pp cross section (140mb). The events were weighted by the cross section when filling the histograms. Several runs were made over the same 150k event sample with a calorimeter of constant 6, 8, 10, 12, 14, and 16 λ thickness. The generated particles pass through a fast simulation of a tracking volume and calorimeter. Muon energy losses were considered. Decays in flight of π/K were calculated in a tracking volume 0.75m in radius and 4.4m in length. Muons from the decays were assumed to be in the direction of the parent hadron with energy thrown according to the kinematics of the two body decays.

Figure 1 shows for two rapidity intervals, a) $\eta < 0.5$, and b) b) 1.0 η 1.5, the

total rate of charged particles exiting the calorimeter as a function of calorimeter depth (solid curve) and the rate from prompt muons + π/K decays in the tracker (dashed curve) and punchthrough particles (dot-dashed curve). Figure 2 shows the rate of charged particles of transverse momenta greater than 10 GeV/c for the same two rapidity intervals. If criteria 1 is satisfied when the fraction of the total rate from hadron punchthrough is less than 1/3, then it can be seen from figure 1, that criteria 1 is satisfied for 12 λ and higher of calorimeter depth. Even if the punchthrough rate were uncertain to a factor of 2 and the dot-dashed curve in figure 2 were revised upward, the punchthrough rate would still be less than 50% of the total rate. Considering only particles with $P_T > 10\ GeV/c$ in figure 2, the rate coming from prompt muons dominates for calorimeter depths of 10 λ and above. So, assuming that we satisfy Criteria 2 if the fraction of the particle rate above 10 GeV/c from hadron punchthrough is less than 1/3 of the total, then Criteria 2 is satisfied in the barrel region for 10 λ and higher calorimeter depth.

Table 1 summarizes the calorimeter depth requirements resulting from Criteria 1 and 2. To satisfy all criteria considered requires a calorimeter of minimum 12 lambda depth over the barrel region. In the next section the evaluation of the calorimeter depth in the endcap region will be described.

Table 1: Summary of Depth requirements

Criteria	Depth at η=0	Depth at η=1.5
1	12 λ	12 λ
2	10 λ	10 λ

In the barrel region, the trigger components proposed for GEM are RPCs. These devices have been tested recently at CERN [5] and found to handle rates up to 50Hz/cm^2 without significant loss of efficiency. Figure 3 shows the rate per unit area (Hz/cm^2) at $10^{33} cm^{-2}/s$ expected in the first layer of the barrel muon system for different calorimeter depths. The first layer is positioned at R=370cm.

At $10^{34} cm^{-2}/s$ luminosity the maximum rate of muon system hits from charged particles would be about 6Hz/cm^2 at η=1.3. This rate is at least an order of magnitude below the limiting rate for the RPCs and the barrel muon system is robust.

Consideration has not been given to detailed muon system performance requirements such as muon identification, triggering, and momentum measurement. However, the results of the above study indicate that 12 λ in the barrel calorimeter sufficiently suppresses the punchthrough rate to levels less than the rate of real muons penetrating the calorimeter.

2.2 Endcap Region [6]

In this section, we examine the rate of charged particles emerging out of the calorimeter and entering the first superlayer (SL1) of the muon system in the endcap region as a function of calorimeter depth. The other two superlayers are exposed to lower rates of particles as soft charged particles, which make it to SL1, will bend and not reach the others. Although, these particles may turn around and hit SL1 for a second time. From charged particle fluxes, the expected chamber occupancies can be calculated. We also study the composition and Pt distribution of exiting particles as a function of calorimeter depth. From these considerations, we draw conclusions on the required calorimeter depth in the endcap region.

The Hit-level Monte Carlo simulation package [7] was used for this study. This package provided trajectories of muons in the muon system in form of hits in chamber layers. The muon system geometry was based on the parameters of the Baseline I [2]. The solenoidal field of 0.8 T was properly simulated including the non-uniformity in the forward regions due to presence of the flux concentrator.

QCD two jet events were generated using ISAJET in the jet Pt range of 4 GeV/c to 2 TeV/c. Decay in flight of π/K mesons inside the inner tracker volume were simulated using GEANT. Tracks with $\eta < 3$ were then passed through a calorimeter modeled in depth as shown in Fig. 4. Four different depths were considered for this study: flat 10 λ in the barrel and endcap, 10 λ in the barrel

increasing to 12 in the endcap as in Fig. 4, similarly 12 to 14 and 14 to 16. The material was a homogeneous mixture of copper and liquid argon for the central and endcap calorimeters. It should be noted that, unlike muons which passed through a full Geant simulation of the calorimeter, the passage of hadrons were simulated using the PCHTHR routine [3], which assumed iron as the absorber material and no magnetic field in the calorimeter.

Tracks leaving the calorimeter were marked by hits placed at the front face of SL1, which is a cylinder of radius 366 cm and of half length (along Z) 566 cm. These dimensions include 10 cm of boron doped polyethylene for neutron shield and 6 cm of air for stay clear area, which were simulated by GEANT.

Fig. 5 shows the flux of charged particles (in Hz/cm^2) at SL1 as a function of rapidity. Unless otherwise stated, the rates are calculated for a luminosity of $10^{33} cm^{-2} s^{-1}$. The four plots give the rates for the four calorimeter depths mentioned above. The turn-around at η=2.5 is due to excluding the tracks with polar angles smaller than the minimum angle covered by SL1 (about 9 degrees). This can be seen from Fig. 6, which shows the charged particle flux as a function of the polar angle θ. The fluxes change by more than two orders of magnitude between η=0.0 and η=2.5. We note that the rates in the barrel region are about a factor of 3 lower than those shown in Section 2.1. There are differences between the two calculations which may account for this discrepancy, however, we regard this as a measure of the precision of these calculations. The agreement, within a factor of 3, between the two rate calculations presented in this note, as well as that described in the LoI [8], indicates that these rates have an uncertainty of a factor of 3.

We further examine the rates, this time in terms of the particle composition. Fig. 7 shows the charged particle rate (in Hz) in the forward endcaps as a function of track ID (GEANT convention) for the four thicknesses 10, 12, 14, and 16 λ. Note that exiting particles are predominately electrons and muons for all depths. Electrons are always present and have a rather soft Pt distribution, indicating that

they are produced in the last layer of calorimeter, hence leaking out. In this sense, additional absorber material will not help reduce the rate of exiting electrons.

Next, we examine the rates in terms of the source of charged particles exiting the calorimeter. Fig. 8 shows the rate (in Hz) as a function of rapidity for prompt muons, decay muons, punchthrough particles (including secondary muons), and muon induced showers (excluding the muon itself). The calorimeter thickness follows the 12 - 14 lambda model. Notice that the rapidity distribution of prompt muons is relatively flat, whereas the punchthrough rate increases steadily with increasing rapidity, and the decay rate increases very rapidly in the endcap region. These features are true of all calorimeter thicknesses considered in this study.

In Fig. 9, we plot the charged particle rate versus calorimeter thickness for two rapidity intervals $1.5 < \eta < 2.0$ and $2.0 < \eta < 2.5$, and for a luminosity of $10^{33} cm^{-2} s^{-1}$. The contributions from prompt and decay muons (prompt + decay) and from punchthrough and muon induced showers (PCHTHR + MuShower) are shown separately. The prompt and decay muons dominate the total rate for all thicknesses in the $2.0 < \eta < 2.5$ region. In fact, it is the decay muons that have the largest rate, simply due to the larger decay path available to π/K mesons in the forward regions. Here, unlike in the barrel, the punchthrough rate and where it falls below the real muon rate are not the criteria for determining the necessary depth of calorimeter. The total rate and chamber occupancy should rather be used.

Table 2 summarizes the occupancies calculated for a single strip (e.g. Cathode Strip Chamber technology) of size typical of those in the forward region nearest to the beam and for a luminosity of $10^{34} cm^{-2} s^{-1}$. The Baseline I design requires an occupancy of $< 3\%$ at this luminosity. A more relevant number may be the 3- or 5-strip occupancy, as a single particle may induce charge on 3 to 5 strips. Assuming 3 strips, a minimum calorimeter depth of 14 λ is clearly required to be able to cope with the rates at the highest SSC luminosities, i.e. an occupancy of $< 3\%$. As mentioned before, there is an uncertainty of factor of 3 (upward!) in these

rate calculations. Therefore, 14 λ should be considered as an absolute minimum calorimeter depth required in the endcap region. In fact, one could argue that a conservative estimate for the necessary depth should be 16 λ, however, note that the decrease in rate from 14 to 16 λ is rather small. Therefore, further rate reduction with increasing calorimeter depth beyond 14 λ does not seem to be appropriate and cost effective. One should rather improve muon chamber rate capability to insure its robustness at higher luminosities.

Table 2. Occupancy versus calorimeter depth.

	CALORIMETER DEPTH			
	10	12	14	16 λ
CHARGED PARTICLE				
RATE 2.0 << 2.5				
L = $10^{34} cm^{-2} s^{-1}$	390	280	160	110 Hz
STRIP SIZE= 30X0.5 cm^2	5850	4200	2400	1650 Hz
SINGLE STRIP	1.8%	1.3%	0.7%	0.5%
OCCUPANCY $3X10^{-6}$	s delay			

It should be noted that muon identification and pattern recognition, as well as triggering and momentum measurement studies may put further constraints on rates in the forward region. Any rate requirements arrived from these studies should be dealt with within the muon system components. We state again that additional calorimetry beyond 14 λ does not result in significant rate reduction; it only amounts to an expensive way of ranging out real muons.

References

[1] Some GEM note here on Hadronic Calorimeter resolution vs λ.

[2] GEM Baseline 1, GEM TN92-76, April 23, 1992.

[3] See for example transparencies talk given by R. McNeil at the GEM Collaboration meeting July 17, 1991. Should write-up a GEM Note on this.

[4] R. McNeil, " How Thick should the GEM Barrel Calorimeter Be", GEM TN92-68, March 10, 1992.

[5] RD5 Collaboration, Status Report, CERN/DRDC/91-53 1992.

[6] M. Mohammadi, GEM Note (endcap cal thickness).

[7] For more details, see "Hit-Level Physics Simulations" section in this report.

[8] GEM Letter of Intent, SSCL-SR-1184, GEM TN-92-49, Nov. 30, 1992.

3.3.2 Calorimetry

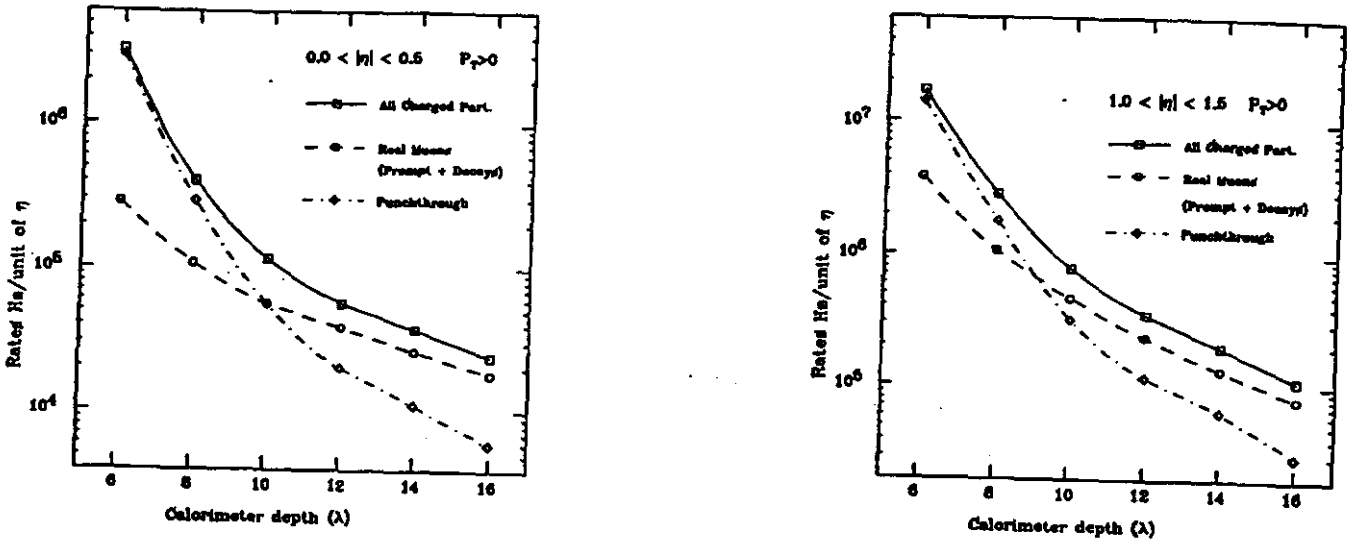

Figure 1. The rate of all Charged particles rates at 10^33 cm^-2/s SSC luminosity exiting the barrel calorimeter for a) |eta|<0.5 and b) 1.0<|eta|<1.5 rapidity intervals. The solid curve is the total rate, the dashed curve is the rate from prompt muons and pi/K decays in the inner tracking region, and the dot-dashed curve is the rate from hadron punchthrough.

3.3.2 Calorimetry

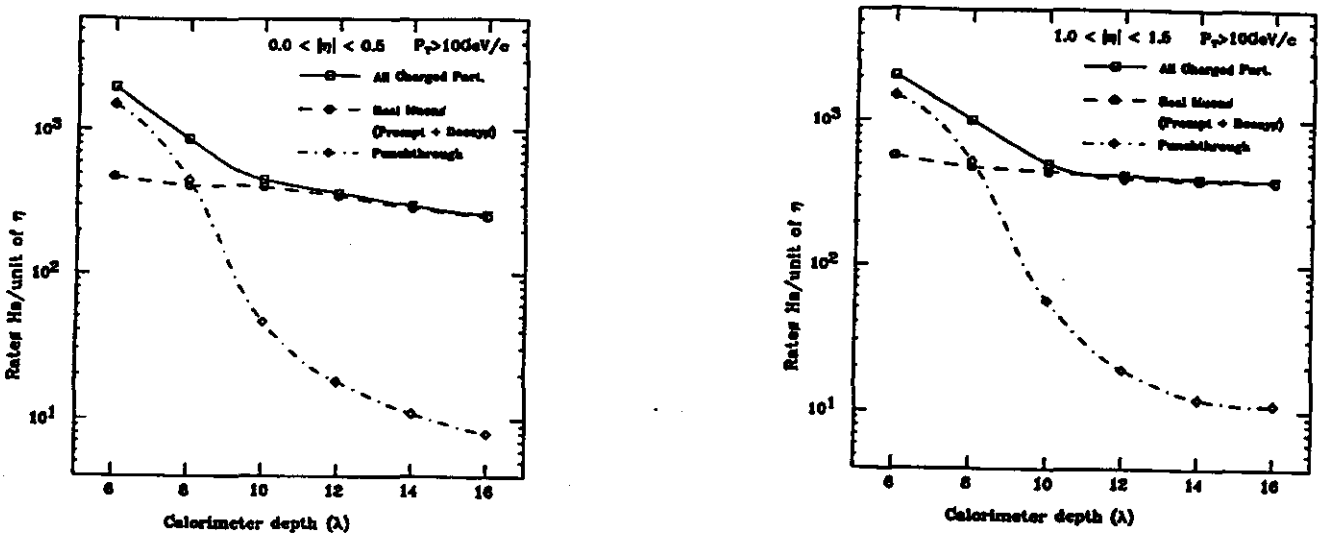

Figure 2. The rate of Charged particles with transverse momentum above 10GeV/c at 10^33 cm^-2/s SSC Luminosity exiting the barrel calorimeter for a) |eta|<0.5 and b) 1.0<|eta|<1.5 rapidity intervals. The solid curve is the total rate, the dashed curve is the rate from prompt muons and pi/K decays in the inner tracking region, and the dot-dashed curve is the rate from hadron punchthrough.

3.3.2 Calorimetry

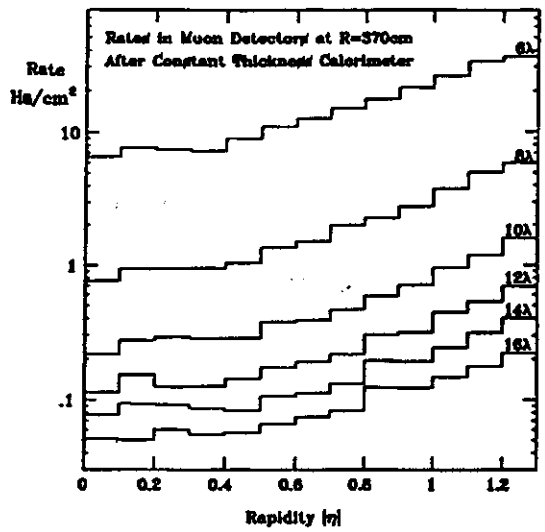

Figure 3. The hit occupancy in the first layer of the GEM barrel muon system at R=370cm at 10^33 cm^-2/s SSC luminosity as a function of rapidity for various constant calorimeter thicknesses.

3.3.2 Calorimetry

Question 6: The PAC notes that the capability of the forward calorimeter to help determine missing transverse energy has not yet been demonstrated.

Perhaps the most demanding requirement on missing transverse energy comes from potential SUSY signatures. For a perfect detector the principal background to the missing transverse energy signature comes from escaping neutrinos in heavy quark jets. The goal set by GEM is to design a detector which does not create any significant additional background to this fundamental physics background. There are two significant sources of detector induced backgrounds, 1) jets at large eta which escape detection down the beam pipe and 2) jets whose transverse energies are mismeasured. The detailed Monte Carlo work of Paige and Vanyashian (GEM TN-92-70) has demonstrated that detector induced backgrounds are small compared to the irreducible neutrino background IF there is full coverage out to eta of about 5.0 and if the transverse energy resolution for jets is at least as good as 10%.

A forward calorimeter with full coverage to eta=5.0 requires that hadronic showers (and electromagnetic showers) be contained for particles impinging anywhere up to eta=5.0. This requires a dense absorber material with short interaction length to prevent significant leakage of showers down the beam pipe. For GEM with a forward calorimeter quite close to the interaction point this is a severe requirement. GEANT simulation (see GEM note by Mike Shupe and John Rutherfoord GEM TN-92-52) shows that a small-sampling-fraction calorimeter with Tungsten absorber which hugs the beam pipe meets this requirement.

The GEM calorimeters in the central and end-cap regions are designed to be hermetic and to measure jet energies with sufficient precision. In the forward region (3.0 <eta < 5.0) contributions to the transverse energy resolution function come more from angle than from energy mismeasurements. It is not a challenge to design a calorimeter with better than 10% energy resolution for the very large energy particles encountered in the forward direction. To meet the necessary angle

resolution it would be desirable to segment the forward calorimeter in the transverse and longitudinal directions. Because hadronic showers are broad compared to the necessary tower sizes, in our Tungsten/LAr forward calorimeter design we have an "EM" section which is 2.3 absorption lengths thick in which more accurate angle measurements are made before the hadronic shower spreads to its maximal size. The transverse segmentation in the last two longitudinal segments is coarser than in the "EM" section corresponding to the less critical pointing information at this depth in the hadronic showers. The "tail catcher" section is used to flag late-developing showers which might leak significant energy out the back and look like missing energy. Since this is a higher order effect, flagging its occurance is sufficient. Detailed GEANT simulation (see again the GEM report of Mike Shupe and John Rutherfoord and a separate GEM report of Geoff Forden GEM TN-91-28) of single hadrons and photons confirms that this design gives transverse energy resolution meeting our goals.

The choice of absorber (Tungsten) and active material (liquid Argon) was driven by considerations of radiation damage. The readout will use the "zero transistor" solution where low impedance microstrip cables will carry the signal to cable terminators (pre-amps) located on the periphery of the endcap calorimeter well away from radiation. The micro- strips are made of Kapton and copper. The electrode structure uses concentric tubes with argon gaps of 100 microns in the "EM" section in order to avoid the positive ion build-up problem (see J. Rutherfoord GEM TN-91-27). Tests of this concept are underway. The drift time in the "EM" section is 20 ns so with shaping times of 20 ns the ballistic deficit will be minimal. While the capacitance in a jet cone is large, the electronics noise is negligible when measured in ET.

Additional issues which we have addressed in preparation for the technical design report are heat deposition and heat transport, electronics noise, physics pile-up, and activation (for personnel access).

3.3.3 Muon System

July 6, 1992

Answers to PAC Questions:

The questions put forth in the Report of SSCPAC December 15-17, 1991 Meeting are answered in turn. For some items, relevant documentation exists. In those cases a short synopsis is given and supporting reports included as enclosures.

(1) *Description of R&D Program:*

There are in four separate technologies which are being studied for the GEM Muon System. They are:

Function:	**Technology:**
Barrel Region:	
Momentum determination	Pressurized Drift Tubes (PDT) Limited Streamer Drift Tubes (LSDT)
Z-coordinate measurement	RPC
Level 1 trigger	Resistive Plate Counters (RPC)
Level 2 trigger	PDT LSDT
Beam Crossing tag	RPC
Endcap Region:	
Momentum determination	Cathode Strip Chambers (CSC)
R-coordinate measurement	CSC
Levels 1 & 2 trigger	CSC
Beam Crossing tag	CSC

Approximately $2.4 M has been allocated to develop these technologies, as well as perform the necessary engineering for the chamber support structure and alignment system [1.1]. Our intention is to be able to make an informed choice of the best chamber technology(ies) for a well documented Technical Design Report. The program consists of the following activities.

(1) Construction of full-scale prototypes of each chamber technology to develop a complete mechanical design. These will be evaluated according to mass manufacturing compatibility and production costs. Special attention will be paid to the maintenance of the required mechanical tolerances needed to achieve the baseline resolution.

(2) Testing of the chambers to evaluate their resolution performance. This includes measuring the single layer resolution with a hardened cosmic ray spectrum provided by the Texas Test Rig (TTR)[1.2],[1.3], which is near completion at the SSCL.

It is expected that the chambers will be ready for testing by late August,1992. Additional tests will be performed on the CSC technology using the RD5 beam at CERN this late summer and fall [1.4].

(3) Determination of the sensitivity to neutrons. Test exposures of CSC, RPC, LSDT, (and PDT) technologies to a ^{252}Cf neutron source are under study. The gas mixture and construction materials are important parameters.

(4) Testing of alignment technologies as to precision and applicability to the GEM muon support structure and chamber technologies.

(5) Conceptual design of the chamber support structure. Attention will be paid to the overall stability, installation, and cost.

Enclosures:

[1.1] "The GEM Muon System R&D/Engineering Plan", Oct. 1991

[1.2] "R&D and Engineering for the Texas Test Rig", Gena Mitselmakher, et al. Nov. 1991.

[1.3] "Monte Carlo Studies of the Texas Test Rig Performance", A. Vanyashin and G. Yost, GEM TN-92-99.

[1.4] "Plans for Participation in the RD5 Experiment at CERN", M. Mohammadi, et al. Feb. 1992.

Note added: This proposal has been accepted at CERN and funded through the TNRLC.

(2) *"Since the rapidity region covered by the resistive plate counters for triggering is quite narrow, 0< $|\eta|$ < 1.32, the proposed trigger based on pad chambers will need to be demonstrated."*

The barrel trigger and beam crossing tag is based on RPCs, which will be instrumented with both ϕ (bend plane) and Z (non-bend plane) coordinate readout. The rapidity region, 0< $|\eta|$ < 1.32, where the RPCs will be located, comprises about 1/2 of our coverage, and thus is "not quite narrow". The RPCs will be constructed in two-gap modules and will be located in each of the three super-layers. This arrangement will enable both a momentum dependent trigger to be formed as well as a measurement of the orthogonal coordinate of the muon track. The RPCs have a measured time jitter of < 1.4 ns (I. Pless - private communication), which is sufficiently fast to unambiguously tag the beam crossing. The bend plane strips will be 1.3 cm wide, while the non-bend plane segmentation varies from 3.9 to 8.9 cm.

Both the endcap trigger and beam crossing tag will be provided by the CSCs. The bend plane strip segments which are used to form the trigger are the 0.5 cm wide strips readout digitally at trigger time. The non-bend plane measurement is provided by means of the anode wires which will be segmented in 5 cm wide electronic channels. Since the maximum drift time of the CSC is < 24 ns per plane, several planes in a super-layer must be "ORed" together to achieve sufficient resolution for the beam crossing tag.

The Level 1 muon trigger is based on a simple logic using hits in super-layers 2 and 3 (SL2 and SL3, respectively) which uses the change of the phi angle, $\Delta\phi$, to measure the curvature (momentum) of the track originating from the interaction point. $\Delta\phi$ is given in terms of the number of readout strips of the RPCs (1.3 cm wide) for a barrel muon, or the number of CSC pickup strips (0.5 cm wide) for an endcap muon. The line formed by the hit in SL2 and the interaction point extrapolated to SL3 gives the position of the muon track for infinite momentum. The difference measured in strips, ΔN_{strip}, between the hit in SL3 and the extrapolated point is a measure of the muon momentum.

The trigger simulation was performed by allowing muon tracks to traverse the calorimeter and to penetrate the three super-layers of the muon system. The details of the GEM magnetic field were included. This is especially important for the endcap region, where the beam power is significantly improved by the Flux Concentrators. In order to know the contributions from different parts of the muon system to the trigger rate, the muon system was divided into the barrel region (η < 1.3) and two endcap regions (Endcap 1: 1.3 < η < 1.7; and Endcap 2: 1.7 < η < 2.4). For trigger efficiency studies, single muons with fixed Pt of 10, 20, 30, 40, and 50 GeV/c were generated. QCD dijets with jet Pt range of 4 GeV/c to 2 TeV/c were also generated to estimate the single muon trigger rates.

Figs. 1a,b,c show the trigger efficiencies for the three angle regions indicated above as functions of the minimum numbers of strips. Note that, even up to Pt = 50 GeV/c in the most forward region of the endcap coverage, there is enough bend power to form a trigger. The corresponding trigger rates were calculated for L = 10^{33} $cm^{-2}sec^{-1}$ and are shown in Figs. 2a, b for the barrel and two endcap regions, respectively, as a function of $\Delta N_{strip\text{-}min}$. For a low Pt cut of 10 GeV/c, the trigger rate would be no larger than 10^3 Hz in the barrel region, and a few times 10^2 Hz in each of the endcap regions.

Even though the above discussion indicates that the segmentation of the trigger chambers and the bend power of the magnet are sufficient to trigger up to 50 GeV/c several other more complicated trigger logics were also tried, especially for the endcaps. Unlike the barrel, low Pt particles, primarily from hadronic punch-through in the calorimeter, sometimes penetrate SL3 in such a way as to mimic high Pt particles in the trigger logic. But the

trajectories generally do not trace back to the intersection point. Hence by comparing a set of redundant measures of the momentum, such as $\Delta\phi 12$ and $\Delta\phi 23$, the number of these particles can be significantly reduced.

Figure Captions:

Fig. 1a The trigger efficiency is shown as a function of ΔNstrip for various values of Pt in the Barrel region.

Fig. 1b Same as Fig. 1a for Endcap region 1.

Fig. 1c Same as Fig. 1a for Endcap region 2.

Fig. 2a The trigger rate (Hz) for $L=10^{33}cm^{-2}s^{-1}$ is shown for the Barrel region as a function of ΔNstrip. To set the trigger for Pt>10 GeV/c only muons with ΔNstrip < 20 would be accepted.

Fig. 2b Same as Fig. 2a for Endcap regions 1 and 2. Refer to Figs. 1b and 1c for Pt cuts in these regions.

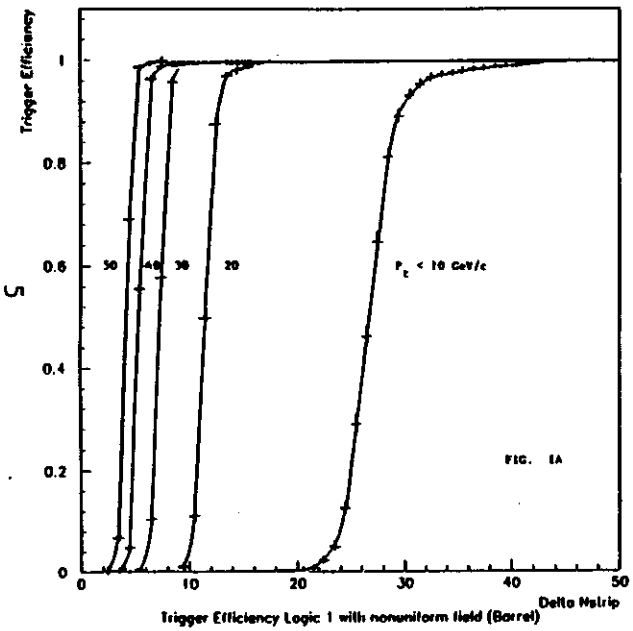

Trigger Efficiency Logic 1 with nonuniform field (Barrel)

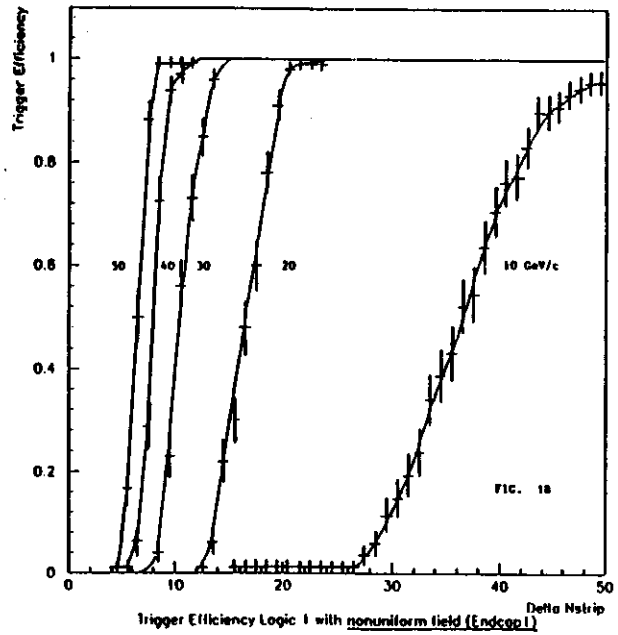

Trigger Efficiency Logic 1 with nonuniform field (Endcap1)

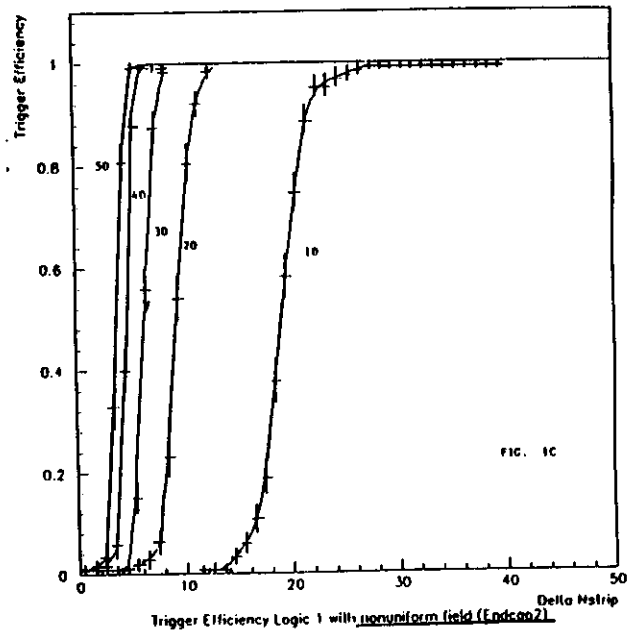

Trigger Efficiency Logic 1 with nonuniform field (Endcap2)

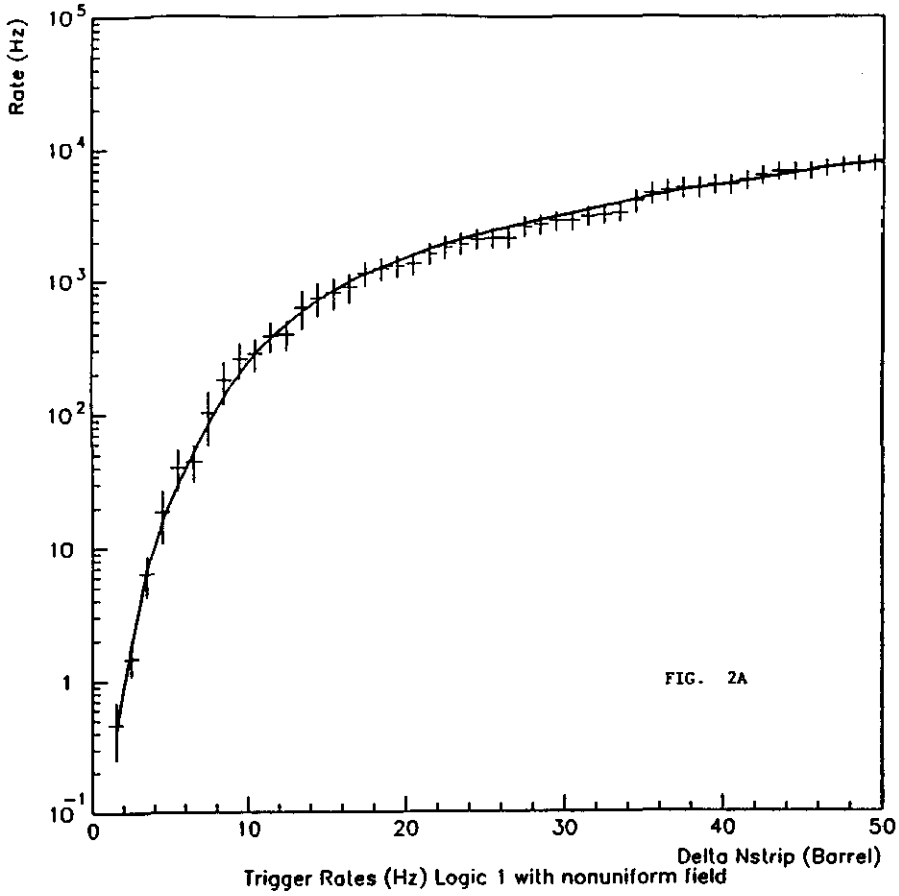

Trigger Rates (Hz) Logic 1 with nonuniform field

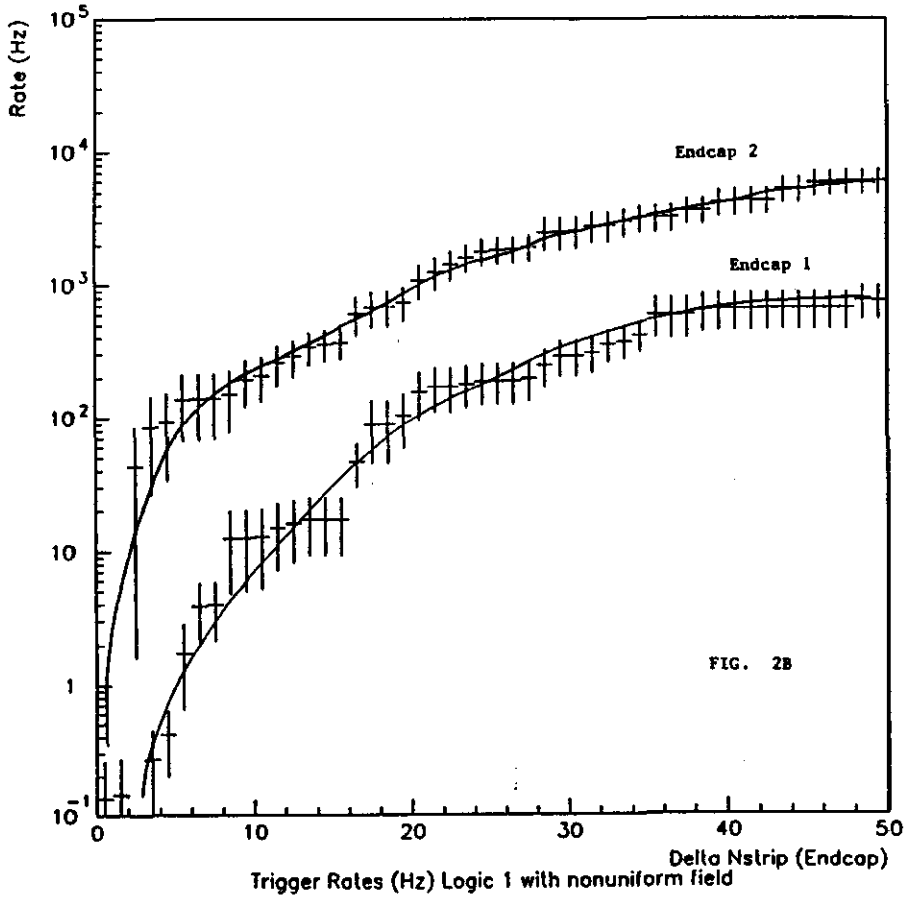

Trigger Rates (Hz) Logic 1 with nonuniform field

(3) *"The collaboration has not yet demonstrated that RPCs and LSDTs are suitable choices for muon detection."*

It is one of the missions of the R&D program outlined above to investigate just these technologies. At the present time, no technology has demonstrated its suitability for the muon system. Both the RPCs [2.1] and the LSDTs [2.2] potentially have several attractive features which make them interesting candidates for the barrel region. We believe them to be worthy of further study.

Summary of RPC Properties:

Function in GEM Muon System:	Barrel: beam crossing time tag Level 1 muon trigger Z-coordinate tracking roads for later analysis
Construction:	dual 2 mm gap 1.3 cm strips - bend plane 4 to 9 cm strips - nonbend plane
Properties:	
plate bulk resistivity	10^{11} Ω cm (typical)
electric field	40 kV/cm
pulse charge	100 pC
pulse risetime	< 3 ns
pulse duration	< 50 ns FWHH
discharge area	0.1 cm^2
recovery time	10 ms
pulse jitter	< 1.4 ns (measured)
Gas	A(2%):Freon(2%):CO_2(86%)
Rate limitation	50 to 100 Hz/cm^2
Efficiency	> 96 % over $1x2m^2$
Random counting rate	5 to 10 x cosmic rate

<u>References:</u>

[3.1] "Descoped SSC R&D Proposal for the GEM Muon Beam Tagging Trigger and Z-Coordinate Measuring System using Resistive Plate Counters", C. Wuest, I. Pless, et al.

[3.2] "Progress in Resistive Plate Chambers", R. Cardarelli, et al. NIM <u>A263</u>,20, (1988).

[3.3] "Study of Muon Triggers and Momentum Reconstruction in a Strong Magnetic Field for a Muon Detector at LHC", M. Della Negra, et al. CERN/DRDC/90-36 (August 1990).

Summary of LSDT Properties:

Function in the GEM Muon System	Barrel: precision sagitta measurement Levels 2 and 3 trigger
Construction	open cathode (top separate) 2.5x2.5 cm^2 cells - 100 μm wire < 1% X0 Al per layer Z-coordinate strips precision wire stringing wire supported every 2 m (typ)
Spatial resolution	100 μm RMS
Pulses	100 mV into 50 Ω 10 ns risetime
Drift time	< 300 ns (typ)
Drift velocity	50 μm/ns (typ)
Gas	A(few %):IB(<10%):CO_2 A(few %):IB(<10%):CO_2:CF_4

Enclosure:

[3.4] "Description of an LSDT Muon System for the GEM Detector", L.S. Osborne, et al. Chapter in the GEM TDR.

(4) *"The thickness of the calorimeter must be sufficient so that the triggering effectiveness will not be compromised by hadron punch-through and thus the system will remain robust at high rate."*

Summary:

Extensive Monte Carlo studies have been performed which indicate that for a calorimeter thickness of greater than 12 λ in the barrel region the charged particle rate in the first super-layer of the muon system is dominated by prompt leptons from the primary vertex, and hadron decay in the central tracker and calorimeter. The hadron punch-through is smaller by a factor of 2.

In the endcap region the particle rate increases quite rapidly as the polar angle decreases. Owing to the energy spectrum of the punch-throughs and the prompt muons, and the geometry of the calorimeter and inner tracker, we find that the charged particle rate is decreased with some efficiency up to 14 λ, but thereafter with diminishing returns. Hence in the forward direction a calorimeter of 14 λ will keep the occupancy low and the trigger operational.

Introduction:

A very important consideration in the design optimization of the muon spectrometer is the level of backgrounds from hadron punch-through and decay. These backgrounds not only affect the ability to observe signals from rare processes at the SSC, but also the ability to form a low-rate muon trigger. An outstanding issue which must be understood before embarking on the construction of the muon spectrometer is the minimum hadron absorber thickness demanded by SSC physics needs. This is particularly important in the GEM detector where all the absorbing material lies inside of the muon system as expensive calorimetry. The thickness of hadron absorber therefore sets the scale in size and cost for both the muon spectrometer and the calorimeter if more depth is required for punch-through suppression than is required for good hadron energy resolution (9-10 λ [2]). In this era of "design to cost" it is therefore very important to study and determine the calorimeter thickness necessary to effectively trigger, identify, and measure muons of physics interest while not overwhelming the GEM detector budget. The current design requirements for calorimeter thickness in the GEM baseline I [2] are 12 λ in the barrel region and 14 λ in the endcap region.

The depth of calorimetry before the muon system was an issue raised by the PAC in its report on the GEM LOI and has been the focus of considerable simulation effort over the past months. Simulation studies of particle rates in the muon spectrometer as a function of calorimeter thickness were performed for both the barrel and endcap regions. For the study, TWOJET events were generated via ISAJET and particle rates outside the calorimeter were determined including prompt muons from quark leptonic decays, muons π/K decays occurring in the inner tracking region, and hadron induced charged particles exiting the calorimeter (punch-through). Neutrons and associated gammas were not considered in the studies. Additional thickness of calorimeter for neutron suppression is not cost effective. Other means to suppress the neutron rate exist ; for example, additional layers of polyethylene doped with Boron. Design requirements for the suppression of the neutron background are currently being studied.

To estimate the punch-through rate, the PCHTHR code [3] was utilized.The PCHTHR code produces 4-vectors for the punch-through particles and was derived from GEANT simulation of single pions of various momenta incident on iron absorber of various thickness. The

resultant punch-through showers were recorded and probability tables prepared for the punch-through probability, shower multiplicity, individual particle type, momentum, spatial position, and exiting angle relative to the incident track. The probability tables are incorporated into a single subroutine which is called for stable hadrons particles incident on the calorimeter. The PCHTHR code, while superior to simple parametrizations, assumes that a lambda of Fe is equivalent to a lambda of any material. It has been found from GEANT simulation that Pb has slightly more absorptive power per lambda than solid Fe. The PCHTHR code also assumes no magnetic field in the calorimeter material. The addition of a non zero magnetic field in the calorimeter should serve to suppress the punch-through. The PCHTHR code can thus be considered a conservative estimate of the punch-through background.

Barrel Region [4]:

For the muon system, the limiting factor will be the rate of particles in the first muon detector layers after the calorimeter. This rate should be sufficiently low that a Level 1 muon trigger can be formed which is efficient for muons of interest, namely muons from Ws and Zs (about 10--20GeV/c in transverse momentum). In considering criteria for evaluating the calorimeter depth, it is useful to consider the source of the particles exiting the calorimeter. Charged particles entering the barrel muon system will be mainly of three sources: 1) Prompt muons from quark decays, 2) the muons from π/K decays in the inner tracking volume before the calorimeter, and 3) the hadron-induced particles leaking out the back of the calorimeter (hadron punch-through. The rate of prompt muons is irreducible. Muons from π/K decays are suppressed in GEM by the very compact tracking region (less than half the size of SDC's). The first two sources produced muons before entering the calorimeter and so the calorimeter material serves merely to range out these muons. Therefore the reason for calorimeter depth beyond that needed for good hadron energy resolution is to reduce the rate of hadron punch-through. Assuming therefore that the calorimeter is not already so thick that it serves only to range muons, then the following two criteria can be defined by which we can gauge the benefits of additional calorimeter thickness:

Criteria 1: The overall particle rate exiting the calorimeter from hadron punch-through should be much less than the sum of the rates from prompt muons and muons from π/K decays.

Criteria 2: The rate of particles with transverse momentum above a trigger threshold from hadron punch-through should be much less than that from prompt muons and muons from π/K decays.

For the determination of particles rates after the calorimeter, TWOJET events have been generated using the ISAJET generator in the JET Pt range 4 GeV/c < Pt < 5000 GeV/c and top quark mass Mt =140 GeV/c^2. The event sample was compiled in various Pt subintervals in order to have increased statistics at high Pt while generating the entire SSC pp cross section (140 mb) The events were weighted by the cross section when filling the histograms. Several runs were made over the same 150k event sample with a calorimeter of constant 6, 8, 10, 12, 14, and 16 lambda thickness. The generated particles pass through a fast simulation of a tracking volume and calorimeter. Muon energy losses were considered. Decays in flight of π/K were calculated in a tracking volume 0.75m in radius and 4.4m in length. Muons from the decays were assumed to be in the direction of the parent hadron with energy thrown according to the kinematics of the two body decays.

Figure 1 shows for two rapidity intervals, a) $|\eta|< 0.5$, and b) $1.0<|\eta|<1.5$, the total rate of charged particles exiting the calorimeter as a function of calorimeter depth (solid curve) and

the rate from prompt muons $+\pi/K$ decays in the tracker (dashed curve) and punch-through particles (dot-dashed curve). Figure 2 shows the rate of charged particles of transverse momenta greater than 10 GeV/c for the same two rapidity intervals. If *criteria* 1 is satisfied when the fraction of the total rate from hadron punch-through is less 1/3, then it can be seen figure 1, that criteria 1 is satisfied for 12 λ and higher of calorimeter depth. Even if the punch-through rate were uncertain to a factor of 2 and the dot-dashed curve in figure 2 were revised upward, the punch-through rate would still be less than 50% of the total rate. Considering only particles with Pt >10 GeV/c in figure 2, the rate coming from prompt muons dominates for calorimeter depths of 10 λ and above. So, assuming that we satisfy *Criteria 2* if the fraction of the particle rate above 10 GeV/c from hadron punch-through is less than 1/3 of the total, then *Criteria 2 is* satisfied in the barrel region for 10 λ and higher calorimeter depth.

Table 1 summarizes the calorimeter depth requirements resulting from *Criteria* 1 and 2. To satisfy all criteria considered requires a calorimeter of minimum 12 λ depth over the barrel region. In the next section the evaluation of the calorimeter depth in the endcap region will be described.

Table 1: Summary of Depth Requirements

Criteria	Depth at $\eta = 0$	Depth at $\eta = 1.5$
1	12 λ	12 λ
2	10 λ	10 λ

In the barrel region, the trigger components proposed for GEM are RPCs. These devices have been tested recently at CERN [5] and found to handle rates up to 50Hz/cm^2 without significant loss of efficiency. Figure 3 shows the rate per unit area (Hz/cm^2) at 10^{33}cm^{-2}/s expected in the first layer of the barrel muon system for different calorimeter depths. The first layer is positioned at R=370cm. At 10^{34}cm^{-2}/s luminosity the maximum rate of muon system hits from charged particles would be about 6Hz at η =1.3. This rate is at least an order of magnitude below the limiting rate for the RPCs and the barrel muon system is robust.

Consideration has not been given to detailed muon system performance requirements such as muon identification, triggering, and momentum measurement These are considered in later sections.

Endcap Region [6]:

In this section we examine the rate of charged particles emerging from the calorimeter and entering the first super-layer (SL1) of the muon system in the endcap region as a function of the calorimeter depth. The other two super-layers are exposed to lower rates of particles as soft charged particles, which make it to SL1, will bend and not reach the others. Although, these particles may turn around and hit SL1 for a second time. From charged particles fluxes, the expected chamber occupancies can be calculated. We also study the composition and Pt distribution of exiting particles as a function of calorimeter depth. From these considerations, we draw conclusions on the required calorimeter depth in the endcap region.

The Hit-level Monte Carlo simulation package was used for this study. This package provided trajectories of muons in the muon system in the form of hits in chamber layers. The muon system geometry was based on the parameters of the Baseline I [2] . The solenoidal field of

0.8 T was properly simulated including the non-uniformity in the forward regions due to the presence of the flux concentrator.

QCD two jet events were generated using ISAJET in the jet Pt range of 4 GeV/c to 2 TeV/c. Decay in flight of π/K mesons inside the inner tracker volume were simulated using GEANT. Tracks with $|\eta| < 3$ were then passed through a calorimeter modeled in depth as shown in Fig. 4. Four different depths were considered for this study: flat 10 λ in the barrel and endcap, 10 λ in the barrel increasing to 12 in the endcap as in Fig. 4, similarly 12 to 14 and 14 to 16. The material was a homogeneous mixture of copper and liquid argon for the central and endcap calorimeters. It should be noted that, unlike muons which passed through a full GEANT simulation of the calorimeter, the passage of hadrons was simulated using the PCHTHR routine [3], which assumed iron as the absorber material and no magnetic field in the calorimeter.

Tracks leaving the calorimeter were marked by hits placed at the front face of SL1, which is a cylinder of radius 366 cm and of half length (along Z) 566 cm. These dimensions include 10 cm of boron doped polyethylene for neutron shield and 6 cm of air for stay clear area, which were simulated by GEANT.

Fig. 5 shows the flux of charged particles (Hz/cm^2) at SL1 as a function of rapidity. Unless otherwise stated, the rates are calculated for a luminosity of 10^{33} cm^{-2} s^{-1}. The four plots give the rates for the four calorimeter depths mentioned above. The turn-around at $|\eta|=2.5$ is due to excluding the tracks with polar angles smaller than the minimum angle covered by SL1 (about 9 degrees). This can be seen from Fig. 6, which shows the charged particle flux as a function of theta. The fluxes change by more than two orders of magnitude between $|\eta|=0.0$ and $|\eta|=2.5$. We note that the rates in the barrel region are about a factor of 3 lower than those shown in Section 2.1. There are differences between the two calculations which may account for this discrepancy, however, we regard this as a measure of the precision of these calculations. The agreement, within a factor of 3, between the two rate calculations presented in this note, as well as that described in the LoI [8], indicates that these rates have an uncertainty of a factor of 3.

We further examine the rates, this time in terms of the particle composition. Fig. 7 shows the charged particle rate (Hz) in the forward endcaps as a function of track ID (GEANT convention) for the four thicknesses 10, 12, 14, and 16 λ. Note that exiting particles are predominantly electrons and muons for all depths. Electrons are always present and have a rather soft Pt distribution, indicating that they are produced in the last layer of the calorimeter, hence leaking out. In this sense, additional absorber material will not help reduce the rate of exiting electrons.

Next, we examine the rates in terms of the source of charged particles exiting the calorimeter. Fig. 8 shows the rate (in Hz) as a function of rapidity for prompt muons, decay muons, punch-through particles (including secondary muons), and muon induced showers (excluding the muon itself). The calorimeter thickness follows the 12 to 14 l model. Notice that the rapidity distribution of prompt muons is relatively flat, whereas the punch-through rate increases steadily with increasing rapidity, and the decay rate increases very rapidly in the endcap region. These features are true of all calorimeter thicknesses considered in this study.

In Fig. 9, we plot the charged particle rate versus calorimeter thickness for two rapidity intervals $1.5 < |\eta| < 2.0$ and $2.0 < |\eta| < 2.5$, and for a luminosity of 10^{33} cm^{-2}s^{-1}. The contributions from prompt and decay muons (prompt + decay) and from punch-through and muon induced showers (PCHTHR + MuShower) are shown separately. The prompt and decay

muons dominate the total rate for all thicknesses in the $2.0 < |\eta| < 2.5$ region. In fact, it is the decay muons that have the largest rate, simply due to the larger decay path available to π/K mesons in the forward regions. Here, unlike in the barrel, the punch-through rate and where it falls below the real muon rate are not the criteria for determining the necessary depth of the calorimeter. The total rate and chamber occupancy should rather be used.

Table 2 summarizes the occupancies calculated for a single strip (e.g. Cathode Strip Chamber technology) of size typical of those in the forward region nearest to the beam and for a luminosity of 10^{34} $cm^{-2}s^{-1}$. The Baseline I design requires an occupancy of < 3% at this luminosity. A more relevant number may be the 3- or 5-strip occupancy, as a single particle may induce charge on 3 to 5 strips. Assuming 3 strips, a minimum calorimeter depth of 14 λ is clearly required to be able to cope with the rates at the highest SSC luminosities, i.e. an occupancy < 3%. As mentioned before, there is an uncertainty of a factor of 3 (upward!) in these rate calculations. Therefore, 14 λ should be considered as an absolute minimum calorimeter depth required in the endcap region. In fact, one could argue that a conservative estimate for the necessary depth should be 16 λ, however, note that the decrease in rate from 14 to 16 λ is rather small. Therefore, further rate reduction with increasing calorimeter depth beyond 14 λ does not seem to be appropriate and cost effective. One should rather improve muon chamber rate capability to insure its robustness at higher luminosities.

Table 2. Endcap Chamber Occupancy versus Calorimeter Depth

	CALORIMETER DEPTH			
CHARGED PARTICLE RATE	10	12	14	16 λ
$2.0 < \|\eta\| < 2.5$				
$L = 10^{34}$ $cm^{-2}s^{-1}$	390	280	160	110 Hz
STRIP SIZE = 30 X 0.5 cm^2	5850	4200	2400	1650 Hz
SINGLE STRIP OCCUPANCY 3 μsec delay	1.8%	1.3%	0.7%	0.5 %

It should be noted that muon identification and pattern recognition, as well as triggering and momentum measurement studies, may put further constraints on rates in the forward region. Any rate requirements arrived from these studies should be dealt with within the muon system components. We state again that additional calorimetry beyond 14 λ does not result in significant rate reduction; it only amounts to an expensive way of ranging out real muons.

References:

[1] Hadronic Calorimeter resolution vs. λ.
[2] GEM Baseline 1, GEM TN92-76, April 23, 1992.
[3] See for example transparencies talk given by R. McNeil at the GEM Collaboration meeting July 17, 1991.
[4] R. McNeil, " How Thick should the GEM Barrel Calorimeter Be," GEM TN92-68, March 10,1992.
[5] RD5 Collaboration, Status Report, CERN/DRDC/91-53 1992.
[6] M. Mohammadi, to be submitted as a GEM Note.
[7] GEM Letter of Intent, SSCL-SR-1184, GEM TN-92-49, Nov. 30, 1992.

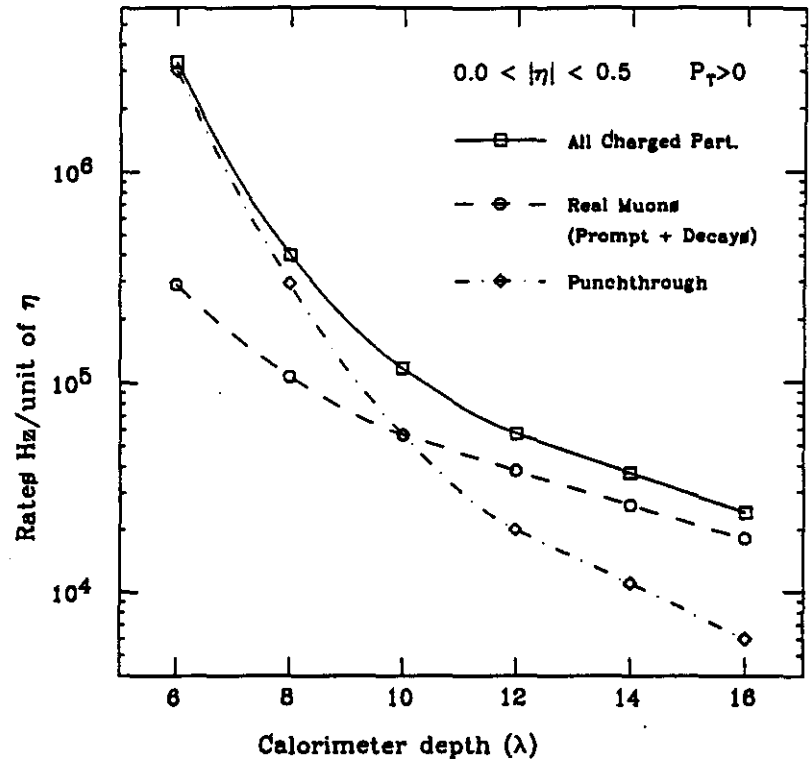

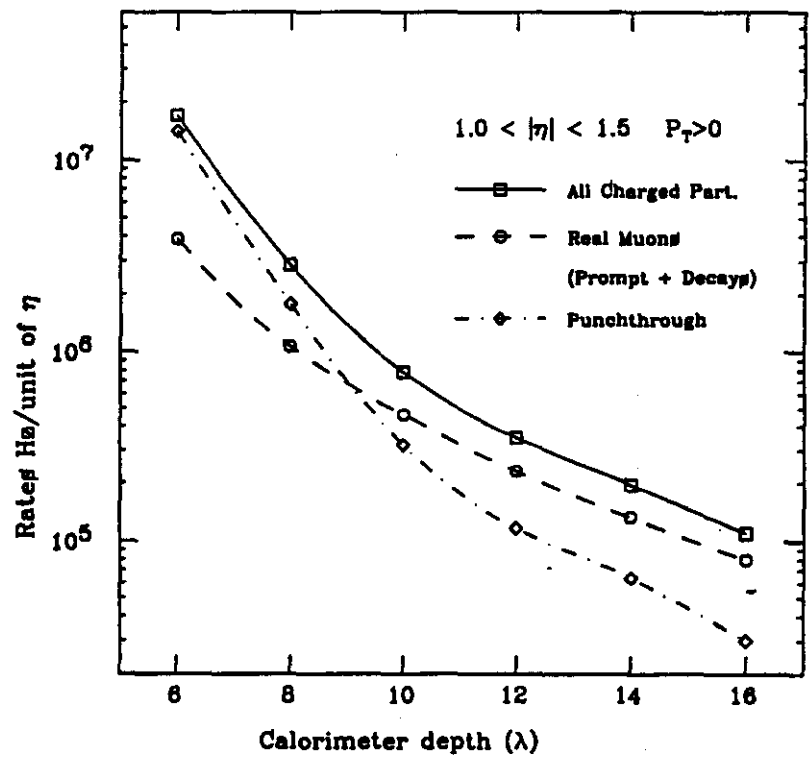

Figure 1. The rate of all Charged particles rates at 10^33 cm^-2/s SSC luminosity exiting the barrel calorimeter for a) |eta|<0.5 and b) 1.0<|eta|<1.5 rapidity intervals. The solid curve is the total rate, the dashed curve is the rate from prompt muons and pi/K decays in the inner tracking region, and the dot-dashed curve is the rate from hadron punchthrough.

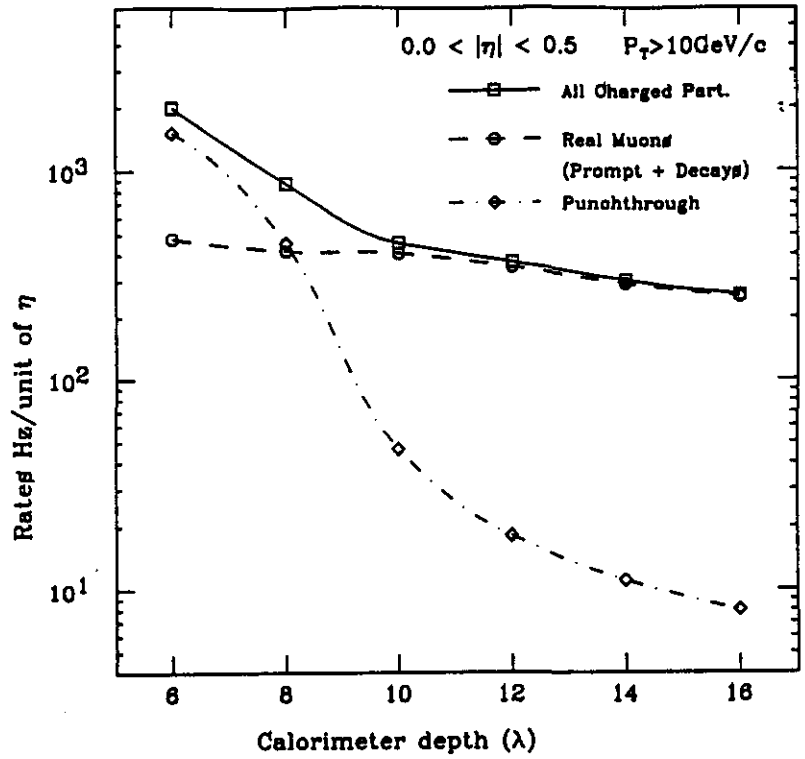

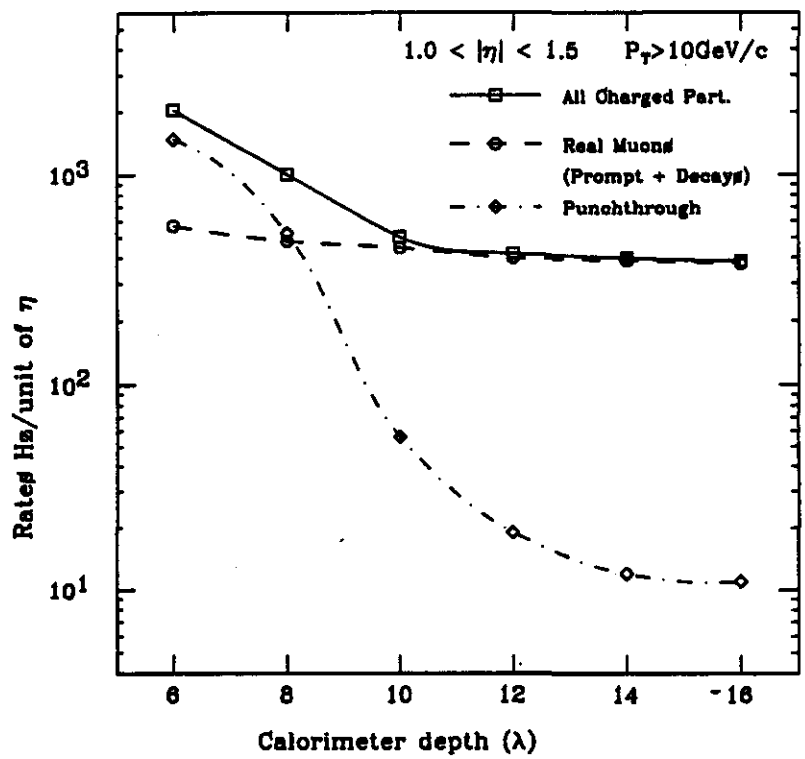

Figure 2. The rate of Charged particles with transverse momentum above 10GeV/c at 10^33 cm^-2/s SSC Luminosity exiting the barrel calorimeter for a) |eta|<0.5 and b) 1.0<|eta|<1.5 rapidity intervals. The solid curve is the total rate, the dashed curve is the rate from prompt muons and pi/K decays in the inner tracking region, and the dot-dashed curve is the rate from hadron punchthrough.

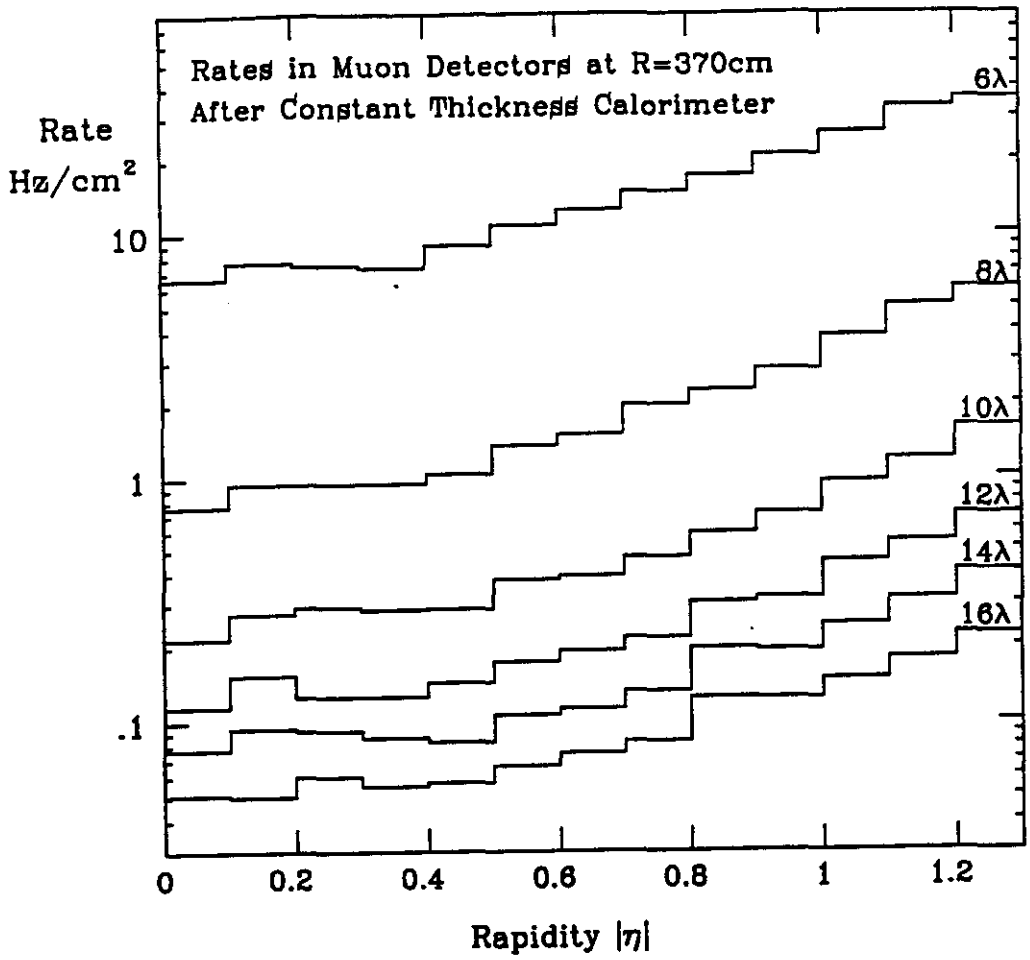

Figure 3. The hit occupancy in the first layer of the GEM barrel muon system at R-370cm at 10^33 cm^-2/s SSC luminosity as a function of rapidity for various constant calorimeter thicknesses.

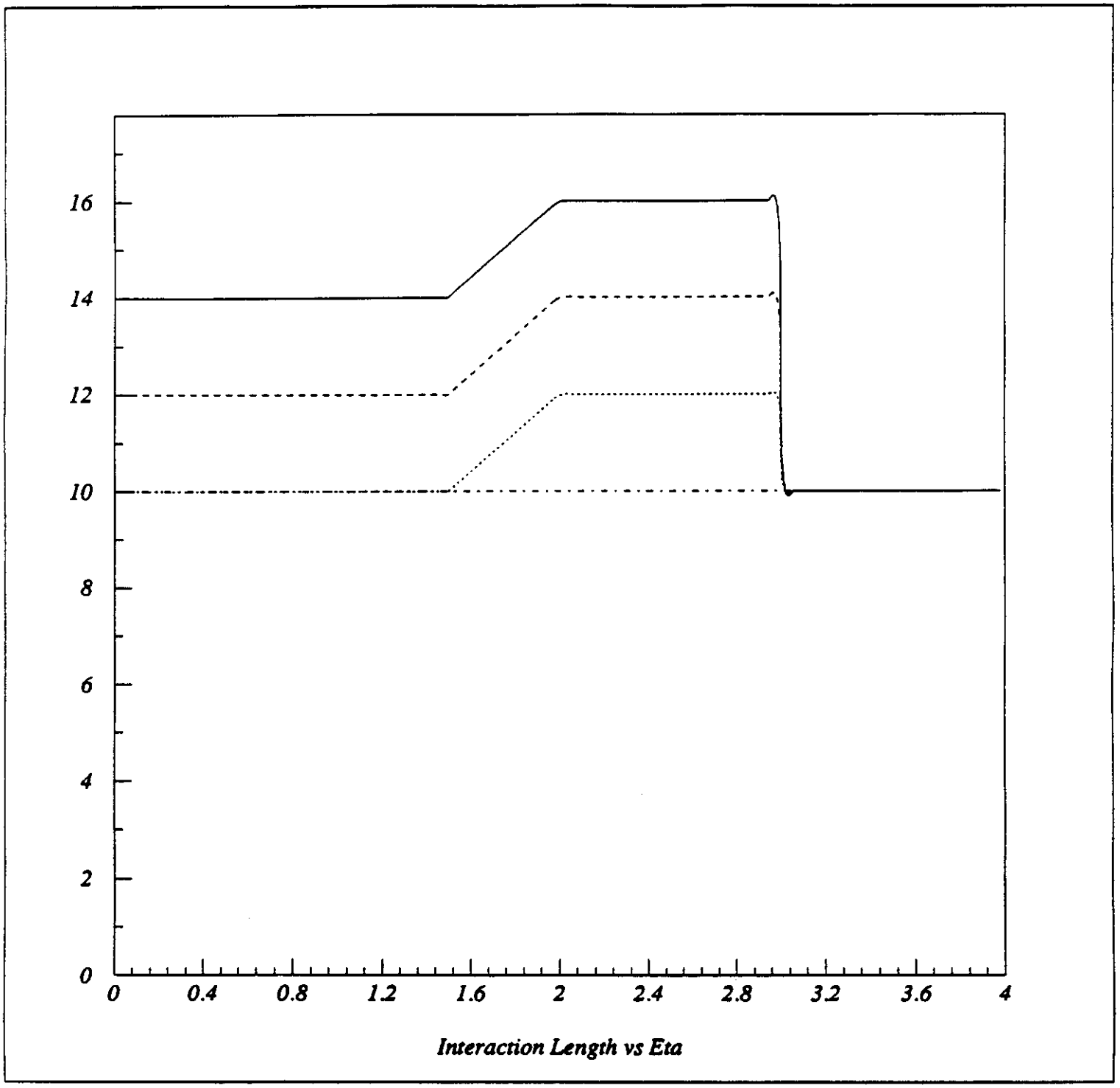

Fig. 4 - Interaction length versus rapidity representing the calorimeter depth model used in the Hit-level Monte Carlo.

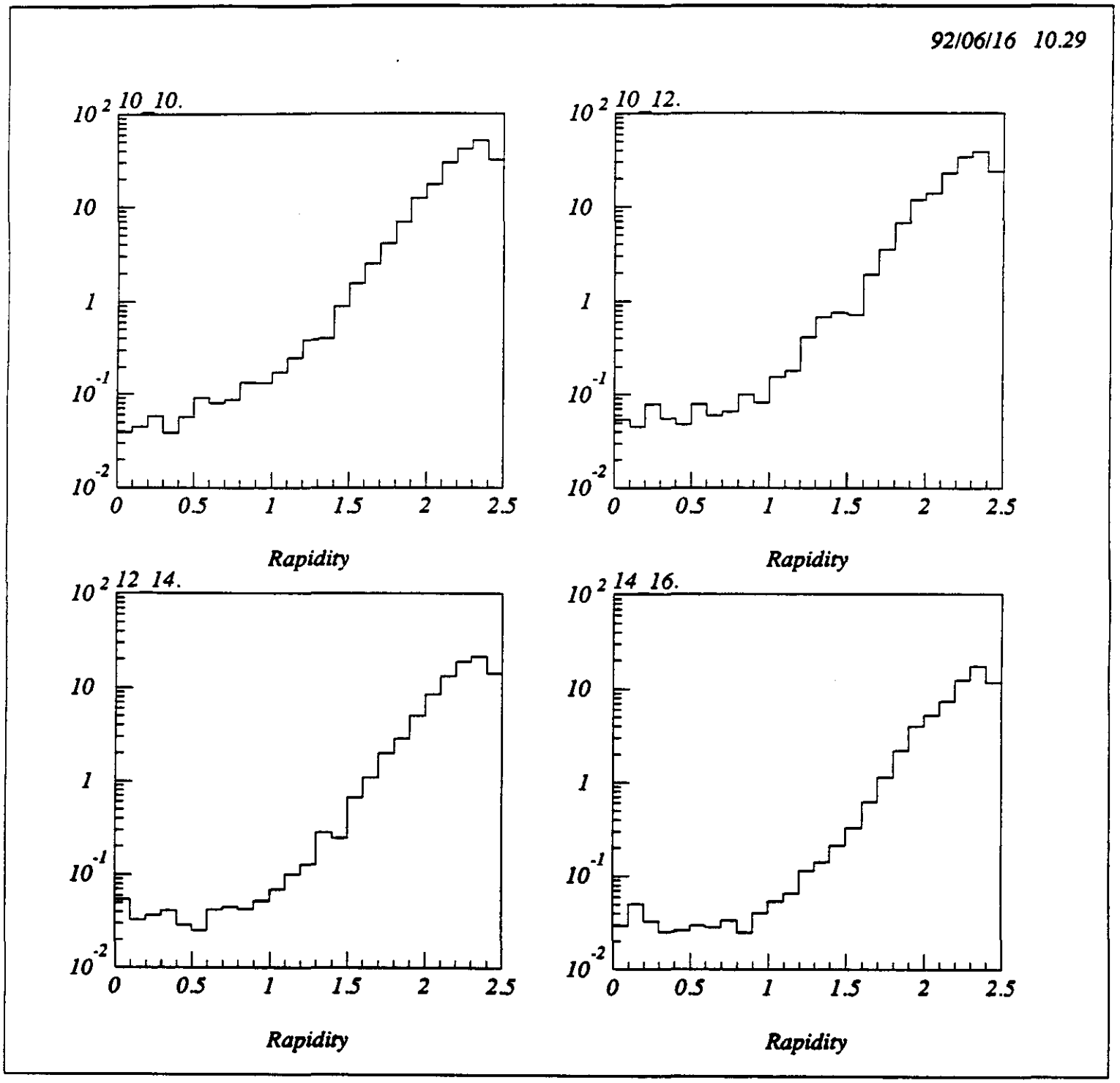

Fig. 5 - Charged particle flux (Hz/cm^2) versus rapidity for four calorimeter depths 10-10, 10-12, 12-14, and 14-16 lambda in the barrel-endcap. (L=10^33 cm^-2 s^-1)

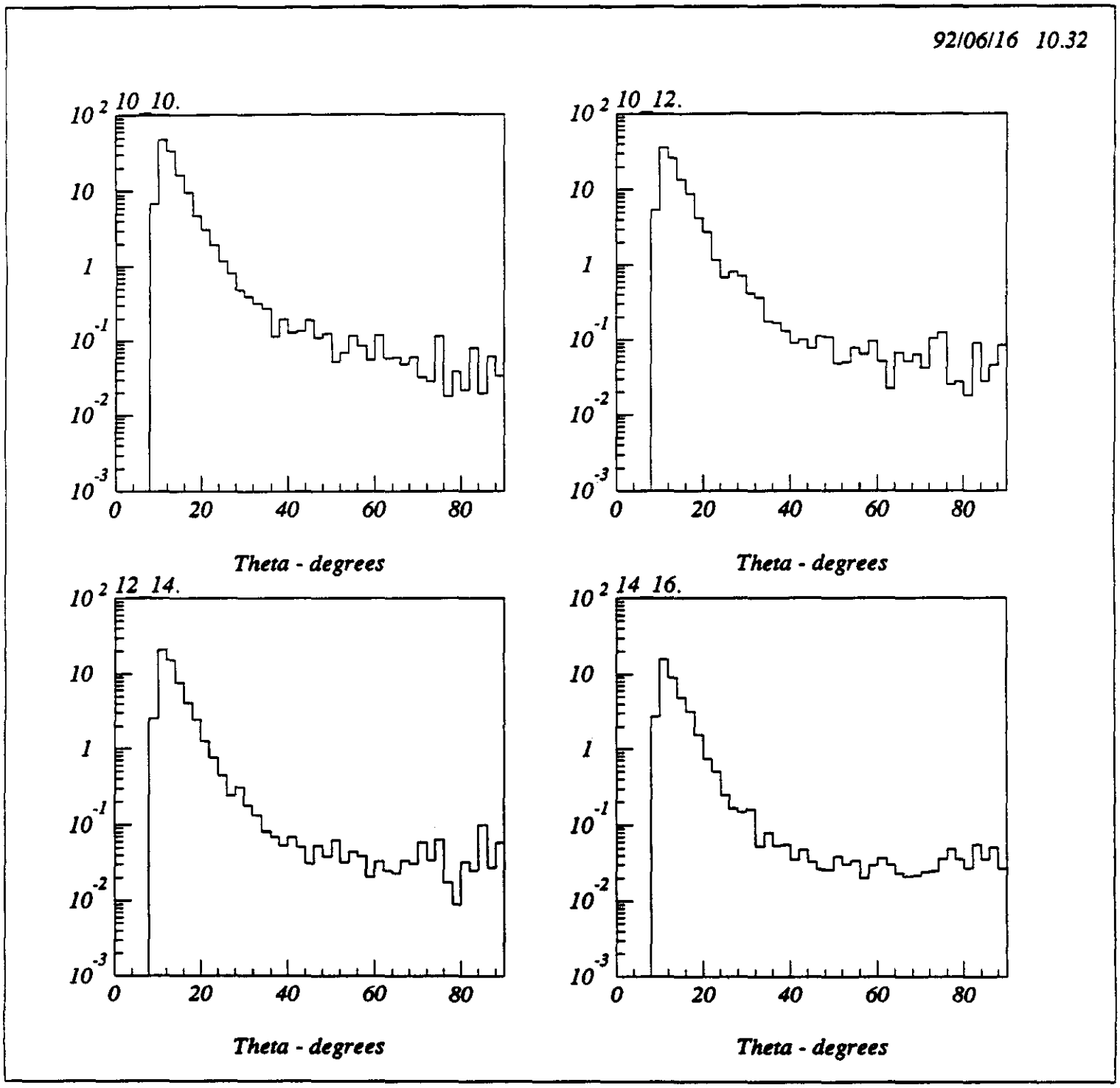

Fig. 6 - Charged particle flux (Hz/cm^2) versus polar angle theta (degrees) for four calorimeter depths. (L=10^33 cm^-2 s^-1)

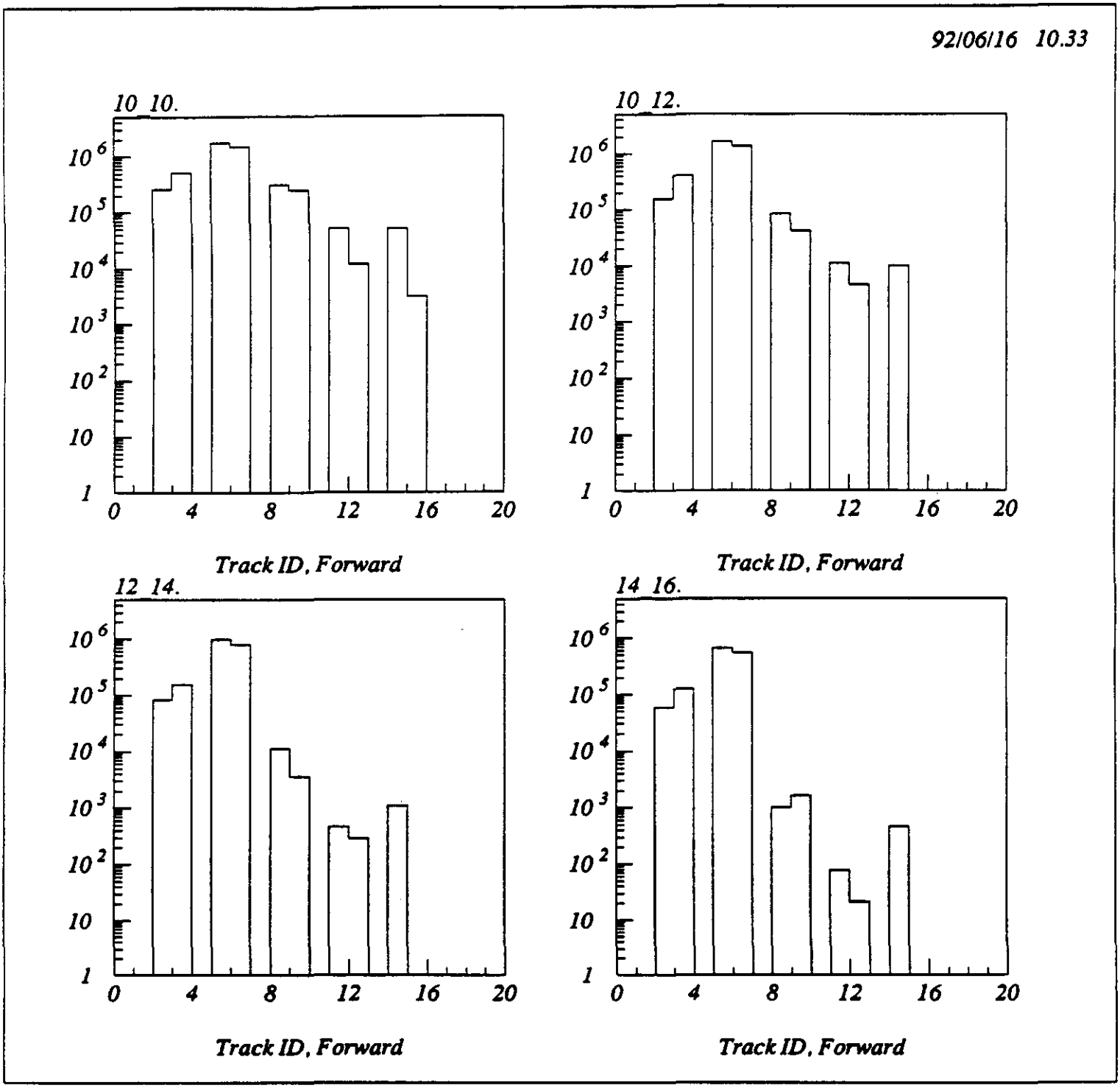

Fig. 7 - Charged particle rate (Hz) in the forward endcap versus track ID for four calorimeter depths. The ID's are: 2 or 3 electrons, 5 or 6 muons, 8 or 9 pions, 11 or 12 kaons, and 15 or 16 protons. (L=10^33 cm^-2 s^-1)

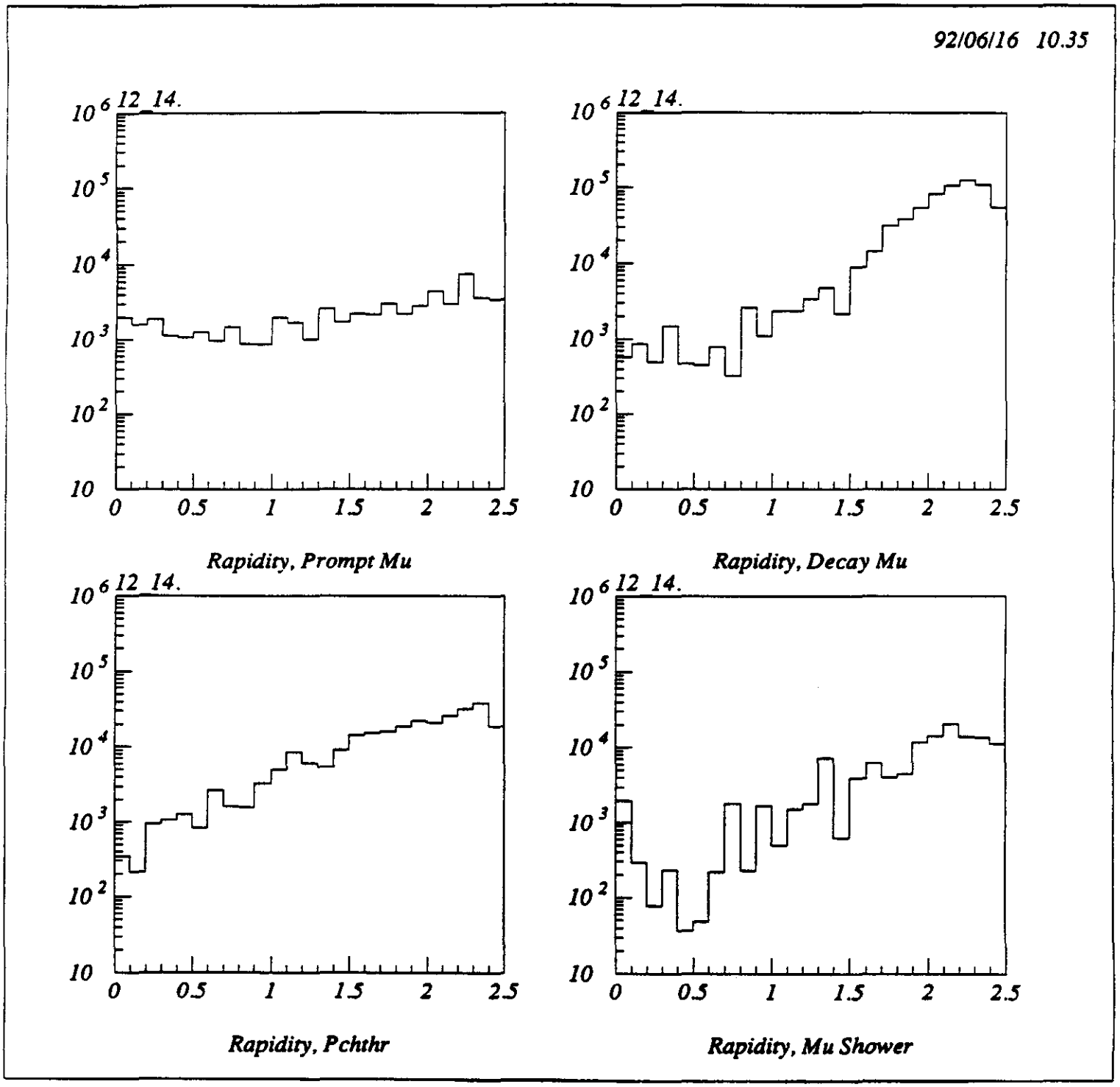

Fig. 8 - Charged particle rate (Hz) versus rapidity for prompt muons, decay muons, punchthrough particles and muon induced showers for a calorimeter depth of 12-14 lambda in the barrel-endcap. (L=10^33 cm^-2 s^-1)

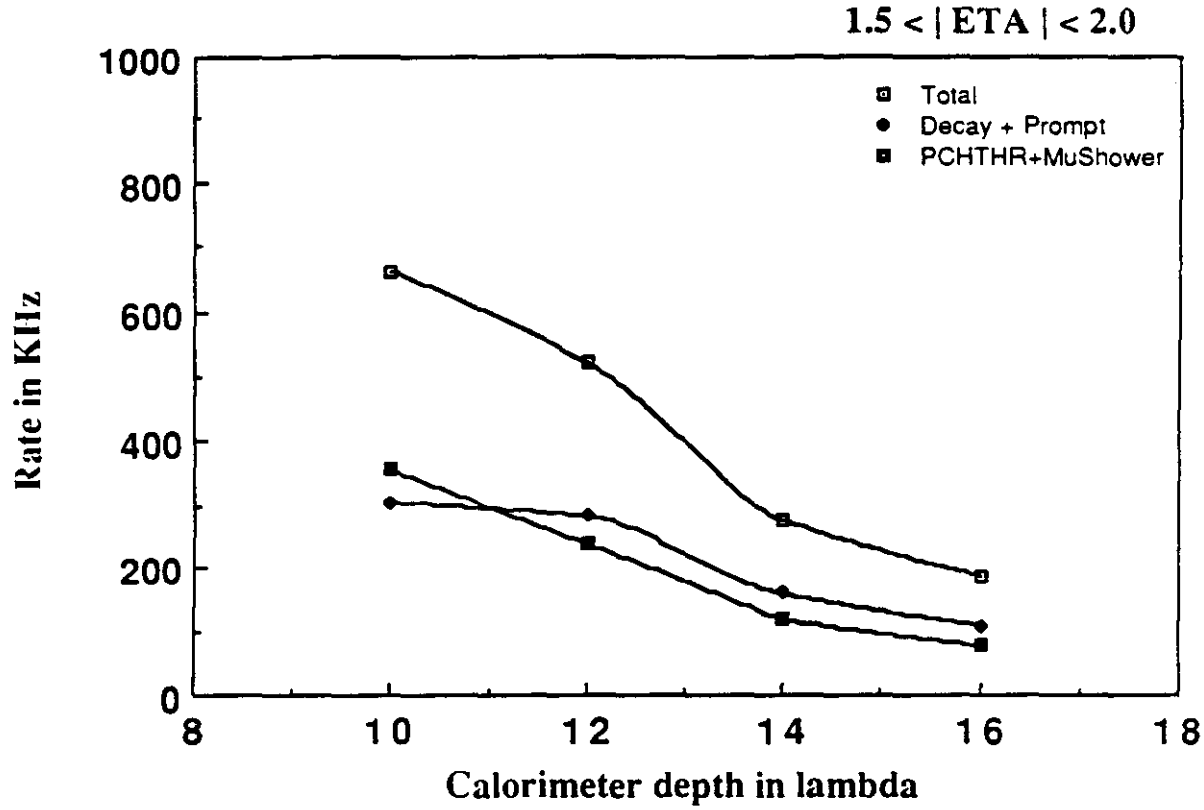

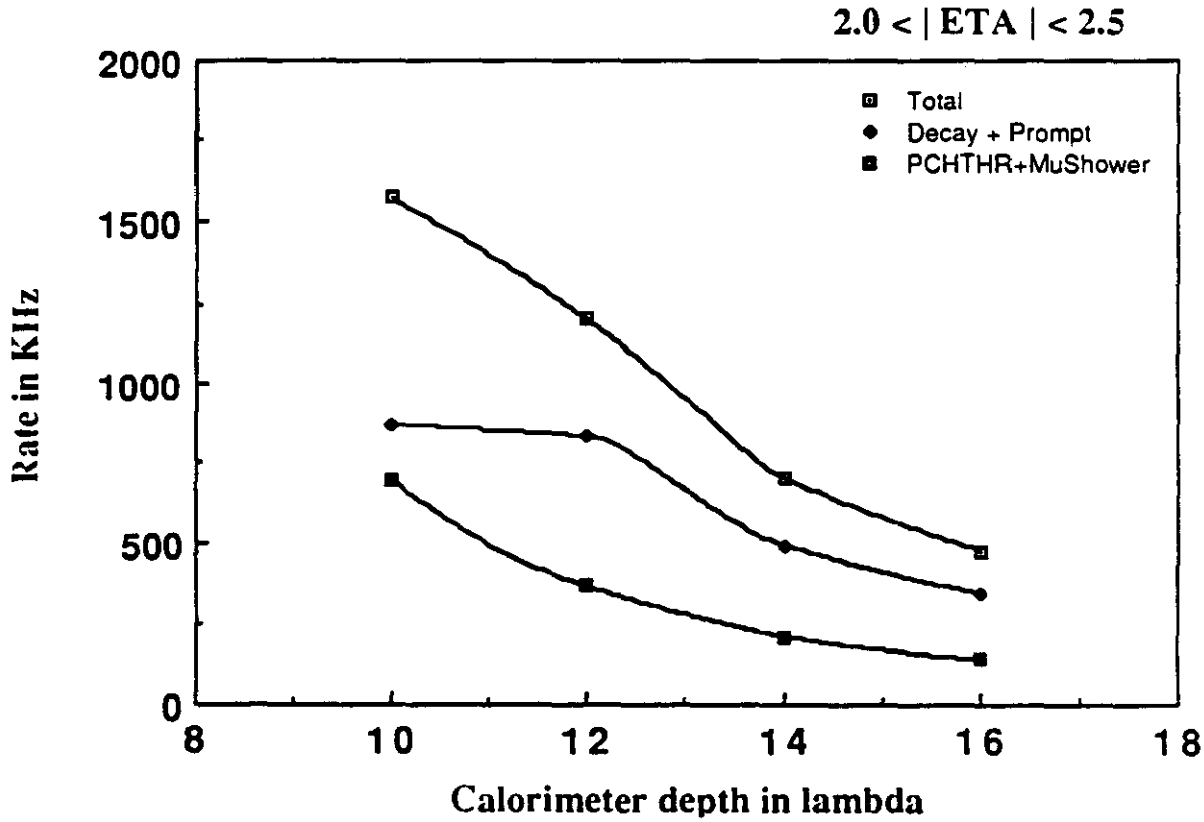

Fig. 9 - Charged particle rate (kHz) versus calorimeter depth (lambda) for two rapidity intervals 1.5<|eta|<2.0 and 2.0<|eta|<2.5. (L=10^33 cm^-2 s^-1)

(5) *There are three levels of alignment: wires, chambers, and chamber packages in the global frame. Each presents its own challenge and will require considerable engineering and significant interaction among the physicists and engineering groups."*

The alignment of the muon chambers is a key aspect of the GEM Muon System design. Since the sagitta of a Pt = 500 GeV/c is only 1.5 mm, which we intend to measure to 5%, the overall error budget in this case is only 75 μm. This requires the chambers to have good single layer resolution, of order 100 μm, that they have small random errors of the placement of the wires/strips of order 50 μm, and most demandingly, that the super-layers be aligned to 25 μm. The alignment concepts [5.1] and requirements [5.2], [5.3] are appended to this report.

Summary of Alignment Requirements:

Item	Value	Reduction Factor for N chambers/SL
Chamber resolution	100 μm (typ)/layer B	$1/\sqrt{N}$
	75 μm (typ]/layer EC	$1/\sqrt{N}$
Relative alignment within super-layer	50 μm	$1/\sqrt{N}$
Relative alignment of super-layers	25 μm	none

Enclosures:

[5.1] "Some Alignment Concepts for the GEM Muon Array", J. Paradiso, GEM-TN-92-124.

[5.2] "Alignment Requirements for the GEM Muon Detector", J. Paradiso, GEM-TN-92-125.

Reference:

[5.3] "Alignment Requirements to Muon System", G. Mitselmakher and A. Zhukov, GEM-TN-92-120.

Enclosure [1.1]

GEM MUON SYSTEM R&D/ENGINEERING PLAN October 1991

Note added [6/28/92]: The R&D task description is according to present plan, but the manpower has changed somewhat.

(1) Introduction

The GEM muon system has the following specifications:

Pseudorapidity coverage:	
Barrel:	$0 < \eta < 1.3$
Endcap:	$1.3 < \eta < 2.5$
Momentum resolution at small momentum:	
Barrel (avg. over rapidity):	1.0%
Endcap (avg. over rapidity):	1.2%
Momentum resolution at large momentum:	
Barrel (avg. over rapidity):	7% p/TeV
Endcap (avg. over rapidity):	7% p/TeV
Radiation lengths in middle module:	
Barrel:	< 10%
Endcap:	< 8%
Systematic sagitta error:	25 μm
Time resolution:	< 5 ns
Level 1 trigger latency time:	< 3 μs
Level 2 trigger latency time:	< 100 μs
Total muon system cost:	< $130M

To achieve these goals the GEM Collaboration has selected the following design for the muon system:

BARREL

Metallic drift tubes to be used for momentum determination and level 2 trigger.

Resistive Plate Chambers (RPC's) to be used for level 1 trigger, bunch crossing tag, and z determination.

ENDCAP

Cathode Strip Chambers (CSC's) to be used for momentum determination, bunch crossing tag, level 1 and 2 triggers, and r determination.

It will be necessary for the barrel drift tubes to achieve a single wire resolution of 100 μm and the CSC's to achieve a single plane resolution of 75 μm to satisfy the above specifications. Two types of drift tubes are under consideration for the barrel: Pressurized Drift Tubes (PDT's), and open profile Limited Streamer Drift Tubes (LSDT's).

The GEM Muon Group consists of 132 physicists and engineers from 21 institutions and 4 countries (USA, China, USSR, Romania). This Group has organized itself into 7 Subgroups to carry out the engineering and R&D activities necessary to bring the current muon system concept to a fully developed design for the GEM Technical Proposal (TP) to be submitted in November 1992. The Subgroups are:

SUBGROUP	DESCRIPTION
CSC	Cathode Strip Chamber Subgroup; coordinated by V. Polychronakos, Brookhaven National Lab.
LSDT	Limited Streamer Drift Tube Subgroup; coordinated bu L. Osborne, MIT
PDT	Pressurized Drift Tube Subgroup; coordinated by S. Ahlen, Boston Univ.
RPC	Resistive Plate Chamber Subgroup; coordinated by I. Pless, MIT, and C. Wuest, Lawrence Livermore National Lab.
ENG	Engineering Subgroup; coordinated by F. Nimblett, Draper Lab.
TTR	Texas Test Rig Subgroup; coordinated by G. Mitselmakher, SSC Lab.
SCARF	Streamer Chamber Assembly and Research Facility Subgroup; coordinated by R. Weinstein, Univ. of Houston

The membership, tasks, and budgets for the Subgroups will be described in subsequent sections. In the next section we give a brief and general overview.

(2) Major Goals for FY92 and the Budget Breakdown Between Subgroups

For the time from December 1991 to September 1992 it will be necessary to complete the following jobs:

i) Decide between PDT's and LSDT's for the barrel. This will be based on tests of modules to be installed in the Texas Test Rig (TTR) which will be built at the SSC Lab. Tests will be done with a hardened cosmic ray spectrum and the decision will be based on cost and performance. Critical issues are alignability, resolution per wire, material thickness, operation stability and safety, and cost and difficulty of assembly.

ii) Build and test a prototype CSC to substantiate preliminary conclusions that this device will perform up to specifications for the endcaps. Critical issues are performance in magnetic fields, channel to channel uniformity and calibratibility, material thickness, and electronics cost.

iii) Develop a base of experience with the use of RPC's to substantiate preliminary conclusions that this device will perform up to specifications for the barrel. Critical issues are time resolution, noise rate, stability of noise rate, RF noise induced in neigboring drift tube detectors, charged particle rate capabilities, and material thickness. A two prong approach will be followed: evaluation of Italian made RPC's, and the construction and evaluation of small prototypes produced with new plate materials.

iv) Carry out engineering design and cost evaluation for the TP. Critical issues are: (a) alignment at the module level (a module being a set of adjacent tracking layers), the sector level (a sector is a set of 3 modules used to make a sagitta measurement), and globally (knowledge of the interaction point and other detectors relative to the muon system sectors); (b) design of system to monitor alignment; (c) thickness of support materials; (d) geometrical efficiency for muon acceptance; (e) formulation of plans for installing, servicing, and operating muon system over life of experiment; and (f) bottoms up cost determination of muon system.

The requested budget for the muon system engineering and R&D for FY92 is $2.7M. It will be divided as follows among the 7 Subgroups:

SUBGROUP	FY92 BUDGET
CSC	$470k
LSDT	$442k
PDT	$378k
RPC	$260k
ENG	$616k
TTR	$200k
SCARF	$64k
TOTAL	$2,430k

Details of the Subgroup R&D/Engineering plans are in the following sections. They are each broken down into a participant list, an overall plan, a descussion of electronics R&D (beyond the amplifier and shaper level), and a discussion of the plan for integration into the TTR in Spring 1992. The Subgroup budgets are collected in the final section.

(3) CSC Subgroup

Participants: 28 people from 4 institutions.

INSTITUTION	PARTICIPANTS
Brookhaven National Lab. (BNL)	Polychronakos, Radeka, Stephani, Yu, Smith, Rogers, O'Connor, Harder, Rescia, Paffrath
Boston Univ. (BU)	Whitaker, Shank, Johnson, Osborne, Warner, Wilson, Hazen, Orlov, Earle
Oak Ridge National Lab. (ORNL)	Todd, Bauer, Britton, Wintenberg
Leningrad Nuclear Physics Institute (LNPI)	Vorobyov, Prokovief, Terentief, Smirnoff, Gratshef

R&D/ENGINEERING PLAN

For FY92 the CSC R&D plan will emphasize the construction and testing of a full scale prototype similar to a complete, 4-layer module of the final endcap detector. Several other activities will be pursued in parallel. These will address specific questions relating to the CSC technology through Monte Carlo studies and the construction and evaluation of small chambers.

The primary goals of the study of the full scale prototype are:

i) Evaluation of construction techniques;

ii) Determination of resolution performance parameters;

iii) Demonstration of feasibility of monolithic multiplexed readout;

iv) Demonstration of trigger capabilities;

v) Determination of precision of bunch crossing assignment using anode wires;

vi) Evaluation of degradation of resolution as a function of angle of incidence.

The module will consist of four independent chambers of size 2 m x 1.28 m, which corresponds roughly to the largest module for the final design. Each chamber will have 256 readout strips, with a pitch of 5 mm, for a total of 1024 channels. Each channel will be equipped with a hybrid preamplifier matched to the strip capacitance. The signals will be shaped and multiplexed in the AMPLEX monolithic chips. All 1024 channels will be read out by a single custom built CAMAC module. To study the various level 1 trigger algorithms under consideration, 32 channels from each of the 4 planes will be equipped with a second, faster shaper (40 ns FWHM), followed by a discriminator. This corresponds to an area of 2 m x 0.16 m which will be instrumented for trigger studies. The 800 anode wires per plane (with a wire spacing of 2.5 mm) will be grouped into 40 channels per plane providing 5 cm wide elements for the determination of the orthogonal coordinate and assignment of the bunch crossing. These channels will be equipped with hybrid amplifiers and shapers followed by discriminators and 4-wide OR circuits. The 40 OR outputs will be read out with commercial TDC units. Note that these earliest-time-of-arrival measurements using the TDC's are done only to study the bunch crossing assignment ability of the device. TDC's would not be used in the final detector.

The full scale prototype will be built at BNL with participation of all groups. The mechanical design will be done jointly by engineering teams from BU and BNL. Construction of parts for the prototype will be done at BU. The design will be completed by January 1992. The strip readout electronics (including a calibration system) will be built at BNL. Anode readout will be the responsibility of ORNL. The electronics for the 128 channels for the trigger implementation will be done by BU and BNL.

Parallel activities will include:

i) Measurements on various gases to find the optimal mixture with regard to drift velocity and Lorentz angle (BU, LNPI).

ii) Detailed simulations of detector performance (BU, LNPI, BNL).

iii) Construction of several small chambers to study cathode optimization and performance in a magnetic field (BU, LNPI).

ELECTRONICS R&D

Some effort will be devoted to fine tune the parameters of the AMPLEX chip as well as the determination of additional functionality necessary for the chip to provide the level 1 trigger signals. Work will also be required to define an additional digital monolithic circuit for control of the AMPLEX chip (supply of local HOLD, RESET, etc.). Nearly half of BNL's electronic engineering budget, as well as some of the ORNL electronic engineering budget, will be devoted to this activity.

TTR PLAN

The CSC prototype is nearly self sufficient with only one CAMAC slot needed to read out all 1024 cathode strip channels. The additional equipment required (40 TDC channels, 128 latching discriminators, 40 OR circuits) will be borrowed from the BNL High Energy Electronics Pool. Jim

Shank (BU) will be the CSC liason person with the TTR for data acquisition. He will be assisted in hardware questions by Vinnie Polychronakos. Thorough testing of the prototype will be done at the place of construction. When moved to the TTR in Spring 1992, Shank, Polychronakos, and other members of the CSC Subgroup will spend whatever time is required at the SSC for completion of the tests.

(4) LSDT Subgroup

Participants: 23 people from 7 institutions.

INSTITUTION	PARTICIPANTS
MIT	Osborne, Kendall, Rosenson, Ross, Taylor, Verdier, Wadsworth
Lawrence Livermore National Lab. (LLNL)	Fackler, Capell, Weanus
LeCroy Corporation (LRS)	Sumner, Hoftiezer
Lousiana State University (LSU)	McNeil, Metcalf
State University of New York at Stony Brook (SUNYSB)	Mohammadi
Vanderbilt University (VU)	Venuti, Panvini
Joint Institute for Nuclear Research, Dubna (JINR)	Korytov, Bonyushkin, Khovansky, Malyshev, Sedykh, Tokmenin

R&D/ENGINEERING PLAN

The LSDT chambers are rectangular boxes containing 4 layers of wires, with each wire located in a covered U-profile cathode The positioning of the wires is achieved by supporting them on accurately machined insulating bridges running across the width of the chamber and through slots in the cathode at the support point. The bridge, in turn, is held against a reference point on the wall of the chamber which can be monitored or aligned from outside. The cathodes are to be made of thin aluminum, possibly coated to minimize secondary electron emission. The cathodes are held in place by a mechanical system separate from the bridges; precision is not required and the weight of the cathodes must not bear on or distort the wire support. At present, we have chosen Mycalex for the bridge material, as it is stable and machinable.

The alignability of the LSDT's is based on the bridge design, which capitalizes on the fact that 12.5 mm machining precision over spans of 1 m are readily achievable with the use of computer controlled machine tools. The cost effectiveness of the LSDT design follows from the development of inexpensive manufacturing methods of similar chambers by the SLD, Aleph, and SCARF groups. The LSDT design has the flexibility of being made to any length desired, with wire supports at any points of choice to control wire sag. The wires can be laid down multiply (as with Iarocci tubes), inspected, and tested for positioning and tension before being covered. Chamber parts can be manufactured in most modern machine shops.

The wires will be operated in limited streamer mode. We have found that the large, fast pulses achieved in this manner provide excellent drift time measurements.[1] Our tests utilized laser beams, cosmic rays, and the 500 GeV test beam at Fermilab. The use of aluminum cathodes makes the tubes themselves good transmission lines that preserve pulse rise time and enable coarse spatial measurements along the wire length by using instrumentation at both ends of the wires. Because the wires lie in cathodes open at the top it is also possible to determine position orthogonal to the drift time direction with instrumented strips placed over the open side. Strip signals correlated with wire signals enable x-y determinations for each track in a single chamber.

The electronics system for the drift time and z measurements is being developed by LRS.[2] They base their design on the LRS MVL407 discriminator chip and the LRS MTD132 TDC chip, the latter achieving sub-ns time resolution. These will be used for prototype measurements. However, it is expected that even faster electronics will be available for the final system.

Below we list the tasks we expect to complete in FY92, adding in parenthesis the institution(s) bearing the corresponding responsibility.

i) Finish assembly and test of 2, 0.5 m wide chambers (MIT);

ii) Measure tube performance in magnetic fields (MIT);

iii) Design and build (D & B) 2, 1 meter wide chambers (MIT & LLNL);

iv) D & B pick-up strip plane (MIT);

v) Investigate and make thinner cathodes (MIT & SUNYSB);

vi) D & B optical window system (MIT);

vii) D & B tiltable chamber stand as a cosmic ray muon telescope (MIT);

vii) Adjoin prototype optical alignment system to the chambers (MIT, Draper Lab.);

viii) Bottoms up cost analysis of the total system (LLNL);

ix) Investigate various materials for use as cathodes (VU);

x) Analyse the data from runs taken at Fermilab on a small prototype, and runs with cosmic rays on the 0.5 m and 1.0 m chambers (MIT, SUNYSB, & LSU);

xi) Simulation studies of the muon system directed toward optimization of the subsystem and integration with the rest of the detector (MIT);

xii) Provide chamber electronics, investigate state of the art electronics for TDC's, and examine scenarios for the use of chambers in a level 1 trigger system (LRS, MIT).

The schedule for completion of the above tasks has the aim of proving the feasibility, quality, and costs of the LSDT system so that it may be compared with other technologies in time for the TP at the end of the year. Milestones are listed below:

MILESTONE	DATE
Delivery of LeCroy electronics for 0.5 m. chmber:	January 1992
Design of thin cathodes:	January 1992
Assembly of 0.5 m chambers:	February 1992
Assembly of 1.0 m chambers:	March 1992
Delivery of 1.0 m. chamber to SSC Lab.:	May 1992
Set final specs. on chambers:	August 1992
Assemble cost figures for EDR:	September 1992

ELECTRONICS R&D

The R&D in electronics breaks up into several categories:

i) Discriminator and shaping on each wire; this is devloped and built by MIT;

ii) TDC units for chamber prototypes-to be available in January 1992 (LRS);

iii) Trigger electronics which will take signals from the TDC units; this might be considered as a first prototype of a more sophisticated version in the final system; this will also be available in January 1992 (LRS);

iv) Begining R&D into faster versions of the TDC's (LRS);

v) Cost estimates for the electronics of the muon system, including cabling and HV system (LRS).

The units for item ii) are essentially the LeCroy 2277 CAMAC modules which use the MTD132 chip, a pipelined TDC with a capacity of 16 hits per channel and a least count of 0.75 nsec. The trigger unit, item iii), will be a custom built CAMAC unit with 32 inputs from 2, 2277 units. The 32 inputs are combined in a pre-defined logic matrix to produce 16 trigger signals. These 16 signals are then used to address a 65,536 bit memory, which contains the trigger decision. The above will be provided for both the 0.5 m chambers and the 1.0 m chambers.

Eventually, a new chip will be designed for any drift time muon system and optimized for that system. Expected improvements in IC processing in the SSC time frame will certainly allow cost, performance, and power dissipation to be enhanced compared to the current circuit. In any event, design concepts can be used to do cost estimates for the final system (item iv). A costing for the total system, similar to the one for EMPACT/TEXAS [2] will be done (item v).

TTR PLAN

We expect to be able to deliver a 1 m x 4 m chamber to the TTR at the SSC Lab in May 1992; the chamber would have been previously tested as a particle detector. The chamber would have 4 layers of wires (the layers being staggered); each layer has 40 wires. However, we would fully instrument only a subset of wires - 8 wires on each layer at a given time. We would include the necessary CAMAC modules and crate for read-out. Someone, probably Dr. A. Korytov, would accompany the apparatus to put it into operating condition. His stay would be limited to setup time due to restrictions in travel funding and the local demands on his time. We would also bring down the necessary programs for reading data out.

We will retain the second 1 m chamber at MIT to continue tests with variants on mechanical structure, chamber gasses, wire materials, cathode materials, etc.

(5) PDT Subgroup

Participants: 53 people from 7 institutions.

INSTITUTION	PARTICIPANTS
Boston Univ. (BU)	Ahlen, Marin, Zhou, Hazen, Earle, Varner
Michigan State Univ. (MSU)	Bromberg, Miller, Joy, Richards, Yosuf
SSC Lab. (SSCL)	Smith, Mitselmakher, Stocker, Villasenor, Yost, Vanyashin, Zimmer-Nixdorf, Prosapio
Joint Institute for Nuclear Research, Dubna (JINR)	Alexeev, Bonyushkin, Fialovszky, Gornushkin, Malyshev, Tokmenin, Vertogradov
Institute of High Energy Physics, Beijing (IHEP)	Xu + 10 others
Institute of Atomic Physics, Bucharest (IAP)	Pascovici, Aculai, Blaj, Bozdoc, Butacu, Ciobanu, Dorobantu, Ighicianu, Popa, Radulescu, Spanu, Stan-Sion, Valeanu, Zimmer

R&D/ENGINEERING PLAN

Round, metal tubes of the sort being considered for the PDT option have been used successfully at colliders in large solenoidal magnetic fields as precision tracking devices: (a) 3 m long stainless steel tubes (2.54 cm diameter, 200 mm wall thickness) are being used in the 1.5 T field at CDF;[3] and (b) 3.7 m long stainless tubes (2.54 cm diameter, 150 mm thickness) were used in the 1.6 T field at HRS.[4] The HRS tubes achieved a diffusion limited spatial resolution of 160 microns using a safe gas ((90% Ar, 9% CO_2, and 1% CH_4). The CDF tubes were operated in limited streamer mode to optimize charge division performance, achieving 200 mm resolution transverse to the wire, and 2.5 mm resolution along the wire.

The symmetry of round, cylindrical tubes operated with axes parallel to magnetic fields enables reliable and precise tracking due to the simple electric field configuration and the independence of the time to space function on angle of incidence. In addition to the CDF and HRS tubes, there have been numerous other examples of the use of round tubes at colliders (mostly as vertex detectors), in magnetic fields as high as 3 T (AMY),[5] with resolutions as good as 45 mm (the MAC drift tubes, with aluminum cathodes, which were operated with a 49.5:49.5:1 Ar-CO_2-CH_4 gas at 60 psia[6]). Furthermore, the cylindrical geometry of tubes enables improvement of resolution through pressurization. The AMY straw drift tubes (25 mm wall thickness), were in fact pressurized iindividually at 21 psia.[5] And tests done on a spare octant of HRS drift tubes at 30 psia[7] have shown that resolution does improve as expected with increasing pressure, implying that a resolution of 100 mm can be achieved with the safe HRS gas at 30 psia.

The current preferances for the tube type for the GEM PDT option are aluminum tubes with 300 micron wall thickness, and about 3 cm diameter. The inner and middle modules would each consist of 8 layers of staggered tubes, and the outer modules would have 4 staggered layers. The number of radiation lengths in the central modules would be X = 8.5%. To keep X small, we favor aluminum over stainless steel material. The main advantage of the latter is reduced reactivity and fewer problems with spurious electrical discharges. However, the PDT's would be operated in saturated proportional, and not limited

streamer mode, so that this is probably not a major concern.

The PDT alignment philosophy is based on accurate placement of wire ends relative to end plate fiducials. This can be achieved with precision machined reference end plates, and precision fabricated end plugs, pins and ferrules. The PDT design does not utilize wire bridges inside the tubes. It is believed that greater alignment precision is possible by calculating wire position from resonant frequency measurements (which provide the ratio of wire tension to wire radius squared, exactly the quantity needed to calculate sag). Such measurements can be made non-invasively with current-magnetic field excitation, and phase shift analysis. Wire holding through crimp and solder techniques will enable long term stability. Measurements have been made by GEM muon group members which have demonstrated that wire position can be predicted correctly within a few mm (for 4 m long wire tensioned at 80% of the yield strength, sag will be about 230 mm, with an electrostatic component in a 3 cm diameter tube of about 5 mm).

The primary goal of the FY92 R&D program for the PDT Subgroup is the demonstration of the suitability of the PDT design for GEM. In particular it must be shown that a cost effective design and assembly procedure can be developed; these must be appropriate for the reliable construction, assembly, testing, and operation of approximately 100,000 drift tubes having gas tight seals for operation at 15 psig, and having wires held stably so that positions can be predicted correctly to within several mm. A two prong program is planned to acvhieve this goal:

(i) TTR PROTOTYPE

A large scale prototype drift tube module will be designed and constructed to be installed into the TTR for the Spring 1992 tests. This will be approximately 4 m long, 1 m wide, with 4 layers of close packed tubes, each layer having 40 tubes. The mechanical design will emphasize quality with regard to (a) reliable, gas tight seals (utilizing o-rings and gaskets, with minimal or no reliance on glue seals); (b) precise placement of wires (to within 20 mm) relative to a precision fiducial end plate; (c) straightness of tubes (to 1/2 mm); (d) derivation of module rigidity through bonding of the tubes (as a kind of honeycomb structure); and (e) reliable assembly procedure which does not require a great deal of technical skill.

To conserve costs only 24 tubes per layer will be outfitted with commercially available electronics. Each tube end will be connected (through a custom built connector) to a coaxial cable which will deliver high voltage to the tube, and will carry the signal from the tube to a high voltage divider/signal router box, from which the signal will be directed to a fast commercial current amplifier (gain of about 200), then to a commercial discriminator (10 mV minimum threshold), and then to a commercial CAMAC based TDC (1 ms full scale, 0.25 ns least count). This electronic configuration has been tested under adverse conditions of a balloon borne experiment,[8] and has been found to have excellent noise suppression characteristics, primarily because the signal is propagated along coaxial cables continuously from the source to the amplifier input.

MSU and SSCL will be responsible for the mechanical design and construction of the prototype, which will be located at the TTR facility at the SSC Lab. BU will be responsible for the electronics for the prototype. This includes selection and procurement of the commercial equipment, design and construction of the HiV dividing boxes, construction of the cables required, and software for the data acquisition. BU will also be responsible for the pressurized gas system, which will be computer controlled and will employ precise pressure monitors, temperature monitors, and input and output electronic flow meters/controllers.

SSCL will provide alignment equipment to enable comparison of absolute track coordinates determined by both the silicon and PDT arrays. The number of tracking layers (4) in the PDT prototype is sufficient to determine internally the single wire resolution independent of alignment errors.

(ii) SPARE HRS OCTANT

A spare octant of the HRS outer drift ube system has been loaned to the BU group by the Indiana University group (led by Harold Ogren) which built these detectors. This octant will be moved to

Boston where a number of tests will be carried out:

(a) Wire tension will be measured 14 years after construction; a comparison with the known initial tension will provide valuable information on long term tension stability with this type of tube design (for HRS the wires were crimped and soldered).

(b) Resolution measurements will be made with various gases and pressures to help select a gas suitable for the TTR test. Detailed measurements of gas drift properties in magnetic fields will be made on selected gases at various pressures and fields at the MIT cyclotron magnet with the BU gas test chamber setup. Such measurements will determine the time-space function required for track reconstruction.

(c) The electronics and acquisition system for the TTR tests will be developed and debugged in Boston on the HRS octant prior to being shipped to the SSCL

ELECTRONICS R&D

There will be no electronics R&D for the PDT's in FY92. The electronics requirements are satisfied by existing commercially available systems. While it is likely that some cost savings could be anticipated with refined systems, it is felt that such work has low priority for 1992. No hardware work is planned on the development of a PDT level 2 trigger.

TTR PLAN

The PDT prototype will be constructed at the SSCL in early Spring 1992, based on the MSU/LANL/SSCL design. The electronics procured and built at BU will be moved to the SSCL in May 1992, and testing of the module will occur during June 1992. Alex Marin and Gary Varner will spend the time required in Dallas to get the acquisition system and electronics for the PDT prototype up and running. All PDT institutions will participate in the data analysis.

(6) RPC Subgroup

Participants: 15 people from 5 institutions.

INSTITUTION	PARTICIPANTS
MIT	Pless, Chang, Hafen, Haridas
Lawrence Limore National Lab. (LLNL)	Wuest, Ables, van Bibber, Bionta, Fackler, Makowiecki
Brown Univ. (BrU)	Widgoff
Indiana Univ. (IU)	Alyea
Univ. of Tennessee (UT)	Bugg, Berridge, Du

R&D/ENGINEERING PLAN

RPC's, developed in Rome ten years ago, are essentially narrow gap spark counters. They operate at a uniform electric field of about 40 kV/cm between parallel electrodes of resistive material. Typically, 2mm thick plates are separated by 2 mm gaps with the use of spacers. The sensitive volume is filled with a gas mixture of 60% argon, 38% isobutane, and 2 % freon. Spatial readout is made via pick up strips insulated from the field electrodes by a polyethylene film. The voltage induced on these pickup strips is about 0.5 V into 50 W, with a measured time resolution of about 1 ns. RPCs have been used in many experiments with the largest having dimensions 0.5 m x 6.0 m. It is planned that the GEM RPCs will have dimensions of up to 3.3 m x 4.0 m.

RPC's have been tested and found to work at rates up to 40 Hz/cm^2, well above those expected in the barrel region of GEM, even at a luminosity of 10^{34} cm^{-2}s^{-1}. They have also been found to work well in close proximity to drift chambers, for which a 25 mm aluminum cover around the RPC's is used as an RF shield.

The RPC R&D program for FY92 will consist of two major areas:

i) Measure the properties of a 1 m x 2 m RPC furnished to MIT by R. Santonico of the Rome 2 University. These properties include:

a) Pulse rise time jitter;
b) Maximum counting rate per unit area;
c) Efficiency;

d) Lifetime.

ii) Measure the properties of a large size RPC produced by the RPC Subgroup.

An RPC test bed will be designed, fabricated, and installed at MIT, under the direction of the MIT group. MIT will also be responsible for the design and implementation of the RPC electronics. Equipment for the test bed will be provided and commissioned by other groups:

i) BrU will provide two scintillation hodoscopes; each hodoscope has two planes, one for x and one for y; each plane consists of 12 scintillators, each being 11 cm wide x 1.27 cm thick x 120 cm long; these will be used to provide timing information which will be used to determine RPC time resolution;

ii) IU will provide a multi-component gas system for the test bed; special emphasis will be placed on non-flammable mixtures for the tests (e.g. 86% CO_2, 10% isobutane, 2% Ar, and 2% freon);

iii) UT will provide 9 drift chambers, each having an area 1 m x 1 m; these will provide tracking information as an aid in understanding RPC performance.

MIT will be responsible for the installation of all RPC's, whether from Italy, or built by LLNL, into the test bed, and for the operation, data acquisition, and maintenance of this facility.

The GEM muon system will require thousands of square meters of reliable RPC's. Activities at LLNL will be focussed on optimizing chamber design and chamber materials with this fact in mind. Thus the emphasis at LLNL will be on the fabrication of large scale prototype RPC's using new materials and manufacturing methods. The FY92 R&D program at LLNL will include the following tasks:

i) Determination of the best plate material (plastic or glass), and coating technique for the large scale prototype RPC and characterization of the resistivity and surface uniformity of the materials. This will be performed by a physicist and the Chemistry and Materials Science (CMS) coatings group, requiring 0.125 FTE of a CMS engineer, and 0.25 FTE of a CMS technician.

ii) Construction of a large scale prototype RPC with dimensions to be determined by funding constraints, but probably 1 m wide and 1 to 4 m long. Construction techniques consistent with large scale production will be tested in the fabrication of this prototype. This effort will require 0.125 FTE of a CMS engineer, 0.25 FTE of a mechanical engineer, o.25 FTE of an electronics engineer and 1 full time physicist.

iii) Characterization of the large scale prototype RPC for noise, operating efficiency (plateau), time resolution and spatial resolution. This includes characterizing the size and temporal duration of the localized dead region after an electron avalanche is generated. Spatial resolution along the long pickup strips can also be studied, with particular attention being paid to uniformity and linearity of the position measurement near the edges of the chamber. Also, chamber lifetime and aging effects will be studied. Tracks will be generated using tagged cosmic rays, radioactive sources, and electrons from the LLNL 140 MeV Linac. This work will be carried out by a 0.25 FTE electronics engineer and 1/4 of a physicist.

ELECTRONICS R&D

None will be done in FY92.

TTR PLAN

An RPC prototype will be moved to the TTR in Spring 1992. It will be necessary to demonstrate that operation of the drift tube prototypes are not degraded by RF interference from the RPC.

(7) ENG Subgroup

Participants: 10 people from 3 institutions.

INSTITUTION	PARTICIPANTS
Draper Lab.	Nimblett, Hamilton + 3 others
SSC Lab. (SSCL)	Smith + 1 other

R&D/ENGINEERING PLAN

The plan described here characterizes the staffing required to implement those engineering tasks necessary to proceed from the current, rather primitive, state of the design of the GEM muon system to the TP in November 1992. This effort requires covering all aspects of the muon system to some level through both a conceptual design phase and the preliminary design phase which will provide the basis for the design, costing and scheduling of the muon system for the TP. The scope of this effort is fixed by the nature of the TP and by the SSC schedule, but the level of detail and the accuracy to which these tasks will be accomplished will be limited by the funds available in FY92.

FY92 activities will consist two basic tasks:

(i) TASK 1 - complete conceptual design of entire muon system for 2 barrel technologies, exclusive of the chamber designs themselves.

This effort will include:

a) Conceptual layouts of proposed chambers (not detailed drawing);

b) Electronic racks and mounting concepts;

c) Cable routing and support concepts;

d) Conceptual design of interfaces to structures, interfaces to magnet support points or other attachment options;

e) Structural support concepts for chambers along with structural analysis and assembly procedures and schedules;

f) Muon system alignment concepts (local and global);

g) Consideration of allotment of space and attachments for muon system (and other systems) service requirements;

h) Consideration of safety air venting, temperature control and air routing through the muon system;

i) Conceptual design for chamber gas systems, including plumbing and surface facility requirements;

j) Initial cost book entries for all of the above.

The costing and overall design concepts will serve as elements in the decision to select one of the two barrel region options by early July 1992. Routine engineering program management and associated travel expenses are also included in this task description and will require a portion of the allotted funding.

To maintain a critical mass on this task will require that the majority of the conceptual design work be done at Draper. However, the global alignment of both the muon system and the overall detector will necessitate interactions among Draper (F. Nimblett), the SSCL (D. Veal), LANL (J. Hanlon) and LLNL (G. Deis). The alignment concept is an area of critical concern which can affect the entire detector architecture and must be addressed very soon in the conceptual design activity.

Expenditures for this task, other than salaries and travel, include computer usage costs, and materials and supplies costs to purchase PC software to improve compatibility within the engineering team and the SSCL and also to provide additional PC based analytical tools to improve group productivity.

(ii) TASK 2 - Preparation for the GEM muon system portion of the Technical Proposal.

Following the selection of the barrel chamber options for the GEM muon system in early July, this task will combine TASK 1 with the chosen chamber options for the barrel and endcaps from the detector subgroup R&D activities to formulate a preliminary design for the GEM muon system. This effort will provide the design, costing and scheduling basis for the TP.

As with the conceptual design task, the overall scope of this task must include all aspects of the muon system design to some level. It is anticipated that the conceptual design activities will provide the basis for prioritizing the various design elements of the preliminary design in a manner that will permit us to place the limited engineering resources onto the most critical items,

whether this criticality be due to technical, cost or schedule risk factors. An additional component of this effort is the need to spend engineering funds on the selected chamber technologies to develop the chamber design detail sufficiently to provide accurate cost estimates based on vendor quotes and to properly integrate the chambers and their alignment structures into the respective support structures. As with the conceptual design, routine engineering program management and associated travel expenses are also included in this task description.

As with TASK 1, most of the efforts of this task will be concentrated at Draper to maintain critical mass. Exceptions to this will involve the alignment task (as described for TASK 1) and those tasks associated with detailed chamber design, which will draw support from LANL, LLNL, BNL, and Draper.

(8) TTR Subgroup

Participants: 8 people from 1 institution.

INSTITUTION	PARTICIPANTS
SSC Lab. (SSCL)	Mitselmakher, Stocker, Villasenor, Yost, Vanyashin, Zimmer-Nixdorf, Prosapio, Smith

R&D/ENGINEERING PLAN

The GEM Collaboration has decided to construct a test facility at the SSCL to evaluate different muon-chamber prototypes during June and July 1992. This evaluation will serve to select the detector technologies that are best suited for the GEM muon system. For this purpose, we will construct the Texas Test Rig (TTR) that will accomodate large scale muon chamber prototypes that will be tested under identical conditions using cosmic muons. The muon technologies to be tested include the PDT's, LSDT's, CSC's and RPC's.

The TTR will consists of an iron toroid magnet, two planes of scintillation counters (one above and the other below the TTR), two layers of Iarocci tubes above and two layers below the magnet, and five compartments to place the muon chambers under test. The dimensions of the largest of the muon-chamber prototypes will be 4 m x 1 m x 0.2 m. Each of the TTR compartments will be about 5 m long, 2.1 m wide and 0.25 m high, so that it can accomodate larger prototypes in the future.

The 1 m thick iron of the magnet will harden the cosmic ray spectrum to muon momenta greater than 1.4 GeV. The muon spectrum can be further hardened (muon momenta greater than 5 to 10 GeV) by imposing offline cuts on the deflection of the muon track before and after it traverses the 1.4 T magnet; this will be done in order to to keep the systematic error introduced by multiple scattering small compared to the expected resolution of the chamber prototypes. We will determine the muon direction above and below the magnetized iron by means of four planes of Iarocci chambers. We are studying two aproaches towards the construction of the magnet: the first is to use the iron from the recently decommissioned D0 Cosmic Ray Telescope from Fermilab; the second is to make our own magnet in a way that is more optimized for our application. We will select one of these options based on several criteria such as cost, performance, viability and schedule. The decision as to which type of magnet we will build will be taken by the end of November 1991. The SSCL group will be responsible for the construction of the magnet. The magnet will be ready by April 1992.

The scintillation counters will provide both the trigger and the the start signal for the TDC's. We expect to have the scintillation counters manufactured for us at Fermilab or LANL. The scintillation counters will be 2.7 m long, 20 cm wide and 2.5 cm thick. We will have two layers of area 5 m x 1.2 m each, which will require 24 counters and 48 phototubes. The scintillation counters will be ready by April 1992.

The coincidence of the signals from the scintillation counters and the four Iarocci chambers will be the trigger for the data acquisition system (DAQ). The SSCL group will provide the trigger electronics, DAQ computer, mass storage, interface cards computer to CAMAC, and crate controllers. The proponents of the technologies will provide the CAMAC crates, the TDC and/or ADC modules, power supplies and the interconnecting cables that are required. The proponents will be responsible for making their prototypes operational at SSCL. The SSCL group will develop the basic data

acquisition software in coordination with the DAQ liason person of each of the proponent institutions.

The SSCL will participate by making computing resources available and helping with the design and construction of the software. However, each proponent will be responsible for providing any technology specific software, including any necessary calibration software.

The Iarocci chambers will provide both the trigger and a measurement of the incoming and outgoing directions of the muons. Each of the four planes of Iarocci chambers will provide x-y position measurement with a cell size of 1 cm for each coordinate. The Institute for Beam Particle Dynamics at the University of Houston will provide the Iarocci chambers with strip boards, front end electronics, CAMAC read out system, gas system, high voltage supply, gas, and monitor/alarm system. The Iarocci tubes will be ready by April 1992.

The prototypes use different gases (mixtures consisting of up to 4 gases). The proponents of each technology will provide their own gas mixers. We will ensure they are being built according to the applicable SSCL safety regulations. The SSCL will provide a complete gas system as a backup system for any of the technologies. The SSCL will also provide exhaust and alarm systems as well as the racks for the gas bottles.

The GEM Muon Group plans to take data for approximately one month in June 1992 to allow enough time for analysis and comparision of the performance of the different prototypes before the due date for the TP. All components being provided by SSCL will be ready by April 1992 to allow installation of the individual technologies by their proponents in May 1992. We will start taking data on June 1, 1992.

(9) SCARF Subgroup

Participants: 7 people from 1 institution.

INSTITUTION	PARTICIPANTS
Univ. of Houston (UH)	R. Weinstein, K. Lau, B. Mayes, J. Pyrlik and 3 others

R&D/ENGINEERING PLAN

The Streamer Chamber Assembly and Research Facility (SCARF) of the Univ. of Houston has developed state of the art facilities for assembling, with outstanding reliability, large quantities of large area limited streamer tubes. The expertise and experience of the SCARF Subgroup is an exceedingly valuable asset to the GEM muon system. An example of the value of this group was indicated in the preceeding section in the description of the tracking chambers to be provided for the TTR. Additional tasks to be taken on by the SCARF Subgroup in support of the GEM muon system during FY92 are indicated in this section.

i) Optimization of cathode surface material is a critical aspect of the development of the CSC concept. The SCARF Subgroup will work on this problem by measuring plateau lengths of U-profile chambers made of extruded Al, extruded Al coated with C, and extruded Al coated with Ni in both streamer and proportional modes. Extruded Al U-channels with 8 or more channels will be obtained from local suppliers. C coating will be done at SCARF. Ni coating will be done by local industry. Plateaus with 100 micron (for streamer mode) and 50 micron (for proportional mode) silver-plated Be-Cu wires and Ar-Isobutane (1:3) gas mixture will be measured. The knees and breakaways will be determined. Afterpusling will be studied. It is expected that most of this task will be completed by June 1992.

ii) As a corollary of the activity listed above, the SCARF Subgroup will provide cost etimates for Ni coated Al, in both U-profiles (LSDT) and tubes (PDT). This information can be made available by April 1992.

iii) An important issue for the CSC task is whether there is any benefit of housing the anode wires in open profile tubes, as opposed to the baseline design of having the wires housed in open chambers. Various opinions on this subject have been espoused throughout the evolution of the GEM muon system design phase. The SCARF Subgroup will work on this problem by constructing a small prototype chamber (1 m x 0.5 m) with strip readouts. The wires for the chamber will be placed in U-profiles with 1 cm cell size. The strips will have 5 mm pitch. The SCARF Subgroup will investigate strip signal size,

multiplicity, and cross talk in both the proportional and streamer modes. It is expected that construction will be completed in June 1992 and that the tests will be completed by September 1992.

iv) The properties of a large gas volume of the barrel drift system will be studied. Air leaks and their effects on the system will be studied. This will be done by August 1992.

If time permits, the SCARF Subgroup will explore the possible use of nitrogen-based gas mixtures (e.g. nitrogen-CF_4) as candidates for inexpensive and nonflammable gases.

(10) References

(1) Toroidal Spectrometer Group Progress Report, SSC Progress Report No.218 (Sept.15, 1991).

(2) EMPACT/TEXAS Tech. Note \# 338, from LeCroy Corp. Nov.26, 1990 (Revised Feb.26, 1991).

(3) S. Bhadra et al., Nucl. Instr. Meth. **A268**, 92 (1988); also see Nucl. Instr. Meth. **A269**, 33 (1988).

(4) G. Baranko, Ph.D. Thesis, Indiana University (1983).

(5) H. Kagan, private communication (1990).

(6) W.W. Ash et al., Nucl. Instr. Meth. **A261**, 399 (1987).

(7) S. Ahlen, unpublished HRS report (1983).

(8) S. Ahlen et al. Phys. Rev. Lett. **61**, 145 (1988).

Enclosure [1.2]

R&D and Engineering for The Texas Test Rig

Participant Institutions:
BNL, BU, DRAPER LAB, JINR, HU, ITEP, INP, LANL, LLNL, MIT, MSU, SSCL

List of Participants from SSCL
M. Botlo, M. Hecht, K. McFarlane, C. Milner, G. Mitselmakher, T. Prosapio, F. Stocker, A. Vanyashin, L. Villasenor, G. Yost, E. Zimmer-Nixdorf

List of Participants from HU
K. Lau, B. Mayes, J. Pyrlik, R. Weinstein

Visitors from:
IFUG/CINVESTAV (MEXICO), INP (ST. PETERSBURG), ITEP (MOSCOW), JINR (DUBNA), MSU (MOSCOW)

INTRODUCTION

The GEM Collaboration has recently decided to construct a test facility at the SSCL to evaluate different muon-chamber prototypes during June and July 1992. This evaluation will serve to select the detector technologies that are most convenient for the GEM Muon System. For this purpose, we will construct the Texas Test Rig (TTR) that will accommodate large scale muon chamber prototypes that will be tested under identical conditions using cosmic muons. The muon technologies to be tested are the following: Pressurized Drift Tubes (PDT), Limited Streamer Drift Tubes (LSDT), Cathode Strip Chamber (SCS), and Resistive Plate Chambers (RPC).

The TTR will consist of an iron toroid, two planes of scintillation counters (one above and the other below the TTR), two layers of Iarocci tubes above and two layers below the magnet, and five compartments to place the muon chambers under test. The dimensions of the largest of the muon-chamber prototypes will be 4m x 1m x 0.2m. Each of the TTR compartments will be about 5m long, 2.1m wide and 0.25m high, so that it can accommodate larger prototypes in the future.

MAGNET

The 1m thick iron of the magnet will harden the cosmic ray spectrum to muon momenta greater than 1.4 GeV. The muon spectrum can be further hardened (muon momenta greater than 5 to 10 GeV) by imposing off-line cuts on the deflection of the muon track before and after it traverses the 1.4 T magnet; this will be done in order to keep the systematic error introduced by multiple scattering small compared to the expected resolution of the chamber prototypes. We will determine the muon direction above and below the magnetized iron by means of four planes of Iarocci chambers. We are studying two approaches toward the construction of the magnet: the first is to use the iron from the recently decommissioned D0 Cosmic Ray Telescope from Fermilab, the second is to make our own magnet in a way that is more optimized for our application. We will select one of these options based on several criteria such as cost, performance, viability and schedule. The decision as to which type of magnet we will build will be taken by the end of November 1991. The SSCL group will be responsible for the construction of the magnet. The magnet will be ready by April 1992.

SCINTILLATION COUNTERS

The scintillation counters will provide both the trigger and the start signal for the TDC's. We expect to have the scintillation counters manufactured for us at Fermilab or LANL. The scintillation counters will be 2.7m long, 20cm wide and 2.5cm thick. We will have two layers of area 5m x 1.2m each, this will require 24 counters and 48 phototubes. The scintillation counters will be ready by April 1992.

DAQ AND TRIGGER ELECTRONICS

The coincidence of the signals from the scintillation counters and the four Iarocci chambers will be the trigger for the data acquisition system (DAQ). The SSCL group will provide the trigger electronics, DAQ computer, mass storage, interface cards computer to CAMAC, and crate controllers. The proponents of the technologies will provide the CAMAC crates, the TDC and/or ADC modules, power supplies and the interconnecting cables that are required. The proponents will be responsible for making their prototypes operational at SSCL. The SSCL group will develop the basic data acquisition software in coordination with the DAQ liaison person of each of the proponent institutions.

DATA ANALYSIS

The SSCL will participate by making computing resources available and helping with the design and construction of the software. However, each proponent will be responsible for providing any technology specific software, including any necessary calibration software.

IAROCCI TUBES

The Iarocci chambers will provide both the trigger and a measurement of the incoming and outgoing directions of the muons. Each of the four planes of Iarocci chambers will provide X-Y position measurement with a cell size of 1 cm for each coordinate. The Institute for Beam Particle Dynamics at the University of Houston will provide the Iarocci chambers with strip boards, front end electronics, CAMAC readout system, high voltage supply, gas and monitor/alarm system. The Iarocci tubes will be ready by April 1992.

GAS SYSTEM

The chamber prototypes use different gases (mixtures consisting of up to 4 gases). The proponents of each technology will provide their own gas mixers. We will ensure they are being built according to the applicable SSCL safety regulations. The SSCL will provide a complete gas system as a backup system for any of the technologies. The SSCL will also provide exhaust and alarm systems as well as the racks for the gas bottles.

SCHEDULE

The GEM Muon Group plans to take data for approximately one month in June 1992 to allow enough time for analysis and comparison of the performance of the different prototypes before the due date for the technical proposal. All components being provided by SSCL will be ready by April 1992 to allow installation of the individual technologies by their proponents in May 1992. We will start taking data on June 1, 1992.

TTR TEXAS TEST RIG

GEM MUON CHAMBERS EVALUATION TEST STAND

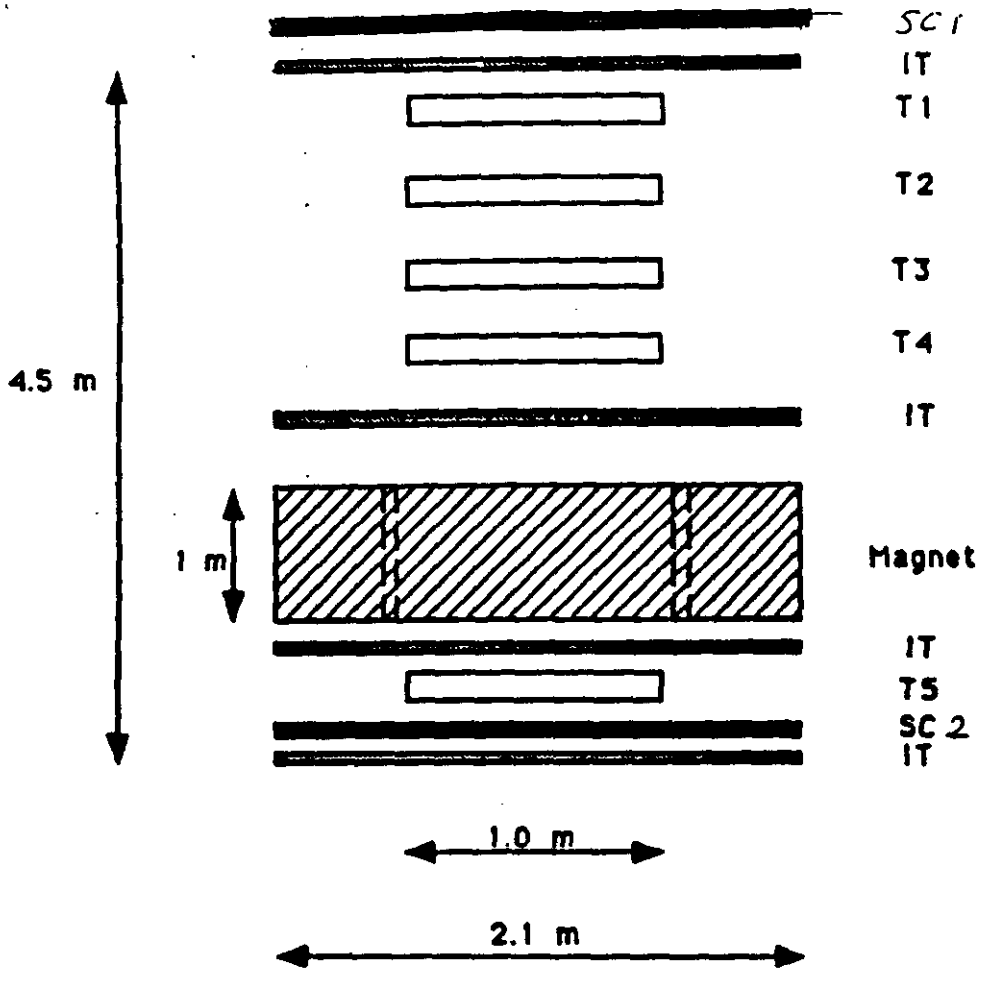

Legend:

T1-T5 Technologies to be Evaluated
- **T1 Pressurized Drift Tubes**
- **T2 Limitied Streamer Drift Tubes**
- **T3 Cathode Strip Chambers, Multiwire Geometry**
- **T4 Cathode Strip Chambers, Open Profile**
- **T5 Resistive Plate Chambers**

SC Scintillator Counters

IT Iarocci-Tube Chambers for Trigger

Monte Carlo Studies of the Texas Test Rig Performance

A. Vanyashin, G. Yost
SSC Laboratory

May 18, 1992

Abstract:

To test the performance of different muon chamber technologies proposed for the GEM experiment at the SSC, the Texas Test Rig (TTR) will be established at the SSC Laboratory. The results of Monte Carlo studies of TTR are presented. An optimized off-line selection algorithm is found.

Monte Carlo Studies of the Texas Test Rig Performance

A.Vanyashin, G.Yost
SSC Laboratory
Dallas, TX 75237

May 18, 1992

Abstract

To test the performance of different muon chamber technologies proposed for the GEM experiment at the SSC, the Texas Test Rig (TTR) will be established at the SSC Laboratory. The results of Monte Carlo studies of TTR are presented. An optimized off-line selection algorithm is found.

1 Introduction

The Letter of Intent for the GEM experiment at the SSC [1] considers four different drift chamber technologies as candidates for the GEM muon chambers. To make a choice between the different muon chamber technologies the Texas Test Rig (TTR) cosmic ray telescope at the SSC Laboratory is proposed as a site to test all the chambers.

The claimed high position resolution (50 - 100 μm) of the drift chambers to be tested makes the multiple scattering effects a factor to be aware of. Two factors will contribute to the measured position resolution. The first factor is the intrinsic position resolution of the drift chambers themselvs and the second factor is the contribution from multiple scattering effects. In principle the multiple scattering contribution is calculable and could be properly subtracted from the observed position resolution. To reduce the systematic error one needs to make multiple scattering effects less than the intrinsic position resolution of the chambers. To reduce multiple scattering effects the cosmic ray muon spectrum needs to be hardened. In Section 2 we present the results of calculations of multiple scattering effects in the most precise chambers to be tested — the Cathode Strip Chambers (CSC). The 1.5 GeV cutoff of the cosmic muon spectrum provided by the 1 m of non-magnetized iron is sufficient to make multiple scattering effects inside CSC less than the intrinsic position resolution of the chambers.

Another way to test prototypes' resolution is to compare hits in the chamber with muon tracks fitted using other technologies. As the overall fit involves tracks, which have traversed larger amounts of material, to achieve high precision one needs to raise the cutoff of low energy muons. To have this additional control over the muon cosmic ray spectrum, the iron shield at the TTR will be magnetized. Four layers of Iarocci tubes (two above and two below the magnet) will be used to select high energy muons. In Section 3 we present the result of Monte Carlo studies leading to a choice of TTR magnet configuration. In Section 4 the results of GEANT MC studies of TTR are presented.

Table 1: Materials used in the Cathode Strip Chambers

Element	Material	Thickness	% of R.L.
Readout board	Cu	0.014"	0.25
	G10	1/16"	0.82

2 Multiple Scattering Effects in Cathode Strip Chambers

Among all the drift chamber technologies considered as candidates for a GEM muon system the Cathode Strip Chambers (CSC) have the best claimed position resolution of 50 μm. Figure 1 presents the layout of these chambers. Table 1 summarizes the material thickness used in MC calculations of the multiple scattering effects.

To estimate the influence of multiple scattering effects we used an algorithm proposed by Frank Taylor [2]. This algorithm uses the difference in the measured incident angles in the upper and the lower part of the chambers as a measure of the CSC position resolution. If there is no multiple scattering inside the chambers the observed distribution of $\theta = \theta_1 - \theta_2$ (see Figure 2 for the angles' definition) would have r.m.s. value of 3.3 $mrad$ due to a 50 μm position resolution in each of four chambers.

Indeed, as $\theta_1 = (x_1 - x_2)/L$, $\theta_2 = (x_3 - x_4)/L$, then

$$\sigma_\theta^{pos.} = \frac{\sqrt{\Sigma\sigma_{x_i}^2}}{L} = 3.3 \times 10^{-3},$$

where x_i is the coordinate of the muon track, measured in each of four chambers, $\sigma_{x_i} = 50$ μm is the position resolution and $L = 30$ mm is the distance between the adjacent chambers in the upper and the lower halves of the CSC (see Figure 1). Figure 3b shows the result of the MC simulation of the difference, with no multiple scattering taken into account.

If one uses the Gaussian approximation for multiple scattering for a 1.5 GeV muon (such a cutoff is provided by an unmagnetized iron shield), one could estimate the r.m.s. angle of deviation due to multiple scattering between θ_1 and θ_2 measurements as

$$\sigma_\theta^{m.s.} = \frac{14.1 MeV}{p}\sqrt{\frac{l}{L_R}}(1 + \frac{1}{9}\log_{10}(\frac{l}{L_R}))$$

If there are 4 G10 plates ($\frac{l}{L_R} = 4.3\%$) placed between the measurements of θ_i then for a 1.5 GeV muon

$$\sigma_\theta^{m.s.} = 2.2\, mrad$$

and the observed r.m.s. $\sigma_\theta^{obs.}$ would be approximately

$$\sigma_\theta^{obs.} = \sqrt{(\sigma_\theta^{pos.})^2 + (\sigma_\theta^{m.s.})^2} \approx 3.8\, mrad.$$

As $\sigma_\theta^{pos.} > \sigma_\theta^{m.s.}$, multiple scattering effects will not dominate measurement errors in $\sigma_\theta^{pos.}$ in the CSC's.

The resulting θ distribution from a GEANT MC of a 1.5 GeV muon track incident normally onto CSC planes is shown at Figure 3a. The CSC materials of (Table 1) were used. One can observe some increase in σ_θ due to a multiple scattering effects. With perfect position resolution, the multiple scattering alone would produce the θ distribution with $\sigma_\theta = 2.2\, mrad$, presented in Figure 3c. The results in Figure 3 are in agreement with our estimates.

3 Cosmic ray spectra with different shield configurations

To have additional control over the muon cosmic ray spectrum the TTR iron shield will be magnetized. Figure 4 shows the outgoing coordinate and angle of a 10 GeV muon track after traversing 1 m of magnetized iron. When the cosmic ray muon traverses the magnetized iron the measured parameters of the muon track will depend on the muon energy. It is possible to make a cut on a muon track position or a muon track angle after the magnet to harden the initial cosmic ray muon spectrum. As large deflections due to multiple scattering will primarily occur only at low momenta, one also could cut on bending angle in the non-bending plane to improve the high energy muon selection.

To optimize the magnet shape we simulated the muon cosmic ray spectra for the four iron shield configurations considered. In all cases we have assumed an iron thickness of 1 m, and an incoming muon cosmic ray spectrum of $1/E^2$. For a magnetized shield a magnetic field inside the iron of 1.5 T was assumed. To compare the different shield configurations and have a sufficient trigger rate, for each configuration the cuts were made in such a way as to retain approximately 50% efficiency for 10 GeV muons (Figure 4).

The resulting muon cosmic ray spectra after the cuts applied on muon position and angles after traversing the shield are presented in Figures 5–6 for two magnet configurations. The split magnet configuration with a 1 m air gap provides better a cutoff of the low energy part of the cosmic muon spectrum. Figures 7–8 shows the selected muon spectra for two possible configurations of unmagnetized iron. Without magnet field the selected muon spectra has more low energy muons than in case of magnetized iron.

The right part of the Figures 5–8 are obtained using a 2σ cut on bending angle for a 10 GeV muon (Figure 4).

4 Off-line Selection of Cosmic Ray Muons in TTR

To achieve high precision in an overall track fit that involves several technologies one need to harden muon cosmic ray spectra further. The TTR Iarocci chambers will provide data for an off-line selection of cosmic ray spectra. To optimize the selection algorithm we made a GEANT MC study of the TTR. In this study realistic cosmic ray spectrum [3] were used. The positions of Iarocci chambers in TTR geometry are not yet determined. Values used in our GEANT MC study are shown in Table 2.

Figure 9 presents an example of the selected spectra for some set of cuts based on Iarocci chambers. To reduce multiple scattering effects one can impose stronger selection cuts. Stronger cuts harden selected spectra, but make muon rate lower. The value to be optimized in a selection algorithm is the mean value of $1/p^2$. This value is proportional to the magnitude of multiple scattering effects, $(\sigma_\theta^{m.s.})^2$, for the selected spectra. Figure 10 plots the muon rate in the upper layer of the TTR Iarocci chambers versus $< 1/p^2 >$. Figure 10 shows that the TTR will provide effective selection of the cosmic ray spectra up to $< 1/p^2 >^{-1/2} \approx 8GeV$. Figure 11 shows the selection efficiency for muons traversing the upper layer of TTR Iarocci chambers. The muon efficiency at high momenta limited by geometrical efficiency, which is determined by magnet area. We assumed perfect efficiency for muon detection in Iarocci chambers in this analysis. Figure 11 shows that off-line analysis will provide up to a 10^{-5} rejection of the low energy cosmic ray muons.

Table 2: TTR Geometry used in GEANT MC studies

Element	Position, cm	X×Y, cm	Thickness, cm
Scintillator 1	495	120×270	2.5
Scintillator 2	485	120×270	2.5
Iarocci tubes 1	450	400×192	1.5
Iarocci tubes 2	240	400×192	1.5
Magnet	166.5	380×110	101.6
Iarocci tubes 3	95	400×192	1.5
Scintillator 3	25	120×270	2.5
Scintillator 4	10	120×270	2.5
Iarocci tubes 4	5	400×192	1.5

5 Conclusions

To test the performance of different muon chamber technologies proposed for the GEM experiment at the SSC the Texas Test Rig (TTR) will be established at the SSC Laboratory. The results of GEANT Monte Carlo studies of the TTR are:

- the 1.5 GeV cutoff of the cosmic muon spectrum provided by 1 m of unmagnetized iron is sufficient to make multiple scattering effects less than the intrinsic position resolution of the chambers,
- to have additional control over the muon cosmic ray spectrum the iron shield at the TTR will be magnetized,
- the TTR provides up to a 10^{-5} rejection (in off-line) of low energy cosmic ray muons.

6 Acknowledgements

We thank Ken McFarlane, Gena Mitselmakher, Luis Villasenor and Frank Taylor for discussions, Frank Stocker and Julia Yarba for providing their programs.

References

[1] GEM Collaboration, GEM Letter of Intent, SSC-LOI004.

[2] F.Taylor, private communication.

[3] Allkofer and Greider, in Cosmic Rays on Earth, Physics Data, Fachinformationszentrum Energie, Physik, 1984 (Table 2.2.4, p. 242).

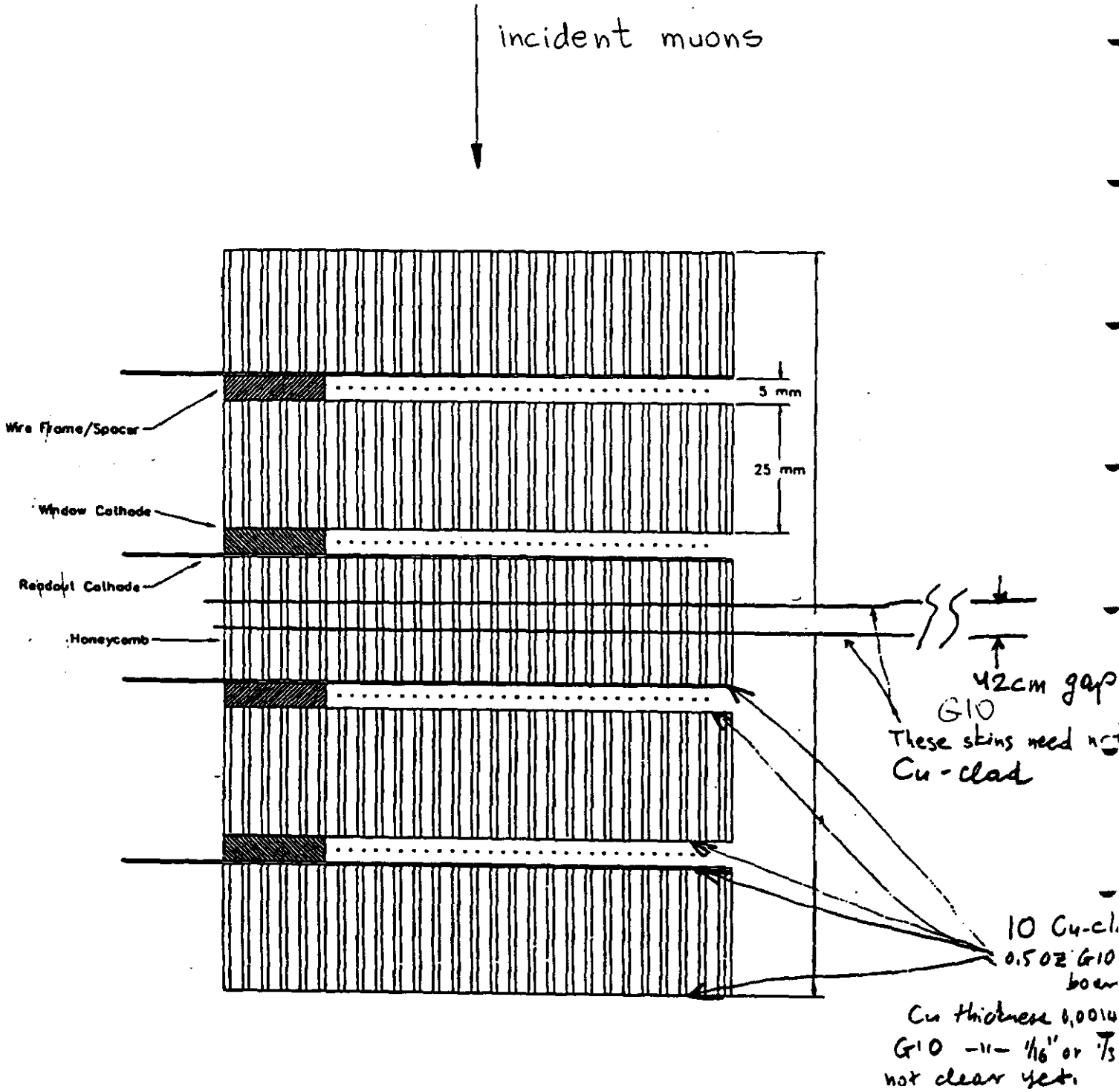

Figure 1: The layout of the Cathode Strip Chambers

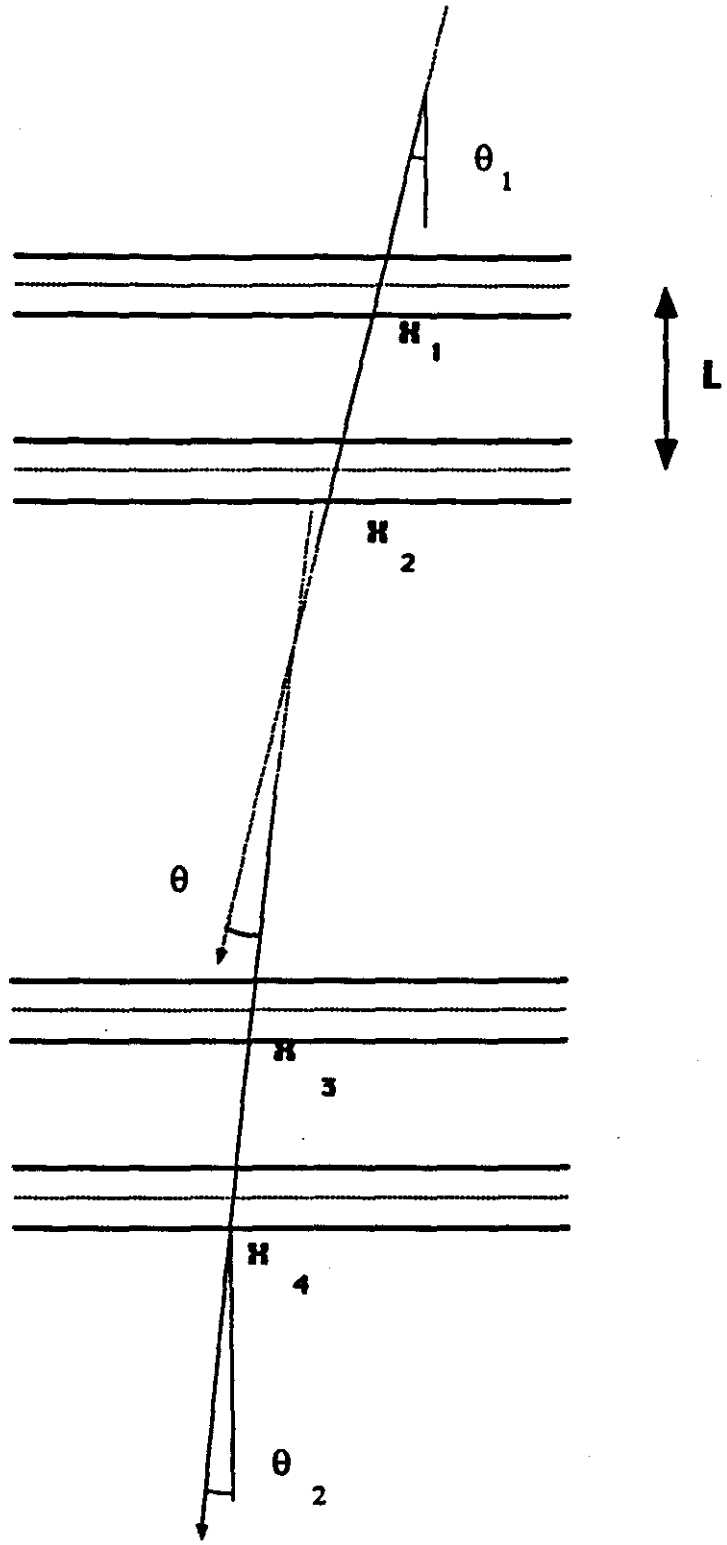

Figure 2: Incident angles measured in the upper and the lower part of the Cathode Strip Chambers are relevant to CSC's position resolution.

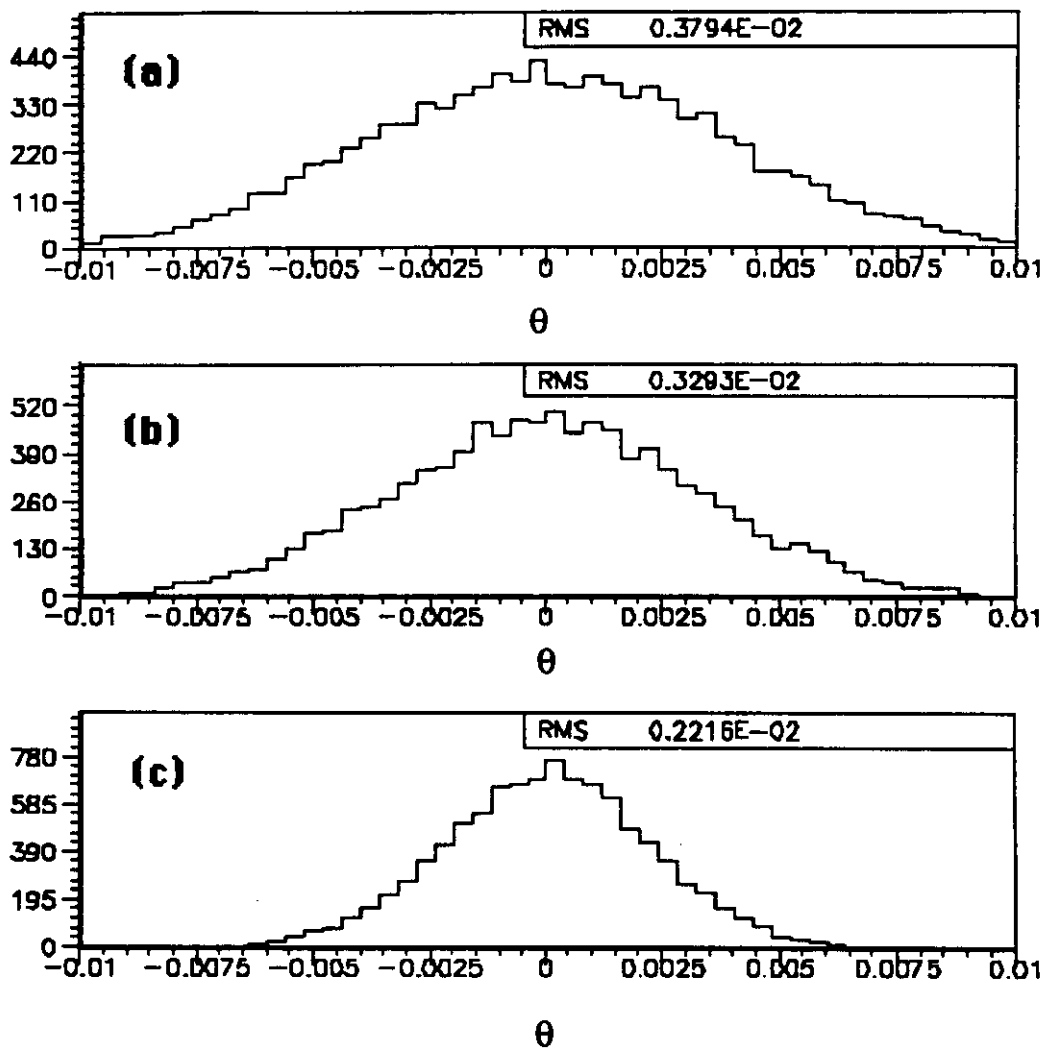

Figure 3: Position resolution in CSC reflected by $\theta = \theta_1 - \theta_2$ (as shown in Figure 2): (a) Multiple scattering plus intrinsic position resolution errors; (b) intrinsic position resolution errors only; (c) multiple scattering only.

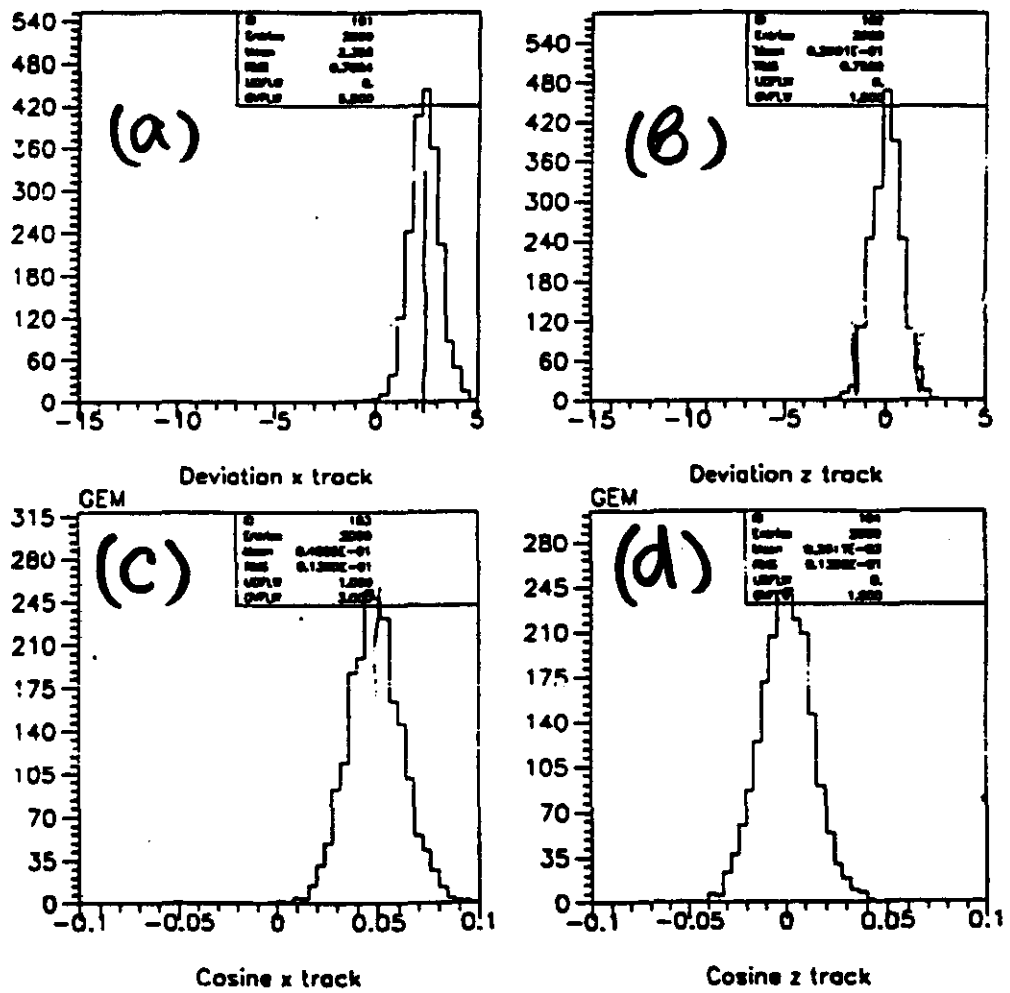

Figure 4: Distribution of the outgoing coordinates and angles of a 10 GeV muon track after traversing 1 m of magnetized iron: (a) distribution of the outgoing coordinate in the bending plane of the magnet; (b) distribution of the outgoing coordinate in the non-bending plane; (c) distribution of the outgoing angle in the bending plane of the magnet; (d) distribution of the outgoing angle in the non-bending plane.

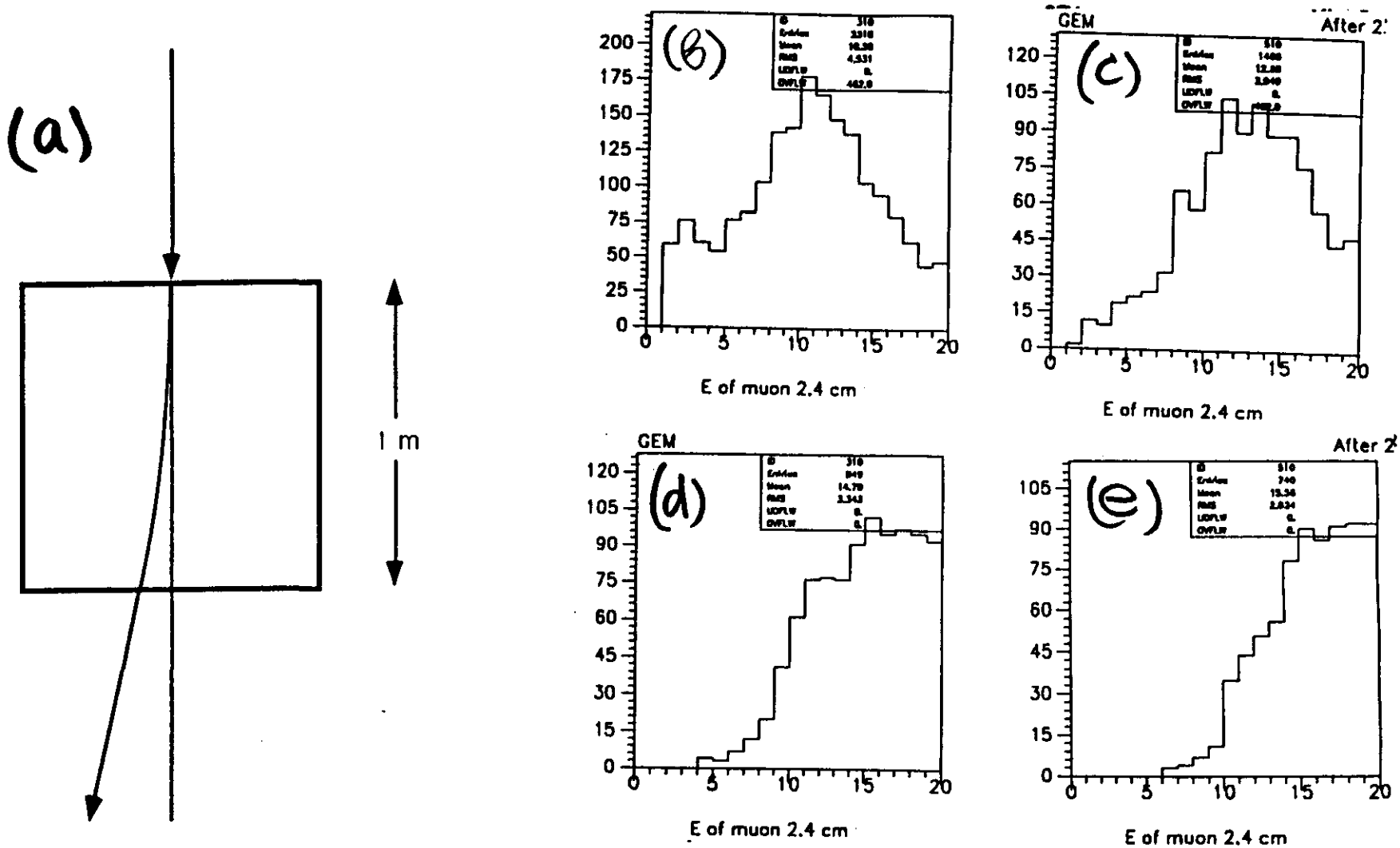

Figure 5: Muon Spectra for a 1 m Fe magnet with a 1.5 T field: (a) Layout of the 1 m magnet configuration; (b) Muon energy spectrum after a cut of 2.4 cm on track deviation in the magnet; (c) same as in (b) with the 2σ cut on deviation in another plane is applied; (d) Efficiency of the cut in (b) versus muon energy; (e) same as in (d) with the 2σ cut on deviation in another plane applied.

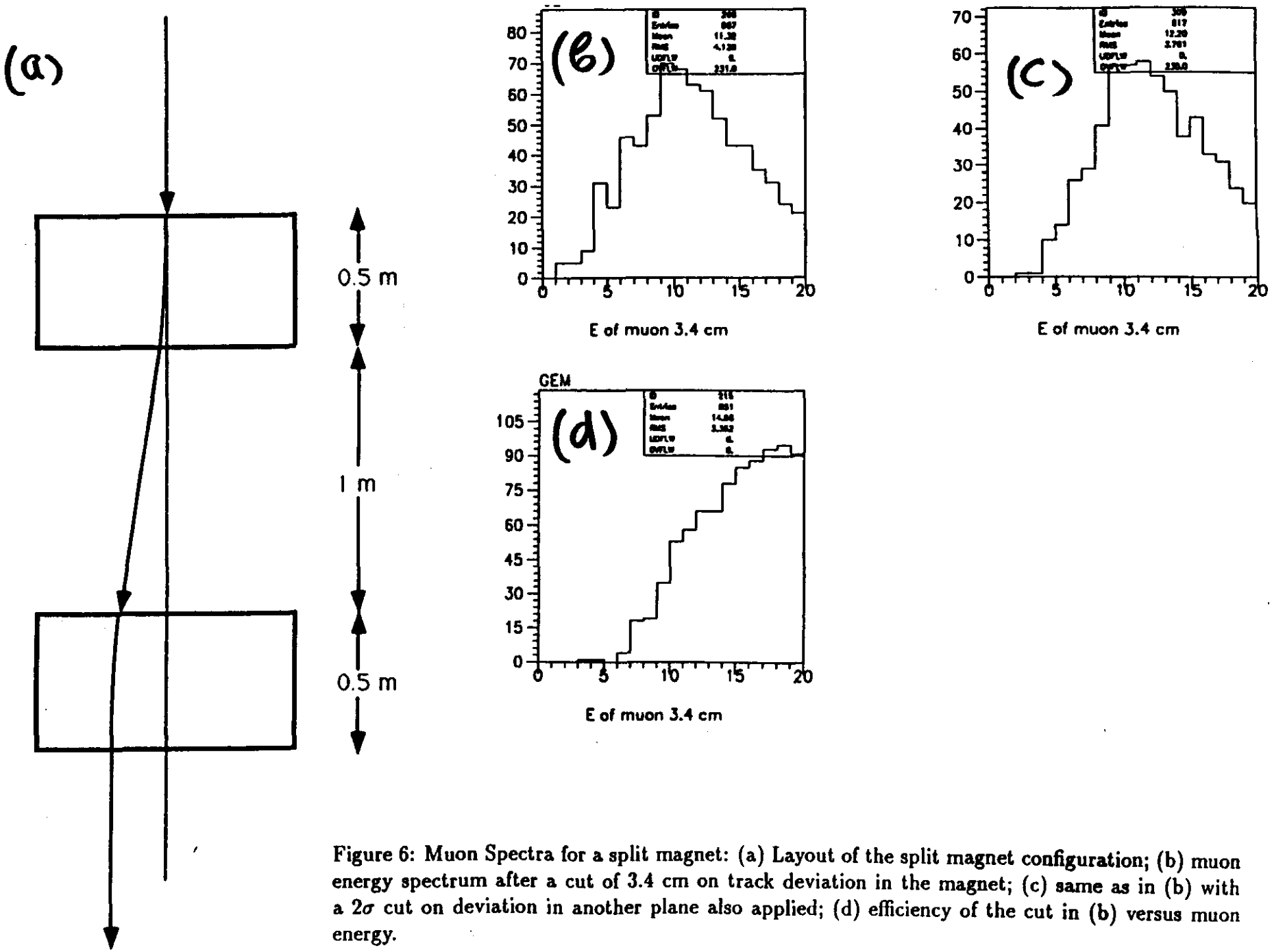

Figure 6: Muon Spectra for a split magnet: (a) Layout of the split magnet configuration; (b) muon energy spectrum after a cut of 3.4 cm on track deviation in the magnet; (c) same as in (b) with a 2σ cut on deviation in another plane also applied; (d) efficiency of the cut in (b) versus muon energy.

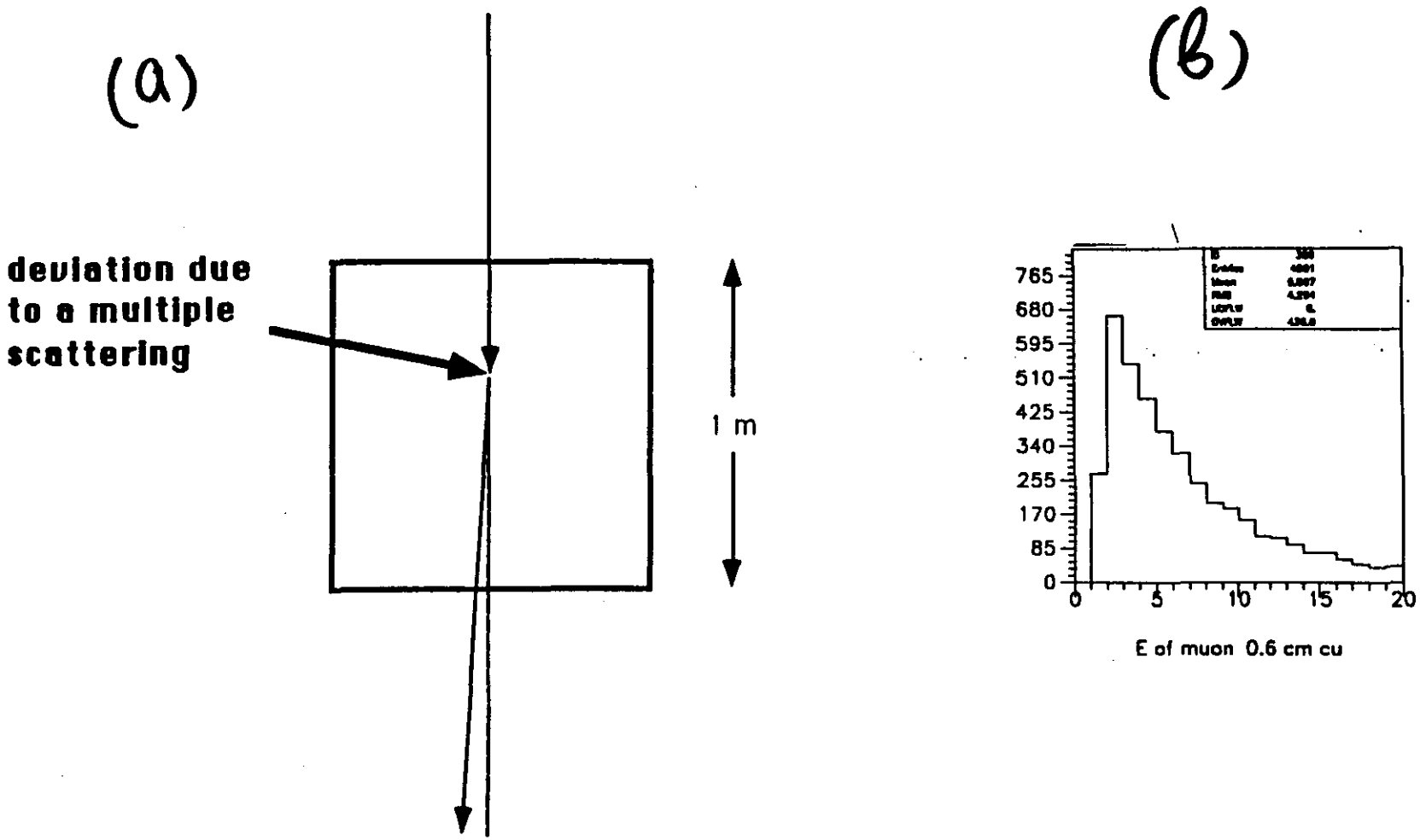

Figure 7: Muon Spectra after traversing 1 m block of an unmagnetized iron: (a) layout of the unmagnetized iron configuration; (b) muon energy spectrum after a 0.8 σ cut on track deviation in the iron.

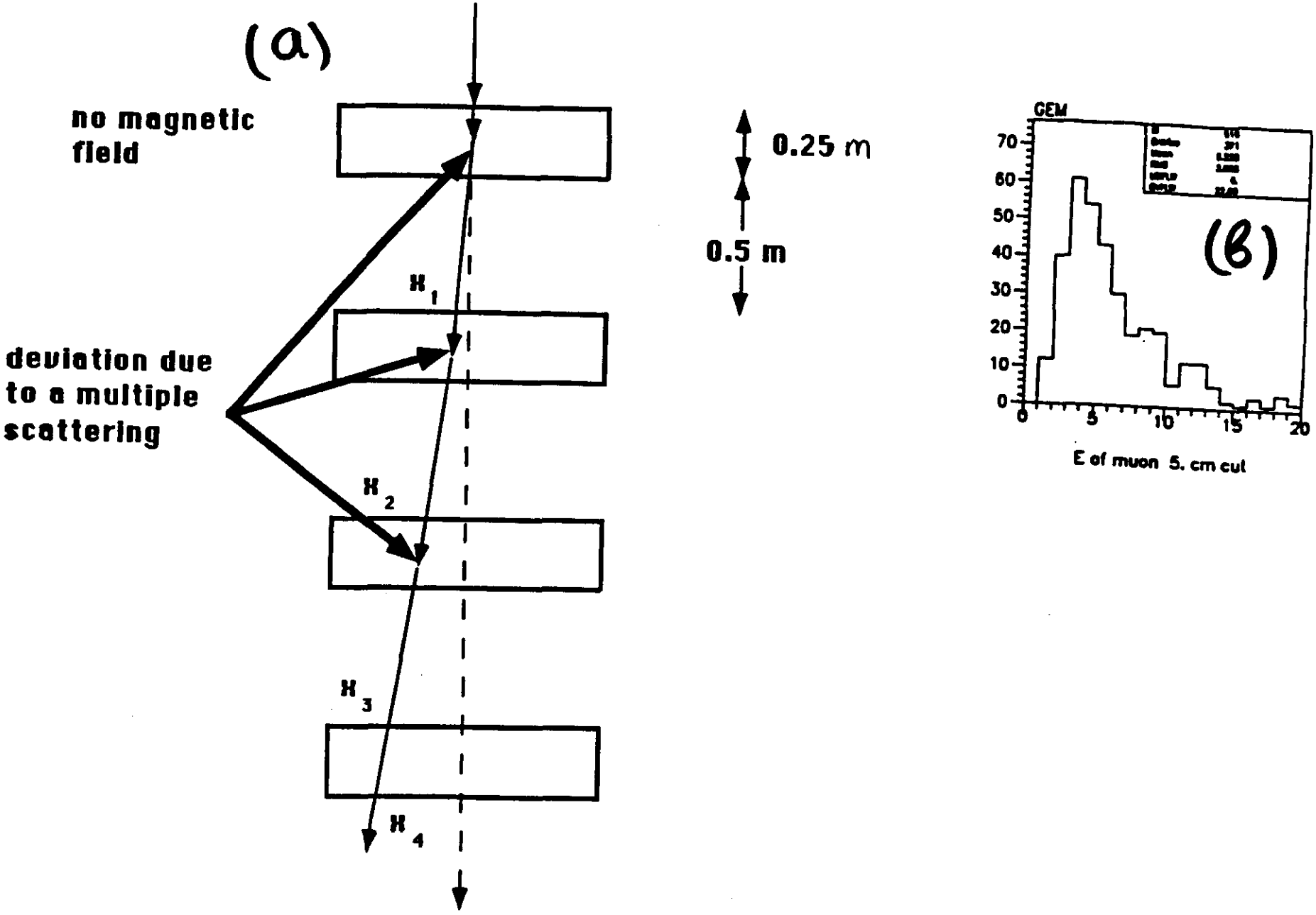

Figure 8: Muon Spectra after traversing 1 m of split iron: (a) layout of the unmagnetized iron configuration (to use multiple scettering effects more efficiently the coordinates of the track are measured in each air gap); (b) muon energy spectrum after a 2 σ cut on track deviations measured in all four chambers applied.

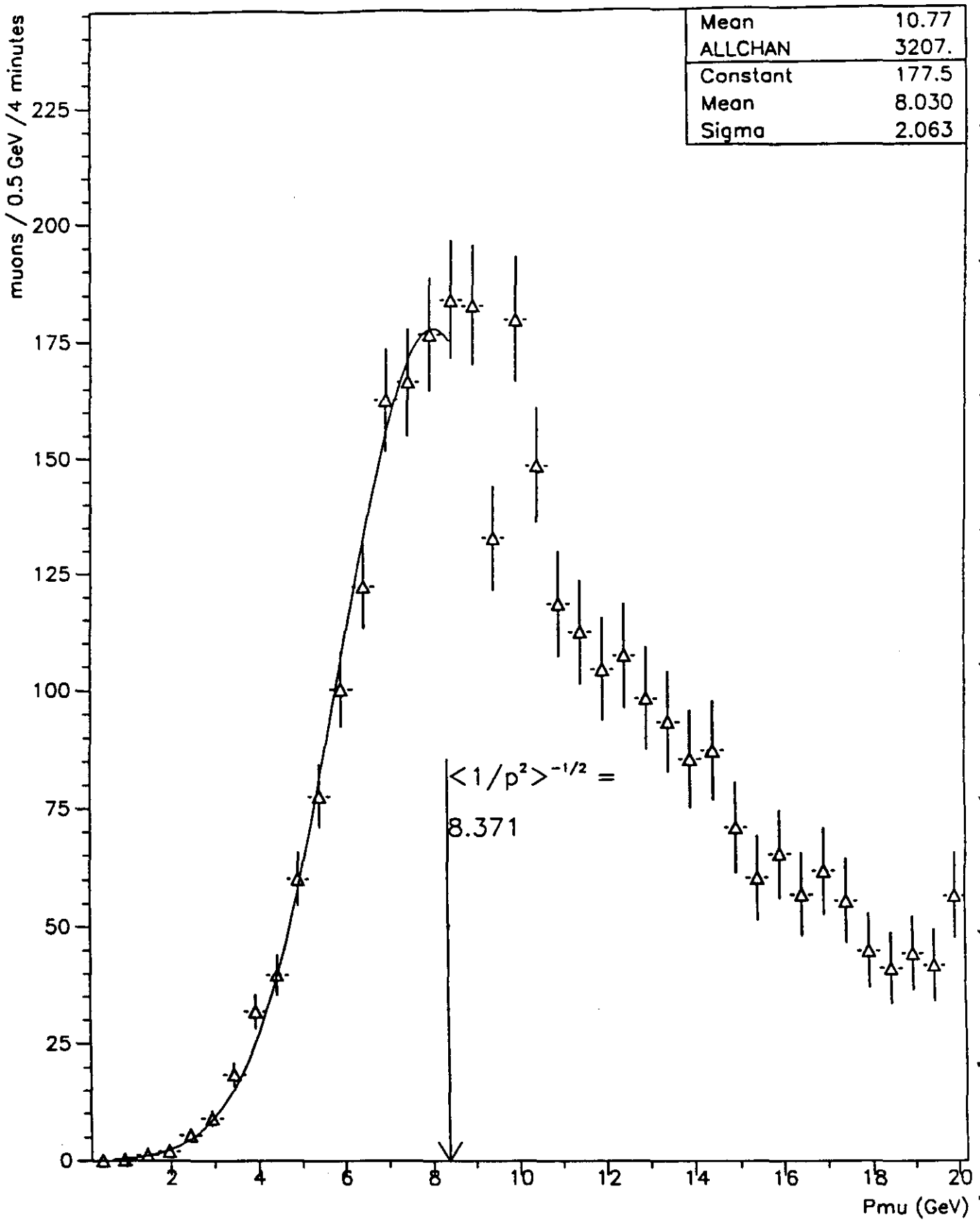

Figure 9: Muon spectrum after off-line selection (1 m 1.5 T magnet).

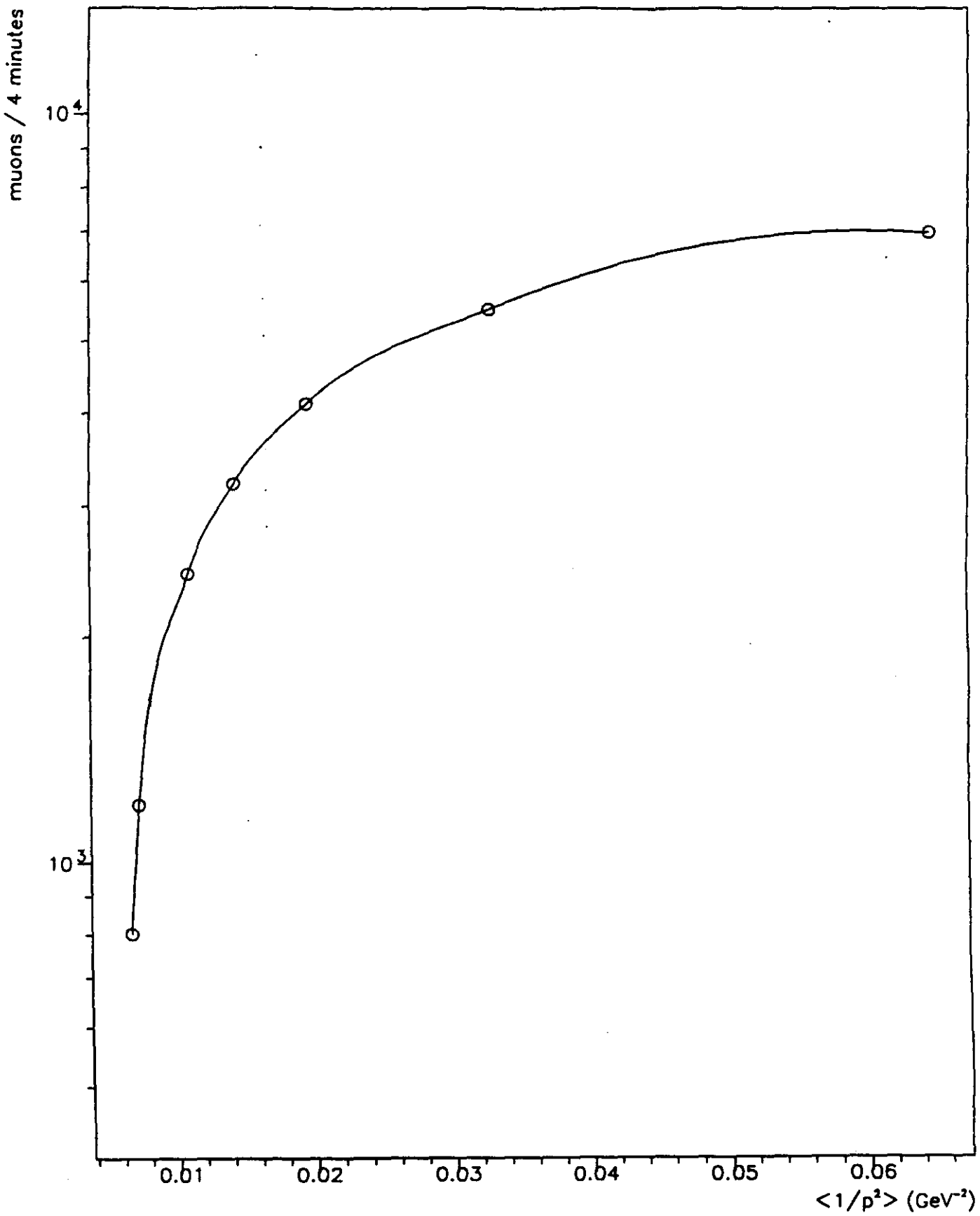

Figure 10: Rate of muons in the upper layer of the TTR Iarocci chambers versus $< 1/p^2 >$ for the selected spectra.

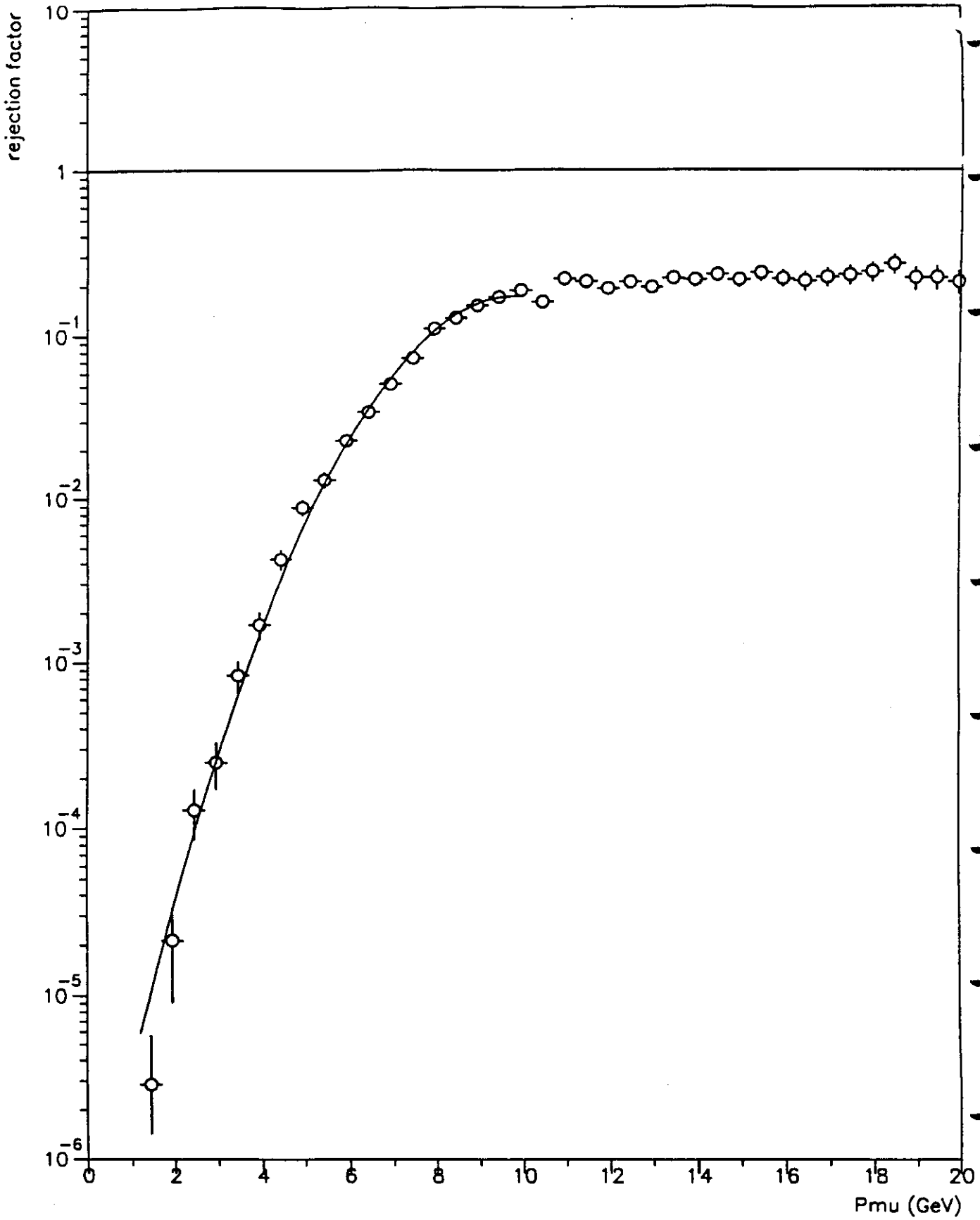

Figure 11: Efficiency of the off-line muon selection in TTR.

Enclosure [1.4]

March 30, 1992

Proposal To The Texas National Research Laboratory Commission

Measurements of Muon Backgrounds and Muon Chamber Performance for the GEM SSC Experiment

A. Johnson, J. Shank, S. Whitaker
Boston University

C. Lyndon, R. McNeil
Louisiana State University

M. Mohammadi*, M. Rijssenbeek, C. Yanagisawa
State University of New York at Stony Brook

[* contactperson]

Contents:

1. Introduction
2. Muon Backgrounds
3. Cathode Strip Chambers
4. RD5 Experiment at CERN
5. Manpower and Resources

References

Budget and Discussion

Faculty Short Resumes

1. Introduction

In designing a high precision muon tracking system for experiments at the SSC, we depend critically on our knowledge of muon backgrounds after many absorption depths of calorimeter. Especially in the forward direction were backgrounds are severe, detailed knowledge of hadron punchthrough is needed. Measurement of this punchthrough, together with realistic test beam studies of chamber resolution, momentum resolution, rate dependence, and trigger efficiency will provide some of the crucial ingredients needed to put together a robust design. For the GEM detector, proposed for the SSC, several types of muon systems are under consideration, varying according to location - central or forward region - and according to detection techniques.

In this proposal, we request funds for performing muon beam tests with the Cathode Strip Chamber (CSC) prototypes, the main technique proposed for muon tracking in the forward regions. We also request funds for extensive hadron punchthrough studies, which will lead to improvements in the simulation code for punchthrough from thick absorbers.

Presently, two CSC prototypes are under construction, at Brookhaven National Lab and at Boston University. Tests were foreseen with cosmic rays only, both locally and at the SSC Lab Muon Cosmic Ray Facility. Such tests, although necessary to test the chamber behaviour, are insufficient to gauge realistically the behaviour of a SSC muon system for the forward region. In the forward regions, particle densities are very high and muon tracking is complicated by increased punchthrough rates, back scatter, and beam halo. In addition to the above personnel, physicists from the Brookhaven National Lab and the Oak Ridge National Lab will also participate in this work but under separate funding.

Over the next few years, the only high energy muon and hadron beams available will be at CERN. Furthermore, there is an R&D effort (the RD5 experiment) presently under way at CERN that aims at making measurements necessary for the design of LHC muon detectors. Here, we present a plan for participation in the RD5 experiment to conduct the above-mentioned muon studies. Our proposed collaboration with RD5 is subject to their final approval. Discussions so far indicate their strong interest and encouragement. A

formal decision by the RD5 collaboration will be made after presentation of this proposal (by V. Polychronakos of BNL, and M. Mohammadi) in the next RD5 collaboration meeting on April 27, 1992.

The muon background and punchthrough studies would initially make use of existing RD5 data. New data with the standard RD5 configuration, and dedicated measurements with different configurations, will be required for further studies and validation of Monte Carlo simulations. Additionally, the cathode strip chambers would be tested in the RD5 setup. The RD5 collaboration is interested in developing large area muon chambers for a detector at LHC. Our testing of this promising new technology as part of a joint program would be beneficial to both groups.

Finally, we stress the urgency of this R&D work in view of the fact that these measurements will help in deciding some of the outstanding issues, such as calorimeter thickness, muon chamber technology, chamber cell size, and type of gas, before the submission of the GEM technical design report. It should also be noted that the first RD5 run is scheduled for July 30, 1992.

2. Muon Backgrounds

We are interested in studying the hadron punchthrough and decays and muon radiation backgrounds, which have consequences in muon trigger rates and pattern recognition. We have done extensive Monte Carlo simulations of these backgrounds. These simulation results should be confronted with reliable test beam measurements in order to fine-tune the Monte Carlo.

Muon backgrounds can be simulated by a code which has the relevant interaction probabilities and can create and track the secondary particles. GEANT including GHEISHA is such a code, widely used in the high energy community. However, due to the inherent simplifying assumptions in the code, it is critical to validate and calibrate its results for thick absorbers (8 and more absorption lengths) using experimental data. Some comparisons of GEANT with data have been performed. For example, Fig. 1 shows the momentum

spectrum $1/N_{inc}dN/dz$, where $z = P_{out}/P_{inc}$, P_{inc} is the incoming hadron's momentum and P_{out} is the exiting particle's momentum after 18.5 absorption lengths measured by experiment E379 [1]. The curve is the result from a GEANT simulation [2], which is in good agreement with the data, both in magnitude and shape. Note that the spectrum is sharply peaked at low momenta. It is important to continue such comparisons with different incident particle momenta and types, and to study other characteristics of the punchthrough shower exiting the absorber.

Full scale GEANT simulation of hadron punchthrough, following all secondaries is very CPU intensive. However, one can utilize GEANT, or experimental data, to produce shower probability tables of sufficient complexity to represent the full-fledged simulation. Such look-up tables already exist for punchthrough studies (PCHTHR) and are used by members of the GEM and SDC collaborations to study rates and optimize their detectors. Fig. 2 shows the particle rate at SSC design luminosity exiting a calorimeter of constant depth in λ following an inner tracking region of 75cm radius [3]. The particle rate is divided into that from punchthrough and muons which enter the calorimeter from the tracking volume, both prompt muons produced at the interaction point and muons from π/K decays. The rate of punchthrough falls below that from real muons only above 12λ and this provides an important criterion in evaluating the optimum depth of calorimeter. Another criterion is the detection efficiency and measurement resolution of muons in or near jets. Here, not only are the multiplicity, and momentum spectrum of the punchthrough particles of interest, but also their lateral spread, exit angles, and particle type.

The present tables in PCHTHR have been derived from simulation of the passage of hadrons through material by GEANT. It is crucial to check the GEANT simulations against experimental data for the particle distributions and to tune the GEANT parameters as necessary. It is also important to understand the limitations of using GEANT (or other simulation codes) for punchthrough showers and, in the event that GEANT proves unable to reproduce experimental data, substitute the actual experimental data to make the shower profiles. For an incident hadron momentum and absorber thickness, punchthrough shower profiles can be expressed in terms of the following quantities necessary to produce

4-vectors of outgoing particles:

a. The probability for any punchthrough to occur, including:

- the probability for the hadron to "sail" through the calorimeter without suffering an interaction;
- the probability for the incident pion or kaon to decay to a muon before it interacts (this produces a stiff muon).

b. The multiplicity of the punchthrough shower (charged particles, P> 1 MeV/c).

c. The particle type of the outgoing punchthrough particles.

d. Momentum spectrum of punchthrough particles.

e. The lateral spread of the punchthrough particles with respect to the projection through the calorimeter of the parent track.

f. The outgoing direction of the punchthrough particles with respect to the incoming direction. This seems to only depend on the outgoing particle momentum.

The relevant correlations between the above quantities must also be included so that the punchthrough shower produced from the tables represents adequately the details of the experimentally produced punchthrough shower. It would be important for the RD5 experiment to be able to produce the above data distributions for comparison with GEANT. It is also necessary to know the dependence of the above distributions on different absorber and chamber materials, and on magnetic field.

Neutrons and gammas exiting the calorimeter produce additional background signals in muon detector components which are sensitive to them. Preliminary simulations show that the flux of neutrons and gammas exiting the calorimeter is orders of magnitude greater than that for charged particles and depends on the material used in the calorimeter. It is therefore important to include the neutron and gamma punchthrough probability distributions in our look-up tables and to validate the GEANT simulations of n/γ punchthrough with experimental data. The sensitivity of muon detector components to neutrons and gammas should be clearly understood before final detector design decisions are taken. The RD5 test beam would enable us to measure the sensitivity of the CSC's to not only charged

particles but also to the neutrons and γ's produced in the tail of the shower.

As for the muon-induced showers, these arise from radiation and delta rays produced by highly energetic muons traversing the material of the calorimeter and muon system. GEANT is generally fast enough to be used fully to simulate this background. Some initial simulations of chambers in zero field at a FNAL testbeam gave encouraging results [4]. But the data were too limited to fully understand the characteristics of the muon-induced showers as a function of magnetic field and different materials of the muon system and final layers of the calorimeter. It is hoped that the CERN test beam could be used to validate muon-induced showers and muon energy loss distributions produced by GEANT.

In summary, a fast hadron punchthrough-shower simulator, which produces realistic punchthrough showers and rates in a relatively short CPU time, will be a valuable tool for muon detection studies. Simulated punchthrough showers will have to be critically compared with experimental data.

3. Cathode Strip Chambers

Detecting and measuring muons in the pseudorapidity interval $2.5 > |\eta| > 1.5$ is widely acknowledged as one of the most difficult experimental challenges at future high energy hadron colliders. Conventional drift chambers or drift tubes are unable to properly handle the rapidly varying muon and background rates in this region. Furthermore, triggering on forward muons presents a formidable challenge. For the GEM experiment at the SSC, we propose to use a system based on multiwire proportional chambers with segmented cathode strip readout. Such a system offers many advantages:

a. Easy cathode segmentation to optimize rates and/or pattern recognition.

b. The same device is used for all functions of the muon system, namely:

- precision momentum measurement;
- measurement of the transverse coordinate;
- bunch crossing assignment;
- level 1 and higher trigger ability.

c. Insensitivity to variations in the gas gain, wire positioning, gas pressure and temperature, etc..

Brookhaven and Boston University, recently joined by Stony Brook, have started a vigorous R&D program to develop and study such a system. A large ($\approx$2x1m^2), trapezoidal, four layer chamber is being constructed, see Fig. 3. Its size is close to that of a foreseen endcap module. The anode wires have a spacing of 2.5 mm and the four anode planes are staggered and their signals OR-ed together to reduce the earliest time of arrival jitter to $\approx$5 nsec. One of the two cathode planes in each layer is segmented in strips of 0.5 cm pitch. Charge interpolation between neighboring strips is expected to provide spatial resolution of the order of $50\mu m$. Such interpolation precision has been achieved in smaller test chambers. For the readout of the cathode strips, we are using a multichannel monolithic preamplifier (the AMPLEX chip developed at CERN) with appropriate hybrid preamplifiers. Work is under way at the BNL Instrumentation Division for the development of an AMPLEX variant suitable for these chambers. Such a custom monolithic circuit-based readout would make a system like this economically and technically feasible.

We plan to test the CSC prototype with cosmic rays, locally and in a test facility under construction at the SSC Laboratory. However, we feel that with the very soft cosmic ray muons it will be difficult to demonstrate the design performance of the chambers. In addition, questions of triggering and problems caused by hadronic punchthrough can only be addressed in a sophisticated high energy accelerator-based setup such as the one built for the RD5 experiment at CERN, allowing for simultaneous acquisition of the shower profile. Because of the CSC's monolithic multiplexed readout, the module requires little additional hardware and is quite portable. It is our belief that testing it in the RD5 setup will result in minimal disturbance of the main RD5 effort. Furthermore, the RD5 collaboration may find this kind of chambers an interesting alternative to the chambers presently under consideration. The honeycomb chambers of the NIKHEF group, which have already been used in the experiment, are very similar in principle to the cathode strip chambers.

4. RD5 Experiment at CERN

The RD5 experiment (Study of Muon Triggers and Momentum Reconstruction in a Strong Magnetic Field for a Muon Detector at LHC - CERN/DRDC/90-36) was first proposed in 1990. The main objectives of the experiment are: punchthrough measurements, muon momentum measurements, trigger studies, and a test of large area muon chambers.

The experimental setup is shown in Fig. 4. There are two magnets, a superconducting solenoid having a field of 3 Tesla (the old EHS magnet), and an absorber magnet having a 1.5 Tesla field. The setup can simulate a solenoidal detector with its return yoke, or a toroidal spectrometer by switching off the EHS magnet. This magnet will only be operational in the 1992 runs. Scintillation counters and multiwire proportional chambers define the incoming muon/hadron beam. A sampling calorimeter with a depth of 10 absorption lengths and made of steel and Honeycomb Strip Chambers is installed inside the EHS magnet. Large area muon drift chambers for accurate muon momentum measurements are located in front, in the middle, and after the absorber magnet. Resistive Plate Chambers (RPC's) are mounted on these muon chambers as well as inside the absorber magnet. These chambers are used to study triggering schemes and to determine t-zero for the drift chambers.

During the summer of 1991, data were taken with beams of hadrons and muons. Preliminary results on punchthrough probability, trigger efficiency, performance of RPC's, and other measurements are summarized in a status report (Status Report of the RD5 Experiment - CERN/DRDC/91-53). The next data-taking runs are scheduled for three 2-week periods: July 30 - August 15, October 15 - 30, and November 13 - 28, 1992.

5. Manpower and Resources

5.1 Computing

Considerable CPU resources exist at LSU. A large cluster of vaxstations are used to run GEANT simulations. There are currently at least 100 mips of Vaxstations running

GEANT. Futhermore, a cluster of 20 SUN's and Decstations are being commissioned. These could also be utilized to perform simulations and/or data analysis for the CERN test beam.

Computing resources available at Stony Brook are: an IBM RS/6000 work-station, two VAX computers 780 and 785, and a cluster of twelve 3100 and 4000 Vaxstations.

We also have access to the Particle Detector Simulation Facility at the SSC Lab. Presently, there is a large amount of CPU available for these studies.

5.2 Personnel

In addition to faculty, postdocs, and graduate students from the universities submitting this proposal and listed below, physicists from the Brookhaven National Lab and the Oak Ridge National Lab are also involved with this project.

BU:	
A. Johnson, J. Shank, S. Whitaker	0.4 FTE
LSU:	
C. Lyndon, R. McNeil	1.0 FTE
student workers	
Stony Brook:	
M. Mohammadi, M. Rijssenbeek, C. Yanagisawa	1.5 FTE
postdoc (search under way) and student workers	

References

[1] K. Lang, Ph.D. Thesis, Univ. of Rochester, UR 908 (1985) (unpublished).

[2] R. McNeil, "Punchthrough simulation studies for a Precision Muon Spectrometer Based on Superconducting Air Core Toroids", EMPACT Note 240 (1990); see also EMPACT Expression of interest for the SSC, (1990).

[3] R. McNeil, "How Thick Should the GEM Barrel Calorimeter Be?", GEM Note 92-68, (1992).

[4] Talk given by A. Koryotov at the GEM Muon Group meeting Oct 17, 1991 at Boston University.

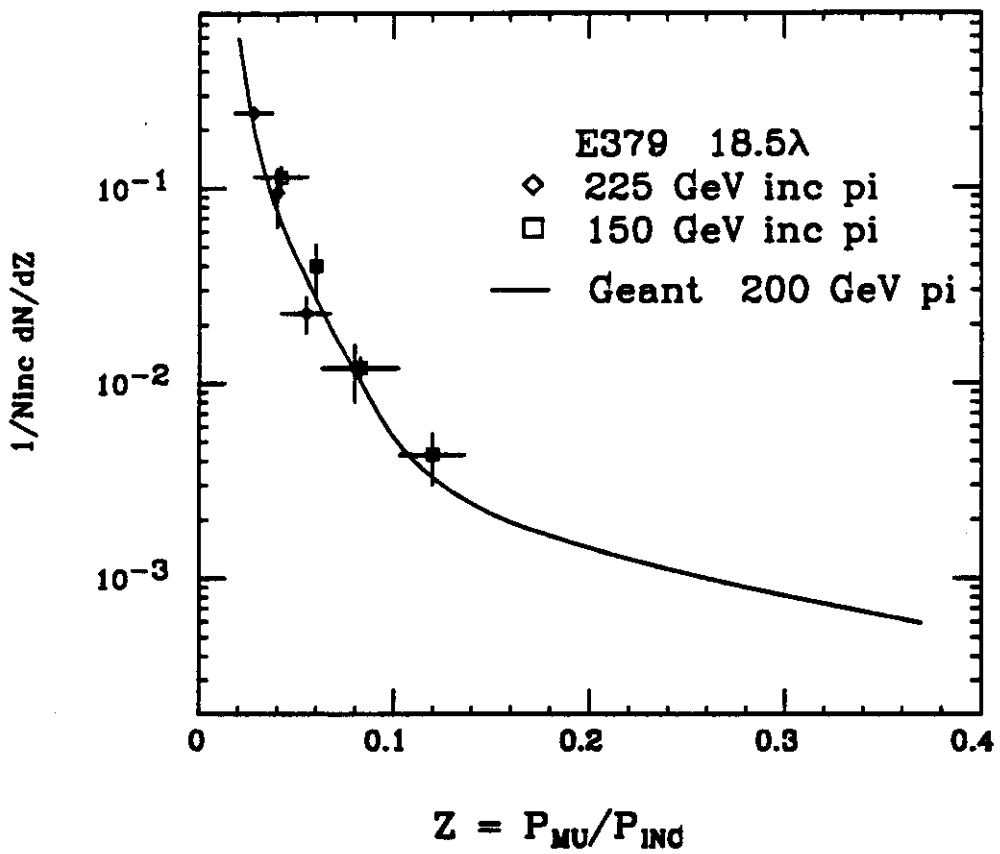

Figure 1. Comparison of momentum spectrum of charged particles after 18.5λ from GEANT simulation and E379 data.

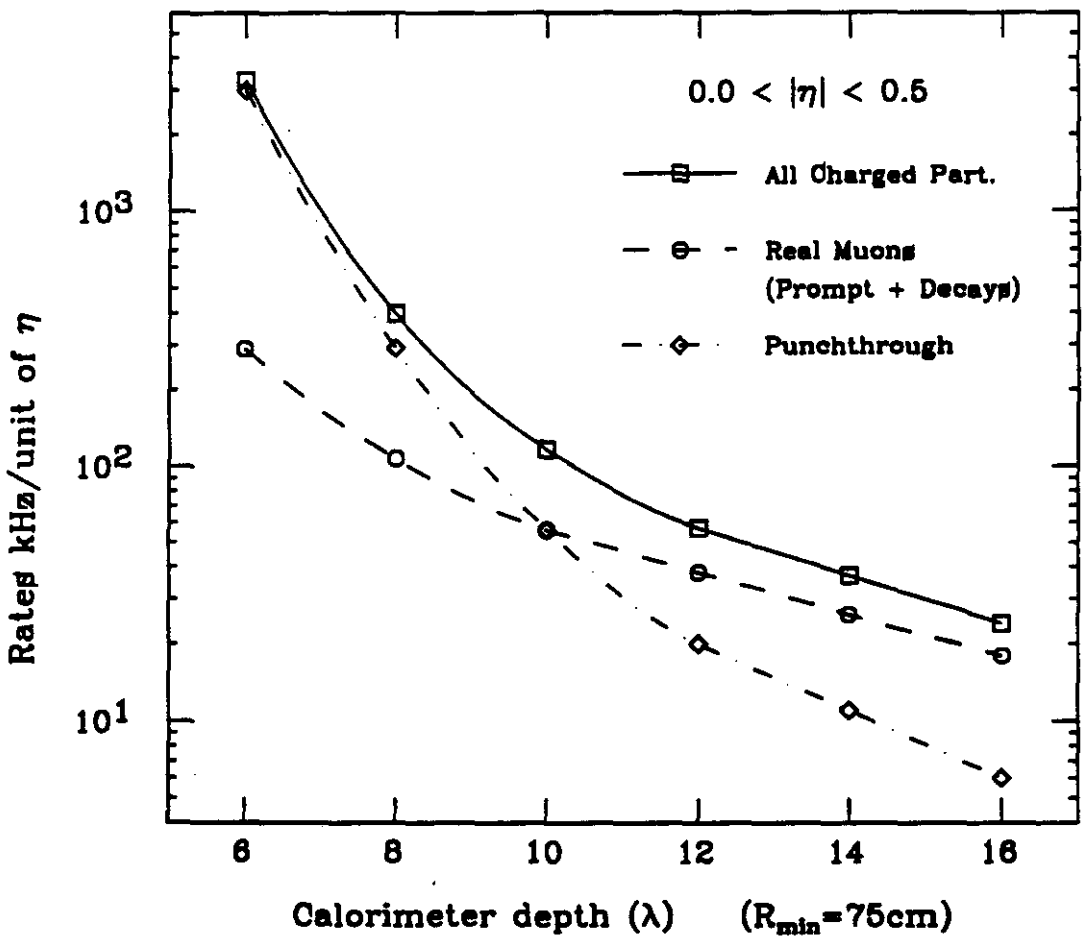

Figure 2. Rates in the central region after constant depth calorimeter at SSC design luminosity.

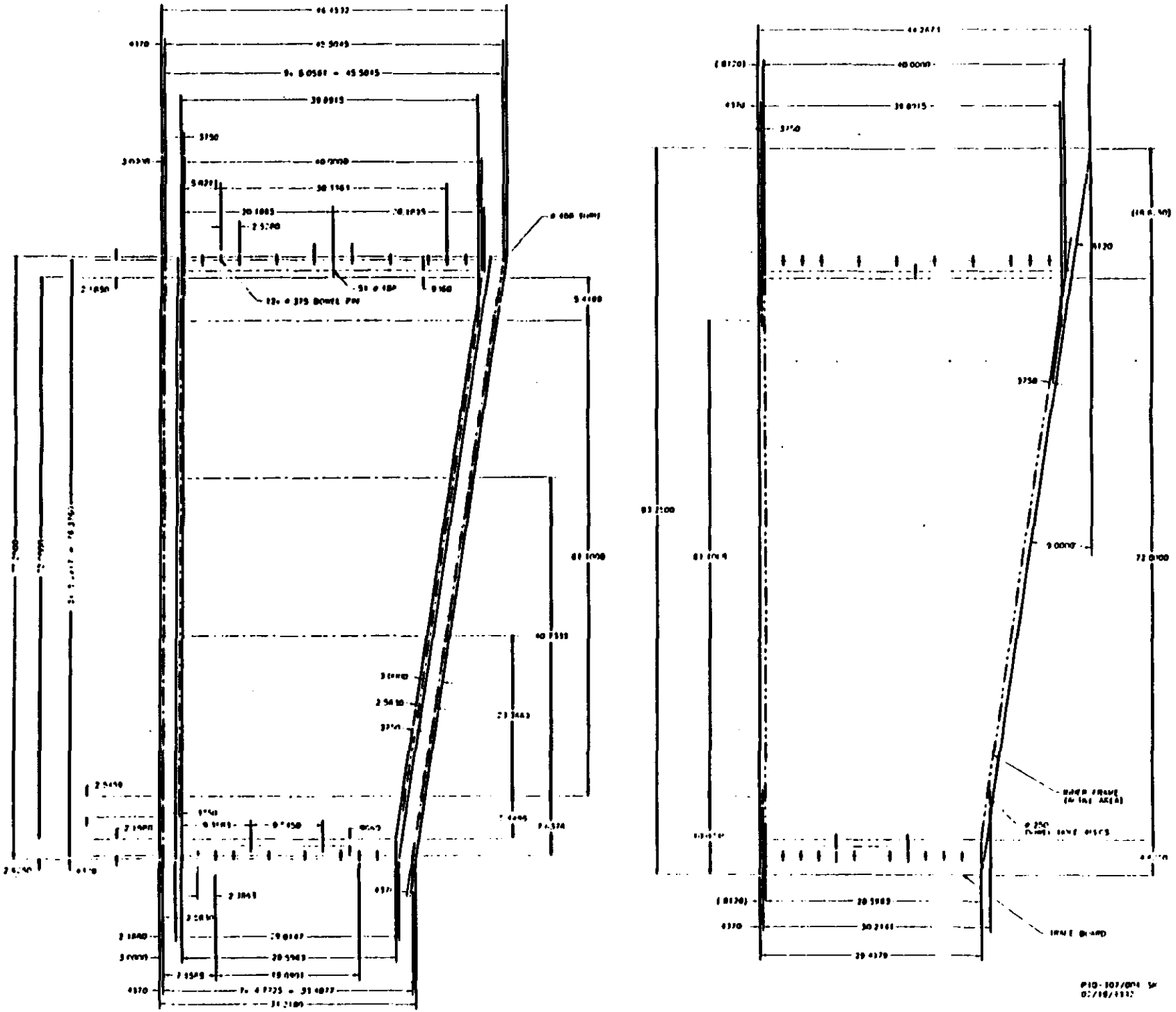

Figure 3a. Front view of GEM forward muon chamber (CSC) prototype.

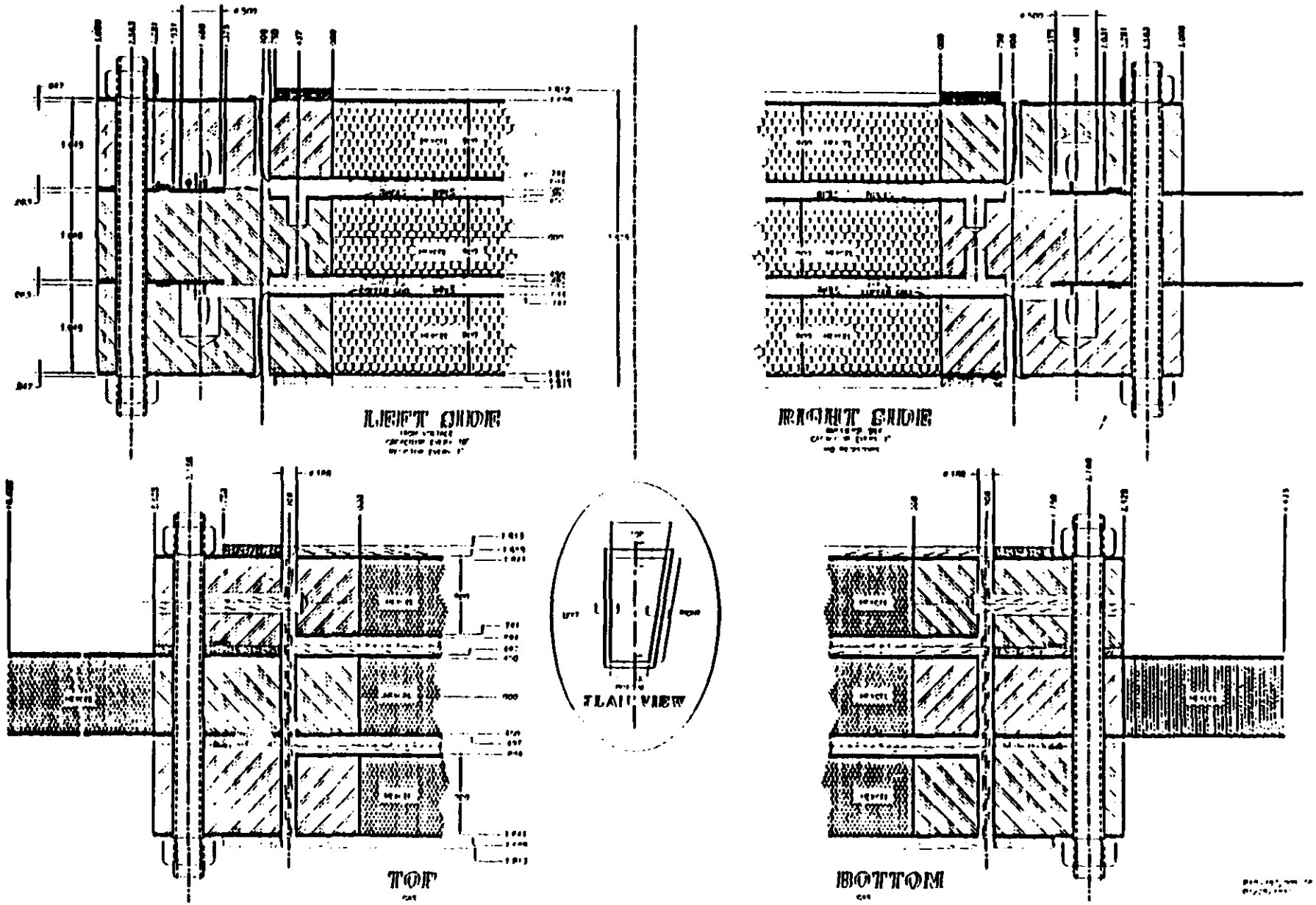

Figure 3b. Cross sections of GEM forward muon chamber (CSC) prototype.

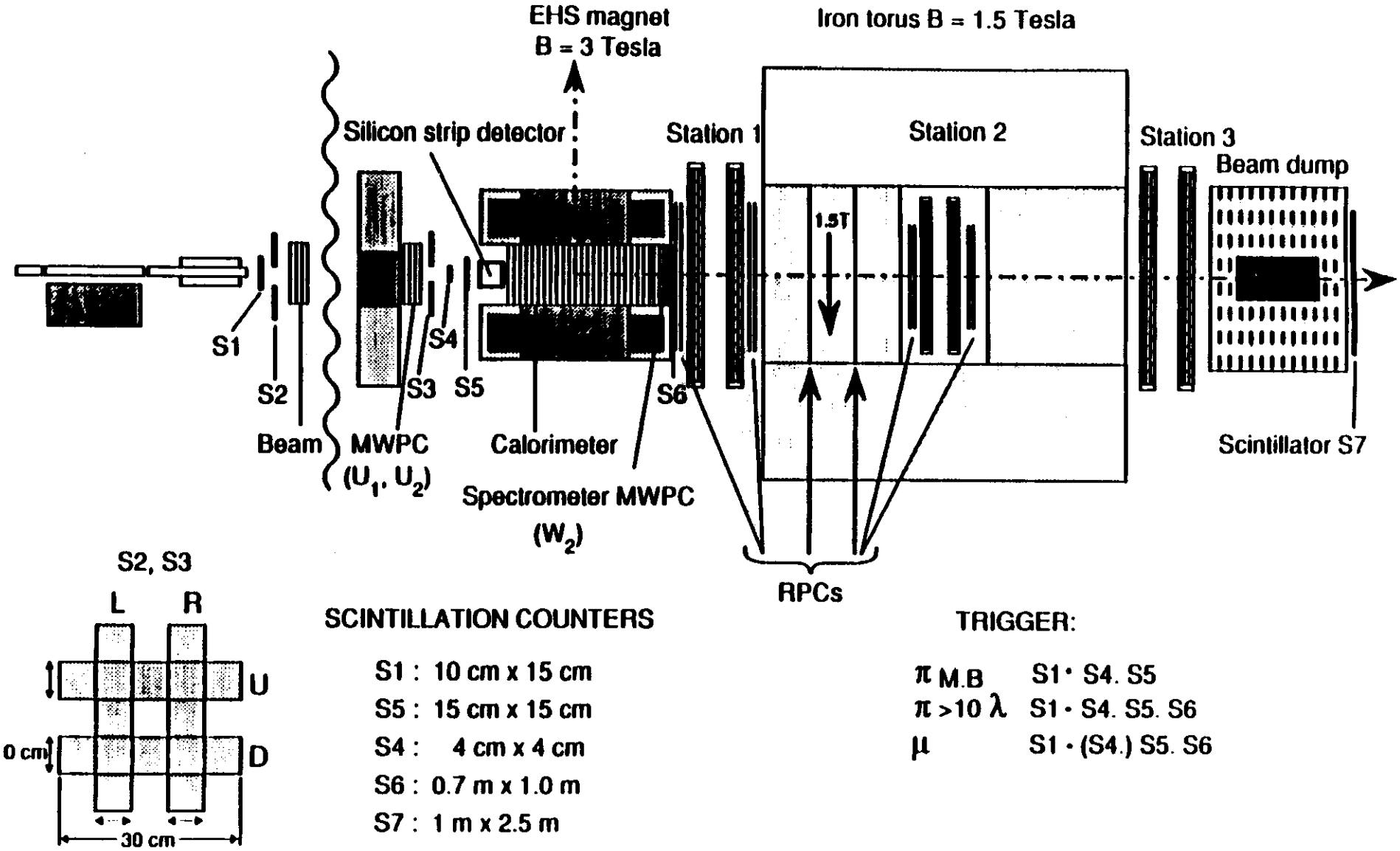

Figure 4. Experimental layout of the CERN RD5 apparatus.

Enclosure [3.4]

LSDT Note
June 29, 1992

TECHNICAL DESIGN REPORT FOR THE LSDT SYSTEM

W. Busza, J. Kelsey, H. W. Kendall, A. Korytov,

H. Linder, E. Nerlich, L. S. Osborne, L. Rosenson, D. Ross,

F. E. Taylor, R. Verdier, B. Wadsworth

Massachusetts Institute of Technology

Laboratory for Nuclear Science

Cambridge, MA

The GEM Limited Streamer Drift Tube Muon System

I. Description of chamber and its operation

A. Desiderata

The GEM muon system must cover over 10^4 m^2 of sensitive area and yet must measure sagittas in muon trajectories which can be as low as hundreds of microns. We list here some of the major desiderata that any such system should be:

1.) Fast; events must be related to their proper collision bunch. A drift system such as we propose should keep delays well below the microsecond level.

2.) Accurate; the per wire measuring error should be kept to 100 μm or better.

3.) Able to measure longitudinal position; this measurement must be in the cm range, 1) for particle mass reconstruction, 2) to disentangle multiple particle outputs from the layers after the calorimeter.

4.) Robust; it must be relatively insensitive to electronic and particle noise. Residual neutrons from the calorimeter are an example of the latter.

5.) Locatable to 25 μm's; the wires must be spatially referenced to this accuracy independent of external conditions such as temperature variations, magnet on/off, wire tension variations, etc.

6.) Usable with non-flammable gas; though at this time a flammable gas has not been arbitrarily excluded, prudence would indicate it will eventually be found too dangerous.

7.) Ammenable to mass production; this not only keeps costs down but will give rise to uniformity of product.

8.) Minimal in material; this is particularly important for the middle superlayer where multiple scattering can contribute to the momentum measurement error. Should be <XX rad. lengths.

9.) Minimally sensitive to backgrounds such as punch through and neutrons.

B. Principle of operation

We have selected a technology based on a drift tube system operating in the streamer mode. This mode of operation has been used widely in many contemporary detectors, SLD, Aleph, Delphi, etc.[1-4]. It has the merit of giving pulses of large amplitude (~100mV) and fast rise time (~10 nsecs); both properties result in a small time jitter in measuring drift times. A further merit is obtained by streamer initiation on first electron arrival; this results in about a factor of 2 better time measurement over proportional mode operation[5]. This responds to items 1, 2, and 4 above. A demerit to the system comes from the higher avalanche gains which can result in faster degradation of tube operation; this latter is much dependent on the gas being used. More on this later.

As in the applications mentioned above, the open cathode tubes allow the placement of pick-up strips facing the wires thereby allowing a measurement of streamer longitudinal position along the wire. We make use of this feature by having pick-up strips perpendicular to the wire. The time correlation with the wire pulse allows an unambiguous x-y measurement of each streamer (item 3).

Several gas mixtures, including non-flammable ones, are available to operate in this limited streamer drift tube mode (LSDT). See item 5.

C. Mechanical description

We wish to make use of the general manufacturing technology used in previous large systems[1-4]. This calls for manufacturing multiple tubes in layers and multiple layers in each gas box. Our basic detector unit has 4 staggered layers of tubes. The gas box varies in width between 0.7 m and 1.2 m in width and 3.7 m and 7.65 m in length. to fit the dimensions called for in each superlayer. We are making the cathode tube layers as complete units; the prototype chambers have such layers made from 10 mil Al. Similar constuction is envisaged for the final system although a simpler and/or cheaper manufacturing method may be found in the future. Note that the positional tolerances for the cathodes is not critical.

The positioning of the wires is critical. The wires are supported by Mycalex bridges that have been grooved accurately to receive the wires; the bridges are, in turn, accurately positioned to an outside reference point. Details of this are related in Sect. X.III.A below.

II. Prototype tests

We have made various test of our proposed technique; the detailed description and results have been, or will be published[6,7,8,10,11]. We summarize these:

1.) An aluminum tube of 2.5 cm cross section with central 100 μm wire was made with a slit window on two opposing sides to allow passage of a laser beam. The laser beam intensity was adjusted to give ionization density comparable to a minimum ionizing particle. The laser beam could be moved with respect to the wire. In this way we could obtain both distance vs. drift time curves for each gas used and each high voltage and, also, a measure of the spatial resolution. The latter gives the contribution to measuring error from electron diffusion and electronic jitter. The results are summarized in Table X.1.

2.) A 0.5 m long prototype chamber was made of four layers, each of four channels of 2.5 cm square aluminum tubes; a schematic cross section is shown in Fig. X.1. In addition, a layer of pick-up strips, orthogonal to the wire direction was placed over one layer to allow an x-y measurement of the pulses. The correlation could be done unambiguously by matching pulse times on wire and strip. The chamber was exposed to 0.5 TeV muons in the Fermilab E665 beam. By fitting muon tracks to the four point measured tracks we obtained the effective single wire measuring resolution; this is listed in Table X.1. Details of the results can be found in references 6 and 7.

In the same beam we placed various materials in front of our chamber to examine the muon induced shower production and to find the degree to which this disrupts the finding

of the muon track. Details of the results can be found in reference 8. We can summarize our findings grossly by stating the reduction of track finding efficiency from ~7% to ~17% with insertion of 10 cm of Pb.

3.) We studied another technology suggested by a Dubna group[9]. The apparatus is described in this reference. This technology is essentially the same as later suggested by the CSC GEM group for use as the muon detector in the end cap region. Details of our results are published in references 6 and 7; a summary of these is shown in Table X.2.

4. We also studied the behaviour of small tubes, as in item 1.) above, again illuminated with a laser beam but operating in a magnetic field. The details of our results can be found in reference 10. A summary of these results is shown in Table X.1. Essentially both resolution and drift times are little affected by the field, whether parallel or perpendicular to the wire.

5. A demerit of operation in the streamer mode is that the large amplification in the streamer avalanche gives rise to UV radiation which can get to the tube walls in spite of the quenching gases used giving rise to secondary electrons which, in turn, give a second pulse. This second pulse is recognizable since it occurs at the drift time from wall to wire after the first pulse.

   We have made tubes with different coatings on the inside wall; namely Al, Al with carbon coating, Ni, Cu, and Ag. We measure the number and pulse height distribution of these secondary pulses as a function of this coating, the high voltage, and the gas composition. Our results can be found in refernce 11. In summary, we found, as expected, that the secondary pulse probability increased with high voltage i.e. with avalanche gain. It was greater with Isobutane, CO_2, and CF_4, in that order. It was relatively independent of the metallic coatings we tried- Al, Cu, Ni, and Ag. However, we found that a carbon coating considerably suppresed the secondary pulses. The

reason for this is still unclear; the work function for carbon is not much different from those of the metals. We are continuing to investigate this.

III. Full chamber

A. Design

A cross sectional view of a full sized chamber is shown in Figure X.2. The chambers are supported and their positions monitored at the points along their length where the bridges holding the wires in place are located. An L-shaped strong back will fasten to the scaffolding; the position monitor (presumed, at this time to be an optical alignment method) is located in the holes provided on the upright of the strong back; a second hole is provided on the other end of the horizontal bar for vertical monitoring of the other side. The slot against which the ends of the wire bridges are mounted are precision machined with respect to the optical hole; the upright part of the L which bears the optical hole has been welded to the side wall before the machining. We have, then, only one transfer surface. The grooves in the bridge which hold the wires are precision machined with respect to the reference edge of the bridge. We have tested the machining capabilities of a CNC on a Mycalex bridge and find that it can locate the grooves in absolute position to less than 10 μm's.

The other side of the bridge is held by a slip pin which controls the height of the bridge (less tolerance required ($\pm 150\mu$m's) but is not constrained by any "breathing" of the Al box. The bridges are not in contact with the cathodes, and suffer bending only under their own weight. This would be excessive in a 1 meter span; a central post is provided to eliminate this sag.

The cathodes are stacked in four layers resting ultimately on the Hexcel bottom. The cathode placement is not critical. The present method for making the cathode planes involves attaching L-shaped beams of 10 mil Al to a substrate of 10 mil Al with thermosetting films. The result is a layer of U-shaped tubes, which, when coverd with the

next layer on top give our required layer of square cross section cathodes with minimal material.

The space over the fourth layer contains the pick-up strip plane for measurements in the longitudinal dirction.

With our design the seperation distance between bridges may be selected. We have chosen to place them at such a seperation that the droop under gravity is always below the desired measuring error rather than trust in making a correction for this, assuming the tension is as planned. This does require more bridges and more optical alignment points and thereby more cost. If one wishes to relax this requirement it can, of course, be done.

Summing all the material in the chamber, excluding the sides, a particle traverses 6.4% of a radiation length.

B. Tests

We have built a 0.5x4.0 m^2 chamber. The purpose was to confront some of the mechanical, electrical, gas handling, and software problems; it was not built with the ultimate mechanical precision required. It works and we can now take cosmic ray data and analyze it. Such an event is shown in Fig. X.3.; the radius of the circles shown around each wire represent the calculated distance of the closest ionization. The wires are connected to one another with short delay lines in pairs at the end opposite the electronics. By measuring time differences in each pair one may get a coarse ($\pm$ 15 cm) measure of the longitudinal position of the track along the wire. The figure shows both the direct pulse and its delayed counterpart on the adjacent wire. Shown also is a straight line fit made to the direct pulses.

C. Electronics

The electronics for the chambers is described in greater detail in Sect. X.Y of this report. It is a straight forward application of, and improvement over present day techniques. We use, at present, a discriminator based on the LeCroy MVL407 and a multichannel TDC Camac module, LeCroy 2277. A block diagram for one channel is shown in Figure X.4. Presumably, the eventual electronics will be a custom chip functionally similar to this but

with improvements in speed and cost. A more detailed description of the electronics for the LSDT system can be found in Sect. V.Z. of this report.

IV. Full system

A. Layout in GEM detector

The layout of the chambers in the GEM detctor is shown in Figures X.5 (side view) and X.6 (end view). We have assumed the 8-8-4 configuration for measurement number in successive layers. It appears prudent to keep the full 8 layers in the chambers just outside the calorimeter in view of the particle disentanglement which will probably be necessary to find the muon track within the punch thorough and shower tracks expected at this point.

The chambers have been overlapped wherever possible to maximize efficiency for getting at least some measurement on every track. We would probably bring the electronics feed through a bulkhead at the top and bottom of the chambers rather than at the end (as done in the prototypes) to minimize dead space; this is always possible with no more than 2 chambers to a super layer. This would occur at the inner junction between two chambers so that the outter, particle sensitve, ends would extend as far as possible.

B. Inventory of chambers

Table X.3 gives an inventory of the chambers with dimensions and number of wires and bridges. The totals for the whole system is also shown.

C. Outline of manufacture

1. Parts procurement

A philosophy behind the LSDT chamber design is that the parts from which the chambers are assembled and which represent a fair fraction of the cost are based on common technology. In this way we can expect the benefits from competitive bidding, common technology, and multiple sources were production times a problem. The work is also accessible to foreign participation though much of it depends on modern machining tecnology i.e. the availability of a CNC machine.

The one technology which has the air of the unusual is the production of thin cathode planes. This is being done for our prototype chambers at Lincoln Laboratory of MIT. They are also taking on the responsibility of locating outside manufacturers who are capable of mass producing the prototypes that they have made and who are also interested in the work. It is from these that we also get cost estimates for the work.

2. Wiring factory

Ultimately the parts must be brought together, the wires strung, and the finished chambers tested. We have had experience in this; the MIT CSC group which forms part of the GEM LSDT group operated the factory which built the modules for the SLD WIC system. It required laying down a comparable number of wires as required here ($\sim 10^5$). We have also had the help of R. Weinstein of the U. of Houston who operates a factory for making Iarocci tubes (SCARF)[4]. Our projected factory makes use of this experience. In order to explain and estimate times and cost we have broken down the steps in the manufacture and testing of chambers; this is illustrated in Fig. X.7.

We wish to make as much use of mass production methods as possible both to minimize costs and to assure a more homogeneous product. Thus, a fair fraction of the total effort is placed into designing and building specialized apparatus for wiring, soldering, checking, and testing the chambers. The details of all this can be found in the back-up material submitted with our cost analysis[13].

V. Costing of full system

The costing of this proposed system is covered in another section of this report, Sect. XX. vskip 0.2in **VI. Performance**

A. Meeting the specifications

We list here some of the specifications which we have high lighted to be used in evaluating the technologies within the GEM muon group and the degree to which they are met

by this LSDT system.

1.) Alignment-chamber: This depends first on the alignment system. For transfer from the this system to the wire bridge we expect $< 25\mu$m's.

2.) Alignment-wires: < 25 μm's.

3.) Wire measurement: < 100 μm's and random. Could be < 60 μm's with Argon-Isobutane.

4.) Dead time per wire: determined by pulse duration, 100 nsec.

5.) Track measurement efficiency per layer: 96%. Loss is due to delta ray production. The efficiency for finding a vector in our 4 layer chamber-getting 3 out of 4 hits- is ZZ%.

6.) 2D capability: available.

7.) Temperature stability: 1 meter of Mycalex expands 10 μm's per ^{o}C.

8.) Noise sensitivity: little-time measurements and the large streamer pulses are relatively immune to noise.

9.) Sensitivity to gas parameters: gas mixture, pressure, and temperature must be monitored.

10.) Safety: The use of Isobutane above the flammability point, 10%, is problematic. However, we can use non-flammable gases though these give poorer resolutions. In any case, the chambers would be run at low pressures ($\sim$ 0.5" of water).

11.) Multiple scattering probability: each 4 layer chamber presents 6.4% of a radiation length.

B. Backgrounds

1.) Punch through

The punch through rates have been calculated[14]. The main problem occurs when a muon is associated with a hadronic jet. These processes have been simulated. The results indicate that a minimum calorimeter thickness of XX interaction lengths should be

used, that the first muon superlayer should have a full 8 measuring layers, and that a 2D measurement on tracks in this layer is desirable.

2.) Neutrons

The sensitivity of our tubes to neutrons has been measured and is reported in reference 15. This was measured both in the direct neutron spectrum from a Cf^{252} source and the moderated spectrum after 30 cm of Boron loaded polyethylene. The "efficiency" was 5.2×10^{-3} and 2.5×10^{-3} respectively with an uncertainty of 50%. Roughly half of this came from a conversion source which was not the gas; it is thought to be some deposit on the inside wall of the tube from insufficient cleaning or condensate from the flowing gas. If we take the neutron flux from the middle barrel region at 4 meters[12] , $.0115 \times 10^{12}$/n/SSC year (a moderated flux), we would get a typical counting rate of $\sim$ 1.8 kHz/wire with no moderator after the calorimeter and, possibly, a factor of ten less with moderator. With no moderator this also amounts to 2.5×10^{-3} Coulombs per cm of wire per year. One Coulomb per cm of wire is considered to be a danger point if no additives are added to the gas.

The above seems reassuring but certain cautions must be expressed. The neutron fluxes at smaller angles are 10^2 and 10^3 times larger; one must make sure that these larger fluxes do not rattle around in the magnet and affect the central angles. The neutron flux calculations should be refined beyond doubts. One must make sure that extra-calorimeter sources, e.g. the accelerator, do not contribute.

3.) Muon generated showers.

During the Fermilab tests (see Sect. II) we investigated the E-M showers produced by muons by measuring the track proliferation in our chambers produced by Pb in front of the chambers. The results were checked against a Monte Carlo simulation with reasonable agreement[14]. An extrapolation of these measurements with the Monte Carlo allows an estimate of track loss (not found); this is 3% for an 8-8-4 muon system but 9% for a 4-8-4 system.

References

1.) A. C. Benvenuti et al. "The Iron Calorimeter and Muon Identifier for SLD", SLAC-PUB-4677, July 1988; NIM **A276**, 94 (1989); NIM **A290**, 353 (1990); NIM **A289**, 463 (1990).

2.) Aleph Technical Report 1983, CERN/LEPC/83-2; LEPC/PI 15 May, 1983.

3.) Delphi Technical Proposal CERN/LEPC 83-3 (1983); NIM **A273** (1988) 841.

4.) K. Lau et al, NIM **A306**, 397 (1991); D. Hungerford et al, NIM **A286**, 155 (1990).

5.) A. H. Walenta, Proceedings of Summer Institute on Particle Physics, SLAC Report, July 1983.

6.) Yu. Bonyushkin et al., NIM **A315**, 55 (1992).

7.) Yu. Bonyushkin et al. (Toroidal Spectrometer Group), SSC Detector R & D Program, Progress Report No. 218, Sept. 1991.

8.) Studies of shower production with Pb

9.) G. Alekseev et al., "The Strip Readout for the EMPACT Muon System", EMPACT/TEXAS Note 242 (1990); Yu. Bonyshkin et al., "Readout for EMPACT Muon System Detectors: Strip Readout Studies", EMPACT/TEXAS Note 327 (1990).

10.) A. Korytov et al. "Studies of LSDT's in a Magnetic Field", GEM Note TN-92-123.

11.) A. Korytov et al, "Studies of Cathode Material for the LSDT", GEM Note TN-92-121.

12.) D. M. Lee, R. E. Prael, L. Waters, GEM Note TN-92-91; L. Waters, private communication.

13.) Cost analysis of the factory

14.) R. McNeil, GEM Note Note TN-92-XX.

15.) A. Korytov et al, "Neutron Sensitivity of LSDT Chambers", GEM Note TN-92-122.

Figures

Fig. X.1 A cross-sectional view of the prototype chamber used in the Fermilab tests.

Fig. X.2 Cross sectional view of a typical full sized chamber

Fig. X.3 Cosmic ray event from a 0.5 m x 4.0 m prototype chamber

Fig. X.4 Electronic block diagram

Fig. X.5 Chamber layout in the GEM detector;side view

Fig. X.6 Chamber layout in the GEM detector ;end view

Fig. X.7 Block diagram of the assembly procedure in the chamber factory

Table X.1: Resolution* and T_{max} for Drift Readout in 2.5 cm. cells								
Gas⟶	A-IB 25 – 75		A-IB-CO_2 2.5 – 9.5 – 88		CO_2 – CF_4 – IB 20 – 69 – 11		CO_2 – CF_4 – IB 40 – 50 – 10	
Ioniz. Source↓	σ (μm)	T_{max} (n sec)	σ (μm)	T_{max} (n sec)	σ (μm)	T_{max} (n sec)	σ (μm)	T_{max} (n sec)
Laser-no mag. field	35	260	55	830	70	280	70	460
Laser- mag. field(0.8 T)	45	278	60	835	75	295		
0.5 TeV Muons	55				95		75	

* Averaged over all drift times

Table X.2: Resolution* for Pick-up Strip Readout (1.0 cm. strips)		
GasAmpl.Mode ⟶ Ioniz.Source ↓	Proportional	Limited Streamer
Laser	45 μm	100 μm
0.5 TeV Muons	85 μm	

* Averaged over all ionization positions

1

Table X.3 Chamber Inventory: GEM LSTD System
for 8-8-4 system, 16 sectors

Barrel

Layer	r(m)	l(m)	w(m)	chmbrs. /sect	total chmbrs	wgt/sect (lbs.)	vol/sect litres	wires /chmbr	bridges /chmbr
1A1a	4.1	3.80	0.70	1	32	236	307	112	12
1A1b	4.1	3.80	0.80	1	32	254	358	128	12
1A2a	4.1	3.80	0.70	1	32	236	307	112	12
1A2b	4.1	3.80	0.80	1	32	254	358	128	12
1B1a	4.3	3.70	0.80	1	32	249	350	128	12
1B1b	4.3	3.70	0.75	1	32	240	325	120	12
1B2a	4.3	4.30	0.80	1	32	278	400	128	12
1B2b	4.3	4.30	0.75	1	32	372	372	120	12
2A1a	6.0	5.60	1.15	1	32	439	764	184	16
2A1b	6.0	5.60	1.00	1	32	402	655	160	16
2A2a	6.0	5.60	1.15	1	32	439	764	184	16
2A2b	6.0	5.60	1.00	1	32	402	655	160	16
2B1a	6.2	5.40	1.00	1	32	392	634	160	16
2B1b	6.2	5.40	1.20	1	32	440	774	192	16
2B2a	6.2	5.90	1.00	1	32	417	688	160	16
2B2b	6.2	5.90	1.20	1	32	468	840	192	16
3A1	7.9	7.45	1.10	2	64	1091	1900	176	20
3A2	7.9	7.45	1.10	2	64	1091	1900	176	20
3B1	8.2	7.25	1.10	1	32	535	926	176	20
3B2	8.2	7.65	1.10	1	32	556	974	176	20
Sect Totals				22		8689	14,251	3,424	344
Gnd Totals					704	278,062	456,032	109,568	11,008

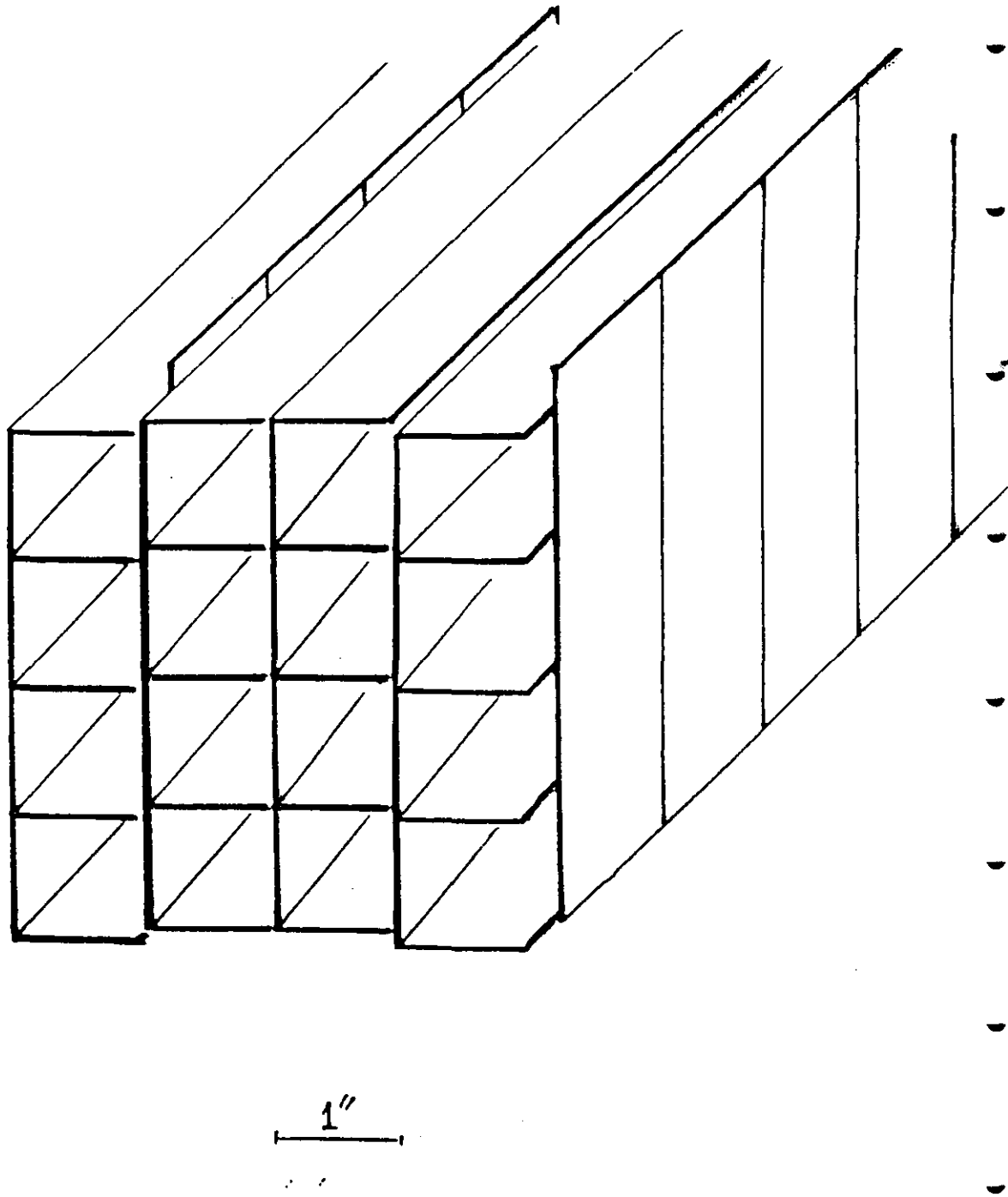

Fermilab Muon Telescope

Fig. X.1 A cross-sectional view of the prototype chamber used in the Fermilab tests.

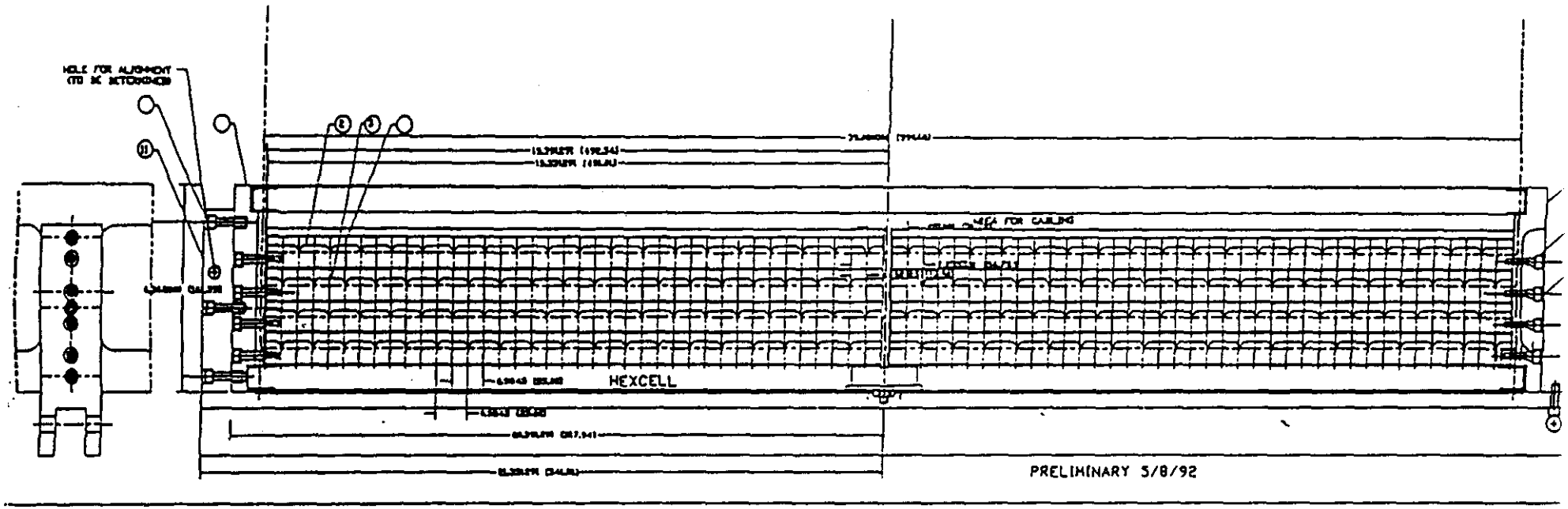

Fig. X.2 Cross sectional view of a typical full sized chamber

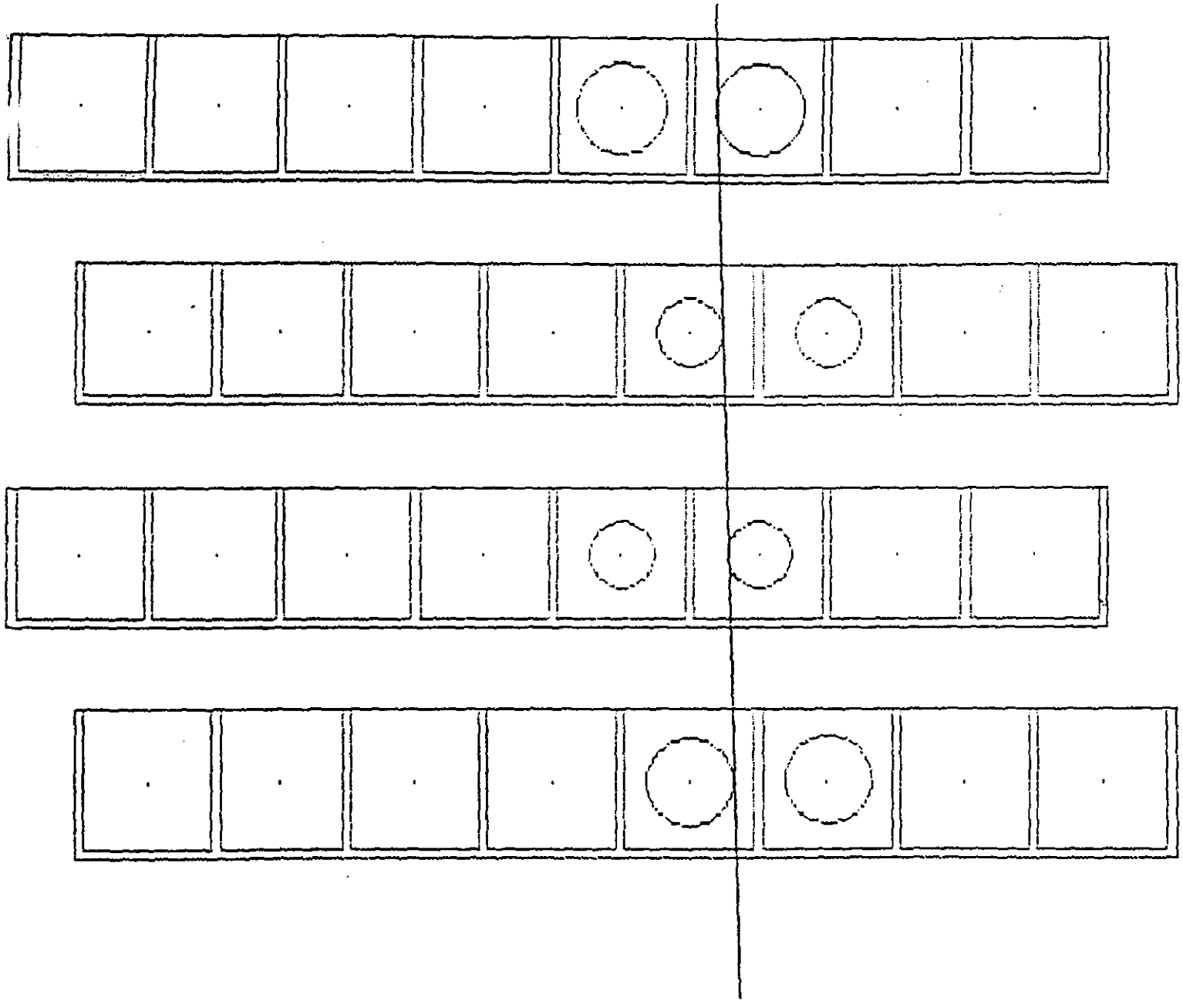

Fig. X.3 Cosmic ray event from a 0.5 m x 4.0 m prototype chamber

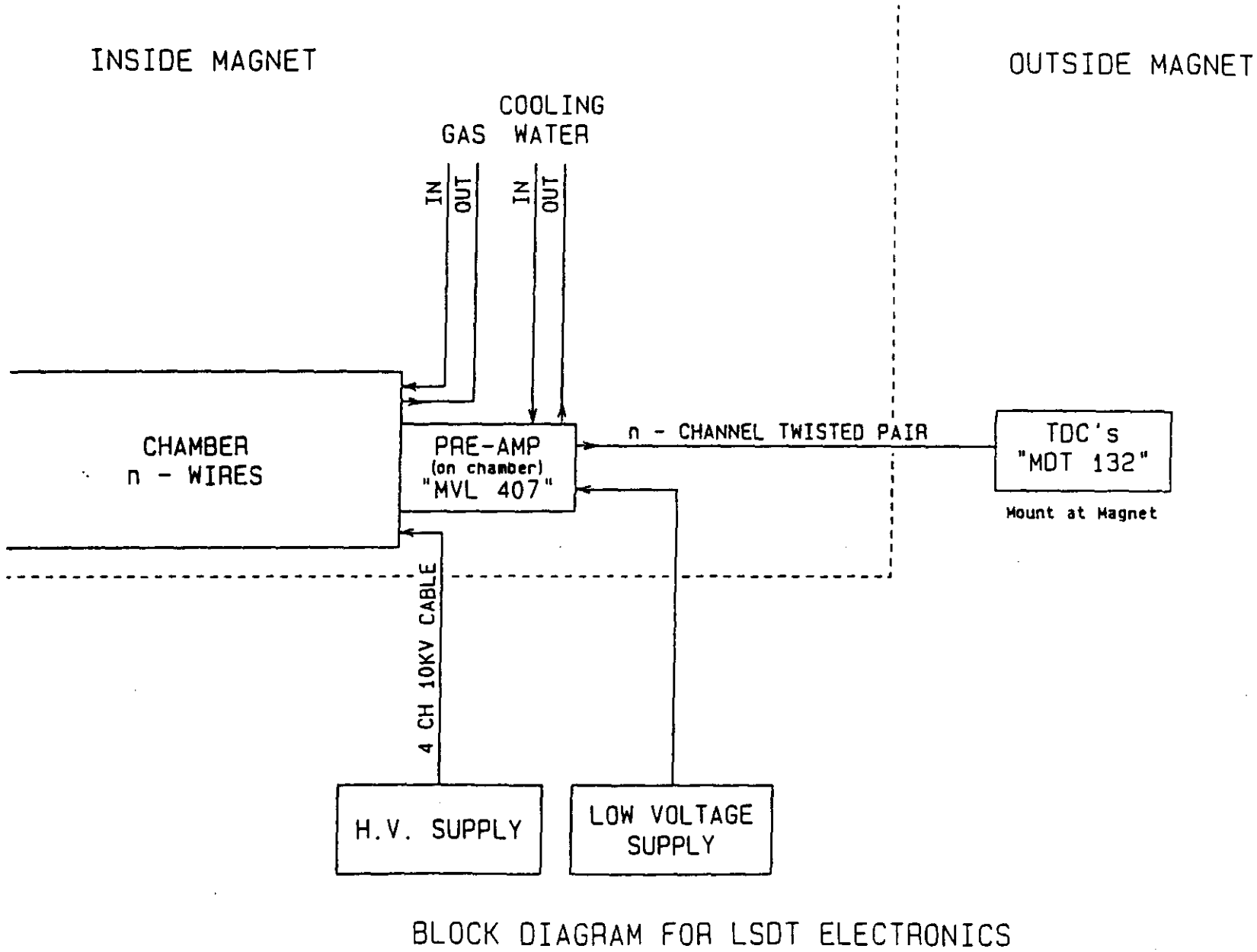

Fig. X.4 Electronic block diagram

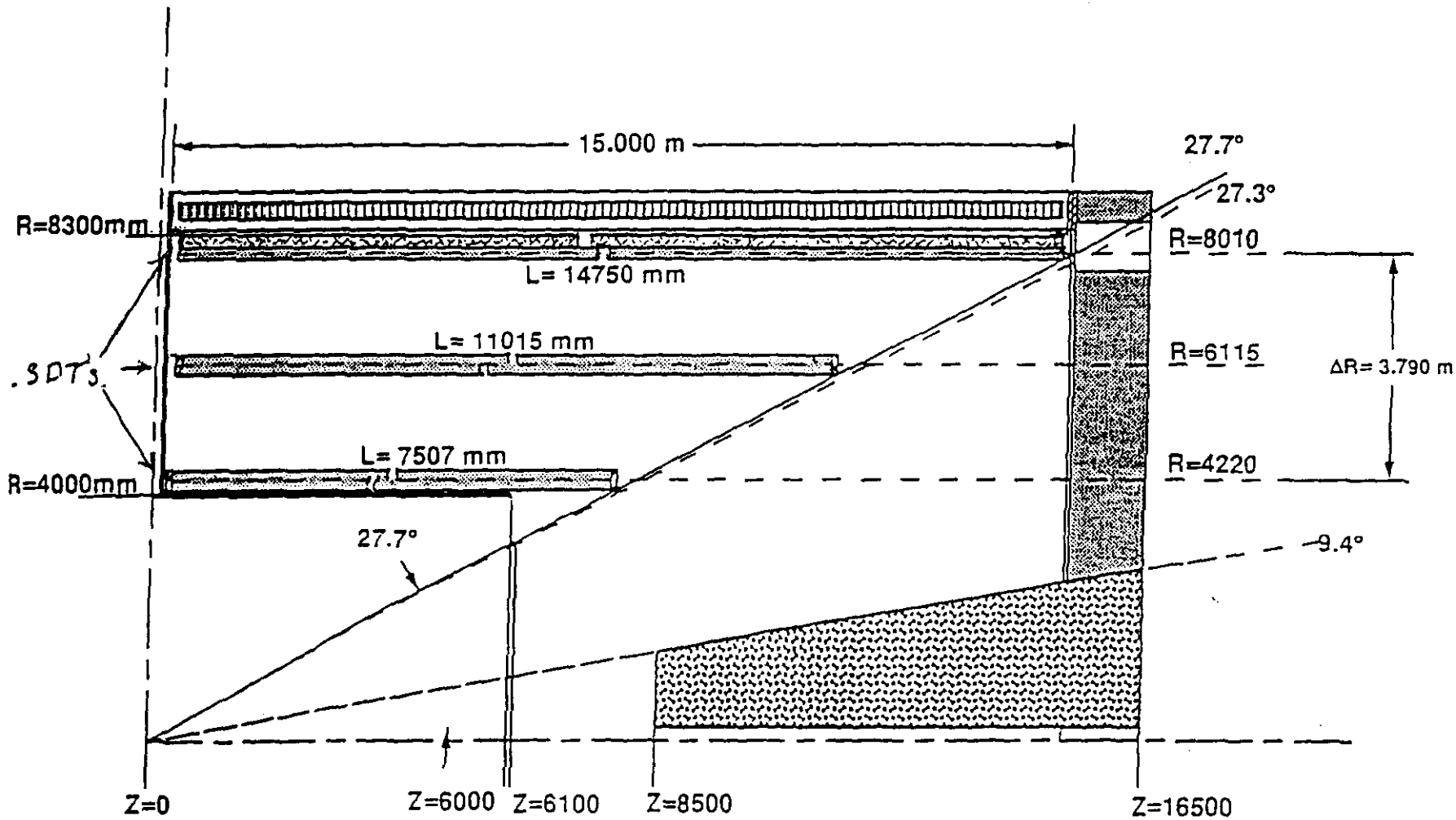

ELEVATION

Fig. X.5 Chamber layout in the GEM detector;side view

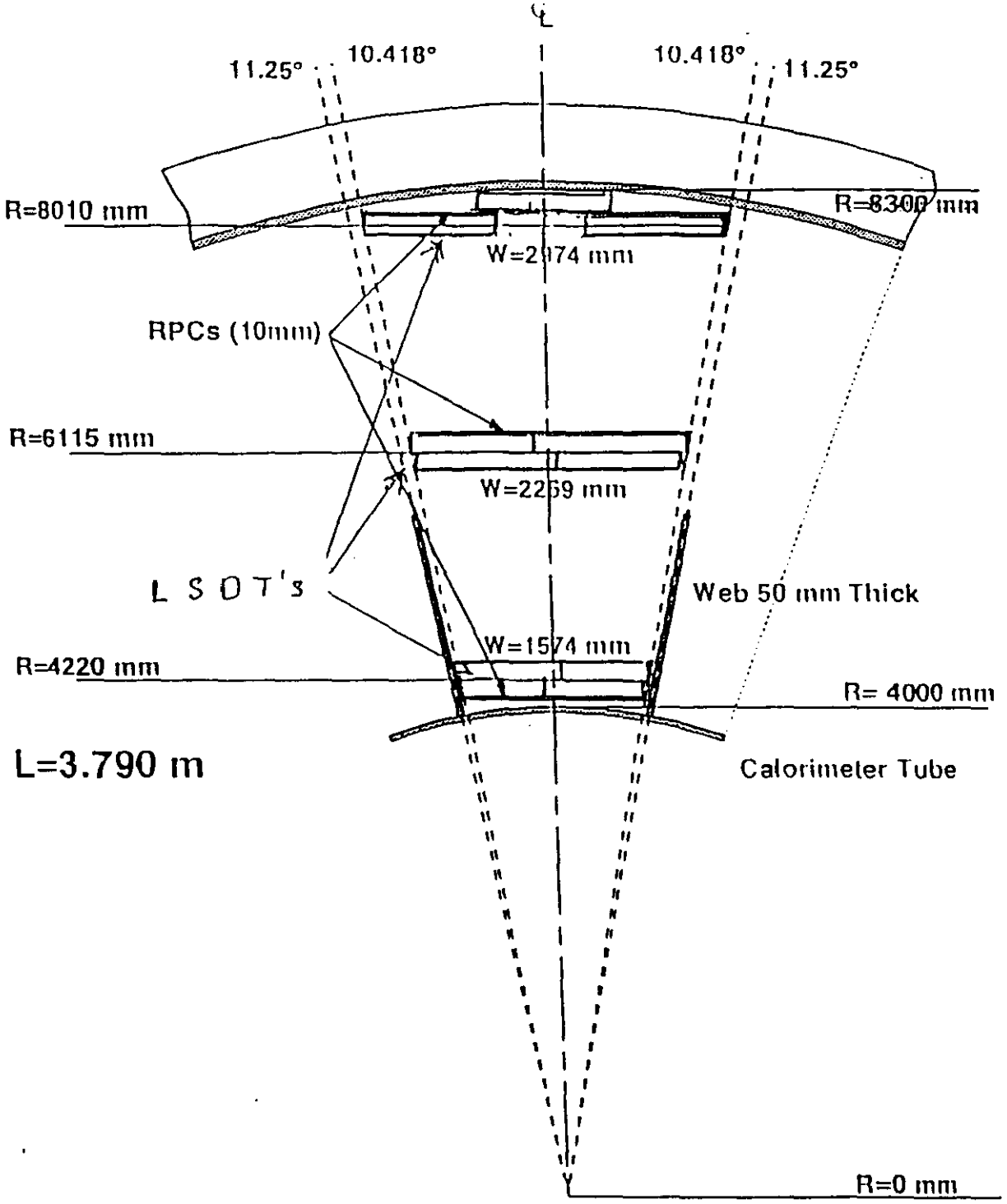

Fig. X.6 Chamber layout in the GEM detector ;end view

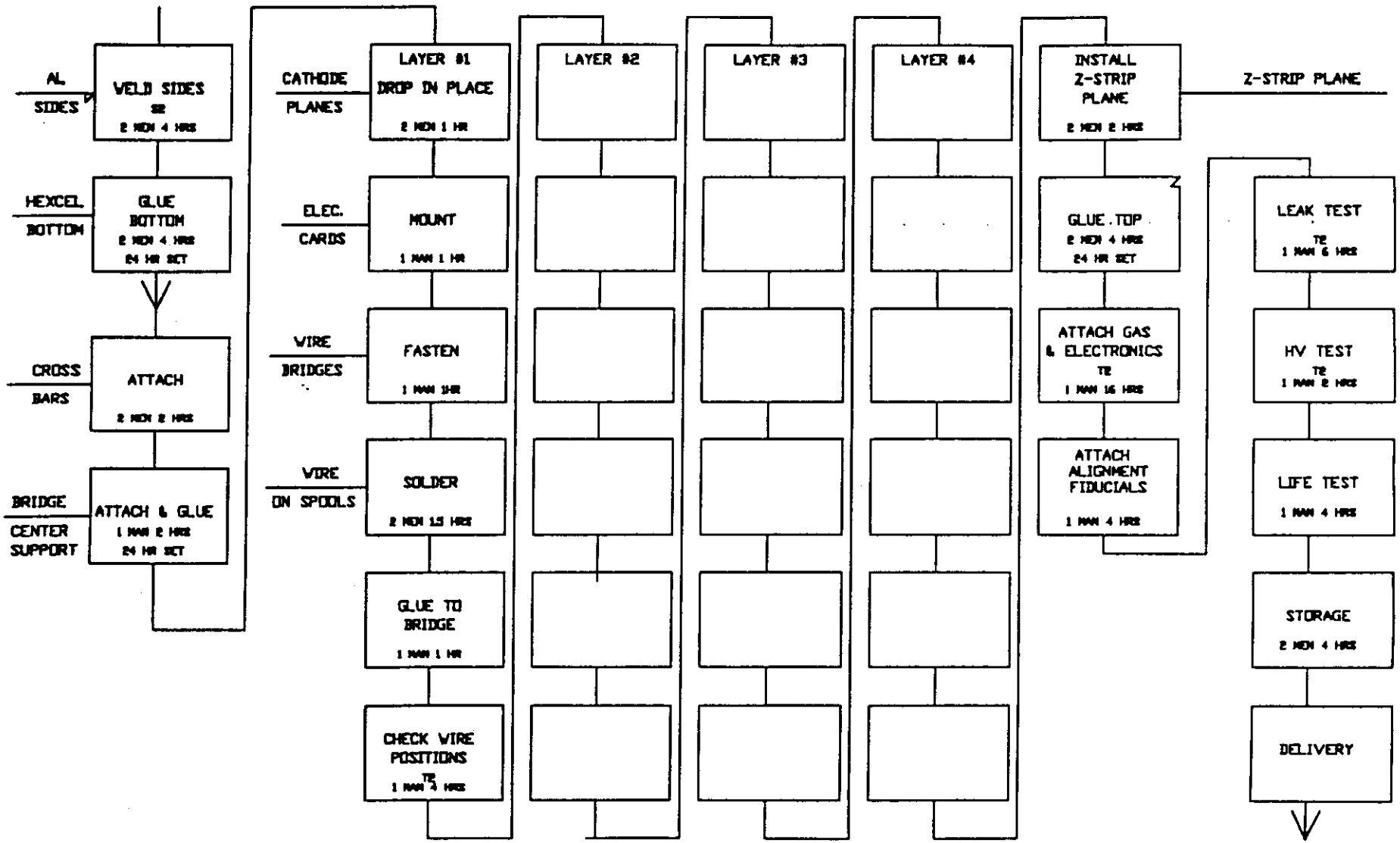

Fig. X.7 Block diagram of the assembly procedure in the chamber factory

Enclosure [5.1]

Some Alignment Concepts for the GEM Muon Array

J. Paradiso
C.S. Draper Laboratory

June 1992

Abstract

This report introduces a basic alignment scheme for the GEM muon detector. Optical straightness monitors are described, and their application discussed. Alternative alignment technologies are suggested and techniques are identified that can provide multipoint measurements. The problem of global alignment is posed, and several concepts are presented to attain the required precision.

Some Alignment Concepts for the GEM Muon Array

-- J. Paradiso, June '92

Each phi sector of the muon detector array (i.e. "hexant") will be instrumented to monitor the relative alignment of its composite drift chamber layers. The most critical such measurement is the deviation in chamber alignment from a straight line along a muon path. If the 3 superlayers are relatively displaced along the muon bending direction, a false sagitta will result, leading to errors in the momentum measurement. In order to retain the quoted 5-10% momentum resolution of the GEM muon detector, the allowed misalignment of sense wires between chamber superlayers must be limited to ±25 μm (in the bending coordinate).

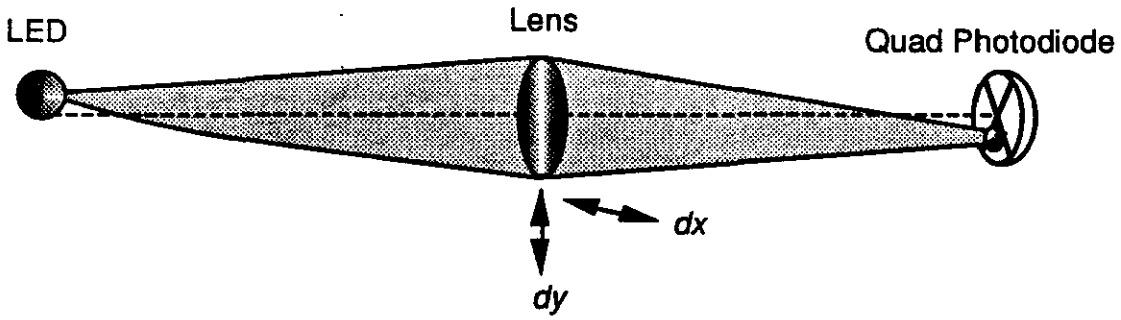

Figure 1: The Basic Straightness Monitor

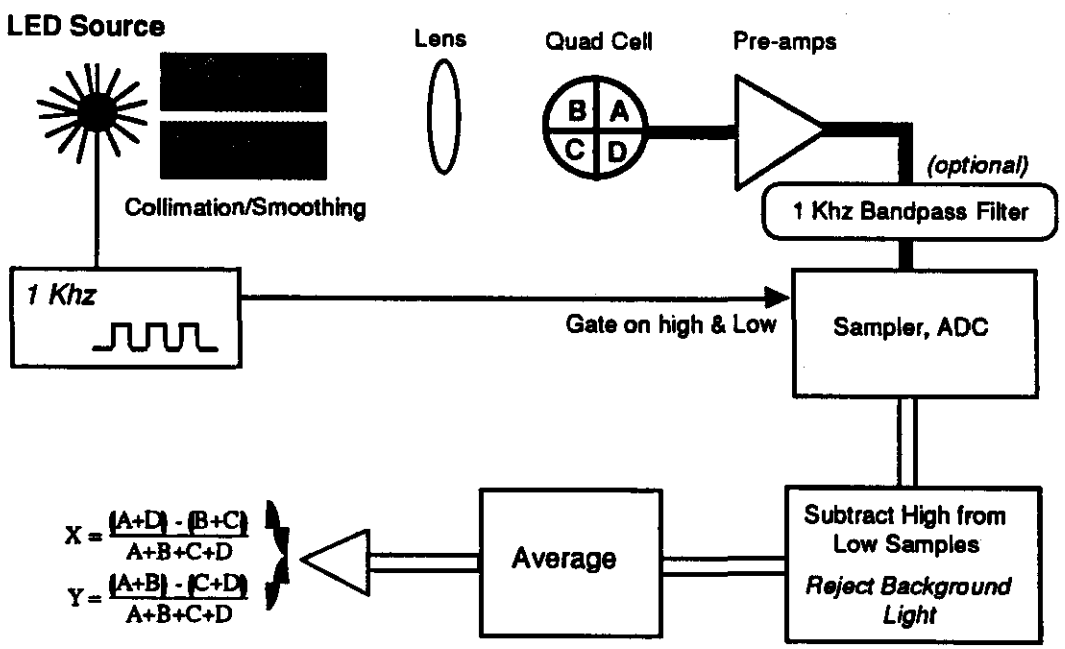

Figure 2: Straightness Monitor Electronics

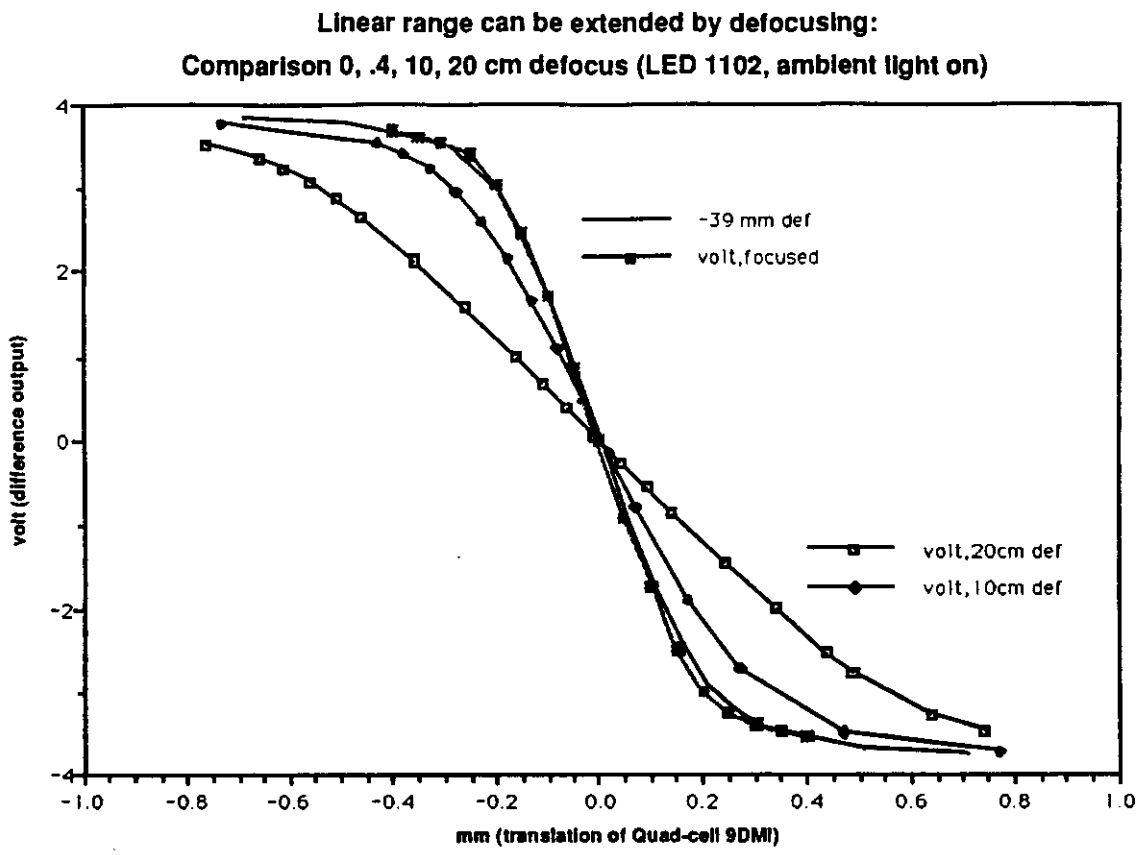

Figure 3: Straightness Monitor Transfer Function

This quantity can be measured by optical insturments based on the "straightness monitors"[1] that were successfully used in the L3 experiment[2]. These are simple devices composed of an LED, lens, and quadrant photodiode, as shown in Fig. 1. An image of a smooth-aperture, collimated source (i.e. LED) is projected onto a planar detector (i.e. quadrant photodiode) through a focusing lens. Displacements of the lens from the line between source and detector are detected by a shift in the illumination centroid at the photodiode. The measured displacement is insensitive to rotations of the components about their optical axes. The LED is modulated by a low-frequency square wave, and synchronously detected to minimize the effects of any ambient light background, as shown in Fig. 2. The straightness monitor components will be fixed to the drift chamber packages such that they precisely reference the sense wire positions. The mounts containing the optical devices and the gain balance between detector quadrants will be precisely adjusted as these components are fabricated. During construction of each muon segment, the straightness monitors will be cross-checked using cosmic ray data and external measurements.

Straightness monitor systems are known to be capable of extremely high resolution (i.e. under 2 μm is commonly achieved[3]), but their practical accuracy is limited by systematic errors, contributed primarily through the mechanics that mount the components. The 6 micron net precision quoted for the L3 monitors[4] is adopted as a baseline accuracy for the GEM straightness system. Since some of the optical path lengths needed for the GEM system can be significantly longer than at L3 (particularly at the endcaps), the effects of thermal gradients and atmospheric disturbances must be ascertained. Recent tests have retained high straightness monitor accuracy over a 9 meter path[5]. Path lengths will be extended by integrating over many samples and randomizing the thermal gradients by maintaining a steady airflow. These devices are quite inexpensive; installed straightness monitor systems have recently been estimated[5] to cost roughly $500. per 3-point string.

The dynamic range of these devices can be quite limited; i.e. the monitors used at L3 have a useful measurement range of roughly 200 μm. Test data from a straightness monitor setup[5] is shown in Fig. 3; the dynamic range for the largest spot (most defocused) approaches 1 mm. Nonhomogeniety of the light spot can affect the linearity of calibration curves; the measurements shown in Fig. 3 employ a special IR LED that incorporates an integral glass ball diffuser lens to smooth the illumination function. By imaging a square rather than a circle, and expanding the image size to occupy more of the diode surface, a wider range can be obtained (ultimately up to several mm).

The range can be also extended by employing different types of detectors that are capable of operating in the magnetic field, such as lateral-effect photodiodes or "photopots", which spatially weight the sensitivity of the quadrants, and imagers like CCDs[6] or photodiode arrays [which are now packaged as devices that intrinsically output an illumination centroid over a wide range; i.e. Ref. 7]. Research in this area is currently proceeding, with the goal of achieving a measurement range above 2 mm; ideally, it should be possible to span a precision measurement across a range of ±5 mm.

The proposed implementation of the straightness monitors is given in Fig. 4, where alignment paths are denoted by dashed lines. Multipoint straightness monitors will be directed along the chamber packages in the z direction. These will be mounted at points that reference the sense wires in a chamber layer (i.e. at positions where the wires are supported, or between chamber package boundaries), and will insure the straightness of wires in each chamber layer. They may be implemented by leapfrogging several sets of standard 3-point monitors (Fig. 5a), or by employing a multipoint alignment scheme, such as provided by the stretched wire alignment technique (SWAT), which has been used to align components to the micron level over large distances[8,9]. To apply the latter

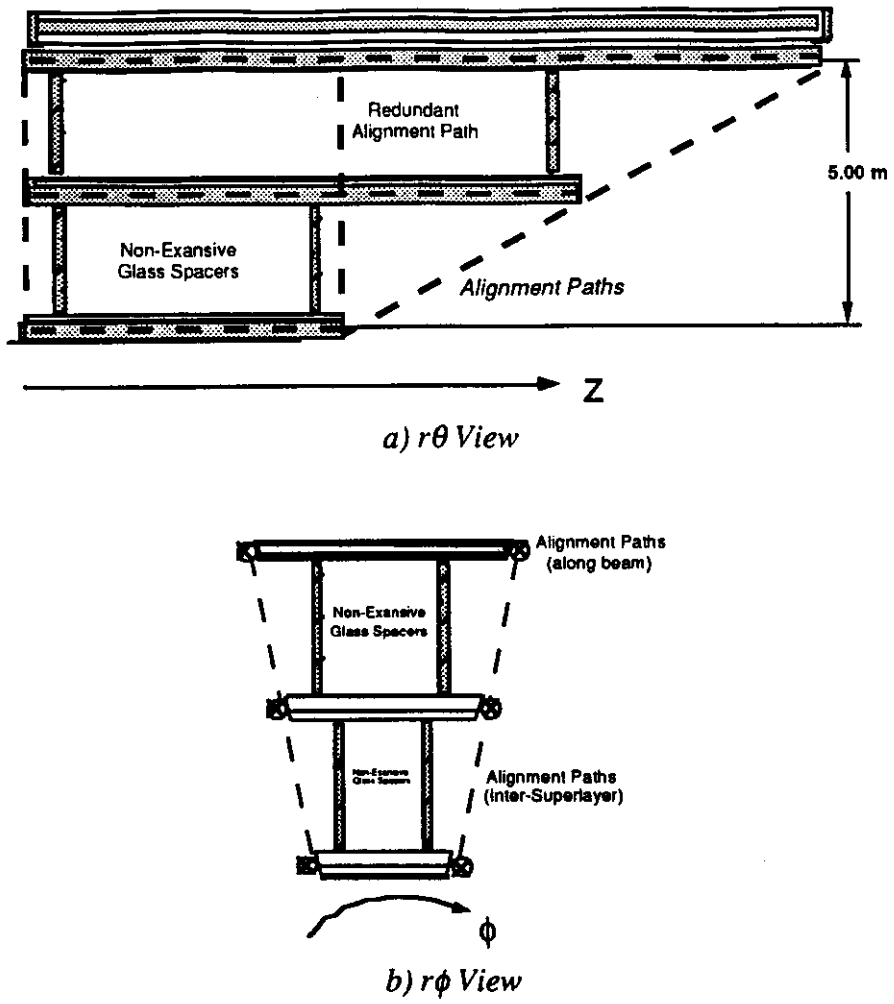

Figure 4: Straightness Monitor Paths in Muon Chamber Barrel

method, a narrow wire will be stretched between the superlayer endpoints in z, and its displacement measured at the locations of the drift chamber wire supports (Fig. 5b). The wire position will be determined relative to the chamber fiducials by an inexpensive optical means (i.e. encapsulated proximity sensors[8], which have been shown to yield a dynamic range of roughly 1 mm; see Fig. 6), or capacitive techniques[9]. By regulating the tension to a known value, the wire sag can be determined and the measurements compensated. In order to reduce sensitivity to structural and atmospheric dynamics, the wire will be stretched to sufficient tension and protected in a tube.

Several optical multipoint alignment schemes (i.e. see Ref. 10) are currently being developed that have intrinsic simplicity and potential reliability advantages over a wire technique. One elegant solution[11] is to use multistrip silicon detectors (making a wafer of about 50 micron thickness, 1-2 cm length, 300 μm strip pitch) to detect the centroid of

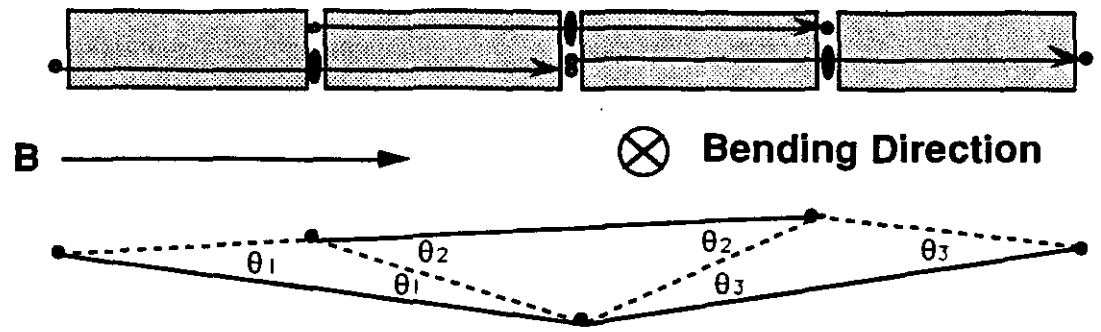

a) Nesting Optical Straightness Monitors Along a Chamber Layer

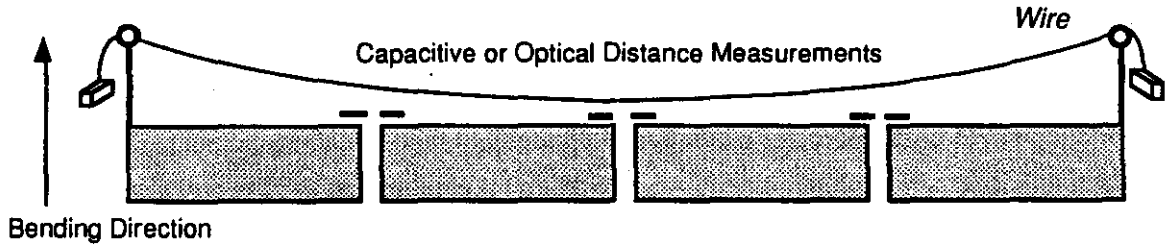

b) SWAT Alignment Along a Chamber Layer

Figure 5: Multipoint Alignment along Beam Axis

illumination of an IR laser that emits at a wavelength (i.e. 1.06 μm) where the silicon wafers are better than 90% transparent. These wafers can then be stacked along the beam, and the beam centroid determined (at the micron level) as projected onto each wafer. Such devices are in initial development; potential difficulties involving fabrication, optical properties (i.e. refraction through the wafer), dust accumulation, and design/cost of readout electronics (i.e. up to 70 preamplifier channels needed per wafer) must be resolved before these techniques can be baselined into the GEM muon array.

The alignment paths that relate different chamber layers are also shown as dashed lines in Fig. 4a. The vertical line at left and angled line at right are needed, as they provide references along the muon path. The vertical line at the center of Fig. 4a represents a redundant alignment path, which will present a useful cross-check (unlike the depiction of Fig. 4a, this path is best implemented as another projective line pointing to the IP; although schemes with 3 or more projective alignment paths are currently under consideration, the loss in θ acceptance may be prohibitively large, particularly at the inner chamber layer).

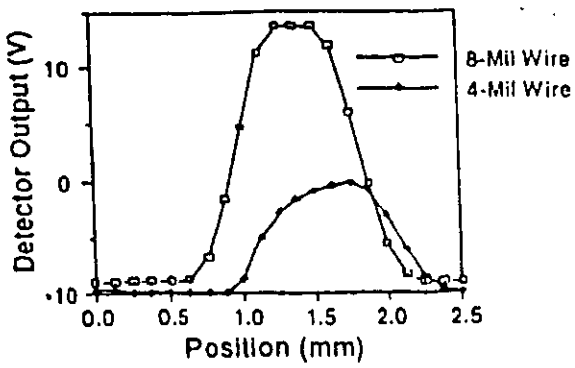

The photodetectors used to measure wire deflections are very sensitive---the output for a 4-mil wire is greater than 20 millivolts per micron of motion!

Figure 6: Measured transfer function of SWAT alignment system (from Ref. 8)

Alignment fixtures are installed at points where the chamber sense wires or pickup strips can be directly referenced (i.e. at points where wire supports [for the limited streamer drift tube option] or drift-tube bulkheads [pressurized drift tubes] are located, or directly on the cathode planes [for cathode strip chambers]). In order to interrelate chamber layers through the straightness monitor scheme of Fig. 4, these fixtures must line up between superlayers, preferably in a projective fashion. Other alignment measuring techniques could relax this requirement; i.e. a "laser beacon"[10,12] can be used to define a plane of illumination, which can then be referenced at various points along the side of a hexant (i.e. distance from the chamber fiducial to the beacon plane defines the sagitta error). Laser beacons require significant mechanical precision (i.e. the rotor must create a plane accurate to 5 μrad[13]), and function in a magnetic field, which has inspired difficulties with similar devices at L3. In addition, sufficient space must be allocated along the edge of the chamber arrays to support the rotor assembly, and optical paths must be guaranteed between the rotor and all sensors. While the laser beacon concept does meet some of the conceptual alignment needs, it will require significant engineering development before becoming a strong alternative.

These alignment paths (i.e. multipoint alignment along a layer, and interlayer alignments) will be instrumented along each side of a muon hexant, as depicted in Fig. 4b. Employing the straightness monitors of Fig. 1 will require lens diameters on the order of 1" (for the 90° path) and 2" (for the 30° path) to ensure sufficient light collection from the LED (a stronger source, such as a spatially stable diode laser, could reduce this diameter, although appreciably increasing the overall expense). The radial displacements of chamber layers (orthogonal to the bending direction) will also couple into the bending measurement at the edges of the hexants in Fig. 4b, producing a needed radial spacing

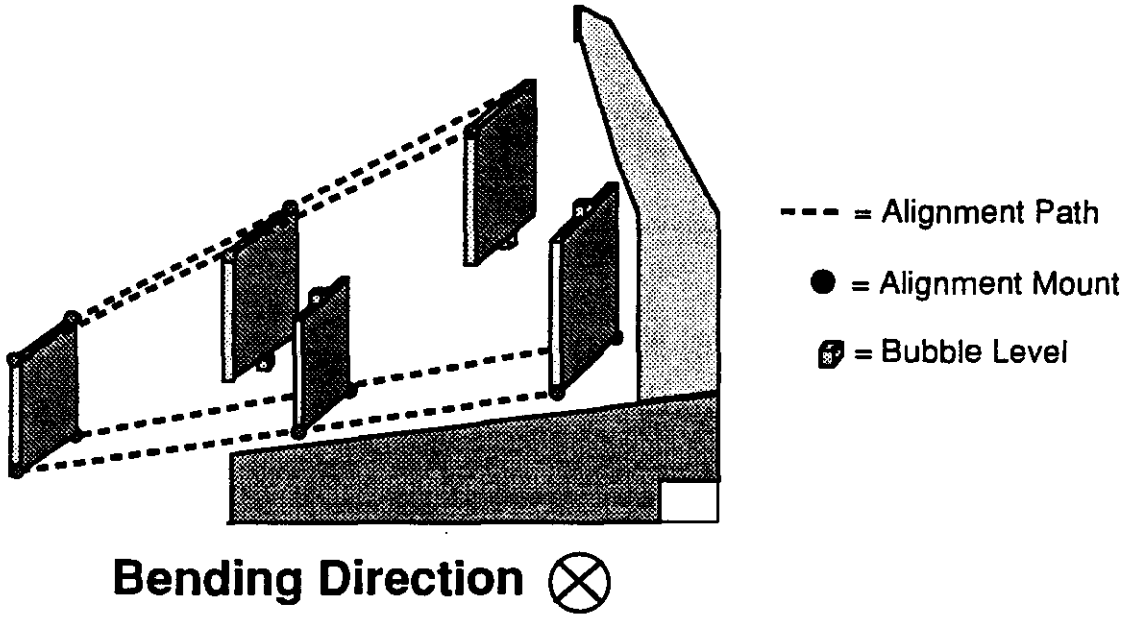

Figure 7: Alignment Paths in the Muon Endcaps

accuracy of 60 μm[14]. Since this is also monitored by the alignment paths directed along the hexant sides, an explicit measurement of the radial layer displacement may not be required; if needed, a precision rod equipped with a range measurement (i.e. capacitive sensor or mechanical gauge) will determine this shift with sufficient accuracy, as shown in Fig. 4 (this measurement will be translated across the multiple chamber packages in a superlayer by the multipoint monitors outlined in Fig. 5). While alignment along the beam (z) axis is not critical, it will nonetheless be precisely measured via the straightness monitor systems, which are sensitive in two coordinates.

The L3 experiment also employed a rotating laser beacon system[12] to determine the coplanarity of the straightness monitor lines, and thus measure the torque in the hexant structure. Since straightness monitors will be directed along the muon paths at maximum and minimum θ (Fig. 4a), and will be installed on both sides of the hexant (Fig. 4b), a "torque" angle (about the z-axis) between alignment lines-of-sight will not create a sagitta error[14], hence the additional planarity measurement is unnecessary.

Alignment paths will be defined at the maximum and minimum θ spanned by the endcap array, as portrayed in Fig. 7. The dashed lines shown in Fig. 7 show a pair alignment paths, one near each ϕ extreme covered by an endcap "hexant" module. These insure that the chamber layers are not twisted in ϕ, which can create an error in the momentum measurement. The alignment mounts will be fixed to precisely defined points

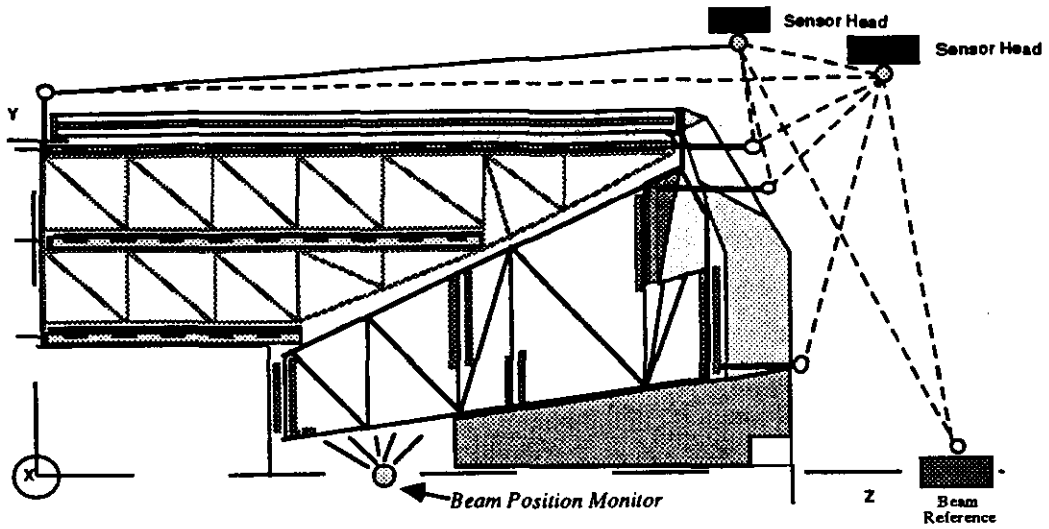

Figure 8: Strategies for Measuring Global Muon System Alignment

on the cathode plane and Hexcell laminate, which will provide a stable reference to the spacepoint measurements. If needed, a measurement of the differential torque between upper and lower chamber layer components (middle, outer layers) can be determined by using bubble levels, of the sort employed in the L3 octant tests[1]. If required, measurements of chamber offsets in the z direction (which couple into the momentum measurement, and must be determined to within 125 μm[14]) can be made with simple mechanical techniques, as suggested for determining the radial chamber spacing in the barrel, or with optical range measuring systems (again, since the alignment lines are projective to the IP, the sagitta error introduced through radial displacement will be detected by the straightness monitors).

Several aspects of the endcap chamber layout are simplified in Fig. 7. In particular, the endcap superlayers are split into several packages displaced along z. This is especially relevant at small θ, where small chambers abound to handle the large rate & occupancy expected at high η. The scheme of Fig. 7 assumes that the superlayer chambers will all be referenced to the straightness monitor fixture, either by precision mechanics or by another (short-range) alignment system. Since the required accuracy is so high here (i.e. the alignment transfer between fixture and chambers should be well below 50 μm, as discussed below), achieving this common alignment reference may not be trivial. A potential alternative here may be to employ a multipoint alignment scheme (i.e. a wire-based "SWAT" technique or a multipoint optical method) to pick a reference off each chamber independently, rather than take a single alignment reading relative to the center of a poorly linked superlayer. Clearly, more detail needs to be established here as the endcap design evolves.

The position of the muon detector components must be determined relative to the interaction region. This will be attempted by tracking muons through the entire detector, thereby tying the muon array to the central tracker (which will find its own reference to the beamline). An independent check of global muon system alignment, however, will aid in reducing systematic error sources. Although a 200 μm precision would be ultimately desired in the $r\phi$ plane for enhanced momentum resolution, an alignment on the millimeter scale will be adequate for most physics goals. Muon events themselves may be sufficient to determine this alignment on-line, provided that enough high-momentum muons will be produced over the full acceptance in η to statistically link the central tracker coordinates to those of the muon array; otherwise a set of automatic survey techniques can monitor the detector position, as depicted in Fig. 8 and discussed below.

A promising method of aligning to the beamline requires placing a pair of beam position monitors inside the detector (on each side, between the calorimeter endcaps and flux concentrators) to dynamically measure the beam location. One can then measure the distance between a point referenced to the beam position monitors and the several positions on the muon array. Since the distances are relatively short, and lines of sight will be readily available to a large portion of the muon array, achieving the required 200 μm accuracy should be possible through a variety of techniques (i.e. optical range/angle, mechanical displacement measurements with thermally invariant rods and/or stress-free structures, etc.). The feasibility of this approach is currently under investigation.

An alternative approach to attaining global muon system alignment is to sight out through holes in the flux concentrator support (and, if possible, through the central membrane gap), to sensors at various reference points in the hall. These sensors, which can be placed in known positions relative to the beamline, can measure the range to several points on the muon detector. The range measurements can be performed by detecting the returned phase of an AM signal modulated onto an optical carrier (as used in commercial surveying equipment[15]). The range measurement is much less sensitive to atmospheric disturbance than an angular measurement; by making many redundant measurements and monitoring the temperature in the hall, it should be possible to achieve the required resolution, although certainly at some expense.

If the dynamic forces on the muon array (mainly due to the shift in shape of the containment vessel as the magnet is powered on and off) are kept small, the change in orientation of the muon hexants can be measured around the vertical with an inexpensive instrumented level system. Together with a model of the structural response, the change in hexant position and orientation may be determined from these measurements, and the initial survey model updated accordingly.

Global alignment for the muon system can be interpreted as the need to direct the radial straightness monitor axes toward the interaction point (as in the scheme depicted by Fig. 4). Optical multipoint alignment techniques that are able to extend the alignment path to the outside of the detector (potentially feasible for the vertical lines near the magnet membrane and the horizontal lines along the z axis; more difficult for the 30° line) may be well suited to determining the global detector alignment. A practical design that incorporates such an approach, however, remains to be determined.

In summary, the precision required by the muon alignment systems is given below (as adapted from Ref. 14, where these figures are presented in more detail): In both the muon barrel and endcaps, the "ϕ" coordinate refers to the bending direction, referenced at the center of each hexant. The "r" coordinate refers to the radial distance from the beamline, and the "z" coordinate is defined to be the beam direction (referenced to the IP). The local alignment ("between superlayers") is assumed to be referenced to the mean position of the composite chambers (the chambers themselves are allowed to have a 50 μm alignment scatter (in ϕ), provided that the superlayer reference is taken at the mean).

Local Alignment (between superlayers)	*Global Alignment (to IP)*
Muon Barrel	
Bending Coordinate (ϕ): 25 μm	ϕ: 5 mm (200 μm goal)
Radial Coordinate (r): 60 μm	r: 10 mm
Beamline Coordinate (z): 1 mm	z: 5 mm
Muon Endcaps	
Bending Coordinate (ϕ): 25 μm	ϕ: 5 mm (200 μm goal)
Radial Coordinate (r): 1 mm	r: 4 mm
Beamline Coordinate (z): 125 μm	z: 10 mm

References

1) Toth, W. E., "Muon Detector Program; Prototype Octant Construction and Evaluation with Production Phase Recommendations", Draper Lab Report CSDL-R-1885, Oct. 1987.

2) Adeva, B. et. al., "The Construction of the L3 Experiment", *Nuc. Inst. and Methods*, A289 (1990), pg. 35.

3) VanderGraff, H., NIKHEF Amsterdam, Personal communication, March, 1992.

4) Duinker, P., et. al., "Some Methods for Testing and Optimizing Proportional Wire Chambers", *Nuc. Inst. and Methods*, A273 (1988), pg. 814-819.

5) Ayer, F. et. al., "The Engineering Development of an Actively Controlled Precise Muon Chamber for the SDC Detector", *Proc. of the SSCIII Conference, New Orleans, LA*, March 1992.

6) Becker, U. and Paradiso, J., "An Optical CCD-based System for Precise Drift Chamber Positioning", *Nuc. Inst. and Methods*, 196, p. 381 (1982).

7) See devices such as the "MULTISCAN" Position-sensitive photodetector (from Technoexan, c/o Semicon Inc., Ontario, Canada), also J. Wyatt et. al., results from the MIT Lincoln Lab vision project.

8) Griffith, L., LLNL, Presentation at GEM Alignment Meeting, SSCL, May 22,1992.

9) Coosemans, W., Lasseur, C., CERN, Geneva, Personal communication, June 9, 1992.

10) Sawicki, R., LLNL, "Muon Chamber Alignment Alternatives", Presentation at SSCL alignment meeting, June 12, 1992.

11) Blum, W., Max Plank Institute, Presentation on silicon multistrip detectors for multipoint alignment, SSCL, June 17, 1992.

12) Seiler, P.G., et al., "The Laser Beacon", L3 Muon Chamber Group Internal Note, 85-4, 1985.

13) Zhukov, V., GEM muon alignment requirements summary, June, 1992.

14) Paradiso, J. "Alignment Requirements for the GEM Muon Detector", June, 1992.

15) Rueger, J.M., Electronic Distance Measurement, Third Edition, Springer-Verlag, 1990.

GEM-TN-92-125

Alignment Requirements for the GEM Muon Detector

J. Paradiso
C.S. Draper Laboratory

June 1992

Abstract

A table of requirements is derived for local and global alignment of the GEM muon detector. Requirements are given for structural accuracy (to which the muon array must be constructed) and precision measurement (where dynamic measurements of detector position may be used to compensate the location of superlayer spacepoints). In order to facilitate the rapid updating of requirements as the detector definition evolves, details are given on the requirement derivation.

Alignment Requirements for the GEM Muon Detector

--J. Paradiso, June '92

1) Introduction

Several phenomena that impact muon system alignment are listed below:

<u>Intrinsic Smears</u>
- **Vertex distribution along z**
- **Multiple scattering in calorimeter**

<u>Needed Structural Accuracy</u>
- **Dynamic range of local alignment system**
- **Alignment of trigger roads**

<u>Precision Measurements</u>
- **Stated momentum precision in bending plane**
- **Align to precision of detector components (muon angle)**
- **Extrapolate $p_\perp$ from measured angle**
- **Mass Resolution**

<u>Pattern Recognition</u>
- **Muon tracking constraints**
- **Track linking with central detector**

<u>Other Effects</u>
- **Line-of-sight deviation from IP**

The "intrinsic smears" arising from the vertex spread along the beamline and multiple scattering in the calorimeter can limit the required alignment accuracy in some coordinates. The accuracy of the structure itself (after it is servoed into position) is driven by the dynamic range of the straightness monitor system (used for local alignment), and the trigger road definition/width. The precision measurements set the needed accuracy of the alignment monitors (which will be used to correct the muon data). The major influence here is the muon $p_\perp$ measurement. Some quantities will require determination of the muon angle; the needed resolutions are quoted here. Pattern recognition considerations may also affect some of these requirements, and track linking with the central detector will induce a limit on the angular error (such effects are not included in this report). Other considerations, such as the sensitivity to torque error in a straight-line alignment system pointing back toward the interaction point, are analyzed.

Figs. 1-4 show simplified views of the GEM muon system, with relevant quantities labeled. Local coordinate offsets are given, plus a net translation of the hexant coordinate system (Δx_G, Δy_G, Δz_G). The angular errors ($\Delta\theta$, $\Delta\phi$) arise from a rotation of the hexant about the IP before translation. Various quantities are assumed in these

derivations; these are listed where relevant, hence may be readily updated, and the results normalized accordingly. The simplified muon system depicted in this analysis has a barrel running from $\theta = 90° \rightarrow 30°$, and an endcap running from $\theta = 30° \rightarrow 10°$.

2) Intrinsic Smears

a) Length of interaction diamond

Assuming the interaction diamond to be of length $\sigma = 7$ cm along the z-axis, we generate a probable error along the beam axis of $\Delta z_G = \pm 4.7$ cm. This error is only relevant to the static structure requirements (in Sec. 3); on an event-by-event basis, the vertex position is measured by the central tracker, hence this is corrected. Since this variation is only an offset along the z-axis, the perceived θ angle is unchanged. The θ accuracy of the structure (which assumes that all muons originate at the IP), however, is smeared by this distribution. In the barrel, the effective shift in θ may be parameterized by $\Delta\theta \approx (D \sin^2\theta_\mu / y_c)$, where $D = \pm 4.7$ cm, and $y_c = 8.53$ m (for the outer RPC layer). This gives $\Delta\theta = \pm 5.5$ mr @ $\theta = 90°$, and $\Delta\theta = \pm 1.4$ mr @ $\theta = 30°$. For the endcap, this relation may be adapted; $\Delta\theta \approx (D \sin\theta_\mu \cos\theta_\mu / z_c)$, where $z_c = 16$ meters. This yields the results: $\Delta\theta = \pm 1.4$ mr @ $\theta = 30°$, and $\Delta\theta = \pm 0.5$ mr @ $\theta = 10°$. Because of the projective geometry of the barrel and endcap structure, an effective smear in the y axis may also be inferred (mainly relevant when specifying the alignment of trigger elements). This parameterizes as $\Delta y_G = \Delta z_G \tan\theta$, and evaluates to $\Delta y_G = \pm\infty$ @ $\theta = 0°$, $\Delta y_G = \pm 2.7$ cm @ $\theta = 30°$, and $\Delta y_G = \pm 8.3$ mm @ $\theta = 10°$. Since the beam diameter is very small (i.e. on the order of 10 μm), there is no significant primary smear generated in the radial axes.

b) Multiple Scattering

Another smear contributing to the global alignment accuracy is due to multiple scattering of muons in the calorimeter. Assuming a 2.5 meter long copper calorimeter (175 radiation lengths), and $\alpha_{ms} = (.015/P(GeV)) \sqrt{\ell/\ell_0}$ (FWHM) , we calculate $\alpha_{ms} = 0.4$ mr at 500 GeV momentum (4.0 mr at 50 GeV). Assuming a maximum momentum of interest to be 500 GeV (these figures can be scaled for other momenta), this error translates directly into polar angle and azimuth: $\Delta\theta, \Delta\phi = \pm 0.2$ mr. Projecting onto the barrel yields: $\Delta z = (r\,\Delta\theta)/\sin\theta$, $\Delta y = (r\,\Delta\theta)/\cos\theta$, $\Delta x = (r\,\Delta\theta)$, where the radius "r" is evaluated at the first chamber layer (since we are projecting back to the IP); $r = y_a/\sin\theta$. For the endcap, we have: $\Delta y = (r\,\Delta\theta)/\cos\theta$, $\Delta z = (r\,\Delta\theta)/\sin\theta$, $\Delta x = (r\,\Delta\phi)$, where r is now

defined along z; $r = z_a/\cos\theta$. Plugging in $y_a = 3.9$ m, $z_a = 6.3$ m, we get (for the barrel): ($\Delta z_G = \pm\infty$, $\Delta y_G = \pm 780$ μm, $\Delta x_G = \pm 780$ μm) at $\theta = 90°$, ($\Delta z_G = \pm 1.6$ mm, $\Delta y_G = \pm 900$ μm, $\Delta x_G = \pm 780$ μm) at $\theta = 30°$, and (for the endcap): ($\Delta z_G = \pm 2.5$ mm, $\Delta y_G = \pm 1.5$ mm, $\Delta x_G = \pm 1.3$ mm) at $\theta = 30°$, ($\Delta z_G = \pm 7.3$ mm, $\Delta y_G = \pm 1.3$ mm, $\Delta x_G = \pm 1.3$ mm) at $\theta = 10°$. For scattering at 50 GeV (the highest energy cut considered for the muon trigger), these factors may be scaled up by an order of magnitude.

3) Structural Accuracy

a) Dynamic range of local alignment systems

It is vital that the structure be designed such that its relative deflection will be within range of the local alignment systems and straightness monitors. In deriving these numbers, a series of assumptions must be taken. The LED/lens straightness monitors currently have a measurement range that (in the best case) is within ±1 mm, and a capture range (with a saturated measurement that indicates the offset direction) of ±3 mm, within which the chamber layers may be servoed into measurement position. After some development, these limits may be extended; i.e. by imaging a wide square on a large quadrant diode (or by using an imaging array), a dynamic range approaching ±5 mm may be attained for the precision measurement. In the current analysis, the conservative estimate of ±1 mm is used (this is also compatible with the present range of measurement obtained from stretched wire techniques). Bear in mind that a servo system or sensor range extension will increase these numbers (which can be scaled accordingly).

For the barrel (Fig. 5), the local x-axis positioning is set directly by the range of the z-axis multipoint and inter-superlayer monitors, thus we derive $\Delta x < \pm 1$ mm (the situation is actually slightly more complicated; the maximum x-axis deviation from a line along the z-axis connecting the chamber packages in a superlayer is ±1 mm, while for a line connecting outer and inner superlayers [fixed at the inner superlayer], the middle superlayer offset is required to be within ±1 mm, yet the outer superlayer can be displaced by ±2 mm [this comes from the requirement of "straightness" along the muon path]). Within a superlayer, the y offset between chamber packages must be within $\Delta y <$ ±1 mm, in order to maintain the range constraint on the z-axis multipoint monitors. Between superlayers, however, the alignment path at $\theta = 30°$ applies the worst-case constraint (since the sensors are angled to be orthogonal to a ray inclined at $\theta = 30°$, $\phi = 11.25°$), namely: $\Delta y_b < \pm(1\text{ mm})\cos 30° = \pm 870$ μm (at $\theta = 90°$, this measurement is limited by the $\Delta\phi$ of a hexant, i.e. $\Delta y_b < \pm(1\text{ mm})\cos 11.25°/\tan 11.25° = 4.9$ mm). The

z offset error is determined by the inter-superlayer monitors; i.e. $\Delta z_b < \pm 1$ mm @ $\theta = 90°$, and $\Delta z_b < \pm(1 \text{ mm}) \cos 30°/\tan 30° = \pm 1.5$ mm @ $\theta = 30°$. For the inter-superlayer monitors, if the measurement is referenced to the inner layer, the upper layer tolerances (Δy_c, Δz_c) are twice the (Δy_b, Δz_b) values (this is only true for the subscripted quantities; the Δy measured by the multipoint monitors along the z-axis must all be within ± 1 mm to stay in range).

For the endcap (Fig. 6), all monitors are considered to be of the 3-point inter-superlayer variety. As above, the measurements are assumed to be referenced to the inner layer; the numbers quoted here are thus relevant for the middle superlayer, and can be doubled for the outer superlayer. Translations along the x & y axes are directly measured (as the sensors are not inclined in these coordinates, and are orthogonal to the z-axis), thus $\Delta x_b < \pm 1$ mm, $\Delta y_b < \pm 1$ mm. Translations along z will project across the sensor, yielding: $\Delta z_b < \pm(1 \text{ mm})/\tan \theta$, thus $\Delta z_b < 1.7$ mm @ $\theta = 30°$ and $\Delta z_b < 5.7$ mm @ $\theta = 10°$.

b) Projective Constraints for the Trigger

The other factor influencing the structural accuracy is the alignment of projective strips for the trigger system. In this analysis, a misalignment of trigger strips was tolerated that caused a loss of up to 10% in projective coincidence (as this loss factor is somewhat arbitrary, it may eventually prove desirable to scale these results to a different figure-of-merit). This analysis does not include effects of z-vertex smearing from the interaction diamond or multiple scattering (which will nonetheless have considerable impact; the effect on chamber alignment from each process is identified separately, and compared in the conclusion of this report). In the measured non-bending coordinates (z in the barrel, y in the endcap), coincidences are required to be of single-strip width, while in the bending coordinate (x in the barrel and endcap), candidate muons are required to have their hits contained in a cone (defined from inner to outer superlayer) of 1° (barrel) or .45° (endcap). This constraint was vaguely derived from the various trigger schemes that are proposed for muons over 50 GeV. This purpose of this analysis is to derive a feel for the alignment requirements for the trigger; it should be updated in a more precise fashion as the trigger definition improves.

Measuring the z-coordinate of the barrel, pickup strips run in the local x-direction (Fig. 2) and are sized projectively, measuring 8.9 cm (at $y_c = 8.53$ cm), 6.5 cm (at $y_c = 6.08$ cm), and 3.9 cm (at $y_c = 4.15$ cm). The nominal angular pitch of these strips is thus $\Delta\theta = 0.6°$. Referencing the coordinates to the inner layer, a 10% loss results when

moving the middle layer by $\Delta z_b = \pm 3.25$ mm or the outer layer by $\Delta z_c = \pm 4.5$ mm. The relative scale of the strip pitch changes when the chamber layers are displaced radially (Δh in Figs. 1 & 2) as: $\Delta z = \Delta h / \tan\theta$. This gives essentially infinite tolerance to Δh at $\theta = 90°$, but produces an effect at smaller angle; at $\theta = 30°$, a $\Delta y_b = \pm 1.9$ mm or a $\Delta y_c = \pm 2.6$ mm will produce a 10% loss in projective overlap between the inner and middle strips.

The x-measuring strips are sized at 1.3 cm in the barrel (this sizing is specified identically for all layers, hence they are essentially non-projective). Assuming that a trigger architecture maps three strips on the middle layer) to 5 strips on the outer layer, the effective middle strip width is 3.9 cm, and the outer strip width is 6.5 cm. The 10% criterion will thus yield allowable bending offsets of $\Delta x_b = \pm 2$ mm for the middle layer and $\Delta x_c = \pm 3.25$ mm for the outer layer. Translating these into Δh errors at the edges of the hexant (i.e. $\Delta x = \Delta h / \tan 11.25°$ as was performed above), yields $\Delta y_b = \pm 1.0$ cm and $\Delta y_c = \pm 1.6$ cm, both fairly loose tolerances.

Looking at the global requirements for the barrel trigger in $r\phi$, we see that an x-translation of the IP (by Δx_G) relative to the hexant centerline (see Fig. 2) will create an angle of $\Delta x_G / y_c$ at the outer chamber layer. If we translate this back to the inner chamber layer, we derive an offset of $\Delta x_a = (y_c - y_a)\ \Delta x_G / y_c$. Using the 10% criterion, we require this shift to lose under 10% net projection, thus (referencing the outer strip width), $\Delta x_a < \pm 3.25$ mm, hence $\Delta x_G < \pm 6.3$ mm. Moving the hexant away from the IP along the local radial axis (y in Fig. 2) changes the aspect of the hexant edges (i.e. the ϕ angles spanned by the inner and outer superlayers relative to the IP are no longer equal [at 22.5°]). This shift (difference in angle to IP from ends of outer and inner superlayers) causes a projective loss at the hexant edges for muons coming from the IP, estimated as $\Delta x = \tan 11.25° \ (y_c - y_a\,[y_c + \Delta y]/[y_a + \Delta y])$. Simplifying and rearranging (assuming Δx small with respect to y_a) yields $\Delta y_G = \Delta x / (\tan 11.25° \ [(y_c/y_a) - 1])$. If we assume our Δx to be the ± 3.25 mm derived from the 10% loss criterion (which may be overly restrictive here), we derive $\Delta y_G = \pm 1.5$ cm; again, a liberal margin.

A similar set of global constraints can be determined for the barrel in $r\theta$. Translating a barrel hexant by Δz_G produces a projective loss at the outermost layer of $\Delta z_G\ [(y_c/y_a) - 1]$. As y_c is nearly twice y_a, the quantity in brackets approaches unity. Using the 10% loss criterion for Δz_c developed above, we derive $\Delta z_G = \Delta z_c = \pm 4.5$ mm. The effect of a radial (i.e. Δy) hexant shift can be determined by the same formula as used for $r\phi$, which now becomes: $\Delta z = \cot\theta\ (y_c - y_a\,[y_c + \Delta y]/[y_a + \Delta y])$, and can be rearranged into: $\Delta y_G = \Delta z / (\cot\theta\ [(y_c/y_a) - 1])$. If we plug in the familiar $\Delta z_c = \pm 4.5$ mm

from the 10% criteria (again, probably conservative), we get a worst-case $\Delta y_G = \pm 2.5$ mm at $\theta = 30°$.

The nonbending coordinate measured by the endcap lies along the local y axis (see Figs. 3 & 4). This is measured by groups of anode wires that span a 5 cm interval (since the chambers within a superlayer are offset by half of this distance, the effective y granularity is divided by $\sqrt{2}$, yielding roughly a 3.5 cm span). If one desires to form a nonbending trigger in the endcap, the y measurements (which don't necessarily line up projectively between superlayers!) must be aligned. If one assumes the 10% loss criterion here, mapping one middle-layer strip to two outer-layer strips (to become vaguely projective), we develop a tolerance of $\Delta y_b = \pm 1.75$ mm, $\Delta y_c = \pm 3.5$ mm. This can also be extended to the Δh between layers, which now lies along the z axis. The major restriction is at $\theta = 30°$, which yields $\Delta z_b = (\pm 1.75 \text{ mm})/\tan 30° = \pm 3.0$ mm, $\Delta z_c = \pm 6.0$ mm.

The bending coordinate is measured by radially-directed 5 mm strips. To become efficient beyond 50 GeV, a trigger coincidence maps a hit in the middle layer to a range of ± 6.5 strips, as extrapolated at the outer layer. Making this a bit more conservative & arbitrary (as we did in the barrel), we assume that we map a hit in the inner layer to a ± 2 cm range in the middle layer and a ± 3.25 cm range in the outer layer, from which we derive requirements of $\Delta x_b = \pm 2$ mm and $\Delta x_c = \pm 3.25$ mm. Extrapolating this to a Δh constraint, we get a worst-case $\Delta h = \Delta x/(\sin 30° \tan 11.25°)$, which produces $\Delta z_b = \pm 2.0$ cm and $\Delta z_c = \pm 3.3$ cm; certainly loose requirements.

Applying the same relation as used in the barrel, the $r\phi$ projection gives a constraint on Δx_G; i.e. $\Delta x_a = (z_c - z_a)\ \Delta x_G/z_c$. Plugging in $\Delta x_a = \pm 3.25$ mm gives $\Delta x_G = \pm 5.6$ mm. A limit on Δz_G can also be estimated from projective loss, as was seen in the barrel: $\Delta z_G = \Delta x/(\tan\theta\ [(z_c/z_a)-1])$. Setting $\Delta x = \pm 3.25$ mm, we get $\Delta z_G = \pm 4.1$ mm @ $\theta = 30°$, and $\Delta z_G = \pm 1.4$ cm @ $\theta = 10°$.

Adapting the $r\theta$ formulae developed for the barrel, we can calculate the projective loss resulting from a global y translation: $\Delta y\ [(z_c/z_a) - 1]$. Requiring this to remain under 10% (and plugging in $\Delta y = \Delta y_c = \pm 3.5$ mm) gives $\Delta y_G = \pm 4.8$ mm, which results in a z requirement of $\Delta z_G = \pm 4.4$ mm @ $\theta = 30°$ and $\Delta z_G = \pm 15$ mm @ $\theta = 10°$.

Since our angles $\Delta\theta$ and $\Delta\phi$ are defined to be rotations about the IP (before applying the global coordinate translations), the trigger is essentially invariant to them; i.e. all stiff tracks will still be projective to the IP. Because a narrow (1 or 2 strip) road was employed in the nonbending trigger definition (which may not be necessary), the nonbending requirements have become more stringent than the requirements in the bending plane; depending on how the trigger is actually defined, this may not be valid,

and the nonbending position tolerances may be appreciably liberalized. Again, this analysis is admittedly based on somewhat crude assumptions, and should eventually be updated with a better-defined trigger scenario.

4) Precision Measurements

a) Stated momentum resolution in bending plane

The figures summarized in this section are the alignment accuracies required to produce the stated momentum resolution i.e. $\Delta p/p = 5\%$ ($\eta = 0$), 10% ($\eta = 2.5$). The muon detector structure need not produce this precision; rather the alignment system will resolve a set of corrections to the chamber positioning for off-line analysis.

The local positioning requirements (within a hexant) are quite exacting. First consider the barrel. In the bending coordinate (referencing measurements to the lower layer), we have the classic figures: $\Delta x_b = \pm 25$ μm and $\Delta x_c = \pm 50$ μm (the doubling of this figure at the outer layer is derived from the nature of this requirement; i.e. deviation of the chamber fiducials from a straight line). This also gives rise to a corresponding Δh requirement at the ϕ extremes of the hexants ($\phi = \pm 11.25°$): $\Delta x = \Delta h \tan 11.25°$. The full ± 25 μm error budget is blown if Δy_b exceeds ± 125 μm or Δy_c grows beyond ± 250 μm. This error is a function of $\tan(\Delta\phi)$, and decreases nearly linearly to zero at the centerline of the hexant. As the subtended angle is small, the tangent is nearly linear, and the mean is readily taken (giving half of the maximum value). Thus, keeping the average contributed error from Δh a factor of 4 below the ± 25 μm Δx error in the quadrature sum will result in a Δh limit of: $\Delta y_b = \pm 63$ μm and $\Delta y_c = \pm 125$ μm.

The situation is analogous in the endcaps, where again, $\Delta x_b = 25$ μm & $\Delta x_c = 50$ μm. The Δh situation is now slightly different; since the endcap chambers are projective to the beam axis, and the lines from the IP to the hexant edges approach the polar (z) axis, the effective $\Delta\phi$ angle is smaller. The sagitta effect becomes: $\Delta x = \Delta h \sin\theta \tan 11.25°$. Plugging in the 25 micron maximum, we blow our budget at $\Delta y_b = \pm 250$ μm ($\theta = 30°$) and $\Delta y_c = \pm 720$ μm ($\theta = 10°$). Again, doing approximate averaging, and keeping the Δh error a factor of 4 lower than the 25 micron maximum Δx contribution yields the tolerances: $\Delta y_b = \pm 125$ μm, $\Delta y_c = \pm 250$ μm ($\theta = 30°$), & $\Delta y_b = \pm 360$ μm, $\Delta y_c = \pm 720$ μm ($\theta = 10°$).

Shifts in the local z axis have no significant effect on the precision momentum measurement. Local Δh shifts also affect the point along the particle path where the

measurement is assumed to be taken, but this error is comparatively insignificant (for a 5% momentum resolution, this Δh position requirement is at least ± 10 cm).

The precision momentum requirements are a function of relative superlayer displacement, and nominally do not involve global alignment. One caveat, however, is a desire to know the position of the beamline relative to the muon array in the $r\phi$ plane, which increases the effective lever arm, thus provides enhanced momentum resolution for very high energy muons (circa 500 GeV and beyond) that scatter less in the calorimeter. This translates into a Δx_G constraint (see Fig. 2); i.e. $\Delta x_G = \pm 200$ μm. Physically, this may be interpreted as the desire to point the axes of the straightness monitors at the IP (in $r\phi$) to within 200 μm (this imposes no $\Delta\phi$ constraint, as ϕ is defined in Fig. 2). If one looks at the requirement of $\Delta x_G = \pm 200$ μm as an angular constraint on the straightness monitor axes (as measured at the outer superlayer), we have pointing needs of $\beta = 23$ μr @ $\theta = 90°$, $\beta = 12$ μr @ $\theta = 30°$ [worst case!]. This parameter is interpreted more as a "goal" than a requirement; i.e. it's not needed to meet the muon detector specifications, but would be a nice extrapolation.

b) Aligning to the ultimate measurement precision

There is no need to specify requirements on global alignment that are significantly more stringent than the possible measurement accuracy of the detector. Figs. 7 & 8 show calculations[1] of the detector resolution in x,z,θ,ϕ, which were made by fitting a muon track through the 3 superlayers (using the quoted resolution), and extrapolating back to the IP. These results include multiple scattering in the calorimeter, giving rise to a family of curves, as shown. The ultimate precision possible occurs at high energy (i.e. beyond 250 GeV for the z coordinate and above 2 TeV for the bending coordinate). Reading off these plots (and normalizing from σ to half-width), we obtain best-case resolutions for the barrel of $\Delta x_G = \pm 330$ μm, $\Delta z_G = \pm 1.3$ cm, $\Delta\theta = \pm 2.7$ mr ($\theta = 90°$), $\Delta\theta = \pm 0.67$ mr ($\theta = 30°$), $\Delta\phi = \pm 0.13$ mr. Doing the same for the endcap, we get: $\Delta x_G = \pm 330$ μm ($\theta = 30°$), $\Delta x_G = \pm 130$ μm ($\theta = 10°$), $\Delta z_G = \pm 1.5$ cm ($\theta = 30°$), $\Delta z_G = \pm 5.3$ cm ($\theta = 10°$), $\Delta\theta = \pm 2.7$ mr, $\Delta\phi = \pm 1.3$ mr. Using the Δz_G or $\Delta\theta$ resolutions, a limit for Δy_G may be estimated. Employing the former technique on the barrel, $\Delta y_G = \Delta z_G \tan\theta$, resulting in the most restrictive limit at $\theta = 30°$, where $\Delta y_G = \pm 1.6$ mm. Doing this to the endcap, we see $\Delta y_G = \pm 9$ mm, essentially independent of θ.

c) Projecting the total momentum

One of the major precision requirements on the polar muon angle (θ) accuracy is generated by the projection from the measured transverse momentum to the total muon momentum:

$$p = \frac{p_\perp}{\sin\theta}$$

Performing a tangent error analysis on this relation yields:

$$\frac{\sigma_p}{p} = \sqrt{\left(\frac{\sigma_{p\perp}}{p_\perp}\right)^2 + \left(\sigma_\theta \cot\theta\right)^2} \qquad (\sigma_\theta \text{ in radians})$$

As a rule of thumb, we decide to keep ($\sigma_\theta \cot\theta$) a factor of four below $\sigma_{p\perp}/p_\perp$, in order that angle error will contribute below 10% to the quadrature error sum. As θ approaches 90°, the muon momentum is totally transverse, hence σ_p is not sensitive to angle error. At $\theta = 30°$, however, we calculate the limit: $\sigma_\theta < 10$ mr [$\Delta\theta = \pm 6.7$ mr] (assuming $\sigma_{p\perp}/p_\perp = 7\%$, as calculated at $p_\perp = 500$ GeV), and at $\theta = 10°$, we see that $\sigma_\theta < \pm 4.4$ mr [$\Delta\theta = \pm 2.9$ mr] (assuming $\sigma_{p\perp}/p_\perp = 7\%$, as quoted).

Using the geometry of the muon array, y_G and z_G tolerances can be inferred from this θ resolution (the projections were given in Sec. 2b on multiple scattering); the position of the innermost chamber layer is taken as the lever arm (producing the tightest requirements). At $\theta = 30°$, we get ($\Delta z = \pm 10$ cm, $\Delta y = \pm 6.0$ cm), and at $\theta = 10°$, we see ($\Delta z = \pm 10$ cm, $\Delta y = \pm 2$ cm); certainly loose requirements!

d) Invariant Mass Resolution

The invariant mass of a muon pair is a function of the 3-momenta and opening angle:

$$m^2 = 4\, p_1\, p_2 \sin^2(\tfrac{1}{2}\theta_{\mu\mu})$$

Performing a tangent error analysis will yield:

$$\frac{\sigma_m}{m} = \sqrt{2\left(\frac{\sigma_p}{p}\right)^2 + \left[\sigma_{\mu\mu} \cot\left(\tfrac{1}{2}\theta_{\mu\mu}\right)\right]^2} \quad (\theta_{\mu\mu} \text{ in radians})$$

At this point, a series of assumptions must be made. First, as above, it is assumed that the angle error term will be a factor of four below the σ_p/p term, in order to achieve under 10% impact in quadrature. Next we assume σ_p/p to be at its quoted best (i.e. 5%). Finally, we must make assumptions about the opening angle. Nominally these will be set from decay kinematics, but we can make a few simplifications. For large angle, with muons nearly back-to-back, the angle error has no impact on the mass resolution. For small angle pairs, the angular term can dominate; however when the angle is below 22.5° (the ϕ span of a hexant), it becomes increasingly probably that both muons will stay within one hexant, thus the global alignment of hexant-to-IP will be of no consequence. The worst-case assumption (i.e. smallest opening angle) adopted here is thus $\theta_{\mu\mu}$ = 11.25°.

Plugging these assumptions into the above relations will yield: $\sigma_{\mu\mu}$ = 2.5 mr. Since we define $\theta_{\mu\mu}$ to be the difference between measured muon angles, the allowed error in each muon angle will be smaller by a factor of $\sqrt{2}$. Assuming the errors in θ and ϕ to be equal (which may need some qualification...), we obtain $\sigma_\theta = \sigma_\phi$ = 1.8 mr, hence $\Delta\theta = \Delta\phi = \pm 1.2$ mr.

Once more, we can apply geometrical projections to estimate equivalent errors induced in the global axes, employing the assumptions (i.e. referencing to the inner layer) & relations explained in the previous section. This yields ($\Delta x_G = \pm 4.7$ mm, $\Delta z_G = \pm 4.7$ mm) @ $\theta = 90°$, ($\Delta x_G = \pm 9.4$ mm, $\Delta y_G = \pm 1.1$ cm, $\Delta z_G = \pm 1.9$ cm) @ $\theta = 30°$, ($\Delta x_G = \pm 7.2$ mm, $\Delta y_G = \pm 8.4$ mm, $\Delta z_G = \pm 4.8$ cm) @ $\theta = 10°$.

Again, the assumptions implicit in this analysis are somewhat rudimentary, and could stand refining.

5) Pattern Recognition

a) Muon Tracking Constraints

No analysis of pattern recognition requirements has been attempted here for tracking in the muon system. Because of the low rate in the barrel, one would assume that pattern ambiguities would be fairly minimal, excepting difficulties from punch-through hadrons, secondary particles exiting the calorimeter together with a muon, and random neutron background. At small θ, the rate is considerably higher, thus pattern matching considerations may begin to impact the alignment needs. A positioning accuracy of Δx, Δy, Δz on the order of ± 1 mm has been discussed in this context, but no supporting analysis has been presented, thus more work is necessary at this point.

b) Track Linking with Central Detector

A neat solution to measuring a precise muon angle is to find the muon track in the central tracker, where it is determined very exactly. In order to accomplish this, one must match a track in the central region (complete with its associated clutter) to a companion seen in the muon detector. One can thus define a fiducial angle around a muon track that determines a cone, within which a match is searched for in the inner tracker. The angle subtended by this cone would provide another driver to the muon alignment accuracy. At this point, no such analysis exists; the best one can ask for, however, is to have the muon system aligned to the limit expected from multiple scattering in the calorimeter, which was discussed in Sec. 2b.

6) Other Effects

a) Line-of-sight deviation from the IP

The alignment accuracies that are quoted can (in some sense) be a function of the type of alignment system that is actually adopted. The baselined GEM alignment scheme (Figs. 5,6) assumes L3-type straightness monitors[2] to measure the bend-plane misalignment between muon superlayers. If these straightness monitor lines-of-sight (LOS) are all projectively oriented toward the IP, "torque error" (in which one LOS is inclined about the z-axis relative to the other LOS) will not affect muon sagitta. This concept is illustrated in Fig. 9, and may be understood intuitively. Assume that a straightness monitor pointing to the IP claims that the chambers are perfectly aligned, although this line is rotated by an angle α about the z-axis. A straight, infinite-momentum muon track originating from the IP at the angle of the LOS will therefore also be fit by the superlayers as a straight line (thus no momentum error is introduced), although it will be seen to be rotated by $-\alpha$ about the z-axis. If the LOS is not pointing toward the IP, a sagitta error can result.

A quantitative analysis, based on an earlier L* derivation, has been performed to ascertain the requirements on pointing the straightness monitor axes at the IP. The situation is illustrated in Fig. 9. Two straightness monitors are considered, one with a vertical LOS pointing at the IP, and another inclined at β_0 to the vertical (the y-intercept of the LOS is assumed to miss the IP (which is defined as the origin) by Δy). The muon from the IP is inclined at β_μ. First the bending (x) coordinates of the superlayer hits are

calculated for the muon, with the chambers rotated about the y-axis in accordance with the torque angle α between the LOS vectors. The bending coordinate of the inner superlayer (x_A) is defined to be zero. We thus state:

$$x_A \equiv 0 \qquad x_B = L_B \sin\alpha\,(z_B/z'_B) \qquad x_C = L_C \sin\alpha\,(z_C/z'_C)$$

$$L_B = y_B - y_A \qquad L_C = y_C - y_A$$

$$z_B = y_B \tan\beta_\mu \qquad z_C = y_C \tan\beta_\mu \qquad z'_B = (y_B + \Delta y)\tan\beta_0$$

$$x_B = \frac{y_B \tan\beta_\mu}{(y_B + \Delta y)\tan\beta_0} L_B \sin\alpha \qquad x_C = \frac{y_C \tan\beta_\mu}{(y_C + \Delta y)\tan\beta_0} L_C \sin\alpha$$

We can then define the sagitta as the offset from a straight line between bottom and top layers, and substitute in the above expressions for x_B & x_C to find the sagitta error.

$$s = x_B - (x_C - x_A)\, L_B/L_C$$

$$s = L_B \frac{\tan\beta_\mu \sin\alpha}{\tan\beta_0}\left(\frac{y_B}{y_B + \Delta y} - \frac{y_C}{y_C + \Delta y}\right)$$

As can be plainly noted in the above expression, $s \rightarrow 0$ as $\Delta y \rightarrow 0$, and the error is largest at high β. Since, in general, $\Delta y << y_C$, y_B, we approximate:

$$s = L_B \frac{\tan\beta_\mu \sin\alpha}{\tan\beta_0} \Delta y \left(\frac{1}{y_B} - \frac{1}{y_C}\right)$$

Assuming a maximum β_μ; then (from Fig. 9) $\beta_\mu \approx \beta_0$. Plugging in barrel parameters ($y_B = 6.3$ m, $y_C = 8.7$ m, $L_B = 2.4$ m), we then obtain:

$$s(\text{mm}) \approx 0.1\, \Delta y \sin\alpha$$

For small Δy, we can readily substitute a misalignment angle (between the LOS at β_0 and a line from the outer layer to the IP [distance R]); $\Delta y \approx R\, \Delta\theta/\sin\beta_0$. This yields:

$$s(\text{rad}) \approx 0.1 \sin\alpha\, R(\text{mm})\, \Delta\beta/\sin\beta_0$$

The above relation can be used to balance torque errors against LOS misalignment errors; i.e. it shows that if 3 mr of torque rotation is present, a LOS misalignment of 3 mr to the IP will generate a worst-case sagitta error of 18 μm (at $\theta = 30°$). Endcap parameters should be similar.

Finally, this analysis can be generalized to account for the misalignment between two projective lines-of-sight and the IP, as shown in Fig. 10. The leftmost LOS makes an angle with the vertical (at the IP) of β_1 and misses the IP with a y-intercept of Δy_1. The rightmost LOS makes an angle with the vertical (at the IP) of β_2 and misses the IP with a y-intercept of Δy_2. Following the steps outlined previously, it becomes simple to produce the following complicated expression:

$$s = L_B \sin\alpha \left(\frac{\tan\beta_\mu\, y_B - \tan\beta_1 (y_B + \Delta y_1)}{\tan\beta_2 (y_B + \Delta y_2) - \tan\beta_1 (y_B + \Delta y_1)} - \frac{\tan\beta_\mu\, y_C - \tan\beta_1 (y_C + \Delta y_1)}{\tan\beta_2 (y_C + \Delta y_2) - \tan\beta_1 (y_C + \Delta y_1)} \right)$$

One can simplify this for the case of small Δy, and hopefully result in a more compact expression, but I'll leave this as an exercise for the reader.

One way to look at global alignment of the muon system to the IP is to consider all of the global quantities quoted in this report to be relative to the straightness LOS. The entire global alignment problem then becomes the need to point the straightness monitors at the IP.

7) Summary

Tables 1 - 4 show a summary of the tolerances calculated in this report. Tables 1 & 3 show the requirements for the structure. The width of the smear processes (scattering in the calorimeter and the interaction diamond length) have been divided by a factor 4 (such that the alignment accuracy would be negligible in a quadrature sum). The multiple scattering is taken at 50 GeV, which will probably represent the maximum desired trigger threshold. Table 1 & 2 show values at each θ extreme covered by the detector component, separated by a "|" character (30°| 90° for the barrel; 10°| 30° for the endcap). Tables 3 & 4 list the smallest of these values over the barrel or endcap θ range. An undefined tolerance (i.e. a quantity in a column that has no dependence on a coordinate specified in the row) is labeled with "∞", while an undefined smear (i.e. uncertainty projected along the y axis due to a smear along z) is labeled with "x".

The rightmost column of these tables shows the final tolerances for superlayer alignment; again, Tables 1/3 give the allowance to which the structure must be constructed, and Tables 2/4 give the measurements needed for position correction. This column consists of the most exacting requirement, or the largest smear contribution (if this surpasses the smallest requirement), taken across each row. The "Ultimate Detector Resolution" column of Tables 2/4 shows the (unscaled) prediction of the best detector resolution, as taken from Figs. 7 & 8. This column is not used in assigning the "summary" resolution column; it is presented only for comparison.

One can see that much of the structural requirement is driven by the limited dynamic range of the straightness monitors. If this range could be extended by a factor of 2 to 3, the constraints on the structure could be loosened in many cases to 2-6 mm. In all cases, the dependence on the z-coordinate is fairly loose. This is due to the large interaction diamond, coarse detector resolution, and irrelevance to the momentum measurement in this coordinate. Since there is no quoted range on the local $z_{b,c}$ tolerances for the momentum measurement (Table 2), such limits have been taken from the dynamic range of the straightness monitor system (Table 1). Since none of the drivers considered for structural alignment have any bearing on θ or ϕ, no tolerance is given for them in the summary of Table 1. In reality, some limits are necessary, particularly on θ, which has considerable effect on detector rate (at small angle) and bending/B_field projection.

In some cases (i.e. global alignment of the endcaps), the required structural alignment is more precise than the need arising from precision measurement. This is driven by the trigger assumptions, which prefer a projective geometry (as the trigger requirements are derived in a very approximate fashion here, these quantities should be investigated further). The 200 μm enhanced-resolution requirement for x_G alignment is presented as a goal in these tables, and has not been propagated into the "Summary" column.

8) References

1) Rosenson, L. (MIT), data generated winter/spring (1992).

2) Duinker, P., et. al., "Some Methods for Testing and Optimizing Proportional Wire Chambers", NIM A273 (1988), pg. 814-819.

	Intrinsic Smears (+4)		Structural Accuracy		
All ±mm and ±mr	Interaction Diamond (7 cm)	Scattering in Calorimeter (50 GeV)	Dynamic Range of Local Alignment	Trigger Roads (10% Loss)	*Summary*
90° / 30°	+4	+4			
Barrel					
Δx(b)			1 | 1	2 | 2	1 | 1
Δx(c)			1 | 1	3.25 | 3.25	1 | 1
Δz(b)			1 | 1	3.25 | 3.25	1 | 1
Δz(c)			2 | 2	4.5 | 4.5	2 | 2
Δy(b)			1 | 0.9	∞ | 1.9	1 | 0.9
Δy(c)			1 | 1	∞ | 2.6	1 | 1
ΔX(g)		2 | 2		6.3 | 6.3	6.3 | 6.3
ΔY(g)	x | 6.8	2 | 2		15 | 2.5	15 | 6.8
ΔZ(g)	12 | 12	x | 4		4.5 | 4.5	12 | 12
Δθ	x | 0.35	0.5 | 0.5			
Δφ		0.5 | 0.5			
30° / 10°					
Endcap					
Δx(b)			1 | 1	2 | 2	1 | 1
Δx(c)			2 | 2	3.25 | 3.25	2 | 2
Δy(b)			1 | 1	1.75 | 1.75	1 | 1
Δy(c)			2 | 2	3.5 | 3.5	2 | 2
Δz(b)			1.7 | 5.7	3 | 10	1.7 | 5.7
Δz(c)			3.4 | 10.4	6 | 20	3.4 | 10.4
ΔX(g)		3.3 | 3.3		5.6 | 5.6	5.6 | 5.6
ΔY(g)	6.8 | 2.1	3.8 | 3.3		4.8 | 4.8	6.8 | 4.8
ΔZ(g)	12 | 12	1.8 | 6.3		4.1 | 14	12 | 12
Δθ	0.35 | 0.13	0.5 | 0.5			
Δφ		0.5 | 0.5			

Table 1: Alignment factors impacting structural accuracy

			Precision Requirements			
All ±mm and ±mr	Scattering in Calorimeter (500 GeV)	Ultimate Detector Resolution	Precision Momentum	Momentum Vector	Mass Resolution	*Summary*
90° / 30°	+4					
Barrel						
Δx(b)			0.025 | 0.025			0.025 | 0.025
Δx(c)			0.05 | 0.05			0.05 | 0.05
Δz(b)						(1 | 1)
Δz(c)						(2 | 2)
Δy(b)			0.063 | 0.063			0.063 | 0.063
Δy(c)			0.125 | 0.125			0.125 | 0.125
ΔX(g)	0.2 | 0.2	0.33 0.33	0.2 | 0.2 (Goal!)		4.7 | 9.4	4.7 | 9.4
ΔY(g)	0.2 | 0.2	x | 1.6		∞ | 60	∞ | 11	∞ | 11
ΔZ(g)	x | 0.4	13 | 13		∞ | 100	4.7 | 19	4.7 | 19
Δθ	0.05 | 0.05	2.7 | 0.67		∞ | 6.7	1.2 | 1.2	1.2 | 1.2
Δφ	0.05 | 0.05	0.13 | 0.13			1.2 | 1.2	1.2 | 1.2
30° / 10°						
Endcap						
Δx(b)			0.025 | 0.025			0.025 | 0.025
Δx(c)			0.05 | 0.05			0.05 | 0.05
Δy(b)						(1 | 1)
Δy(c)						(2 | 2)
Δz(b)			0.125 | 0.360			0.125 | 0.360
Δz(c)			0.25 | 0.72			0.25 | 0.72
ΔX(g)	0.33 | 0.33	0.33 | 0.13	0.2 | 0.2 (Goal!)		9.4 | 7.2	9.4 | 7.2
ΔY(g)	0.38 | 0.33	9 | 9		60 | 20	11 | 8.4	11 | 8.4
ΔZ(g)	0.18 | 0.63	15 | 53		100 | 100	19 | 48	19 | 48
Δθ	0.05 | 0.05	2.7 | 2.7		6.7 | 2.9	1.2 | 1.2	1.2 | 1.2
Δφ	0.05 | 0.05	1.3 | 1.3			1.2 | 1.2	1.2 | 1.2

Table 2: Alignment factors impacting Precision Measurements

	Intrinsic Smears (+4)		Structural Accuracy		
All ±mm and ±mr	Interaction Diamond (7 cm)	Scattering in Calorimeter (50 GeV)	Dynamic Range of Local Alignment	Trigger Roads (10% Loss)	*Summary*
	+4	+4			
Barrel					
Δx(b)			1	2	1
Δx(c)			1	3.25	1
Δz(b)			1	3.25	1
Δz(c)			2	4.5	2
Δy(b)			1	1.9	1
Δy(c)			1	2.6	1
ΔX(g)		2		6.3	6.3
ΔY(g)	6.8	2		2.5	6.8
ΔZ(g)	12	4		4.5	12
Δθ	0.35	0.5			
Δφ		0.5			
Endcap					
Δx(b)			1	2	1
Δx(c)			2	3.25	2
Δy(b)			1	1.75	1
Δy(c)			2	3.5	2
Δz(b)			1.7	3	1.7
Δz(c)			3.4	6	3.4
ΔX(g)		3.3		5.6	5.6
ΔY(g)	2.1	3.3		4.1	4.1
ΔZ(g)	12	6.3		4.4	12
Δθ	0.13	0.5			
Δφ		0.5			

Table 3: Most Restrictive Alignment Factors (Structural Accuracy)

			Precision Requirements			
All ±mm and ±mr	Scattering in Calorimeter (500 GeV)	Ultimate Detector Resolution	Precision Momentum	Momentum Vector	Mass Resolution	*Summary*
	÷4					
Barrel						
Δx(b)			0.025			0.025
Δx(c)			0.05			0.05
Δz(b)						1
Δz(c)						2
Δy(b)			0.063			0.063
Δy(c)			0.125			0.125
ΔX(g)	0.2	0.33	0.2 (Goal!)		4.7	4.7
ΔY(g)	0.2	1.6		60	11	11
ΔZ(g)	0.4	13		100	4.7	4.7
Δθ	0.05	2.7		6.7	1.2	1.2
Δφ	0.05	0.13			1.2	1.2
Endcap						
Δx(b)			0.025			0.025
Δx(c)			0.05			0.05
Δy(b)						1
Δy(c)						2
Δz(b)			0.125			0.125
Δz(c)			0.25			0.25
ΔX(g)	0.33	0.13	0.2 (Goal!)		7.2	7.2
ΔY(g)	0.33	9		20	8.4	8.4
ΔZ(g)	0.63	15		100	19	19
Δθ	0.05	2.7		2.9	1.2	1.2
Δφ	0.05	1.3			1.2	1.2

Table 4: Most Restrictive Alignment Factors (Precision Measurement)

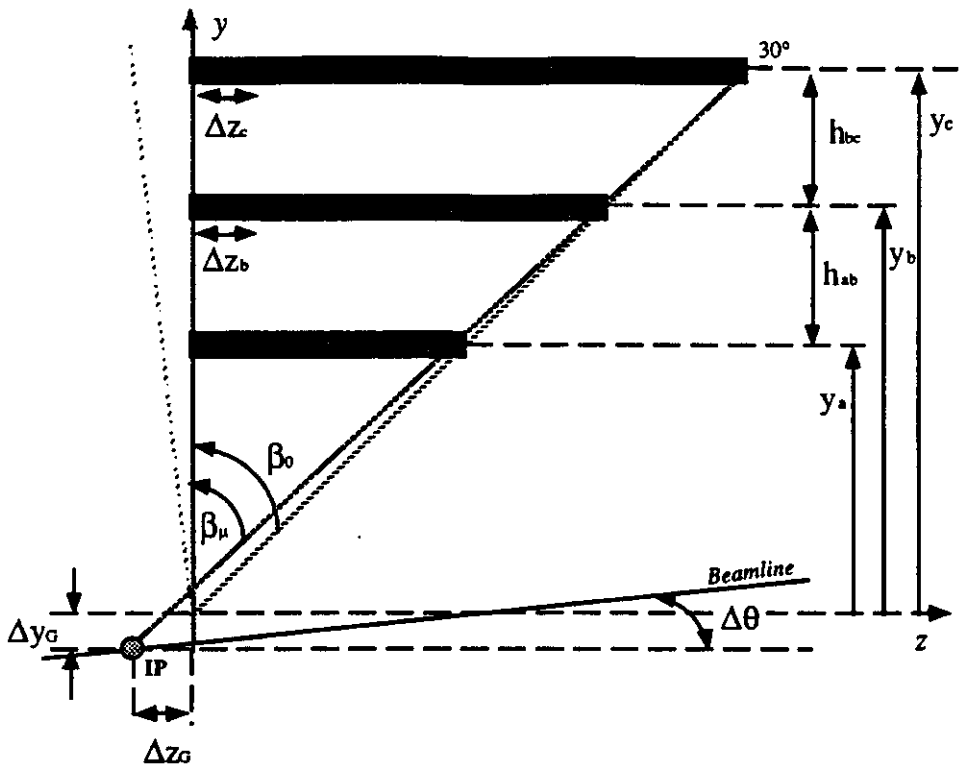

Figure 1: Barrel Requirements Definition; rθ

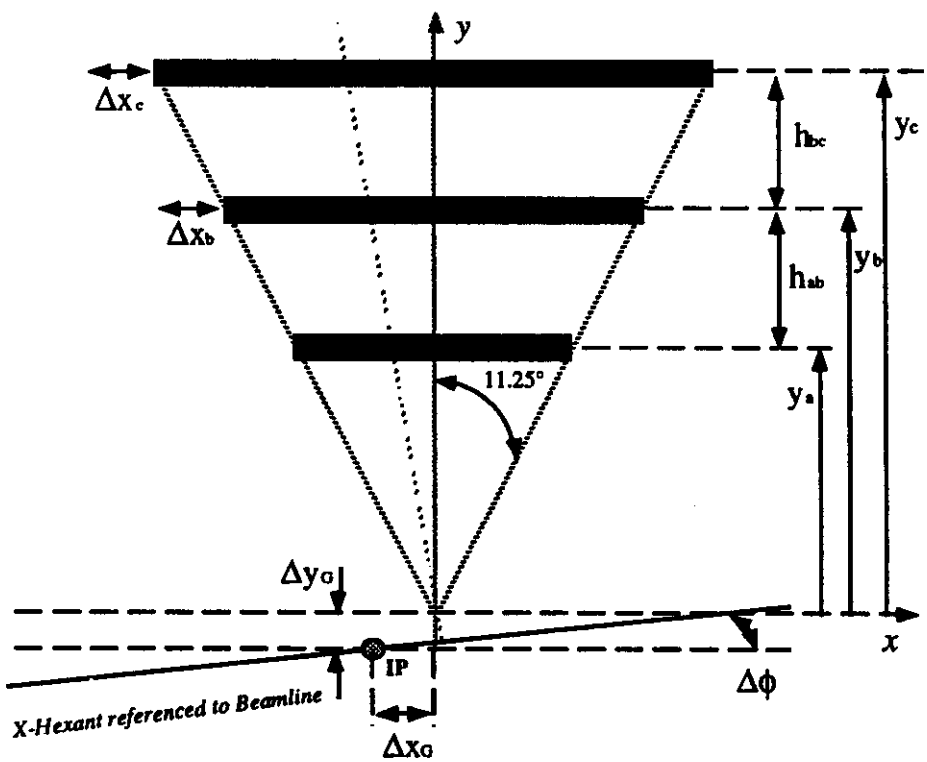

Figure 2: Barrel Requirements Definition; rϕ

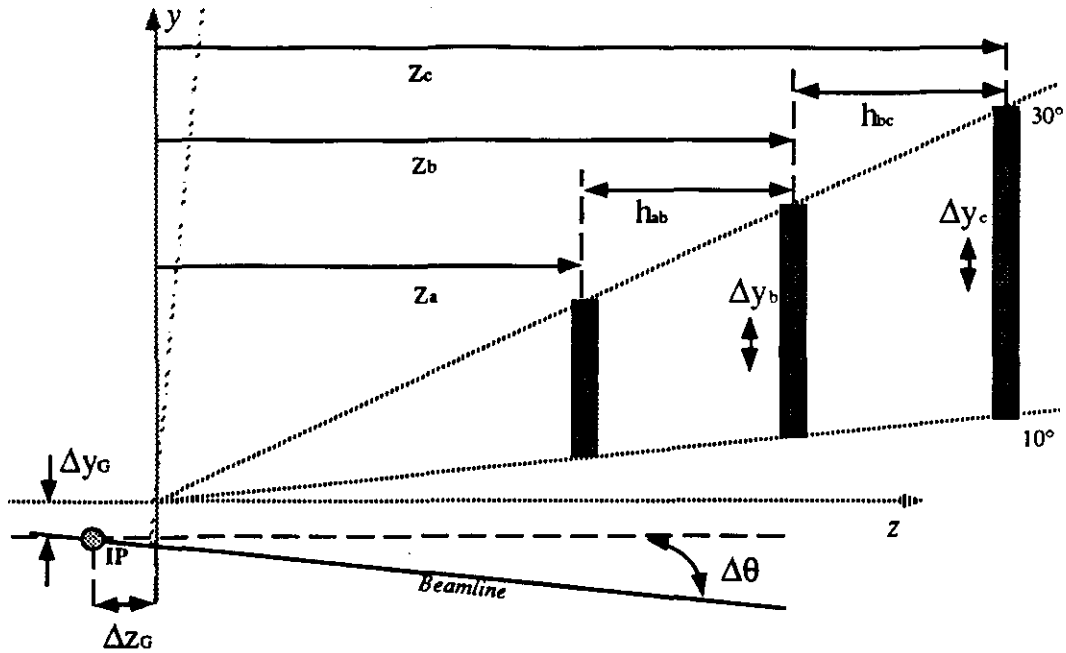

Figure 3: Endcap Requirements Definition; rθ

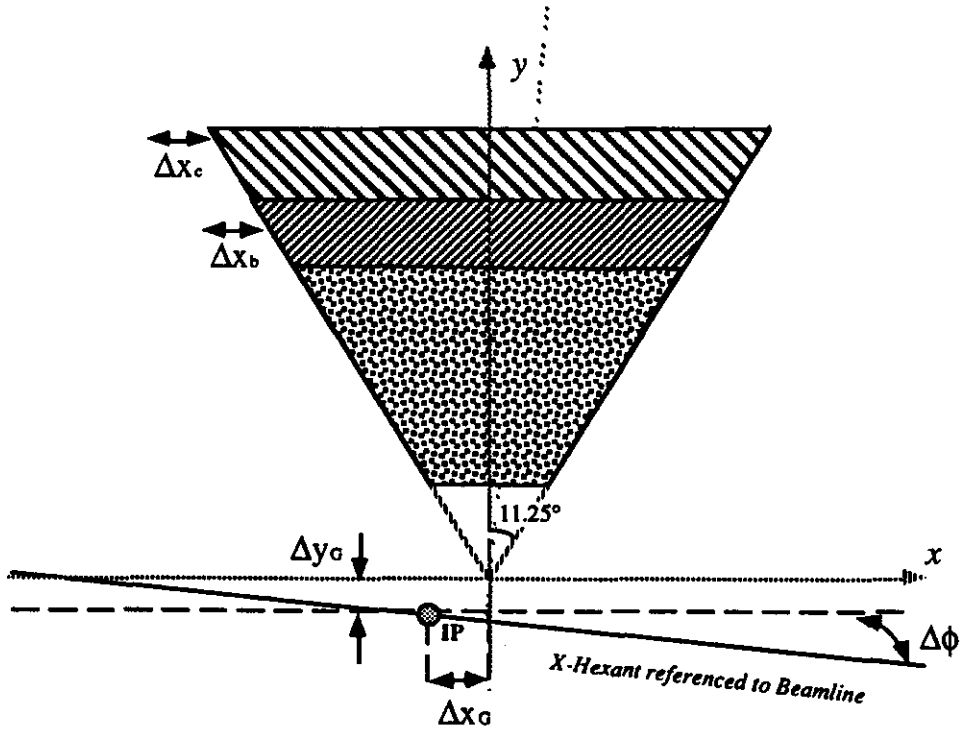

Figure 4: Endcap Requirements Definition; rϕ

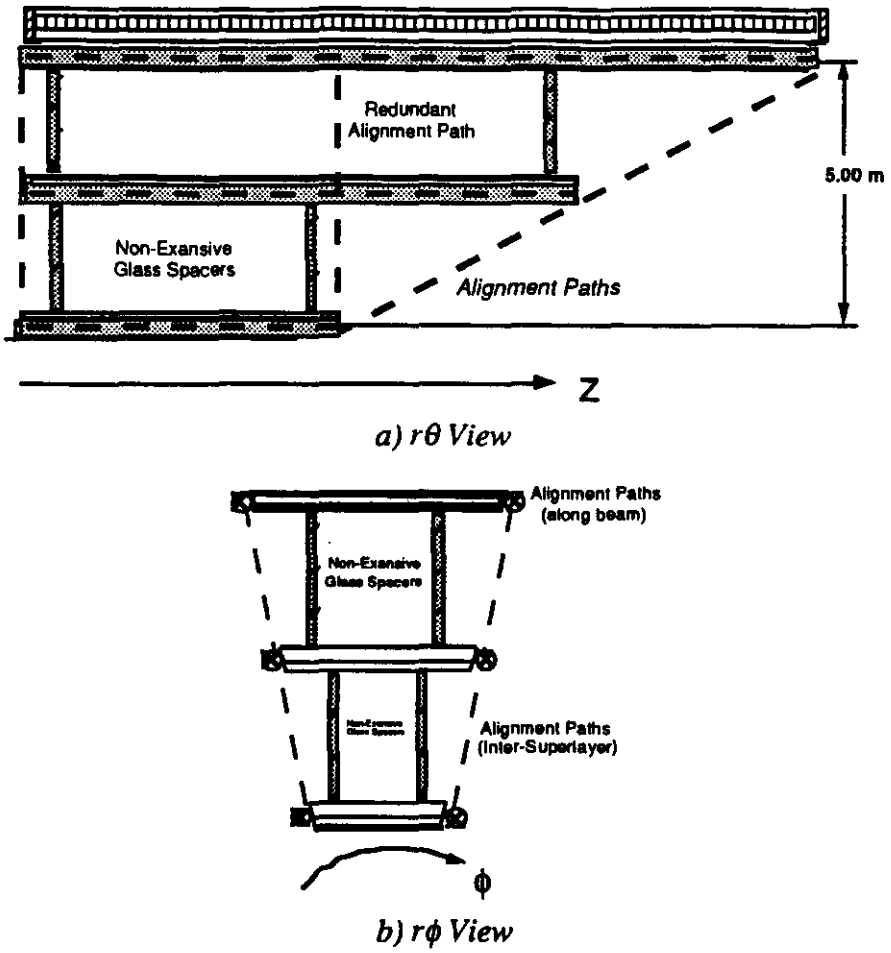

Figure 5: Possible scheme for aligning muon barrel

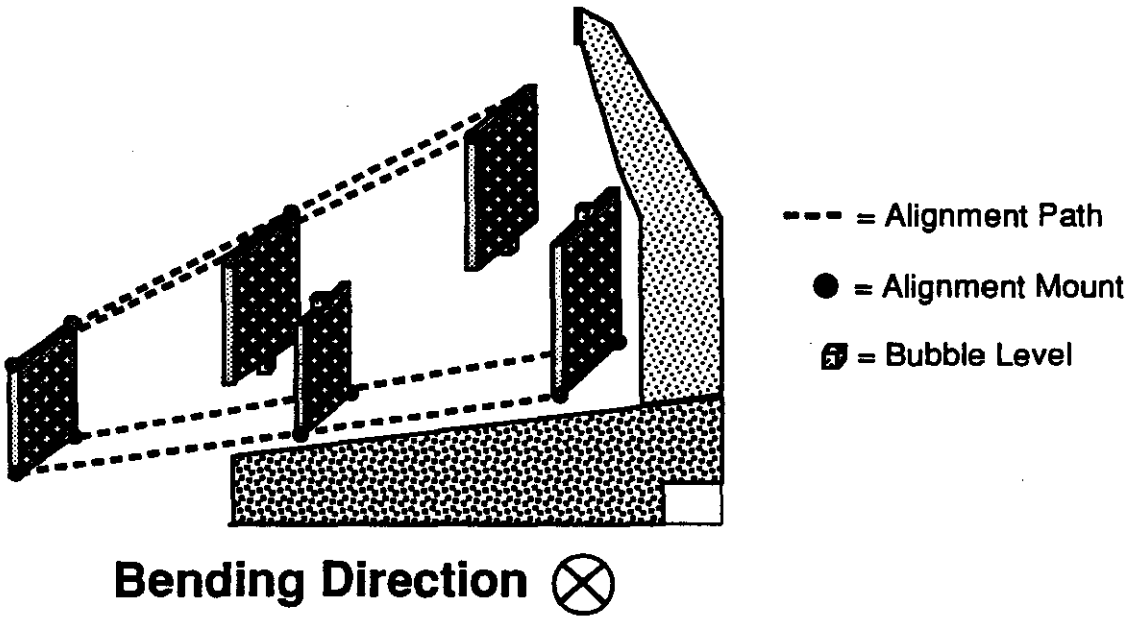

Figure 6: Possible scheme for aligning muon endcap

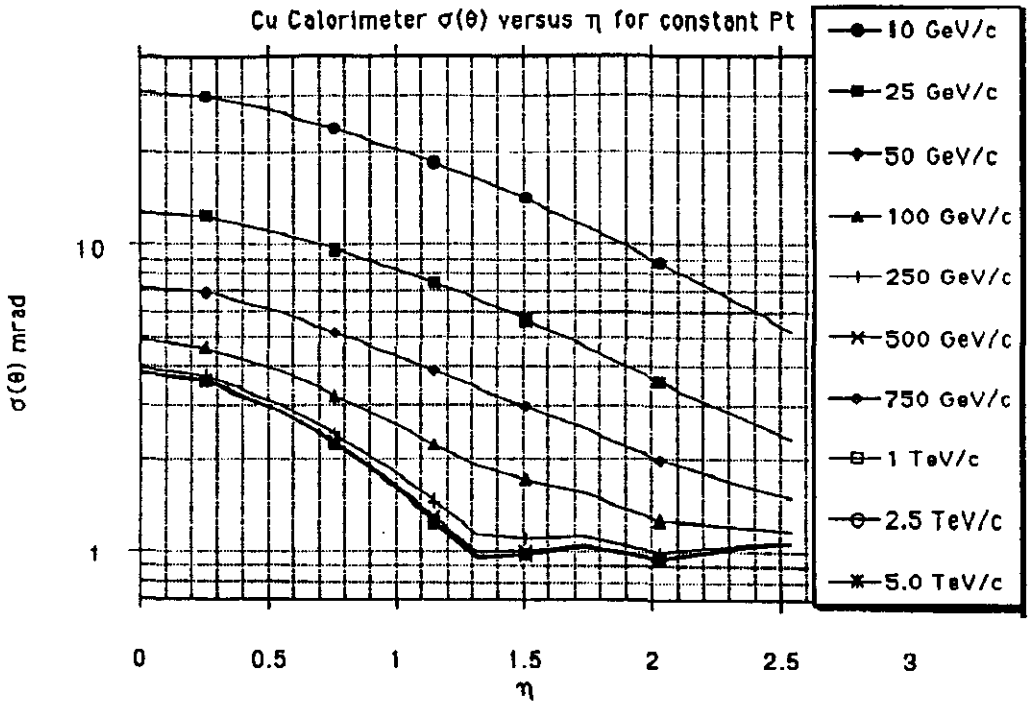

Figure 7a: θ resolution in muon detector

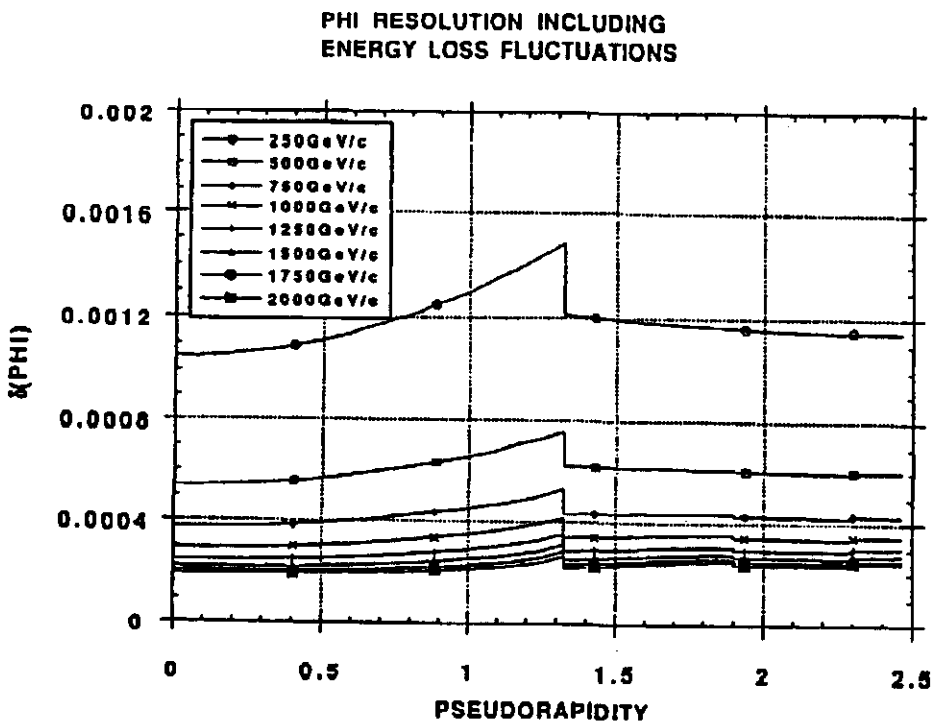

Figure 7b: ϕ resolution in muon detector

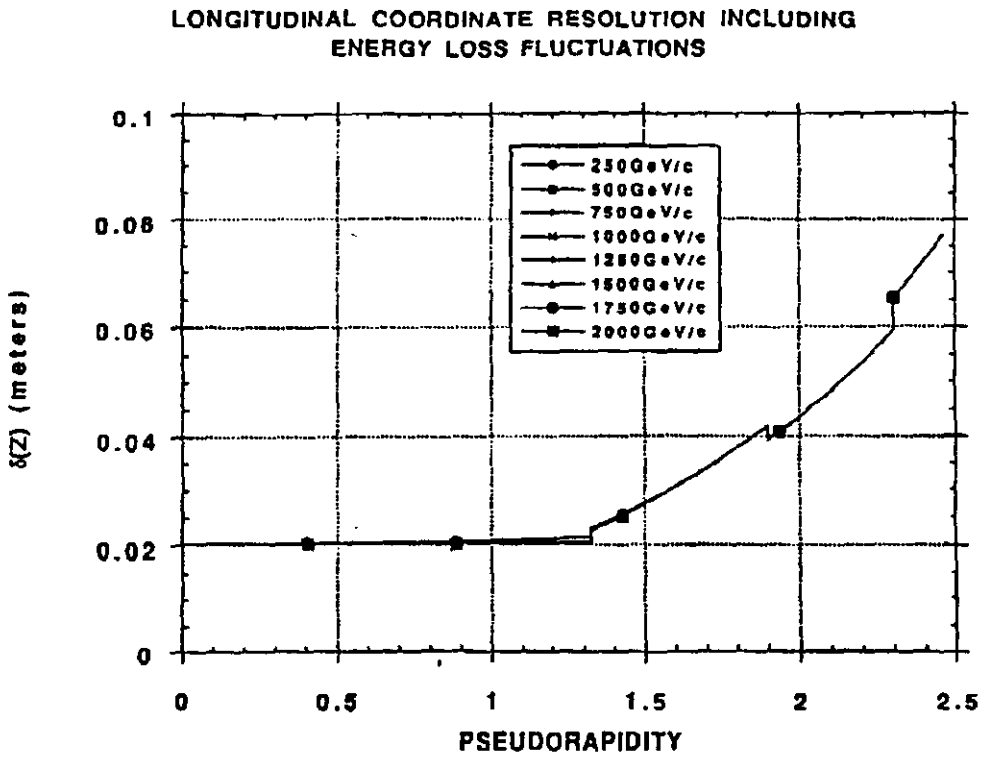

Figure 8a: z resolution in muon detector

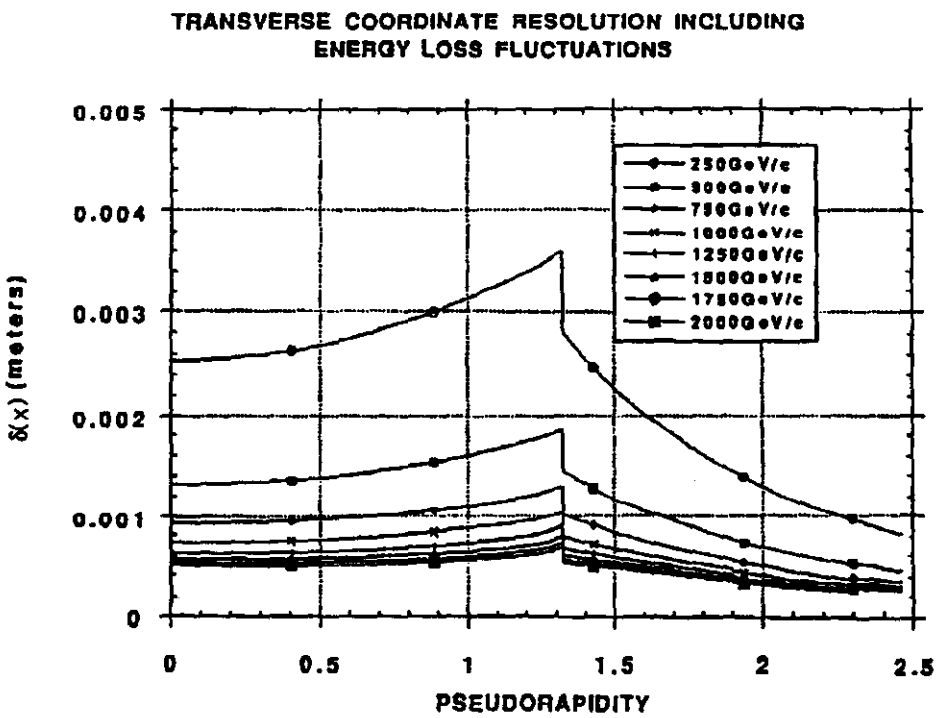

Figure 8b: x resolution in muon detector

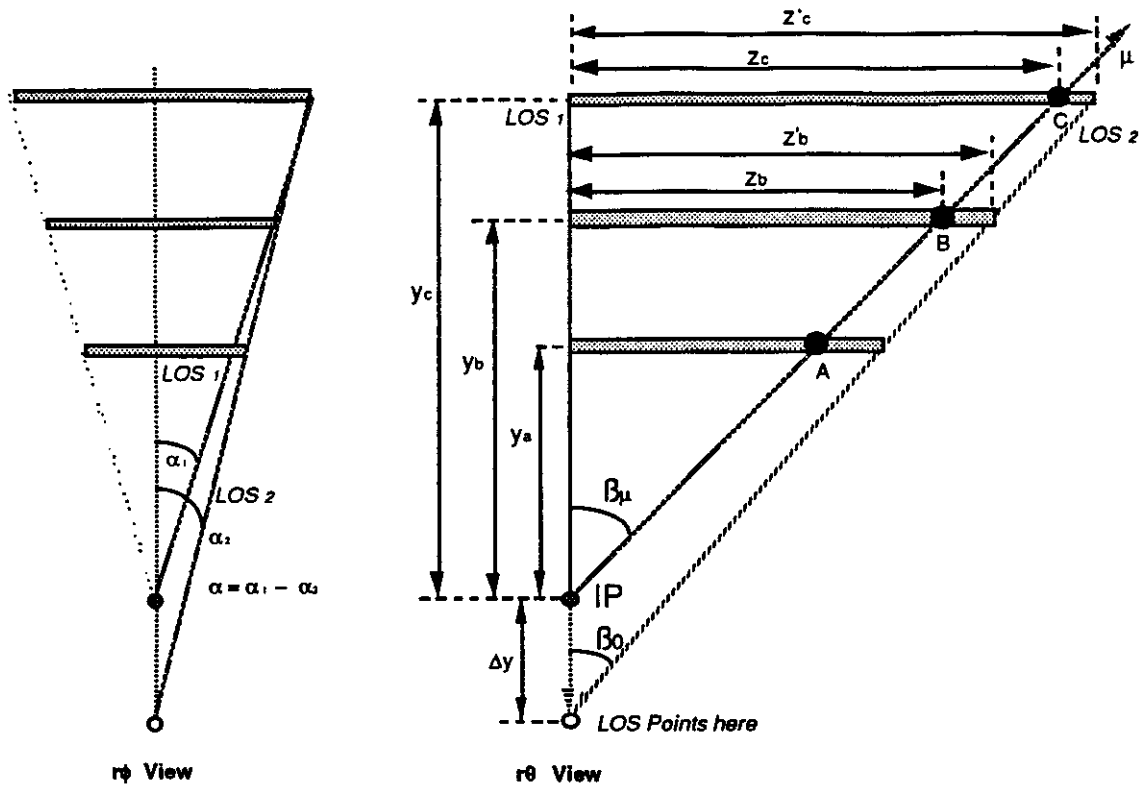

Figure 9: Analysis of sagitta error from superlayer torque

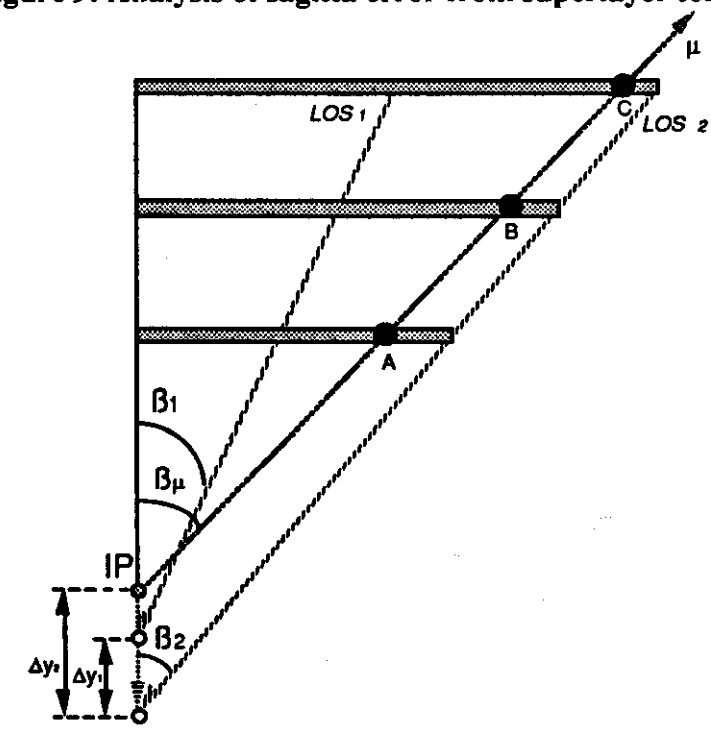

Figure 10: General analysis of sagitta error from superlayer torque

3.3.4 Tracking

3.3.4 Tracking

Question 1: The projected momentum resolution demands very good intrinsic resolution in the silicon and the interpolating pad chambers (IPCs), and places challenging demands on the alignment and stability of the complete system.

The intrinsic resolution of the silicon detectors is expected to be 14 micron for 50 μpitch. For our geometry, that includes two single sided silicon detectors in a sandwich configuration, the net resolution per sandwich configuration (a plane) is 10 microns. Included in this figure is the contributions from 2 position measurements, one from the Rϕ side and one from the z-side, digital averaging and full charge sharing in the silicon detector. The 10 micron resolution is the result of a full calculation of the physics response of the detector.

To achieve the design momentum resolution of the GEM Central Tracker, the IPCs must provide a position measurement good to 2% of the cathode pad width. The measurement technique employed in the IPCs has been in wide use for a number of years, and the conditions which determine the position resolution in a geometric charge division measurement are now well understood. At low anode charge levels, the electronic noise in the readout system is the dominant determining factor in the position resolution obtained. At higher charge levels, irreducible effects such as delta ray production and diffusion limit the position resolution to a value which is generally close to one percent of the anode to cathode spacing, if the cathode pad width is optimized for the chamber geometry. Space charge and aging effects in the IPCs limit the gas gain to values below 5×10^4, implying that electronics noise will be the dominant contribution to position resolution in the IPCs. The position resolution obtained as a function of electronics noise is given by

$$\delta x_c/l_a = \Delta Q/Q_T\sqrt{2+3(x_c/l_a)^2}$$

where l_a is the cathode pad width, x_c is the measured position, and $\Delta Q/Q_T$ is the ratio of the electronics noise to the total cathode signal. The total induced cathode signal expected at the design gas gain is 2×10^5 electrons. Our front end electronics is being designed with a maximum noise requirement of 1000 electrons RMS, leading to a position resolution from electronics noise of better than 50 microns. The front end preamp and shaper, which represents the dominant source of electronics noise in the readout chain, has been prototyped and tested, and meets these design requirements for an input capacitance typical of the baseline IPC design, and a 25 ns shaper peaking time. In the near future, these amplifier prototypes will be used on IPC prototypes now under test. These IPCs prototypes have been constructed and tested by members of the GEM Central Tracker group using front end electronics similar to the custom ICs being developed for the GEM IPCs, but with peaking times of approximately 100 ns. The position resolution achieved using these prototypes under exposure to x-rays is better than 50 microns, as shown in Figure 1. The position resolution is dominated in these tests by the range of the 5 KeV photoelectron generated the gas by the x-ray, not electronics noise. Scaling the

electronics noise observed in the 100 ns peaking time electronics to a 25 ns system leads to a expected position resolution from electronics noise of slightly better than 50 microns.

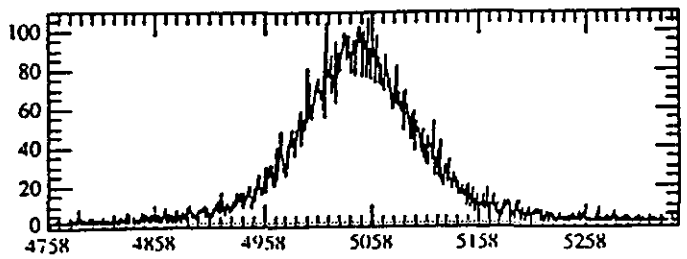

Fig. 1
IPC Position Resolution (Microns)

The Central Tracking specifications for and IPC internal Alignment Stability are:

	Phi	R	Z	(microns)
Silicon Wafers	5	80	250	
IPC	25	250	250	

For both detectors the Phi stability specification is the tightest. Sources of instability that will be minimized include: thermally induced strains, and thermal shifts, material property changes due to radiation exposure, creep, or moisture, and dimensional changes due to externally induced strain or vibration sources. It is practical to minimize these effects but impossible to eliminate them. Since the potential to exceed the stability specifications exists, it is important to plan into the design the ability to detect the instabilities and deal with them.

Design features of the Silicon Tracker include the application of state of the art high stability performance materials to meet the mechanical stability and an evaporative cooling system to provide isothermalization of the entire detector. Composite materials with selected properties will minimize mismatches in coefficients of thermal expansion and be insensitive to moisture effects. The closed loop thermo-siphon evaporative cooling system will minimize the coolant flow rate and induced vibrations, and provide a uniform thermal equilibrium and with a minimum system mass. The IPC mechanical support system will also include the application of advanced composites and stable strain relief mounting. Environmental isolation is also provided with an enclosed containment and gas control. Unlike the Silicon Ladders, the IPC electronics and cooling system are thermo-mechanically isolated off of the Cathode Pad surface for increased stability.

The Alignment plan for Silicon Tracker is developed around defining placement, measurement and stability. In order to minimize the cost of assembly, the Silicon Ladders will be assembled and installed into the subassemblies with modest precision, then precisely optically inspected. This procedure will put the emphasis into defining the positions of the Silicon Microstrips relative to each other in the subassemblies. Each subassembly will contain a fiber optic motion sensor that will measure the critical relative displacements. By installing the fiber optic sensors on large subassemblies, their relative displacements can be continuously monitored.

Question 2: The total amount of material in the silicon layers and the IPCs (including support frames, electronics, cooling systems and cables) is very substantial and will generate substantial background. It needs to be kept as small as practical to avoid major difficulties, especially in the forward direction. The choice of single-sided silicon detectors doubles the amount of silicon. It is not clear that this choice would substantially increase the radiation hardness.

The choice of whether we use either single sided or double sided silicon wafers must consider the following:

- Radiation resistance
- Radiation lengths
- Capacitance
- Cost

The radiation resistance for single-sided detectors has been studied and found to be reasonably radiation resistant. The fixed target experiment E789 at Fermilab has accumulated over $1x10^{13}$ particles/cm 2 on their silicon wafers without loss of performance. These detectors were tested in the LAMPF beams and found to operate satisfactorily up to $7x10^{13}$ particles/cm2 [Kap]. Studies by the Silicon Tracking Subsystem R&D program have demonstrated that single-sided detectors can be operated up $6x10^{13}$ particles without serious loss in pulse height [Pit]. These studies have shown that type inversion occurs a $\sim 2x10^{13}$ after which an increase in voltage is needed to obtain depletion of the silicon detector. The maximum voltage that can be applied to the detectors before breakdown determines the radiation level that can be tolerated. At a fluence of $6x10^{13}$ the detectors require a depletion voltage of about 150 volts. Se Figure 1. A variety of studies have shown that the neutron fluence limit of single-sided silicon detectors is $>10^{14}$ where again the upper limit depends on the depletion voltage required [Lin]. Studies of the radiation resistance of double-sided detectors have recently been completed by several groups and their conclusions show that double-sided detectors have comparable radiation tolerance as the single-sided detectors [Sai].

The capacitance of the strip of the silicon detectors is an important parameter because the noise level of the anticipated front end bipolar preamplifier scales with the square of the detector capacitance and the power requirements the input preamplifier with a shaping time of 20 ns increase with increasing detector capacitance [Spi]. We want to keep the

signal to noise (S/N) to >12 and the power requirements for each strip as low as possible. In single-sided detectors the major contribution to the total strip capacitance is the interstrip capacitance (80-90%). Typical values for the capacitance for a 50 micron pitch detector is 1.2 pf/cm. There is little data on the stability of the capacitance under irradiation. For double-sided detectors the p side is the same as the p side for the single-sided detectors but the n side has the additional complication of an intermediate p implant between the n strips to provide the necessary isolation between n strips. The undesirable result of the intermediate p strip is an increase in the strip capacitance to larger values of only 30 to 50% increase over the p side capacitance [Yam]. It appears possible to design an amplifier that will satisfy the S/N requirement for the p side with a power budget of 1-3mW per strip. However, this power budget presents serious problems to the cooling system and structural design. The increase in the S\N and power for the n side is a potential drawback and leads one to favor all single-sided detectors.

The radiation length for a 300 micron thick silicon detector is .0032. In the GEM silicon tracker we have 6 layers of detectors so that if we use double-sided detectors the total radiation length budget for silicon alone would be .0192 and if we use a sandwich of two single-sided detectors the radiation length budget would be .0385. We expect the support structure for the two different options to be comparable. The total radiation length budget for the entire Central Tracker has not been fully determined but we expect it to be about .15 excluding the polyethylene shield. We therefore expect the fractional increase of the radiation length to be about 15%, i.e. for .13 to .15 depending on whether a 300 micron double-sided detector is implemented or a sandwich of 2- 300 micron single-sided detectors is implemented. The increase in radiation length will be studied by Monte Carlo but it doesn't appear to be a serious problem.

The cost for the silicon detectors depends on the complexity of the fabrication process and the yields from the 4 inch silicon ingot. We have requested quotations from a number of possible vendors who have indicated verbally that the cost of a single-sided detector would be between 2-5 times less expensive than a double-sided detector due primarily to the increased complexity in the processing for the double-sided detector and consequently a poorer yield. Since the wafer cost for the silicon tracker is a cost leader, any reduction in the wafer cost would be welcome.

Two considerations lead us to prefer single-sided detectors, cost and capacitance. Radiation resistance appears not to be a determining factor and radiation length is a minor problem. If the cost and capacitance issues can be resolved than our preference would be to use the double-sided option. Additional R&D is needed on the double-sided detector. We believe, however, that the single-sided option is viable and a decision could be made in that direction without degrading the performance of the Central tracker.

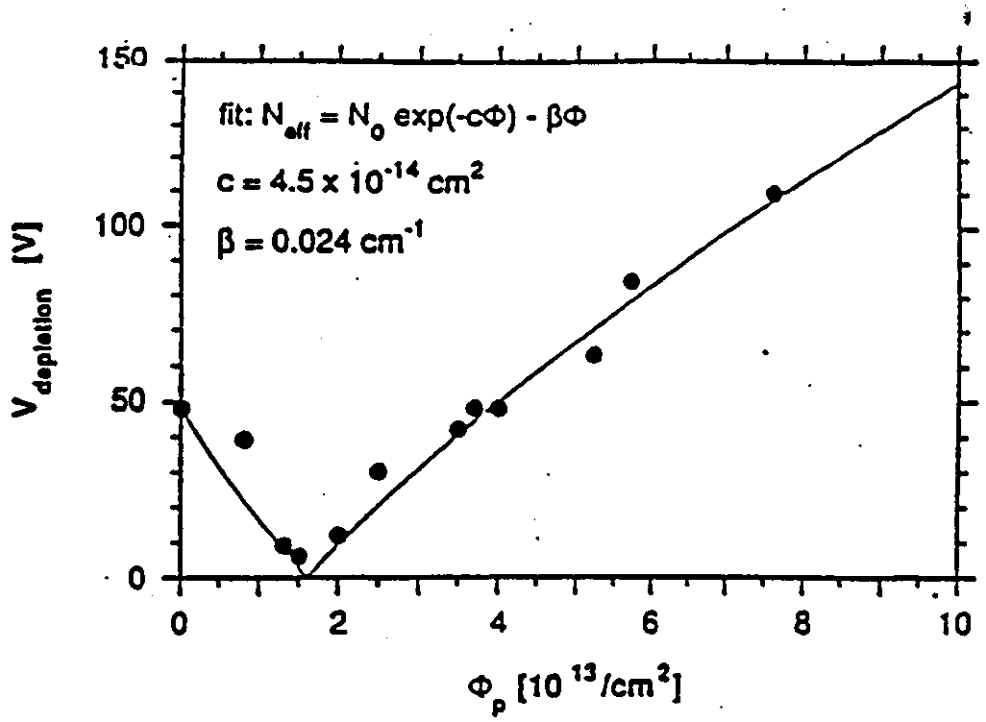

Depletion voltage versus proton fluence for SI detectors. Type inversion occurs at $\Phi = 1.5 \cdot 10^{13}/cm^2$. The line is the best fit according to equations (1) and (2).

1

2(Kap) J. Kapustinsky, private communication, J. Kapustinsky et. al., FERMILAB- Conf-90/214-E (1990).
(Pit) D. Pitzl et. al., UC Santa Cruz preprint SCIPP 91/05.
(Lin) G. Lindstrom, et. al., Radiation Effectsin Si-Detectors and Calorimeter Considerations, FERMILAB Conf 90.
(Sai) K. Saito, et. al., Development and Test of Double Sided Silicon Detectors, Nagoya University preprint; K. Yamamoto, private communication.
(Spi) H. Spieler, private communication.
(Yam) K.Yamamoto, private communication.
(GRO) D. Groom, Radiation Levels in SSC Calorimetry, SSC-229, July 1989.

Question 3: In the forward direction, the placement of a large number of detectors at a radial distance of 10 cm represents a serious risk to their operation. Furthermore, it is not proven that the proposed performance goals can be achieved in this region.

Ten double layers of silicon detectors extend in to a 10cm radius in the forward direction in order to provide tracking coverage out to $\eta \approx 2.5$ and stay within the constraint of the tracking volume. Impact parameter measurements are directly related to this inner radius. The impact parameter measurement does deteriorate as η approaches 2.5, but b-decay requirements are still met. With occupancies well below one percent we are confident that the higher track density at the inner radius will not degrade performance.

The inner silicon detectors will experience the largest radiation exposure and are expected to be the first devises to fail. After operating for several years we expect to deactivate them and this is being designed into the system so that only the inner wafer can be removed while retaining full operation of most of the forward system.

Question 4: The proposed R&D program focuses on the IPCs, their read-out electronics and chamber prototyping, and a demonstration of a position resolution of 1% of the strip width, as well as mechanical engineering of a light support structure of high precision and rigidity. This effort should be fully supported. Due to the similarity of the designs, the silicon detector R&D should be closely coordinated with the parallel effort by the SDC collaboration on mechanics and read-out electronics.

The R&D program presented to the PAC is being pursued by the Tracker Group as described, and we agree with the points raised.

Question 5: Detailed Monte Carlo studies to evaluate the pattern recognition problems in the central and forward tracker, taking into account realistic background effects as well as integration and dead times, have not yet been presented.

The first studies of the GEM Central Tracker pattern recognition have now been completed with the GEANT simulation of GEM and the results are presented in Chapter 7 (of the GEM Central Tracker) Volume V of the GEM Technical Design Report.

Question 6: The tracking group is at present seriously understaffed.

This was true last December. Since then however the group has grown steadily. The tracking group now has 12 institutions and 88 scientists and is still growing. Important additions include the University of Oregon group (J. Brau et. al.) and the Moscow State University group, both of which have extensive expertise with silicon, and the Taiwan group with important connections to Taiwanese electronics industry.

The present tracking group is as follows:

Academia Sinica, Taiwan, R.O.C.
A. Antos, Y.C. Chen, T. L. Chu, M. Huang, S. C. Lee, A. Sumarokov, P.K. Teng, M.J. Wang, P. Yeh

Brookhaven
P.O.'Connor, V. Radeka, G. Smith, B. Yu

Indiana University
B. Bower, M. Gebhard, R. Heinz, S. Mufson, J. Musser, J. Pitts

Los Alamos
R. Barber, J.G. Boissevain, M. Brooks, D. Brown, M. Cafferty, B. Cooke, K. Fuller, S.F. Hahn, C. Johnson, J. Kapustinsky, W.W. Kinnison, D.M. Lee, G.B. Mills, D. Neeper, R. Prael, G.H. Sanders, W.E. Sondheim, T. Thompson, J. VanAnne, L. Waters, B. Weinstein

Moscow State University
G. Bashindzhagyan, Y. Fisyak, D. Karmanov, E. Kuznetsov, A. Larichev, M. Merkin, A. Savin, A. Voronin, V. Zhukov

Nanjing University
E. Chen, D. Gao, M. Qi, D.X. Xie, N.G. Yao, Z.W. Zhang

Rutgers University
F. Jacques, M. Kalelkar, R.J. Plano, P. Stamer, G.B. Word

SSCL
K. Morgan, I. Sheer, J. Thomas

University of Albany
H. Alam, I.J. Kim, B. Neman, J. O'Neill, H. Severini, C.R. Sun, . Zhichao

University of Michigan
D. Kouba, D. Levin, S. McKee, G. Tarle

University of Oregon
A. Arodzero, J. Brau, R. Frey, K. Furuno, D. Strom

Yale University
C. Baltay, R. Ben-David, D. Dong, W. Emmet, S. Manly, S. Sen, Y. Sinnot, J. Turk, E. Wolin

3.3.5 DAQ & Trigger

3.3.5 DAQ and Trigger

PAC Remark: " . . . the amount of work remaining for a TDR is prodigious. A detailed schedule including functional specification, design and review, prototype development and system testing, and production plans should be developed and compared with projected physicist and engineering manpower."

Answer: In the months since the PAC's December meeting, considerable progress has been made in the areas of front-end electronics. Substantial efforts, led and staffed by experienced engineers and physicists, are underway for the readouts of the silicon vertex detector, the central tracker IPC's, the calorimeter, and the CSC's. Functional specifications and schedules have been developed for each of these systems, and detailed board- and chip-level design efforts are underway. A number of integrated circuit designs have been or will soon be submitted for fabrication. The muon drift-wire and RPC readouts are not yet being pursued as vigorously, but their requirements are very similar to those of existing systems, reducing the need for special development efforts. We recognize, however, that this situation must soon be remedied and we are working to bring this effort up to speed. The attached table shows the staffing of the various efforts. Highest priority has been given to the front-end elements, since these will be mounted in or on the detector and are therefore coupled to the detector installation schedule. Trigger designs are being developed in conjunction with their corresponding front-end readouts.

A GEM electronics systems integration group has been formed at the SSCL. These engineers interact with the mechanical engineers working on systems integration, SSCL facilities engineers, and the electronics engineers working on detector readouts.

A group having its nucleus at the SSCL has recently been formed to work out the design of the high-level DAQ—i.e. data collection, event building, and Level 3 processing.

We have adopted a "matrix management" approach to the electronics work.

In this approach, most of the people involved in developing detector readouts are active members of a detector working group as well the electronics group. This ensures that the designs develop in such a way as to be compatible with both the detector to be instrumented as well as the general trigger/DAQ framework. Although this presents potential organizational problems and results in onerous meeting schedules for some, owing to the generally cooperative spirit and diligence on the part of the affected individuals, these difficulties have been largely avoided.

We are gratified at the rate of progress in assembling a professional electrical engineering team for GEM. We realize, however, that we must continue to build strength in this area both within the U.S. and abroad.

PAC Remark: " The cost estimates appear low, and the review process ought to be compared with SDC estimates. "

Answer: Considerable effort has been expended since last January on refining the GEM electronics cost estimate. A reasonably complete estimate based on a parametric model developed by LeCroy was recently reviewed at the SSCL. In parallel to that effort, work has started on a set of "bottom up" estimates for each subsystem. We anticipate that these efforts will result in generally reduced contingency allocations and, in certain cases, reduced base costs. Comparison with SDC reveals comparable overall electronics costs.

Table of Electrical Engineers & Physicists

Subsystem/Task	EE's	Responsible Physicist
Central Tracker		
Si Microstrip	Sangkoo Hahn (LANL)	Geoff Mills (LANL)
	Brad Cooke (LANL)	
CT Pad Chambers		Jim Musser (IU)
Preamps	Paul O'Connor (BNL)	
Analog Pipes	Chuck Britton (ORNL)	
Calorimeter		John Parsons (Nevis)
Preamps	Sergio Rescia (BNL)	David Lissauer (BNL)
Analog Pipe	Bill Sippach (Nevis)	
	Herb Cunitz (Nevis)	
Digital Pipe		Peter Denes (Princeton)
Trigger		Bill Cleland (Pitt)
Muons		Maged Atiya (BNL)
CSC		V. Polychronakos (BNL)
Preamps U.S.	Paul O'Connor (BNL)	
Preamps C.I.S.	Dvornikov, Malyshev,	Mikhail Baturistsky
	Mamedov (Integral)	(Byelorussian State Univ.)
Arch. U.S.	Bob Wixted (SSCL)	
Arch. C.I.S.	Dimitri Smoline (Dubna)	
Drift Wire	Dick Sumner (LeCroy)	Lou Osborne (MIT)
RPC's		Irwin Pless (MIT)
Muon Trigger		Maged Atiya (BNL)
DAQ	Alex Booth (SSCL)	Michi Botlo (SSCL)
	Mark Bowden (SSCL)	
Integration	N. Lau (LLNL/SSCL)	Dan Marlow (Princeton)
	Ken Freeman (SSCL)	
Preamps	Veljko Radeka (BNL)	
Management		Dan Marlow (Princeton)
		Mike Shaevitz (Nevis)